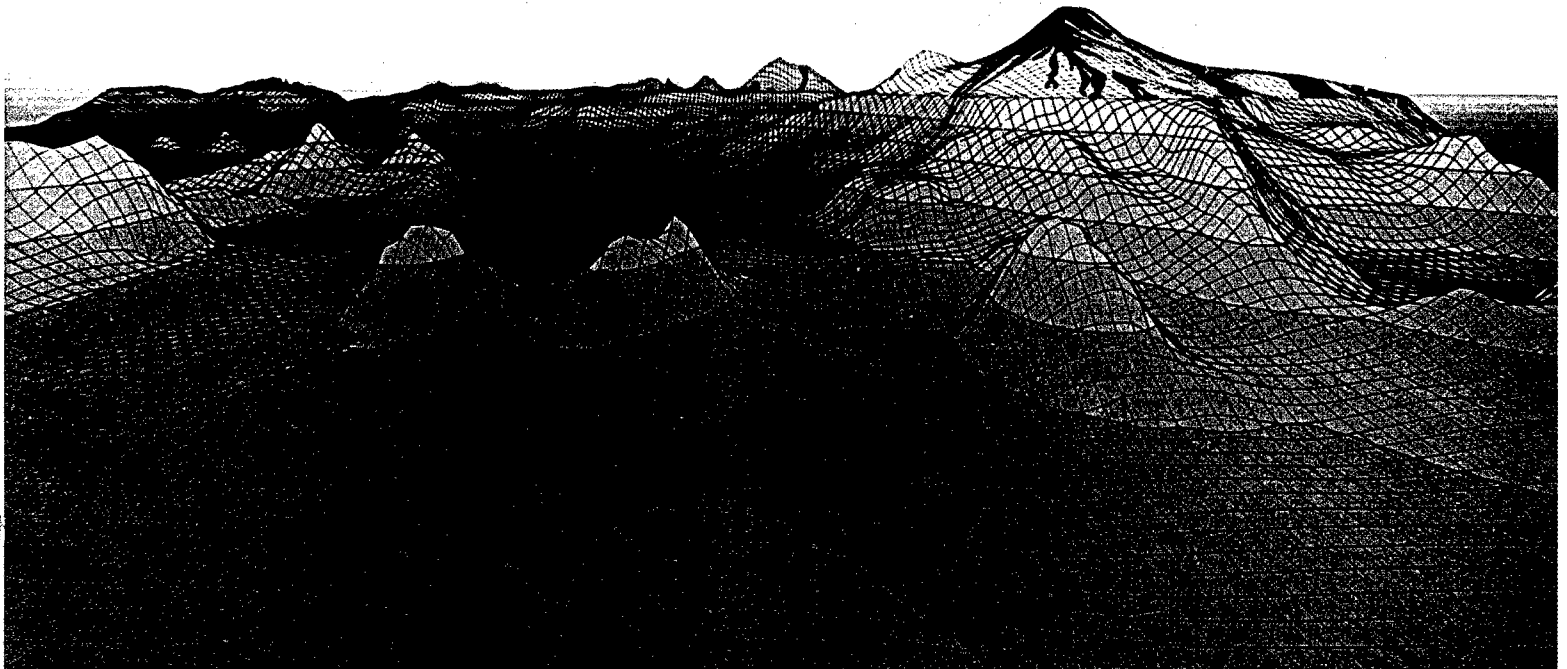


‘Aha Huliko‘a



FROM STIRRING TO MIXING

DISTRIBUTION STATEMENT A
Approved for Public Release
Distribution Unlimited

20021009 042

Proceedings
Hawaiian Winter Workshop
University of Hawaii at Manoa
January 16–19, 2001

‘Aha Huliko‘a

FORUM ON TURBINE ENERGY
TRANSFERS AND TURBULENCE
IN A STRATIFIED OCEAN

IN A STRATIFIED OCEAN

PROCEEDINGS
‘Aha Huliko‘a
Hawaiian Winter Workshop
University of Hawaii at Manoa
January 16–19, 2001

PETER MÜLLER
DIANE HENDERSON
editors

Sponsored by the U.S. Office of Naval Research,
the School of Ocean and Earth Science and Technology,
and the Department of Oceanography, University of Hawaii

(Cover image from Dynamic Graphics)

SOEST Special Publication • 2001

FOREWORD

The twelfth ‘Aha Huliko’^a Hawaiian Winter Workshop, was held from January 16 to 19, 2001 in Honolulu, Hawaii. Its topic was “From stirring to mixing in a stratified ocean.”

Stirring and mixing are the physical processes that convert variance from the eddy to the molecular scale and that may need to be parameterized in ocean models. This scale range is highly complex and contains many physical processes. The workshop focused especially on

- (1) The parameterization of mesoscale eddies
- (2) General approaches to stirring, including the application of ideas from dynamical systems theory
- (3) Inertial instability, submesoscale motions, and vortical motions
- (4) The interplay of isopycnal and diapycnal processes
- (5) Processes in the surface mixed layer
- (6) The stirring and mixing of biologically active tracers
- (7) Mixing efficiency, i.e. the fraction of energy lost from the mean flow that produces a vertical buoyancy flux, and
- (8) Differential mixing of heat and salt.

There is a need not to just understand these processes, but also to parameterize them in a form that can be implemented in ocean circulation models.

The lectures of the workshop are published in these proceedings. The order of the papers loosely follows the agenda of the workshop, covering observations, theoretical analyses, and numerical modeling results. Also included is a summary of the workshop.

The workshop was supported by the Office of Naval Research grant number N00014-00-1-0168. It was hosted by the Department of Oceanography, School of Ocean and Earth Science and Technology, University of Hawaii. The excellent facilities and the capable staff of the Imin Conference Center contributed greatly to the success of the meeting. The local organization and logistical arrangements were expertly handled by Ms. Sharon Sakamoto. This proceedings volume came into existence through the creative and dedicated research of the scientists who gathered in Hawaii and provided the articles that follow.

Peter Müller

Diane Henderson

Department of Oceanography

School of Ocean and Earth Science and Technology

1000 Pope Road

University of Hawaii

Honolulu, Hawaii 96822

^a ‘Aha Huliko’^a is a Hawaiian phrase meaning an assembly that seeks into the depth of a matter.

This work is related to Department of the Navy Grant N00014-98-1-0207 issued by the Office of Naval Research.
The U. S. government has a royalty-free license throughout the world in all copyrightable material herein.



PARTICIPANTS

T. McDougall

E. Chassignet

L. St.Laurent M. Barry C. Garrett

M. Fiadeiro, R. Ferrari, J. McWilliams, D. Luther

G. Carnevale

M. Guiles D. Kirwan, D. Rudnick, T. Paluszakiewicz
L. Seuront

B. Young

D. Marshall

M. Briscoe A. Mahadevan W. Munk Y. Zu A. Natarov

D. Kelley K. Richards, S. Sakamoto B.L. Hua, P. Müller

G. Holloway P. Killworth P. Haynes S. Drijfhout A. Tandon

CONTENTS

<p>Stirring and mixing: What are the rate-controlling processes? <i>Chris Garrett</i></p> <p>Geostrophic eddies, abyssal recirculations, and zonal jets <i>David P. Marshall, Susan T. Adcock, and Claire E. Tansley</i>.....</p> <p>Parameterisation of eddies in coarse resolution models <i>Peter D. Killworth</i></p> <p>Are there principles to guide eddy parameterizations? <i>Greg Holloway</i></p> <p>Representing the effects of mesoscale eddies in coarse-resolution ocean models <i>T. J. McDougall</i></p> <p>Viscosity parameterization and the Gulf Stream separation <i>Eric P. Chassignet and Zulema D. Garrafo</i></p> <p>Characterization of tracer cascade in physical space <i>B.L. Hua, P. Klein, and G. Lapeyre</i>.....</p> <p>Pathways for advective transport <i>A.D. Kirwan, Jr., J. Toner, and B.L. Lipphardt, Jr.</i></p> <p>From stirring to mixing of momentum: cascades from balanced flows to dissipation in the oceanic interior <i>James C. McWilliams, M. Jeroen Molemaker, and Irad Yavneh</i></p> <p>Decay of Agulhas rings due to cross-frontal secondary circulations <i>S.S. Drijfhout</i></p> <p>Vertical shear plus horizontal stretching as a route to mixing <i>Peter H. Haynes</i>.....</p> <p>Spirals on the sea: A manifestation of upper-ocean stirring <i>Walter Munk and Laurence Armi</i></p> <p>On the horizontal variability of the upper ocean <i>Daniel L. Rudnick</i></p> <p>The temperature-salinity relationship of the mixed layer <i>R. Ferrari</i>.....</p> <p>Water mass transformation due to mixed layer entrainment and mesoscale stirring: In series or parallel? <i>A. Tandon</i></p> <p>Biogeochemical variability in the upper ocean <i>A. Mahadevan</i>.....</p> <p>Stirring and mixing of biologically reactive tracers <i>K.J. Richards, S.J. Brentnall, P. McLeod, and A.P. Martin</i></p> <p>Browning bugs and superprocesses <i>W.R. Young</i></p>	<p>1</p> <p>9</p> <p>17</p> <p>29</p> <p>33</p> <p>39</p> <p>45</p> <p>53</p> <p>59</p> <p>67</p> <p>73</p> <p>81</p> <p>87</p> <p>95</p> <p>105</p> <p>113</p> <p>117</p> <p>123</p>
---	---

Describing intermittent processes in the ocean: Univariate and bivariate multiscaling procedures <i>Laurent Seuront</i>	131
Laboratory experiments on diapycnal mixing in stratified fluids <i>M.E. Barry, G.N. Ivey, K.B. Winters, and J. Imberger</i>	145
Simulations of internal-wave breaking and wave-packet propagation in the thermocline <i>G.F. Carnevale, P. Orlandi, M. Briscolini, and R.C. Kloosterziel</i>	153
Mixing and diapycnal advection in the ocean <i>Louis C. St. Laurent, John M. Toole, and Raymond W. Schmitt</i>	175
Differential diffusion in bistable conditions <i>Greg Holloway, Ann Gargett, and Bill Merryfield</i>	187
Six questions about double-diffusive convection <i>Dan E. Kelley</i>	191
Meeting Report: From stirring to mixing in a stratified ocean <i>Peter Müller and Chris Garrett</i>	199

Stirring and mixing: What are the rate-controlling processes?

Chris Garrett

Department of Physics and Astronomy, University of Victoria, Victoria,
British Columbia, Canada

Abstract. The parameterization of unresolved processes in oceanographic models is complicated by the interplay of processes on a wide variety of space and time scales. The lack of spectral gaps further complicates the situation, though perhaps not as seriously as might be feared. Understanding the interaction of different processes, and determining which one is critical, or rate-controlling, may be aided by thinking in terms of a triple decomposition into mean, eddies and turbulence. Particular physical processes reviewed include the fate of energy released in baroclinic instability and the ultimate thermohaline frontolytic mechanism on mean isopycnal surfaces. Both of these issues may have implications for diapycnal mixing rates. Another important question reviewed briefly is that of the efficiency of conversion of turbulent kinetic energy to mean potential energy; we do not know what “external” parameters determine it. The kinematic details of overturning are also discussed in terms of the probability distribution of displacements from a stably stratified buoyancy profile.

1. Introduction

The behavior of the ocean is affected by a variety of processes occurring at space and time scales that are too small to be resolved explicitly in models. The influence of these processes then needs to be parameterized in terms of variables that are explicitly included in the models.

Following a “Reynolds decomposition” of variables into a (slowly changing) mean and fluctuations, we therefore seek a representation of the eddy fluxes $\overline{u'_i C'}$ for a scalar C and $\overline{u'_i u'_j}$ for momentum, where the prime superscript denotes the fluctuation. For the scalar C it is usual to assume that the eddy flux is related by a tensor to the local gradient of the mean \overline{C} , as would be appropriate in a mixing length theory in which the fluctuations are related to particle displacements that are small compared with the distance over which the mean changes significantly. Thus

$$\overline{u'_i C'} = -T_{ij} \partial \overline{C} / \partial x_j. \quad (1)$$

The symmetric part K_{ij} of T_{ij} is diagonalizable and is likely to represent down-gradient diffusion parallel to the principal axes of the tensor. The antisymmetric part S_{ij} of T_{ij} has an associated “skew flux” \mathbf{F}_s given

by

$$F_{si} = -S_{ij} \partial \overline{C} / \partial x_j = (\mathbf{D} \times \nabla \overline{C})_i \quad (2)$$

where $\mathbf{D} = -(S_{23}, S_{31}, S_{12})$. This flux is perpendicular to $\nabla \overline{C}$ and may be written as

$$\mathbf{F}_s = -(\nabla \times \mathbf{D}) \overline{C} + \nabla \times (\mathbf{D} \overline{C}). \quad (3)$$

The second term of this is non-divergent and so does not affect the evolution of \overline{C} . The first term is advective with a velocity \mathbf{U}_s which may be written

$$U_{si} = \partial S_{ij} / \partial x_j. \quad (4)$$

This standard formalism (e.g., *Rhines and Holland* 1977; *Moffatt* 1983; *Middleton and Loder* 1989) is purely kinematic. In practice, however, it seems likely that K_{ij} describes large mixing rates along mean isopycnals and a very much smaller diapycnal mixing rate, whereas \mathbf{U}_s is related to the difference between Lagrangian and Eulerian mean flows. Values for K_{ij} and \mathbf{U}_s appropriate for the oceans in their present state could conceivably be obtained from appropriate and sufficient observations. However, extrapolation of limited measurements and the requirements of models that seek to be predictive for different ocean states require that we obtain formulae for K_{ij} and \mathbf{U}_s in terms of resolved variables. This, in turn, requires that we understand the processes responsible for the fluxes.

Many problems immediately arise. One is the validity of a representation of the fluxes in terms of local mean gradients. There are clearly examples in the ocean in which ocean properties are advected by coherent eddies over larger distances than those over which mean gradients are reasonably constant. This is likely to be even more of a problem for momentum, which may be carried long distances by waves. Such situations call for different forms of parameterization but will not be considered here.

Another fundamental difficulty is associated with the decomposition into mean and fluctuations. This essentially assumes that there is a spectral gap of some sort between the mean and fluctuations, allowing an assumption that the mean changes little over a time or space scale large enough for the determination of statistically accurate eddy fluxes. This important issue will be discussed, albeit naively, in Section 2.

A further basic issue concerns the extent to which different ocean processes are in parallel or in series. If in parallel, which is dominant? If in series, which one controls the eddy flux, leaving the other just to do what it has to? This will be discussed in Section 3, followed by a discussion in Section 4 of the possible insights to be gained from a “triple decomposition” into mean, eddies and turbulence. Section 5 addresses the inter-relationship of isopycnal stirring and diapycnal mixing, and Section 6 speculates on the factors that may determine the “mixing efficiency” with which mechanical energy input, such as that from breaking internal waves, is converted to an increased potential energy of the mean state. Some clues on this may come in the future from careful analysis of overturning motions in the ocean, so some recent ideas and results on this topic are summarized in Section 7.

2. The Spectral Gap

At mid-latitudes, internal waves may overlap in spatial scale with other, quasi-geostrophic, motions, but have different time scales. Thus, in determining the effect of the former on the latter, one could presumably exploit the existence of a spectral gap in the frequency domain. Near the equator the internal wave time scales may be longer and overlap with the time scales of other motions, so that a separation does not appear to be possible in either time or space. Nonetheless, a “dynamical gap” still exists, which is what permits one to talk separately about the two classes of motion, and one assumes that it will still be possible to parameterize the effects of the waves on the other motions.

Motions other than internal waves (and even smaller phenomena such as those associated with double diffusive processes) may, of course, have a continuous spec-

trum, without any spectral gap. This would appear to make parameterization of small scales impossible. The success of Large Eddy Simulations (e.g., *Metais* 1998) has shown, however, that the details of unresolved scales may be unimportant if their only role is to absorb variance that is generated at larger scales and cascades to small scales. This could occur in three-dimensional turbulence, with the only requirement being that the start of the inertial subrange be resolved.

In the ocean, of course, as in the atmosphere, the cascade may be partly to larger, rather than smaller, scales so that the details of the small-scale behavior do affect large scales after a finite time. This is the classic problem of chaotic behavior and lack of predictability. On the other hand, experience in the atmosphere suggests that, while “weather” is unpredictable, “climate” may be predictable (e.g., *Mote and O’Neill* 2000). Maybe we can hope for the same in the ocean.

A naive view might thus be that the lack of a spectral gap is less important than might have been feared. Either separation is possible using a dynamical gap, or unresolved scales do not have a back effect on resolved scales, or the back effect does not affect the climatic state of the ocean. The issue is, however, one that should be kept under review.

3. Are Processes in Parallel or in Series? What is Rate-Controlling?

In three-dimensional turbulence at high Reynolds number, the turbulent scalar flux $\overline{\mathbf{u}C'}$ is in parallel with a much smaller molecular flux $-\kappa\overline{\nabla C}$, with κ the molecular diffusivity. The turbulent flux does depend on the presence of the molecular diffusivity in series; as stressed by *Nakamura* (1996) and *Winters and D’Asaro* (1996), the total flux may be thought of as being purely diffusive, but across a highly convoluted surface of constant concentration. The value of the molecular diffusivity does not determine the value of the turbulent flux; reducing the molecular diffusivity would just lead to an increase in the streakiness, or fine-scale gradients, of the scalar.

Mathematically this can be summarized from the equation for the rate of change of the concentration variance

$$\begin{aligned} \frac{\partial \overline{C'^2}}{\partial t} + \nabla \cdot (\overline{\mathbf{u}'C'^2} + \overline{\mathbf{u}'C'^2} - \kappa\overline{\nabla C'^2}) + 2\overline{\mathbf{u}'C'} \cdot \nabla \overline{C} \\ = -2\kappa\overline{\nabla C'} \cdot \nabla \overline{C}. \end{aligned} \quad (5)$$

This is just the Osborn-Cox formula (*Osborn and Cox* 1972) if C is the temperature. If the time-dependent and divergence terms on the left hand side of (5) are neglected on the grounds of stationarity and spatial ho-

mogeneity, there is a balance between variance production and dissipation. The turbulent eddy flux may remain the same when κ is reduced provided that the mean square gradient of the concentration fluctuations is increased.

One might say that the turbulent and molecular fluxes act in parallel, with the former dominating, but that the processes also act in series, with the turbulent stirring being the rate-controlling process. The molecular diffusion just does what it has to; it is essential but does not control the flux.

One can think of similar situations in the environment. For example, the meridional flux of potential temperature in the atmosphere is controlled by the eddy flux associated with weather systems. The eddy flux relies on the presence of radiative air mass modification in series, but the magnitude of the flux does not depend on the details of this.

On the other hand, the heat flux across the north wall of the Gulf Stream may appear to be just a function of the rate of meander formation and subsequent generation of warm core rings, which then lose their excess heat through air-sea interaction. Many of the rings, however, recirculate and rejoin the Gulf Stream before they have fully decayed (e.g., Olson 1991). Presumably, therefore, the northward heat flux in this case depends, at least partly, on the actual strength of the air-sea interaction which acts in series with the initial eddy flux.

4. Triple Decomposition

When there is some small-scale turbulence acting in series with larger scale eddies, some insight may be obtained from a triple decomposition of the concentration field into mean, eddies and turbulence (Joyce 1977; Davis 1994). It is assumed that there is a spectral gap between the mean and the eddies, and another gap between the eddies and the turbulence. We write $C = C_m + C_e + C_t$, with subscripts m , e and t denoting mean, eddies and turbulence, respectively. For any quantity Q we write \bar{Q} for the average of Q over a time, or space scale, large compared with the scale of the turbulence but short compared with that of the eddies, and $\langle Q \rangle$ for the average of Q over a time or space scale long compared with that of the eddies but short compared with that of the mean state.

Assuming stationarity, so that variances do not change with time, and homogeneity, so that divergence terms may be ignored, it is straightforward to derive

$$\langle \bar{\mathbf{u}_t} \bar{C}_t \rangle \cdot \nabla C_m + \langle \mathbf{u}_e C_e \rangle \cdot \nabla C_m = -\frac{1}{2} \langle \chi \rangle \quad (6)$$

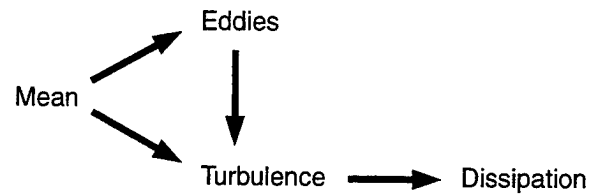


Figure 1. A simple schematic of the path of scalar concentration variance from mean to dissipation via eddies and turbulence.

$$\langle \bar{\mathbf{u}_t} \bar{C}_t \rangle \cdot \nabla C_m + \langle \bar{\mathbf{u}_t} \bar{C}_t \cdot \nabla C_e \rangle = -\frac{1}{2} \langle \chi \rangle \quad (7)$$

$$\langle \mathbf{u}_e C_e \rangle \cdot \nabla C_m - \langle \bar{\mathbf{u}_t} \bar{C}_t \cdot \nabla C_e \rangle = 0 \quad (8)$$

where $\chi = 2\kappa \bar{\nabla C' \cdot \nabla C'}$ is the rate of dissipation of scalar variance, as before.

The first equation here is just the Osborn-Cox equation if one does no separate averaging over the time scales, essentially lumping eddy and turbulent fluctuations together. The second equation, however, shows that the dissipation may be regarded as coming from the production of variance by the turbulence acting on both the mean state and the fluctuations produced by the eddies. The third equation is just the difference of the previous two and shows that variance generated by the eddies acting on the mean state must be passed on to dissipation by the turbulence acting on the eddy fluctuations. The situation is summarized in Figure 1, showing the pathway from production to dissipation via the eddies as well as directly from the turbulence acting on the mean state.

The molecular, turbulent and eddy fluxes are all in parallel in determining the total flux at a fixed point, but it is not necessary for the eddy flux to dominate the turbulent flux in the same way as the turbulent flux dominates the molecular flux in the simple case. Just as considered by Nakamura (1996) and Winters and D'Asaro (1996) for the simple case, one may think of the flux in different ways. At a fixed point, or across the contours of the overall mean scalar, the flux is made up of the molecular, turbulent and eddy fluxes all acting in parallel. Alternatively, the flux is purely molecular across the contours of the instantaneous concentration field. A third way of viewing the problem, however, is with respect to contours of C obtained by averaging over the turbulence but not the eddies. In this case the flux is carried by the turbulence and molecular diffusion in parallel. If the contours defined this way are not very convoluted it implies that the transport across a fixed surface is dominated by the turbulence rather than by the eddies.

There are likely to be variations on this theme, but

it does seem that a triple decomposition may provide insight in some situations, bearing in mind, however, that there may not be convenient spectral gaps between the mean, eddies and turbulence.

5. The Relationship Between Isopycnal Stirring and Diapycnal Mixing?

We tend to think of adiabatic processes associated with mesoscale eddies in the ocean as being independent of small-scale diabatic mixing processes caused by things like breaking internal waves. It is important to consider whether this is true, and, if not, what implications it might have for the parameterization of diapycnal mixing. Two previously studied problems will be briefly reviewed here. The first concerns the ultimate fate of the available potential energy released into eddies in baroclinic instability; the second concerns the final dissipation mechanism for thermohaline fronts that are presumably generated by adiabatic stirring on isopycnal surfaces.

5.1 Does baroclinic instability lead to diapycnal mixing?

A popular parameterization scheme for the relaxation of mean isopycnals by baroclinic instability in the ocean was proposed by *Gent and McWilliams* (1990). It represents the horizontal components of the skew velocity by $(\kappa \nabla_h b / b_z)_z$, where b is the buoyancy field. *Gent et al.* (1995) showed that the effect of this is close to that of having a vertical eddy viscosity $A_v = (f^2/N^2)\kappa$ acting on the mean flow. The appropriateness of this scheme over one invoking the mixing of potential vorticity is discussed elsewhere in this volume. The point to be made here is that, as discussed by *Tandon and Garrett* (1996), one needs to consider the ultimate fate of the mean available potential energy released to the eddies. It seems unlikely that it is dissipated adiabatically by internal friction in the ocean. Some of the eddy damping may occur via air-sea interaction or by viscous damping in the boundary layer at the sea floor, but one also needs to consider the possibility that the energy is lost in the fluid interior and that some fraction of this appears, through diapycnal mixing, as an increase of the basic potential energy.

As discussed by *Tandon and Garrett* (1996), the rate of release from the mean flow is $(f^2/N^2)\kappa|\mathbf{u}_{hz}|^2$ for an equivalent eddy viscosity, as above, acting on the vertical shear \mathbf{u}_{hz} of the mean horizontal flow \mathbf{u}_h . Using the thermal wind equation $|\mathbf{u}_{hz}| = f^{-1}|\nabla_h b|$ this energy loss rate becomes $s^2\kappa N^2$ where $s = |\nabla_h b|/N^2$ is the mean isopycnal slope. If the rate of creation of mean potential energy is at a rate R_f times this, and is ex-

pressed as $K_v N^2$, then the vertical eddy diffusivity is $K_v = R_f s^2 \kappa$ and could be as large as $10^{-3} \text{ m}^2 \text{s}^{-1}$ in places like the Southern Ocean. *Tandon and Garrett* (1996) argue that this could have a significant effect on tracers, though it is unlikely to significantly augment the spin-down of the mean flow already associated directly with the Gent and McWilliams mechanism.

The problem thus seems to warrant continued investigation. Strong internal wave activity and inferred high dissipation have been reported for the Southern Ocean by *Polzin and Firing* (1997). They suggest that the waves originate as lee waves generated by strong flows over a rough sea floor, and that these strong flows include currents associated with the mesoscale eddies. In that case the internal waves would indeed be associated with the decay of the baroclinic eddies, though the mixing in the water column would not be associated with the local current shear. It is worth considering whether there could additionally be some direct local connection between the mesoscale eddy current shear and the excitation of internal waves.

5.2 Are thermohaline fronts dissipated passively or actively?

Compensating lateral gradients of potential temperature and salinity can exist on isopycnal surfaces in the ocean. Purely adiabatic stirring of these gradients will presumably lead to density-compensated thermohaline fronts. Some small-scale mixing mechanisms must occur to prevent the temperature and salinity gradients from increasing without limit.

The gradients could, of course, become sharp enough that molecular diffusion alone removes them. Alternatively, there might be some small-scale lateral mixing mechanism, perhaps involving vortical modes, which would hasten the transfer to molecular scales. Both of these possibilities could be described as "passive" in the sense that the small-scale mixing mechanism was in place already, and just copes with the extra variance produced by the isopycnal stirring.

Another, more likely, passive mechanism was explored by *Haynes and Anglade* (1997) and is reviewed by Haynes in this volume. The fundamental idea is that the vertical shear of the stirring process leads to the development of vertical scalar gradients at the same time as lateral gradients. Sharp gradients develop in the vertical as well as laterally, with diapycnal mixing then acting to smooth them. *Haynes and Anglade* (1997) argue that a lateral frontal width of a few kilometres is a plausible outcome for reasonable values of the vertical shear.

An alternative mechanism for the thermohaline frontolysis was proposed by *Garrett* (1982) and reviewed

by *Garrett* (1989). He suggested that as the front develops, it will be unstable to thermohaline intrusions which would limit the further narrowing of the front, effectively dissipating the lateral variance production by larger-scale stirring. This might be termed an "active" process in that it introduces extra diapycnal mixing that would not have occurred without the lateral stirring. The associated diapycnal eddy diffusivity is inevitably negative for density (as is the case for density for any process driven double-diffusively), but is likely to be positive for salinity and can take either sign for temperature, depending on the circumstances. The process deserves further study if the effective diapycnal diffusivities that one would add to a model for large-scale oceanic behavior reach significant values. If the diffusivities are very small one would argue that the process is interesting scientifically but just does what it has to without having any large-scale impact.

The formula suggested for the effective diapycnal diffusivity of salt is

$$K_s = 10^{-3} D^2 N (g\beta |\nabla_h S| / N^2)^3 \quad (9)$$

where D is the diameter of the mesoscale eddies doing the stirring, β the density coefficient for salinity and $|\nabla_h S|$ is the lateral gradient of the large-scale salinity field (over a scale larger than that of the eddies causing the stirring). The value of K_s is clearly very sensitive to the lateral salinity gradient and only likely to be significant in a few places such as the Mediterranean salt tongue where it is large (*Garrett*, 1989).

The model also predicts the thickness of the intrusions to be about $\frac{1}{2}(g\beta |\nabla_h S| / N^2)D$. This could be compared with data in any systematic examination of CTD profiles. Of course the intrusions would only be found in the narrow frontal regions. The width of these was predicted to be

$$W \simeq 0.08(g\beta |\nabla_h S| / N^2)DN\Omega^{-1} \quad (10)$$

where Ω is the large scale strain rate (say 10^{-6}s^{-1} or less typically).

Presumably this active frontolytic mechanism only occurs if the width from (10) is larger than the width in the passive mechanism proposed by *Haynes and Anglade* (1997). The particular values for W tabulated by *Garrett* (1989) show that this may be the case, though clearly there is considerable uncertainty in both models.

One location for which information is available is the site of the North Atlantic Tracer Release Experiment (*Ledwell et al.* 1993). In this experiment an artificial tracer injected at a depth of about 300 m was teased out into streaks by a strain rate estimated as $3 \times 10^{-7}\text{s}^{-1}$ and reached a width of about 3 km. This width was

found by *Haynes and Anglade* (1997) to be plausible for the mechanism they described, though with considerable uncertainty associated with the lack of information on the vertical shear of eddy currents.

To apply the model considered here, we need to assume that at the same time as the tracer became streaky, the associated lateral convergence would lead to thermohaline frontogenesis. The large-scale isopycnal salinity gradient in this region is approximately 10^{-7}m^{-1} , and $N^2 \simeq 1.8 \times 10^{-5}$ so that $g\beta |\nabla_h S| / N^2 \simeq 4 \times 10^{-5}$. If we take $D \simeq 100$ km, then (10) gives a frontal width of about 5 km. This is also close to the observed width. A point against this interpretation is that no intrusive features were reported, though *Garrett's* (1982) model would predict them to be only 2 m in vertical extent with very small temperature and salinity signatures and so perhaps not readily observable.

It also seems quite likely that in this particular situation neither of the models discussed here constituted the ultimate lateral mixing process, but that the mixing was actually accomplished by small-scale vortical modes. The discussion is perhaps somewhat academic anyway; even if *Garrett's* (1982) mechanism were the ultimate frontolytic process in the NATRE region, the regional average diapycnal mixing rate for salt, using (9), would be less than $10^{-8}\text{m}^2\text{s}^{-1}$ and so utterly negligible. (The smallness of this value is partly associated with the small area occupied by the thermohaline fronts.)

Perhaps the realistic conclusion at this stage is that we do not know in general what the frontolytic mechanism is, that it may vary from place to place, and that in a few situations it may be important to know what it is if it introduces further diapycnal mixing.

6. Mixing Efficiency

An important issue in considering the relationship of stirring to mixing in the diapycnal sense is that of the mixing efficiency: how much of the energy being put into stirring motions is converted to the potential energy of the basic state? The topic is discussed by Barry elsewhere in these proceedings and also by *St. Laurent and Garrett* (2001).

The standard approach is to write

$$K_v = \Gamma\epsilon/N^2, \quad \Gamma = R_f/(1 - R_f), \quad (11)$$

where R_f is the flux Richardson number, representing the fraction of energy put into the stirring motions that produces a diapycnal buoyancy flux rather than being dissipated.

It is customary to choose Γ to be about 0.2, based on comparisons of different methods of measuring the di-

apycnal diffusivity (e.g., *Oakey* 1982), but there seems to be no reason why it should be a universal constant. *Ivey and Imberger* (1991) argue that Γ varies considerably in a two-dimensional space described by two dimensionless parameters. One is the “overtake Froude number” $Fr_T = (L_R/L_C)^{2/3}$, where $L_R = (\epsilon/N^3)^{1/2}$ is the Ozmidov scale and L_C is “the scale of the most energetic overtake”. The other parameter is the “overtake Reynolds number” $Re_T = (L_C/L_K)^{4/3}$, where $L_K = (\nu^3/\epsilon)^{1/4}$ is the Kolmogorov scale.

We note, however, that Fr_T is an “internal” dimensionless parameter, with its value determined by the turbulent mixing itself rather than by the physical processes driving the mixing. It thus does not seem to be a satisfactory descriptor. We might also expect that Γ should be independent of Re_T for large values of the latter or, equivalently, of the turbulent Reynolds number $\epsilon/(\nu N^2) = Fr_T^2 Re_T$ when this is large.

Thus one still seeks “external” dimensionless parameters on which Γ might depend. One wonders whether Γ might be less if the shear is persistent (compared with N^{-1}) at a particular location; then for much of the time the turbulence is mixing water that is already well mixed, hence with less buoyancy flux resulting. This persistence might be associated with the frequency content of the internal wave spectrum (with an enhancement of low frequency energy, such as that at inertial and tidal frequencies) increasing the persistence and reducing Γ . Alternatively, persistence could be a consequence of greater exceedance of some stability criterion: if the Richardson number goes well below 1/4 at its minimum, then its duration below 1/4 is increased over a case in which it just barely goes below 1/4.

Perhaps an apparent dependence of Γ on $\epsilon/(\nu N^2)$ might just be because this parameter is acting as a proxy for some other indicator of mixing strength that does not involve the viscosity ν .

A test in the field could of course come from simultaneous data on ϵ and the temperature microstructure dissipation rate χ if both were available, as in *Oakey* (1982). If only velocity microstructure data and coarser density data were available one could proceed via a comparison of Thorpe and Ozmidov scales. The former, L_T , is the r.m.s. displacement in reordering a density profile to be stable. The latter, L_O , is defined as $(\epsilon/N^3)^{1/2}$. If we write $L_O = \alpha L_T$, then $K_v = \Gamma \epsilon/N^2$ implies that

$$K_v = \Gamma \alpha^2 N L_T^2. \quad (12)$$

With $\Gamma \simeq 0.2$ and $\alpha \simeq 0.79$ (*Dillon* 1982) or 0.66 (*Crawford* 1986) this gives $K_v \simeq 0.1 N L_T^2$. This latter result seems likely to be a consequence of the dynamics of overturning and more likely to be a general result than a fixed proportionality between L_O and L_T . Hence if α

is found to differ from 0.8, one could use (12) to imply $\Gamma \simeq 0.1 \alpha^{-2}$. Interestingly, *Ferron et al.* (1998) found $\alpha \simeq 0.95$ in the energetic abyssal mixing in the Romanche Fracture Zone. As they point out, the error bars on all these values of α are such that they could be consistent with a universal value, but we note that the higher value they find might also imply a lower mixing efficiency.

7. The Probability Distribution of Thorpe Displacements

The existence of statically unstable portions of a water column is clear evidence for vertical stirring and mixing. The nature of this stirring is usually characterized by the single parameter of the Thorpe scale, as discussed above. Recently, however, *Stansfield et al.* (2001) have suggested that more information might be available from the actual probability distribution $P_1(L)$ of the Thorpe displacement L (the particle displacement in the reordering process). The Thorpe scale L_T is simply $(\int_0^\infty L^2 P_1(L) dL)^{1/2}$. Now

$$P_1(L) = \int_0^\infty H P_3(L/H) P_2(H) dH / \int_0^\infty H^2 P_2(H) dH \quad (13)$$

where $P_2(H)$ is the probability distribution of overturns of thickness H (an overturn being a closed set of displacements) and $P_3(L/H)$ is the normalised probability distribution of displacement L .

Stansfield et al. (2001) do not offer any model for $P_2(H)$, but suggest a very simple kinematic model for $P_3(L/H)$, based on the assumption that each particle has an equal probability of going to any other location in the overturn. This is equivalent to the assumption that any rearrangement of the elements that make up an overturn is equally likely. If the overturn is made up of n points, then we may take $L/H = m$ for $0 \leq m \leq n$ and it is easy to show that $P(0) = 1/n$ and otherwise $P(m) = 2(n-m)/n^2$. Then $L_T^2 = H^2/6$ for large n .

There are subtleties associated with this model as it is necessary to exclude the rearrangements that do not constitute a single overturn, but these are not critical if n is larger than about 20 or so. Figure 2 shows $P_3(L/H)$ for winter and summer data from Juan de Fuca Strait. While the error bars are not shown here, there are clearly more small displacements, and fewer medium and large displacements, in the data than in the model. There is little reason to regard the model as anything other than a convenient reference, but it seems possible that examination of $P_3(L/H)$ and also $P_2(H)$ in different settings might reveal different mixing regimes and possibly provide an indicator of different mixing efficiencies.

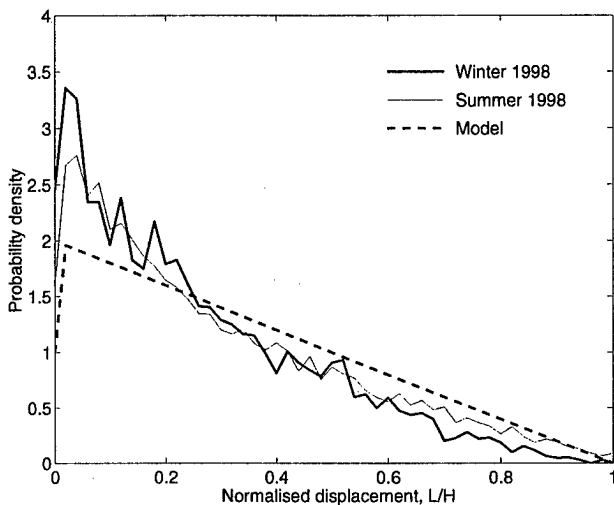


Figure 2. The probability distribution of displacements, normalised by the overturn height, from winter 1998 (thick line) and summer 1998 (thin line) data from Juan de Fuca Strait. The dashed line is the prediction of a simple kinematic model, assuming 50 points in a profile (though this number only affects the value of L/H at which the model prediction rises to from 1 to 2.) From Stansfield et al. (2001).

Conclusions

This short review has attempted to raise some of the issues of stirring and mixing in the ocean, bearing in mind that a primary goal is to derive parameterizations of small-scale processes that have a significant impact on important aspects of the ocean's behavior. An overriding issue is the need for formulae, not just numbers, for any parameterization in a model that aspires to predictive capability. If, in a model of a particular resolution, several sub-grid-scale processes appear to be acting together, it is clearly important to decide which processes are rate-controlling so that theoretical and observational programs can be focused on them.

Acknowledgments. I thank Peter Müller for inviting my participation in this interesting workshop and ONR for its support. Lou St. Laurent provided helpful feedback on a draft of this paper. I thank him and Peter Haynes for discussion.

References

- Crawford, W. R., A comparison of length scales and decay times of turbulence in stably stratified flows. *J. Phys. Oceanogr.*, 16, 1847–1854, 1986.
- Davis, R. E., Diapycnal mixing in the ocean: the Osborn-Cox model. *J. Phys. Oceanogr.*, 24, 2560–2576, 1994.
- Dillon, T. M., Vertical overturns: a comparison of Thorpe and Ozmidov length scales. *J. Geophys. Res.*, 87, 9601–9613, 1982.
- Ferron, B., H. Mercier, K. Speer, A. Gargett, and K. Polzin, Mixing in the Romanche Fracture Zone. *J. Phys. Oceanogr.*, 28, 1929–1945, 1998.
- Garrett, C., On the parameterization of diapycnal fluxes due to double diffusive intrusions. *J. Phys. Oceanogr.*, 12, 952–959, 1982.
- Garrett, C., Are diapycnal fluxes linked to lateral stirring rates? *Proceedings of the Fifth 'Aha Huliko'a Hawaiian Winter Workshop*, 317–327, 1989.
- Gent, P. R. and J. C. McWilliams, Isopycnal mixing in ocean circulation models. *J. Phys. Oceanogr.*, 20, 150–155, 1990.
- Gent, P. R., J. Willebrand, T. J. McDougall, and J. C. McWilliams, Parameterizing eddy-induced tracer transports in ocean circulation models. *J. Phys. Oceanogr.*, 25, 463–474, 1995.
- Haynes, P. and J. Anglade, The vertical-scale cascade in atmospheric tracers due to large-scale differential advection. *J. Atmos. Sci.*, 54, 1121–1136, 1997.
- Ivey, G. N. and J. Imberger, On the nature of turbulence in a stratified fluid. Part 1. The energetics of mixing. *J. Phys. Oceanogr.*, 21, 650–658, 1991.
- Joyce, T. M., A note on the lateral mixing of water masses. *J. Phys. Oceanogr.*, 7, 626–629, 1977.
- Ledwell, J. R., A. J. Watson, and C. S. Law, Evidence for slow mixing across the pycnocline from an open-ocean tracer-release experiment. *Nature*, 364, 701–703, 1993.
- Metais, O., Large-eddy simulations of three-dimensional turbulent flows: Geophysical applications. In "Ocean modeling and parameterization" ed. E.P. Chassignet and J. Verron. Kluwer Academic Publishers, 351–372, 1998.
- Middleton, J. F. and J. W. Loder, Skew fluxes in polarized wave fields. *J. Phys. Oceanogr.*, 19, 68–76, 1989.
- Moffatt, H. K., Transport effects associated with turbulence with particular attention to the influence of helicity. *Rep. Prog. Phys.*, 46, 621–664, 1983.
- Mote, P. and A. O'Neill (Eds.), Numerical Modeling of the Global Atmosphere in the Climate System. NATO Science Series C 550, Kluwer, 2000.
- Nakamura, N., Two-dimensional mixing, edge formation, and the permeability diagnosed in an area coordinate. *J. Atmos. Sci.*, 53, 1524–1537, 1996.
- Oakey, N. S., Determination of the rate of dissipation of turbulent energy from simultaneous temperature and velocity shear microstructure measurements. *J. Phys. Oceanogr.*, 12, 256–271, 1982.
- Olson, D. B., Rings in the ocean. *Ann. Rev. Earth Plan. Sci.*, 19, 283–311, 1991.
- Osborn, T. R. and C. S. Cox, Oceanic fine structure. *Geophys. Fluid Dyn.*, 3, 321–345, 1972.
- Polzin, K. and E. Firing, Estimates of diapycnal mixing using LADCP and CTD data from I8S. *International WOCE Newsletter*, 29, 39–42, 1997.
- Rhines, P. B. and W. R. Holland, A theoretical discussion of eddy-driven mean flows. *Dyn Atmos. Oceans*, 3, 289–325, 1977.
- St. Laurent, L. and C. Garrett, The role of internal tides in mixing the deep ocean. *J. Phys. Oceanogr.*, submitted,

- 2000.
- Stansfield, K., C. Garrett, and R. Dewey, The probability distribution of the Thorpe displacement within overturns in Juan de Fuca Strait. *J. Phys. Oceanogr.*, in press, 2001.
- Tandon, A. and C. Garrett, On a recent parameterization of mesoscale eddies. *J. Phys. Oceanogr.*, 26, 406–411, 1996.
- Winters, K. B. and E. A. D'Asaro, Diascalar flux and the

rate of fluid mixing. *J. Fluid Mech.*, 317, 179–193, 1996.

This preprint was prepared with AGU's L^AT_EX macros v4, with the extension package 'AGU++' by P. W. Daly, version 1.6a from 1999/05/21.

Geostrophic eddies, abyssal recirculations, and zonal jets

David P. Marshall, Susan T. Adcock, and Claire E. Tansley

Department of Meteorology, University of Reading, Reading, United Kingdom

Abstract. A characteristic property of geostrophic turbulence is that energy undergoes an inverse cascade to large spatial scales, whereas potential enstrophy cascades directly to small spatial scales. In the presence of weak dissipation, such as in the ocean, energy is therefore quasi-conserved whereas potential enstrophy is always dissipated. As a consequence geostrophic eddies only partially mix potential vorticity along isopycnals, with the amount of mixing being dependent on the energy available in the initial state. To illustrate these ideas, two oceanographic applications are considered: the generation of abyssal recirculations around topographic features and the formation of inertial zonal jets. A new eddy parameterization is developed that dissipates potential enstrophy subject to the constraint of conserving energy. Results obtained using the parameterization are compared with those from an eddy-resolving calculation. Possible extensions of these ideas are discussed, including the possibility of incorporating additional constraints such as conservation of angular momentum.

Introduction

The ocean contains an intense geostrophic eddy field, with a dominant energy-containing scale of order 100 km at midlatitudes. In order to obtain plausible turbulent cascades of dynamic and passive tracers it is necessary for models to resolve even finer spatial scales of order 10 km (e.g., *Roberts and Marshall*, 1998), and consequently ocean climate models are unlikely to adequately resolve the geostrophic eddy field for several years. Development of parameterizations of unresolved geostrophic turbulent processes therefore remains an important task for ocean modelling and climate prediction. But at least as importantly, development of parameterizations is also an excellent strategy for testing and further advancing our understanding of geostrophic turbulence and its impact on the large-scale circulation.

The performance of numerical ocean models has recently been transformed by the widespread adoption of the *Gent and McWilliams* (1990) parameterization (hereafter GM). The key idea behind their parameterization is that geostrophic eddies adiabatically rearrange fluid parcels along isopycnals, without changing the density of individual fluid parcels. Consequently GM represents the eddy flux of a passive tracer through both a diffusion along isopycnals and an advection by an “eddy-induced transport velocity” (*Gent*

et al., 1995). These adiabatic conservations properties have led to a series of dramatic improvements in ocean models, including improved global temperature distribution, improved poleward and surface heat fluxes, and improved occurrence of deep convection (*Danabasoglu et al.*, 1994).

Nevertheless there remain significant shortcomings of GM. For example, the eddy-induced transport in GM is chosen to mimic the effects of baroclinic instability by extracting potential energy from the mean flow, thus driving the ocean towards a state of rest with flat isopycnals. In contrast a number of studies suggest that under appropriate conditions, geostrophic eddies can homogenize the potential vorticity field along isopycnals (*Holland and Rhines*, 1980; *Rhines and Young*, 1982; *Marshall et al.*, 1999). These results have led to alternative closures for the eddy-induced transport in terms of isopycnic gradients of potential vorticity (*Treguier et al.*, 1997; *Killworth*, 1997). However other studies suggest that while eddies may mix potential vorticity along isopycnals, the potential vorticity field is not necessarily homogenized (e.g., *Bretherton and Haidvogel*, 1976; *Wang and Vallis*, 1994).

In this paper we review two oceanographic phenomena in which eddies mix the potential vorticity field along isopycnals without making the potential vorticity uniform. Firstly we consider the formation of anticy-

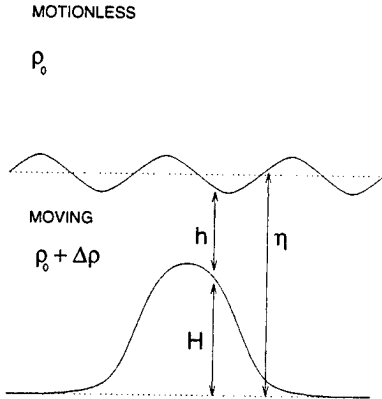


Figure 1. The inverted shallow water model. Motion is confined to a dynamically active abyssal layer, thickness h , overlying variable bottom topography, height H . The height of the layer interface is $\eta = H + h$. (From Adcock and Marshall, 2000.)

clonic recirculations around topographic features (also known as “cold domes”). We diagnose the nature of the turbulent cascades in the formation of such recirculations, based on which we develop a new energy-conserving eddy parameterization. Secondly we consider the formation of inertial zonal jets embedded within a larger-scale flow. Finally we discuss some possible extensions and wider implications of our results.

Abyssal recirculations

In this section we review the results of some numerical experiments illustrating the interactions between geostrophic eddies and the mean circulation in the presence of variable bottom topography (Adcock and Marshall, 2000). The experiments are performed using an “inverted” shallow-water model, in which motion is confined to a dynamically active abyssal layer, thickness h , overlying variable bottom topography, height H (Figure 1). While highly idealized, this model captures the following key ingredients: a geostrophic eddy field, a Rossby deformation radius, a variable isopycnal interface, and variable bottom topography. In these experiments, we simply initialize with an ensemble of balanced geostrophic eddies and integrate forwards in time for 40 model years.

The equations of motion can be written:

$$\frac{\partial u}{\partial t} + u \frac{\partial u}{\partial x} + v \frac{\partial u}{\partial y} - fv + g' \frac{\partial \eta}{\partial x} = -A \nabla^4 u, \quad (1)$$

$$\frac{\partial v}{\partial t} + u \frac{\partial v}{\partial x} + v \frac{\partial v}{\partial y} + fu + g' \frac{\partial \eta}{\partial y} = -A \nabla^4 v, \quad (2)$$

$$\frac{\partial h}{\partial t} + \frac{\partial}{\partial x}(hu) + \frac{\partial}{\partial y}(hv) = 0. \quad (3)$$

Here $\eta = h + H$ is the height of the layer interface, u, v are the velocity components in the x, y directions respectively, $f = f_0 + \beta y$ is the Coriolis parameter where $f_0 = 0.7 \times 10^{-4} \text{ s}^{-1}$ and $\beta = 2 \times 10^{-11} \text{ m}^{-1} \text{ s}^{-1}$, and $g' = 0.02 \text{ m s}^{-2}$ is the reduced gravity. We solve in a square domain (dimension 1000 km) containing a seamount of height 500 m. The mean value of η is 750 m. A scale-selective biharmonic dissipation is employed in the momentum equations to dissipate preferentially at the grid ‘1scale; in our reference experiment we employ a dissipation coefficient of $A = 2.5 \times 10^8 \text{ m}^4 \text{ s}^{-1}$. The equations are discretized on a C-grid with a grid spacing of 5 km. Further details can be found in Adcock and Marshall (2000).

Figure 2 shows the evolution of the interface height (equivalent to streamlines for the geostrophic flow). The initial interface height field reveals a series of geostrophic eddies with maximum geostrophic velocities of order 30 cm s^{-1} . After 4 months there is the first indication of the interface rising over the seamount. After 5 years there is an intense “cold dome” over the seamount and an associated anticyclonic recirculation with velocities of order 40 cm s^{-1} . This intense recirculation remains even after 40 years. The amplitude of the recirculation is dependent on the amplitude of the initial eddy field. Notice that at all stages the interface height field, and thus also the energy field, remains trapped at scales comparable to, or larger than, the deformation radius.

In Figure 3 we show the equivalent snapshots of the potential vorticity field,

$$Q = \frac{f + \zeta}{h}, \quad (4)$$

where $\zeta = \partial v / \partial x - \partial u / \partial y$ is the relative vorticity. At leading order, potential vorticity variations are dominated by the variations in the bottom topography, with high values of potential vorticity found over the seamount and low values found off the seamount. After 4 months there is clear evidence of the direct cascade of the potential vorticity field towards small spatial scales with filaments of high potential vorticity moving off the seamount and filaments of low potential vorticity moving onto the seamount. After 5 and 40 years, the maximum value of the potential vorticity is significantly reduced over the seamount, but note that the potential vorticity field is not made uniform. The reduced potential vorticity is associated with increased layer thickness over the seamount, and hence the cold doming and the anticyclonic circulation. In contrast, a uniform potential vorticity state would require a far

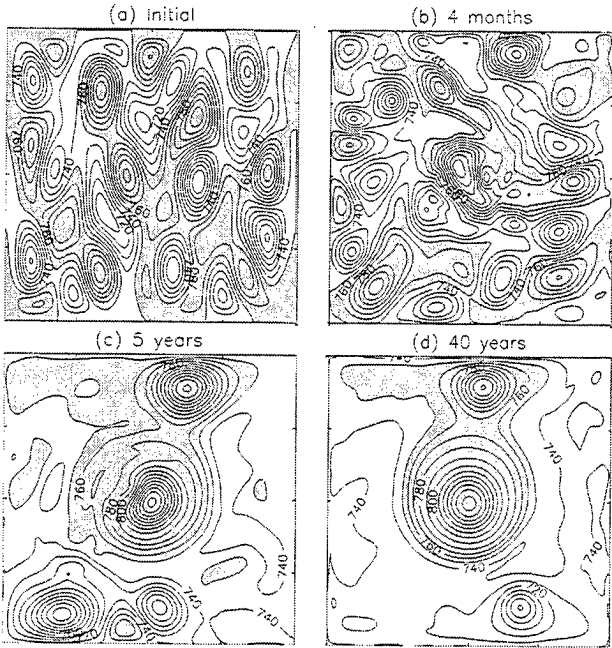


Figure 2. Interface height, η (shading indicates values greater than 750 m). (a) Initial conditions; (b) after 3 months; (c) after 5 years; (d) after 40 years. Contour interval=10m. (From Adcock and Marshall, 2000.)

greater doming of the layer interface over the seamount, which is impossible without an input of energy.

More quantitatively we can consider the evolution of the net available energy

$$E = \rho_o \iint \left\{ \frac{h(u^2 + v^2)}{2} + \frac{g'h(h+2H)}{2} \right\} dx dy, \quad (5)$$

and the net potential enstrophy,

$$\Lambda = \iint \frac{hQ^2}{2} dx dy, \quad (6)$$

the latter being a measure of the variance of the potential vorticity field and thus the extent to which the potential vorticity field is mixed. Figure 4(a) shows the available energy over the first five model years for different values of biharmonic momentum dissipation. The amount of energy dissipated increases with the coefficient of momentum dissipation, but in each case the energy dissipated is small compared with the energy that would be dissipated if the eddies were spinning the ocean down towards a state of rest. Figure 4(b) shows the potential enstrophy over the same period. The potential enstrophy rapidly decreases below the level consistent with spin-down towards a state of rest, but similarly never approaches the level consistent with a state of uniform potential vorticity. The evolution of the potential enstrophy is remarkably insensitive to the level

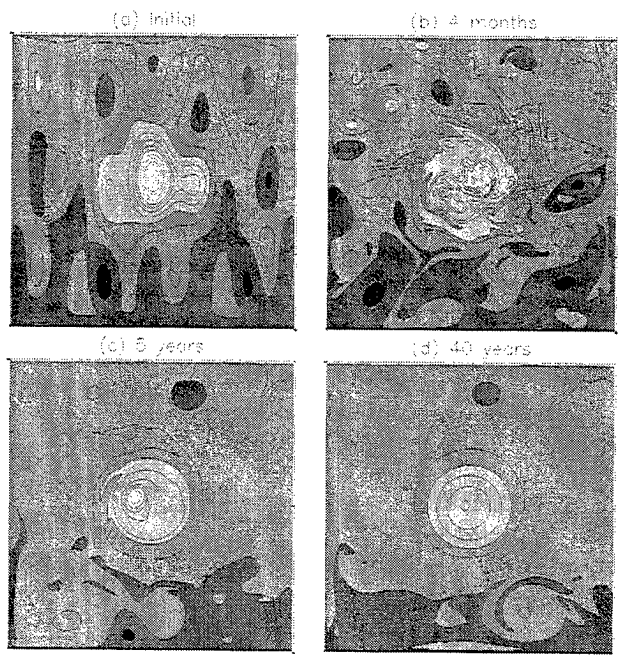


Figure 3. Potential vorticity in the abyssal layer. (a) Initial conditions; (b) after 3 months; (c) after 5 years; (d) after 40 years. Contour interval= $2 \times 10^{-8} \text{ m}^{-1} \text{s}^{-1}$. (From Adcock and Marshall, 2000.)

of momentum dissipation. These results suggest that eddies are neither driving the model ocean down towards a state of rest, as assumed in GM, nor towards a state of uniform potential vorticity. Instead the ocean is driven towards a state of minimum potential enstrophy, subject to the constraint of (nearly) conserving the net available energy (c.f. Bretherton and Haidvogel, 1976).

An energy-conserving parameterization

The above results can be exploited to develop a new geostrophic eddy parameterization. As in GM we represent the eddies through a rearrangement of fluid parcels or “eddy-induced transport”, \mathbf{U}^* , such that the continuity equation becomes

$$\frac{\partial h}{\partial t} + \nabla \cdot (h\mathbf{u} + \mathbf{U}^*) = 0. \quad (7)$$

We write the eddy-induced transport in the form

$$\mathbf{U}^* = U_0 \mathbf{a}, \quad (8)$$

where

$$\frac{\iint \mathbf{a} \cdot \mathbf{a} dx dy}{\iint dx dy} = 1. \quad (9)$$

Here U_0 is taken as an externally prescribed parameter controlling the rate at which rearrangements occur,

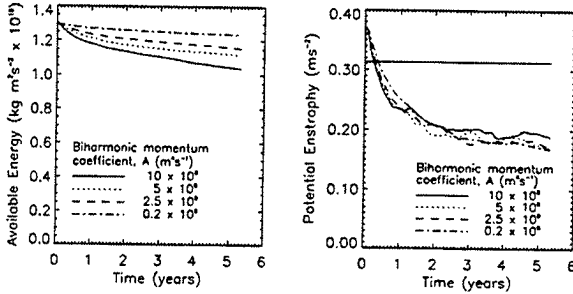


Figure 4. Evolution of (a) the total available energy and (b) the total available potential enstrophy over the first five years. The four curves correspond to different coefficients of biharmonic momentum dissipation. The thick solid line in (a) corresponds to the energy of the minimum energy state in which the ocean is at rest. The upper thick line in (b) corresponds to the potential enstrophy of the minimum energy state and the lower thick line corresponds to the potential enstrophy of the uniform potential vorticity state. (From Adcock and Marshall, 2000.)

while \mathbf{a} describes the *spatial pattern* of these rearrangements.

We now seek the form of \mathbf{a} that, in a given time interval Δt , maximizes the dissipation of potential enstrophy,

$$-\Delta\Lambda = \Delta t \iint \mathbf{U}^* \cdot \nabla \frac{Q^2}{2} dx dy. \quad (10)$$

subject to conserving the total available energy,

$$\Delta E = \Delta t \iint \mathbf{U}^* \cdot \nabla B dx dy = 0, \quad (11)$$

where $B = g'\eta + (u^2 + v^2)/2$ is the Bernoulli potential. Taking variations, $\delta\mathbf{a}$, in order to maximize (10), subject to the constraints (9) and (11), gives

$$\mathbf{U}^* = \kappa \left(\nabla \frac{Q^2}{2} + \lambda \nabla B \right). \quad (12)$$

Here κ is a Lagrange multiplier determined uniquely by (9), and λ is a Lagrange multiplier determined uniquely by the energy constraint (11).

The first term in (12) corresponds to a potential vorticity closure for \mathbf{U}^* , whereas to leading order the second term corresponds to the GM closure. The new parameterization thus contains elements of both the GM and potential vorticity closures, and results in partial, but not total, mixing of potential vorticity.

To illustrate the use of the parameterization, in Figure 5 we show the results of three parallel simulations, the first at 5 km resolution with resolved geostrophic turbulence, the second at 40 km resolution and including the parameterization of the geostrophic turbulence,

and the third at 40 km resolution with neither resolved nor parameterized turbulence. The integrations are initialized with the same eddy field shown in Figure 2(a). In the high-resolution case (Figure 5a, b) an intense anticyclonic recirculation is evident after 30 model weeks. The coarse resolution case with the parameterized turbulence (Figure 5c, d) is able to reproduce a plausible anticyclonic recirculation, whereas the coarse resolution case without the parameterized turbulence (Figure 5e, f) produces only a very weak recirculation. Note that the maximum value of the potential vorticity over the seamount is much higher in the latter case. While there are some differences, particularly in the details of the circulation off the seamount, we are encouraged by the ability of the parameterization to reproduce a plausible doming of the layer interface over the seamount.

Zonal jets

The formation of abyssal recirculation gyres represents a situation in which potential vorticity mixing is limited by the amount of energy available in the initial state. However even in the situation that there is a ready supply of energy, the inverse cascade of energy to large spatial scales can still restrict the extent to which potential vorticity can be mixed. This issue is a topic of ongoing research, but here we present some preliminary results that highlight some of the issues involved.

Specifically we consider eastward flow past a cylinder in a barotropic β -plane channel. The flow is maintained through a sponge layer (shaded region on the figures) within which the zonal velocity is relaxed towards a uniform value. These experiments were originally designed to study the dynamics of flow separation; further details can be found in Tansley and Marshall (2001), Marshall and Tansley (2001). Here we focus on just one aspect of these flows: the formation of zonal jets.

We solve the nondimensional barotropic vorticity equation

$$\frac{\partial \zeta}{\partial t} + \mathbf{u} \cdot \nabla \zeta + \hat{\beta} v = \frac{1}{Re} \nabla^2 \zeta, \quad (13)$$

where $\zeta = \partial v / \partial x - \partial u / \partial y$ is the relative vorticity,

$$Re = \frac{UL}{\nu} \quad (14)$$

is the Reynolds number, and

$$\hat{\beta} = \frac{\beta L^2}{U} = \frac{L^2}{L_R^2} \quad (15)$$

is a non-dimensional “ β -parameter” or the “Rhines number”; the latter term is motivated by the “Rhines scale”, $L_R = \sqrt{U/\beta}$, that controls the meridional scale of zonal jets in geostrophic turbulent flows (Rhines,

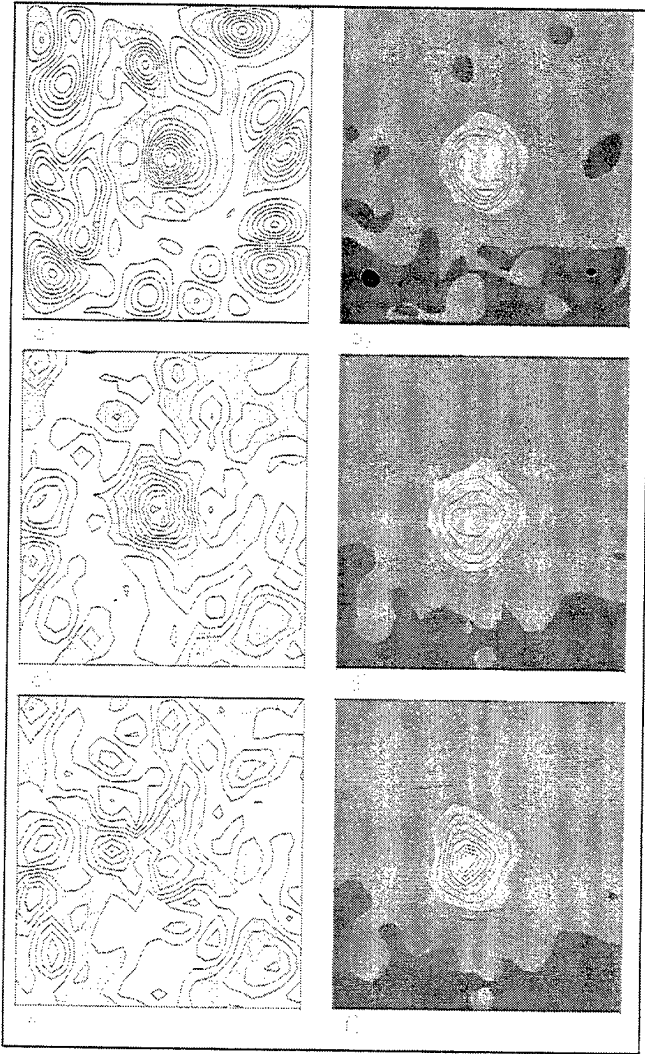


Figure 5. Snapshots of the interface height (panels a, c, e) and potential vorticity (panels b, d, f) after 30 weeks of integration. Panels a and b correspond to the 5 km resolution case with resolved turbulence; panels c and d correspond to the 40 km resolution case with the parameterization; panels e and f correspond to the 40 km resolution case without the parameterization. Contour intervals as in Figures 2 and 3. (From Adcock and Marshall, 2000.)

1975). Here L is the diameter of the cylinder, U is the mean zonal velocity, ν is the coefficient of lateral viscosity, and β is the gradient in the Coriolis parameter.

Here we show solutions only for the value $\hat{\beta} = 75$, and for three values of the Reynolds number. The latter controls the level of dissipation, and hence the amplitude of the eddy field. The streamfunction (ψ , defined such that $u = -\partial\psi/\partial y$, $v = \partial\psi/\partial x$) is shown in Figure 6 and the vorticity ($q = \zeta + \beta y$) is shown in Figure 7.

Even at the lowest Reynolds number of 25 (panels

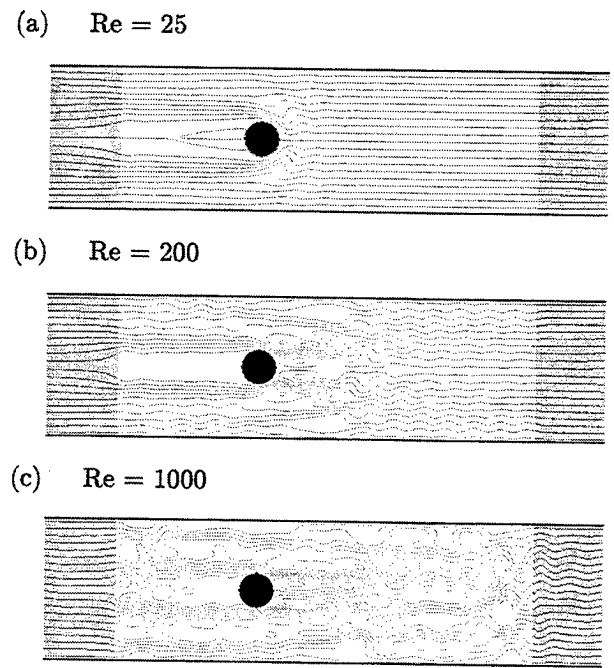


Figure 6. Streamfunction (nondimensionalized) from three solutions with $\hat{\beta} = 75$ and (a) $Re = 25$, (b) $Re = 200$, (c) $Re = 1000$. Contour interval = 0.2. Shading indicates the sponge layer within which the zonal velocity is relaxed towards a uniform value. (From Tansley and Marshall, 2001.)

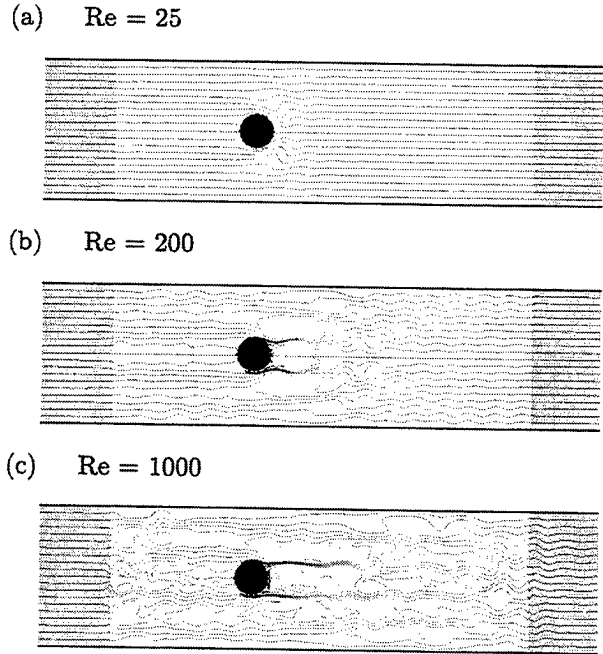


Figure 7. Vorticity (nondimensionalized) from three solutions with $\hat{\beta} = 75$ and (a) $Re = 25$, (b) $Re = 200$, (c) $Re = 1000$. Contour interval = 15. (From Tansley and Marshall, 2001.)

a), the circulation is significantly altered from the non-rotating case (not shown). Rather than a separated region downstream of the cylinder, we find a separated region upstream of the cylinder. This is related to the westward propagation of Rossby waves, and the ability of the circulation to accommodate western boundary currents, but not eastern boundary currents (e.g., see Merkine, 1980; Page and Johnson, 1990; Tansley and Marshall, 2001). There is a slight hint of a strongly damped Rossby wave downstream of the cylinder, but no turbulent eddies.

However at the higher Reynolds numbers of 200 (panels b) and 1000 (panels c), the circulation is fundamentally altered downstream of the cylinder. At these higher Reynolds numbers, the Rossby waves break to form a turbulent wake. Within this wake there is a direct cascade of enstrophy and an inverse cascade of energy; the latter is arrested in the meridional direction at the Rhines scale (Rhines, 1975), leading to the formation of a series of zonal jets. These jets extend further downstream of the cylinder at the higher value of the Reynolds number since the turbulent wake itself extends further downstream.

Just as in the formation of the abyssal recirculations, the vorticity is mixed by the eddy field, but it is not made uniform. Rather there are "plateaus" of nearly uniform vorticity, separated by narrow regions of enhanced vorticity gradient. Confirmation that the eddy field is responsible for *accelerating* the zonal jets is given in Figure 8, which shows the convergence of the eddy vorticity flux ($-\nabla \bar{\zeta}' \bar{u}'$, where the overbar and primes represent time-mean and time-varying components), and the mean dissipation of vorticity through the right-hand side of (13). While the eddy term contains a rich structure, there is an unambiguous tendency to enhance the vorticity gradient across, and hence accelerate, the zonal jets. In contrast the dissipation acts to decelerate the jets.

Discussion

In this paper we have considered the impact of geostrophic eddies on the large-scale circulation from the perspective provided by geostrophic turbulence theory. Energy undergoes an inverse cascade to large spatial scales, whereas potential enstrophy cascades directly to small spatial scales. Consequently we argue that geostrophic eddies only partially mix potential vorticity along isopycnals, with the amount of mixing being dependent on the energy available in the initial state.

The need for an energetic constraint is clear in the formation of abyssal recirculations, since energy is required to raise isopycnals over a seamount. However we suggest that an energetic constraint might also be ap-

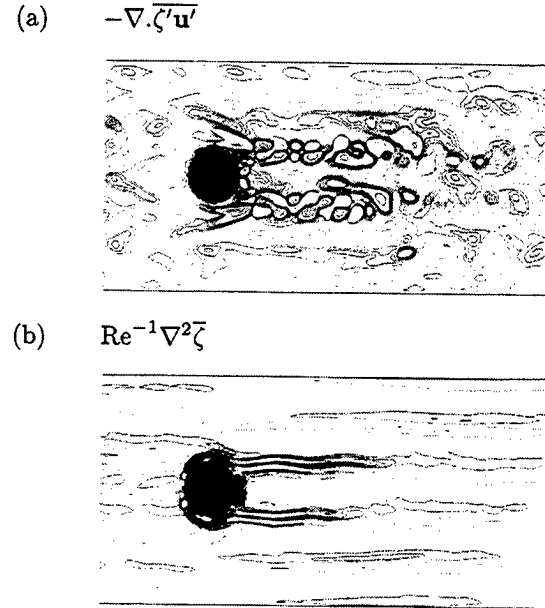


Figure 8. (a) Convergence of the eddy vorticity flux and (b) mean frictional dissipation from the solution with $Re = 1000$ and $\beta = 75$. Two contour intervals are employed: 1.0 between values of -4.5 and 4.5; and 10.0 for values of greater magnitude; shading indicates negative contours. Only the central portion of the channel is shown. (From Tansley and Marshall, 2001.)

propriate even in the case in which unconstrained mixing of potential vorticity leads to a net decrease in energy, since energy remains trapped at relatively large spatial scales. In Figure 9 we speculate on the implications for the slumping of a baroclinic front. According to GM, the eddy-induced transport acts to flatten the isopycnals, with a single overturning cell extending across the baroclinic front. However this slumping will result in a release of potential energy which must be converted to kinetic energy. Alternatively we suggest that the eddy-induced transport may initially be confined to a series of localized overturning cells that act to convert available potential energy into the kinetic energy of zonal jets. This kinetic energy will in turn be dissipated through bottom drag and/or internal wave breaking, allowing further slumping to proceed. If this hypothesis is correct, then the rate at which eddies transport fluid, and tracers, across a baroclinic front should be dependent on the nature and level of dissipation in an eddy-resolving calculation. Work is in progress to explore these issues.

There is also a distinct possibility that there are additional constraints on the mixing of potential vorticity. For example in a zonal domain with no topographic variations, one should expect angular momentum to be conserved (e.g., Marshall, 1981). It is also unclear how

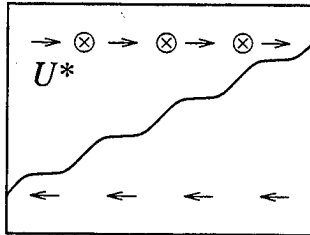


Figure 9. A hypothesis for the impact on an energetic constraint on the slumping of a baroclinic front. We suggest that the eddy-induced transport (U^*) may be confined to a series of localized overturning cells that act to convert available potential energy into the kinetic energy of zonal jets. The overall meridional transport will then depend crucially on the dissipation of the jets by bottom friction and/or internal wave breaking.

these constraints are modified in the presence of explicit forcing and dissipation, and indeed whether one should take into account the input of energy from smaller, unresolved spatial scales as suggested by Holloway (1987). There is also the possibility of energy transfer to small spatial scales in the presence of small-scale variations in bottom topography. These issues all require further study.

We have developed a simple energy conserving eddy parameterization in this paper. In principle it should be possible to incorporate additional constraints as required. However there are some significant limitations of our approach. In particular we apply our energy constraint in a global, rather than local, sense. The alternative approaches of Sadournay and Basedevant (1985) and Holloway (1992) may provide more practical ways forward.

Acknowledgments. DPM would like to thank Peter Müller and Chris Garrett for organizing a most stimulating and thoroughly enjoyable workshop. This work was funded by the U.K. Natural Environment Research Council.

References

- Adcock, S. T., and D. P. Marshall, Interaction of geostrophic eddies and the mean circulation over large-scale bottom topography, *J. Phys. Oceanogr.*, **30**, 3223-3338, 2000.
- Bretherton, F. P., and D. B. Haidvogel, Two-dimensional turbulence above topography, *J. Fluid Mech.*, **78**, 129-154, 1976.
- Danabasoglu, G., J. C. McWilliams, and P. R. Gent, The role of mesoscale tracer transports in the global ocean circulation, *Science*, **264**, 1123-1126, 1994.
- Gent, P. R., and J. C. McWilliams, Isopycnal mixing in ocean circulation models, *J. Phys. Oceanogr.*, **20**, 150-155, 1990.
- Gent, P. R., J. Willebrand, T. J. McDougall, and J. C. McWilliams, Parameterizing eddy-induced tracer trans-
- ports in ocean circulation models, *J. Phys. Oceanogr.*, **25**, 463-474, 1995.
- Holland, W. R., and P. B. Rhines, 1980, An example of eddy-induced ocean circulation, *J. Phys. Oceanogr.*, **10**, 1010-1031, 1980.
- Holloway, G., Systematic forcing of large-scale geophysical flows by eddy-topography interaction, *J. Fluid Mech.*, **184**, 463-474, 1987.
- Holloway, G., Representing topographic stress for large-scale ocean models, *J. Phys. Oceanogr.*, **22**, 1033-1046, 1992.
- Killworth, P. D., On the parameterization of eddy transfer, *J. Mar. Res.*, **55**, 1171-1197, 1997.
- Marshall, D. P., and C. E. Tansley, An implicit formula for boundary current separation, *J. Phys. Oceanogr.*, **31**, 1633-1638, 2001.
- Marshall, D. P., Williams, R. G., and M.-M. Lee, The relation between eddy-induced transport and isopycnal gradients of potential vorticity, *J. Phys. Oceanogr.*, **29**, 1571-1578, 1999.
- Marshall, J. C., On the parameterization of geostrophic eddies in the ocean, *J. Phys. Oceanogr.*, **11**, 257-271, 1981.
- Merkine, L. O., Flow separation on a β -plane, *J. Fluid Mech.*, **99**, 399-409, 1980.
- Page, M. A., and E. R. Johnson, Flow past cylindrical obstacles on a beta-plane, *J. Fluid Mech.*, **221**, 349-382, 1990.
- Rhines, P. B., Waves and turbulence on a beta-plane, *J. Fluid Mech.*, **69**, 417-433.
- Rhines, P. B., and W. R. Young, Homogenization of potential vorticity in planetary gyres, *J. Fluid Mech.*, **122**, 347-367.
- Roberts, M. J., and D. P. Marshall, Do we require adiabatic dissipation schemes in eddy-resolving ocean models? *J. Phys. Oceanogr.*, **28**, 1998, 2050-2063.
- Sadournay, R., and C. Basedevant, Parameterization of subgrid scale barotropic and baroclinic eddies in quasi-geostrophic models: anticipated potential vorticity method, *J. Atmos. Sci.*, **42**, 1353-1363, 1985.
- Tansley, C. E., and D. P. Marshall, Flow past a cylinder on a β -plane, with application to Gulf Stream separation and the Antarctic Circumpolar Current, *J. Phys. Oceanogr.*, 2001, in press.
- Treguier, A. M., I. M. Held, and V. D. Larichev, Parameterization of quasigeostrophic eddies in primitive equation ocean models, *J. Phys. Oceanogr.*, **27**, 567-580, 1997.
- Wang, J., and G. K. Vallis, Emergence of Fofonoff states in inviscid and viscous ocean circulation models, *J. Mar. Res.*, **52**, 83-127, 1994.

Parameterisation of eddies in coarse resolution models

Peter D. Killworth

Southampton Oceanography Centre, Southampton, England

Abstract. Some requirements on eddy parameterisations are discussed, especially the implications of expressing them in terms of the quasi-Stokes velocity and the modified mean, rather than Eulerian mean, density. The difference between the two means is second-order in perturbation amplitude and thus small in the fluid interior (where formulae to connect the two exist). Near horizontal boundaries, the differences become first order, and so more severe. Existing formulae for quasi-Stokes velocities and streamfunction also break down here. The layer in which the largest differences between the two mean densities occur is the vertical excursion of a mean isopycnal across a deformation radius, at most about 20 m thick. Most climate models would have difficulty in resolving such a layer. It is shown that extant parameterisations appear to reproduce the Eulerian, and not modified mean, density field and so do not yield a narrow layer at surface and floor either. Both these features make the quasi-Stokes streamfunction appear to be non-zero right up to rigid boundaries, so that we must query what are the relevant surface and floor quasi-Stokes streamfunction conditions, and what are their effects on the density fields. To answer this, a variety of eddy parameterisations is employed for a channel problem, and the time-mean density is compared with that from an eddy-resolving calculation. The parameterisations were only successful if the vertical component of the quasi-Stokes velocity vanished at top and bottom as in current practice, but all were almost equally successful given proper tuning. One parameterisation, based on linear instability theory, is extended to a global geometry. In low and mid-latitudes, because the predominant orientation of the instability wavevector is north-south, the main quasi-Stokes flow is east-west, only becoming the more traditional north-south at higher latitudes.

1. Introduction

The ocean component of climate models is necessarily of coarse resolution, and it does not possess eddies. This paper discusses various aspects of the issue of representing eddies in such models. First, it discusses the extant parameterisations (Section 2). Section 3 examines some hitherto unappreciated details, with reference to the ‘modified mean density’ concept; it is shown that the difference between this density and the Eulerian mean is largest at surface and floor. The region that this difference occupies is too shallow to be resolved by coarse models, so that eddy effects occur in what appears to such models as a delta-function. Current parameterisations do not generate solutions which include these differences, even with adequate resolution. Some eddy-resolving channel experiments are used in Section 5 to explore whether the relevant boundary condition is that of no eddy flux (formally correct beyond the thin layer) or not; the conclusion is that the usual boundary

condition must be employed. Last, a parameterisation based on linear instability theory (introduced in Section 4) is extended in Section 6 from channel simulations to the global domain and is briefly compared with the *Gent and McWilliams* (1990) parameterisation. The directionality of linear instability at low and mid-latitudes is such that the ‘bolus’ fluxes are oriented east-west, rather than north-south, at these latitudes, because the beta effect constrains maximal instability to a north-south orientation (which yields east-west fluxes).

2. Background

A variety of schemes has been suggested to include eddy effects in coarse-resolution ocean models. These schemes divide into two categories. The first, which we shall be examining here, involves adding terms to represent the additional thickness flux by baroclinic eddies (*Gent and McWilliams*, 1990; *Greatbatch and Lamb*, 1990; *Gent et al.*, 1995; *Visbeck et al.*, 1997; *Treguier*

et al., 1997; Killworth, 1997, 1998; Greatbatch, 1998). The second (Neptune) involves a representation of the statistical properties of eddies on the mean flow (*Eby and Holloway*, 1994; *Merryfield and Holloway*, 1997), and will not be discussed in detail here. Methods to represent propagating features (e.g. Agulhas rings) do not seem yet to be available.

Eddy parameterisations have been designed with various criteria in mind by different authors. Initial requirements include mimicking both baroclinic instability – “reducing APE”, in some sense, and barotropic instability – “reducing lateral shear”, as well as the Neptune approach of making the ocean resemble a rectified eddying ocean. All these are quasi-steady in nature and ignore the fact that instability generates variability on weeks to decades through nonlinear interactions. I am not aware of any parameterisation which attempts to put temporal variability into the ocean (by stochastic forcing, perhaps), so that coupled ocean-atmosphere models, even with parameterisations, are unlikely to possess a realistic degree of self-induced oceanic variability.

Two other pragmatic requirements are that parameterisations should not induce erroneous ocean behaviour (e.g. breaking conservation laws such as momentum), and should ensure that the numerics of the models behave (the original concept behind eddy diffusivity, of course).

The manner in which a parameterisation is couched depends on what belief structure about eddy behaviour is used. In the literature already are suggestions for thickness smoothing, potential vorticity (q) conservation, energy loss, energy conservation, and q smoothing. These effects are usually placed in the tracer equations, but it is possible to include effects in momentum equations also. There are potential difficulties near horizontal surfaces, discussed later.

2.1 Formulations

Most authors seek an “equivalent to the bolus velocity”, namely some

$$(u^+, v^+, w^+)$$

which is fully three-dimensional and non-divergent, such that $\bar{\mathbf{u}} + \mathbf{u}^+$ advects (a form of) the density adiabatically – i.e. build in our belief that density (or neutral density) effects are adiabatic. This is usually represented as a 2-dimensional streamfunction

$$\Psi = (\psi_1, \psi_2)$$

such that

$$u^+ = \psi_{1z}, v^+ = \psi_{2z}, w^+ = -\nabla_H \cdot \Psi.$$

The most logical approach to date is the transient-residual-mean (TRM) theory introduced by McDougall (1998, and earlier references therein); *McDougall and McIntosh* (2001, hereafter MM) give more detail on the same material. Another, highly related, approach is to use density-weighted averaging (cf. *Greatbatch*, submitted ms; *de Szoeke and Bennett*, 1993). The TRM theory applies to low-pass temporally averaged quantities and deduces a quasi-Stokes velocity \mathbf{u}^+ which is related, but not identical, to the bolus velocity. (The two are not identical because the background mean flow involves averages on two different surfaces, though they are frequently similar.) Formulae have been derived for small perturbations by *McDougall* (1998) and MM, involving only averages at constant depth. The quasi-Stokes vector streamfunction is given to second order in amplitude by

$$\Psi = -\frac{\overline{\mathbf{u}'_H \rho'}}{\bar{\rho}_z} + \frac{\mathbf{u}_{Hz}}{\bar{\rho}_z} \left(\frac{\bar{\phi}}{\bar{\rho}_z} \right),$$

where the suffix H denotes the horizontal component, and $\phi = (1/2)\bar{\rho}^{1/2}$. The vertical derivative of Ψ is the horizontal component of \mathbf{u}^+ . The second term is usually small compared with the first and is neglected henceforth.

Since eddying motions are believed to conserve density, this implies that the definition of density must be modified. *McDougall* (1998) shows that rather than using the Eulerian mean density $\bar{\rho}$ at a (vertical) point (EMD for short), one should interpret density as being the inversion of the mean depth of a given density (termed the ‘modified mean density’ $\tilde{\rho}$, or MMD for short). The difference between these two fields $\tilde{\rho}$ and $\bar{\rho}$ is again of second order in small quantities and is thus very small where the TRM theory is formally valid. However, the time derivatives of EMD and MMD differ by $O(1)$ amounts because of the above discussion. The MMD is advected by the (Eulerian) mean flow and by the quasi-Stokes velocity:

$$\tilde{\rho}_t + \nabla \cdot [(\bar{\mathbf{u}} + \mathbf{u}^+) \tilde{\rho}] = 0.$$

We shall see that near horizontal boundaries, the small-amplitude formulae of *McDougall* (1998) and MM to convert EMD to MMD break down. In fact, the two fields differ at first, not second, order in the small quantities. (This is nothing to do with the question of neutrally stable and mixed layers, which are beyond the scope of this paper.)

The earliest parameterisation was a simple pair of diffusivities: $\kappa_H \nabla_H^2 \bar{\rho} + \kappa_V \bar{\rho}_{zz}$. This suffers from the well-known Veronis effect, in that fluid within a density class is not conserved. The now classic GM parameter-

isation (*Gent and McWilliams*, 1990) takes

$$\Psi = -\kappa \frac{\nabla_H \bar{\rho}}{\bar{\rho}_z}$$

though the density is arguably $\tilde{\rho}$ and not $\bar{\rho}$. This both conserves layer thickness (which, note, is an integral, not a conserved quantity) and “smooths” them. It fits conveniently into the isopycnic mixing tensor formalism of *Solomon* (1981) and *Redi* (1982). *Visbeck et al.* (1997) give a variant with horizontally varying diffusion coefficient based on baroclinic instability. *Killworth* (1997) uses an approximate solution to (single wave) baroclinic instability, obtaining a three-dimensionally varying diffusion coefficient, which vanishes for stable flow. The scheme mixes q in *one direction*, not down-gradient. Thus

$$\mathbf{u}_H^+ = \kappa \mathbf{A} \cdot \frac{\partial}{\partial z} \left(\frac{\nabla_H \bar{\rho}}{\bar{\rho}_z} \right) + \frac{\beta}{f} \kappa \mathbf{A}_2$$

$$\mathbf{A} = \begin{pmatrix} \cos^2 \theta & -\sin \theta \cos \theta \\ -\sin \theta \cos \theta & \sin^2 \theta \end{pmatrix}$$

and θ is the angle the instability wavevector makes with the x -axis. The approach is usually written in terms of the quasi-Stokes streamfunction. Many other suggestions appear in the literature, mostly untested (*Marshall*, this volume-MAYBE) shows a different approach, which is tested in simple physical situations).

2.2 Inferences from eddy-resolving simulations

There have been several efforts to use eddy-resolving computations to enlighten choices about eddy parameterisation. To date, these have produced not completely consistent results.

Lee et al. (1997) indicate that q is fluxed in a three-layer channel model, and not layer thickness. *Roberts and Marshall* (2000), however, find in a depth-co-ordinate model that the divergent part of the temperature flux is not well correlated with mean temperature gradient; the equivalent for q is moderately well correlated, as are the eddy-induced transport velocity. *Wilson* (2000), however, in a three-layer channel model with forcing varying downstream, finds varying agreement with both thickness and q flux (thickness having better agreement than q) and large areas in the middle layer in which the fluxes are not correlated with either gradient, suggesting the importance of the rotational component. This latter is emphasised by *Drijfhout and Hazeleger* (2001) in a gyral eddy-resolving model; they show that the zonally averaged northward mean thickness gradients are well correlated with the zonally averaged divergent eddy thickness fluxes, while the equivalent for q is much less well correlated.

Estimates of eddy-induced diffusivities also vary. There are strong suggestions that diffusivity varies vertically (*Treguier* 1999; *Robbins et al.*, 2000) as well as theoretical suggestions of lateral variation (*Visbeck et al.*, 1997; *Killworth*, 1997).

The boundary conditions on surface and floor of the TRM streamfunction, which should apparently be zero values in both locations, also remain unclear. Both *Treguier* (1999) and *Gille and Davis* (1999) estimate the streamfunction, which takes extreme values at both top and bottom of the channels they considered.

There is no strong evidence that any single globally tested parameterisation (a) gives similar fluxes (rotational and divergent?) to observed values from eddy-permitting/resolving models or (b) uniformly improves water masses and tracers. GM has by far the largest suite of tests, and while the evidence is clear that – mostly – temperature/salinity distributions are favourably affected by its use (e.g. *Knutti et al.*, 2000 for a 2.5-dimensional model), the response of other tracers deteriorates (*England and Rahmstorf*, 1999).

This should not be surprising: physical eddies have many effects, and the extant parameterisations are aimed at a small subset of those effects.

3. Some details about TRM streamfunctions

3.1 Differences between EMD and MMD

The TRM approach is to work from density coordinates to locate what “density” variable is conserved by a flow consisting of a mean ($\bar{\mathbf{u}}$) plus a quasi-Stokes velocity (\mathbf{u}^+). *McDougall* (1998) shows that this density (the modified mean density) is the inversion of the average height of a density surface,

$$\bar{z}(x, y, \rho, t) \rightarrow \tilde{\rho}(x, y, z, t)$$

for some averaging operator. Then

$$\tilde{\rho}_t + \nabla \cdot \{(\bar{\mathbf{u}} + \mathbf{u}^+) \tilde{\rho}\} = 0.$$

MM show that for small amplitude variability, and to second order accuracy,

$$\tilde{\rho} = \bar{\rho} + \hat{\rho} = \bar{\rho} + O(\alpha^2)$$

$$\hat{\rho} = -\left(\frac{\bar{\phi}}{\bar{\rho}_z}\right)_z, \bar{\phi} = \frac{1}{2} \left(\overline{\rho'^2}\right)$$

$$\Psi = -\frac{\overline{\mathbf{u}'_H \rho'}}{\bar{\rho}_z} + \frac{\mathbf{u}_{Hz}}{\bar{\rho}_z} \left(\frac{\bar{\phi}}{\bar{\rho}_z}\right)$$

where the second term is usually small and will be neglected here.

These formulae work well *except near the surface and floor*, where there are *first-order* differences between $\bar{\rho}$ and $\tilde{\rho}$. These differences are produced by the advection of fluid laterally: any fluid of a light density which is ever present at some (x, y) has an entry in the modified mean density. The differences occur over a distance which is first-order in perturbation amplitude. Fig. 1 shows the near-surface behaviour for a flow whose density is given at some horizontal location by

$$z - z_0 = F(\rho - \rho_0) + \alpha G(\rho - \rho_0, t)$$

$$\bar{G} = 0.$$

(The solution is for $G(t) = \sin t$.) The behaviour is caused by time-averaging near surface or floor only being valid when the resulting depth z is within the fluid.

The length scale in Fig. 1 is proportional to eddy amplitude. For linear theory, it appears as a delta-function boundary layer. When the eddies have finite amplitude, the vertical length scale over which the two densities differ noticeably is of order

$$z' \sim \rho'/\bar{\rho}_z \sim a |\nabla_H \bar{\rho}/\bar{\rho}_z|$$

which is the typical vertical excursion made when moving a short horizontal distance (a) along a mean isopycnal which moves significantly vertically only on the gyre scale ($L \gg a$). This depth is small for ocean, though not for the atmosphere. Even with fairly optimistic estimates, it is hard to produce a vertical scale much larger than 20 m. So *the distance over which the MMD and EMD differ significantly is not resolved in most climate models*, being concentrated in the last grid point (save in regions such as the Antarctic Circumpolar Current). Thus the near-boundary differences between the two mean densities will probably appear to climate models as single grid-point effects, i.e. delta functions. *McIntosh and McDougall (1996)* show diagnostics from FRAM which support this.

No parameterisation of which I am aware succeeds in reproducing the MMD even given adequate vertical resolution. Fig. 2 shows channel model results for a 4-year and along-channel average of an eddy-resolving calculation, with surface relaxation and parameters designed to permit the lighter near-surface and denser near-bottom fluid present in the MMD to be resolved by the 10-m grid spacing (the relevant depth being 50-60 m). Also shown is a two-dimensional calculation using GM (other parameterisations will give similar poor results). It is clear that the “pushing forward” of warm isopycnals present in the MMD is not present. Differences are very small at the lower boundary because eddy amplitudes were small there also. The presence of

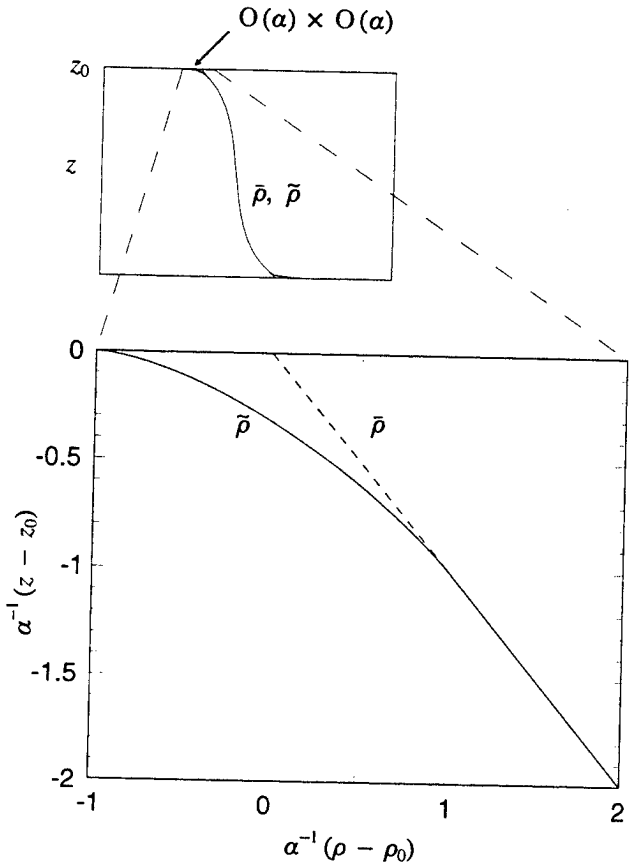


Figure 1. The differences between Eulerian mean and modified density. The upper diagram shows that the densities are very close to each other in the fluid interior (differing by $O(\alpha^2)$, where α is the small amplitude of the fluctuations). In a zone of size α near surface and floor, the two densities differ by a much larger amount, $O(\alpha)$, as indicated in the exploded lower view (which is actually the exact solution for sinusoidal time variation and uniform interior density gradient).

a mixed layer (not treated here) makes no difference to this argument, since it merely moves the region where EMD and MMD differ slightly lower (usually to worse resolution).

Because the resolution does not permit the resolution of the layer where MMD and EMD differ, not all the eddy fluxes can be represented. Fig. 3 shows the physical near-surface situation contrasted with what is represented in a coarse-resolution model. At the least density which the model is capable of representing, the quasi-Stokes streamfunction is non-zero (its value, correctly, representing the lateral eddy flux within the unresolved layer, which thus appears as a delta-function).

An argument can be made that one could relax the condition of $\psi_1 = \psi_2 = 0$ on surface and floor since the model being run (a) cannot distinguish the EMD and

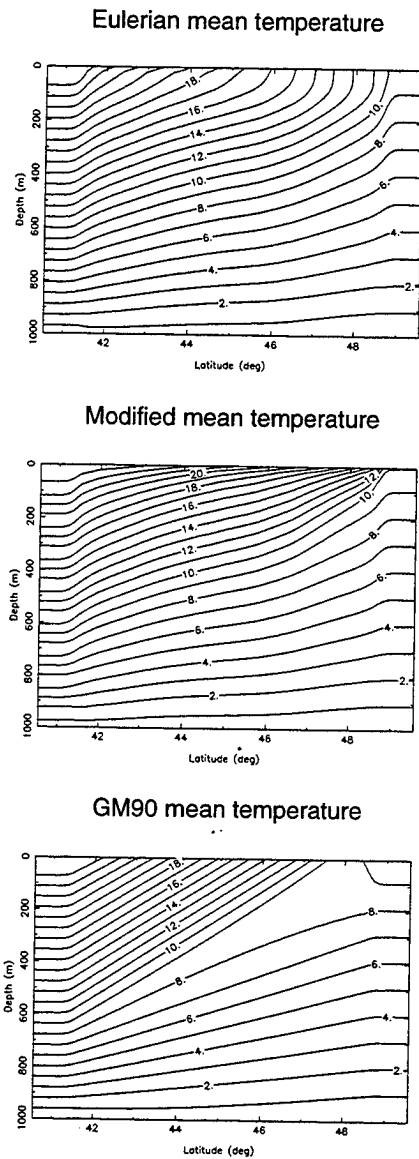


Figure 2. The Eulerian and modified mean density for a 4-year and along-channel average of an eddy-permitting channel model discussed in the text. (The average over the previous 4 year period is almost identical.) The problem was chosen to provide a larger vertical range over which the EMD and MMD differ than would hold for the real ocean, so that the vertical resolution (10 m) was adequate. Also shown is a typical two-dimensional parameterisation steady-state result, in this case following Gent and McWilliams (1990), using an eddy diffusion of $2000 \text{ m}^2 \text{ s}^{-1}$. While the latter does not reproduce the EMD particularly well (true for a wide range of diffusivities), it does not reproduce the MMD at all where this differs from the EMD. This appears to hold for most extant parameterisations.

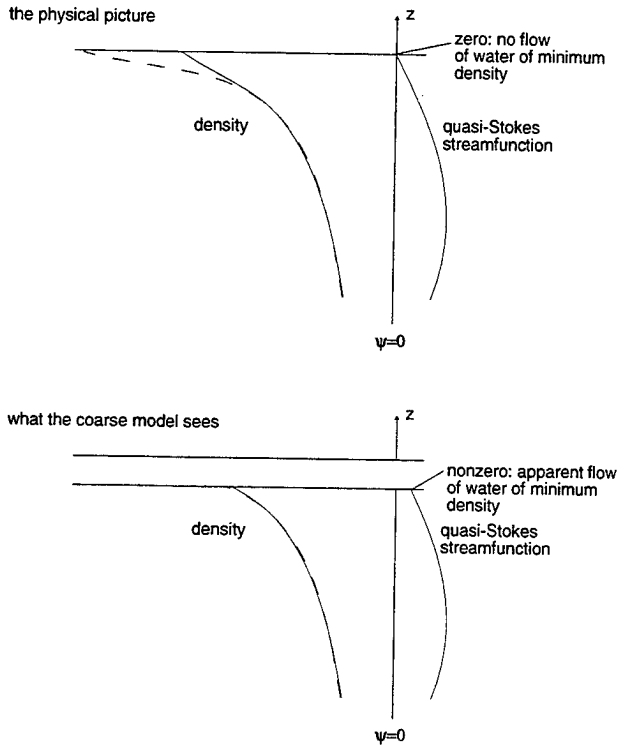


Figure 3. Misrepresentation of quasi-Stokes fluxes when the shallow layer is not resolved by the model

the MMD and (b) does not resolve the missing layer. This is investigated below.

3.2 Mass and available potential energy

The differences between the two densities have two important effects. The first is directly concerned with the interpretation of mean density. It is straightforward to see that the low-pass time filtered net mass in a water column, which is a uniquely defined value, is the same whether EMD or MMD is used:

$$\begin{aligned} \overline{\int \rho dz} &= \int \bar{\rho} dz \quad (\text{averaging at constant depth}) \\ &= \overline{\int \rho z_p d\rho} = \int \bar{\rho} z_p d\rho = \int \tilde{\rho} dz \\ &\quad (\text{averaging at constant density}). \end{aligned}$$

(As Fig. 1 suggests, $\tilde{\rho}$ is lighter at the surface, but the shortfall is made up at the floor.)

The same does *not* hold for potential energy, because of the noncommutative averaging operators on products of quantities. For small amplitude, the differences between EMD and MMD potential energies are $O(\alpha^2)$, and occur due to $O(\alpha^2)$ differences in the interior over a depth range of order unity, and $O(\alpha)$ differences over $O(\alpha)$ depth ranges.

It is shown in *Killworth* (2001) that

$$\Delta PE = \int_{-H}^0 z(\bar{\rho} - \bar{\rho}) dz < 0.$$

The difference between the two PE expressions lies in the variability, fundamentally a part of the MMD. It involves an integral in density space of the mean square depth fluctuations; the proof is straightforward, either from the *McDougall* (1998) formulae or by direct evaluation, and is not given here.

Thus the low-pass filtered potential energy of a fluid column (a uniquely defined quantity) is only correctly evaluated using EMD, and is consistently underestimated using the MMD; correction terms can be derived, and involve knowledge of the variability. This implies that energetics cannot consistently be produced for coarse models including parameterisations.

4. Creating a parameterisation

The *Gent and McWilliams* (1990) parameterisation has the virtue of simplicity and elegance, although to function globally various modifications have to be made, typically those of ‘tapering’ neutral density slopes when they become too large. Other parameterisations are usually less elegant, and so need more modifications. The depth-co-ordinate version of *Killworth* (1997) is briefly discussed here before comparisons are made in channel and global geometries.

The parameterisation uses linear theory, following *Robinson and McWilliams* (1974). Linear theory is not always a good predictor of the behaviour of a nonlinear eddying system, as *Edmon et al.* (1980) demonstrate, but it makes an indicative starting point (and holds in the same parameter range as the *McDougall* (1998) formulae). The system is assumed to be slowly varying in the horizontal, compared with the local deformation radius. The equations for small perturbations varying as $\exp ik(x \cos \theta + y \sin \theta - ct)$ are

$$(\tilde{u} - c) \left\{ \left(\frac{f^2 p_z}{N^2} \right)_z - k^2 p \right\} + \tilde{q}_y p = 0$$

$$\tilde{q}_y = \beta \cos \theta - \left(\frac{f^2}{N^2} \tilde{u}_z \right)_z \quad (q \text{ in direction } \theta)$$

$$\tilde{u} = u \cos \theta + v \sin \theta \quad (\text{velocity in direction } \theta)$$

In the case of a channel geometry, θ is identically zero.

All quantities can be expressed in terms of the pressure perturbation, for example:

$$\overline{v' \rho'} = -\frac{k \cos \theta}{2f \rho_0 g} \operatorname{Re}(ipp_z^*); \psi_2 = -\frac{k \cos \theta}{2f \rho_0^2 N^2} \operatorname{Re}(ipp_z^*)$$

$$\text{diffusivity } \kappa = \frac{kc_i}{2f^2 \rho_0^2} \left| \frac{p}{\tilde{u} - c} \right|^2$$

$$u^+ = -\frac{\kappa \sin \theta \tilde{q}_y}{f}; v^+ = \frac{\kappa \cos \theta \tilde{q}_y}{f}.$$

Thus to estimate Ψ , all that is needed is an approximate solution to the instability problem. The deformation radius is estimated from

$$C = \frac{1}{\pi} \int_{-H}^0 N(z) dz, a = C/f$$

and wavenumber from the *Eady* (1949) result

$$k = 0.51/a.$$

The angle θ is estimated from a crude solution maximising the growth rate based on standard deviations of u and v over depth. As shown by *Gill et al.* (1974), θ is small for east-west flow as in the channel case, but is near $\pi/2$ if u is small and v nonzero except in high latitudes where β is small. The approximate vertical structure of κ and p is found by two iterations of an approximate (small wavenumber) solution of the problem, and κ is scaled by Aac_i . Here A is an $O(1)$ constant: 3 is found to be optimal. The use of c_i , the imaginary part of the phase speed, ensures that there is no mixing where flow is stable, though there is always instability when v is non-zero, as *Pedlosky* (1987) shows.

The resulting streamfunction possesses two terms. The first is $-\kappa$ times the slope of the isopycnals normal to the angle of instability, which has similarities to the GM formulation. The second, extra term, has no such easy interpretation. Here the diffusivity κ varies three-dimensionally.

5. Channel model comparisons

The discussion in Section 3 suggests that the surface and floor conditions on the TRM in coarse resolution models are not obvious (Fig. 2 being a good example). This section examines solutions to two-dimensional emulations of the three-dimensional channel model of *Killworth* (1998), using a variety of formulations to represent the eddy terms, specifically to examine the boundary condition question.

The model covered a longitude range of 2.6° , a latitude range of 5.2° , centred on 30°N , and a shallow depth of 300 m. The grid spacings were 0.02° east-west, 0.018° north-south and 20 m vertically, with viscosities $50 \text{ m}^2 \text{ s}^{-1}$ (horizontal) and $5 \times 10^{-4} \text{ m}^2 \text{ s}^{-1}$ vertically and diffusivities $10 \text{ m}^2 \text{ s}^{-1}$ horizontally and 10^{-4} vertically. Starting from a narrow temperature front with uniform salinity, relaxation towards the initial temperature values in bands at north and south of the channel provided a source of potential energy. This method

has the advantage that there are no regions of unstable or neutral stratification, thus avoiding difficulties about parameterisations in such regions. Averages were computed over time and longitude over 7.25 years between days 300 and 2950.

Two-dimensional (latitude-depth) simulations were then run using a variety of two-dimensional parameterisations on a Cartesian grid, and the 4000-day computations (steady in almost all cases) compared with the averages from the three-dimensional run. Comparisons were made with the temperature field as a function of y (north) and z , and with the baroclinic u velocity.¹ The comparisons are not ideal. Like other published work, they are of Eulerian means only, and over a period probably an order of magnitude too short for a good statistical comparison. (However, the fields in Fig. 3 were visually unaltered by averaging over another period of similar length, so the statistics may be better than we suggest.)

Comparisons were made both visually and using a stringent measure of explained variance due to *Visbeck et al.* (1997). In each case, any free parameters in the parameterisation were adjusted to maximise the agreement with the eddy-resolving average. No parameterisation reproduced the ‘pushing forward’ of isopycnals in the MMD, so that direct comparisons with it are not useful.

Fig. 4 shows the three-dimensional time- and along-channel-averaged solution. To provide a yardstick for the various parameterisations, Fig. 5 shows the two-dimensional temperature field using only advection by the actual (two-dimensional) velocity fields plus a horizontal diffusivity of $200 \text{ m}^2 \text{ s}^{-1}$, which clearly gives results very close to the three-dimensional results.

The other parameterisations used were (in order of appearance in Figs. 6–10) the following:

GM90 (*Gent and McWilliams*, 1990, which has a constant diffusivity); Fig. 6

K97 (more properly, the depth co-ordinate version of *Killworth*, 1997, discussed earlier, which computes a variable diffusivity); Fig. 7

GMs (*Gent and McWilliams*, 1990, but with the streamfunction non-zero at the surface); Fig. 8

Ks (*Killworth* 1997, adapted as discussed below); Fig. 9

VP (computing $(v' \rho')_y$ directly from small-amplitude formulae, also discussed below); Fig. 10

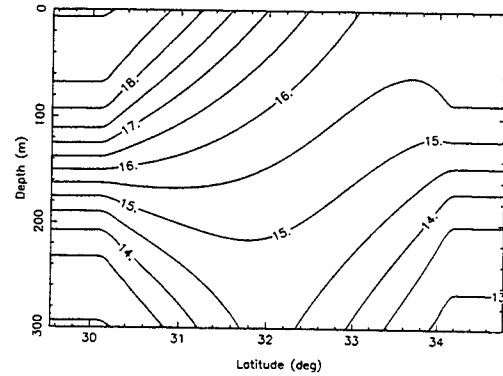


Figure 4. Contours of temperature ($^{\circ}\text{C}$; contour interval 0.5°C) for the time- and along-channel-averaged three-dimensional eddy-resolving calculation.

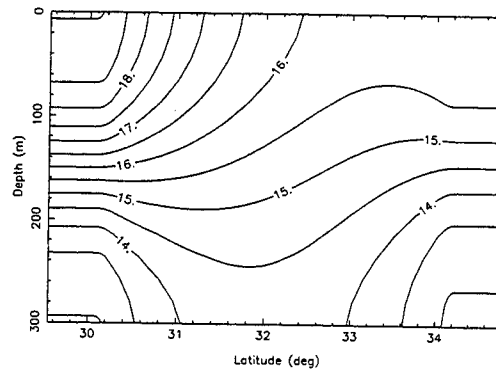


Figure 5. Two-dimensional simulation of Fig. 4, using a horizontal diffusivity of $200 \text{ m}^2 \text{ s}^{-1}$

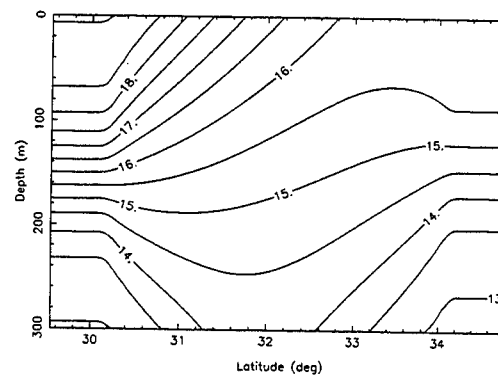


Figure 6. As Fig. 4, but using the *Gent and McWilliams* (1990) parameterisation, with $\kappa = 160 \text{ m}^2 \text{ s}^{-1}$

¹As discussed by *Killworth* (1998), the two-dimensional runs have no depth-averaged u field, so that only the baroclinic u can be compared. The barotropic u field, as noted by *Killworth*, plays a not inconsiderable role in the dynamics.

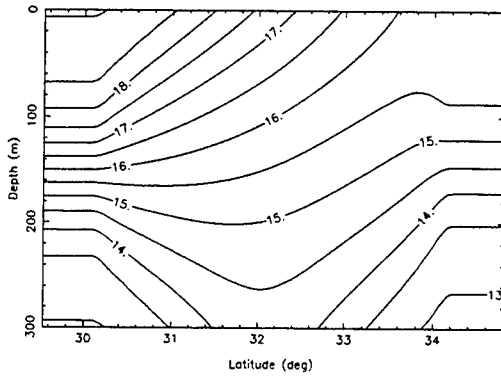


Figure 7. As Fig. 4, but using the Killworth (1997) parameterisation with $A = 3$.

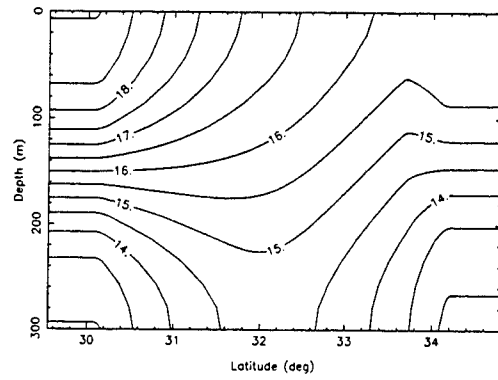


Figure 10. As Fig. 4, but using a direct parameterisation of $(v' \rho')$ _y directly from linear theory, with $A = 3$

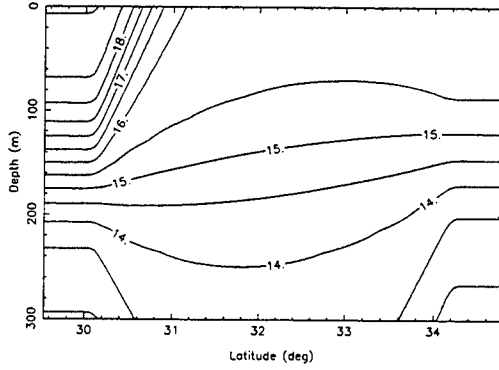


Figure 8. As Fib. 4, but using the Gent and McWilliams parameterisation modified so that the streamfunction does not vanish at surface or floor, with $\kappa = 1200 \text{ m}^2 \text{ s}^{-1}$

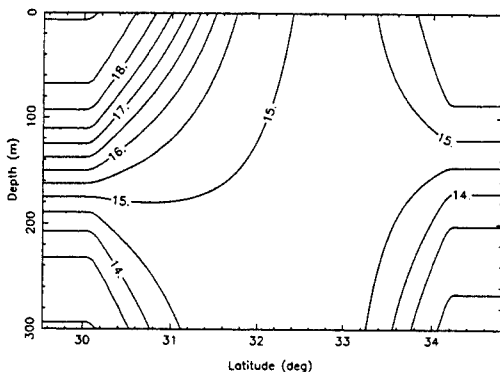


Figure 9. As Fig. 4, but using the Killworth (1997) parameterisation, modified so that the streamfunction does not vanish at surface or floor, with $A = 5$

The GM parameterisation is handled as in the MOM3 code (*Pacanowski and Griffies, 1999*), with the TRM streamfunction dropping to zero over the last grid point. The diffusivity κ is taken as a constant. The K97 parameterisation is as discussed earlier. The third parameterisation, GMs, attempts to emulate a nonzero value of streamfunction at surface and floor. This is not an easy task numerically, since many apparently straightforward approaches generated numerical instabilities. These included extrapolation of either the isopycnic slope or the streamfunction to the boundary, and computation of boundary values using one-sided interpolation formulae. A slightly unsatisfactory approach which set the streamfunction at surface (floor) to the values immediately below (above) was eventually used; the disadvantage being that the v^+ field vanished in the top and bottom grid points. The fourth parameterisation, Ks, does the same thing for K97.

The last parameterisation, for the EMD, directly evaluates $(v' \rho')_y$ (very similar answers are found for $(v' \rho')_y + (w' \rho')_z$) directly from small-amplitude theory, again using Killworth's (1997) scalings. Neither calculation requires boundary conditions since the normal velocity must vanish at boundaries. Direct attempts to parameterise the flux divergence usually suffer from Veronis effects (*Veronis, 1975*); however, this approach does not, since the terms have the same conservation properties (for the flux terms) as the original system.

The most accurate version of the GM90 parameterisation for this problem has a κ of $160 \text{ m}^2 \text{ s}^{-1}$, a little lower than that cited in Killworth (1998). The results for the GM90 (Fig. 6) are very similar to those of pure diffusion (5), although slightly less accurate in the u field. The similarity is surprising since the GM90 includes the strong northward (southward) advection near

the surface (floor) which is not present in the simple diffusive case.

The most accurate version of the K97 parameterisation (Fig. 7) has $A = 3$, as used in Killworth (1998) for the same problem. As Fig. 7 shows, this parameterisation is the only one to produce the ‘doming’ of the 15.5° isotherm near the northern boundary with any accuracy.

If w^+ is not required to vanish at surface and floor, then for this geometry the parameter values used hitherto are insufficient to reproduce the three-dimensional solution. This is because the high northward advection near-surface is now lacking. For the GM90 parameterisation (Fig. 8), κ needed to be increased an order of magnitude (to $1200 \text{ m}^2 \text{ s}^{-1}$) in order to reproduce an approximation to the three-dimensional fields. Although the temperature field looks reasonable, the corresponding velocity is poorly reproduced, due to the strong surface front near the southern boundary. A similar finding holds for the K97 parameterisation (Fig. 9). Thus permitting non-zero w^+ at surface and floor has not achieved a higher accuracy than maintaining zero w^+ , for this problem and choice of parameterisations.

The final parameterisation (VP) does not use the (v^+, w^+) formulation, but simply inserts a parameterisation for mixing directly. The results (Fig. 10) again show an accurate representation of the three-dimensional result.

In terms, then, of reproducing the *Eulerian* mean density, most schemes were successful. The K97 and VP were only marginally superior to the others, and schemes which permitted nonzero quasi-Stokes streamfunctions at the surface were quite inferior.

6. Global parameterisations

Although various theoretical suggestions for parameterisations have been made, relatively few have been tested in global models. GM has been shown to be robust (provided that tapering arrangements are included to prevent poor behaviour in weakly stratified environments). The K97 parameterisation is here extended to work globally, within the MOM3 code (Pacanowski and Griffies, 1999). This represents a TRM streamfunction as an extra term within the 3×3 isopycnic mixing tensor, as

$$\begin{pmatrix} A_I & 0 & A_IS_x + \psi_1 \\ 0 & A_I & A_IS_y + \psi_2 \\ A_IS_x - \psi_1 & A_IS_y - \psi_2 & A_IS^2 + A_D \end{pmatrix} \begin{pmatrix} \rho_x \\ \rho_y \\ \rho_z \end{pmatrix}$$

where S_x, S_y are the isopycnal slopes in the x and y directions, A_I is the isopycnal diffusion, and A_D the diapycnal diffusion.

First, there is also an element of tapering. In the expressions for ψ_1 and ψ_2 (not shown here) the first term, as noted earlier, includes an expression which is the product of the diffusivity and the isopycnal slope normal to the orientation of the fastest growing wavenumber. This slope is tapered in precisely the same way as in isopycnal mixing. Second, because the K97 formulation is essentially quadratic in shear (κ increases with shear, and operates on the shear) rather than linear as in GM, an abrupt start, e.g. from observed temperature and salinity, could lead to instabilities. The diffusivity – and hence streamfunctions – within a column are rescaled if necessary so that $\kappa < \kappa_{\max} = 10^4 \text{ m}^2 \text{ s}^{-1}$.

The role of baroclinic instability near the equator is unclear. While GM does not depend on position, any scheme involving q mixing must make choices near equator which reflect (a) that the role of baroclinic instability is less near the equator than at mid-latitude and (b) that it is the east-west density gradient which is predominantly creating flows, and so should be preferentially decreased by eddies. In addition, preliminary results analysing OCCAM output (de Vries and Drijfhout, personal communication) suggest that the TRM streamfunction is much larger near the equator than a simple constant-diffusion GM would predict.

In any event, an engineering ‘fix’ is required. At present, the Coriolis parameter \hat{f} is taken as the maximum of f and some f_{\min} (N. Hemisphere sign convention), and the deformation radius is defined from the mid-latitude and equatorial values by

$$a_{mid} = C / |\hat{f}|; a_{eq} = \sqrt{(C/2\beta)};$$

$$a = \min(a_{mid}, a_{eq}); k = 0.51/a_{mid}$$

which both avoids large wavenumbers and permits the approximate solution to continue to function reasonably.

The last modification is that velocity shears are consistently used in the calculation instead of density gradients, since thermal wind fails near the Equator. Near the surface these include the Ekman contribution. This is removed in the surface layer (the model has no mixed layer) by extrapolating the effective surface velocity from the next two depths.

The above changes have been implemented in MOM3, and run in a $2^\circ \times 2^\circ$ near-global configuration (77°S – 77°N) for one year only, since various features of the parameterisation remain under experiment. Monthly windstress and surface forcing were employed using standard MOM3 options. Typical parameter values were used, including an isopycnal diffusivity of $10^3 \text{ m}^2 \text{ s}^{-1}$. A parallel run used the GM formulation, which is an option in MOM3, with $\kappa = 10^3 \text{ m}^2 \text{ s}^{-1}$. This failed

after 3 months with erroneously high velocities in the Arctic. Results from the last snapshot files are shown from both runs. Normal diagnostics such as overturning streamfunction are not useful with such short runs, and for reasons of space only one elementary diagnostic is given here.

Figures 11 and 12 show the near-surface (level 1) horizontal TRM velocities superimposed on temperature contours for K97 and GM at the second level (depth 37.5 m) of the model, at the respective ends of their runs. Interestingly, neither set of TRM velocities are particularly small compared with the mean flow. The K97 TRM flow is predominantly east-west at latitudes less than about 40° . This is caused by the north-south orientation of the fastest growth rate, at least with the approximation used here. Another approximation, casting the continuous flow onto a 2-layer system and maximising growth rate over wavenumber and angle, followed by using this in the vertical iteration scheme used normally in K97, gives similar answers. It is possible that both approximations miss other, stronger growth rates at higher wavenumber. Gill *et al.* (1974) give some examples, but the indication from their work and from Pedlosky's (1987) book is that the orientation is expected to be close to north-south under most circumstances, as Fig. 11 suggests. Thus the restriction of the TRM flow to represent q mixing along a single orientation only yields TRM flows which are in the east-west direction in midlatitudes (despite the fact that density gradients are for the most part much stronger north-south than east-west in ocean data). Only in the subpolar areas is the β -effect reduced sufficiently that north-south TRM flows appear, e.g. in the Antarctic Circumpolar Current. However, the equatorial TRM flows in Fig. 11 are smooth and well-behaved, in contrast to the GM flows in Fig. 12 which are rather noisy. In the subtropics, both K97 and GM have weak TRM flows. However, in the subpolar region the GM TRM flows are more uniform and slightly stronger poleward than their K97 counterparts.

7. Discussion

The eddy parameterisation issue is far from resolved for many reasons. Even if the belief structure is adopted that mixing is done by eddies, it is unclear what should be mixed. The role of divergent and rotational fluxes remains unclear. Coarse models do not usually possess the vertical resolution to distinguish Eulerian and MM density near the surface and floor, save in weakly stratified regions.

Nonetheless, simple, clean parameterisations such as GM seem to improve much (but not all) of a coarse model response. There are indications that mixing co-

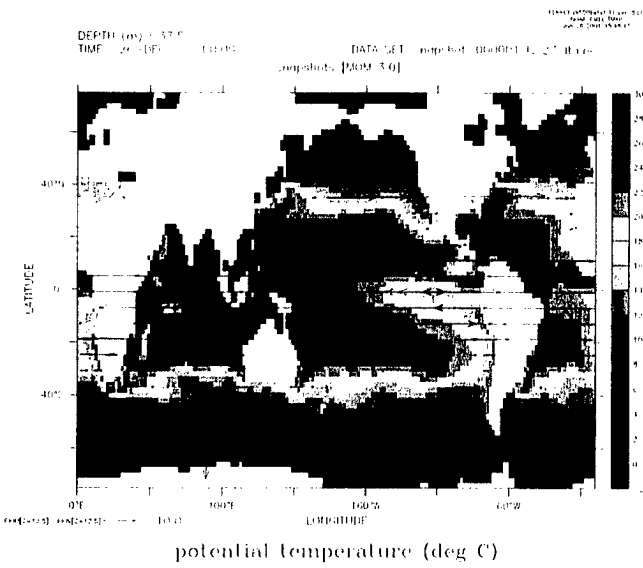


Figure 11. Global K97 results for near-surface temperature and horizontal TRM fluxes, after 1 year's integration

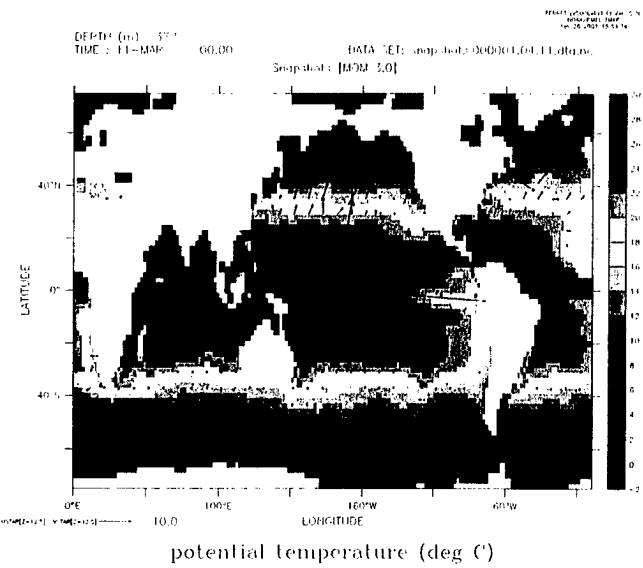


Figure 12. GM equivalent, after 3 months' integration

efficients vary spatially, but it is unclear whether this is O(1) in importance; recall that the channel simulations showed almost indistinguishable results between GM, with a constant diffusivity, and K97, where the diffusivity varied by two orders of magnitude. Similarly, more complicated parameterisation schemes appear to function as well as (sometimes better, sometimes not) simple schemes. Again it is unclear how important the simple-complex distinction is. Certainly it is not proven that any complicated scheme performs better globally than a simple one.

In the near future, careful intercomparisons of different schemes against trusted, statistically reliable three-dimensional eddy-resolving calculations will be required. This needs the community to invest in fine-resolution closed-gyre forced and free calculations run to some form of equilibrium to use as the testbeds for parameterisations. Some of these need to be explicitly time-varying, e.g. on seasonal scales. (Should seasonal variation be included within, or without, the averaging interval for eddy fluxes when applied, say, to annual mean coarse resolution modelling?) The community should also be encouraged to seek other ways of casting the parameterisation problem (e.g., the approach by Marshall in this volume).

Acknowledgments. My thanks to George Nurser for parts of Fig. 2.

References

- de Szoeke, R.A., and A.F. Bennett, Microstructure fluxes across density surfaces. *J. Phys. Oceanogr.*, 23, 2254-2264, 1993.
- Drijfhout, S.S., and W. Hazeleger, Eddy mixing of potential vorticity versus thickness in an isopycnic ocean model". *J. Phys. Oceanogr.*, 31, 481-505, 2001.
- Eady, E.T., Long waves and cyclone waves. *Tellus*, 1, 33-52, 1949
- Eby, M., and G. Holloway, Sensitivity of a large-scale ocean model to a parameterisation of topographic stress. *J. Phys. Oceanogr.*, 24, 2577-2588, 1994.
- Edmon, H.J., B.J. Hoskins, and M.E. McIntyre, Eliassen-Palm Cross Sections for the Troposphere. *J. Atmos. Sci.*, 37, 2600-2616, 1980.
- England, M.H., and S. Rahmstorf, Sensitivity of Ventilation Rates and Radiocarbon Uptake to Subgrid-Scale Mixing in Ocean Models. *J. Phys. Oceanogr.*, 29, 2802-2828, 1999.
- Gent, P.R., and J.C. McWilliams, Isopycnal mixing in ocean circulation models. *J. Phys. Oceanogr.*, 20, 150-155, 1990.
- Gent, P.R., J. Willebrand, T.J. McDougall, and J.C. McWilliams, Parameterizing Eddy-Induced Transports in Ocean Circulation Models. *J. Phys. Oceanogr.*, 25, 463-474, 1995.
- Gill, A.E., J.S.A. Green, and A.J. Simmons, Energy parti-
- tion in the large-scale ocean circulation and the production of mid-ocean eddies. *Deep-Sea Res.*, 21, 499-528, 1974.
- Gille, S.T., and R.E. Davis, The influence of mesoscale eddies on coarsely resolved density: An examination of subgrid-scale parameterisation. *J. Phys. Oceanogr.*, 29, 1109-1123, 1999.
- Greatbatch, R.J., Exploring the relationship between eddy-induced transport velocity, vertical momentum transfer, and the isopycnal flux of potential vorticity. *J. Phys. Oceanogr.*, 28, 422-432, 1998.
- Greatbatch, R.J., and K.G. Lamb, On parameterizing vertical mixing of momentum in non-eddy resolving ocean models. *J. Phys. Oceanogr.*, 20, 1634-1637,
- Killworth, P.D., On the parameterisation of eddy transfer. Part I: Theory. *J. Mar. Res.*, 55, 1171-1197, 1997.
- Killworth, P.D., On the parameterisation of eddy transfer. Part II: Tests with a channel model. *J. Mar. Res.*, 56, 349-374, 1998.
- Killworth, P.D., Boundary conditions on quasi-Stokes velocities in parameterizations. *J. Phys. Oceanogr.*, 31, 1132-1155, 2001.
- Knutti, R., T.F. Stocker, and D.G. Wright, The effects of subgrid-scale parameterizations in a zonally averaged ocean model. *J. Phys. Oceanogr.*, 30, 2738-2752, 2000.
- Lee, M.M., D.P. Marshall, and R.G. Williams, On the eddy transfer of tracers: advective or diffusive. *J. Mar. Res.*, 55, 483-505, 1997.
- McDougall, T.J., Three-dimensional residual mean theory. pp. 269-302 in *Ocean Modeling and parameterisation*, eds. E. P. Chassignet and J. Verron. Kluwer, 451 pp., 1998.
- McDougall, T.J., and P.C. McIntosh, The temporal-residual-mean velocity Part II: Isopycnal interpretation and the tracer and momentum equations. *J. Phys. Oceanogr.*, 31, 1222-1246, 2001.
- McIntosh, P.C., and T.J. McDougall, Isopycnal averaging and the residual mean circulation. *J. Phys. Oceanogr.*, 26, 1655-1660, 1996.
- Merryfield, W.J., and G. Holloway, Topographic stress parameterisation in a quasi-geostrophic barotropic model. *J. Fluid Mech.*, 341, 1-18, 1997.
- Pacanowski, R.C., and S.M. Griffies, MOM 3.0 manual, Geophysical Fluid Dynamics Laboratory, Princeton, NJ, 680 pp., 1999.
- Pedlosky, J., *Geophysical Fluid Dynamics*. 2nd ed. Springer Verlag, 710 pp., 1987.
- Redi, M., Oceanic isopycnal mixing by coordinate rotation. *J. Phys. Oceanogr.*, 12, 1154-1157, 1982.
- Roberts, M.J., and D.P. Marshall, On the validity of down-gradient eddy closures in ocean models. *J. Geophys. Res.*, 105, 28,613-28,628, 2000.
- Robbins, P.E., J.F. Price, W.B. Owens, and W.J. Jenkins, The importance of lateral diffusion for the ventilation of the lower thermocline in the sub-tropical North Atlantic. *J. Phys. Oceanogr.*, 30, 67-89, 2000.
- Robinson, A.R., and J.C. McWilliams, The baroclinic instability of the open ocean. *J. Phys. Oceanogr.*, 4, 281-294, 1974.

- Solomon, H., On the representation of isentropic mixing in ocean circulation. *J. Phys. Oceanogr.*, 1, 233-234, 1971.
- Treguier, A.M., Evaluating eddy mixing coefficients from eddy-resolving ocean models: A case study. *J. Mar. Res.*, 57, 89-108. 1999.
- Treguier, A.M., I.M. Held, and V.D. Lariehev, On the parameterisation of quasi-geostrophic eddies in primitive equation ocean models. *J. Phys. Oceanogr.*, 27, 567-580, 1997.
- Veronis, G., The role of models in tracer studies. In *Numerical Models of the Ocean Circulation*. Natl. Acad. of Sci., 133-146, 1975.
- Visbeck, M., J. Marshall, T. Haine, and M. Spall, On the specification of eddy transfer coefficients in coarse resolution ocean circulation models. *J. Phys. Oceanogr.*, 27, 381-402, 1997.
- Wilson, C., The role of mesoscale eddies and its representation in numerical models. PhD thesis, University of Liverpool, 128 pp., 2000.

This preprint was prepared with AGU's *LATeX* macros v4, with the extension package 'AGU++' by P. W. Daly, version 1.6a from 1999/05/21.

Are there principles to guide eddy parameterizations?

Greg Holloway

Institute of Ocean Sciences, Sidney, B.C., Canada

Abstract. A “list as long as your arm” has described the range of principles that may be attempted for possible eddy parameterization schemes. We feel uncomfortably an attitude of “try and see” whether any particular principle “works” in any particular application. This note summarises a discussion which followed the body of presentations at ‘Aha. We ask if principles from general physics, especially notions of the 2nd Law and entropy, can help clear a way. We ask if such ideas offer practical means to advance practical knowledge, and where major impediments may lie.

A discussion

These pages follow notes taken throughout ‘Aha Huliko’a, and from ideas discussed in part during the ‘Aha discussion time. The issues were framed by David Marshall and further by Peter Killworth. Surveying approaches that have been taken to providing a basis for eddy parameterization, one is daunted by the length of the list and the tentative character of the entries. What “should” eddies do? On the list we find (as examples)

- Eddies should flatten isopycnals.
- Eddies should maximally dissipate APE (available potential energy).
- Eddies should mix PV (potential vorticity).
- Eddies should mix layers thickness along layers.
- Eddies should maximally dissipate enstrophy.
- Eddies should reduce MKE (mean kinetic energy).
- Eddies should relax toward certain rectified (“neptune”) flows.
- ... and so on.

“Should” eddies do any of this? While we pose this list in terms of eddy parameterizations, another ‘Aha topic—stratified mixing—would generate yet another list. Are we dispirited? To “help,” Bill Young inserted an estimate of the number of active degrees of freedom in the ocean, suggesting 10^{28} “per cell” or 10^{37} if one includes biology. (There was a little dispute about numbers, but the key message is the numbers are “big”—far, far bigger than modern supercomputers are able to prognose, which are more like 10^7 to 10^9 .) Given such circumstances, Walter Munk asked if we deem the situation hopeless.

Answering Walter’s question depends upon what ocean modelling seeks to do. If our modelling project amounts to trying to invent a steam engine from molecular dynamics simulation of water vapour, it may well be hopeless in our lifetimes. If we would invent a steam engine based on thermodynamic functions, in part from empiricism and in part from statistical physics, it may not be so hopeless. Importantly we need to turn the huge number of degrees of freedom from threat to opportunity.

When we recognize that we’ve no ability nor practical interest to know the ocean in all its 10^{37} (or whatever) details, we naturally turn to probabilities of oceans. Mel Briscoe asked if we would predict evolution of probabilities distributions or if we limit attention to moments (expectations) from those probabilities. Framing issues in terms of moments might render the task manageable?

Lessons in our coffee cups?

A difficulty may be in part “cultural” insofar as we, as a community, have little orientation toward statistical physics, basing ocean dynamics instead on the classical mechanics of GFD amended with sundry by-guess-and-by-golly mixing coefficients. During ‘Aha two other themes recurred. We were reminded of the oft-cited stirring cream into coffee. And we were reminded of the influence Carl Eckart brought, seeking to base physical oceanography upon underlying physics. Although we cannot invite Carl’s direct input, we might seek in a spirit after Carl to ask why does cream in coffee turn brown. Here I only substitute my own comment. I should hope the answer is *not* because stirring causes enhanced mixing (diffu-

sion). I should hope the answer is that internal interactions within the coffee cup transition the probabilities of cream and of coffee to a distribution with higher entropy. Practically, the useful representation of this idea may well be that stirring leads to enhanced mixing. We see this as a result following from the underlying basis, after which we might quasi-empirically parameterize cups, teaspoons, manners of agitation, etc.

In the case of stirring cream into coffee, one is quite inclined merely to nod to the entropy discussion before proceeding directly to parameterizing the stirring-mixing. Were the topic of ocean eddies this simple, we would hardly speak of so simple a matter at ‘Aha Huliko’ā. But eddies are not simple. Then stirring-mixing intuitions, post-hoc modified by criteria such as listed at the outset of this note, are notoriously unreliable. Was there something more to learn in our coffee cups?

Dynamics of moments of probable seas

The following story is not yet clear, in part because the methods are so little explored. Here I make a sketch, indicating some research directions, practical results, relations to issues David and Peter framed, and current challenges.

First we embrace the idea that oceans are known only in probability. The detailed state of the ocean might be expressed in a state vector \mathbf{y} , whose dimension could well be 10^{37} , or whatever. We don’t know \mathbf{y} . We only speak of elemental probability $dP = P(\mathbf{y})d\mathbf{y}$ that the actual value of \mathbf{y} falls within a phase volume $d\mathbf{y}$ about any given \mathbf{y} . So far the discussion is aerie-faerie. What we really would like to access are moments of P , such as $\mathbf{Y} = \mathbf{y} dP$ with the integral over all \mathbf{y} . Importantly, the dimension of \mathbf{Y} need no longer be 10^{37} . We can “project out” as much of \mathbf{y} as we care not to consider, perhaps taking as only “lumped” (space-time averages) over \mathbf{y} . (My notation could be embellished!) Dimensions of \mathbf{Y} might be only 10^7 or 10^3 or maybe only 10. The key consideration is that these \mathbf{Y} are moments of probabilities. That distinction can get lost when, for example, we look at output of GCMs and see maps of velocities, temperatures, elevations or whatever. Even when we admit that the \mathbf{Y} are grid-cell-averaged variables, we tend still to speak of “velocity” rather than “velocity moment of probability of,” for example. So what?

The “so what” gets us when we write dynamic equations. Too easily we look up equations for velocity or temperature or such from textbooks, the only ambiguity arising from nonlinearities which, averaged over space-time volumes need some closure “approximations”. Were we to ask instead for the equation of motion of the temperature moment of the probable state, say, we might (1) grow tired and (2) pause on our way to the textbook. Until we are clear what are the dependent variables in the problem, assuming equations of motion is premature.

Next steps are, in part, familiar. Linear terms in equations of $d\mathbf{y}/dt$ commute with expectation and averaging operators, so linear terms in $d\mathbf{Y}/dt$ are “as usual”. Nonlinearities in $d\mathbf{y}/dt$ can be expressed in parts as corresponding nonlinearities among components of \mathbf{Y} , which again may look familiar following “usual” Reynolds averaging. And there is “more,” the “stuff” that connects the \mathbf{Y} to all the $P(\mathbf{y})$ which we do not know. $d\mathbf{Y}/dt = \mathbf{f}(\mathbf{Y}) + \mathbf{X}$, where “ \mathbf{f} ” express the “familiar” equations from textbooks and “ \mathbf{X} ” are the unknowns (of course).

Two routes to “ \mathbf{X} ”

The question of “ \mathbf{X} ” should be seen in context of nonequilibrium statistical mechanics, a gloriously unsolved problem. There are two avenues. I have tended to follow Lars Onsager, seeing in “ \mathbf{X} ” the generalized thermodynamic forcing $\mathbf{X} = \kappa \bullet \nabla_{\mathbf{Y}} S$ where $S = -\int \ln(P) dP$ is entropy, denotes the gradient of entropy with respect to the \mathbf{Y} , and κ supplies the coupling with which $\nabla_{\mathbf{Y}} S$ force $d\mathbf{Y}/dt$. As we don’t know P , hence we don’t know S , or $\nabla_{\mathbf{Y}} S$ and we don’t know κ , all this looks like useless window dressing. Maybe not. If we can determine some $\mathbf{Y} = \mathbf{Y}^*$ for which $\nabla_{\mathbf{Y}} S$ is small (in the sense much smaller than $\nabla_{\mathbf{Y}} S$ at the actual \mathbf{Y}) we could try to expand $\kappa \bullet \nabla_{\mathbf{Y}} S \approx \kappa \bullet \nabla^2_{YY} S \bullet (\mathbf{Y} - \mathbf{Y}^*)$. Call $\kappa \bullet \nabla^2_{YY} S = C$ so it doesn’t look so scary and we have only two problems: what is \mathbf{Y}^* and what is C ?

\mathbf{Y}^* is usually obtained by thinking about $d\mathbf{Y}/dt = \mathbf{f}(\mathbf{Y})$ under idealized circumstances, where we suppose many excited degrees of freedom while omitting all external forcing and internal dissipation (here regarded as “external” to dynamics of \mathbf{Y}). Dynamics sometimes are further simplified, e.g. to quasi-geostrophy, to make calculation of \mathbf{Y}^* tractable.

Subject to integrals of the motion of idealized $d\mathbf{Y}/dt = \mathbf{f}(\mathbf{Y})$, \mathbf{Y}^* is the \mathbf{Y} that maximizes S , i.e., $\nabla_{\mathbf{Y}}S = 0$.

Aside: This point has confused onlookers more than any other. The “theory” appears to be to maximize entropy. But such a result would only apply to a mathematical idealization (an isolated, unforced, nondissipative system) arguably far from Earth’s oceans. What needs be emphasized is that the *whole idea* is to use \mathbf{Y}^* as a means to access *non-zero* $\nabla_{\mathbf{Y}}S$ in order to complete the actual equations of motion of actual \mathbf{Y} . This is not a “maximum entropy” theory of anything.

Couplings C remain to be estimated and, in my work to date, are largely fudged. (\mathbf{Y}^* isn’t so great either.) At this time the point is not to find “the answer” (don’t I only wish!), but rather to identify the parts of the answer which may yield to successive efforts. At C I encounter the same kinds of semi-empirical, largely fudged, by-guess-and-by-golly estimations which are characteristic of our ability to represent oceanic turbulence.

Here let me mention a second approach to “X,” recently advanced by Joel Sommeria and colleagues. The idea is to find an expression for overall production of entropy, dS/dt , which can be maximized with respect to \mathbf{Y} . \mathbf{X} is then the force on $d\mathbf{Y}/dt$ which maximizes dS/dt . Although both the derivation of dS/dt and the assignment of constraints for maximizing dS/dt have raised new issues and new uncertainties, the maximum entropy production approach offers an important complement to the entropy gradient forcing which I have pursued. Happily, Igor Polyakov has compared the two approaches in a case of Arctic ocean modeling and finds pleasingly similar results.

So what?

A reader can well ask: if we are only stirring cream into coffee, isn’t this entropy talk a lot of bother? Indeed if only ocean eddies were as simple as the coffee, we should hardly bother. For much of what we do about ocean mixing parameterizations, effort to recast the discussion in terms of entropy calculus would (most likely) only append a superstructure over what—practically—we do anyway. On the other hand, during this ‘Aha there were two very different areas of research where results were not “simple” in the sense of coffee turning brown.

First recall David’s results in two-layer flow over topography. Numerical experiments do not lead to flattening isopycnals (reducing APE) and do not lead to uniform PV. What are eddies doing? The suggestion, which would need to be quantified suing actual code for actual geometry of David’s experiments, is that eddies move the two-layer flow to nearly the highest entropy it can attain. One approach may be, if the code David used can be run in dissipationless, conservative mode, then the model itself can be let run to reveal \mathbf{Y}^* . There is no reason \mathbf{Y}^* should reflect either minimum APE or uniform PV. When actual dissipation and forcing (if present) cause actual \mathbf{Y} to depart from \mathbf{Y}^* , eddy fluxes should arise in the model (testably) approximately proportionally to $\mathbf{Y}^* - \mathbf{Y}$.

Peter reminded us of an older illustration from statistical mechanics, recalling a hypothetical Arctic circulation (from myself from ‘Aha Huliko’a, 1993!) in which rectified (“neptune”) flows were induced by eddies. While those early results were barotropic, extensions to baroclinic flow apply to David’s case.

A different result that stirred controversy during ‘Aha was George Carnevale’s simulation of internal wave breaking. When George evaluated vertical buoyancy flux, $w b'$, where buoyancy $b = (p_0 - p)/p_0$ is the fractional deficit of density about reference p_0 and w is vertical velocity, spectral contributions were positive (upwards) over nearly all k . In particular $w b'(k) > 0$ over all k that were “turbulent” by any measure of “turbulence”. Because the experiments were stably stratified, mean $db/dz > 0$ and the turbulence from internal wave breaking forced b up the b -gradient (on average), “anti”-mixing. This is not stirring the cream into the coffee! What was wrong? Sentiments at ‘Aha ranged from (1) the experiments were performed improperly (wrong large scale forcing) to (2) analyzing outcome in “ z ” is wrong, and density coordinates should be used.

Or maybe George had things right, as indeed (I think) explains the differential diffusion which I report elsewhere in these proceedings. If George was right, why $w b'(k) > 0$? Again I’ll only speculate without direct access to George’s output, but I believe that wave “breaking” efficiently scatters potential energy PE (as b'^2) to higher wavenumbers. Over most k , the result was $PE > KE$ at each k . In these experiments without Coriolis, \mathbf{Y}^* for internal gravity modes equipartitions PE and KE. Thus $w b'(k) > 0$, converting PE \Rightarrow KE, is driven by $\mathbf{Y} - \mathbf{Y}^*$.

Does this help? A shortened list of guiding principles can read only “ $dS/dt > 0$ ” but the ongoing practical challenge is to put this idea to work. Progress is slow because the methods are unfamiliar. But I think tangible practical progress is being made.

Representing the effects of mesoscale eddies in coarse-resolution ocean models

T.J. McDougall

CSIRO Marine Research, Hobart, Tasmania – Australia

Abstract. Mesoscale eddies in the ocean mix fluid parcels in a way that is highly constrained by the stratified nature of the fluid—so much so that much of our intuition about ocean mixing comes from thinking in density coordinates. Temporal-residual-mean (TRM) theory provides the link between the different views that are apparent from averaging turbulent flow in height coordinates and in density coordinates. The TRM theory reduces the parameterization problem from three dimensions to two dimensions and it shows how the divergent part of the relevant eddy density flux is skew-symmetric in height coordinates and that the total advection velocity can be adiabatic. The Gent-McWilliams scheme is best interpreted as a scheme for implementing the temporal residual mean. The TRM theory has very specific things to say about how the tracers in coarse-resolution models should be interpreted and how the skew diffusion streamfunction should approach zero at boundaries. Here it is emphasized that the extra advection in the TRM theory is not the bolus transport because the extra TRM advection is non-divergent and diapycnal in character while the bolus velocity is divergent and adiabatic. When using eddy-permitting numerical model results to deduce a parameterization for mesoscale eddies, it is very important to use the full TRM theory, and in so doing, the parameterization task is simplified somewhat.

Introduction

Gent and McWilliams (1990) realized that when averaging in density coordinates, the thickness-weighted average velocity involves the bolus velocity, defined as the flow along density surfaces caused by the correlation between the horizontal velocity and the thickness between adjacent density surfaces. This motivated them to recommend additional terms in the tracer conservation equations. For several years these extra terms were interpreted as being undesirably diapycnal in character; for example it was emphasized that while the flow at any point in space was forced to be diapycnal by the mixing scheme, the area-averaged flow was not diapycnal.

The paper of *Gent et al.* (1995) pointed out the important property that the total flow (the sum of the resolved-scale and the eddy-induced velocity) did not have a diapycnal component. *Gent et al.* (1995) also cast the scheme in terms of a two-dimensional streamfunction and they pointed out the sign-definite sink of domain-averaged gravitational potential energy that the scheme provides. While the motivation of both *Gent and McWilliams* (1990) and *Gent et al.* (1995) came from the bolus velocity of den-

sity coordinates, it is argued below that the *Gent et al.* (1995) mixing scheme is not a parameterization for the bolus velocity but rather is a parameterization for the extra streamfunction of the temporal-residual-mean (TRM) theory. The TRM theory says unambiguously how one must interpret the variables that are carried by coarse-resolution ocean models and it also provides the physical justification for the tapering of the extra streamfunction to zero at ocean boundaries. We begin with a quick revision of the theory and then discuss some common misconceptions about the *Gent et al.* (1995) parameterization scheme.

The temporal-residual-mean approach

The averaging operator (the overbar) here is defined to be a low-pass temporal average and primed quantities are the deviations from this low-passed value. For simplicity the equation of state is taken to be linear (*McDougall and McIntosh*, 2001) have derived the TRM theory for a non-linear equation of state). The usual conservation equations for Eulerian-averaged density and for half the density variance are

$$\bar{\gamma}_t + \nabla \cdot (\bar{\mathbf{U}}\bar{\gamma}) = \bar{Q} - \nabla \cdot (\bar{\mathbf{U}}'\bar{\gamma}') \quad (1)$$

$$\bar{D}_t \bar{\phi} = \bar{Q}'\bar{\gamma}' - \bar{\mathbf{U}}'\bar{\gamma}' \cdot \nabla \bar{\gamma} + O(\alpha^3). \quad (2)$$

Here $\bar{\phi} \equiv 1/2 \bar{\gamma}'^2$ is half the density variance measured at a fixed point in space, and the terminology $O(\alpha^3)$ indicates terms that are of cubic or higher order in perturbation amplitude. Q represents the effects of molecular diffusion and small-scale mixing processes.

In order to develop residual-mean conservation equations that apply to unsteady flows we need to admit the possibility that the Eulerian-mean density may not be the most appropriate mean density to appear in the mean density conservation equation. For example, the Eulerian-mean density, $\bar{\gamma}(x, y, z, t)$, describes a density surface whose average height is not that of the original Eulerian averaging, z . The appropriate mean density is the one whose surface is, on average, at the height of the averaging. This density can be expressed in terms of $\bar{\gamma}$ and $\bar{\phi}$ by

$$\tilde{\gamma} = \bar{\gamma} - (\bar{\phi}/\bar{\gamma}_z)_z + O(\alpha^3). \quad (3)$$

The distinction here is between averaging density at a given height, z , and averaging the height of a given density surface $\gamma = \tilde{\gamma}$. McDougall and McIntosh (2001) used the density variance equation (2) to rewrite the mean density conservation equation (1) as

$$\begin{aligned} \tilde{\gamma}_t + \nabla \cdot (\bar{\mathbf{U}}\tilde{\gamma}) &= \bar{Q}^* - \nabla \cdot (\mathbf{U}^*\tilde{\gamma}) - \nabla \cdot \mathbf{M} + O(\alpha^3) \\ &= \bar{Q}^* - \nabla \cdot (\mathbf{A}\nabla\tilde{\gamma}) - \nabla \cdot \mathbf{N} + O(\alpha^3) \end{aligned} \quad (4)$$

where

$$\mathbf{U}^+ \equiv \nabla \times (\Psi \times \mathbf{k}) = \Psi_z - \mathbf{k}(\nabla_H \cdot \Psi), \quad (5)$$

$$\bar{Q}^* \equiv \bar{Q} + \left[-\frac{\bar{Q}'\bar{\gamma}'}{\bar{\gamma}_z} + \frac{\bar{Q}_z}{\bar{\gamma}_z} \left(\frac{\bar{\phi}}{\bar{\gamma}_z} \right) \right]_z, \quad (6)$$

$$\Psi = -\frac{\bar{\mathbf{V}}'\bar{\gamma}'}{\bar{\gamma}_z} + \frac{\bar{\mathbf{V}}_z}{\bar{\gamma}_z} \left(\frac{\bar{\phi}}{\bar{\gamma}_z} \right) + O(\alpha^3) \quad (7)$$

and \mathbf{M} and \mathbf{N} are non-divergent fluxes, expressions for which are given in *McDougall and McIntosh* (2001). The anti-symmetric tensor \mathbf{A} is defined in terms of the two components of the quasi-Stokes streamfunction, $\Psi = (\Psi^x, \Psi^y)$, as

$$\mathbf{A} \equiv \begin{bmatrix} 0 & 0 & \Psi^x \\ 0 & 0 & \Psi^y \\ -\Psi^x & -\Psi^y & 0 \end{bmatrix}. \quad (8)$$

Isopycnal Interpretation The upper line of equation (4) shows that the modified density, $\tilde{\gamma}$, is advected with the TRM velocity, $\bar{\mathbf{U}}^* = \bar{\mathbf{U}} + \mathbf{U}^+$, where both the Eulerian-mean velocity, $\bar{\mathbf{U}}$, and the quasi-Stokes velocity, \mathbf{U}^+ , are non-divergent. This equation shows that the TRM velocity only has a component through the modified density surfaces because of the modified diabatic source term, \bar{Q}^* . This is in contrast to the Eulerian-mean velocity, because (see (1)) the Eulerian-mean velocity, $\bar{\mathbf{U}}$, flows through the Eulerian-mean density surfaces due not only to the diabatic source term, \bar{Q} , but also due to the mesoscale eddy flux of density.

A Taylor series expansion shows that the horizontal component of the TRM velocity, $\bar{\mathbf{V}}^*$, is the same as the thickness-weighted horizontal velocity that is found by averaging in density coordinates, $\hat{\mathbf{V}}$. That is

$$\hat{\mathbf{V}} \equiv \hat{\mathbf{V}} + \mathbf{V}^B = \bar{\mathbf{V}} + \Psi_z + O(\alpha^3) = \bar{\mathbf{V}}^* + O(\alpha^3) \quad (9)$$

where $\hat{\mathbf{V}}$ is the horizontal velocity averaged on a density surface and the bolus velocity, $\mathbf{V}^B = \bar{\mathbf{V}}|_{\bar{\gamma}} z'_z$, is due to correlation between the horizontal velocity evaluated on the density surface and the thickness between density surfaces. Because of (9) it can be shown (McDougall and McIntosh, 2001) that the TRM conservation statement for density in the upper line of (4) is the same as is found by thickness-weighted averaging in density coordinates. The key to making this connection is to simply ignore the non-divergent flux, \mathbf{M} , in (4). The same Taylor series approach shows that the modified source term, \bar{Q}^* , is the thickness-weighted source term of density coordinates.

The skew diffusion approach in the second line of (4) is preferable numerically because the quasi-Stokes streamfunction is less spatially differentiated than in the advective approach of the upper line of (4) (*Griffies*, 1998). The skew diffusion of density is given by

$$-\mathbf{A}\nabla\tilde{\gamma} = -\tilde{\gamma}_z \Psi + \mathbf{k}(\Psi \cdot \nabla_H \tilde{\gamma})$$

and if it takes the *Gent et al.* (1995) form of the quasi-Stokes streamfunction, then the parameterization of mesoscale mixing that was used before GM90 is equivalent to retaining the horizontal component of this skew flux but ignoring the vertical component.

The Taylor series approach also furnishes a physical explanation of the quasi-Stokes streamfunction, Ψ ; at any height, z , Ψ is the contribution of temporal perturbations to the horizontal transport of water that is denser than $\tilde{\gamma}(z)$, the density of the surface having time-mean height z .

The TRM analysis procedure can also be applied to the tracer conservation equations (see *McDougall and McIntosh*, 2001) and one finds that the terms required to account for the mixing by mesoscale eddies are (i) the epi-neutral mixing of passive substance along the local neutral tangent plane (*Griffies et al.*, 1998) and (ii) the skew diffusion of tracer with the same skew diffusion tensor as for density, namely (8). It is this second term that corresponds to the *Gent and McWilliams* (1990) scheme. The extra mixing term can be regarded as an extra advection by the quasi-Stokes velocity, U^+ , or as the skew diffusion term, $-\nabla \cdot (\mathbf{A} \nabla \hat{\tau})$. An important new finding of the TRM theory is that the tracer conservation equation is written in terms of the thickness-weighted tracer of density coordinates, $\hat{\tau}$. This finding completes the correspondence between each of the terms in the TRM conservation equations and those that arise in density coordinates.

Cubic order terms and exact TRM equations. All of the above results are accurate to cubic order in perturbation amplitude. Recent unpublished work has demonstrated that away from solid boundaries the cubic terms that appear in the above expressions are quite small in comparison with the quadratic order terms that are to be parameterized. It has also been shown by *McDougall and McIntosh* (2001) that the conservation equations are exact if the quasi-Stokes streamfunction is in fact as described in the physical explanation above, rather than as defined in (7). The exact form of the quasi-Stokes streamfunction which leads to exact tracer conservation equations is

$$\Psi \equiv \overline{\int_z^{z+z'} \mathbf{V} dz''} \quad (10)$$

which is the temporal average of the vertical integral of the horizontal velocity integrated between the fixed height, z , and the instantaneous height of the density surface, $z + z'$. If we were ever clever enough to parameterize this form of the quasi-Stokes streamfunction, the job of parameterizing the skew diffusion by mesoscale eddies would be complete and the analogy with the equations found by averaging in density coordinates would be exact. The parameterization task for coarse-resolution ocean models is then to parameterize (10).

In summary, I believe the important practical features of the TRM theory are that

- (i) it demonstrates exactly how one must interpret the tracers that are carried by eddyless ocean models,
- (ii) it shows that the job of parameterizing the dynamical effects of mesoscale eddies is reduced to the task of parameterizing the quasi-Stokes streamfunction, (10) (or (7) in the approximate form), and

(iii) the physical interpretation of the quasi-Stokes streamfunction demands that it be tapered smoothly to zero at ocean boundaries (as opposed to other suggestions of having delta functions at the boundaries or of allowing flow through the boundaries).

The rest of this paper will attempt to correct some common misconceptions about the *Gent et al.* (1995) scheme, and then to make some remarks about the task of deducing eddy parameterizations from eddy-permitting models. But first, some comments are in order about other ways of averaging the conservation equations.

Comparison with other averaging approaches. There are other ways of averaging the conservation equations, for example the ‘effective’ approach following *Plumb and Mahlman* (1987), the “stochastic” approach of *Dukowicz and Smith* (1997), and the Lagrangian-mean approach of *Andrews and McIntyre* (1978). To date these approaches have proved less useful than the TRM theory for the following reasons. When the “effective” approach is extended to temporal averaging in three dimensions (as opposed to zonal averaging) one finds that the density which is advected by the “effective” velocity is devoid of a physical interpretation and, in particular, does not have a connection to averaging in density coordinates. Similarly, the extra two-dimensional streamfunction of the “effective” approach is written in terms of the first order approximations to Lagrangian displacements of fluid parcels and is similarly not amenable to an isopycnal interpretation.

In the stochastic approach both the eddy diffusion coefficient and the mean velocity are written in terms of probability density functions of the eddy motions, but what is missing is a connection to the Eulerian-mean velocity that is naturally carried by the momentum equations in a coarse-resolution model. Consequently, various authors have made different assumptions as to what the mean velocity in the “stochastic” approach might be, with correspondingly different interpretations of the mean variables and of the things that need to be parameterized. For example, the papers of *Dukowicz and Smith* (1997) and *Dukowicz and Greatbatch* (1999) both use the same ‘stochastic’ theory but have different conclusions because of different assumptions about the physical meaning of the ‘stochastic’ velocity.

The Lagrangian-mean theory of *Andrews and McIntyre* (1978) is beautifully general but the Lagrangian-mean velocity is divergent at leading order and the Lagrangian-mean tracer values are not readily observable. The beauty of the TRM theory is that it provides a one-to-one match between every variable (tracer, density and velocity) that arises in the TRM approach with the same variable that arises when averaging in density coordinates. Since the rate of oceanic diapycnal mixing is so small in relation to the lateral fluxes of mesoscale eddies, it is imperative to cleanly separate these two types of mixing processes, and all of our

intuition in this regard comes from thinking and averaging in density coordinates. It is this direct link to averaging in density coordinates that makes the TRM approach attractive for z -coordinate models.

Neither GM90 nor the quasi-Stokes velocity is the bolus velocity

The stated aim of *Gent and McWilliams* (1990) and of *Gent et al.* (1995) was to provide a parameterization for the bolus velocity and it was argued that this should be directed down the isopycnal gradient of thickness so that the extra horizontal velocity would be $\kappa(\nabla_H \tilde{\gamma}/\tilde{\gamma}_z)_z$. However, in order to make the streamfunction a locally determined quantity, and particularly to ensure a sign-definite sink of gravitational potential energy, the diffusivity was moved inside the vertical derivative so that the streamfunction of *Gent et al.* (1995) became $\kappa\nabla_H \tilde{\gamma}/\tilde{\gamma}_z$. This form also allowed the boundary conditions at the top and bottom of the ocean to be easily satisfied by having the diffusivity go to zero.

If one makes the most elementary assumption for the first term in (7) that the horizontal density flux is directed down the horizontal gradient of $\tilde{\gamma}$ with diffusivity κ (that is, $\overline{V' \gamma'} = -\kappa \nabla_H \tilde{\gamma}$) and if one ignores the second term in (7), the quasi-Stokes streamfunction becomes $\Psi = \kappa \nabla_H \tilde{\gamma}/\tilde{\gamma}_z$, exactly as we advocated in *Gent et al.* (1995) and as used by many subsequent authors. In this way, this simple Fickian assumption on the horizontal flux of density has enabled us to interpret the *Gent et al.* (1995) scheme as a particular parameterization for the quasi-Stokes streamfunction of the TRM theory. But from (9) it immediately follows that the GM90 and *Gent et al.* (1995) schemes are not parameterizations for the bolus velocity because the horizontal component of the bolus velocity is different from the horizontal quasi-Stokes velocity, Ψ_z , by the amount $\bar{V} - \tilde{V}$ which is the difference in the horizontal velocity averaged at constant depth and at constant density.

The movement of the diffusivity inside the vertical derivative in the *Gent et al.* (1995) expression for the eddy-induced horizontal velocity, $(\kappa \nabla_H \tilde{\gamma}/\tilde{\gamma}_z)_z$, far from being a weakness of *Gent et al.* (1995) because of the weaker connection to the bolus transport, is actually a very important strength of the GM90 scheme. Consider for example the situation where the slopes of density surfaces are independent of height so that the original idea of down-gradient thickness flux would mean that the eddy-induced horizontal velocity was zero at all heights except for delta functions of eddy-induced horizontal velocity at the top and bottom.

Finite-amplitude baroclinic instability operating on such an initial condition will lead to the simultaneous relaxation (in the mean) of isopycnals throughout the entire water column, not merely at the boundaries of the domain. The TRM approach can achieve this property by allowing the diffusivity, κ , to be a function of height. In this way the quasi-Stokes velocity of the TRM theory can achieve a more realistic parameterization of baroclinic instability than is possible with a down-gradient scheme. This type of depth-dependent diffusivity is being pursued by *Killworth* (2001). The same criticism applies to an up-gradient potential vorticity mixing scheme which has often been suggested as a parameterization for Ψ_z . When there is no epineutral gradient of potential vorticity in the whole water column, we do not expect baroclinic instability to cause mean motion and relaxation of isopycnals only in delta function boundary layers as would occur with a potential vorticity parameterization.

In addition to the issue of having the diffusivity inside the vertical derivative, there are two other compelling reasons why the eddy-induced velocity of *Gent et al.* (1995) (which we are interpreting as the quasi-Stokes velocity of the TRM theory) is neither the bolus velocity nor the down-gradient thickness flux. The first of these is that the quasi-Stokes velocity is three-dimensionally non-divergent whereas the epineutral flux of thickness is divergent (see *McDougall and McIntosh*, 2001). The second reason is that the bolus velocity and the epineutral thickness flux have no diapycnal component, whereas the quasi-Stokes velocity has a large diapycnal component (see for example, Figure 6b of *Hirst and McDougall*, 1998). These differences arise through the use of the streamfunction (that is, the continuity equation) to construct the vertical component of both the quasi-Stokes velocity and of the eddy-induced velocity in the *Gent et al.* (1995) scheme.

The task of parameterizing the effects of mesoscale eddies is very different for isopycnal models than for height-coordinate models. In an isopycnal model the extra horizontal velocity that is needed is indeed the bolus velocity. The sum of the bolus velocity and the resolved-scale horizontal velocity of an isopycnal model, \tilde{V} , gives the thickness-weighted velocity of isopycnal coordinates, \hat{V} . In sharp contrast to the large diapycnal component of the quasi-Stokes velocity of height-coordinate models, the bolus advection that is needed in isopycnal models has zero diapycnal component (see *McDougall and McIntosh*, 2001).

Some issues in parameterizing Ψ

It is argued above that the effects of mesoscale eddies enter the tracer conservation equations through (i) the symmetric diffusion tensor which represents the passive

epineutral mixing of tracer, and (ii) the skew diffusion tensor (8) whose elements are the quasi-Stokes streamfunction, (10), of TRM theory. Some authors have suggested that Ψ_z should be parameterized as being up the gradient of potential vorticity (measured along the local neutral direction). Apart from the small meridional change in the Coriolis parameter, this suggestion is the same as the down-gradient thickness idea. *McDougall and McIntosh* (2001) have argued that irrespective of whether or not these suggestions turn out to be a good parameterization for Ψ_z , they leave open the question of the vertical component of the quasi-Stokes velocity. Equivalently, this down-potential vorticity parameterization does not address the issue of how Ψ_z behaves at the top and bottom boundaries of the ocean. *McDougall and McIntosh* (2001) have shown that this uncertainty means that the contribution of this parameterization to the meridional flux of heat is quite uncertain. This uncertainty is equivalent to the practical difficulty that arises when parameterizing the bolus velocity in coarse-resolution layered ocean models where, in practice, the interface height is smoothed rather than actually introducing a parameterized bolus velocity to the model. The key to overcoming this considerable uncertainty in the meridional heat flux is to parameterize the quasi-Stokes streamfunction, Ψ_z , itself, rather than its vertical derivative.

There are other rather general problems with the down-gradient potential vorticity parameterization. *Cummins* (2000) has pointed out that such a parameterization can lead to a fictitious torque which spontaneously generates angular momentum while *Adcock and Marshall* (2000) have shown that energy conservation is violated as the scheme attempts to homogenize potential vorticity (or thickness) along neutral density surfaces.

While our skill in parameterizing the quasi-Stokes streamfunction is clearly in its infancy, some eddy-permitting models are showing intriguing results. For example, *Treguier* (1998) has analyzed a primitive equation model for the zonally averaged bolus velocity and has found a small diffusivity for use in the quasi-Stokes diffusivity. Such a result would be expected to have some benefits so long as the models remain stable with these smaller diffusivities. The two benefits that come to mind are avoiding the slowing of the horizontal circulation of the subtropical gyres that occurs with the larger values of the quasi-Stokes diffusivity, and reducing the intrusion of Antarctic Bottom Water into the North Atlantic which is too strong with present values of the quasi-Stokes diffusivity (*Hirst and McDougall*, 1998).

Given the above problems with both the down-gradient thickness and the up-gradient potential vorticity schemes, it seems that the way forward for the foreseeable future will

be to stay with the general *Gent et al.* (1995) form of the quasi-Stokes streamfunction, $\Psi = \kappa \nabla_H \tilde{\gamma} / \tilde{\gamma}_z$, but to allow the diffusivity, κ , to be a function of space.

It must be pointed out (following *Tandon and Garrett*, 1996) that the adiabatic nature of the TRM velocity implies that the eddy kinetic energy of mesoscale eddies cannot be dissipated in the ocean interior but rather must be dissipated near the upper and/or lower boundaries. This seems a rather special restriction on the energy budget.

When seeking to determine a parameterization for the quasi-Stokes streamfunction from the output of eddy-permitting ocean models, it is important to use the correct TRM conservation equations. For example, *Gille and Davis* (1999) have analyzed an eddy-permitting primitive equation model of a zonal channel with respect to the conservation of the Eulerian-mean density, $\bar{\gamma}$, rather than the modified density of (4), and they also considered only the first term in the expression, (7), for the quasi-Stokes streamfunction. Analyzing model data in this way leaves the extra forcing term,

$$\left(-\overline{U' \gamma} \cdot \nabla \bar{\gamma} / \bar{\gamma}_z \right)_z , \quad (11)$$

in the density conservation equation and *Gille and Davis* (1999) conclude that this term is too large to ignore and needs to be parameterized. *McDougall and McIntosh* (2001) have shown that this extra source term does not arise when the full residual-mean transformation is performed. Rather, all that needs to be parameterized is the quasi-Stokes streamfunction.

Similarly, *Roberts and Marshall* (2000) have examined the divergent part of the horizontal density flux and found that it was directed as much perpendicular to the mean density gradient as down the mean gradient. Unpublished work has shown (at least for the Southern Ocean) that while this is true of the first term in the expression, (7), when the second term is also included, the full quasi-Stokes streamfunction is much closer to being directed down the mean density gradient. This supports the contention that it is very important in efforts aimed at finding parameterizations for mesoscale turbulence that the conservation equations are carefully and accurately derived. When all the terms are kept, as has been done in the above TRM equation set, the parameterization task seems to be more promising than when leading order terms are ignored.

Conclusions

The intimate relationship between averaging in density coordinates and the TRM conservation equations is what provides the satisfying physical interpretations for the various quantities that arise in the TRM approach. For example, the quasi-Stokes streamfunction, (10), provides a com-

pelling link between the coordinate systems since it is the contribution of temporal perturbations to the horizontal transport of water that is denser than $\tilde{\gamma}(z)$, the density of the surface having time-mean height z . I have argued that the parameterization task we face is to parameterize the quasi-Stokes streamfunction; not the horizontal bolus velocity, not the down-gradient flux of thickness and not the up-gradient flux of potential vorticity. While it might seem tedious to keep track of all the leading order terms (second order in perturbation quantities) in the conservation equations, when seeking to parameterize mesoscale eddies, it is becoming more obvious that we cannot afford to ignore these leading order terms.

References

- Adcock, S.T., and D.P. Marshall, interactions between geostrophic eddies and the mean circulation over large-scale bottom topography. *J. Phys. Oceanogr.*, 30, 3223-3238, 2000.
- Andrews, D.G., and M.E. McIntyre, An exact theory of nonlinear waves on a Lagrangian-mean flow. *J. Fluid Mech.*, 89, 609-646, 1978.
- Cummins, P.F., Remarks on potential vorticity mixing over topography and momentum conservation. *Deep-Sea Res.*, 47, 737-743, 2000.
- Dukowicz, J.K., and R.J. Greatbatch, The bolus velocity in the stochastic theory of ocean turbulent tracer transport. *J. Phys. Oceanogr.*, 29, 2232-2239, 1999.
- Dukowicz, J.K., and R.D. Smith, Stochastic theory of compressible turbulent fluid transport. *Phys. Fluids*, 9, 3523-3529, 1997.
- Gent, P. R., and J. C. McWilliams, Isopycnal mixing in ocean circulation models. *J. Phys. Oceanogr.*, 20, 150-155, 1990.
- Gent, P.R., J. Willebrand, T.J. McDougall, and J.C. McWilliams, Parameterizing eddy-induced tracer transports in ocean circulation models. *J. Phys. Oceanogr.*, 25, 463-474, 1995.
- Gille, S.T., and R.E. Davis, The influence of mesoscale eddies on coarsely resolved density: An examination of subgrid-scale parameterization. *J. Phys. Oceanogr.*, 29, 1109-1123, 1999.
- Griffies, S.M., The Gent-McWilliams skew-flux. *J. Phys. Oceanogr.*, 28, 831-841, 1998.
- Griffies, S.M., A. Gnanadesikan, R.C. Pacanowski, V. Larichev, J.K. Dukowicz, and R.D. Smith, Isoneutral diffusion in a z-coordinate ocean model. *J. Phys. Oceanogr.*, 28, 805-830, 1998.
- Hirst, A.C., and T.J. McDougall, Meridional overturning and dianeutral transport in a z-coordinate ocean model including eddy-induced advection. *J. Phys. Oceanogr.*, 28, 1205-1223, 1998.
- Killworth, P.D., Boundary conditions on quasi-Stokes velocities in parameterizations, submitted to *J. Phys. Oceanogr.*.
- McDougall, T.J., and P.C. McIntosh, The temporal-residual-mean velocity. Part II: Isopycnal interpretation and the tracer and momentum equations. *J. Phys. Oceanogr.*, 31, 1222-1246, 2001.
- Plumb, R.A., and J.D. Mahlman, The zonally-average transport characteristics of the GFDL general circulation/transport model. *J. Atmos. Sci.*, 44, 298-327, 1987.
- Roberts, M.J., and D.P. Marshall, On the validity of downgradient eddy closures in ocean models. *J. Geophys. Res.*, 105, 28,613-28,627, 2000.
- Tandon, A., and C. Garrett, On a recent parameterization of mesoscale eddies. *J. Phys. Oceanogr.*, 26, 406-411, 1996.
- Treguier, A.M., Evaluating eddy mixing coefficients from eddy resolving ocean models: a case study. *J. Mar. Res.*, 57, 89-108, 1998.

Viscosity parameterization and the Gulf Stream separation

Eric P. Chassignet and Zulema D. Garraffo

Rosenstiel School of Marine and Atmospheric Science, University of Miami, Miami, Florida - USA

Abstract. Recent advances in computer architecture allow for numerical integration of state-of-the-art ocean models at basin scale with a grid resolution of $1/10^\circ$ or higher. At that resolution, the Gulf Stream's separation at Cape Hatteras is well simulated, but substantial differences from observations are still observed in its path, strength, and variability. Several high resolution ($1/12^\circ$) North Atlantic simulations performed with the Miami Isopycnic Coordinate Ocean Model (MICOM) are discussed and the results suggest that, even with such a fine grid spacing, the modeled large scale circulation is still quite sensitive to choices in forcing and viscosity parameterization.

1. Introduction

Until recently, most ocean general circulation models (OGCMs) had great difficulties in reproducing the basic pattern of the Gulf Stream. The modeled Gulf Stream had in general the tendency to separate far north of Cape Hatteras and to form a large stationary anticyclonic eddy at the separation latitude [see *Dengg et al.* (1996) for a review]. Simulations with grid resolution of $1/10^\circ$ or higher are now able to realistically represent the Gulf Stream separation (*Paiva et al.*, 1999; *Smith et al.*, 2000; *Hurlbert and Hogan*, 2000). These results support the view that a good representation of the inertial boundary layer is an important factor in the separation process (*Özgökmen et al.*, 1997). The fine mesh size also resolves the first Rossby radius of deformation everywhere in the subtropical gyre (marginally in the subpolar gyre), therefore providing a good representation of baroclinic instability processes (*Paiva et al.*, 1999; *Smith et al.*, 2000).

However, despite the more realistic behavior, the representation of the Gulf Stream separation differs from one simulation to the next, sometimes significantly. This paper discusses some of the factors influencing the modeled circulation in the Miami Isopycnic Coordinate Ocean Model (MICOM). It will be shown that even with such a fine grid spacing, the viscosity parameterization remains of importance for the modeled large scale ocean circulation.

2. Mean sea surface height fields

Figures 1 and 2 display the mean sea surface height (SSH) from two MICOM simulations with an horizon-

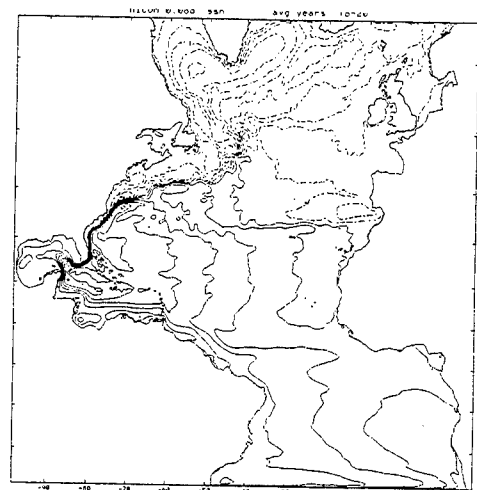


Figure 1. 3-year-mean model SSH field for the $1/12^\circ$ COADS-forced MICOM. The viscosity operator is a combination of biharmonic ($A_4 = V_D \Delta x^3$, with $V_D = 1$ cm/s) and Laplacian ($A_2 = \max[.1 \Delta x^2 \times \text{deformation tensor}, V_D \Delta x]$, with $V_D = .5$ cm/s).

tal resolution of $\Delta\phi = 1/12^\circ$. The horizontal grid is defined on a Mercator projection with the resolution given by $\Delta\phi \times \Delta\phi \cos(\phi)$, where ϕ is the latitude. The first simulation (Fig. 1), configured from 28°S to 65°N , was integrated with MICOM for 20 years using monthly climatological COADS-based forcing (including freshwater flux) plus a weak restoration to monthly climatological surface salinity (*Paiva et al.*, 1999, *Garraffo et al.*, 2001a,b). The second simulation (Fig. 2), configured from 28°S to 70°N , including the Mediterranean Sea, was first spun-up for 6 years with MICOM us-

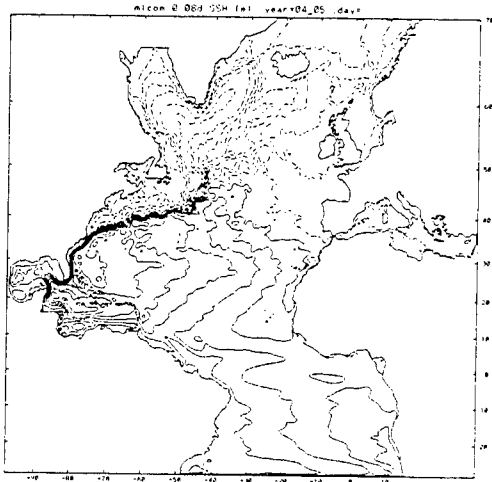


Figure 2. 2-year-mean model SSH field for the $1/12^\circ$ ECMWF-forced MICOM. The viscosity operator is the same as for the COADS-forced run (see caption of Fig. 1).

ing monthly climatological ECMWF atmospheric fields (including freshwater flux) plus a weak restoration to monthly climatological surface salinity, and is presently further integrated using 6-hourly ECMWF forcing from 1979 to 2000.

In both simulations, the simulated Gulf Stream path agrees well with observations until the location of the New England Seamounts chain. Eastward of the chain, the ECMWF-forced run (Fig. 2) exhibits a path that agree well with observations everywhere. In the COADS-forced run (Fig. 1), the path east of the New England Seamounts chain is displaced northward by about 1° to 2° . This northward shift in the COADS-forced run is associated with a larger than observed seasonal migration of the path [observed annual signal of up to 100 km, north of the mean from August to November and south of the mean from March to June (A. Mariano, 1999, personal communication)]. This higher than observed seasonal shift results primarily from the fact that the MICOM bulk Kraus-Turner mixed layer is on the average deeper in the COADS-forced run than in the ECMWF-forced run (not illustrated). The deepening of the mixed layer in winter induces a decrease in the magnitude of the upper layer velocities because MICOM's mixed layer does not allow vertical shear (Kraus and Turner, 1967). A deeper mixed layer in the COADS-forced run therefore implies a Gulf Stream that is less inertial than in the ECMWF-forced run. The end result is that in the latter run, the modeled Gulf Stream path agrees well with observations and does not exhibit a higher than observed seasonal shift in latitude eastward of the New England seamounts chain.

The impact of the seamounts on the Gulf Stream path and variability was further investigated in a 3-year sensitivity experiment with COADS forcing in which the bottom topography was modified by removing the New England seamounts. The impact of removing the seamounts on the Gulf Stream path was found to be negligible (not illustrated).

3. Importance of the viscosity parameterization

When the grid spacing reaches a certain threshold, the energy cascade from the small to the large scales should be properly represented by the model physics. Dissipation should then be prescribed for numerical reasons only in order to remove the inevitable accumulation of enstrophy on the grid scale. This is the reason why higher order operators such as the biharmonic form of friction have traditionally been favored in eddy-resolving or eddy-permitting numerical simulations (*Holland*, 1978; *Bryan and Holland*, 1989; *Smith et al.*, 2000). Higher order operators remove numerical noise on the grid scale and leave the larger scales mostly untouched by allowing dynamics at the resolved scales of motion to dominate the subgrid-scale parameterization (*Griffies and Hallberg*, 2000).

In addition to numerical closure, the viscosity operator can also be a parameterization of smaller scales. One of the most difficult tasks in defining the parameterization is the specification of the Reynolds stresses in terms of only the resolved scales' velocities [see *Pedlosky* (1979) for a review] and the common practice has been to assume that the turbulent motion acts on the large scale flow in a similar manner as molecular viscosity. However, the resulting Laplacian form of dissipation removes both kinetic energy and enstrophy over a broad range of spatial scales, and its use in numerical models in general implies less energetic flow fields than in cases with more highly scale-selective dissipation operators. In order to assess the impact of the dissipation operator on the Gulf Stream system, several sensitivity experiments were performed with MICOM using Laplacian and biharmonic operators for the viscosity in the momentum equations.

The mean SSH of two simulations performed with two different magnitudes of the biharmonic viscosity coefficient are displayed in Figs. 3 and 4, respectively (COADS-forced run). When a relatively small value of the biharmonic viscosity coefficient is used (see caption of Fig. 3 for details), the western boundary current is seen to separate from the coast early at the Charleston bump before Cape Hatteras (Fig. 3). A similar result was observed with the $1/10^\circ$ Los Alamos Parallel Ocean Model (POP) during the spin-up phase in which both

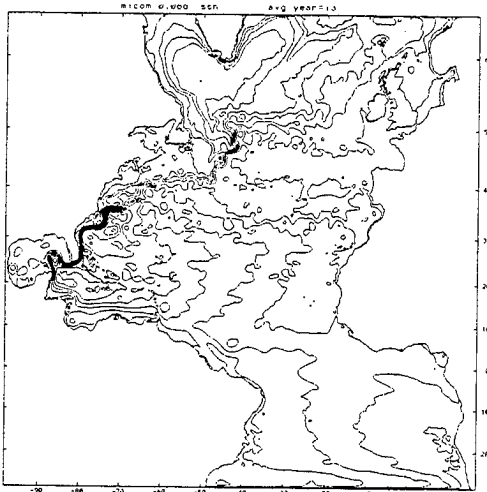


Figure 3. 1-year-mean model SSH field with a biharmonic viscosity operator; $A_4 = \max [0.1 \Delta x^4 \times \text{deformation tensor}, V_D \Delta x^3]$, with $V_D = 1 \text{ cm/s}$.

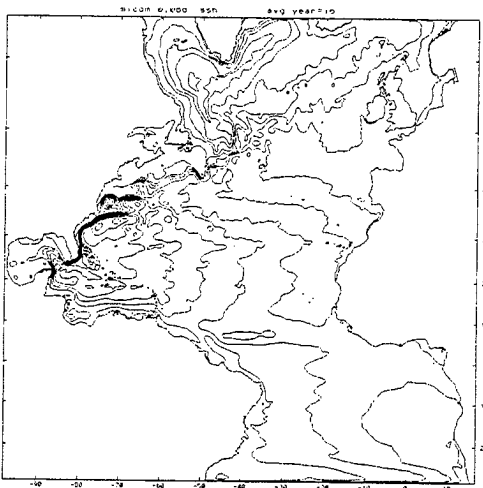


Figure 4. 1-year-mean model SSH field with a biharmonic viscosity operator; $A_4 = \max [\Delta x^4 \times \text{deformation tensor}, V_D \Delta x^3]$, with $V_D = 2 \text{ cm/s}$.

the viscosity and diffusion had to be increased by a factor of 3 in order to eliminate this feature (*Smith et al., 2000*). An increase in the magnitude of the biharmonic viscosity operator in MICOM did indeed also eliminate the early detachment seen in Fig. 3, but it also led to the establishment of a permanent eddy north of Cape Hatteras (Fig. 4). This eddy results from a series of warm core (anticyclonic) rings that propagate westward, collide with the western boundary, and are only weakly dissipated by the biharmonic viscosity operator. This behavior is reminiscent of other simulations performed with biharmonic dissipation (*Smith et*

al., 2000). The fact that this permanent eddy only appears with biharmonic operators seems to indicate an incorrect representation of the eddy/mean flow and/or of the eddy/topography interactions, possibly because of the scale selectiveness of the higher order operator that allows features that are marginally resolved by the grid spacing. In all simulations, the grid spacing is such that both the inertial and the viscous boundary layers are resolved (very well for the inertial and minimally for the viscous).

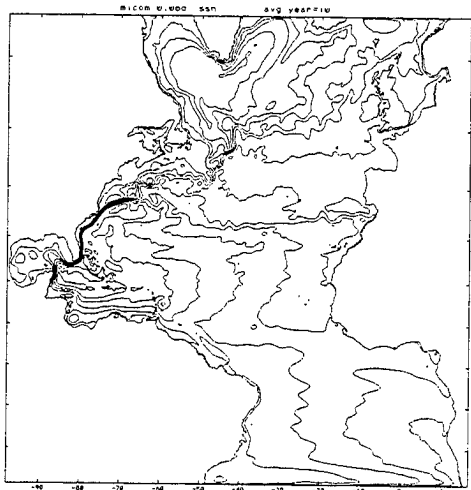


Figure 5. 1-year-mean model SSH field with a Laplacian viscosity operator; $A_2 = \max [0.1 \Delta x^2 \times \text{deformation tensor}, V_D \Delta x]$, with $V_D = 1 \text{ cm/s}$.

The mean SSH of the simulation performed with the Laplacian viscosity operator is displayed in Fig. 5 (COADS-forced run). The magnitude of the Laplacian viscosity coefficient is the minimum value needed for numerical stability. In that simulation (Fig. 5), the Gulf Stream separates well from the coast, but does not penetrate further than the New England Seamounts.

Overall, neither the Laplacian nor the biharmonic viscosity operator alone provide satisfactory results regarding the Gulf Stream system behavior. With the biharmonic operator, eddies are found to retain their structure for longer periods of time than with a Laplacian operator, but with undesirable effects on several features of the large scale circulation. With the Laplacian operator, the western boundary current and its separation are well represented, but with a weak penetration of the Gulf Stream.

With a Laplacian (harmonic) dissipation operator, the evolution of a wave $c(t)e^{ikx}$ is damped exponentially with a spin-down time $\tau_2 = A_2^{-1} \left(\frac{2}{\Delta x} \sin \left(\frac{k \Delta x}{2} \right) \right)^{-2}$. In the case of a biharmonic operator, the spin-down time is $\tau_4 = A_4^{-1} \left(\frac{2}{\Delta x} \sin \left(\frac{k \Delta x}{2} \right) \right)^{-4}$. For comparison purposes,

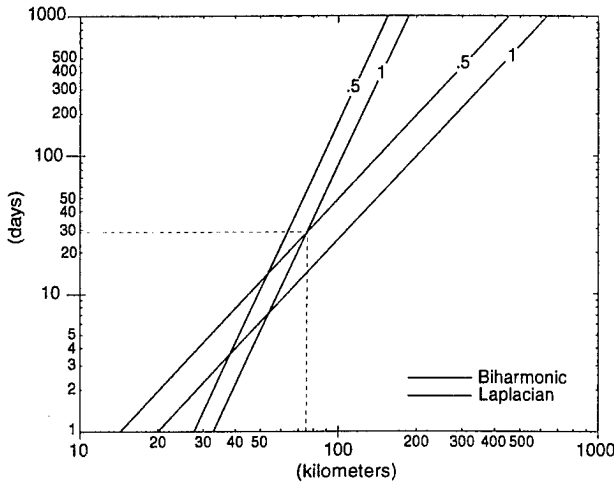


Figure 6. Laplacian and biharmonic decay time scale as a function of the wavelength k for values of the diffusive velocity $V_D = .5$ and 1 cm/s, respectively.

constant harmonic and biharmonic viscosity coefficients can be expressed as a function of a diffusive velocity V_D and the grid spacing Δx as $A_2 = V_D \Delta x$ and $A_4 = V_D \Delta x^3$, respectively. Examples of spin-down times for both operators are given in Fig. 6 for the average grid spacing of the MICOM simulations (6 km). For the same diffusive velocity, the biharmonic operator more strongly selects the small scales to dissipate and leaves the large scales relatively untouched.

The Laplacian experiment of Fig. 5, when contrasted to the biharmonic experiments of Figs. 3 and 4, suggests that some damping of the larger scales is necessary for a reasonable western boundary current behavior. The best separation/penetration results were obtained in the COADS-forced and the ECMWF-forced runs shown in Figs. 1 and 2 in which the viscosity operator was prescribed as a combination of the biharmonic and Laplacian operators. The main motivation for combining the two operators (see caption of Fig. 1 for details) was to be able to retain the scale selectiveness of the biharmonic operator and to provide some damping at the larger scales [performed in this case by the Laplacian operator for k greater than 80 km (Fig. 6)]. This allowed us to reduce the magnitude of the Laplacian coefficient A_2 by 50% and, at the same time, ensure numerical stability with an effective damping of the smaller scales via the biharmonic operator (Fig. 6). When combined, the individual diffusive velocity V_D specified for each operator is smaller than the minimum value that is needed for numerical stability when only one of the operators is specified.

4. Summary and discussion

These results appear to suggest that, in a realistic setting, even with such a fine grid spacing, the modeled large scale ocean circulation is strongly dependent upon the choices made for the viscosity operators. Furthermore, it appears that the cascade of energy from the small scales to the larger scales may not take place as anticipated and that some large scale information is needed for a proper representation of the western boundary current. In the experiments described in this paper, the latter is taking place via the Laplacian viscosity operator. Hyperviscosity (∇^{2n} operator with $n \geq 2$) is often used in numerical simulations of turbulent flows to extend the range of the inviscid inertial cascade. It has, however, been argued that it may also contribute non-trivial spurious dynamics (Jiménez, 1994). While it can be firmly stated that a resolution of $1/10^\circ$ is sufficient for the Gulf Stream to separate from the coast at Cape Hatteras (Paiva et al., 1999; Hurlburt and Hogan, 2000; Smith et al., 2000), it is not yet clear what is the optimal resolution for a correct Gulf Stream penetration and variability. A four-fold increase in resolution from $1/16^\circ$ to $1/64^\circ$ with the Laplacian operator in the hydrodynamic (i.e. no thermal forcing) Navy Layered Ocean Model (NLOM - Hurlburt and Hogan, 2000) brought the SSH variability to observed levels without altering the pattern of the large scale circulation. While numerical simulations at the above-noted resolutions are becoming more common, they still demand the latest in computing facilities. A four-fold increase in resolution for the thermodynamically forced models cannot be realistically implemented with the present computer resources. Thus, further evaluation of the impact of various dissipation operators on the large scale circulation should be pursued.

Acknowledgments. The authors wish to acknowledge the support of the National Science Foundation (OCE-95-31852 and OCE-00-00042). Eric Chassignet also wish to express his thanks to Chris Garrett and Peter Müller for inviting him to the 'Aha Huliko'a Hawaiian Winter Workshop.

References

- Bleck, R., and E.P. Chassignet, Simulating the oceanic circulation with isopycnic coordinate models. *The Oceans: Physiochemical Dynamics and Resources*. The Pennsylvania Academy of Science, 17-39, 1994.
- Bleck, R., C.G.H. Rooth, D. Hu, and L.T. Smith, Salinity-driven transients in a wind- and thermohaline-forced isopycnic coordinate model of the North Atlantic. *J. Phys. Oceanogr.*, 22, 1486-1505, 1992.
- Bryan, F.O., and W.R. Holland, A high resolution simulation of the wind- and thermohaline-driven circula-

- tion in the North Atlantic Ocean. In *Parameterization of Small-Scale Processes*. Proceedings 'Aha Huliko'a Hawaiian Winter Workshop. U. of Hawaii. January 17-20, 1989. P. Muller and D. Henderson, Eds., 1989.
- Dengg, J., A. Beckmann, and R. Gerdes, The Gulf Stream separation problem. In *The Warmwatersphere of the North Atlantic Ocean*, W. Krauss, (Ed.), Gebr. Borntraeger, Berlin, 253-290, 1996.
- Garraffo, Z.D., A.J. Mariano, A. Griffa, C. Veneziani, and E.P. Chassignet, Lagrangian data in a high resolution numerical simulation of the North Atlantic. I: Comparison with *in-situ* drifter data. *J. Mar. Sys.*, 29, 157-176, 2001a.
- Garraffo, Z.D., A. Griffa, A.J. Mariano, and E.P. Chassignet, Lagrangian data in a high resolution numerical simulation of the North Atlantic. II: On the pseudo-Eulerian averaging of Lagrangian data. *J. Mar. Sys.*, 29, 177-200, 2001b.
- Griffies, S.M., and R.W. Hallberg, Biharmonic friction with a Smagorinsky-like viscosity for use in large-scale eddy-permitting ocean models. *Mon. Wea. Rev.*, 128, 2935-2946, 2000.
- Holland, W.R., The role of mesoscale eddies in the general circulation of the ocean - Numerical experiments using a wind-driven quasigeostrophic model, *J. Phys. Oceanogr.*, 8, 363-392, 1978.
- Hurlbut, H.E., and P.J. Hogan, Impact of $1/8^\circ$ to $1/64^\circ$ resolution on Gulf Stream model-data comparisons in basin-scale subtropical Atlantic Ocean models. *Dyn. Atmos. Oceans*, 32, 283-330, 2000.
- Jiménez, J., Hyperviscous vortices. *J. Fluid Mech.*, 279, 169-176, 1994.
- Kraus, E.B., and J.S. Turner, A one dimensional model of the seasonal thermocline, II. The general theory and its consequences, *Tellus*, 19, 98-105, 1967.
- Özgökmen, T., E.P. Chassignet, and A. Paiva, Impact of wind forcing, bottom topography, and inertia on mid-latitude jet separation in a quasi-geostrophic model. *J. Phys. Oceanogr.*, 27, 2460-2476, 1997.
- Paiva, A.M., J.T. Hargrove, E.P. Chassignet, and R. Bleck, Turbulent behavior of a fine mesh ($1/12$ degree) numerical simulation of the North Atlantic. *J. Mar. Sys.*, 21, 307-320, 1999.
- Pedlosky, J., *Geophysical Fluid Dynamics*, Springer-Verlag, New York, 624 pp., 1979.
- Smith, R.D., M.E. Maltrud, F.O. Bryan, and M.W. Hecht, Numerical simulations of the North Atlantic Ocean at $1/10^\circ$. *J. Phys. Oceanogr.*, 30, 1532-1561, 2000.
-
- Eric P. Chassignet, RSMAS/MPO, University of Miami, Miami, FL, 33149, USA. (e-mail: echassignet@rsmas.miami.edu)

This preprint was prepared with AGU's LATEX macros v4, with the extension package 'AGU++' by P. W. Daly, version 1.6a from 1999/05/21.

Characterization of tracer cascade in physical space

B.L. Hua, P. Klein, and G. Lapeyre

Laboratoire de Physique des Océans, IFREMER, BP 70; 29280 Plouzan; France

Also at Laboratoire de Météorologie Dynamique, 24 Rue Lhomond, 75230 Paris Cedex 05; France

Abstract. Geophysical turbulent fluids are characterized by the presence of organized energetic structures which control tracer transport and stirring, while enabling a tracer cascade down to the smallest scales. In order to understand the physical mechanisms involved in this turbulent tracer cascade, we focus on the dynamics underlying the formation of tracer gradients which are necessarily associated to this cascade. We show that the dynamics of tracer gradients in physical space is mainly governed by their orientation with respect to the compressional eigenvector of the strain tensor. This relative angle results from the competition between strain and the "effective rotation" (due to both vorticity and rotation of strain axes). The implication is that tracer gradients (be they passive or active) should align with specific directions of the flow field, which depends only on the local velocity and acceleration gradient tensors in physical space. Most of the tracer stirring is thus occurring at specific locations that can be identified analytically. These results have been confirmed by direct numerical simulations and enable a better characterization of the cascade in physical space.

1. Introduction

The widely observed tracer cascade toward small spatial scales in geophysical flows is known to result from stirring by mesoscale eddies. It corresponds to the formation of strong horizontal gradients, such as those indicated by the chlorophyll concentration at the sea surface as observed by satellite (Figure 1). Another observed characteristic is that horizontal gradients of different tracer fields are often found at the same locations in physical space. This is consistent with the interpretation that such locations result from the common topology of the underlying flow that advects the different tracer fields. This is observed for instance in Figure 2, which presents airborne measurements of different mixing ratios in the southern stratosphere, showing sharp horizontal gradients coinciding at several locations (*Tuck et al., 1992*). On the other hand, the different strengths of the relative mixing ratios $|\nabla c|/c$ (where c is the mixing ratio) that are observed in Figure 2, are the result of the differences in the past history of the tracer fields, which may be caused by differences in their sources, forcings and sinks.

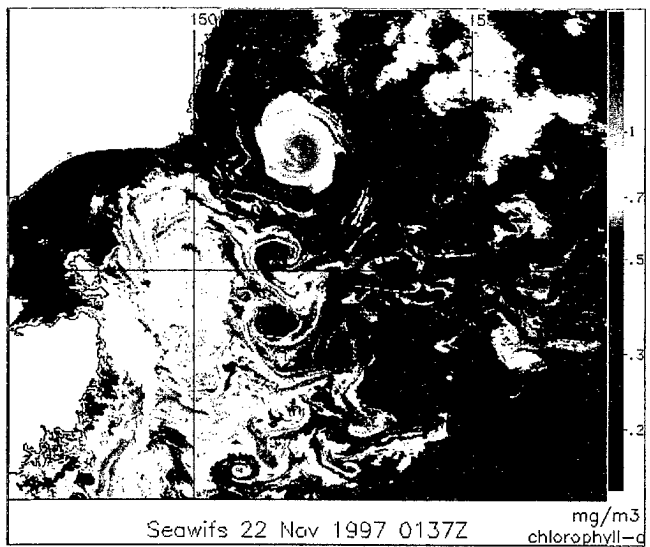


Figure 1. Chlorophyll concentration as observed by SEA-WIFF

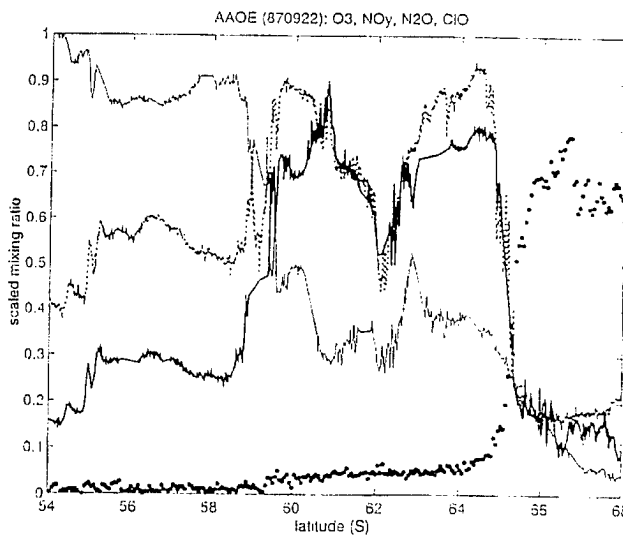


Figure 2. Different mixing ratios measured in the southern stratosphere (from Tuck *et al.*, (1992)).

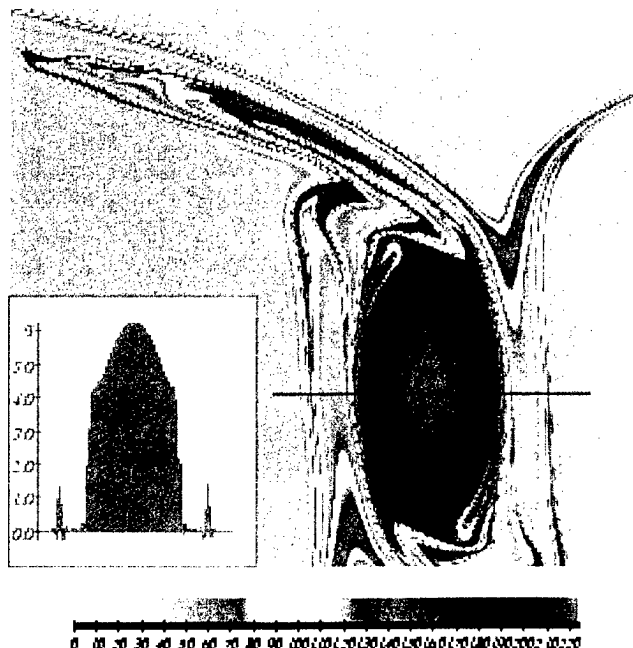


Figure 3. Vorticity field of an isolated vortex submitted to a externally prescribed strain field (Mariotti *et al.*, 1994).

However, the existence of intense gradients in tracer distribution does not always imply the occurrence of strong mixing of the tracer field. Figure 3 presents the vorticity distribution of an isolated vortex which is influenced by an externally prescribed strain field (Mariotti *et al.*, 1994). This setup leads to a constant erosion of the vortex structure, which is taking place through the ejection of filaments which will eventually be destroyed by small-scale mixing. However, as seen in the insert of Figure 3, the distribution of vorticity observed along a horizontal mid-section across the vortex shows a significant reinforcement with time of the gradients at the vortex boundary. Such a phenomenon is the opposite of mixing and corresponds to the formation of a barrier to transport that inhibits exchanges across the vortex boundary.

Our main purpose has been to attempt to characterize dynamically this tracer cascade in physical space. The specific objectives are to study the equations governing the dynamics of tracer gradients in order to localize the barriers to mixing as well as the regions of filament production. The chosen approach is to use information from both the velocity \vec{u} and acceleration fields $\frac{D\vec{u}}{Dt}$ in order to go beyond the simple kinematic approach of the chaotic advection literature, which relies on the sole knowledge of the velocity field.

In what follows, we have moreover made the assumption that as far as oceanic mesoscale eddies are concerned, the classical framework of the quasigeostrophic turbulence is a valid first step.

The paper is organized as follows. We first recall the basic ingredients that influence the evolution of tracer gradient by considering simple flows (section 2). The equations governing the dynamics of tracer gradients are then studied in section 3, leading to the prediction of preferred alignment of tracer gradients with specific orientations for different regions of the flow, which are found to depend on the tensors of velocity gradient and acceleration gradients $\nabla \vec{u}$ and $\nabla \frac{D\vec{u}}{Dt}$. Section 4 presents results from numerical simulations of two-dimensional turbulence in free-decay, providing evidence of statistical validation of alignment properties of the tracer cascade in physical space. Section 5 summarizes our results and mentions possible applications of the tracer gradient dynamics.

2. Simple flows

For a pure strain field, the streamfunction field $\psi = \sigma_{xy}$ corresponds to the blue isolines of Figure 4, where σ denotes the strain-rate magnitude. An initial tracer blob (red continuous isoline) will be stretched with time into an elongated pattern (the red dotted isoline) and the tracer gradient ∇q (black vector) will tend to align

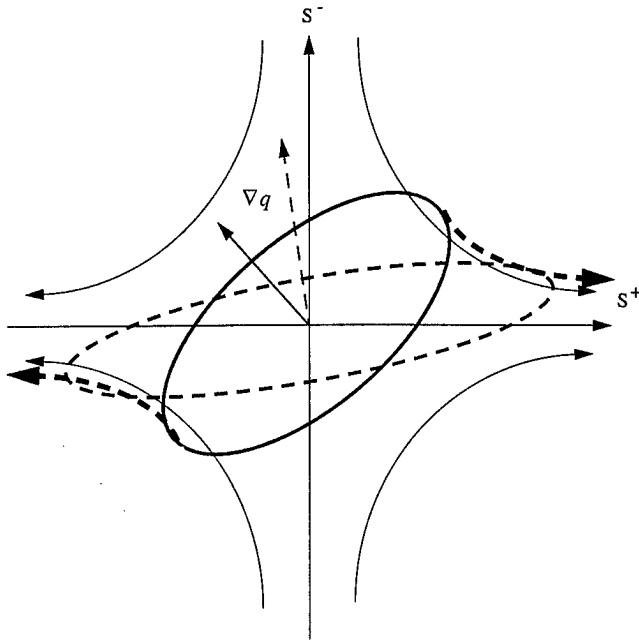


Figure 4. Pure strain field

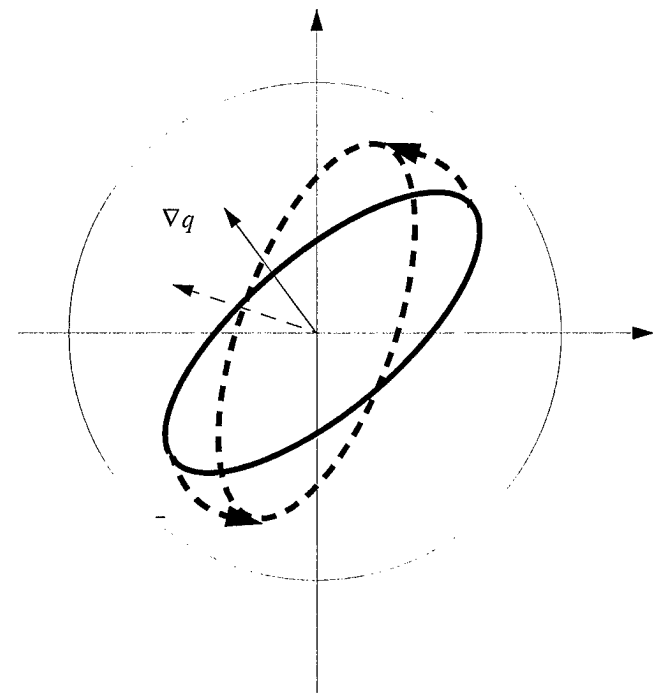


Figure 5. Pure vorticity field

with time with the compressional principal axis of the strain tensor (denoted by S^- in Figure 4). This alignment is associated with an exponential growth of the tracer gradient norm.

In the case of a pure vorticity field the streamfunction field is $\psi = \frac{\omega}{2}(x^2 + y^2)$, where ω denotes the vorticity. The initial tracer blob (red dotted isoline) simply rotates with time (the red continuous isoline) and so does the tracer gradient vector (Figure 5). There is no growth of the tracer gradient norm. The above simple limits can be obtained from the results of *Okubo* (1970) and *Weiss* (1991). For a passive tracer q that obeys the conservation equation

$$\frac{Dq}{Dt} = 0,$$

its gradient will obey

$$\frac{D\nabla q}{Dt} = -[\nabla \vec{u}]^* \nabla q. \quad (1)$$

$[\nabla \vec{u}]^*$ denotes the transpose of the velocity gradient tensor for which eigenvalues are $\pm \lambda^{1/2}$, where $\lambda = \sigma^2 - \omega^2$ depends on the competition between strain and vorticity. Both authors made the assumption that $[\nabla \vec{u}]^*$ is slowly varying along a Lagrangian trajectory ($\frac{D[\nabla \vec{u}]}{Dt} \sim 0$) so that the tracer gradient equation can be integrated, yielding

$$\nabla q = \nabla q_0 \exp(\pm \lambda^{1/2} t).$$

Thus in regions where the strain rate dominates ($\lambda > 0$), there is an exponential growth of the gradient norm,

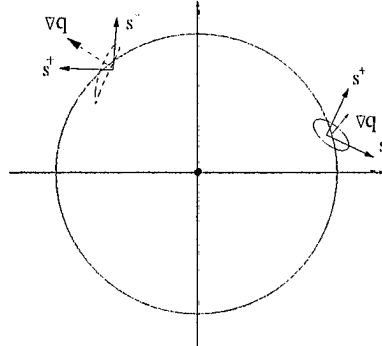


Figure 6. Finite size axisymmetric vortex

while in regions where vorticity dominates ($\lambda < 0$), the solution corresponds to a simple rotation of the gradient vector.

It is easy to find simple counterexamples where the Okubo-Weiss results do not hold (*Pierrehumbert and Yang*, 1993). Consider the case of an axisymmetric vortex of finite size, such that outside the vortex core, the vorticity is $\omega = 0$, while the strain rate is $\sigma \neq 0$ and streamlines are still circular. In such a region, $\lambda = \sigma^2 - \omega^2 = \sigma^2 > 0$ and the Okubo-Weiss criterion predicts an exponential growth. However, such a case can be integrated analytically (*Lapeyre et al.*, 1999) and the solution is found to correspond to a continuous rotation of the tracer gradient with a linear growth of

its norm with time. The Okubo-Weiss criterion fails because the rotation of the principal axes of the strain-rate tensor has not been taken into account, and this implies $\frac{D\nabla\vec{u}}{Dt} \neq 0$. Along the circular Lagrangian trajectories (Figure 6), the principal axes constantly rotate so that the tracer gradient vector cannot align with the compressional strain axis, and the initial tracer blob (continuous red line) is mostly linearly distorted with time. Other simple counterexamples can be constructed, involving a rotation of the strain-rate principal axes, where the Okubo-Weiss criterion fails and can be found for instance in Young (1999).

3. Dynamics of tracer gradient

The equation that governs the dynamics of tracer gradient (1) can be explicit as

$$\frac{D\nabla q}{Dt} = -\frac{1}{2} \begin{pmatrix} \sigma_n & \sigma_s + \omega \\ \sigma_s - \omega & -\sigma_n \end{pmatrix} \nabla q, \quad (2)$$

where the following quantities have been used

$$\begin{aligned} \sigma_n &= \partial_x u - \partial_y v \\ \sigma_s &= \partial_x v + \partial_y u \\ \sigma^2 &= \sigma_n^2 + \sigma_s^2 \\ \omega &= \partial_x v - \partial_y u. \end{aligned}$$

It is important to note that equation (2) is a vector equation and corresponds to two degrees of freedom that can be chosen as the tracer gradient norm $|\nabla q|$ and its orientation θ ,

$$\nabla q = |\nabla q| \begin{pmatrix} \cos \theta \\ \sin \theta \end{pmatrix}.$$

An angle ϕ that characterizes the orientation of the strain axes with respect to the coordinate axis (Figure 7) can be introduced

$$\begin{pmatrix} \sigma_n \\ \sigma_s \end{pmatrix} = \sigma \begin{pmatrix} \sin 2\phi \\ \cos 2\phi \end{pmatrix}.$$

The two scalar equations for the norm $|\nabla q|$ and the gradient orientation θ are derived in Lapeyre *et al.* (1999).

$$\frac{D \log |\nabla q|^2}{Dt} = -\sigma \sin(2(\theta + \phi))$$

$$2 \frac{D\theta}{Dt} = \omega - \sigma \cos(2(\theta + \phi))$$

Both scalar equations depend only on the relative angle

$$\zeta = 2(\theta + \phi)$$

(Figure 7) between ∇q and the compressional axis S^- . We have seen in previous simple examples that it is this relative angle that determines the growth rate with

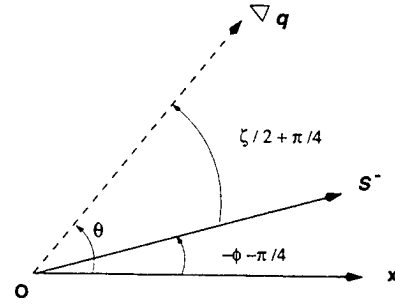


Figure 7. definition of angles ϕ , θ and ζ

time of the gradient norm. Introducing a nondimensional Lagrangian time which is related to the strain-rate magnitude

$$\tau = \int_0^t \sigma(t') dt',$$

one can rewrite both scalar equations as

$$\begin{aligned} \frac{D \log |\nabla q|^2}{D\tau} &= -\sin \zeta \\ \frac{D\zeta}{D\tau} &= r - \cos \zeta. \end{aligned} \quad (3)$$

The orientation equation (3b) involves a nondimensional parameter r which is defined as

$$r = \frac{\omega + 2D\phi/Dt}{\sigma} = \frac{\text{effective rotation}}{\text{strain rate}}$$

The dimensionless parameter r is the ratio between “effective rotation”¹ in the strain basis (i.e. the rotation effects due to both the vorticity and the rotation of the principal axes of the strain-rate tensor) and the magnitude of the strain rate (which tends to align the gradient with a strain eigenvector).

An important remark is that r remains invariant in a change of coordinates involving solid body rotation, while the Okubo-Weiss eigenvalues λ do not remain invariant in such a change of coordinates. The new physics that have been taken into account correspond to the quantity $\frac{D\phi}{Dt}$ that takes into account the fact that the principal axes of strain can vary along a Lagrangian trajectory, also implying that $\frac{D\nabla\vec{u}}{Dt} \neq 0$.

Note that the dynamics of the orientation equation (3b) is completely independent of the actual value of the gradient norm $|\nabla q|$, and the solution to (3b) will depend on the actual value of r , whether $r > 1$ or $r < 1$.

Strain-dominated regions

By definition, this corresponds to $|r| < 1$. Making the weaker assumption that both r and the strain mag-

¹We follow the terminology of Dresselhaus and Tabor (1991).

nitude σ are slowly varying along a Lagrangian trajectory, the equation for the orientation ζ has two fixed points $\zeta_{\pm} = \pm \arccos r$, an unstable one ζ_+ , and a stable one ζ_- . One expects a rapid alignment of the tracer gradient with the stable orientation ζ_- , leading to an exponential growth rate of $\sigma\sqrt{1-r^2}$ for the tracer gradient norm (Lapeyre et al., 1999). Conversely, the unstable orientation ζ_+ corresponds to a strong decay of $|\nabla q|$. In the case where $|r| = 1$, there is an algebraic growth of $|\nabla q|^2$ with time.

“Effective rotation”-dominated regions

In regions where the effective rotation dominates, $|r| > 1$. There is no fixed point solution to equation (3) and one has a nonuniform rotation of gradient. Since $\frac{D\zeta}{Dt}$ is variable the gradient tends to spend most of its time near the direction with minimal rotation rate ($D^2\zeta/Dt^2 = 0$). The most probable orientation of this direction is α such that (Klein et al., 2000)

$$\alpha = \arctan\left(\frac{s}{r}\right) + (1 - \text{sign}(r))\frac{\pi}{2},$$

which depends on another nondimensional parameter s which is defined as

$$s = -\frac{D(\sigma^{-1})}{Dt},$$

which measures how rapidly the stirring time scale σ^{-1} varies along a Lagrangian trajectory. In such a situation, the gradient norm presents only a weak growth or decay rate of $-\sigma s/\sqrt{r^2 + s^2}$.

The two nondimensional parameters r and s suffice to characterize the topology of stirring as well as the time evolution of the tracer gradient magnitude (growth or decay). For instance, a saddle point corresponds to the values $r = 0$ and $s = 0$, the axisymmetric vortex flow to the values $|r| = 1$ and $s = 0$ and the strong rotation limit to $|r| \gg 1$.

Finally, one can show that r and s depend on both the velocity gradient tensor $\nabla \vec{u}$ and on the acceleration gradient tensor $\nabla \frac{D\vec{u}}{Dt}$.

4. Numerical simulations

In order to test the above analytical predictions for alignment of the tracer gradient, numerical simulations of freely decaying turbulence have been performed at a resolution of $(1024)^2$.

Figure 8 displays the vorticity field in a portion of the domain where a strong vorticity filament is being stretched between two cyclonic vortices. The color code is such that red/brown corresponds to positive vorticity and blue to negative values. The corresponding field



Figure 8. vorticity ω



Figure 9. $r = \frac{\omega + 2D\phi/Dt}{\sigma}$

of the parameter r is given in Figure 9, where green indicates regions where the strain dominates, blue and red correspond to regions where effective rotation dominates. In the latter regions, red corresponds to the case when vorticity contributes the largest part of the effective rotation while blue corresponds to the opposite situation. Strips of yellow correspond to $|r| = 1$.

The parameter r presents sharp transitions and also a smooth behaviour along the longitudinal direction of the filamentary patterns. The vortex cores are regions with $r < -1$ because of large ω . Their periphery is composed of regions with $r^2 < 1$ because of large σ and regions with $r > 1$ because of large $\frac{D\phi}{Dt}$. For each vortex, we observe opposite signs of r between its core and the part on its periphery where effective rotation is strong. In these regions, $\omega + 2\frac{D\phi}{Dt}$ is dominated by $2\frac{D\phi}{Dt}$ which is of opposite sign of ω . This indicates that a characterization of the stirring properties of vortices must take into account this rotation rate.

The results for the alignment of the tracer gradient in strain-dominated regions, where $r < 1$, are checked against the analytical prediction $\zeta \approx \zeta_-$ in Figure 10, which presents the joint p.d.f. of $\zeta + \pi/2$ and r , and the bold curve is $\cos \zeta$. The relation $\cos \zeta \sim r$ is well corroborated and this strongly validates the analytical solution. On the other hand, a joint p.d.f. between $\zeta + \pi/2$ and ω/σ , which corresponds to the assumption of Okubo-Weiss that implies $\frac{D\phi}{Dt} = 0$, does not present such a correlation, and no alignment occurs for Okubo-Weiss criterion (Figure 11). This further emphasizes the quantitative importance of the rotation of the strain

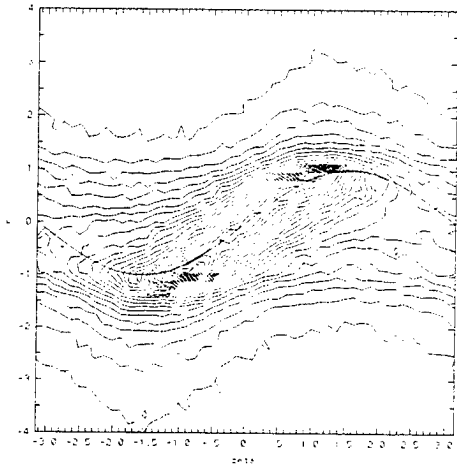


Figure 10. PDF of $\zeta + \pi/2$ and $r = \frac{\omega + 2\frac{D\phi}{Dt}}{\sigma}$

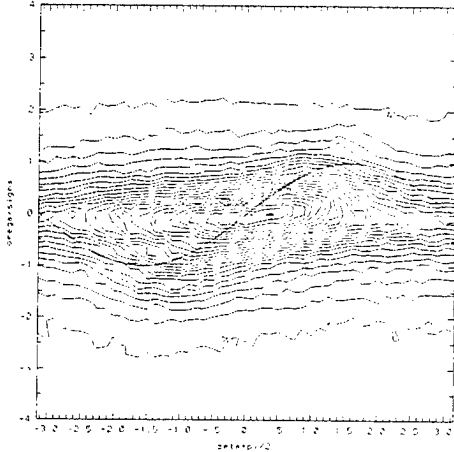


Figure 11. PDF of $\zeta + \pi/2$ and ω/σ for Okubo-Weiss results

axes.

The results for the alignment of the tracer gradient for regions where effective rotation dominates, $r > 1$ are checked against the analytical prediction $\zeta \approx \alpha$ in Figure 12, where the joint p.d.f. of ζ and α is plotted. Again, the numerical simulations confirm that there exist preferred directions of alignment of the tracer gradient that depends on r and s .

5. Discussion

To summarize, the dynamics of tracer gradients as a function of the flow topology can be captured by two regimes. The first one is well characterized solely by

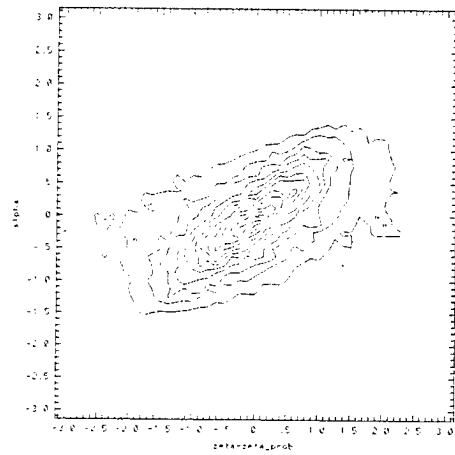


Figure 12. PDF of ζ and α

the parameter r

$$r = \frac{\omega + 2\frac{D\phi}{Dt}}{\sigma},$$

that measures the competition between the strain rate and the effective rotation which takes into account both the vorticity and the rotation rate of the principal axes of the strain-rate tensor along a Lagrangian trajectory (Lapeyre et al., 1999). Strong gradient growth occurs when $|r| < 1$. The second regime needs another parameter s

$$s = -\frac{D(\sigma^{-1})}{Dt}$$

that measures the variation of the stirring time scale (σ^{-1}) along a Lagrangian trajectory (Klein et al., 2000), and weaker growth/decay of the tracer gradient occurs for $|r| > 1$.

In both regimes, the flow topology enforces preferred orientations for the tracer gradient vector, which will depend on both local properties of the velocity gradient tensor $\nabla \vec{u}$ and also on the long-range spatial influence of the acceleration gradient tensor $\nabla \frac{D\vec{u}}{Dt}$ (Ohkitani and Kishiba, 1995; Hua and Klein, 1998). Both $\nabla \vec{u}$ and $\nabla \frac{D\vec{u}}{Dt}$ are entirely diagnostic for quasi-geostrophic dynamics and their computation only involves the resolution of Poisson problems in which right-hand sides are nonlinear functions of the streamfunction field at a given time (Hua et al., 1998).

These predictions based on tracer gradient dynamics have been applied to two other problems which are also related to the more general issue of stirring.

The first case corresponds to the detection of invariant manifolds (i.e. the attracting/repelling material lines associated with local maxima of particle dispersion or equivalently to local maxima of tracer gradients) by

computing the persistence of hyperbolicity defined as

$$\tau_r = \int_{|r|<1} \sigma dt,$$

along a Lagrangian trajectory in regions where $|r| < 1$ for a finite time. This technique enables us to locate the presence of such manifolds in the immediate vicinity of coherent vortices, as well as in the "far field" (Lapeyre *et al.*, 2001). For the second case, we have applied the analytical prediction of the time evolution of the tracer gradient norm to the predictability problem with the aim of identifying the regions of most rapid growth of the dynamical structures (Riviére *et al.*, 2001). The underlying idea is that initial perturbations that are responsible for the rapid growth of the structures in a given flow can be viewed as perturbations of the initial potential vorticity field of the flow. As such, their dynamics are closely linked in physical space to the regions which present the largest growth in potential vorticity gradients. Potential vorticity being a tracer field, the above analytical predictions can be used to identify the "sensitive" regions of most rapid growth.

References

- Dresselhaus, E., and M. Tabor, The stretching and alignment of material elements in general flow fields, *J. Fluid Mech.*, **236**, 415–444, 1991.
- Hua, B. L., and P. Klein, An exact criterion for the stirring properties of nearly two-dimensional turbulence, *Physica D*, **113**, 98–110, 1998.
- Hua, B. L., J. C. McWilliams, and P. Klein, Lagrangian accelerations in geostrophic turbulence, *J. Fluid Mech.*, **366**, 87–108, 1998.
- Klein, P., B. L. Hua, and G. Lapeyre, Alignment of tracer gradients in two-dimensional turbulence using second order Lagrangian dynamics, *Physica D*, **146**, 246–260, 2000.
- Lapeyre, G., P. Klein, and B. L. Hua, Does the tracer gradient vector align with the strain eigenvectors in 2-D turbulence ?, *Phys. Fluids A*, **11**, 3729–3737, 1999.
- Lapeyre, G., B. L. Hua, and B. Legras, Comments on "Finding invariant manifolds in two-dimensional velocity fields", *Chaos*, in press.
- Mariotti, A., B. Legras, and D. G. Dritschel, Vortex stripping and the erosion of coherent structures in two-dimensional flows, *Phys. Fluids A*, **6**, 3954–3962, 1994.
- Ohkitani, K., and S. Kishiba, Nonlocal nature of vortex stretching in an inviscid fluid, *Phys. Fluids A*, **7**, 411–421, 1995.
- Okubo, A., Horizontal dispersion of floatable particles in the vicinity of velocity singularity such as convergences, *Deep-Sea Res.*, **17**, 445–454, 1970.
- R. T. Pierrehumbert, and H. Yang, Global chaotic mixing on isentropic surfaces, *J. Atmos. Sci.*, **50**, 2462–2480, 1993.
- Riviére, G., B. L. Hua and P. Klein, An analytical Lagrangian approach to predictability based on potential vorticity gradients, *what?*, 2001 in prep.
- Tuck, A. F., T. Davies, S. J. Hovde, M. Noguer-Alba, D. W. Fahey, S. R. Kawa, K. K. Kelly, D. M. Murphy, M. H. Profitt, J. J. Margitan, M. Loewenstein, J. R. Podolske, S. E. Strahan, and K. R. Chan, Polar stratospheric cloud processed air and potential vorticity in the northern hemisphere lower stratosphere at mid-latitudes during winter, *J. Geophys. Res.*, **97**, 7883–7904, 1992.
- Weiss, J., The dynamics of enstrophy transfer in two-dimensional hydrodynamics, *Physica D*, **48**, 273–294, 1991.
- Young, W. R., Lecture notes on Stirring and Mixing, *Geophysical Fluid Dynamics Summer School* 1999, Woods Hole.

This preprint was prepared with AGU's LATEX macros v4, with the extension package 'AGU++' by P. W. Daly, version 1.6a from 1999/05/21, with modifications by D. E. Kelley, version 1.0 from 2001/03/26, for the 'Aha Huliko'a Hawaiian Winter Workshop.

Pathways for advective transport

A. D. Kirwan, Jr., M. Toner, and B. L. Lipphardt, Jr.

University of Delaware, Newark, Delaware-USA

Abstract. Advective transport in the ocean fundamentally is Lagrangian in nature. At model grid scales, this transport is parameterized by eddy or turbulent exchange coefficients in analogy to molecular diffusion. Nevertheless, much of the transport is by advection on scales larger than the grid cell yet smaller than basin scale. Moreover, flow at these scales tends to be nonstationary in time and irregularly distributed in space. Recently we have successfully used concepts from dynamical systems theory to analyze observations of such flows. The analysis is based on constructing, from synoptic observations of currents, material boundaries within the flow field that are not apparent in time varying Eulerian velocity fields. Here a short description of the approach is given and an application to the Gulf of Mexico is described where the analysis precisely identifies the boundaries of coherent vortical structures as well as pathways for advective transport.

Introduction

In a perceptive paper, Eckart (1948) developed a paradigm for ocean stirring and mixing in the ocean. He hypothesized this as occurring in three stages: the initial stage where coherent structures are formed, a stirring phase characterized by local strong gradients of fluid properties and localized but intense small scale advection, and a final stage in which small scale mixing obliterates the gradients and produces a uniform distribution of properties.

As Eckart's analysis is particularly pertinent to the results described here, it is appropriate to review his theory. The starting point is the diffusion equation for a substance C:

$$\frac{\partial C}{\partial t} + u_j \frac{\partial C}{\partial x_j} = K \frac{\partial^2 C}{\partial x_i \partial x_j} \quad (1)$$

Here, the indicial notation in which repeated subscripts in a term are summed over the range of the spatial domain. The remaining terms are standard.

Taking the gradient of (1) yields

$$\begin{aligned} & \frac{\partial}{\partial t} \left(\frac{\partial C}{\partial x_p} \right) + u_j \frac{\partial}{\partial x_j} \left(\frac{\partial C}{\partial x_p} \right) \\ & + \frac{\partial u_j}{\partial x_p} \left(\frac{\partial C}{\partial x_j} \right) = K \frac{\partial^2}{\partial x_i \partial x_j} \left(\frac{\partial C}{\partial x_p} \right) \end{aligned} \quad (2)$$

The last term on the LHS is sometimes referred to as "frozen-in." Frozen-in fields are not uncommon in hydrodynamics. The potential vorticity equation is one widely recognized example of a frozen-in field. Evolution equations for fields that include the frozen-in term change in

time like a differential line element moving with the fluid. Moreover, these terms can be used to construct Lagrangian invariants for the basic field. Although frozen-in fields and associated Lagrangian invariants are of fundamental interest in the theory used below, they are not pursued here. Interested readers are referred to Kuz'min (1984) for details.

As is well known in theoretical hydrodynamics, the velocity gradient term in (1) can be divided into an isotropic tensor whose eigenvalue is the fluid divergence, a traceless and symmetric deviator (called the velocity strain rate or deformation), and a skew-symmetric tensor called the spin, which is one half the vorticity. These quantities are denoted respectively as Δ_{jp} , Φ_{jp} , Ω_{jp} . Δ_{ij} accounts for the change in volume of a fluid parcel with no change in its shape or orientation, Φ_{jp} describes the change of shape of the parcel without change in volume or orientation, and Ω_{jp} quantifies the changes in orientation with no shape or volume changes.

What effect does the frozen-in term have on uncertainty in the gradients of C? To examine this, multiply (2) by $\frac{\partial C}{\partial x_p}$ and take the ensemble average. It is seen that the vorticity term sums to zero so that the evolution equation for the variance of the gradient C reduces to

$$\begin{aligned}
 & \partial \langle \partial C / \partial x_p, \partial C / \partial x_p \rangle / \partial t + \\
 & u_j \partial \langle \partial C / \partial x_p, \partial C / \partial x_p \rangle / \partial x_j + \\
 & 2\Delta \langle (\partial C / \partial x_p)(\partial C / \partial x_p) \rangle + \\
 & 2\Phi_{jp} \langle (\partial C / \partial x_p)(\partial C / \partial x_j) \rangle = \\
 & K\partial^2 \langle \partial C / \partial x_p, \partial C / \partial x_p \rangle / \partial x_i \partial x_j - \\
 & 2K \langle (\partial^2 C / \partial x_p \partial x_i)(\partial^2 C / \partial x_p \partial x_j) \rangle
 \end{aligned} \tag{3}$$

In (3) Δ is $1/3$ of the divergence of the velocity field and the angled brackets are the ensemble average operator. The noteworthy item about (3) is that the vorticity Ω does not effect the evolution of the variance of the gradient, even though it is the largest of the gradient terms. The physical explanation is that this merely reorients the variance but does not change its value. By far, the dominant frozen-in term in (3) involves the deformation Φ .

The heuristic picture that emerges from this is that the vorticity is the dominant frozen-in term in (2) while the deformation is critical in (3). Thus, in the Eckart picture, the vorticity is important in large-scale circulation effects on the gradient (stirring) while the fluid deformation is important in the final stage of mixing.

Here some ideas from dynamical systems theory are applied to quantify the Eckart paradigm. The next section reviews the requisite material from dynamical systems. This is applied to a reduced gravity primitive equation model in section 3 and then to interactions of rings and the Loop Current in the Gulf of Mexico.

Review of dynamical systems theory

The analysis focuses on those regions in the flow field that are dominated by fluid deformation and not vorticity. Generally these are small and ephemeral. As deformation dominates in these regions, one expects particle trajectories to move exponentially fast away from these regions or approach a critical point in the flow field. This is generally the case, but under appropriate conditions there is a special or distinguished trajectory that does neither. In the dynamical systems literature, such trajectories are called distinguished hyperbolic trajectories or DHTs. DHTs possess an important flow property, they are the seeds for the material surfaces, or manifolds in the dynamical systems literature, that define the barriers and pathways to advective transport.

Identifying the DHT and constructing the manifolds is still at a trial and error state. It is hoped that improvements in this phase of the analysis will soon improve this phase of the analysis so no attention is given here to this matter. Interested readers should consult *Guckenheimer and Holmes* (1983) or *Wiggins* (1990).

The essential ideas are contained in an example due to Ide (2000). Consider a flow field given by

$$\begin{aligned}
 dx/dt &= (y - \sin t)/2 \\
 dy/dt &= (x - 3 \cos t)/2
 \end{aligned} \tag{4}$$

The particle paths resulting from this flow are

$$\begin{aligned}
 x &= (X - 1)\cosh(t/2) + Y \sinh(t/2) + \cos t \\
 y &= (X - 1)\sinh(t/2) + Y \cosh(t/2) - \sin t
 \end{aligned} \tag{5}$$

Here (X, Y) are the starting positions. Consider first the particle that starts at $X=1, Y=0$. The trajectory of this particle is a circle. This trajectory differs from all other particle trajectories, which exhibit exponential time behavior. For example, particles starting along the line $y=1-x$ will flow towards the DHT as it executes its circular trajectory. All other particles will flow away from the DHT along the line $y=x-1$. The lines $y = \pm(x-1)$ define the inflowing and outflowing manifolds for this example.

It is important to note that particles cannot cross the quadrants delineated by the eigen-directions since they are asymptotes for the trajectories. Thus, the curves along the eigen-directions are the manifolds. The inflowing manifold is along the northwest-southeast direction and the outflowing manifold is along the other eigen-direction. Although the deformation is everywhere constant, locally the manifolds emanate from the DHT and so they move in space and time.

In natural settings one expects a multitude of DHT within a domain. Thus, one could expect a complicated web of intersecting inflowing and outflowing manifolds associated with different DHT. Such intersections are called principal intersection points or PIP. Particles flowing along an outflowing manifold will transfer to the inflowing manifold at a PIP. Examples of this are demonstrated below.

Manifolds in a reduced gravity primitive equation model

Here a few examples of DHT and manifolds are given for a reduced gravity primitive equation model. The model domain is 2000 km on a side and the forcing is by a meridional wind stress. See *Poje and Haller* (1999) for details.

Figure 1 shows the flow field with several manifolds and DHT. Note that the two eddies north of the jet are connected by manifolds. This implies some mass exchange between these structures. Also note the manifolds bounding the jet. These indicate that there is no advective transport across the jet in those regions. In fact, the only communication between the waters on either side of the

jet are through manifolds that develop when eddies are shed.

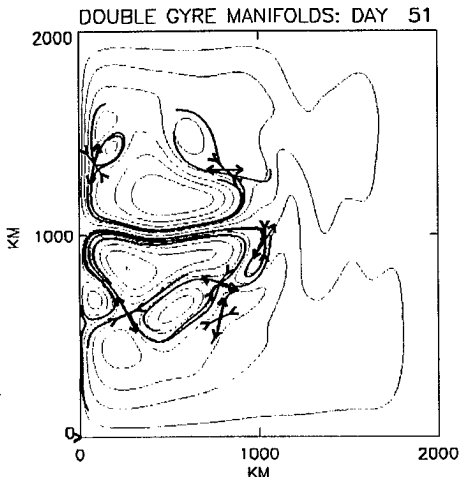


Figure 1. Flow field with several manifolds and DHT.

Figure 2 depicts an example of the power of manifolds to channel advective stirring. Two blobs are started in about 50 kilometers apart. The one just to the east is initialized around a DHT so it is expected to be stretched along the outflowing manifold. The other blob is initialized near a principal intersection point or the intersection of an inflowing manifold of one DHT and the outflowing manifold of another DHT. It is attracted nearly equally to both and so the stretching effects are canceled. The result is that this blob is advected parallel to the outflowing manifold but with negligible stretching.

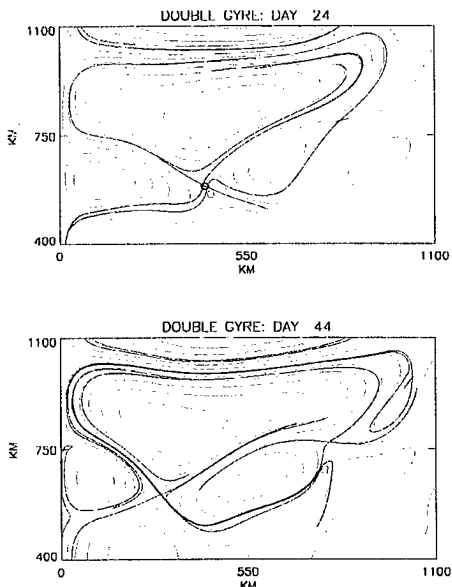


Figure 2. Manifolds that channel advective stirring.

Interactions of rings with the Loop Current

The purpose of this section is to apply the dynamical systems methods illustrated above to ocean data. To do this we use the University of Colorado model of the Gulf of Mexico. This is a 24-layer primitive equation model with 1/12 degree resolution, realistic bottom topography, and modified Mellor Yamada turbulence closure. It also is run in a predictive mode assimilating altimeter data, ABTs, and NOGAPS winds. For more details on the model and an assessment of its performance see *Toner et al* (2000).

Figure 3 shows a time slice of the model sea surface height and currents at 50 meters. Attention is directed to the eastern portion of the model domain where the Yucatan Current enters the Gulf and makes a large loop before egressing through the Straits of Florida. To the west of the Loop Current is a large anticyclonic ring that was shed several months before, and to the east is the Tortugas Eddy, a large semi-permanent cyclone sitting near the western most Florida Key. *Kutnetzov et al* (2000) provide more details of the flow field.

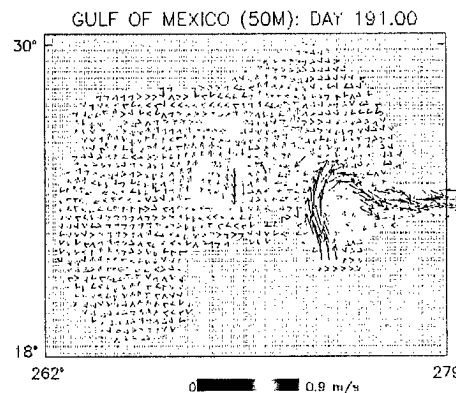


Figure 3. Time slice of the model sea surface height and currents at 50 m.

Four DHTs were located in this region and inflowing and outflowing manifolds were calculated for each. These are shown in Figures 4 and 5. It is important to note that the manifolds provide precise (but not necessarily accurate) delineations of the boundaries of the coherent structures noted above. Since they represent boundaries to advective transport the manifolds provide a quantitative measure of the size and shape of these structures.

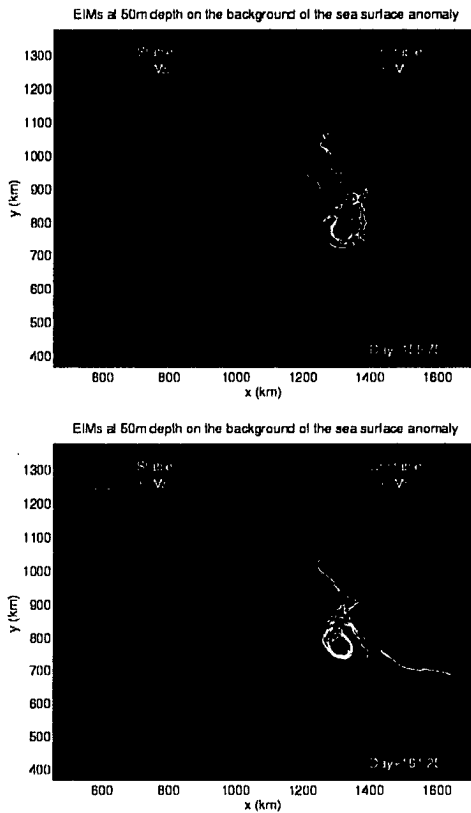


Figure 4. Inflowing and outflowing manifolds calculated for four DHTs.

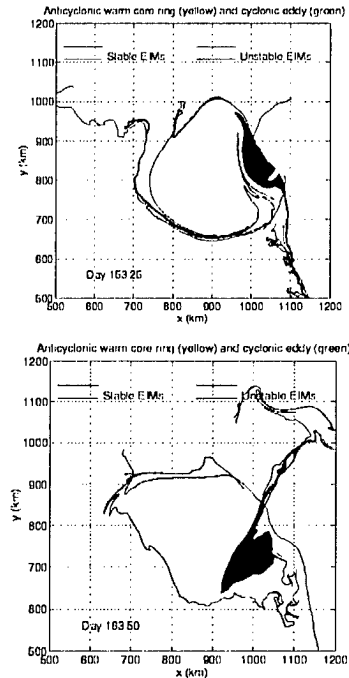


Figure 5. Evolution of a small cyclone originally to the northeast of the large anticyclonic ring.

Figure 5 shows the evolution of a small cyclone originally to the northeast of the large anticyclonic ring. As seen in this figure the cyclone moves anticyclonically around the ring and actually cuts off approximately 20%. This phenomenon was missed in the original examination of the Eulerian model velocities and height fields. The Lagrangian analysis used here highlighted this event.

Summary and discussion

This analysis is based on concepts from dynamical systems theory. The basic ingredients are hyperbolic points or saddle points and DHTs. The former is characterized by real eigenvalues of the velocity gradient at stagnation points. They have special significance in this approach in that they often signify a nearby DHT. These latter objects serve as seeds for calculating inflowing and outflowing manifolds or material boundaries that determine the advective transport pathways through a maze of coherent flow structures. In complex flows, such as the Loop Current region of the Gulf of Mexico, manifolds connect regions of intense mixing. In the language of Eckart (1948), the manifolds delineate stirring regimes and connect regions of intense mixing.

These pathways have now been found in simple time dependent QG and primitive equation models and in data assimilative GCMs (Samelson, 1992). Additionally, these techniques have been applied to merged drifters, moorings and MODAS data set on the LATEX Shelf (Schulz, 1999). It seems then they are telling us that stirring and mixing in the ocean may be highly time- and space-dependent and are governed by relatively simple processes determined by Lagrangian analysis. However, quantification of the importance of manifolds and DHTs to stirring and mixing, relative to traditional exchange processes, will have to await extension of these methods to three dimensions.

A comment on the stretching of blobs when they approach a DHT along an inflowing manifold is appropriate. The analysis indicates that a blob may be stretched hundreds of kilometers along the outflowing manifold, a purely advective process. We know of no observational evidence for this. Rather, it seems more likely that the blob undergoes intense small scale mixing and may lose its identity. But, both the reduced gravity primitive equation model and the assimilative model of the Gulf of Mexico include sophisticated and well-tuned mixing parameterizations. That the models are unable to predict the likely evolution of the blob in near a DHT suggests a deficiency in the present generation of mixing parameterizations.

Acknowledgments. We are grateful to the Office of Naval Research for supporting this research and to Chris Garrett and Peter Müller for convening this conference. We also thank Lakshmi Kantha for the Gulf of Mexico model runs and to Chris Jones and Leonid Kutnetzkov for the manifold calculations.

References

- Eckart, C., An analysis of the stirring and mixing processes in incompressible fluids, *J. Mar. Res.*, **VII**, 265-275, 1948.
- Guckenheimer, J. and P. Holmes, Nonlinear Oscillations, Dynamical Systems, and Bifunctions of Vector Fields, Springer-Verlag, New York, 459 pp, 1983.
- Ide, K., F. Lekien, and S. Wiggins, Distinguished hyperbolic trajectories in time dependent fluid flows: Analytical and computational approach for velocity fields defined as data sets, under review, 2001.
- Kuz'min, G.A., Ideal Incompressible Hydrodynamics in terms of the vortex moment density, *Phys. Lett.*, **96A**, 2, 88-90, 1983.
- Kuznetsov, L., M. Toner, A.D. Kirwan, Jr., C.K.R.T. Jones, L. Kantha, and J. Choi, Interactions of the Loop Current and adjacent rings in the Gulf of Mexico, submitted, 2000.
- Poje, A.C. and G. Haller, Geometry of cross-stream mixing in a double-gyre ocean model, *J. Phys. Oceanogr.*, **29**, 1649-1665, 1999.
- Samelson, R.M., Fluid exchange across a meandering jet, *J. Phys. Oceanogr.*, **22**, 431-440, 1992.
- Schulz W.J., Ocean Surface Maps from Blending Disparate Data through Normal Mode Analysis, PhD thesis, Old Dominion University, Norfolk, VA 23529, December 1999. Also available as Center for Coastal Physical Oceanography Technical Report No. 99-02.
- Toner, M., A.D. Kirwan, Jr., L. Kantha, and J. Choi, Can general circulation models be assessed and their output enhanced with drifter data?, *J. Geophys. Res.*, **106**, 19,563-19,580, 2001.
- Wiggins, S. Introduction to Applied Nonlinear Dynamical Systems and Chaos, Springer-Verlag, New York, 672 pp., 1990.

From stirring to mixing of momentum: cascades from balanced flows to dissipation in the oceanic interior

James C. McWilliams¹, M. Jeroen Molemaker¹, and Irad Yavneh²

Abstract. Under the influences of stable density stratification and Earth's rotation, large-scale flows in the ocean and atmosphere have a mainly balanced dynamics—sometimes called the slow manifold—in the sense that there are diagnostic hydrostatic and gradient-wind balances that constrain the fluid acceleration. The nonlinear balance equations are a successful approximate model for this regime, and we have identified mathematically explicit limits of their time integrability. We hypothesize that these limits are indicative, at least approximately, of the transition from the larger-scale regime of inverse energy cascades of anisotropic flows to the smaller-scale regimes of forward energy cascade to dissipation of more nearly isotropic flows and intermittently breaking inertia-gravity waves. In the oceans these regime transitions occur mostly in the scale range of 0.1–10 km—in between the mesoscale and fine-structure—where Rossby (Ro), Froude (Fr), and Richardson (Ri) numbers are typically neither small nor large. In pursuit of testing this hypothesis we have revisited several classical problems, including gravitational, centrifugal/symmetric, elliptical, barotropic, and baroclinic instabilities. In all cases we find definite evidence, albeit still incompletely understood, of fluid-dynamical transitions in the neighborhood of loss of balanced integrability.

Introduction

The general circulation of the ocean is forced by surface fluxes of heat, water, and momentum primarily at large space and long time scales. The circulation has comparably large and long scales, as well as important smaller ones associated with equatorial zonal and lateral boundary currents and with the dominant instability modes at mesoscales. All of these circulation elements approximately satisfy geostrophic, hydrostatic, and incompressible dynamical balances.

How does the energy dissipation occur for the general circulation in an equilibrium balance with the generation by surface fluxes? Some of the dissipation undoubtedly occurs within turbulent boundary layers near the surface and bottom. Some dissipation also occurs through creation of internal gravity waves by flow over

topography, with subsequent wave propagation into the interior and a wave-dynamical cascade (sometimes involving breaking) down to dissipation at small scales. Each of these routes to dissipation involves an extraction of energy from the circulation near the vertical boundaries, although the bulk of the energy resides in the vertical interior. A more local route is directly through the interior, turbulent cascade dynamics of the circulation. In oceanic general circulation models, the local route to dissipation is implied by the use of eddy diffusivities to parameterize this cascade. The purpose of this article is to examine the mechanism for the local route to dissipation, without here trying to assess the relative contributions among these alternative routes.

Our conceptual view of the mechanism is the following:

Large- and mesoscale circulations typically satisfy a balanced dynamics (as defined below), which have little interaction with the inertia-gravity wave field;

¹Institute of Geophysics and Planetary Physics, University of California at Los Angeles, Los Angeles, CA 90095-1567, USA

²Department of Computer Science, Technion, Haifa 32000, ISRAEL

balanced turbulent cascades are very inefficient in energy dissipation;

there are explicitly specifiable limits to the regime of balanced dynamics that are violated sometimes for the circulation;

violation of these limits leads to energy transfer to unbalanced motions;

turbulent cascades are much more efficient in their dissipation.

In this view the important bottleneck in the local route to dissipation is loss of balance and its evolutionary consequences.

Confirming or refuting this hypothesis is quite challenging, since it involves the connectedness of turbulent cascades spanning several dynamical regimes. Even diagnosis of the degree of balance can be subtle. In lieu of making a more general test of the hypothesis as yet, here we focus on the special situation of the linear instability of balanced steady currents in a rotating, stratified fluid in relation to the conditions for loss of balance. Since fluid instabilities have been the subject of much prior research, we will tell the story from both historical perspectives of early discovery and personal perspectives of the implications for the hypothesis above—skipping over most of the literature in between.

Balanced Dynamics

The essential basis for the approximations of balanced dynamics is velocity anisotropy. In a rotating, stratified fluid with Coriolis frequency f and Brunt-Väisälä frequency N and away from boundaries, the evolution from general initial conditions or forcing by the process called geostrophic (or balanced) adjustment leads to a local anisotropy with $u, v \gg w$, while radiating away inertia-gravity waves. Here z and w are the coordinate and velocity components in the vertical direction, antiparallel to gravity, and (x, y) and (u, v) are their horizontal counterparts. The condition for this to occur are that the Rossby and Froude numbers,

$$Ro = V/fL \quad \text{and} \quad Fr = V/NH, \quad (1)$$

are not too large (where V , H , and L are characteristic values for (u, v) , z , and (x, y)). Under these conditions the vertical momentum balance is approximately hydrostatic,

$$\phi_z \approx b, \quad (2)$$

($\phi = p/\rho_o$ is the geopotential function, $b = g[1 - \rho/\rho_o]$ is the buoyancy, and ρ_o is the mean density); the diver-

gence of the horizontal momentum balance is approximately

$$\nabla^2 \phi \approx \nabla \cdot f \nabla \psi + 2[\psi_{xx}\psi_{yy} - \psi_{xy}^2], \quad (3)$$

which is called gradient-wind balance (∇ is the horizontal gradient operator); and the horizontal velocity is weakly divergent and thus can be approximately represented by a streamfunction,

$$u \approx -\psi_y \quad \text{and} \quad v \approx \psi_x. \quad (4)$$

The maximal truncation of the incompressible (Boussinesq) equations consistent with these approximations and conservation of either energy (in Cartesian coordinates, (x, y, z)) or potential enstrophy (in isopycnal coordinates, (X, Y, b)) is called the balance equations (Lorenz [1960]; Gent and McWilliams [1984]). (Many alternative models have been proposed for balanced dynamics; among the better ones, their similarities seem more important than their differences.) The balance equations contain no inertia-gravity wave solutions; so they are often taken as a dynamical-systems model for the (advection) slow manifold. They have second-order asymptotic accuracy as $Ro \sim Fr \rightarrow 0$, whereas the traditional geostrophic balance and quasi-geostrophic equations have only first-order accuracy (Gent and McWilliams [1983]). They have been shown in many analyses to accurately represent the observed state and evolution of large-scale flows in the atmosphere and ocean; for example, they often are used for initialization of weather forecasts, even ones for hurricanes. An important aspect of this accuracy is the weakness of inertia-gravity wave generation by balanced motions when Ro and Fr are not large.

The advective dynamics of balance or quasigeostrophic equations—called geostrophic turbulence—yields an inverse turbulent cascade of energy towards larger scales in (x, y, z) , hence away from dissipation by molecular viscosity at small scales, and a forward cascade of potential enstrophy (i.e., variance of potential vorticity) to its dissipation at small scales (Charney [1971]; McWilliams et al. [1994]). (This behavior is analogous to the turbulence in a two-dimensional fluid.) In the enstrophy inertial range, Ro and Fr are invariant as the scale decreases, at least in the limit of $Ro, Fr \rightarrow 0$. There is as yet much less experience with balanced turbulence at finite values of Ro and Fr , but available solutions indicate that it is only modestly more dissipative of energy (Yavneh et al. [1997]). It remains an open question how consistently Ro and Fr avoid increasing in the forward cascade, either in the balance equations or

more fundamental fluid dynamics: at small scales does the cascade in balanced turbulence generate inconsistencies with its justifying assumptions and how leaky is the slow manifold to unbalanced motions? Nevertheless, our present understanding is that the balance equations do not provide an efficient route to energy dissipation away from boundaries: they imply more stirring than mixing for momentum.

Loss of Balance

An analysis for the solvability of the balance equations is made in *Yavneh et al.* [1997] and *McWilliams et al.* [1998]. To be able to integrate forward in time from a balanced state, several necessary conditions must be satisfied everywhere within the domain. Where these are violated, there is a change of type of the partial differential system and the initial- and boundary-value problem becomes ill-posed. For the balance equations in isopycnal coordinates (i.e., *Gent and McWilliams* [1984]) and $f \geq 0$, the conditions for loss of balance are the following:

1. Change of sign of vertical stratification, $N^2 = \frac{\partial b}{\partial z}$;
2. Change of sign of absolute vorticity, $A = f + \zeta^{(z)} = f + v_X - u_Y$ (where the horizontal derivatives denoted by capital letters are in isentropic coordinates);
3. Change of sign of $A - |S|$ (where $S^2 = (u_X - v_Y)^2 + (v_X + u_Y)^2$ is the variance of the strain rate).

None of these conditions occurs in the quasigeostrophic limit, since $A, A - |S| \rightarrow f + \mathcal{O}(Ro)$ and $N \rightarrow N_o + \mathcal{O}(Ro)$, where $N_o(z)$ is the resting-state stratification. Note the greater susceptibility of anticyclonic regions (i.e., with $\zeta^{(z)}/f < 0$) in the second and third conditions; furthermore, note the greater susceptibility to the third condition, since $A - |S| \leq A$. The first and second conditions also are related to the potential vorticity, $q = AN^2$. Since potential vorticity is conserved on parcels, except for mixing effects, there is thus an evolutionary inhibition for an unforced flow to spontaneously develop a violation of the first and second conditions. However, there is no such constraint with respect to the third condition, which indicates another sense in which there may be a greater susceptibility to the third condition.

Instability and Cascade

We now ask what happens when there is a loss of balance as defined above. Obviously any further integration of the balance equations is precluded. So the question must be answered in a more fundamental fluid dynamics, such as the incompressible Boussinesq equations, which have no restriction on Ro and Fr for their validity. In general, our expectation is that some inertia-gravity waves and/or more nearly isotropic turbulence will be generated—instigating some degree of enhanced dissipation—where there is a loss of balance. However, the efficiency of their generation is uncertain, as is whether the subsequent evolution systematically departs from balanced dynamics or relaxes back towards it (e.g., as a geostrophic adjustment or selective cascade and dissipation processes). In the rest of this article, we address the issue of generation and subsequent evolution only in a very particular context, viz., the linear instabilities of rotating, stratified flows which are steady, inviscid, balanced solutions of the Boussinesq equations. While this is far from the general circumstances of fluid evolution, it does provide a cleanly posed question that also is one that can be answered in part by reference to the extensive literature on fluid instabilities.

Instability Types

Now we attempt to interpret the known instabilities in relation to the conditions for loss of balance for rotating, stratified flows where Ro and Fr are not large. It is probably unprovable that any such taxonomy of instability types can be complete and unique; however, after all the research that has gone into this topic, the landscape has become fairly well mapped.

Quasigeostrophic Inflectional Instability

Consider the instability of a geostrophic parallel flow $U(y, z)$ with background stratification $N_o(z)$ and Coriolis frequency $f(y)$ in the quasigeostrophic limit, $Ro, Fr \rightarrow 0$. Following *Rayleigh* [1880] and *Drazin and Howard* [1966] and ignoring vertical-boundary effects, one can derive a “Rayleigh theorem” from the potential vorticity equation that a necessary condition for inviscid instability of a non-symmetric (i.e., $\partial_x \neq 0$), normal-mode fluctuation is that the mean potential vorticity gradient,

$$N_o^{-2} Q_y = \frac{df}{dy} - U_{yy} - \left(\frac{f}{N_o} \right)^2 U_{zz}, \quad (5)$$

change sign within the domain. This is called an inflection-point instability since it involves the horizontal and/or vertical curvature of U ; depending upon which curvature is dominant, the instability is labeled barotropic or baroclinic instability. The unstable mode is itself geostrophically balanced. This is the only type of instability that occurs in the quasigeostrophic limit. It has an analytic continuation to finite Ro and Fr , where it can be expected to remain balanced over some range of these parameters. Thus, its onset conditions have nothing to do with the limits of balance, and it represents a mode of stirring within balanced dynamics.

Gravitational Instability

The condition for the onset of gravitational instability in the limit of vanishing viscosity is $N^2 < 0$ (*Rayleigh* [1916]; *Chandrasekhar* [1961]). This coincides with the first condition for loss of balance, and the mode of instability is unbalanced (e.g., the vertical momentum balance is non-hydrostatic).

Symmetric Centrifugal Instability

For a balanced, parallel flow $U(y, z)$, the necessary and sufficient condition for inviscid instability of a parallel-symmetric perturbation is a change of sign of potential vorticity $q(y, z)$ (*Hoskins* [1974]). This coincides with the second condition for loss of balance. (This is a 2D problem rather than a 3D one, and *McWilliams et al.* [1998] show that the third condition is not germane in this situation.) For a balanced, axisymmetric, azimuthal flow $U(r, z)$, the conditions for the inviscid instability of an axisymmetric perturbation are the change of sign of either the absolute vorticity A or the absolute circulation $C = \frac{1}{2}fr + U$ (*Rayleigh* [1916]; *Ooyama* [1966]). *McWilliams et al.* [1998] show that these coincide with the second or third conditions, respectively, for loss of balance in this case. Thus, the boundaries for onset of symmetric centrifugal instability, which has unbalanced growing modes, occur exactly at the limits of balanced evolution.

Elliptical Instability

The inviscid instability of the balanced, elliptical, two-dimensional, barotropic flow in an unbounded domain,

$$\Psi(x, y) = \frac{1}{2}(\alpha x^2 + \beta y^2), \quad 1 > \frac{\beta}{\alpha} > 0, \quad (6)$$

was originally analyzed for $f = N = 0$ (*Pierrehumbert* [1986]; *Bayly* [1986]; *Craik and Criminale* [1986]) and

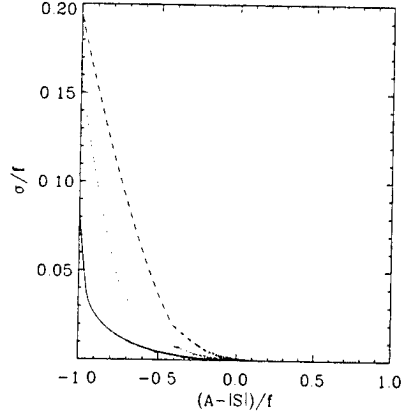


Figure 1. Growth rate, σ/f , for the elliptical flow (6), maximized over vertical wavenumber. Curves are shown for $\beta/\alpha = 0.25$ (dashed), 0.11 (dotted), and 0.026 (solid). The corresponding abscissa values for the second condition for loss of balance are -0.6, -0.8, and -0.95 (see text).

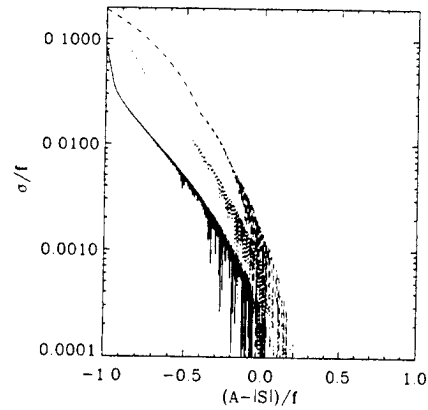


Figure 2. As figure 1, but with logarithmic ordinate. The evident noise is because of intermittent underestimates of σ due to incomplete optimization searches over the very narrow unstable bands in vertical wavenumber.

later extended to $\text{Ro}, \text{Fr} < \infty$ by Miyazaki [1993]. The unstable modes occur in bands of the vertical wavenumber. They have temporally oscillatory horizontal wavenumbers and exhibit exponential growth averaged over a wavenumber oscillation period.

The problem was revisited in McWilliams and Yavneh [1998] from the perspective of loss of balance: elliptical instability disappears in the quasigeostrophic limit and its onset nearly, but not precisely, coincides with the third condition for loss of balance (see Figures 1–2). The unstable mode is unbalanced. For this basic flow the vorticity and strain rate are spatially uniform and unequal in magnitude. The abscissa, $(A - |S|)/f$, = +1 in the quasigeostrophic limit, = 0 at the third condition for loss of balance, = $-(\alpha - \beta)(\alpha + \beta)$ at the second condition for loss of balance, and $> +1$ for cyclonic flows. Cyclonic elliptical flows are stable for $\alpha, \beta = \mathcal{O}(f)$.

Taylor-Couette and Barotropic Instabilities

Consider Taylor-Couette flow in the gap between two axisymmetric, rotating cylinders,

$$U(r) = A r + \frac{B}{r}, \quad (7)$$

which is a viscous steady solution commonly studied in laboratory experiments. The classical instability for this flow is centrifugal (*Taylor* [1923]; *Chandrasekhar* [1961]), whose onset in the inviscid limit coincides with the second condition for loss of balance. In a neutrally stratified fluid, this is the only type of linear instability, since this profile does not have an inflection point. However, for a stably stratified fluid with small Fr , this barotropic shear flow has another class of unbalanced instabilities at finite Ro in the anticyclonic regime (*Molemaker et al.* [2001]; *Yavneh et al.* [2001]), but there is not any instability for the quasigeostrophic limit, $\text{Ro} \rightarrow 0$, nor for cyclonic flows with $\text{Ro} = \mathcal{O}(1)$. For this new class an infinite but countable set of unstable modes exist, which differ in their cross-stream structure, each with a different narrow band of vertical wavenumbers. In Figures 3–4, the growth rates are shown for the first three modes in the thin-gap limit where $\zeta^{(z)}$ and S are nearly uniform and equal in magnitude. As with elliptical flow, the strength of the instability strongly increases in the neighborhood of the third condition for loss of balance. (And, in this case, $(A - |S|)/f \approx -1$ corresponds to the second condition.) The instability can be shown to involve a resonance of shear-modified neutral modes (as required in any eigenvalue problem whose eigenfrequency is either real or a

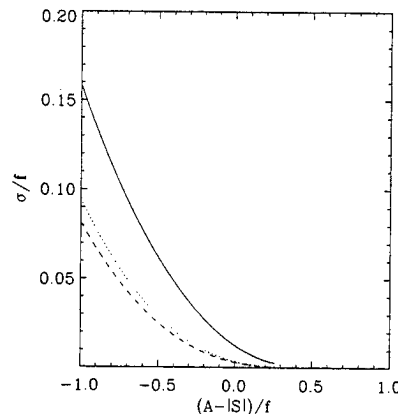


Figure 3. Growth rate, σ/f , for Taylor-Couette flow (7) in a narrow gap, maximized over vertical wavenumber. Curves are shown for the three gravest modes in cross-stream structure.

complex-conjugate pair); for the gravest unstable mode the resonance involves a pair of Kelvin waves propagating cyclonically along each cylinder wall, and for the other modes, one of the Kelvin modes is replaced by an inertia-gravity mode. Thus, the instability has an unbalanced dynamics. An explicit formula can be obtained for the unstable growth rate of the gravest mode,

$$\frac{\sigma}{f} \sim e^{-\gamma/\text{Ro}} \sim e^{-2\gamma/(1-X)}, \quad (8)$$

asymptotically as $\text{Ro} \equiv \max |\zeta^{(z)}|/f \rightarrow 0^+$ and $X \equiv (A - |S|)/f \rightarrow 1^-$ (with $\gamma = 2$ (analytically) for the gravest mode and $\gamma \approx 3$ (computationally) for the higher modes; n.b., X is the abscissa in Figures 3–4). This asymptotic regime is accurately realized even in the neighborhood of the third condition for loss of balance, which implies that there is an extremely rapid weakening of σ with Ro and X in this neighborhood, but not an abrupt cessation at any critical value near $X = 0$.

Recently we have also solved the linear, inviscid stability problem for a barotropic boundary current along a straight coastline (at $x = 0$),

$$V(x) = V_0 \exp(-\alpha x), \quad (9)$$

in a uniformly rotating, stratified fluid in a semi-infinite domain (i.e., $x \geq 0$). This profile also does not have an inflection point. In addition to no normal flow at the boundary, we prescribe a radiation condition at a sufficiently distant location in the interior by matching the solution to an outwardly radiating, free inertia-gravity

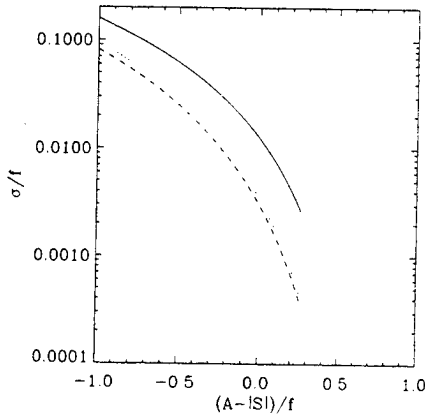


Figure 4. As figure 3, but with logarithmic ordinate

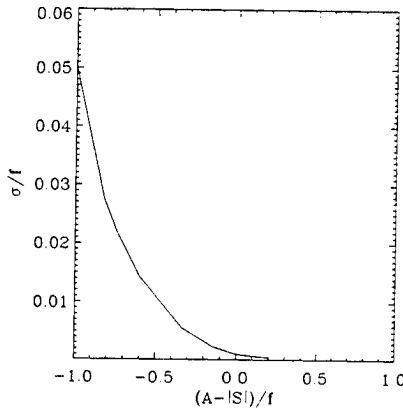


Figure 5. Growth rate, σ/f , for the parallel boundary current (9), maximized over along-stream and vertical wavenumbers. The abscissa value is based upon the minimum over x which occurs at $x = 0$.

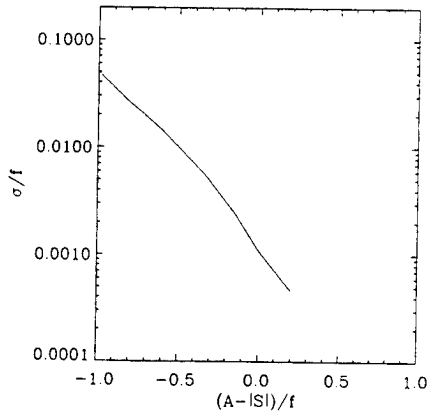


Figure 6. As figure 5, but with logarithmic ordinate

wave,

$$\frac{\partial u}{\partial x} = iku, \quad (10)$$

where k is a cross-stream wavenumber determined from vertical and along-stream wavenumbers and eigenfrequency using the dispersion relation of an inertia-gravity wave. Again there are unbalanced unstable modes for anticyclonic flows (i.e., $V_o/f > 0$) away from the quasigeostrophic limit. In contrast with Taylor-Couette flow, with its discrete spectrum of modes in the cross-flow direction, here there is a continuous set of unstable modes for any along-stream and vertical wavenumber pair (and its corresponding cross-stream k). In Figures 5-6, growth rates are shown for optimal along-flow and vertical wavenumbers, indicating yet again a rapid increase of the growth rate in the vicinity of the third condition for loss of balance; the functional form of $\sigma[Ro]$ here appears to be close to that for the higher-mode, Taylor-Couette instabilities. Again, a resonance can be diagnosed with a shear-modified Kelvin mode and an inertia-gravity mode.

In summary, the three different barotropic, anticyclonic, rotating, stratified, shear flows analyzed in this and the preceding section all have an unbalanced instability whose strength rapidly increases in the vicinity of the third condition for loss of balance (in addition to the unbalanced, centrifugal instability in the vicinity of the second condition). In the hydrostatic limit, this instability is related to ageostrophic, parallel, anticyclonic flow instability in a shallow-water layer (*Satomura [1981]; Griffiths et al. [1982], et seq.*)

Baroclinic and Kelvin-Helmholtz Instabilities

Consider a steady, spatially uniform vertical shear flow, $U(z) \propto z$, in a uniformly stratified and rotating fluid in a vertically bounded domain with non-isopycnal boundaries. We define the Richardson number for this flow by $Ri = N_o^2/U_z^2$, which is equivalent to a Fr^{-2} . The balancing buoyancy field is $B(y, z) = N_o^2 z - f U_z y$, and the associated quantities in the second and third conditions for loss of balance are

$$A = f \left[1 - \frac{1}{Ri} \right], \quad A - S = f \left[1 - \frac{2}{Ri} \right]. \quad (11)$$

Notice that this flow regime is anticyclonic since $A/f < 1$. Thus, we can make the following categorization for this flow in terms of Ri and in relation to the conditions for loss of balance:

- The quasigeostrophic limit occurs for $Ri \rightarrow \infty$. It has a geostrophic baroclinic instability (*Charney*

[1947]; Eady [1949]), whose “inflection point” in this particular case occurs at the vertical boundaries (see above).

- The third condition is satisfied if $Ri < 2$.
- The second condition is satisfied if $Ri < 1$.
- The classical (non-rotating) condition for the onset of Kelvin-Helmholtz instability (Miles [1961]; Howard [1961]) is satisfied if $Ri < \frac{1}{4}$.
- The first condition is satisfied if $Ri < 0$; this is gravitational instability (see above).

Analyses of this problem in Stone, [1966, 1970] and Nakamura [1988] show that a centrifugal instability does occur near $Ri = 1$ for both zonally symmetric and asymmetric fluctuations and that another ageostrophic instability (with shorter zonal wavelengths than the geostrophic instability) occurs for even larger values of Ri , though its onset value is not well determined. This latter instability is shown in Figure 2 of Stone [1970], with an accompanying remark that it has “growth rates $[\text{Im}\sigma]$ which decrease as Ri increases, and may in fact still be unstable for $Ri \geq 2$, but if so the growth rates were too small to be found by our numerical method, because of the near singular behavior of the coefficients of the differential equation when $\text{Im}\sigma$ is very small.” Confirmation is presented in Figure 8 of Nakamura [1988] which shows that $\text{Im}\sigma$ is strongly decreasing as Ri increases; it is somewhat unclear exactly how large a Ri value he obtained unstable solutions for, but his figure suggests it is at least as large as $Ri = 2$. An interpretation of the shortwave instability is presented (p. 3261): it involves a resonance between a boundary-trapped shear mode and an inertia-gravity mode, with an “inertia critical level” that limits the vertical extent of the eigenmode. Thus, although further examination is needed of the behavior of $\text{Im}\sigma$ in the vicinity of the third condition for loss of balance, the instabilities for this flow appear to support quite well the hypothesis we have advanced.

The Rest of the Quest

We have presented here a survey of the known instabilities of rotating, stably stratified fluids. Barotropic and baroclinic inflectional instabilities are the only types that occur in the quasigeostrophic limit, and several others arise in the neighborhood of the limits of balance as determined from the balance equations. These latter include gravitational, symmetric centrifugal, and elliptical, as well as presently unnamed variants

of barotropic and baroclinic instabilities. The instability onset is generally understood to be sharp with respect to the N^2 and A conditions for loss of balance, which correspond to the gravitational and centrifugal instabilities. We have shown for the elliptical, Taylor-Couette, and barotropic boundary-current instabilities that the onset behaviors are smooth in the transition across the $A - |S|$ condition, though still quite steep, with exponential or steeper dependences for the growth rate, $\sigma(A - |S|)$. The onset behavior near the $A - |S|$ condition has yet to be as well determined in the ageostrophic baroclinic instability problem, but previous studies indicate it is also steep. Kelvin-Helmholtz instability does not fit in this categorization scheme because its onset occurs well beyond the A and $A - |S|$ conditions.

Thus, we conclude that these problems give confirmation, *pro tem*, of the hypothesis that the limits of balance are indicative of transition from the larger-scale regime of inverse energy cascades in anisotropic flows to the smaller-scale regimes of forward energy cascade to dissipation of more nearly isotropic flows and intermittently breaking inertia-gravity waves. There is still need for refining our understanding of $\sigma(Ri, Ro, Fr)$ in the neighborhood of the conditions for loss of balance, especially for the less familiar third condition. Now that we know that pure barotropic and baroclinic instabilities fit the hypothesis, it would be worthwhile to further test it with more general shear profiles (e.g., the “coastal” $V(x, z)$ profile that Barth [1994] has shown to have an ageostrophic baroclinic instability). Beyond these linear instability problems lies the challenge of aptly diagnosing flow evolution near the loss of balance conditions in general nonlinear initial- and boundary-value problems. Nevertheless, we interpret the results in hand as indicating that the loss-of-balance transitions are steep but fuzzy, consistent with the view that the balanced slow manifold is itself modestly fuzzy and leaky to more efficiently cascading, unbalanced motions.

Acknowledgments. The authors appreciate support from the National Science Foundation, Office of Naval Research, and The Fund for the Promotion of Research at the Technion.

References

- Barth, J.A., Short-wavelength instabilities on coastal jets and fronts, *J. Geophys. Res.*, 99, 16095–16115, 1994.
- Bayly, B.J., Three-dimensional instability of elliptical flow, *Phys. Rev. Lett.*, 57, 2160–2163, 1986.
- Charney, J.G., The dynamics of long waves in a baroclinic westerly current, *J. Met.*, 4, 135–163, 1947.

- Charney, J., Geostrophic turbulence, *J. Atmos. Sci.*, **28**, 1087–1095, 1971.
- Chandrasekhar, S., *Hydrodynamic and Hydromagnetic Stability*. Oxford University Press, 1961.
- Craik, A.D.D., and W.O. Crimale, Evolution of wavelike disturbances in shear flow: a class of exact solutions of the Navier-Stokes equations, *Proc. R. Soc. London Ser. A*, **406**, 13–26, 1986.
- Drazin, P.G., and L.N. Howard, Hydrodynamic stability of parallel flow of inviscid fluid, *Adv. Appl. Mech.*, **9**, 1–89, 1966.
- Eady, E.T., Long waves and cyclone waves, *Tellus*, **1**, 33–52, 1949.
- Gent, P.R., and J.C. McWilliams, Regimes of validity for balanced models, *Dyn. Atmos. Oceans*, **7**, 167–183, 1983.
- Gent, P.R., and J.C. McWilliams, Balanced models in isentropic coordinates and the shallow water equations, *Tellus*, **36A**, 166–171, 1984.
- Griffiths, R.W., P.D. Killworth, and M.E. Stern, Ageostrophic instability of ocean currents, *J. Fluid Mech.*, **117**, 343–377, 1982.
- Hoskins, B.J., The role of potential vorticity in symmetric stability and instability, *Q. J. Royal Met. Soc.*, **100**, 480–482, 1974.
- Howard, L.N., Note on a paper of John W. Miles, *J. Fluid Mech.*, **10**, 509–512, 1961.
- Lorenz, E.N., Energy and numerical weather prediction, *Tellus*, **12**, 364–373, 1960.
- McWilliams, J.C., J.B. Weiss, and I. Yavneh, Anisotropy and coherent structures in planetary turbulence, *Science*, **264**, 410–413, 1994.
- McWilliams, J.C., and I. Yavneh, Fluctuation growth and instability associated with a singularity of the Balance Equations, *Phys. Fluids*, **10**, 2587–2596, 1998.
- McWilliams, J.C., I. Yavneh, M.J.P. Cullen, and P.R. Gent, The breakdown of large-scale flows in rotating, stratified fluids, *Phys. Fluids*, **10**, 3178–3184, 1998.
- Miles, J.W., On the stability of heterogeneous shear flows, *J. Fluid Mech.*, **10**, 496–508, 1961.
- Miyazaki, T., Elliptical instability in a stably stratified rotating fluid, *Phys. Fluids A*, **5**, 2702–2709, 1993.
- Molemaker, M.J., J.C. McWilliams, and I. Yavneh, Instability and equilibration of centrifugally-stable stratified Taylor-Couette flow, *Phys. Rev. Lett.*, **86**, 5270–5273.
- Nakamura, N., Scale selection of baroclinic instability—Effects of stratification and nongeostrophy, *J. Atmos. Sci.*, **45**, 3253–3267, 1988.
- Ooyama, K., On the stability of the baroclinic circular vortex: a sufficient condition for instability, *J. Atmos. Sci.*, **23**, 43–53, 1966.
- Pierrehumbert, R.T., Universal short-wave instability of two-dimensional eddies in an inviscid fluid, *Phys. Rev. Lett.*, **57**, 2157–2159, 1986.
- Rayleigh, Lord, On the stability, or instability, of certain fluid motions, *Proc. London Math. Soc.*, **9**, 57–70, 1880.
- Rayleigh, Lord, On the dynamics of revolving fluids, *Proc. R. Soc. London A* **93**, 148–154, 1916.
- Satomura, T., An investigation of shear instability in a shallow water, *J. Met. Soc. Japan*, **59**, 148–167, 1981.
- Stone, P.H., On non-geostrophic baroclinic instability, *J. Atmos. Sci.*, **23**, 390–400, 1966.
- Stone, P.H., On non-geostrophic baroclinic instability: Part II, *J. Atmos. Sci.*, **23**, 721–726, 1970.
- Taylor, G.I., Stability of a viscous fluid contained between two rotating cylinders, *Phil. Trans. R. Soc. London A*, **233**, 289–343, 1923.
- Yavneh, I., A.F. Shchepetkin, J.C. McWilliams, and L.P. Graves, Multigrid solution of rotating, stably stratified flows: The balance equations and their turbulent dynamics, *J. Comp. Phys.*, **136**, 245–262, 1997.
- Yavneh, I., J.C. McWilliams, and M.J. Molemaker, Non-axisymmetric instability of centrifugally stable, stratified Taylor-Couette flow, *J. Fluid. Mech.*, in press.

This preprint was prepared with AGU's *LATeX* macros v4, with the extension package 'AGU++' by P. W. Daly, version 1.6a from 1999/05/21.

Decay of Agulhas rings due to cross-frontal secondary circulations

S.S. Drijfhout

Royal Netherlands Meteorological Institute, De Bilt, The Netherlands

L. de Steur, and P.J. van Leeuwen

Institute for Marine and Atmospheric Research, Utrecht University, Utrecht, The Netherlands

Abstract. A series of idealized numerical experiments is presented to study the evolution of an Agulhas ring. The modeled ring is a circular symmetric idealization of ring Astrid, as measured by a cruise in March 2000. In particular, the hypothesis is tested that mixing is mainly due to cross-frontal secondary circulations. Both the role of beta-decay and shear instabilities in setting-up cross-frontal mixing is studied. The largest mixing of ring water with its surroundings occurs in the first months after shedding when the heat loss is maximal. Therefore, it is tested whether buoyancy forcing is able to enhance cross-frontal circulations. It is concluded that for realistic initial conditions the observed decay can be accounted for by adiabatic decay associated with cross-frontal circulations. The adiabatic decay appears to be a nonlinear function of the ring strength, possibly enhanced by the instability of the ring. The relative decay for weaker, stable rings is more than twice as weak. For a wide parameter range all modeled rings are unstable for a mode-2 perturbation and split. Observations suggest that most rings do not split and are not as unstable as suggested by the model. What causes this mismatch and how it affects the decay rate is still unclear. Realistic cooling is observed to slightly retard the split and marginally stabilize the ring. The decay rate is enhanced with typically 30%. For weaker rings the impact of cooling becomes less.

Introduction

In Autumn 1999, the Netherlands consorted observational and modeling program MARE (Mixing of Agulhas rings Experiment) was started (*Lutjeharms et al., 2000*). The main goal is to estimate the proportion of Agulhas leakage that contributes to the upper branch of the thermohaline circulation and identify the dominant mixing processes that determine that proportion. The experiment is motivated by the observation that the sea surface height anomaly of Agulhas rings most rapidly decays just after shedding (*Schouten et al., 2000*). Figure 1 shows the mean sea surface height (SSH) anomaly of 11 Agulhas rings as a function of age. During the first 5 months the decay is fast: 5 cm per month. After 10 months the rings decay very slowly: 0.5 cm per month. As a result, in the early phase when Agulhas rings cross the Benguela Current, the associated density anomaly for a large part is mixed away into the surroundings. The Benguela Current is thought to be the main agent for the North Atlantic Deep Water (NADW) return flow

in that region (*De Ruijter et al., 1999*). So, the mixing process(es) associated with the fast decay regime in the early phase of Agulhas rings mainly determines the proportion of Agulhas leakage that contributes to the NADW return flow.

To determine the mixing associated with the fast decay regime from measurements only, requires an observational database that contains an amount of detail which is not feasible with present day measurement techniques. Therefore, MARE consists of a hierarchy of modeling efforts to support the observational program. Here, we report a series of model simulations initialized with a circular symmetric idealization of ring Astrid, as measured by the first MARE cruise. In particular, we test the hypothesis that mixing is mainly due to cross-frontal secondary circulations. That is, the associated mixing is predominantly adiabatic (stirring). The stirring itself may have various dynamical origins which can be adiabatic (e.g., β -decay, baroclinic instability), or diabatic (e.g., cooling, double diffusion).

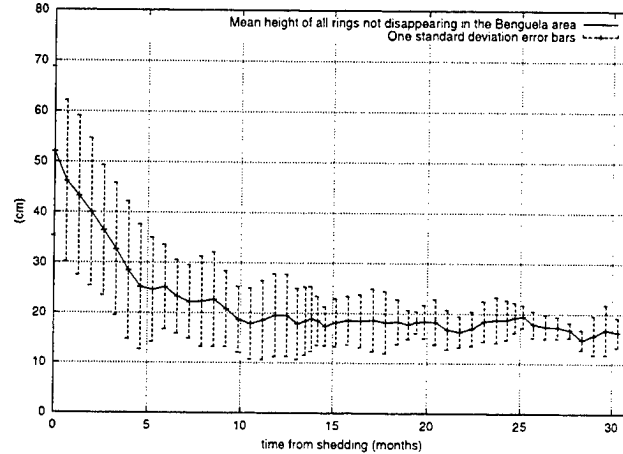


Figure 1. Mean SSH anomaly (and bars of 1 standard deviation) of Agulhas rings plotted against their age from Schouten *et al.* (2000).

Both observations and modeling efforts have shown that secondary circulations may arise due to internal instabilities (e.g., Pollard and Regier, 1992; Spall, 1995). In the case of convective chimneys, cooling sets the stage for baroclinic instability. Stirring is associated with baroclinic instability-driven intrusions (Legg and McWilliams, 2000). As the largest mixing of ring Water with its surroundings coincides with maximum heat loss, we test whether cooling is able to maintain/enhance cross-frontal stirring and whether this is the main driving agent for the decay of Agulhas rings.

Experimental setup

The simulations we analyze have been performed with MICOM 2.7, which is an extended version of the ocean general circulation model described by Bleck and Smith (1990). The horizontal resolution is 0.05° in longitude and latitude and there are 12 layers in the vertical. Computations were carried out on a 201×201 periodic domain with a flat bottom at 4000 m depth. The model was initialized with a circular symmetric idealization of ring Astrid. First, for 12 selected depth intervals, the average σ_0 outside the ring was calculated from the measurements. These σ_0 values were assigned to the isopycnic layers. Then, the σ_0 value at 50 m depth outside the ring (the bottom of layer 1) was estimated, and the depth of this σ_0 level was assessed as a function of the radial distance from the ring center. The curve, so obtained, was fitted to a linear profile (solid body rotation) inside the ring, and an $\exp(-r)^2$ profile outside the ring. The bounding edge between inside and outside was defined by the velocity maximum

of the ring.

The same profile was used for all layer depths, implying an equivalent barotropic structure. The amplitude as a function of layer number was obtained by evaluating the σ_0 values at the undisturbed layer depths outside the ring, and then calculating the depth of this σ_0 level at the ring center. The temperature profile was obtained in an analogous way and the salinity profile was calculated from the associated temperature and σ_0 values. The barotropic pressure gradient was assumed to compensate the baroclinic pressure gradient in the deepest layer. The initial velocity field was obtained by demanding cyclogeostrophic balance.

Due to the periodic boundary conditions there is a discontinuity in f and potential vorticity at the north/south boundary. This does not affect the ring structure, which is initialized in the middle of the domain, but it affects the barotropic waves that radiate away from the ring. As the barotropic waves re-enter the domain due to the periodic boundary conditions, they interact with the ring and this interaction is influenced by the north/south potential vorticity discontinuity. The impact on the ring of this interaction with the barotropic wave field is assumed to be small and not to affect the evolution characteristics of the ring.

In a few simulations the model was forced with uniform cooling to 16°C , with an average wind field of 7 m/s. This value was estimated from the wintertime SST for the same ring, as measured during the second MARE cruise. Initially, temperature in the surface layer was 18.43°C outside the ring, 20.53°C at the ring center. A uniform cooling to 16.0°C implies entraining layer 2 and part of layer 3 with initial values of 12.82°C outside the ring and 14.58°C at the ring center. Layer 3 is between 100 and 200 m depth outside the ring, between 320 and 520 m depth at the ring center.

Results

Stability characteristics

The stability of the modeled ring appeared to be highly sensitive to details of the initial profile, that is, both the horizontal shape and vertical profile. Horizontal shapes that feature vorticity maxima within the ring (e.g., an $\exp(-r)^2$ profile) generally induce quickly developing instabilities. Also, the vertical profile matters. Two different profiles with the same two-layer integrated properties (σ_0 and interface displacement) may show completely different stability behavior. In this case, the amplitude of the barotropic and first baroclinic mode is the same, but the amplitude of the higher baroclinic modes differ. Apparently, the amplitude of the higher baroclinic modes have a strong impact on

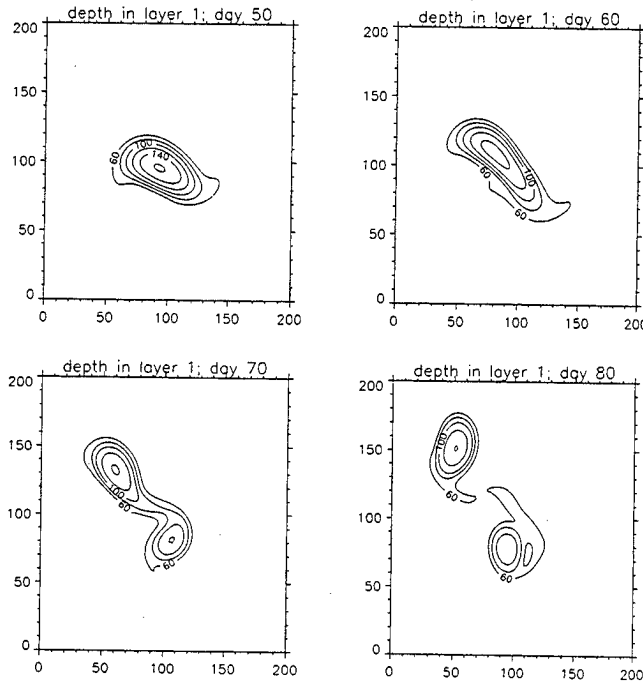


Figure 2. Thickness of the upper layer at days 50, 60, 70 and 80 with $\alpha=1$. Contour interval is 20 m.

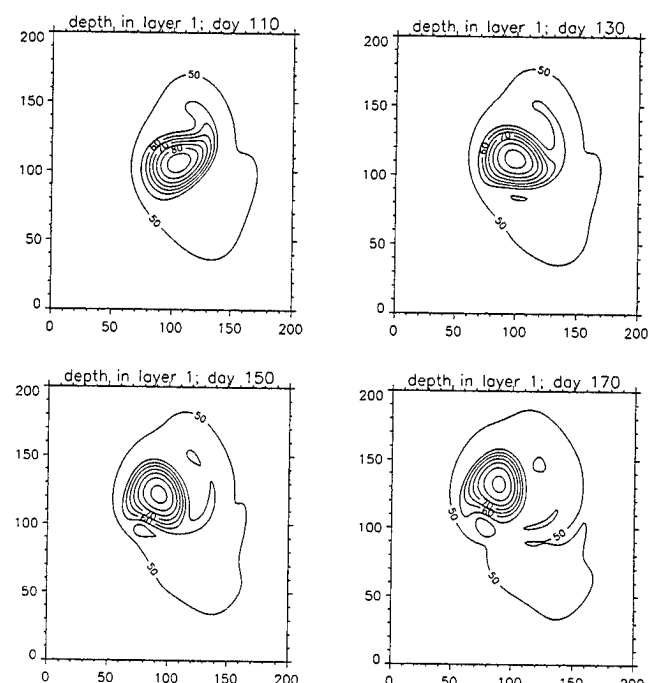


Figure 3. Thickness of the upper layer at days 110, 130, 150 and 170 with $\alpha=0.33$. Contour interval is 5 m.

the stability characteristics of the ring, and as a result, the two-layer stability results of Dewar *et al.* (1999) do not simply extrapolate to a multilayer setting.

All runs we discuss here use nearly the same parameter setting, which is derived from ring Astrid. The only parameter we vary is the overall strength. In all runs both the barotropic pressure gradient and interface displacements are multiplied with one and the same factor α . With $\alpha = 1$ the ring mimics ring Astrid. This ring is unstable for a mode-2 perturbation and the ring splits after 80 days. Figure 2 shows the evolution of upper layer thickness between day 50 and 80. At day 50 the ring has become ellipsoidal. At day 60 it is even more elongated. At day 70 a neck is forming in the middle, and at day 80 the ring is split into a slightly weaker and a stronger half.

The ring remains unstable while decreasing α to 0.5. When we decrease α further to 0.44 the ring becomes stable, that is, the ring sheds off satellites that become increasingly smaller and weaker relative to the parent ring with decreasing α . Figure 3 shows the evolution of upper layer thickness between day 110 and 170 for $\alpha = 0.33$. The ring becomes much less ellipsoidal. It develops streamers from which at intervals small satellites are cut off.

The strong tendency of ring Astrid to split is remarkable. Schouten *et al.* (2000) tracked 20 Agulhas rings using TOPEX/Poseidon satellite altimetry. Of those

20, 6 split, and 14 remained stable. As the strength of Astrid appears not to be a critical parameter, either the density stratification, or, the vertical profile of the rings should enhance the stability. In our calculations a change in stratification did not have a very strong impact, while a change in vertical profile in general made the ring more unstable. An alternative explanation could be that for the observed rings (nonlinear) interaction with the background flow, or, with other rings and cyclones could prevent splitting. Also, the bathymetry could stabilize the rings.

Decay

When calculating the SSH anomaly as a function of time for the unforced runs with $\alpha = 1$, it appears that the decay rate is consistent with the fast decay regime shown in Fig. 1. The cross-frontal mass exchange is associated with a single-cell secondary circulation that implies upwelling at the back of the ring and downwelling at the face of the ring (Fig. 4a). Here, back and face are defined along the β -induced movement. On the basis of potential vorticity considerations we would expect f -plane subduction to occur at the edge of the ring and upwelling in the middle when some sort of confluence is present near the ring edge (e.g., Pollard and Regier, 1992; Spall, 1995). This confluence can be provided for by the developing baroclinic instability. Apparently, the instability process develops slowly for Agulhas rings, so

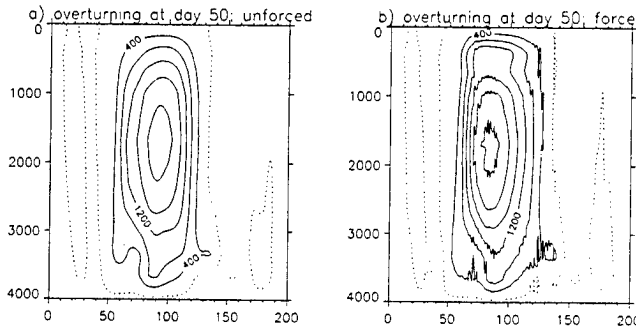


Figure 4. Meridional overturning at day 11 with $\alpha=1$. Units are in milliSverdrups. a) left panel unforced run; b) right panel run with cooling.

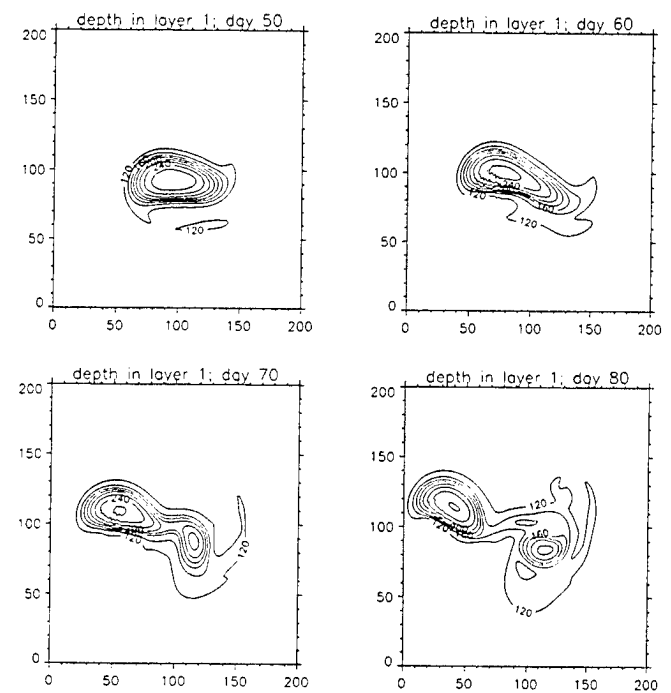


Figure 5. Thickness of the upper layer at days 50, 60, 70 and 80 with $\alpha=1$, and cooling turned on.

that the associated confluence is too weak to overcome the β -induced movement. The resulting single-cell overturning slightly extends across the ring boundaries and is associated with adiabatic stirring of the ring's density anomaly across its boundaries. When the ring is stable the associated adiabatic decay is (relatively) more than twice as slow, too weak to account for the observed fast decay regime. It is disturbing that the observed rings seem less unstable but still show a decay rate that is only found for modeled rings that are unstable.

When we allow for cooling, convection initially modifies the β -induced overturning cell. Figure 4b shows the meridional overturning at the same stage (day 50) as Fig. 4a, but now with cooling turned on. The convection-induced modification on the overturning is small. The only effect is more small-scale structure. The decrease of SSH as a function of time is enhanced by 30%. This is due to the direct effect of heat release through the surface. For stable rings the impact of cooling is smaller; too small to recover the observed fast decay regime. The impact of convection on the baroclinic instability is weak. This is contrary to the case of convective chimneys. There, the stratification is already weak, and cooling can significantly change the initial stratification and reduce the Rossby radius. This may have a severe impact on the stability characteristics of the convective chimneys (Legg and McWilliams, 2000). In case of Agulhas rings, the stratification is much stronger and the depth penetration of the effect of cooling is much less. As a result the Rossby radius is hardly reduced by convection, and the dominant effect is the reduction of vertical shear in the upper layers. Subsequently, cooling slightly stabilizes the ring and the instability process develops marginally slower. Figure 5 shows the evolution of upper layer thickness for $\alpha = 1$ with cooling turned on at day zero. Comparing Figs. 5 and 2 we observe only small differences; the splitting process occurs somewhat later in the case when cooling

has been turned on.

Discussion and Conclusions

Both adiabatic (β)-decay and baroclinic instability seem to account for the observed initial fast decay of Agulhas rings. The overturning associated with the β -induced movement implies cross-frontal mass exchange. Baroclinic instability mainly occurs for a wavenumber-2 disturbance which leads to ring splitting. The splitting itself hardly affects the SSH and density anomalies of the associated rings. Weaker, stable rings decay relatively more than twice as slow. Either the decay rate is a nonlinear function of the ring strength, or, baroclinic instability speeds up the overall decay. In that case, adiabatic decay does not explain the fast decay regime of the observed rings, as these seem more stable than the modeled rings. From the observed rings 30% split (Schouten et al., 2000), while in the model a reduction in ring strength by a factor of 2 relative to observed still leads to a split.

The impact of cooling on the decay of Agulhas rings is rather modest. Both the strong stratification and relatively weak air/sea temperature contrasts seem to be responsible for this. Cooling on the eddy scale is strong; $115 \text{ W m}^{-2} \text{ K}^{-1}$ (Drijfhout and Walsteijn 1998). In a Gulf Stream-like environment, cooling of rings significantly affects the regional heat balance and the decay of warm-core Gulf Stream rings. In the case of Agul-

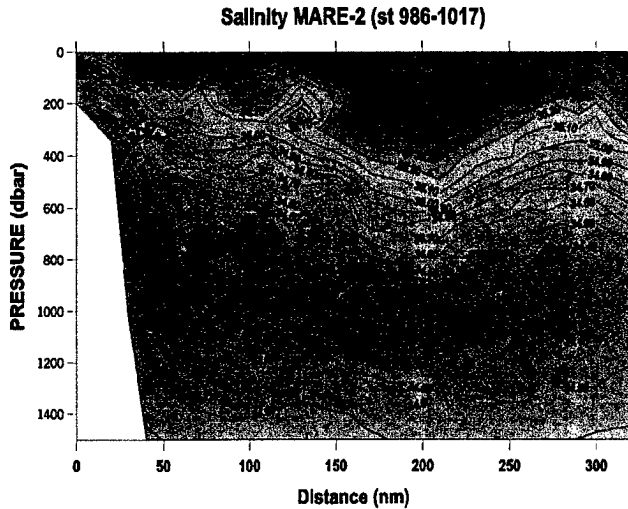


Figure 6. Zonal section of salinity through ring Astrid, taken at the second MARE cruise.

has rings, however, in general the depth penetration of cooling is too small to have such large impacts on the density and SSH anomaly of the rings. The decay rate is typically enhanced by 30%; for weaker rings the impact of cooling becomes less.

In our opinion, the most likely candidate to affect the decay of Agulhas rings we have overlooked so far, seems to be interleaving by double-diffusive driven thermohaline intrusions. Both in case of meddies and warm core Gulf Stream rings, double-diffusive driven interleaving has been identified as a main candidate in the decay of the mesoscale feature (e.g., Tang *et al.*, 1985, Ruddick, 1992). A zonal section through the edge of ring Astrid obtained from MARE-2 shows thermohaline intrusions to be operative between 100 and 150 nm from the coast and at 200 m depth (Fig. 6). A further analysis of the data is needed to identify whether these thermohaline intrusions have a double-diffusive origin. Also, the present numerical model has to be severely extended to be able to account for the development of double-diffusive-driven thermohaline intrusions. Such a study is left for the future.

References

- Bleck, R. and L.T. Smith, A wind-driven isopycnic coordinate model of the north and equatorial Atlantic ocean. 1. Model development and supporting experiments. *J. Geophys. Res.*, 95, 3273–3505, 1990.
- De Ruijter, W.P.M., A. Biastoch, S.S. Drijfhout, J.R.E. Lutjeharms, R.P. Matano, T. Pichevin, P.J. Van Leeuwen, and W. Weijer, Indian-Atlantic interocean exchange: Dynamics, estimation and impact. *J. Geophys. Res.*, 104, 20885–20910, 1999.
- Dewar, W.K., P.D. Killworth, and J.R. Blundell, Primi-
- tive-equation instability of wide ocean rings. Part II: Numerical studies of ring stability. *J. Phys. Oceanogr.*, 29, 1744–1758, 1999.
- Drijfhout, S.S. and F.H. Walsteijn, Eddy-induced heat transport in a coupled ocean-atmospheric anomaly model. *J. Phys. Oceanogr.*, 28, 1744–1758, 1998.
- Legg, S. and J.C. McWilliams, Temperature and salinity variability in heterogeneous oceanic convection. *J. Phys. Oceanogr.*, 30, 1188–1206, 2000.
- Lutjeharms, J.R.E., W.P.M. De Ruijter, H. Ridderinkhof, H. Van Aken, C. Veth, P.J. Van Leeuwen, S.S. Drijfhout, J.H.F. Jansen, and G.-J.A. Brummer, MARE and ACSEX: new research programmes on the Agulhas Current system. *S. Afr. J. Sci.*, 96, 105–110, 2000.
- Pollard, R.T., and L.A. Ringer, Vorticity and vertical circulation at an ocean front. *J. Phys. Oceanogr.*, 22, 609–625, 1992.
- Ruddick, B., Intrusive mixing in a Mediterranean salt lens-intrusion slopes and dynamical mechanisms. *J. Phys. Oceanogr.*, 22, 1609–1625, 1992.
- Schouten, M.W., W.P.M. De Ruijter, and P.J. Van Leeuwen, Translation, decay and splitting of Agulhas rings in the southeastern Atlantic Ocean. *J. Geophys. Res.*, 105, 21913–21925, 2000.
- Spall, M.A., Frontogenesis, subduction and cross-front exchange at upper ocean fronts. *J. Geophys. Res.*, 100, 2152–2168, 1995.
- Tang, C.L., A.S. Bennett, and D.J. Lawrence, Thermohaline intrusions in the frontal zones of a warm-core ring observed by batfish. *J. Geophys. Res.*, 90, 8928–8942, 1985.
- S. S. Drijfhout, Royal Netherlands Meteorological Institute, P.O Box 201, 3730 AE De Bilt, The Netherlands. L. de Steur and P. J. van Leeuwen, Institute for Marine and Atmospheric Research, Utrecht University, P.O. Box 80005, 3508 TA, Utrecht, The Netherlands. (e-mail: drijfhou@knmi.nl; steur@phys.uu.nl; leeuwen@phys.uu.nl)

This preprint was prepared with AGU's L^AT_EX macros v4, with the extension package 'AGU++' by P. W. Daly, version 1.6a from 1999/05/21.

Vertical shear plus horizontal stretching as a route to mixing

Peter H. Haynes

Department of Applied Mathematics and Theoretical Physics, University of Cambridge, UK

Abstract. The combined effect of vertical shear and horizontal stretching leads to thin, sloping structures in tracer fields, whose vertical length scale is much smaller than their horizontal length scale. These structures are then vulnerable to vertical mixing processes. This effect needs to be taken into account when interpreting the horizontal structure of oceanic (and atmospheric) tracers and may explain recent oceanographic observations.

1. Introduction

In both atmosphere and ocean it is useful to divide velocity fields into isentropic or isopycnal parts, which move fluid parcels along potential temperature or potential density surfaces, and diabatic or diapycnal parts, which move fluid parcels across such surfaces. This is because diabatic or diapycnal motion can be accomplished only by non-conservative physical processes such as radiative heating (in the atmosphere) and molecular diffusion of temperature enhanced by three-dimensional turbulence (in atmosphere and ocean). In large parts of the atmosphere and ocean, such processes are weak in some average sense, so that diabatic or diapycnal velocities must be much smaller than isentropic or isopycnal velocities.

The process of stirring may therefore be regarded as layerwise two-dimensional, in the sense that differential advection by the quasi-horizontal isentropic/isopycnal velocity field acts independently on each isentropic or isopycnal surface to distort tracer fields into complex geometrical configurations. If atmospheric and oceanic flows were purely two-dimensional, similar to many numerical simulations or laboratory experiments, then stirring would simply strengthen horizontal spatial gradients of tracer fields until horizontal diffusion became competitive with advection and mixing occurred. But in layerwise two-dimensional atmospheric and oceanic flows, horizontal advection that varies in the vertical may also act to increase vertical gradients, thereby enhancing the effects of vertical diffusion, or more complicated vertical mixing processes. The fact that vertical scales are almost always observed to be considerably smaller than horizontal scales suggests that mixing diffusion rather than horizontal mixing is the dominant process.

Most previous theoretical investigations of stirring

and mixing of tracers have focussed on models of quasi-isotropic flows, either in two or three dimensions. The considerations above suggest that the most relevant model for the atmosphere and the ocean is an anisotropic model in which the vertical velocity is zero, but the horizontal velocities depend on the vertical coordinate. *Haynes and Anglade* (1997, hereafter HA97) used such an anisotropic model to study the enhancement of vertical gradients by horizontal stirring plus vertical shear. This is a relatively simple extension to previous work, but essential if theoretical results are to be relevant to real flows. The HA97 work was motivated primarily by the stratosphere. This article reviews and expands on some of the arguments in that paper, focussing in particular on the implications for stirring and mixing in the ocean.

The model to be presented is based on the paradigm of ‘chaotic advection’, that flows that are smoothly varying in space and time may lead to patterns of advected tracer that are spatially highly complex. One of the requirements on a chaotic advection flow is that there is a useful division of scales between the smallest active scale in the advecting velocity field and the diffusive scale (or more generally scale at which genuine mixing processes act). The case of three-dimensional turbulence, for example, does not fall into this category, since the velocity field has complex spatial structure at scales down to the diffusive scale and it may be argued that the stirring of tracer features at any scale larger than the diffusive scale is dominated by the flow at the same scale (rather than at the large scale). In fact the chaotic advection paradigm is relevant in three-dimensionally turbulent flows for tracers with diffusivity much less than the momentum diffusivity (large Schmidt number). The tracer field may then have non-trivial structure on a spatial scale smaller than the Kolmogorov scale, with the flow at the Kolmogorov

scale providing the ‘large-scale’ stirring. This is often called the Batchelor regime of turbulence and has been studied as an important special case in recent theoretical work on tracer fields in turbulent flows (e.g. see *Shraiman and Siggia*, 2000 and references therein).

In the stratosphere it seems to be useful to consider tracer fields to be determined by the stirring effect of the large-scale flow (varying on spatial scales of hundreds to thousands of kilometers) and by the mixing effect of localised patches of three-dimensional turbulence, with vertical scales of a hundred meters or so and horizontal scales of a few kilometers. There is no strong evidence of active stirring by eddies on scales from a few hundred down to tens of kilometers, and in this range of scales the chaotic advection paradigm is therefore relevant.

Similarly in the ocean one might argue that mesoscale eddies with scales of tens of kilometers are the dominant part of the flow in stirring the tracer field at scales from a few tens of kilometers down to the scale of small-scale mixing events.

The structure of the paper is as follows. Section 2 describes a simple model problem of steady flow including both horizontal stretching and vertical shear, focussing on the spreading of a tracer from a point release in such a flow. Section 3 discusses some aspects of tracer evolution in more general random flows. Section 4 considers application of these ideas to the observations of *Ledwell et al.* (1993) (hereafter L93). Section 5 gives a brief discussion of the possible competing role of mixing by double-diffusive intrusions. Section 6 describes some possible future lines of research.

2. Steady flow model

The simplification allowed by the chaotic advection paradigm is that there is a finite scale below which the flow may be considered as a linear function of the space coordinates, i.e. the velocity field may be expanded as a (multidimensional) Taylor series about some reference location and only the linear term in the series retained. The effects of small-scale mixing events may be represented by a diffusion term (but more sophisticated representations are also possible).

We follow HA97 in considering first a steady linear flow that has the two ingredients of horizontal strain, Γ , plus vertical shear, Λ . In much of the atmosphere and ocean it is relevant to consider the parameter regime $\Lambda \gg \Gamma$, i.e. vertical shear much larger than horizontal strain. This may be argued from the observed fact that horizontal length scales tend to be larger than vertical scales or by appealing to theoretical arguments that the ratio of horizontal to vertical scales is of order f/N (Prandtl’s ratio), where f is the Coriolis parameter and

N the buoyancy frequency. f/N is $O(100)$ in the atmosphere and in the oceanic thermocline and perhaps reduces to $O(10)$ in the deep ocean.

The flow is taken to have components $(\Gamma x, -\Gamma y + \Lambda z, 0)$ in the x , y and z directions respectively, where (x, y, z) are Cartesian coordinates, with z vertical. The steadiness assumption implies that the horizontal strain Γ and the vertical shear Λ are constants. The equation for the evolution in this flow of a tracer with concentration $\chi(x, y, z, t)$ is therefore

$$\frac{\partial \chi}{\partial t} + \Gamma x \frac{\partial \chi}{\partial x} + (\Lambda z - \Gamma y) \frac{\partial \chi}{\partial y} = \kappa \left(\frac{\partial^2 \chi}{\partial x^2} + \frac{\partial^2 \chi}{\partial y^2} + \frac{\partial^2 \chi}{\partial z^2} \right), \quad (1)$$

where κ is the diffusivity, assumed constant.

HA97 considered sinusoidal solutions of this equation. Another useful solution of this equation, and indeed of the equation for tracer concentration in any flow where velocity components are linear functions of space coordinates (including time-dependent flows), is an ellipsoidal Gaussian solution, i.e. an exponential function of a negative definite quadratic function of x , y and z . This is conveniently obtained by considering the second-order spatial moments of the solution, such as $m_{xx} = \int x^2 \chi dV / \int \chi dV$, m_{xy} etc. The six moments are sufficient to determine the quadratic function and the constraint that the total amount of tracer remains constant then determines the coefficient of the exponential function. In the above flow, the equations for the moments may be shown to be

$$\frac{d}{dt} m_{xx} = 2\Gamma m_{xx} + \kappa \quad (2)$$

$$\frac{d}{dt} m_{xy} = \Lambda m_{xz} \quad (3)$$

$$\frac{d}{dt} m_{xz} = \Gamma m_{xz} \quad (4)$$

$$\frac{d}{dt} m_{yy} = -2\Gamma m_{yy} + 2\Lambda m_{yz} + 2\kappa \quad (5)$$

$$\frac{d}{dt} m_{yz} = -\Gamma m_{yz} + \Lambda m_{zz} \quad (6)$$

$$\frac{d}{dt} m_{zz} = \kappa \quad (7)$$

These equations may be solved straightforwardly. For brevity we consider the case where all moments tend to zero as $t \rightarrow 0^+$, corresponding to a point release. Then the solutions are

$$m_{xx} = \frac{\kappa}{\Gamma} e^{2\Gamma t} \quad (8)$$

$$m_{xy} = m_{xz} = 0 \quad (9)$$

$$m_{yy} = \frac{\kappa\Lambda^2}{\Gamma^3} \{2\Gamma t + 4e^{-\Gamma t} - e^{-2\Gamma t} - 3\} + \frac{\kappa}{\Gamma} \{1 - e^{-2\Gamma t}\} \quad (10)$$

$$m_{yz} = 2\frac{\kappa\Lambda}{\Gamma^2} \{\Gamma t - 1 + e^{-\Gamma t}\} \quad (11)$$

$$m_{zz} = 2\kappa t \quad (12)$$

First consider the case where $\Lambda = 0$, i.e. the case of purely two-dimensional flow. Then $m_{xx} = \kappa(e^{2\Gamma t} - 1)/\Gamma$ and $m_{yy} = \kappa(1 - e^{-2\Gamma t})/\Gamma$. For small times, $t \ll \Gamma^{-1}$, diffusion dominates and both m_{xx} and m_{yy} increase linearly with time. When $t \sim \Gamma^{-1}$ advection by the horizontal strain flow becomes competitive with diffusion. The tracer elongates in the direction of the stretching axis, so that for $t \gg \Gamma^{-1}$, $m_{xx} \sim \kappa e^{2\Gamma t}/\Gamma$, whilst in the direction of the compression axis a steady-state balance between strain and diffusion is achieved, with $m_{yy} \sim \kappa/\Gamma$. At all times the only vertical transport is through diffusion, so m_{zz} increases linearly with t at all times.

What is the effect of adding vertical shear, i.e. taking $\Lambda \neq 0$ (with $\Lambda \gg \Gamma$)? The elongation of the tracer along the stretching axis of the horizontal strain axis is unchanged. However, the spreading of the tracer in the direction of the compression axis is rather different. Examination of the expression for m_{yy} above shows that there are three regimes. For $t \lesssim \Lambda^{-1}$ (regime I) there is purely diffusive spreading as above. For $\Lambda^{-1} \lesssim t \lesssim \Gamma^{-1}$ (regime II) the diffusive spreading of the tracer in the vertical allows the vertical shear to augment the spreading in the horizontal, so that $m_{yy} \sim \kappa\Lambda^2 t^3$. Finally when $t \sim \Gamma^{-1}$ horizontal advection begins to inhibit the horizontal spreading, so that for $t \gtrsim \Gamma^{-1}$ (regime III), $m_{yy} \sim \kappa\Lambda^2/\Gamma^2$. These three regimes are depicted graphically in Figure 1. Note that m_{yy} continues to increase with time, in contrast to the case with $\Lambda = 0$. In regime III $m_{yy} \sim \Lambda m_{yz}/\Gamma \sim \Lambda^2 m_{zz}/\Gamma^2$ suggesting that the y and z scales of the tracer patch are in the ratio Λ/Γ . Indeed what happens is that the tracer patch forms a sheet that slopes at angle Γ/Λ (from the horizontal) in the (y, z) plane. The extent of the sheet in the vertical direction is $(\kappa t)^{1/2}$, therefore the extent of the sheet in the horizontal (y) direction is $\Lambda(\kappa t)^{1/2}/\Gamma$. This explains the dominant behaviour of m_{yy} , m_{yz} and m_{zz} . In order to deduce the spread of the tracer on a given horizontal surface it is useful to consider $m_{yy} - 2\Lambda m_{yz}/\Gamma + m_{zz}\Lambda^2/\Gamma^2$, i.e. the moment of $(y - \Lambda z/\Gamma)^2$. It is straightforward to show that

$$\begin{aligned} m_{yy} - 2\Lambda m_{yz}/\Gamma + m_{zz}\Lambda^2/\Gamma^2 &= \\ \frac{\kappa}{\Gamma} \left(1 + \frac{\Lambda^2}{\Gamma^2}\right) (1 - e^{-2\Gamma t}) &\simeq \frac{\kappa \Lambda^2}{\Gamma \Gamma^2} (1 - e^{-2\Gamma t}). \end{aligned} \quad (13)$$

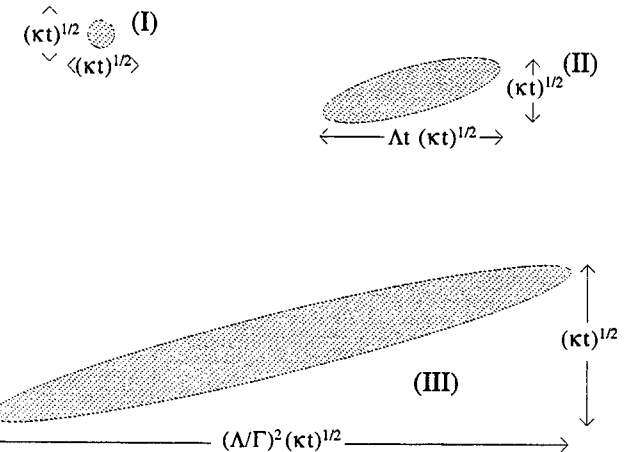


Figure 1. The spread of tracer in the (y, z) in each of regimes I ($t \lesssim \Lambda^{-1}$), regime II ($\Lambda^{-1} \lesssim t \lesssim \Gamma^{-1}$) and regime III ($\Gamma^{-1} \lesssim t$).

Thus the spread of the tracer on a given horizontal surface is $(\kappa/\Gamma)^{1/2} \Lambda/\Gamma$. The effect of the vertical shear is therefore to increase the equilibrium width of the tracer patch by a factor Λ/Γ .

In summary, the effect of the vertical shear is to lead to sloping structures in the tracer field with aspect ratio (ratio of horizontal length scale to vertical length scale) $\alpha = \Lambda/\Gamma$. The equilibrium width of these structures is larger by a factor α than would be the case without vertical shear. One might say that it is *as if* a horizontal diffusivity $\kappa\alpha^2$ were acting.

3. Time-dependent flow models

In a flow that varies in space and time, the velocity gradient encountered by a fluid parcel changes with time as the particle moves through the flow. The evolution of small-scale tracer features is therefore governed by the equation for tracer evolution in a time-dependent linear flow. In the study of turbulence there is a long tradition of considering the effect of a linear flow that varies randomly in time (using so-called ‘random-straining’ models). This approach has been used most recently by various authors to give a rather complete description of the statistics of tracer fields in Batchelor-regime turbulence. [See Balkovsky and Fouzon, 1999 and Falkovich *et al.*, 2001 for further details of this work.]

The random-straining model most relevant to the atmosphere and ocean is non-standard in that the statistics of the velocity gradient tensor is not isotropic (since the vertical velocity is zero, but the vertical gradient of the horizontal velocity is not). HA97 considered such random-straining models and showed that the important predictions of the steady flow model presented in

Section 2 carried over, in the sense that the tracer field was predicted to form sloping sheets, with an aspect ratio α that depended on the statistics of the horizontal strain and vertical shear fields.

We review some of the HA97 results below, emphasising the dependence of α on the different flow parameters. One particular goal is to identify conditions under which α is not simply equal to the aspect ratio Λ/Γ of the flow itself.

It is convenient to consider the normalised gradient of the tracer field, defined by $\mathbf{k}(t) = \chi^{-1} \nabla \chi$, evaluated at the position $\mathbf{x} = \mathbf{X}(t)$ following a fluid parcel. \mathbf{k} might be considered as a local wavenumber of the tracer field in the case where the tracer field varies rapidly in space compared to the velocity field. It may be shown from the gradient of the tracer advection equation that

$$\frac{d\mathbf{k}}{dt} = -(\nabla \mathbf{u}) \cdot \mathbf{k} \quad (14)$$

where the scalar product on the right-hand side applies to the second index of the tensor $\nabla \mathbf{u}$. The evolution of \mathbf{k} therefore depends on the time series of $\nabla \mathbf{u}$ (encountered following the point $\mathbf{X}(t)$). In a random-straining model the effect of turbulent flow on gradients of tracer (or line elements) is considered as a kinematical problem, in which the tensor $\nabla \mathbf{u}$ is taken to be given by a random time series, without addressing questions of the flow dynamics.

For the layerwise two-dimensional flows of interest here, the matrix W of components of the velocity gradient tensor, with $W_{ij} = \partial u_i / \partial x_j$, has $W_{31} = W_{32} = W_{33} = 0$. (The index 3 is taken to correspond to the z coordinate.) It is useful to write $\mathbf{k} = (\mathbf{k}^{(h)}, m)$, with $\mathbf{k}^{(h)}$ the horizontal wavenumber and m the vertical wavenumber, and define $\mathbf{W}^{(h)}$ to be the 2nd rank tensor with components W_{11}, W_{21}, W_{12} and W_{22} , and Λ to be the vector with components (W_{13}, W_{23}) . It then follows that

$$\frac{dk_i^{(h)}}{dt} = -W_{ji}^{(h)} k_j^{(h)} \quad (15)$$

and

$$\frac{dm}{dt} = -W_{j3} k_j^{(h)} = -\Lambda_j k_j^{(h)} \quad (16)$$

In what follows the summation convention is used for repeated suffices and the suffices run through the values $\{1, 2\}$. Equation (15) is just that for the tracer wavenumber in two-dimensional (horizontal) flow. Note that it may be solved independently of (16). Thus variation in the z -direction makes no difference to the evolution of the horizontal wavenumber vector. However (16) shows that the vertical wavenumber evolves through the vertical shear (in the horizontal flow) acting on the horizontal wavenumber vector.

To formulate a suitable random-straining model we assume that each of the six non-zero components of the matrix W is a realisation of a random function of time, with average (over all realisations) zero. We also assume that the wavenumber at $t = 0$ is randomly chosen and is statistically independent of the W_{ij} . Equation (16) may be integrated to give

$$m(t) = m(0) + \int_0^t \Lambda_j(t') k_j^{(h)}(t') dt' \quad (17)$$

and then squaring, and taking the ensemble average, it follows that

$$\langle m(t)^2 \rangle = \langle m(0)^2 \rangle + \int_0^t dt' \int_0^t dt'' \langle \Lambda_j(t') k_j^{(h)}(t') \Lambda_k(t'') k_k^{(h)}(t'') \rangle, \quad (18)$$

where $\langle \cdot \rangle$ denotes the ensemble average, over all realisations of the flow field and all realisations of the initial wavenumber vector.

Useful quantitative estimates are possible if a number of further assumptions are made concerning the statistics of the velocity gradient tensor. The first is that the components of Λ are independent of all components of $\mathbf{W}^{(h)}$, i.e. that the vertical shear is statistically independent of the horizontal deformation. It follows that Λ is also independent of $\mathbf{k}^{(h)}$ so that averages of terms involving Λ and terms involving $\mathbf{k}^{(h)}$ may be taken separately in (18). The second important assumption is stationarity, from which it follows $|\langle \Lambda_j(t') \Lambda_k(t'') \rangle| \sim \Lambda^2 g(\sigma_\Lambda |t' - t''|)$, for some function g , where σ_Λ is an inverse correlation time for the vertical shear and $\Lambda^2 = \langle \Lambda^2 \rangle$.

In order to estimate the integral appearing in (18) it is also necessary to have information on the evolution of the horizontal wavenumber. This follows exactly as in the random straining models of isotropic two-dimensional flow considered by Kraichnan (1974) and others. The basic predictions of these theories are that the horizontal wavenumber increases exponentially in time, at a rate, S say, governed by the statistics of the horizontal strain field and depending in particular on the root mean square rate of strain, Γ say, and on the inverse correlation time σ_h for the horizontal strain field. Detailed analysis of explicit models (Kraichnan, 1974; Chertkov et al., 1995; HA97) suggests that $S \sim \Gamma \min(\Gamma/\sigma_h, 1)$.

Again, making suitable stationarity assumptions, this suggests that $|\langle k_i^{(h)}(t') k_j^{(h)}(t'') \rangle| \sim k_0^2 e^{S(t'+t'')} h(\mu |t' - t''|)$, where $k_0^2 = \langle \mathbf{k}^{(h)}(0)^2 \rangle$. The inverse time scale μ and the precise form of the function $h(\cdot)$, depend on the statistics of the horizontal strain field, but explicit calculation in various models suggests that $\mu \sim S$.

Substituting these estimates into (18) it follows that, for large times, when the second term on the right-hand side dominates the first,

$$\langle m(t)^2 \rangle \sim \frac{\Lambda^2 k_0^2 e^{2St}}{S^2} \min\left\{1, \frac{S}{\sigma_\Lambda}\right\}. \quad (19)$$

Note that the dominant contribution to the first integral, over t'' , performed in (18) comes from a neighbourhood of $t'' = t$ of size $\min\{S^{-1}, \sigma_\Lambda^{-1}\}$ and that to the second integral, over t' , comes from a neighbourhood of $t' = t$ of size S^{-1} .

The ratio α of horizontal length scale to vertical length scale, or, equivalently, the ratio of vertical wavenumber to horizontal wavenumber may therefore be estimated as

$$\begin{aligned} \alpha^2 &\sim \frac{\langle m(t)^2 \rangle}{\langle k^{(h)}(t)^2 \rangle} \sim \frac{\Lambda^2}{S^2} \min\left\{1, \frac{S}{\sigma_\Lambda}\right\} \\ &\sim \frac{\Lambda^2}{\Gamma^2} \max\left(1, \frac{\sigma_h^2}{\Gamma^2}\right) \min\left\{1, \frac{\Gamma}{\sigma_\Lambda} \min\left(1, \frac{\Gamma}{\sigma_h}\right)\right\}. \end{aligned} \quad (20)$$

with the last estimate following from the estimate for S .

This semi-quantitative analysis suggests that the vertical wavenumber increases exponentially at the same rate as the horizontal wavenumber, and that the ratio α is equal to the ratio of vertical shear to horizontal strain, Λ/Γ , multiplied by a number that depends on σ_h/Γ and σ_Λ/Γ . These predictions agree with explicit calculations based on suitably formulated random-straining models. (See HA97 for more details.)

Figure 2 summarises the variation of the aspect ratio α with the parameters σ_h and σ_Λ . Note that α is anomalously large (i.e. greater than Λ/Γ) when the horizontal strain varies on a timescale that is shorter than both the inverse horizontal strain rate and the timescale of variation of the vertical shear. On the other hand, α is anomalously small (i.e. less than Λ/Γ), when the vertical shear varies on a timescale that is shorter than both the inverse horizontal strain rate and the timescale of variation of the horizontal strain. As might be expected, in the limit where $\sigma_h \ll \Gamma$ and $\sigma_\Lambda \ll \Gamma$ the estimate for α agrees with that obtained for the steady flow considered in the previous section.

Note that in this section we have not considered the effects of diffusion explicitly. Nonetheless, it is plausible that diffusion acts in a similar way to that deduced from the steady flow model in Section 2, i.e. diffusion κ acts on structures in the tracer field that slope with aspect ratio α and the result, e.g. in achieving a balance between diffusion and horizontal straining, is that it is as if there is a horizontal diffusivity with magnitude $\kappa\alpha^2$. This is supported (with certain limitations) by explicit calculations in *Vanneste and Haynes (2001)*.

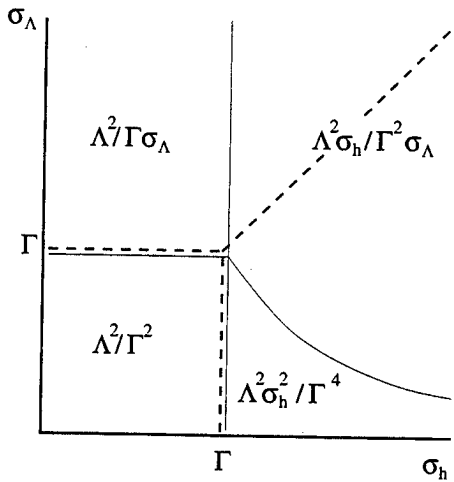


Figure 2. Scaling of α^2 (where α is aspect ratio of horizontal to vertical scale) with parameters Γ (horizontal strain rate), Λ (vertical shear), σ_h (inverse correlation time for horizontal strain) and σ_Λ (inverse correlation time for vertical shear). The thin dashed lines delimit the regions where the different estimates hold. The thick dashed lines delimit the regions where α scales as the aspect ratio of the velocity field (Λ/Γ) (lower left-hand region), is larger than that aspect ratio (right-hand region) and is smaller than that aspect ratio (upper region).

4. Application to the Ledwell et al. (1993) observations

In the tracer release experiment reported by L93 the dispersion of a tracer in the ocean thermocline was followed over a period of several months. The vertical (cross-isopycnal) diffusion could be estimated directly and a value of vertical diffusivity κ_v of about $10^{-5} \text{ m}^2 \text{s}^{-1}$ was inferred. In the horizontal the tracer was, in the later stages of the experiment, observed to be confined to thin streaks, whose width apparently reached an equilibrium value of about 3 km. This was interpreted as the stretching out of the tracer patch by the mesoscale eddy field, resulting in filaments of tracer whose width was the equilibrium value determined by a balance between horizontal stretching (which tends to reduce the width of the filament) and horizontal dispersive effects, perhaps associated with small-scale mixing processes (which tend to increase the width of the filament). From the observed length of the tracer filament it was estimated that the average stretching rate experienced was about $3 \times 10^{-7} \text{ s}^{-1}$. It followed that if the horizontal dispersive effects could be represented by an effective horizontal diffusivity κ_h , it must have a value of about $3 \text{ m}^2 \text{s}^{-1}$ ($\simeq (3 \text{ km})^2 \times 3 \times 10^{-7} \text{ s}^{-1}$). Thus $\kappa_h/\kappa_v \simeq 3 \times 10^5$. Previous work by *Young et al. (1982)*, taking account of the combined effect of vertical mixing and horizontal advection by inertio-gravity waves had

suggested $\kappa_h/\kappa_v \simeq (N/f)^2 \simeq 1500$, i.e. 200 times too small to account for the L93 observations.

HA97 noted that the combined effect of horizontal stretching and vertical shear could account for the value of κ_h/κ_v if the aspect ratio α was about 500. According to the analysis presented in Section 3 this requires $\Lambda \sim 1.5 \times 10^{-4} \text{ s}^{-1}$, based on the estimate $\alpha \sim \Lambda/S$ (which holds if $\sigma_\Lambda \lesssim S$, i.e. the correlation time for the vertical shear must be larger than S^{-1}). This value of vertical shear (equivalent to 15 cm s⁻¹ per km) does not seem indefensible as realistic.

If the models described in this article are to be relevant to the L93 observations, one might ask further whether the observed morphology of the tracer is consistent with the model predictions. First it is clear that in a flow with finite length scales the exponential stretching in a single direction predicted by the model in Section 2 must break down when the largest length scale of the tracer patch (or, at this stage, tracer filaments) becomes comparable to the length scale of the flow. What happens is simply that the filaments meander on the length scale of the flow (as observed in countless laboratory and numerical experiments). Perhaps more crucial is the shape of tracer filaments in cross-section. The model of Section 2 predicts that this will ultimately be highly elongated, so that the tracer is actually concentrated within sloping sheets. However, this applies on time scales much greater than Γ^{-1} , where Γ is the strain rate and therefore, in the steady model, the stretching rate. For times comparable to Γ^{-1} (see Figure 1), the tracer distribution is not sheet-like, but it is simply the case that the filament cross section has much larger horizontal extent than vertical extent (by a factor α). The observing period reported by L93 is such that $\Gamma t \lesssim 6$, so that sheet-like features are not necessarily expected. [Note that the extent of the sheets is proportional to $(\Gamma t)^{1/2}$.]

5. Possible effects of double diffusion

Garrett (1982) (hereafter G82) noted that the stirring by mesoscale eddies of temperature and salinity along isopycnal surfaces would lead to large local gradients in these quantities manifested as thermohaline fronts. These in turn might lead to double-diffusive intrusions. G82 argued that the sharpening of gradients of temperature and salinity by stirring would be halted by the mixing effects of the intrusions when the growth rate of the intrusions was equal to the convergence acting on the fronts, i.e. to the stretching rate associated with the stirring process. He gave the formula (based on previous theoretical and experimental work)

$$\lambda_{max} = 0.075 \frac{g\beta S_x}{N} \quad (21)$$

for the maximum growth rate λ_{max} of the intrusions, where g is the gravitational acceleration, $\beta = \rho^{-1}(\partial\rho/\partial S)_T$ is the rate of change, at constant temperature, of density with salinity, and S_x is the salinity gradient in the neighbourhood of the front. He argued that if the front had width L_f then the approximate value of S_x would be $S_x = \tilde{S}_x L_{eddy}/L_f$ where \tilde{S}_x was the large-scale salinity gradient and L_{eddy} was the typical size of the mesoscale eddies. If s is the stretching rate then it follows that L_f is given by the formula

$$L_f = 0.075 \frac{g\beta S_x}{N} \frac{L_{eddy}}{s}. \quad (22)$$

For the values of s and L_f observed by L93 (taking L_f to be the width of the filaments) and assuming $L_{eddy} \sim 100$ km, this would require $g\beta S_x/N \simeq 10^{-7} \text{ s}^{-1}$. This is, in fact, considerably weaker than the values suggested by G82 as examples. This therefore appears to leave open the possibility that it is the mixing effects, along isopycnal surfaces, of double diffusive intrusions, rather than any process directly related to 'background' vertical mixing, that determines the width of the filaments observed by L93. On the other hand it is not at all clear that the filaments of a tracer injected at an arbitrary location will match the regions of enhanced gradients in temperature and salinity whose distribution is set on the large scale and therefore feel the same mixing effects.

6. Discussion

The work reported in HA97 may be extended in various ways, some of which are relevant to oceanographic considerations. For example, *Vanneste and Haynes* (2001) have considered the effect of vertical shear on the horizontal wavenumber spectrum of passive tracers, in particular on the range of scales where the effects of diffusive mixing become important. In particular this work highlights the limitations of estimating the effective horizontal diffusivity as $\kappa\alpha^2$. The recent theoretical work on Batchelor-regime turbulence has made explicit predictions about probability density functions for tracer concentrations, tracer concentration differences (over a finite distance) and tracer concentration gradients and this work needs to be extended to the layerwise two-dimensional case if it is to be applicable to real atmospheric and oceanic flows.

Much insight into atmospheric tracer distributions has been obtained by using models driven by observed velocity fields, or velocity fields extracted from quasi-realistic global models. Approaches have included full numerical integrations of the tracer evolution equation (e.g. on an isentropic surface), non-diffusive reconstructions of tracer fields by following back trajectories to an

initial condition and calculations of the statistical properties of large numbers of trajectories, e.g. to give the distribution of finite-time stretching rates. See, for example, the papers by *Schoeberl and Newman* (1995), *Ngan and Shepherd* (1999) and *Hu and Pierrehumbert* (2001). All of these methods have substantial savings over integrations of a full model including tracer equations and dynamical equations and some may be worth applying in the oceanic context. Velocity fields might be extracted from eddy-resolving models for this purpose, but as a first step it might be worth considering 'synthetic' velocity fields that are generated quite artificially to have a plausibly realistic spatial and temporal structure in space and time.

Acknowledgments. I am grateful to Chris Garrett for bringing possible double-diffusive effects to my attention.

References

- Balkovsky, E. and A. Fouxon, Universal long-time properties of Lagrangian statistics in the Batchelor regime and their application to the passive scalar problem. *Phys. Rev. E*, **60**, 4164–4174, 1999.
- Chertkov, M., Falkovich, G., Kolokolov, I. and V. Lebedev, V., Statistics of a passive scalar advected by a large-scale two-dimensional velocity field: analytic solution. *Phys. Rev. E*, **51**, 5609–5627, 1995.
- Falkovich, G., I. Kolokolov, V. Lebedev, and S. Turitsyn, Statistics of soliton-bearing systems with additive noise. *Phys. Rev. E*, **63**, 025601(R), 2001.
- Garrett, C., On the parametrization of diapycnal fluxes due to double-diffusive intrusions. *J. Phys. Oceanogr.*, **12**, 952–959, 1982.
- Haynes, P. H. and J. Anglade, The vertical-scale cascade of atmospheric tracers due to large-scale differential advection. *J. Atmos. Sci.*, **54**, 1121–1136, 1997.
- Hu, Y. and R.T. Pierrehumbert, The advection-diffusion problem for stratospheric flow. Part I: Concentration probability. *J. Atmos. Sci.*, **58**, 1493–1510, 2001.
- Kraichnan, R. H., Convection of a passive scalar by a quasi-uniform random straining field. *J. Fluid Mech.*, **64**, 737–762, 1974.
- Ledwell, J. R., Watson, A. J. and C. S. Law, Evidence for slow mixing across the pycnocline from an open-ocean tracer-release experiment, *Nature*, **364**, 701–703, 1993.
- Ngan, K. and T.G. Shepherd, A closer look at chaotic advection in the stratosphere. Part I: Geometric structure. *J. Atmos. Sci.*, **56**, 4134–4152, 1999.
- Schoeberl, M. R. and P. A. Newman, A multiple-level trajectory analysis of vortex filaments. *J. Geophys. Res.*, **100**, 25801–25815, 1995.
- Shraiman, B. I. and E. D. Siggia, Scalar turbulence. *Nature*, **405**, 639–646, 2000.
- Vanneste, J. and P. H. Haynes, The role of diffusion and vertical shear in determining stratospheric tracer spectra, *J. Atmos. Sci.* (submitted), 2001.
- Young, W. R., Rhines, P. B., Garrett, C. J. R., Shear-flow dispersion, internal waves and horizontal mixing in the ocean. *J. Phys. Oceanogr.*, **12**, 515–527, 1982.

This preprint was prepared with AGU's LATEX macros v4, with the extension package 'AGU++' by P. W. Daly, version 1.6a from 1999/05/21.

Spirals on the sea: A manifestation of upper-ocean stirring

Walter Munk and Laurence Armi

Scripps Institution of Oceanography, La Jolla, California

Abstract. Spiral eddies were first seen in the sun glitter on the Apollo Mission 30 years ago; they have since been recorded on SAR missions and in the infrared. The spirals are globally distributed, 10–25 km in size and overwhelmingly cyclonic. They have not been explained. Under light winds favorable to visualization, linear surface features with high surfactant density and low surface roughness are of common occurrence. We have proposed that frontal formations concentrate the ambient shear and prevailing surfactants. Horizontal shear instabilities ensue when the shear becomes comparable to the Coriolis frequency. The resulting vortices wind the linear features into spirals. The hypothesis needs to be tested by prolonged measurements and surface truth. Spiral eddies are a manifestation of a sub-mesoscale oceanography associated with upper ocean stirring; dimensional considerations suggest a horizontal diffusivity of order $10^3 \text{ m}^2 \text{s}^{-1}$.

Introduction

The first photographs of spiral eddies appear to have been taken on Apollo-Saturn in October 1968. In the late 70s SEASAT with its synthetic aperture radar (SAR) confirmed the early discoveries from crewed space flights (Stevenson 1998, 1999). But most of the existing material was collected by Paul Scully-Power (the first and so far only oceanographer-astronaut) on 5–13 October 1984: “Far and away the most impressive discovery... is that of the submesoscale ocean (less than 100 km) is far more complex dynamically than ever imagined... Patterns of this complexity could be seen to be interconnected for hundreds and hundreds of kilometers” (Scully-Power 1986).

The spiral pattern whose global distribution was reported by Scully-Power is at an awkward scale, virtually impossible to recognize from shipboard, and too large to be encompassed even from high-flying aircraft. Discovery had to await space missions.

Spiral Images in the Sun Glitter and in SAR

Figures 1 and 2 show a visual and SAR image, respectively, of spiral streak patterns. Spirals are globally distributed (Figure 3). Typical spiral dimensions are from 10 to 20 km, with streaks 50 to 100 m wide. Spirals are overwhelmingly cyclonic, wound anti-clockwise (viewed from above) in the northern hemisphere, clockwise in the southern hemisphere. Ship wakes crossing the streaks (not shown) have a cyclonic offset with

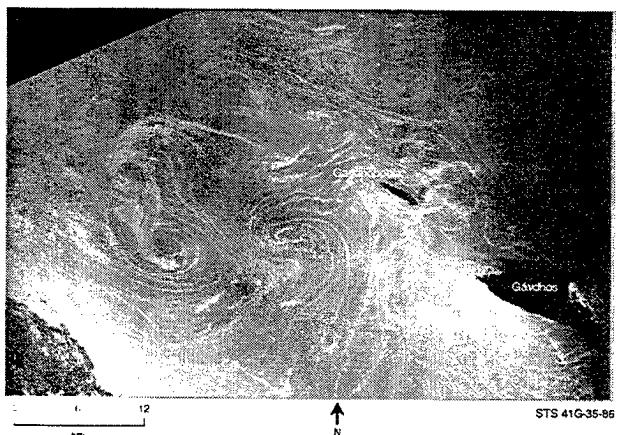


Figure 1. A pair of interconnected spirals in the Mediterranean Sea south of Crete. This vortex pair has a clearly visible stagnation point between the two spirals, the cores of which are aligned with the pre-conditioning wind field. 7 October 1984.

shears up to 10^{-3} s^{-1} . We need to refer to *Munk et al.* (2000) (henceforth *MAFZ*) for a more representative selection (13 images out of 400 collected).

The observational material poses three questions:

- (A) How are the spirals wound?
- (B) How is symmetry broken in favour of cyclonic rotation?
- (C) What makes spirals visible?
On SAR images the streaks are always dark, indicat-

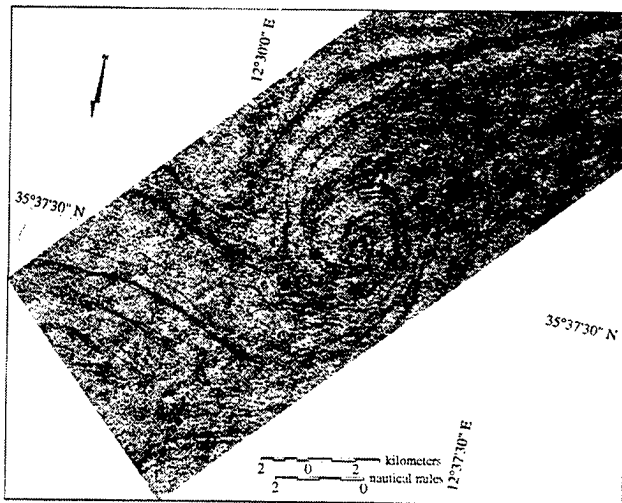


Figure 2. Spirals in the Mediterranean Sea visualized with Shuttle XSAR. The streaks are differentially smooth. 9 October 1994.

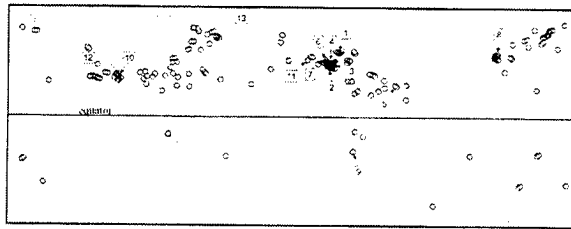


Figure 3. Distribution of spiral eddies from Scully Power (1986) visual observations and our collection of 400 images. The 13 numbered locations refer to MAFZ.

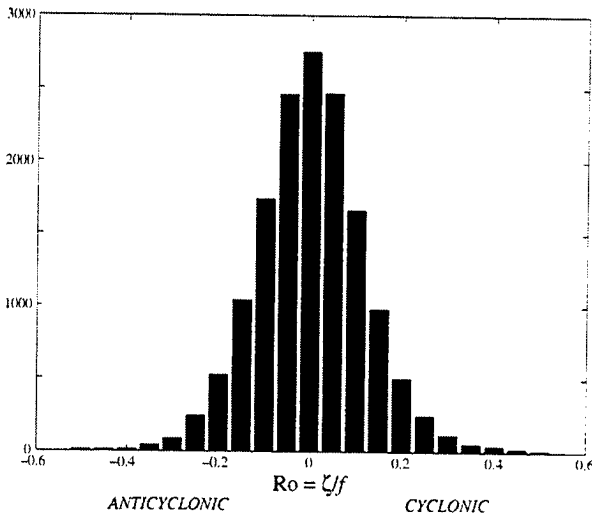


Figure 4. Rossby number in the upper 250 m sampled at 3 km spacing along 140° W from 25° N to 35° N in the North Pacific (Rudnick and Ferrari 1999).

ing a reduced scattering cross-section, e.g. differentially smooth water. Natural biogenic surface films are organized by near-surface convergence into linear streaks with over 40% surfactant coverage at low winds. The concentration is associated with nearly inextensible surface films which dissipate capillaries and short gravity waves. The film thickness required to dampen the short waves is only 0.01 to 0.1 μm . On the optical images the smooth streaks are bright in the inner sun glitter (which requires low rms slopes for reflection of the sun into the camera) and dark in the outer glitter. The situation is complex and not well understood, and we refer to MAFZ (1225-30, 1236-7) for further discussion.

But evidently the third question can be restated as follows: What is the circulation pattern that collects the surfactant material into streaks (which are subsequently wound into a spiral pattern)? Multiple stripes at kilometer spacing presumably are associated with helical circulation rolls in the atmospheric boundary layer. In addition, frontal instabilities can concentrate and distort the surfactant, as we shall see.

Ambient Ocean Vorticity

Measurement of surface velocity shear du/dy along 1000 km of roughly northward track in the North Pacific (Rudnick and Ferrari 1999) indicate values of order 10^{-5}s^{-1} . The situation is conveniently portrayed by a distribution of Rossby Numbers

$$\text{Ro} = \zeta/f \quad (1)$$

where $\zeta = \partial v / \partial x - \partial u / \partial y$ is the vertical component of vorticity (cyclonic is positive) and f is the Coriolis frequency (Figure 4). The distribution is symmetric, with very few values exceeding $\frac{1}{4}$. There are a few outliers showing a slight preference of cyclonic vorticity for large $|\text{Ro}|$, and this has since been confirmed (Rudnick, this volume).

The above paper also shows that the shear is distributed over a broad band of scales, from kilometers to hundreds of kilometers.

Horizontal Shear Instability

Starting from parallel shear flow with an inflection point, Figure 5 shows a numerical simulation of the development of the most unstable mode (Corcos and Sherman 1976, 1984). Time is in units of the initial reciprocal shear at the stagnation point. The numerical experiment was intended to model a vertical shear flow, but may as well be interpreted in terms of a horizontal shear flow. There is no implication of the sense of rotation; in fact we have reversed the published drawing from anticyclonic to cyclonic rotation.

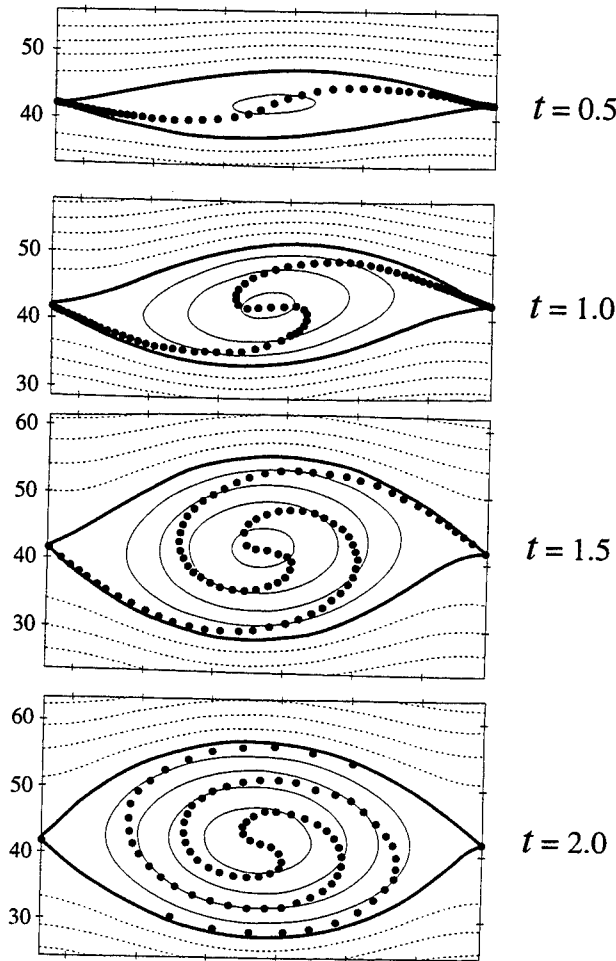


Figure 5. Computer simulations of a developing shear instability (Corcos and Sherman 1984). The four panels show the streamlines at times 0.5, 1.0, 1.5, 2.0 (in units of the initial reciprocal shear). Heavy line is the “cat’s-eye” streamline through the stagnation points. The dots represent particle positions initially placed on the interface; they are initially crowded near the two stagnation points to allow for a subsequent large strain. The model allows for diffusion and viscosity. We have reversed the original figure from anticyclonic to cyclonic rotation.

Streamlines show the development of Kelvin’s celebrated “cat’s-eye” solution. Particles inserted along the interface exhibit the growth of a spiral.

It is instructive to compare this numerical experiment with *Stuart’s* (1967) steady-state solution for a non-rotating incompressible equal-density fluid (Figure 6). The streamlines are given by

$$\Psi(x, y) = -k^{-1}U \log(\cosh ky - \alpha \cos kx). \quad (2)$$

For $\alpha = 0$ we have $u = -\partial\Psi/\partial y = -U \tanh ky$. It is

readily shown that vorticity is conserved:

$$D\zeta/Dt = 0, \quad \zeta = -\nabla^2\Psi \quad (3)$$

where D/Dt is the substantial derivative (following a particle). The circulation $\Gamma = \int \zeta dx dy = 4\pi U k^{-1}$ is the same for all four panels. The streamlines through the two stagnation points separate the “core circulation” from an exterior circulation which is not all that different from the case $\alpha = 0$. The fractional core circulation

$$\Gamma_C/\Gamma = 4\pi^{-1} \tan^{-1} \sqrt{a} \quad (4)$$

increases with increasing α . The four panels give independent steady-state solutions for different values of the independent parameter α , but we are tempted, by comparison of the two figures, to interpret the Stuart solution as a developing instability for a slowly increasing $\alpha(t)$. In MAFZ we demonstrate that an initial particle injection produces mature spirals, as in the Corcos and Sherman numerical experiment, some of them resembling the vortex pair in the Cretan Sea (Figure 1). The proposed response to question A is that the spirals are a manifestation of a horizontal shear instability.

There is as yet no breaking of symmetry. In fact, replacing $D\zeta/Dt = 0$ by

$$D(\zeta + f)/Dt = 0 \quad (5)$$

does not change the developing streamline pattern, so that planetary vorticity is conserved in the f -plane. But the developing pressure patterns are fundamentally modified (MAZD figure 22). Starting with the Stuart solution of a low pressure in the core (regardless of the sense of rotation) and gradually turning on the coriolis parameter f , the core pressure remains a LOW for the cyclonic case but switches to a HIGH for the anticyclonic case. Clearly there is here the dynamics for breaking symmetry.

Breaking Symmetry: the Hoskins-Bretherton Jet

Hoskins and Bretherton (1972) have solved a problem of frontogenesis with conservation of density and potential vorticity,

$$D(\rho, q)/Dt = 0, \quad \rho q = (f + \zeta) \bullet \nabla \rho \quad (6)$$

where D/Dt is the substantial derivative. The starting point is a vertically mixed layer with a horizontal density transition from warm and light in the south (say) to cold and heavy in the north (Figure 7, left). The initial density gradient develops into an eastward “thermal wind”, as shown. A deformation field $\gamma =$

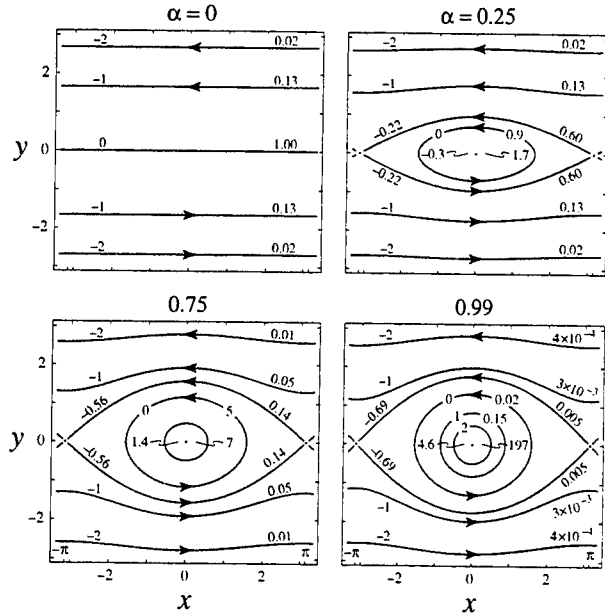


Figure 6. Stuart's (1967) solution portraying a steady flow conserving vorticity. Streamlines designate both dimensional streamlines $\Psi = -\log q$, $q = \cosh y - \alpha \cos x$, and lines of constant vorticity $\zeta = (1 - \alpha^2)q^{-2}$, with values indicated in each panel to the left and right, respectively. For $\alpha = 0$ the velocity profile is $u = -\tanh y$. Stagnation points at $x = \pm\pi$, $y = 0$ are connected by the stagnation stream lines separating the closed "core" circulation from the outer flow. With increasing α a larger fraction of the circulation is concentrated within the core.

$\partial u / \partial x - \partial v / \partial y$ is superposed, causing the initially vertical isopycnals to tilt northward. Up to this point there has been no breaking of symmetry, all directions can be reversed.

In the subsequent development we use "north" and "east" only for convenient reference to the figure. The northward tilting of isopycnals is not uniform; the northern isopycnals converge at the surface, and the southern isopycnals diverge. Accordingly the associated eastward thermal jet has a strong cyclonic shear at its northern (left) flank and a weak anticyclonic shear at its southern (right) flank. At time 2.5 (measured in γ^{-1} units) the associated Rossby numbers are $\text{Ro}^+ = +1$ and $\text{Ro}^- = -0.3$, respectively.

At this stage the underlying rate of strain no longer determines the rate of development. Rather, the isopycnal "collapse" takes the form of a "Rossby Adjustment Problem" with $f^{-1} \approx 10^{-4} \text{s}^{-1}$ taking the place of $\gamma^{-1} \approx 10^{-5} \text{s}^{-1}$ as the relevant time scale (Ou 1984). In the short time interval between 2.5 to 2.75 γ^{-1} the cyclonic shear grows from $\text{Ro}^+ = 1$ to $\text{Ro}^+ = 3$, and

at $2.89 \gamma^{-1}$ the density gradient at the left flank develops $\text{Ro}^+ = \infty$, while anticyclonic shear remains at $\text{Ro}^- = -0.3$.

The crucial point is that starting at a time when Ro^+ is of order +1 the cyclonic shear zone becomes a breeding ground for spiral eddies long before appreciable anticyclonic vorticity has been generated. In Figure 4 the third panel has been emphasized because at this time the vertical shear at the surface at the front reaches a value of $du/dz = 2N$ (N is the buoyancy frequency) corresponding to a Richardson number $(N/(du/dz))^2 = \frac{1}{4}$ and suggesting the onset of vertical shear instability.

An independent consideration has to do with the visibility of the spiral arms, presumably the result of the alignment and concentration of surfactants. Consider an elementary surface area $\delta x \delta y$ at time zero. With the developing front the area is elongated along the x -axis on both flanks of the developing jet. But in accordance with the Hoskins and Bretherton theory, at the time $2.75 \gamma^{-1}$ the area has expanded (by a factor $\frac{7}{4}$) on the anticyclonic side, while it has contracted (to $\frac{1}{4}$ the original area) on the cyclonic side. Thus the frontal theory has the elements to account for both the visibility and sense of rotation of the spiral eddies. But when examined in detail the story is not as clear-cut as presented here, and we must refer to MAFZ for a more complete discussion.

Breaking Symmetry: the Margules Front

In the traditional Margules treatment of a sharp front, anticyclonic fronts are ruled out by the condition of static stability. For a "softened Margules front" (MAFZ) there is a gravitational stability limit to the anticyclonic shear, but no such limit to the cyclonic case.

Breaking Symmetry: Anticyclonic Instabilities

To further confuse the issue, there is another independent set of processes to explain the dominance of cyclonic vortices. It follows from the Rayleigh criterion of stability (extended to include Coriolis acceleration) that cyclonic circular vortices are stable and anticyclonic vortices are unstable (MAFZ 6.21), and this leads to an "inertial instability" criterion $\text{Ro} < -1$ which goes back to Pedley (1969). Oceanographers are familiar with the vertical shear (Richardson) instability for $du/dz > 2N$ but surprisingly unfamiliar with the horizontal shear (Pedley) instability for $du/dy > f$.

There is ample numerical evidence for instabilities

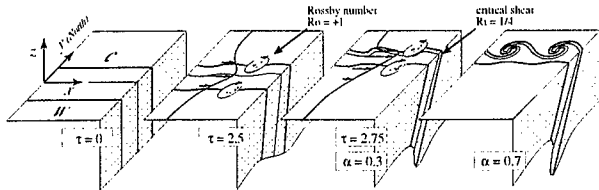


Figure 7. Cartoon for the generation of ocean spirals (see text).

that impede the development of anticyclonic vortices but have no such effect on cyclonic vortices. (*Lesieur et al.*, 1991, *Potylitsin and Peltier* 1998). The distinction is equally clear in laboratory experiments (*Bidokhti and Tritton* 1992). *Kloosterziel* (1990) observed that "it is virtually impossible to create anticyclonic vortices ... by simply stirring the fluid locally. But cyclonic vortices are easily created in this way! In the anticyclonic case stirring leads to turbulent motion and the generation of waves whereas by cyclonic stirring a well-defined smooth vortex forms."

With regard to question B, it is unresolved whether the dominance of cyclonic vortices is associated with a dominance in cyclonic horizontal shear early in the formation process, or with the relative instability of anticyclonic vortices in the mature stage.

Stirring and Mixing

The proposed formation of spiral eddies is cartooned in Figure 7. The geostrophically balanced ambient ocean vorticity of order $\pm 10^{-1} f$ is enhanced by local frontogenic processes, with concentration of surfactant along a converging line. When the frontal shear becomes comparable to f , instabilities lead to cross-frontal flow accompanied by a cat's-eye circulation pattern. The cat's-eye circulation twists the convergence line and neighboring linear features into a cyclonic spiral which stretches and further thins the lines of surfactant concentration. It is a text-book example of horizontal stirring.

We have not made any serious attempt at estimating the relevant diffusivity. The best we can do is a dimensional argument for $\kappa = cl'u'$ with $c = \frac{1}{4}$ (typical for turbulent shear flows, *Tennekes and Lumley* 1972). Taking the minor axis of a Stuart core as the characteristic length l' , the maximum velocity along the stagnation streamline for u' and $\alpha = 1$ for a mature 20 km spiral yields $\kappa = 10^3 \text{ m}^2 \text{ s}^{-1}$ (MAFZ).

Testing the Hypothesis

Our hypothesis is based on observational material which consists almost entirely of unrelated glimpses in x, y -space on the sea surface. For a satellite in a low earth orbit (LEO) a given point remains within view for only about 6 s. What is required here are prolonged stares or frequent repeat visits coordinated with shipboard observations (Figure 8). We cannot think of any x, y, z, t ocean processes that had been properly identified from measurements in half the coordinate space. We must assume that there are serious flaws in the foregoing presentation.



Figure 8. The proposed experiment. SAR imagery from an overhead drone is examined by the authors on shipboard in real time. The image shows the position of the vessel which is about to enter a spiral streak.

Following his 41-G space mission in October 1984, *Scully-Power* (1986) wrote: "The almost ubiquitous occurrence (of spiral eddies), whenever submesoscale dynamics was revealed in the sun glitter, indicates that they are perhaps the most fundamental entity in ocean dynamics at this scale. The difficulty is in explaining their structure." The only serious attempt at analysis has been in a Norwegian Doctoral dissertation which explores baroclinic instabilities in a narrow cyclonic shear

zone (*Eldevik and Dysthe 1999*). Why has the problem received so little attention in the thirty years since discovery? We assert that the fashion during these years has been statistical rather than phenomenological descriptions of ocean features, and here we are concerned with a truly phenomenological problem.

References

- Bidokhti, A.A., and D.J. Tritton, The structure of a turbulent free shear layer in a rotating fluid. *J. Fluid Mech.*, **241**, 469-502, 1992.
- Corcos, G.M., and F.S. Sherman, Vorticity concentration and the dynamics of unstable free shear layers. *J. Fluid Mech.*, **73**, 241-264, 1976.
- Corcos, G.M., and F.S. Sherman, The mixing layer: deterministic models of a turbulent flow. Part I. Introduction and the two-dimensional flow. *J. Fluid Mech.*, **139**, 29-65, 1984.
- Eldevik, T., and K.B. Dysthe, Short frontal waves: can frontal instabilities generate small scale spiral eddies, *Selected Papers of the ISOFRP* (ed. A. Zatsepin and A. Ostrovskii), UNESCO, 1999.
- Hoskins, B.J., and F.P. Bretherton, Atmosphere frontogenesis models: mathematical formulation and solution. *J. Atmos. Sci.*, **29**, 11-37, 1972.
- Kloosterziel, R.C., Barotropic vortices in a rotating fluid. Phd thesis, University of Utrecht, the Netherlands, 1990.
- Lesieur, M., S. Yanase, and O. Métais, Stabilizing and destabilizing effects of a solid-body rotation upon quasi-two-dimensional shear layers. *Phys. Fluids A*, **3**, 403-407, 1991.
- Munk W, L. Armi, K. Fischer, and F. Zachariasen, Spirals on the Sea. *Proc. R. Soc. London A*, **456**, 1217-1280, 2000.
- Ou, Hsien Wang, Geostrophic Adjustment: A Mechanism for Frontogenesis. *J. Phys. Oceanogr.*, **14**, 994-1000, 1984.
- Pedley, T.J., On the stability of viscous flow in a rapidly rotating pipe. *J. Fluid Mech.*, **36**, 177-222, 1969.
- Potylitsin, P.G., and W.R. Peltier, Stratification effects on the stability of columnar vortices of the *f*-plane. *J. Fluid Mech.*, **355**, 45-79, 1998.
- Rudnick, D.L., and R. Ferrari, Compensation of horizontal temperature and salinity gradients in the ocean mixed layer. *Science*, **283**, 526-529, 1999.
- Scully-Power, P., Navy Oceanographer Shuttle observations, STS 41-G Mission Report. Naval Underwater Systems Center, NUSC Technical Document 7611, 1986.
- Stevenson, R.E., Spiral eddies: the discovery that changed the face of the oceans. *21st Century Sci. Technol.*, **11**, 58-71, 1998.
- Stevenson, R.E., A view from space: the discovery of nonlinear waves in the ocean's near surface layer. *21st Century Sci. Technol.*, **12**, 34-47, 1999.
- Stuart, J.T., On finite amplitude oscillations in laminar mixing layers. *J. Fluid Mech.*, **29**, 417-440, 1967.
- Tennekes, H., and J.L. Lumley, *A First Course in Turbulence*. MIT Press, 1972.

This preprint was prepared with AGU's L^AT_EX macros v4, with the extension package 'AGU⁺⁺' by P. W. Daly, version 1.6a from 1999/05/21, with modifications by D. E. Kelley, version 1.0 from 2001/03/26, for the '*Aha Huliko'a Hawaiian Winter Workshop*.

On the horizontal variability of the upper ocean

Daniel L. Rudnick

Scripps Institution of Oceanography, La Jolla, California

Abstract. The last decade has seen a tremendous increase in the number and quality of observations of horizontal structure in the upper ocean. Many of these data have been made possible by the widespread use of towed vehicles and shipboard Doppler sonars. We review what these observations have revealed about processes in the upper ocean, with special emphasis on mid-latitudes and horizontal scales of 1-100 km. Fronts are one of the most prominent features of the mixed layer on these scales. The vertical/across-front circulation created at a front may be quantified assuming quasigeostrophic dynamics. Typical of the mixed layer are fronts that are warm and salty on one side, and cool and fresh on the other such that the density contrast across the front is small. The ubiquitous existence of such compensated fronts suggests that horizontal mixing in the mixed layer is an increasing function of the horizontal density gradient. Arguments based on the conservation of potential vorticity indicate that 10-km-scale (roughly the Rossby radius of deformation) eddies in the mixed layer should be predominantly cyclonic. Recent observations of mixed-layer vorticity are positively skewed.

Introduction

The database of small horizontal scale upper ocean observations has grown significantly in recent years due to the increased use of towed vehicles (such as SeaSoar), shipboard Acoustic Doppler Current Profiler (ADCP) and Global Positioning System (GPS) navigation. A brief review of these measurements is the purpose of this paper, with special emphasis on the mid-latitude open ocean on scales of 1-100 km.

Relevant characteristics of the instruments used in upper ocean surveying are as follows. SeaSoar is a towed vehicle capable of cycling from the surface to over 300 m every 3-4 km at a tow speed of 4 m s^{-1} . SeaSoar usually carries a CTD, providing measurements of temperature, salinity, and pressure. A 150-kHz ADCP in typical use allows horizontal resolution of velocity quite similar to that of a SeaSoar, with vertical coverage of 200-300 m. High quality GPS navigation is a key part of the surveying system, especially for retrieving the best absolute velocity. P-code receivers, in use on many research vessels, offer positional accuracy of about 3 m.

Observations are used to address three issues. (1) The anatomy of an upper ocean front is discussed, including the vertical/across-front circulation and associated heat flux. (2) Compensation of horizontal temperature and salinity gradients in the mixed layer is shown common. (3)

Cyclonic vorticity is preferred at small horizontal scales in the mixed layer. For each of the above issues, we discuss what the observations suggest about mixing in the ocean.

The anatomy of an upper ocean front

The most common use of the SeaSoar/ADCP/GPS system has been to survey individual features in the upper ocean. Such a survey of the Azores Front in the North Atlantic, done in March 1992, demonstrates many phenomena common to oceanic fronts [Rudnick and Luyten, 1996]. The survey, consisting of a series of north/south sections separated by one-quarter of a degree in longitude, reveals a sharp density front (Figure 1). Horizontal velocity approaches 0.5 m s^{-1} , and is generally directed parallel to isopycnals. This intuitive result has two implications. First, surveying techniques are accurate enough that coherent velocity and density fields can be measured. Second, and more importantly, the rate of change and vertical advection of density must be small. The velocity field is in the form of a jet strongest at the density front. The jet, and its associated straining, causes streamers in the alongfront direction. Enhanced horizontal variability is typical of frontal regions [Ferrari and Rudnick, 2000].

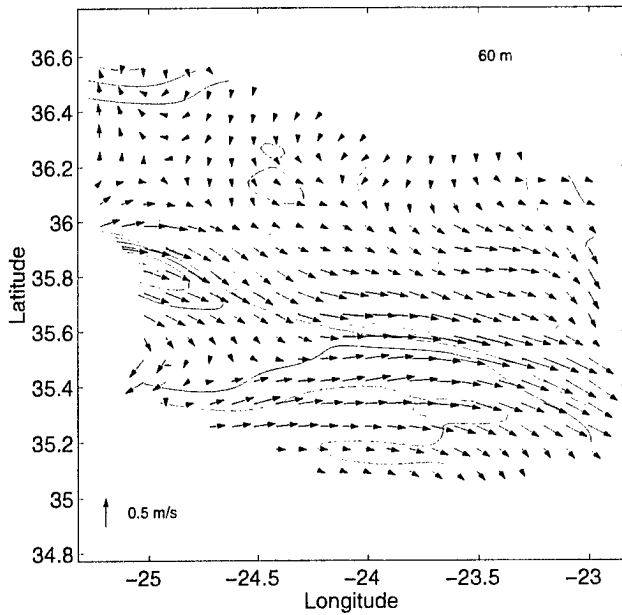


Figure 1. Potential density and horizontal velocity in the mixed layer at the Azores Front. The contour interval is 0.025 kg m^{-3} , and the velocity scale is shown. Note the jet directed along the density front.

The vertical/across-front structure is seen in a north/south section along 24.25°W (Figure 2). Mixed-layer depth trends from about 100 m deep in the northern part of the section to roughly 150 m in the south. The mixed-layer base is marked as a region of strong stratification. The front is apparent as isopycnals slope upward and to the north across the mixed layer. One can think of the structure almost as a piece of the mixed-layer base peeling off and intersecting the surface. Because the survey is from late winter, following a period of relative calm, restratification is just beginning. A shallow stratified layer lies over the mixed layer north of the front. Isopycnals retain a strong slope in the thermocline beneath the surface front. The Azores Front is, in fact, a permanent feature that penetrates to a depth of 2000 m [Gould, 1985]. There is some suggestion of subduction, as mixed-layer water from the north side of the front appears to slide southward and below the outcropping front.

The simplest dynamical balance one can imagine testing is thermal wind. Such a test is possible by comparing the independently measured fields of velocity shear and density (Figure 2). Strong shear of the correct sign is apparent along the outcropping isopycnals in the mixed layer, and downward and southward beneath the mixed layer. Alternating bands of positive and negative shear are apparent at the mixed layer base north of the front. These shears are

clearly out of thermal wind balance, and are likely near-inertial.

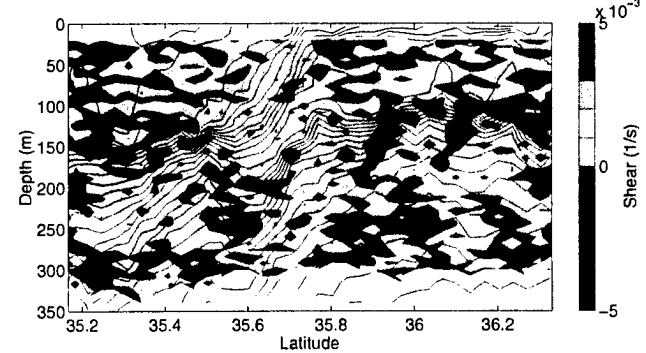


Figure 2. North/south section of potential density and vertical shear of velocity. The contour interval of density is 0.025 kg m^{-3} . Note the high shear along the sloping front.

The vertical velocity field may be inferred assuming quasi-geostrophic dynamics. This assumption is reasonable because the front is observed to be nearly in thermal wind balance. Derivation of the resulting omega equation [Hoskins *et al.*, 1978] relies on the elimination of the time derivative terms in the momentum and density equations. The omega equation can be written

$$\nabla^2(N^2 w) + f^2 \frac{\partial^2 w}{\partial z^2} = 2\nabla \cdot \mathbf{Q}, \quad (1)$$

where

$$\mathbf{Q} = \frac{g}{\rho_0} \left(\frac{\partial \mathbf{u}_g}{\partial x} \cdot \nabla \rho, \frac{\partial \mathbf{u}_g}{\partial y} \cdot \nabla \rho \right), \quad (2)$$

and \mathbf{u}_g is geostrophic velocity, the divergence operator is two-dimensional and other symbols have their usual meaning. Forcing of the omega equation is a function of the density and geostrophic velocity fields.

The elliptic omega equation is solved for the survey of the Azores Front [Rudnick, 1996]. A band of downwelling exists near and to the north of the front (Figure 3). Upwelling appears on the south side of the front especially at about 24°W . A region of strong downwelling occurs in the SW corner where the flow is southward. The tendency for downwelling on the dense (cold) side of the front and upwelling on the less dense (warm) side results in a net heat flux averaged over the horizontal area of the survey. The heat flux peaks at the base of the mixed layer at about 15 W m^{-2} . This heat flux is comparable to, or larger than, climatological values compiled on 1° grids [Marshall *et al.*, 1993].

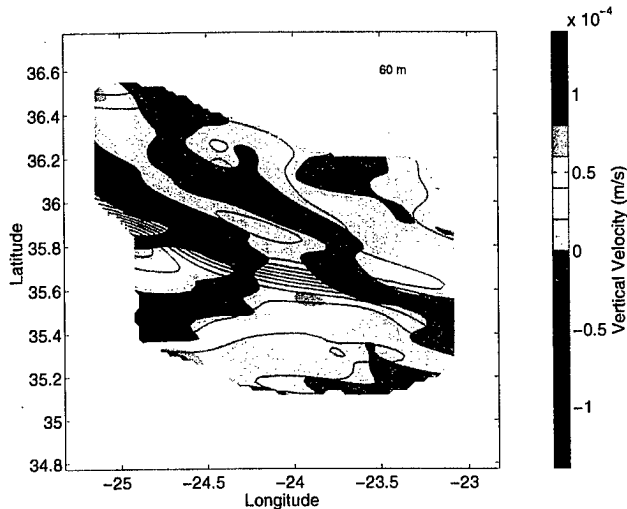


Figure 3. Vertical velocity and potential density in the mixed layer at the Azores Front. The contour interval for potential density is 0.025 kg m^{-3} . The white contour indicates zero vertical velocity. Note the band of downwelling in and to the north of the front.

A simple theory of a semi-geostrophic front [Hoskins and Bretherton, 1972] helps to understand the observations. The two-dimensional model relies on the assumption that the across-front momentum balance is exactly geostrophic, but the alongfront balance includes horizontal and vertical advection (see Appendix). The front is formed by a large-scale deformation of an initially vertically uniform layer with weak horizontal density gradients. The solution (Figure 4) is shown at time $4/\alpha$, where α is the rate of strain. The large-scale strain estimated from the velocity field of Figure 1 is approximately 10^{-6} s^{-1} , so the dimensional time would be 46 days. Sloping isopycnals

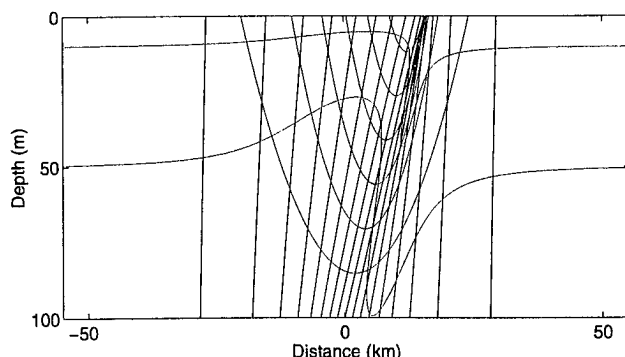


Figure 4. The semi-geostrophic model of frontogenesis at time $4/\alpha$. Black lines are isopycnals with a contour interval of 0.2 kg m^{-3} . Lines of constant along-front velocity (blue) have an interval of 0.1 m s^{-1} . The red lines show the positions of particles initially at 10 and 50 m.

are pinched at the surface forming a front. An essential feature of this model is that an infinitely sharp front is formed in a finite time. Alongfront velocity is in the form of a surface intensified jet with the dense (positive vorticity) side sharper than the light (negative vorticity) side. As the solution is Lagrangian, it is a simple matter to determine the position of particles. The initial 10 and 50 m surfaces have been stirred to be multi-valued as a function of horizontal position. Strong localized downwelling occurs on the dense side of the front with weaker, more diffuse, upwelling on the less dense side. This pattern of vertical velocity is consistent with the observations.

Temperature/salinity compensation

Mixed-layer thermohaline fronts are often observed to have a gradient from warm and salty to cool and fresh such that the density contrast across the front is small. This phenomenon is termed compensation because temperature and salinity compensate in their effects on density. Compensation has been known for some time at large and meso scales [Rodden, 1975; Rodden, 1984]. More recently, compensation has been shown to exist at horizontal scales as small as 10 m [Ferrari and Rudnick, 2000; Rudnick and Ferrari, 1999].

The existence of compensation in the mixed layer is consistent with theory proposed by Young [1994] and Ferrari and Young [1997]. Consider a vertically mixed layer with an initially random distribution of temperature and salinity. Temperature and salinity gradients compensate in their effect on density in some regions, while in others density gradients exist. Density gradients slump due to gravity, creating sloping isopycnals. Vertical mixing results in weakened horizontal density gradients. This process is essentially shear dispersion [Taylor, 1953] where the shear is due to slumping density gradients, and the mixing is caused by any of the processes that make the mixed layer vertically uniform. Temperature/salinity gradients that are compensated do not slump and therefore do not experience shear dispersion. The net effect is that density gradients diffuse while compensated gradients persist.

Compensation is manifest as a strong correlation between temperature and salinity in a horizontal SeaSoar tow in the N. Pacific winter mixed layer [Ferrari et al., this volume]. Temperature and salinity fluctuations coincide at all resolved scales. The observations are thus consistent with a horizontal diffusivity that is an increasing function of horizontal density gradient.

An important question is under what conditions is compensation typical of the world's oceans. This question is addressed using SeaSoar data from the midlatitude, northern hemisphere Pacific, Atlantic, and Indian Oceans during all seasons [Rudnick and Martin, 2001]. The relevant

quantity is the density ratio R , defined as the ratio of the effect of a horizontal change of temperature on density divided by that of salinity on density. For a compensated thermohaline front, $R=1$.

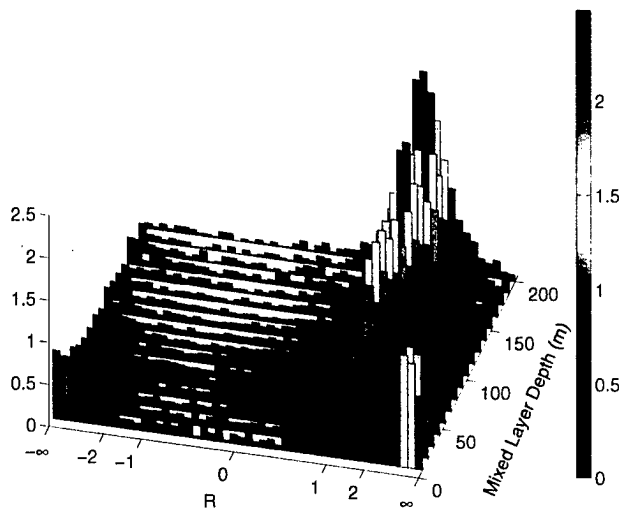


Figure 5. The conditional probability density function (pdf) of mixed-layer density ratio as a function of mixed-layer depth from the global ocean. Each row of bars represents the conditional pdf for the given mixed-layer depth. Height, and color shading, of the bars indicate the pdf magnitude. The density ratio is typically 1 for mixed layers deeper than 75 m.

The conditional probability density function (pdf) of mixed-layer density ratio as a function of mixed-layer depth summarizes results from the global ocean (Figure 5). For mixed-layers deeper than 75 m a density ratio near 1 is typical, while shallower mixed layers have a poorly defined density ratio. The shallowest mixed layers are temperature dominated as the density ratio approaches infinity. Mixed-layer depth may be considered a proxy for the strength of vertical mixing. The results suggest that vertical mixing is essential to the establishment of compensation in the mixed layer. This observation is consistent with the slumping and mixing model where vertical mixing is an essential process. On the other hand, compensation should not be expected in shallow mixed layers where vertical mixing is weak.

A density ratio of two is typical of the thermocline beneath the mixed layer [Schmitt, 1981]. This phenomenon is believed to be caused by salt fingering [Schmitt, 1994]. What is remarkable is the sharpness of the transition from $R=1$ to $R=2$ across the mixed-layer base, especially when the mixed layer is deep [Ferrari and Rudnick, 2000; Rudnick and Martin, 2001]. The change in density ratio from the mixed layer to the thermocline is a reflection of the different mixing processes working in the two regions.

Mixed-layer vorticity

Rapidly rotating vortices in the ocean are, in theory, predominantly cyclonic. A simple explanation invokes the conservation of potential vorticity as in the two-dimensional Hoskins and Bretherton semigeostrophic model (Figure 4). The potential vorticity for this model is

$$q = \frac{1}{\rho_0} \left[\frac{\partial \rho}{\partial z} \left(f + \frac{\partial v}{\partial x} \right) - \frac{\partial \rho}{\partial x} \frac{\partial v}{\partial z} \right]. \quad (3)$$

The initial state of the model is one of zero q as the layer is vertically uniform and velocities are zero. As the front sharpens, gradients of density and velocity increase, but q must remain zero. Because of thermal wind, the second term above is always positive (in the northern hemisphere). To conserve q then, the first term must be negative. As static stability requires $\partial \rho / \partial z \leq 0$, absolute vorticity must remain positive. If the relative vorticity is to be the magnitude of f or larger, it must thus be cyclonic.

The discussion above has relevance to the symmetric instability [Hoskins, 1974]. The symmetric instability considers an exactly circular vortex, so a two-dimensional model (radial/vertical) is sufficient. Instability occurs if the potential vorticity, given by (3), is positive. Hoskins points out that a statically stable, motionless state cannot evolve frictionally and adiabatically to a state subject to symmetric instability.

The relevant length scale in the ocean is the Rossby radius of deformation for the mixed layer, of order 10 km. The impediment to making accurate measurements of small-scale vorticity using shipboard ADCP data has been navigation. With the advent of military grade (P-code) GPS, this problem has been solved.

Vorticity is estimated using data of 3-km horizontal resolution from a cruise in the North Pacific during the winter of 1997 [Rudnick, 2001]. Because a SeaSoar was used, underway estimates of mixed-layer depth are available. The pdf of mixed-layer relative vorticity normalized by planetary vorticity has a mode near zero and is positively skewed (Figure 6). The skewness is apparent as a relatively thick tail at a normalized vorticity of 0.5. The skewness of vorticity is 0.36, and is considered statistically significant. The skewed vorticity is likely the velocity signature of spiral eddies seen in photographs of the sea surface [Munk *et al.*, 2000]. The contribution of these eddies to mixing in the ocean is an open question.

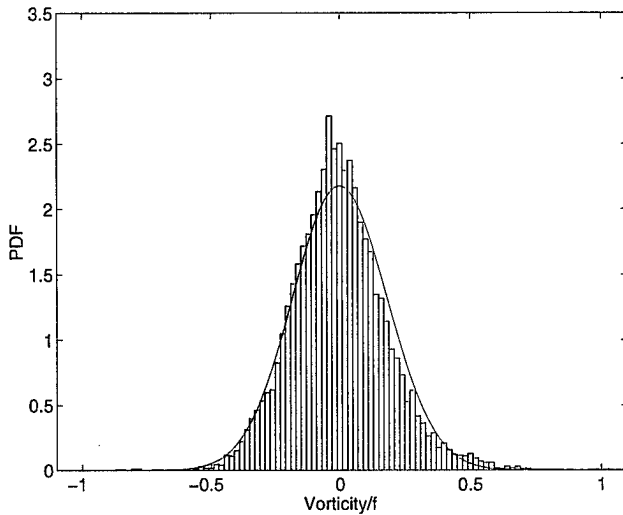


Figure 6. Probability density function (pdf) of relative vorticity normalized by planetary vorticity in the mixed layer. A normal distribution with zero mean and standard deviation, 0.18, equal to the observations is shown (solid line). The skewness, equal to 0.36, is apparent as the relatively high value of the pdf near a normalized vorticity of 0.5.

Summary

Shipboard surveys using SeaSoar and ADCP have greatly improved our knowledge of small-scale horizontal variability in the upper ocean. Oceanic fronts are observed to be in approximate thermal wind balance. A restratifying across-front circulation can be inferred, implying a heat flux of order 10 W m^{-2} when averaged over a 100 km^2 region surrounding the front. Temperature/salinity compensation is typical in the mixed layer, especially when the mixed layer is deep. The observed compensation is consistent with the slumping and mixing model of Young and colleagues, and a horizontal diffusivity that is a growing function of density gradient. Mixed-layer vorticity is skewed positive because the largest vorticities are positive. The observed skewness is consistent with potential vorticity conservation.

Appendix

The following is a review of the *Hoskins and Bretherton* [1972] two-dimensional semi-geostrophic model of frontogenesis. A novelty is that the solution is in fully Lagrangian coordinates, in contrast to the mixed Eulerian/Lagrangian solution in Hoskins and Bretherton.

The semi-geostrophic equations appropriate for a front in the x -direction are

$$-fv = -\frac{1}{\rho_0} \frac{\partial p}{\partial x} \quad (\text{A1})$$

$$\frac{Dv}{Dt} + fu = -\frac{1}{\rho_0} \frac{\partial p}{\partial y} \quad (\text{A2})$$

$$0 = -\frac{\partial p}{\partial z} - \rho g \quad (\text{A3})$$

$$\frac{D\rho}{Dt} = 0 \quad (\text{A4})$$

$$\frac{\partial u}{\partial x} + \frac{\partial v}{\partial y} + \frac{\partial w}{\partial z} = 0 \quad (\text{A5})$$

where

$$\frac{D}{Dt} = \frac{\partial}{\partial t} + u \frac{\partial}{\partial x} + v \frac{\partial}{\partial y} + w \frac{\partial}{\partial z}.$$

Here, y is the along-front direction, z is vertical, ρ_0 is a constant reference density, and f is a constant Coriolis parameter. Ertel's potential vorticity (3) is conserved following fluid particles

$$\frac{Dq}{Dt} = 0 \quad (\text{A6})$$

Assume a solution consisting of a geostrophic confluent flow plus a two-dimensional component,

$$u = -\alpha x + u'(x, z, t) \quad (\text{A7})$$

$$v = \alpha y + v'(x, z, t) \quad (\text{A8})$$

$$\frac{p}{\rho_0} = f\alpha xy - \left(\alpha^2 + \frac{d\alpha}{dt} \right) \frac{y^2}{2} + \frac{p'}{\rho_0}(x, z, t) \quad (\text{A9})$$

$$\rho = \rho(x, z, t) \quad (\text{A10})$$

$$w = w(x, z, t). \quad (\text{A11})$$

Note that the parameter α may be a function of time.

Substitution of (A7-11) into (A1-5) yields the equations

$$\frac{DM}{Dt} + \alpha M = 0 \quad (\text{A12})$$

$$\frac{\partial u}{\partial x} + \frac{\partial w}{\partial z} = -\alpha \quad (\text{A13})$$

$$f \frac{\partial v'}{\partial z} = -\frac{g}{\rho_0} \frac{\partial \rho}{\partial x}, \quad (\text{A14})$$

where

$$M = v' + fx.$$

These together with conservation of density (A4) are the equations we need to solve.

The prognostic equations (A12) and (A4) can be solved immediately in Lagrangian coordinates, with no explicit dependence on along-front position,

$$M = M_0(x_0, z_0)e^{-\beta} \quad (\text{A15})$$

$$\rho = \rho(x_0, z_0), \quad (\text{A16})$$

where

$$\beta(t) = \int_0^t \alpha(t') dt',$$

and x_0 and z_0 are the initial across-front and vertical positions of particles.

A useful identity expresses the Eulerian spatial gradient of a dependent variable h in Lagrangian coordinates,

$$\left(\frac{\partial h}{\partial x} \right)_z = \frac{\partial(h, z)}{\partial(x_0, z_0)} \left[\frac{\partial(x, z)}{\partial(x_0, z_0)} \right]^{-1}. \quad (\text{A17})$$

where the subscript z on the lhs makes clear that z is held constant. Using (A17), (A13-14) can be written in Lagrangian coordinates as

$$\frac{\partial(x, z)}{\partial(x_0, z_0)} = e^{-\beta} \quad (\text{A18})$$

$$f \frac{\partial(x, M)}{\partial(x_0, z_0)} = -\frac{g}{\rho_0} \frac{\partial(\rho, z)}{\partial(x_0, z_0)}. \quad (\text{A19})$$

The solution in Lagrangian coordinates (A15-16) is simple. The challenge is the transformation back to Eulerian coordinates (A18-19). These equations are nonlinear, and possibly difficult to solve depending on the initial and boundary conditions used.

Potential vorticity may be written

$$q = \frac{1}{\rho_0} \frac{\partial(M, \rho)}{\partial(x, z)} = \frac{1}{\rho_0} \frac{\partial(M_0, \rho)}{\partial(x_0, z_0)}, \quad (\text{A20})$$

and is necessarily conserved, as can be readily seen by its expression in Lagrangian coordinates.

Consider a layer initially vertically uniform in density. Suppose also that the initial horizontal density gradient is so small that along-front velocity and its vertical shear are negligible. Using these initial conditions, solutions are

$$M = fx_0e^{-\beta} \quad (\text{A21})$$

$$\rho = \rho(x_0). \quad (\text{A22})$$

Substituting these into the thermal wind equation (A19) and integrating yields

$$x = z \frac{g}{f^2 \rho_0} \frac{\partial \rho}{\partial x_0} e^\beta + A(x_0, t), \quad (\text{A23})$$

where $A(x_0, t)$ is to be determined from boundary conditions. Derivatives of x with respect to x_0 and z_0 can be derived from (A23) and substituted into the continuity equation (A18). Integrating the result with respect to z_0 gives

$$z \frac{\partial A}{\partial x_0} + z^2 \frac{g}{2f^2 \rho_0} \frac{\partial^2 \rho}{\partial x_0^2} e^\beta = z_0 e^{-\beta} + B(x_0, t). \quad (\text{A24})$$

We use boundary conditions that particles on the top and bottom boundaries remain there

$$z(z_0 = \pm H) = \pm H. \quad (\text{A25})$$

Evaluating (A24) at the boundaries, and using (A23), yields expressions for the integration constants

$$A = x_0 e^{-\beta} \quad (\text{A26})$$

$$B = H^2 \frac{g}{2f^2 \rho_0} \frac{\partial^2 \rho}{\partial x_0^2} e^\beta. \quad (\text{A27})$$

The solutions for x and z are thus

$$x = x_0 e^{-\beta} + z \frac{g}{f^2 \rho_0} \frac{\partial \rho}{\partial x_0} e^\beta \quad (\text{A28})$$

$$z - z_0 + (z^2 - H^2) \frac{g}{2f^2 \rho_0} \frac{\partial^2 \rho}{\partial x_0^2} e^{2\beta} = 0. \quad (\text{A29})$$

The solution in Figure 4 has an initial density profile that is an arctan with a length scale of 500 km, in a layer 200 m deep.

A few features of the solution are worthy of note. The absolute vorticity is

$$\frac{\partial M}{\partial x} = f \left[1 + z \frac{g}{f^2 \rho_0} \frac{\partial^2 \rho}{\partial x_0^2} e^{2\beta} \right]^{-1}. \quad (\text{A30})$$

Vorticity becomes infinite in a finite time, provided the initial density profile has nonzero curvature. This will happen first on the boundaries.

The slope of an isopycnal,

$$\left(\frac{\partial x}{\partial z} \right)_{x_0} = \frac{g}{f^2 \rho_0} \frac{\partial \rho}{\partial x_0} e^\beta, \quad (\text{A31})$$

depends only on x_0 and t , so the isopycnal is a straight line.

The Richardson number is given by

$$Ri = \frac{N^2}{(\partial v / \partial z)^2} = \frac{f}{\partial M / \partial x}. \quad (\text{A32})$$

Therefore, (A30) implies that Ri becomes zero in a finite time in the region of strong vorticity and subduction at the

front. Ri is 1 elsewhere. Mixing must become important as the front sharpens.

Acknowledgments. This paper reviews observations from several experiments over the last fifteen years. I thank the many PIs who are responsible for making these experiments successful. The Office of Naval Research and the National Science Foundation provided the funding for most of the work reviewed here. During the preparation of this paper, I was supported by NSF under grant OCE98-19521.

References

- Ferrari, R., and D. L. Rudnick, Thermohaline variability in the upper ocean, *J. Geophys. Res.*, **105**, 16,857-16,883, 2000.
- Ferrari, R., and W. R. Young, On the development of thermohaline correlations as a result of nonlinear diffusive parameterizations, *J. Mar. Res.*, **55**, 1069-1101, 1997.
- Gould, W. J., Physical oceanography of the Azores front, *Prog. Oceanogr.*, **14**, 167-190, 1985.
- Hoskins, B. J., The role of potential vorticity in symmetric stability and instability, *Quart. J. Roy. Meteor. Soc.*, **100**, 480-482, 1974.
- Hoskins, B. J., and F. P. Bretherton, Atmospheric frontogenesis models: mathematical formulation and solution, *J. Atmos. Sci.*, **29**, 11-37, 1972.
- Hoskins, B. J., I. Draghici, and H. C. Davies, A new look at the ω -equation, *Quart. J. R. Met. Soc.*, **104**, 31-38, 1978.
- Marshall, J. C., A. F. G. Nurser, and R. G. Williams, Inferring the subduction rate and period over the North Atlantic, *J. Phys. Oceanogr.*, **23**, 1315-1329, 1993.
- Munk, W., L. Armi, K. Fischer, and F. Zachariasen, Spirals on the sea, *Proc. R. Soc. Lond. A*, **456**, 1217-1280, 2000.
- Roden, G. I., On North Pacific temperature, salinity, sound velocity and density fronts and their relation to the wind and energy flux fields, *J. Phys. Oceanogr.*, **5**, 557-571, 1975.
- Roden, G. I., Mesoscale oceanic fronts of the North Pacific, *Ann. Geophys.*, **2**, 399-410, 1984.
- Rudnick, D. L., Intensive surveys of the Azores Front, 2, Inferring the geostrophic and vertical velocity fields, *J. Geophys. Res.*, **101**, 16,291-16,303, 1996.
- Rudnick, D. L., On the skewness of vorticity in the upper ocean, *Geophys. Res. Lett.*, *in press*, 2001.
- Rudnick, D. L., and R. Ferrari, Compensation of horizontal temperature and salinity gradients in the ocean mixed layer, *Science*, **283**, 526-529, 1999.
- Rudnick, D. L., and J. R. Luyten, Intensive surveys of the Azores Front, 1, Tracers and dynamics, *J. Geophys. Res.*, **101**, 923-939, 1996.
- Rudnick, D. L., and J. Martin, P., On the horizontal density ratio in the upper ocean, *Dyn. Atmos. Oceans*, *in press*, 2001.
- Schmitt, R. W., Form of the temperature-salinity relationship in the central water: Evidence for double-diffusive mixing, *J. Phys. Oceanogr.*, **11**, 1015-1026, 1981.
- Schmitt, R. W., Double diffusion in oceanography, *Ann. Rev. Fluid Mech.*, **26**, 255-285, 1994.
- Taylor, G. I., Dispersion of soluble matter in solvent flowing slowly through a tube, *Proc. R. Soc. Lond. A*, **219**, 186-203, 1953.
- Young, W. R., The subinertial mixed layer approximation, *J. Phys. Oceanogr.*, **24**, 1812-1826, 1994.

The temperature-salinity relationship of the mixed layer

R. Ferrari

Woods Hole Oceanographic Institution, Woods Hole, Massachusetts - USA

F. Paparella, D.L. Rudnick and W.R. Young

Scripps Institution of Oceanography, La Jolla, California - USA

Abstract. The surface mixed layer of the ocean is often characterized by density compensation between the horizontal temperature and salinity gradients. In this contribution we present a combination of theoretical arguments and numerical simulations to investigate how compensation might emerge as a result of processes at work within the mixed layer. The dynamics of the mixed layer are investigated through a simple model. The model consists of a pair of coupled advection-diffusion equations for heat and salt. The coupling arises through a nonlinear diffusion operator proportional to the buoyancy gradient, which parameterizes the combined effect of slumping and mixing of small-scale horizontal buoyancy gradients. Numerical solutions of the mixed layer model show that the nonlinear diffusion creates compensation between the temperature and salinity gradients, while the stirring field maintains alignment between the two gradients. The results of this work suggest a new parameterization of the horizontal fluxes of heat and salt for numerical models of the mixed layer.

1. Introduction

Observations show that the thermohaline structure of the surface mixed layer (ML) of the ocean is largely compensated. In other words, temperature and salinity fronts coincide so that the resulting density contrasts are small relative to the individual contributions of heat and salt. This phenomenon has been known for some time for certain fronts at scales of a few tens to one hundred kilometers (Roden, 1975; Rudnick and Luyten, 1996). Recent high-resolution observations have shown that compensation exists down to horizontal scales of tens of meters in the North Pacific (Rudnick and Ferrari, 1999; Ferrari and Rudnick, 2000) and throughout the global ocean on scales of kilometers (Rudnick and Martin, 2001). An example from a horizontal tow in the ML of the Subtropical North Pacific is given in Figure 1. Notice how almost all fluctuations of temperature are mirrored in salinity so that density gradients are minimized.

One explanation of these observations is that atmospheric forcing conspires to create and juxtapose water masses with compensating properties. However the ratio of heat to freshwater density fluxes is variable in large scale maps (Schmitt *et al.*, 1989) and in time series at a point (Weller *et al.*, 1985), so internal ocean

dynamics is required to account for the observed compensation. Young (1994) and Ferrari and Young (1997) propose a more satisfactory explanation that relies on regulating mechanisms at work in the ML. These theoretical arguments suggest that compensation is the result of the preferential diffusion of horizontal density gradients which occurs because of the combined action of *unbalanced motions* and *vertical mixing*.

The physical explanation of the theory of Young and collaborators is as follows. Horizontal gradients of temperature and salinity can arise in the ML in response to non homogeneous atmospheric forcing and entrainment of thermocline waters. At some locations temperature and salinity will compensate each other exactly, whereas in other locations temperature and salinity will create strong horizontal density gradients. Much of the ML will lie between these two extremes. The strong density gradients slump under the action of gravity and tend to restratify the ML. Vertical mixing eventually arrests this unbalanced motion by remixing the ML. This mechanism is essentially thermohaline shear dispersion, where the shear is driven by the horizontal density gradient, and the vertical mixing results from the variety of processes that mix the ML. On the other hand, compensated fronts are balanced and therefore do not experience shear dispersion. The net result is that density

fronts are diffused, while compensated fronts persist.

The preferential diffusion of horizontal density gradients can be represented with mixing parameterizations in which the transport of heat and salt depends nonlinearly on the density gradient, e.g., with diffusivities proportional to some power of the density gradient (Young, 1994; Ferrari and Young, 1997). In this paper we examine the establishment of thermohaline compensation by implementing these nonlinear diffusive parameterizations in a simple model of the ML. Numerical solutions show that the thermohaline structure of the ML is generated by a balance between the mesoscale straining field, that acts to increase temperature and salinity gradients, and the nonlinear diffusion, that arrests the formation of density gradients but not of compensated gradients. In agreement with observations, temperature and salinity gradients tend to be aligned, because both heat and salt are advected by the same straining field, and compensated.

The mechanism of compensation described above implicate vertically sheared currents within the ML and it is not included in numerical models with bulk MLs. In the last section of the paper we show how to simplify the nonlinear diffusive parameterization so that it can be implemented in ocean circulation models to improve the representation of ML thermohaline dynamics.

The paper is organized as follows. In section 2, we revisit the arguments of Young and collaborators in the context of the parameterization of diapycnal fluxes in the ML. In section 3, we describe numerical simulations used to test the nonlinear diffusive parameterization of heat and salt transports in the ML. In section 4, we suggest a simplified version of the nonlinear diffusive parameterization to be implemented in bulk ML models. Finally, conclusions are offered in section 5.

2. Horizontal transport of heat and salt in the mixed layer

Let us consider the dispersion of some tracer of concentration θ in the ML. We model the ML as a vigorously mixed, shallow layer, characterized by a small aspect ratio, i.e., with a depth H much less than the horizontal scale. The main point here is that there are two very different time scales: a fast time scale τ_V over which the layer is mixed vertically over the depth H and a longer time scale τ_H associated with horizontal transports.

The mathematical model for the transport of a tracer θ stirred by an incompressible velocity field \mathbf{u} is the familiar advection-diffusion equation,

$$\partial_t \theta + \mathbf{u} \cdot \nabla \theta = \kappa \nabla^2 \theta, \quad (1)$$

together with appropriate boundary conditions. The operator on the RHS represents the diffusion of tracer fluctuations by molecular motions and κ is the molecular diffusivity. The equation in (1) is appropriate to describe the transport of θ at scales from a few millimeters to thousands of kilometers. However, the resulting description is overly complicated. Our goal is to derive a simpler model that describes transports in the ML at large scales and long times by averaging the equation in (1) over short times and short scales. The key step in the analysis is to find appropriate scales for the averaging so that we can derive a closed equation for the averaged concentration $\bar{\theta}$ by folding all the details of the small scale motions in a suitable operator \mathcal{D} that depends on averaged variables, i.e.,

$$\partial_t \bar{\theta} + \bar{\mathbf{u}} \cdot \nabla \bar{\theta} = \mathcal{D}(\bar{\mathbf{u}}, \bar{\theta}), \quad (2)$$

where $\bar{\mathbf{u}}$ is the averaged velocity field.

Some very popular ML models, referred to as bulk models (e.g. Kraus and Turner, 1967), choose to average over the depth H of the ML and the characteristic time of vertical mixing τ_V . This choice is quite natural, because the turbulent fluxes that homogenize vertically the ML are due to processes such as convection and Langmuir cells, characterized by coherent eddies which span the depth H and have an aspect ratio close to one. In these models, the operator \mathcal{D} parameterizes all the processes that maintain the ML well mixed in the vertical. A problem arises when bulk ML are implemented in circulation models that resolve horizontal scales that are orders of magnitude larger than H . In this case one has to average the tracer equation over H in the vertical, but over a scale $L > H$ in the horizontal. A typical solution is to parameterize in series the motions on scales shorter than H and those on scales between H and L ¹. That is, the same operator \mathcal{D} is retained to describe the fluxes that mix vertically the ML, but a lateral effective eddy diffusivity is introduced to parameterize the fluxes at larger scales. Here we show that unbalanced horizontal motions with characteristic scales between H and L act in parallel with the turbulent motions on scales shorter than H . Therefore it is necessary to modify the operator \mathcal{D} and parameterize all unresolved motions together.

Let us average equation (1) over the depth H in the vertical, over a scale $L > H$ in the horizontal and over a time $\tau_H > \tau_V$. The scales L and τ_H have only lower bounds, but are not specified for the moment. We obtain the Reynolds' averaged equation,

$$\partial_t \bar{\theta} + \bar{\mathbf{u}} \cdot \nabla_H \bar{\theta} = -\nabla_H \cdot \overline{\mathbf{u}' \theta'} + \kappa \nabla_H^2 \bar{\theta} + \mathcal{F}. \quad (3)$$

¹See Garrett (2001) for a discussion of parameterizations of unresolved motions in parallel and in series.

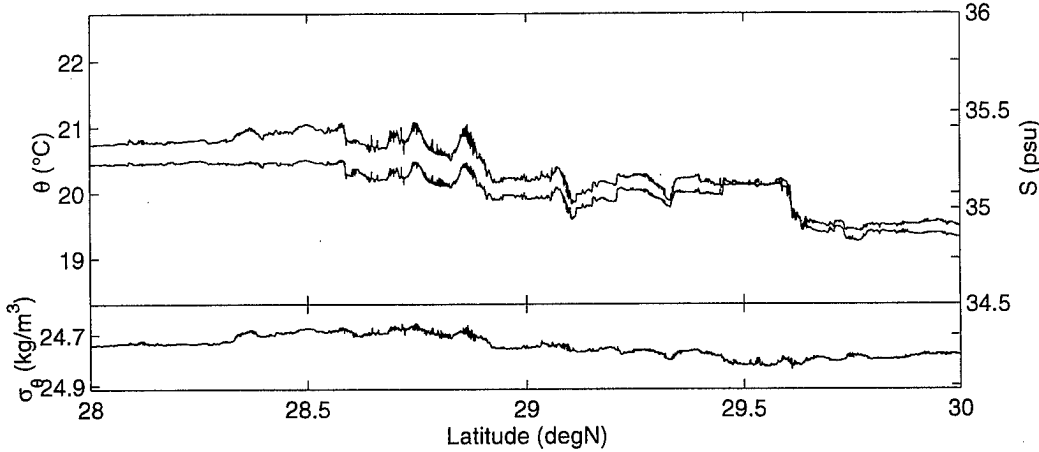


Figure 1. Potential temperature (red line), salinity (blue line) and potential density (black line) from a horizontal SeaSoar tow at 50 m in Subtropical North Pacific, at 140 degrees west, between 28 and 30 degrees north. This depth is in the middle of the local mixed layer. The vertical axis for temperature and salinity are scaled by the respective expansion coefficients so that excursions of temperature and salinity show the change they imply on density.

Here $\bar{\theta}$ and \bar{u} are the averaged velocity and averaged tracer concentration and θ' and u' are departures from those averages. \mathcal{F} represents the flux of tracer induced by the boundary conditions at the top and bottom of the ML. The notation ∇_H is used to remind that derivatives are taken only in the horizontal, because the averaged quantities do not depend on the vertical coordinate. In order to simplify the discussion, we assume that H is a constant independent of position (for more on this point see Young, 1994; Garrett and Tandon, 1997).

The next step is to express the first term on the RHS (called “eddy flux divergence”) in terms of averaged quantities. Mixing-length theories are a common way to achieve this goal. The argument goes that a fluid particle carries the value of a conserved, and hence transferable, tracer for some length l' , before it is mixed with its new surroundings. We give a vectorial nature to l' to allow for situations which are not isotropic. If the particle has a concentration of scalar typical of its surroundings then the eddy flux of tracer θ is given by

$$\overline{u'\theta'} = -\overline{u'l'} \cdot \nabla_H \bar{\theta}, \quad (4)$$

where it is assumed that $\nabla_H \bar{\theta}$ varies little over distances comparable with the mixing length l' . The tensor $\overline{u'l'}$ defines the eddy diffusivity.

In the special case when the statistics of the velocity field are homogeneous and isotropic, the eddy diffusivity tensor is a constant, and the eddy transport assumes the

form of a down-gradient Fickian diffusion:

$$\overline{u'\theta'} = -k \nabla_H \bar{\theta}, \quad (5)$$

This kind of closure is commonly applied to ML models and the two relevant scalars (temperature and salinity) are diffused with the same eddy diffusion coefficient, and are independent from each other.

However in the ML there are lateral inhomogeneities in the buoyancy² field at scales larger than H . Horizontal buoyancy gradients slump under the action of gravity and drive horizontal eddy fluxes. Therefore we expect the transport of tracer to be in the direction of and to increase with $\nabla_H B$. This breaks the assumptions of homogeneity and isotropy. Therefore a down-gradient Fickian diffusion cannot be used to model the ML at scales larger than H . A more appropriate expression for the diffusivity tensor is,

$$\overline{u'l'} = \gamma f(|\nabla_H \bar{B}|) \nabla_H \bar{B} \nabla_H \bar{B}, \quad (6)$$

where γ is a constant and $f(|\nabla_H \bar{B}|)$ a non-dimensional function whose form depends on the details of the hydrodynamic instabilities that dominate in the eddy field. The expression (6) is rationalized as follows. According to mixing-length theories, the diffusivity tensor

²Buoyancy B is defined as $\rho = \rho_0 [1 - g^{-1} B]$, where ρ is the fluid's density, ρ_0 is a constant reference density and g is the acceleration of gravity. With this definition, B has the dimensions of acceleration.

can be expressed in terms of the characteristic velocity \mathbf{v}_{eddy} and length l_{eddy} of the transfer process, that is $\mathbf{u}'\mathbf{l}' \propto \mathbf{u}_{eddy} l_{eddy}$. In our case the length scale is given by $l_{eddy} = \mathbf{u}_{eddy} \tau_V$, where τ_V is the time for which the slumping process acts, before it is arrested by the turbulent fluxes that mix vertically the ML. The eddy velocity is in the direction of $\nabla_H \bar{B}$ with a magnitude proportional to $|\nabla_H \bar{B}|$. Thus we get the expression in (6), where the tensor $\nabla_H \bar{B} \nabla_H \bar{B}$ arises from the direction of the eddy velocity field and $\gamma f(|\nabla_H \bar{B}|)$ is a positive semidefinite term that determines the magnitude of the flux. Notice that both the unbalanced motions at scales larger than H and the turbulent fluxes at scales shorter than H enter in the closure in 6. That is the processes of slumping and mixing act in parallel.

Plugging (6) into (4) gives the eddy tracer flux,

$$\overline{\mathbf{u}'\theta'} = -\gamma f(|\nabla_H \bar{B}|) (\nabla_H \bar{B} \cdot \nabla_H \bar{\theta}) \nabla_H \bar{B}. \quad (7)$$

Notice that, even though the flux is in the direction of $\nabla \bar{B}$, $\overline{\mathbf{u}'\theta'} \cdot \nabla \bar{\theta} < 0$. Thus the flux of tracer tends to be down the tracer gradient, but only the projection of the tracer gradient along the direction of the buoyancy gradient contributes to the flux.

We now apply the closure in (7) to the advection-diffusion equations for heat and salt in the ML,

$$\begin{aligned} \partial_t T + \mathbf{u} \cdot \nabla T = \\ = \gamma \nabla \cdot [f(|\nabla B|) (\nabla B \cdot \nabla T) \nabla B] + \mathcal{F}_T, \end{aligned} \quad (8)$$

$$\begin{aligned} \partial_t S + \mathbf{u} \cdot \nabla S = \\ = \gamma \nabla \cdot [f(|\nabla B|) (\nabla B \cdot \nabla S) \nabla B] + \mathcal{F}_S, \end{aligned} \quad (9)$$

where \mathcal{F}_T and \mathcal{F}_S represent the thermohaline fluxes from the top and bottom of the ML. We dropped overbars and we replaced ∇_H with ∇ for convenience, but keep in mind that all variables are averaged over scales larger than H and times longer than τ_V and that derivatives are taken only in the horizontal. We assume a linear equation of state and measure T and S in buoyancy units units, so that,

$$B = T - S. \quad (10)$$

The nonlinear advection-diffusion equations (8) and (9), together with (10), form a closed system whose solution is fully determined once the forcings \mathcal{F}_T and \mathcal{F}_S and the large scale velocity field \mathbf{u} are prescribed.

By adding and subtracting (8) and (9), we obtain closed equations for buoyancy and spice $V = T + S$ (*Veronis*, 1972; *Munk*, 1981), viz.,

$$\begin{aligned} \partial_t B + \mathbf{u} \cdot \nabla B = \\ = \gamma \nabla \cdot [f(|\nabla B|) (\nabla B \cdot \nabla B) \nabla B] + \mathcal{F}_B, \end{aligned} \quad (11)$$

$$\begin{aligned} \partial_t V + \mathbf{u} \cdot \nabla V = \\ = \gamma \nabla \cdot [f(|\nabla B|) (\nabla V \cdot \nabla B) \nabla B] + \mathcal{F}_V, \end{aligned} \quad (12)$$

where $\mathcal{F}_B = \mathcal{F}_T - \mathcal{F}_S$ and $\mathcal{F}_V = \mathcal{F}_T + \mathcal{F}_S$. We can now see how the equations in (11) and (12) model the development of compensation in the ML. The product $f(|\nabla B|) (\nabla B \cdot \nabla B)$ must be an increasing function of $|\nabla B|$ to be consistent with our assumption that eddy fluxes are driven by buoyancy gradients. Under this constraint, the nonlinear diffusion always dissipates buoyancy, even more so when $|\nabla B|$ is large. Also spice is dissipated where $|\nabla B|$ is large. However large values of $|\nabla V|$ can survive in regions where $|\nabla B|$ is small. In terms of temperature and salinity this means that compensated fronts, for which $\nabla T \approx \nabla S$ persist, while buoyancy fronts are short lived.

Young (1994) and *Ferrari and Young* (1997) derive formally equations of the form of those in (8) and (9) to parameterize the transport of heat and salt on horizontal scales of a few kilometers in the ML. These theoretical works are examples of the closures we have been discussing when the averaging is done over the depth of the ML, over horizontal scales of a few kilometers and time scales of a few hours. Nonlinear diffusion arises because the horizontal transport of heat and salt is by shear dispersion, and the shear flow doing the dispersion is driven by slumping horizontal buoyancy gradients. The strength of the shear dispersion increases as the horizontal buoyancy gradient squared, that is $f(|\nabla B|) = 1$ in (8) and (9).

At scales larger than the Rossby radius of deformation Ro , unbalanced motions are influenced by rotation in the form of baroclinic instability. Therefore, if one is to parameterize the transport of heat and salt on horizontal scales larger than Ro , say 10 km for a typical ML, the closure must include the transports due to eddies generated at baroclinically unstable gradients. *Green* (1970) and *Stone* (1972) derived expressions for the tracer fluxes generated by baroclinic waves. Their results predict that the baroclinic eddy fluxes across a buoyancy gradient are proportional to the absolute value of the diapycnal buoyancy gradient. *Green* and *Stone* considered only zonally-averaged models and did not investigate the direction of the fluxes. If their arguments are extended to two horizontal dimensions to parameterize diapycnal fluxes of heat and salt in the ML, one obtains nonlinear diffusion equations of the form in (8) and (9) with $f(|\nabla B|) = |\nabla B|^{-1}$. Notice, however, that a full parameterization of baroclinic instability should include the eddy fluxes along isopycnals as well (*Marshall and Shutts*, 1981). This issue is not pursued further here, because we focus on the role of diapycnal fluxes on the establishment of the temperature-salinity relationship in the ML.

Chris Garrett, during the meeting, suggested that symmetric instability might also drive thermohaline

fluxes in the ML. *Haine and Marshall* (1997) used numerical simulations to study what hydrodynamical instabilities control the transfer of buoyancy through the ML on scales of some tens of kilometers. Their conclusion is that nonhydrostatic baroclinic instability provides the dominant mode of lateral buoyancy transfer. However symmetric instability plays an important role during the slumping process by setting to zero potential vorticity along isopycnal surfaces. Clearly more work need to be done to formulate a closure that takes into account the effects of both symmetric and baroclinic instabilities.

3. Thermohaline alignment and compensation in the mixed layer

The nonlinear advection-diffusion equations in (8) and (9) are now used to investigate how compensation appears in the ML. Suppose that spatial variations in temperature and salinity are created by surface fluxes that vary on large horizontal scales. Mesoscale stirring will create small-scale temperature and salinity gradients by stretching and folding the large scale thermohaline patterns. Large density gradients will disappear quickly as a result of nonlinear diffusion, while compensated gradients will persist for longer times. Thus we expect that the temperature and salinity gradients present at small scales at any particular moment will be typically compensated. We are now going to test this scenario with a numerical model.

3.1. Numerical model

The parameterization in (8) and (9) is tested with numerical simulations in which temperature and salinity are advected using a velocity field generated by solving the equivalent barotropic equations in the streamfunction-vorticity formulation,

$$\partial_t \zeta + J(\psi, \zeta) = -\mu \zeta + \nu \nabla^6 \zeta + \mathcal{F}_\zeta, \quad (13)$$

where ψ is the streamfunction, $\zeta = \nabla^2 \psi$ the relative vorticity and J the Jacobian operator. The forcing \mathcal{F}_ζ is applied in spectral space at a scale of 6 km with constant amplitude and random phases. The bottom drag coefficient is set to $\mu = 3 \cdot 10^{-6} \text{ s}^{-1}$ and the hyper-viscosity to $\nu = 3 \cdot 10^6 \text{ m}^6 \text{ s}^{-1}$. The result is a two-dimensional turbulent field with meandering vortices of a diameter of approximately 3 km (half the forcing scale) and RMS velocities of 0.1 m s^{-1} (Figure 2). The domain of integration is a biperiodic square of $51.2 \times 51.2 \text{ km}^2$ with a mesh of 100 m. This is a poor model of the mesoscale dynamics of the ML. In particular we are neglecting feedbacks between the buoyancy and the velocity fields. But our goal is to show that compensation develops at

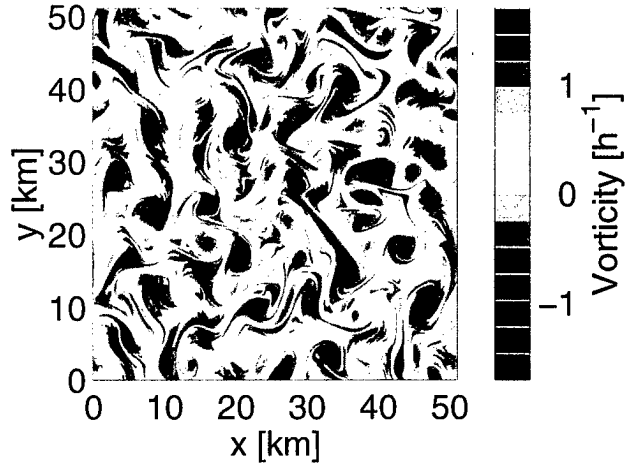


Figure 2. Snapshot of the vorticity field obtained by integrating the equivalent barotropic equations. The typical size of vortices is about 3 km, that is half the wavelength of 6 km at which the vorticity equation is forced.

scales small scales, regardless of the details of the stirring field and, in this context, the model in 13 suffices.

The temperature and salinity equations in (8) and (9) are integrated with $f(|\nabla B|) = 1$, that is we use the closure in *Young* (1994) and *Ferrari and Young* (1997). The value of γ is set to $10^{14} \text{ m}^2 \text{ s}^3$ appropriate for typical ML parameters (details in *Ferrari and Young*, 1997). However the qualitative results discussed in the rest of this paper do not depend on the particular choice of $f(|\nabla B|)$.

Temperature and salinity are forced with orthogonal sinusoidal patterns, that is we set $\mathcal{F}_T = F_0 \cos qx$ in the RHS of (8) and $\mathcal{F}_S = F_0 \sin qy$ in the RHS of (9). The sinusoids have a wavelength equal to the domain size, i.e., $q = 2\pi/51.2 \text{ km}^{-1}$. The amplitude F_0 is chosen such as to have thermohaline fluctuations of 1°C and 0.35 psu, at the scale of the domain. These forcings do not impose any correlation between temperature and salinity fluctuations. Further details on the numerical code are given in *Ferrari and Paparella* (2001).

3.2. Complex density ratio

It is common to quantify compensation in terms of the density ratio, defined as the change in buoyancy due to temperature divided by the change in buoyancy due to salinity,

$$R_{1D} \equiv \frac{\hat{\ell} \cdot \nabla T}{\hat{\ell} \cdot \nabla S}, \quad (14)$$

where temperature and salinity are defined in buoyancy units, and $\hat{\ell}$ is the direction along which the cut is taken.

In two-dimensions, it is convenient to introduce a

complex density ratio as,

$$R \equiv \frac{T_x + i T_y}{S_x + i S_y}. \quad (15)$$

The complex density ratio has both a magnitude and a phase, $R = |R| \exp(i\phi)$: $|R|$ is the ratio of the magnitudes of the temperature and salinity gradients and ϕ is the angle between them. If the gradients are parallel ($\phi = 0^\circ$) or antiparallel ($\phi = 180^\circ$), there is *thermohaline alignment* and the definition of R in the complex plane is equivalent to that in (14) regardless of the orientation of \vec{l} . When $|R| > 1$, the change in buoyancy due to temperature is greater than the change in buoyancy due to salinity along the direction of ∇B , that is $|\nabla B \cdot \nabla T| > |\nabla B \cdot \nabla S|$ and the buoyancy-front is temperature-dominated. The opposite is true if $|R| < 1$ and the buoyancy-front is salinity-dominated. The particular case $|R| = 1$ and $\phi = 0^\circ$ describes *thermohaline compensation*.

Because the magnitude of the complex density ratio is infinite when the salinity gradient vanishes, we characterize fronts in terms of the phase ϕ and the Turner angle,

$$Tu \equiv \arctan |R|, \quad (16)$$

choosing the branch where $0 \leq Tu \leq \pi/2$. All statistics will be computed in terms of ϕ and Tu . For convenience, results are discussed in terms of ϕ and $|R|$, because their values are more familiar.

In the following we use the joint pdf $P(Tu, \phi)$ to describe the degree of alignment and compensation in the ML. The joint pdf is normalized according to

$$\int_0^{\pi/2} dTu \int_0^{2\pi} d\phi P(Tu, \phi) = 1. \quad (17)$$

3.3. Results of numerical simulations

For the simulations we use kilometers to measure distances and hours to measure time. Therefore vorticity is given in h^{-1} and buoyancy in km h^{-2} . We set to zero the initial vorticity, temperature and salinity. After an initial transient of several eddy turnover times, kinetic energy, enstrophy, temperature and salinity variances settle to a constant value; i.e. the system reaches an equilibrium between the variance input by the forcing at large scales and dissipation at small scales.

In Figures 3 and 4, we show snapshots of spice and buoyancy 700 h after the beginning of the simulation. It is difficult to recognize in these snapshots the large scale patterns of buoyancy and spice imposed by the forcing described in section 3.1. But the sinusoidal patterns emerge clearly if one averages the fields over times of the order of a few hundred hours. At small scales the

two fields are remarkably different. A comparison of the black contours in the two figures shows that gradients of spice are sharper than those of buoyancy: buoyancy contours are evenly spaced, while spice contours are extremely packed in a few regions and widely spaced in others. Sharp spice gradients with no signature in buoyancy imply $\nabla T \approx \nabla S$, i.e., thermohaline compensation.

The small scale variability in Figures 3 and 4 is produced by stirring the large scale thermohaline patterns. The temperature and salinity gradients, computed across the grid spacing of 100 m, are typically aligned. Alignment occurs because the isolines of T and S are stretched by the same stirring field and thus both tracers end up with gradients pointing in the same directions (Hua, 2001). This is shown through the joint pdf $P(Tu, \phi)$ (Figure 5). The overwhelming majority of points in the pdf have angles very close to either $\phi = 0^\circ$ or $\phi = 180^\circ$. But this is not the whole story, because not all values of $|R|$ are equally probable along those two angles. The pdf has a clear peak at $R = 1$. This is the signature of nonlinear diffusion which selectively dissipates all gradients whose density ratio is different from one and establishes compensation. Stirring alone does not produce a single peak in the pdf, because it acts only on the relative orientation of ∇T and ∇S but not on the ratio of their magnitudes. This was checked by running a simulation in which the nonlinear diffusion was set to zero. In this limit, the pdf $P(Tu, \phi)$ is indeed collapsed along the angles $\phi = 0^\circ$ and $\phi = 180^\circ$, but it does not have a single mode.

Compensation is not maintained always and everywhere in the domain. There are regions, in Figures 3 and 4, where buoyancy and spice gradients are comparable. This happens when the stirring field momentarily creates large buoyancy gradients at small scales. These gradients do not persist for long, though, because nonlinear diffusion restores compensation in a few hours. At any time, a one dimensional cut through the domain shows many compensated fronts and some rare buoyancy fronts. This result agrees with the thermohaline structure found by Ferrari and Rudnick (2000) in the ML of the Subtropical North Pacific (Figure 1), where almost all temperature and salinity fluctuations are compensated.

4. Implications for numerical models of the mixed layer

In the previous sections we have suggested that the thermohaline compensation observed in the ML is consistent with preferential diffusion of horizontal buoyancy gradients. The theoretical argument implicates vertically sheared currents within the ML as the agent which produces the preferential horizontal transport of

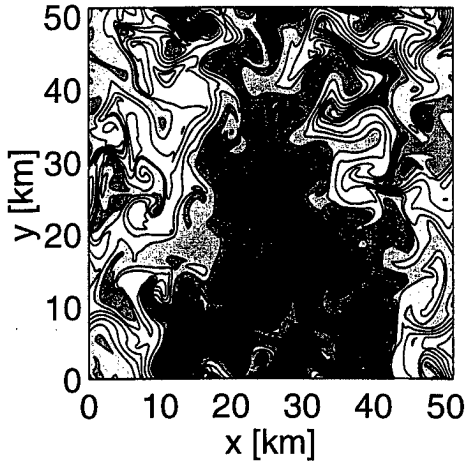


Figure 3. Snapshots of spice at the same time of figures 2 and 4. The colored pattern hints at the large-scale sinusoidal checkerboard, imposed on the spice field through the thermohaline forcing.

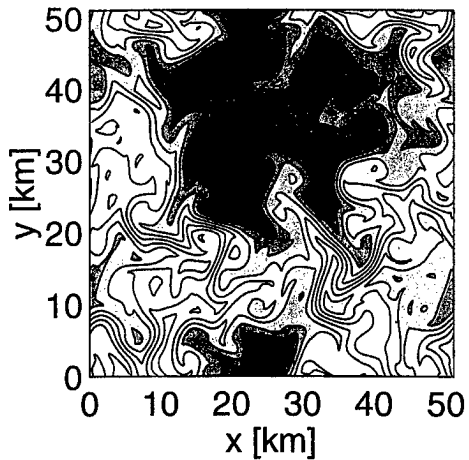


Figure 4. Snapshots of buoyancy at the same time of figures 2 and 3. The colored pattern hints at the large-scale sinusoidal checkerboard, imposed on the buoyancy field through the thermohaline forcing. At small scales buoyancy shows less structure and milder gradients than spice. Regions with large spice fluctuations with no signature in buoyancy are the trademark of compensation.

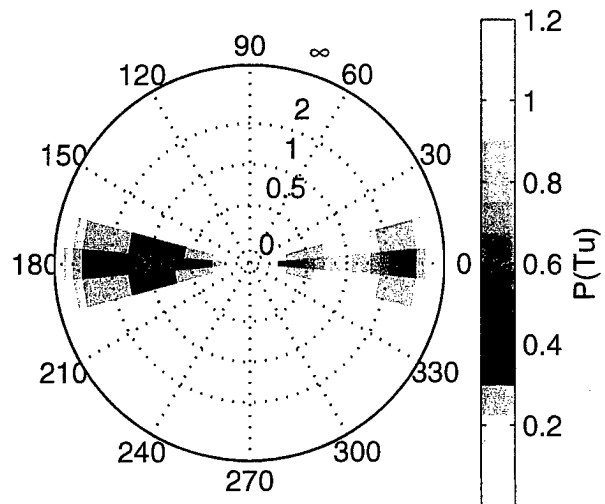


Figure 5. Joint pdf $\mathcal{P}(\text{Tu}, \phi)$ of the complex density ratio R defined in section 3.2. The azimuthal position in the radar plot indicates the angle between the temperature and the salinity gradients, while the radial displacement is the ratio of their magnitudes. The pdf is an average over 200 hours during which the simulation was in equilibrium. Nearly all points lie along the line of alignment, that is at angles $\phi = 0^\circ$ and $\phi = 180^\circ$. The maximum of the pdf is at $R = 1$ and shows that thermohaline fronts are typically compensated.

density. Numerical models with bulk MLs do not include this physics. The purpose of this last section is to suggest a simple parameterization of ML horizontal transports that might improve the representation of thermohaline dynamics in numerical models with bulk ML.

Bulk ML parameterizations ignore the potential energy stored in horizontal buoyancy gradients. But we contend that the release of this potential energy plays an important role in establishing compensation. The system in (11) and (12) describes the horizontal dynamics of the vertically-averaged fields and could be implemented in a bulk ML model. However the nonlinear diffusive terms on the RHS of (11) and (12) are difficult to integrate numerically. In small regions with large buoyancy gradients the diffusive constraint on the time stepping becomes severe (Ferrari and Paparella, 2001) and the whole calculation proceeds very slowly. The path we follow here is to derive a substitute model that retains the basic physics of (11) and (12), but that is easy to integrate numerically. That is we write a linear model that diffuses horizontal buoyancy gradients more efficiently than spice gradients in the following way,

$$B_t + \mathbf{u} \cdot \nabla B = \kappa_B \nabla^2 B, \quad (18)$$

$$V_t + \mathbf{u} \cdot \nabla V = \kappa_V \nabla^2 V. \quad (19)$$

By setting $\kappa_B \gg \kappa_V$ buoyancy gradients decay faster than spice gradients. The main advantage of the model in (18) and (19) over that in (11) and (12) is that the diffusivities are independent of the buoyancy gradients and therefore the diffusive constraints on the time stepping do not grow unbounded.

In order to match observations, the two diffusivities κ_B and κ_V must be chosen such that compensation happens mostly at scales below 10 km (Ferrari and Rudnick, 2000). That is the dissipation cutoff scale for buoyancy must be of the order of 10 km, while the dissipation cutoff scale for spice must be smaller. The dissipation cutoff scale for buoyancy can be estimated as,

$$L_{diss} \approx \sqrt{\frac{\kappa_B}{\sigma}}, \quad (20)$$

where σ is the RMS strain rate of to the mesoscale eddy field \mathbf{u} . A reasonable strain rate in the ML is of the order of 10^{-5} s^{-1} . By imposing $L_{diss} \approx 10 \text{ km}$, it follows that $\kappa_B \approx 10^3 \text{ m}^2 \text{ s}^{-1}$. The choice of κ_V is somewhat arbitrary, but it should be a couple of orders of magnitude smaller than κ_B , so that there is at least a decade between the cutoff scales of spice and buoyancy.

The final step is to write the linear model in (18) and (19) in terms of temperature and salinity, by using once more the linear expressions for buoyancy $B = T - S$ and spice $V = T + S$,

$$T_t + \mathbf{u} \cdot \nabla T = \kappa_+ \nabla^2 T - \kappa_- \nabla^2 S, \quad (21)$$

$$S_t + \mathbf{u} \cdot \nabla S = \kappa_+ \nabla^2 S - \kappa_- \nabla^2 T, \quad (22)$$

where $\kappa_+ = (\kappa_B + \kappa_V)/2$ and $\kappa_- = (\kappa_B - \kappa_V)/2$. The coupling between the salt and heat fluxes in (21) and (22) is formally similar to the Soret and DuFour effects that operate on a molecular level (Caldwell, 1973). The main difference is that, in the present case, all terms in the RHS of (21) and (22) are of the same order and none can be neglected. Only for $\kappa_B = \kappa_V$, the coupling between temperature and salinity disappears.

The parameterization in (21) and (22) has been tested by integrating the equations with the velocity field and thermohaline forcings described in section 3.1. The lower panel of Figure 6 shows the pdf of the meridional density ratio at a scale of 3 km obtained with the linear model. The pdf has a clear peak at $R = 1$, as in the observations (upper panel of Figure 6). Notice that the large scale density ratio for the same simulation is uniform. Thus compensation is a result of the parameterization in (21) and (22), and is not due to the external forcing.

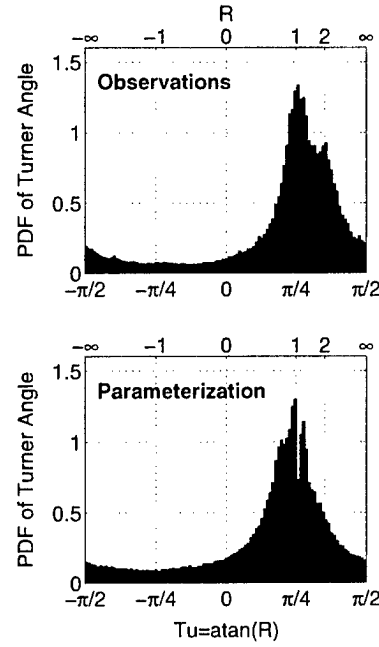


Figure 6. Probability density function of the horizontal mixed-layer Turner angle across a distance of 3 km along 25–35 degrees in the North Pacific (upper panel) and across the same distance in a simulation with the proposed mixed layer parameterization (lower panel). The values of Turner angle and density ratio are indicated on the upper and lower axes. The pdfs have a peak close to $R = 1$ and represent thermohaline fields characterized by buoyancy compensation.

5. Conclusions

We have shown that the ubiquitous compensation of thermohaline gradients observed in the ML is consistent with the theoretical arguments of Young (1994) and Ferrari and Young (1997). Compensation can be explained as the preferential diffusion of horizontal buoyancy gradients which occurs because unbalanced motion due to these gradients is stronger in the ML than in the more nearly geostrophic interior. The horizontal pressure gradients associated with the buoyancy gradients produce “exchange flows” which act to restratify the ML in the vertical. The turbulent fluxes, that continuously mix the ML in the vertical, oppose the restratification and weaken the horizontal buoyancy gradients. This process is essentially shear dispersion of buoyancy, where the shear flow is driven by the density gradients themselves.

The theoretical arguments of Young and collaborators implicate that eddy fluxes of heat and salt in the ML are in the direction of the buoyancy gradients and act to weaken the horizontal buoyancy stratification. That is, the thermohaline diapycnal fluxes remove the energy stored in horizontal buoyancy gradients. The sit-

uation is reversed below the ML base, where the available potential energy is believed to be removed by adiabatic processes. The difference in the two cases is that there are strong diabatic motions in the ML at small scales, while flows are mostly along isopycnals in the ocean interior. Expressions like the one in (7) might be a first step toward a better parameterizations of diapycnal fluxes in the ML.

We implemented the nonlinear diffusive parameterization of heat and salt in a simple, idealized model of the ML. Numerical simulations showed that buoyancy-driven diffusion is complemented and locally enhanced by the mesoscale stirring field. The strain in the velocity field continuously creates thermohaline gradients at small scales. Nonlinear diffusion selectively removes buoyancy gradients. As a result at any single time typical temperature and salinity gradients are compensated, in agreement with the observations of *Ferrari and Rudnick* (2000). Our model does not include any feedback between the velocity field and buoyancy, as due to rotation. An obvious direction for future research is to investigate whether this feedback plays an important role in the establishment of the temperature-salinity relationship of the ML.

Our discussion emphasized the role of diapycnal fluxes in removing horizontal buoyancy gradients. A question arises as to what maintains the long-lived buoyancy fronts observed at some locations in the ML (e.g. *Roden*, 1975; *Rudnick and Luyten*, 1996). First, these fronts have horizontal scales of a few tens of kilometers. The buoyancy-driven fluxes, discussed above, are mostly active at scales shorter than, say, 10 kilometers and are weaker at larger scales. Second, ML fronts are believed to be maintained by surface forcing or by convergences in the velocity field. When this is the case, the diapycnal thermohaline fluxes do not remove completely the buoyancy gradient. Instead an equilibrium is reached between nonlinear diffusion and forcing. The result is a buoyancy front in which temperature and salinity partly oppose each other, but do not compensate. Observations indeed show partial cancellation of the thermohaline components at many ML fronts.

We also derived a linear model that reproduces the preferential diffusion of horizontal buoyancy gradients. The linear parameterization produced realistic distributions of the density ratio in a simple, idealized model of the ML. It remains an open question whether the new parameterization would produce realistic diapycnal fluxes and water mass conversions, if implemented in high-resolution ocean models with bulk ML.

Acknowledgments. Ferrari wishes to acknowledge the support of the National Science Foundation (OCE96 -

16017) and the WHOI Postdoctoral Fellowship. Ferrari, Rudnick and Young wish to express their thanks to Chris Garrett and Peter Müller for organizing and inviting us to the 'Aha Huliko'a Hawaiian Winter Workshop.

References

- Caldwell, D.R., Thermal and Fickian diffusion of sodium chloride in a solution of oceanic concentration, *Deep-Sea Res.*, 20, 1029–1039, 1973.
- Ferrari, R., and W. R. Young, On the development of thermohaline correlations as a result of nonlinear diffusive parameterizations, *J. Mar. Res.*, 55, 1069–1101, 1997.
- Ferrari, R., and Rudnick, D.L., Thermohaline structure of the upper ocean. *J. Geophys. Res.*, 105, 16857–16883, 2000.
- Ferrari, R., and Paparella, F., Compensation and alignment of thermohaline gradients in the mixed layer, in preparation for *J. Phys. Oceanogr.*, 2001.
- Ferrari, R., D.L. Rudnick, and W.R. Young, Parameterization of horizontal diffusivities in the mixed layer, in preparation for *J. Phys. Oceanogr.*, 2001.
- Garrett C., and A. Tandon, The effects on water mass formation of surface mixed layer time-dependence and entrainment fluxes, *Deep-Sea Res.*, 44, 1991–2006, 1997.
- Garrett, C., Stirring and mixing: what are the rate controlling processes?, in *From stirring to mixing in a stratified ocean*, Proceedings of the 12th 'Aha Huliko'a Hawaiian Winter Workshop, in press, 2001.
- Green, J.A., Transfer properties of the large-scale eddies and the general circulation of the atmosphere, *Quart. J. Roy. Meteorol. Soc.*, 96, 157–185, 1970.
- Haine T.W.N., and J. Marshall, Gravitational, Symmetric, and Baroclinic Instability of the Ocean Mixed Layer, *J. Phys. Oceanogr.*, 28, 634–658, 1997.
- Hua, B.L., Tracer cascade in geostrophic turbulence, in *From stirring to mixing in a stratified ocean*, Proceedings of the 12th 'Aha Huliko'a Hawaiian Winter Workshop, in press, 2001.
- Kraus, E.B., and J.S. Turner, A one dimensional model of the seasonal thermocline, II. The general theory and its consequences, *Tellus*, 19, 98–105, 1967.
- Large, W.G., G. Danabasoglu, S.C. Doney, and J.C. McWilliams, Sensitivity to surface forcing and boundary layer mixing in a global ocean model: Annual-mean climatology, *J. Phys. Oceanogr.*, 27, 2418–2447, 1997.
- Marshall J., and J. Schutts, A note on rotational and divergent eddy fluxes, *J. Phys. Oceanogr.*, 11, 1677–1680, 1981.
- Mellor G.L., and T. Yamada, A hierarchy of turbulent closure models for planetary boundary layers, *J. Atmos. Sci.*, 31, 1791–1806, 1974.
- Munk, W., *Evolution of Physical Oceanography*, (B.A. Warren and C. Wunsch, eds.), Chapter 9. MIT Press, Cambridge, Massachusetts. 198.
- Roden, G.I., On north Pacific temperature, salinity, sound velocity and density fronts and their relation to the wind and energy flux fields, *J. Phys. Oceanogr.*, 5, 557–571, 1975.

- Rudnick, D. L., and J. R. Luyten, Intensive survey of the Azores Front, 1, Tracers and dynamics, *J. Geophys. Res.* 101, 923–939, 1996.
- Rudnick, D.L., and J.P. Martin, On the horizontal density ratio in the upper ocean, submitted to *Dynamics of the Oceans and the Atmosphere*, 2001.
- Rudnick, D.L., and R. Ferrari, Compensation of horizontal temperature and salinity gradients in the ocean mixed layer, *Science*, 283, 526–529, 1999.
- Schmitt, R. W., P. S. Bodgen, and C. E. Dorman, Evaporation minus precipitation and density fluxes for the North Atlantic, *J. Phys. Oceanogr.* 9, 1208–1221, 1989.
- Stommel, H., A conjectural mechanism for determining the thermohaline structure of the oceanic mixed layer, *J. Phys. Oceanogr.*, 23, 142–148, 1993.
- Stone P.H., A simplified radiative-dynamical model for the static stability of rotating atmosphere, *J. Atmos. Sci.*, 96, 157–185, 1972.
- Veronis, G., On properties of seawater defined by temperature, salinity and pressure. *J. Mar. Res.*, 30, 227–255, 1972.
- Weller, R.A., J.P. Dean, J. Marra, J.F. Price, E.A. Francis, and D.C. Boardman, 3-dimensional flow in the upper ocean, *Science*, 227, 1552–1556, 1985.
- Young, W.R., The subinertial mixed layer approximation, *J. Phys. Oceanogr.*, 24, 1812–1826, 1994.

R. Ferrari, Woods Hole Oceanographic Institution,
MS#21, Woods Hole, Massachusetts, USA. (e-mail:
rferrari@whoi.edu)

This preprint was prepared with AGU's L^AT_EX macros v4, with the extension package 'AGU++' by P. W. Daly, version 1.6a from 1999/05/21, with modifications by D. E. Kelley, version 1.0 from 2001/03/26, for the '*Aha Huliko'a Hawaiian Winter Workshop*.

Water mass transformation due to mixed layer entrainment and mesoscale stirring: In series or parallel?

A. Tandon

Physics Department, College of Engineering, and School for Marine Science and Technology,
University of Massachusetts, North Dartmouth MA 02747. (e-mail: atandon@umassd.edu)

Abstract. The convergence of advective and diffusive buoyancy flux must match the air-sea buoyancy flux between two outcropping isopycnals. This leads to a diagnostic framework for water mass transformation in which a myriad of different processes can be incorporated under a unifying balance. We review how the diapycnal advection due to ubiquitous mixed layer entrainment can be included in this framework, and we estimate its contribution to the large scale transformation. We also consider how decomposing the flow and buoyancy field into mean, eddy and turbulent parts leads to clarifying the interaction of mixed layer and mesoscale (or sub-mesoscale) eddies in the overall large scale balance.

1. Introduction

Quantifying the water mass changes and finding the water mass formation rates for specific density classes are central to understanding the diabatic ocean circulation. Accurate quantification of water mass formation rates is also important for understanding variability in oceanic heat and freshwater fluxes and their contribution to climate.

The current description of water mass transformation was formulated by *Wal in* (1982), who proposed that the poleward surface drift in the ocean can be determined directly by the air-sea heat flux $-B_0$ at the surface.¹ This led *Wal in* to suggest the relation

$$F(T) = B_0 \frac{dS}{dT} \quad (1)$$

where F is the cross-isotherm advection (volumetric flow rate), and dS is the area enclosed between the two isotherm outcrops as shown in Figure 1.

This relationship was subsequently successfully used in diagnostic calculations (*Tziperman* 1986, *Speer and Tziperman* 1992). These calculations showed close correspondence between the water mass formation derived by the diathermal advection from the *Wal in* relation and the estimated rates of water mass formation for

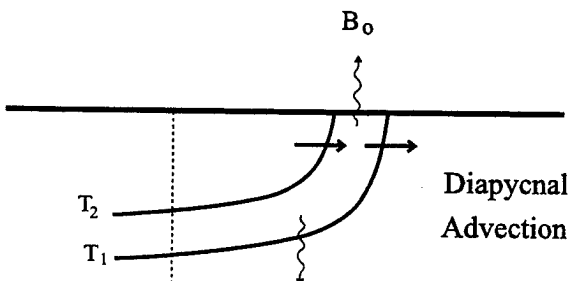


Figure 1. A schematic of the diapycnal advection $F(T)$ considered by *Wal in* (1982). The net surface heat flux is balanced by a net advective flux at the surface.

Sub-Tropical mode water and the Sub-Polar Mode Water from observations. However, the *Wal in* (1982) formulation assumed negligible mixing in the upper ocean.

In the same year that *Wal in* proposed his ideas about this diathermal advection, *Niiler and Stevenson* (1982) sought to constrain the values of diapycnal mixing by considering the heat budget of the isotherms that outcrop in the tropics and are subject to net heat gain through the year as shown in Figure 2.

In this case, since by definition the net change in the mean annual isothermal position is zero, there cannot be a net diathermal advection and the net heat flux must be balanced by a net diffusive flux due to mixing. Therefore, at least in the limiting case of closed mean isopycnal surfaces, the role of diffusive flux due to mixing cannot be ignored, and the surface drift of

¹The interest in water mass formation rate in specific density classes has followed various diagnostics, e.g. in *Wal in* (1982) arising out of considering budgets with heat fluxes and isotherms, and in other studies, the distribution of isopycnals and buoyancy fluxes. Thus we retain the symbol B_0 for both surface heat fluxes and surface buoyancy fluxes.

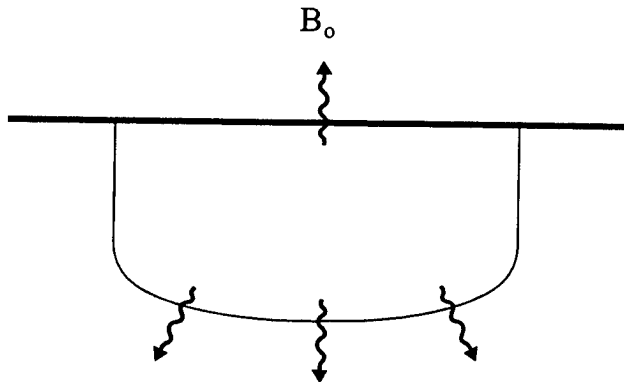


Figure 2. A schematic of the outcropping tropical annual mean isotherms considered by Niiler and Stevenson (1982). The net surface heat flux must be balanced by a net diffusive flux due to mixing.

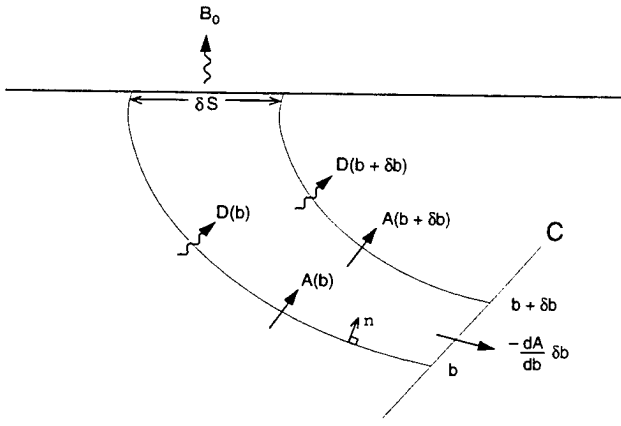


Figure 3. Air-sea buoyancy flux $B_0 \delta S$ between two outcropping isopycnals b and $b + \delta b$ must be balanced by convergence of diapycnal advective flux due to advection $A(b)$ and diffusive flux $D(b)$. From Garrett et al. (1995).

Walin (1982) cannot achieve this balance.

This realization led Garrett et al. (1995) to clarify the Walin formulation. They insisted that considering the diapycnal advection about any averaged isopycnal position would require diapycnal mixing, since otherwise the isopycnal would simply be advected around by the flow. As Figure 3 shows, the convergence of the diapycnal advective and diffusive fluxes must match the air-sea buoyancy flux between two isopycnals.

The Walin (1982) approach was thus generalized by

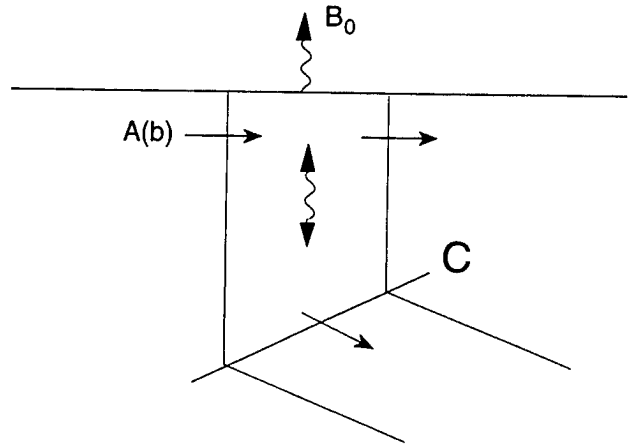


Figure 4. Garrett et al. (1995)'s ideal case. With no horizontal mixing and only vertical mixing, $D(b)$ can be ignored and the diapycnal advection equals the air-sea transformation, or, $A = F$.

Garrett et al. (1995) as

$$A(b) = F(b) - \frac{dD}{db} \quad (2)$$

where $D(b)$ is the diapycnal diffusive flux across the isopycnal b . Formal derivations of this relation appear in Garrett et al. (1995) and in Marshall et al. (1999).

$D(b)$ consists of many mixing processes that can result in diffusive flux across isopycnal b . There will be contributions to D from diffusive mixing in the thermocline, while horizontal diffusive fluxes due to mesoscale stirring would arise near the ocean surface, and tidal mixing near rough bathymetry for the isopycnals that intersect with the ocean bottom in such regions. In so far as the balance in the upper ocean is concerned, if the control volume is chosen to be bounded by two isopycnals b and $b + \delta b$ and a control surface at the bottom of the mixed layer (Figure 4), Garrett et al. (1995) showed that for negligible horizontal mixing and with vertical isopycnals, vertical mixing $D(b)$ makes no contribution and the net diapycnal advection is only due to the air-sea transformation, that is,

$$A(b) = F(b) \quad (3)$$

where $F(b) = -B_0 \frac{dS}{db}$ is the air-sea transformation, with the negative sign due to the convention that the diapycnal advection from less buoyant to more buoyant water mass is considered positive (reversing the signs of Walin's convention in Figure 1). This is an important idealization, since in this case the diapycnal advection can be fully diagnosed by surface buoyancy flux and surface buoyancy outcrop distribution.

Speer (1997) evaluated $F(b)$ and $A(b)$ using a hydrographic section at 11°S , as shown in the schematic

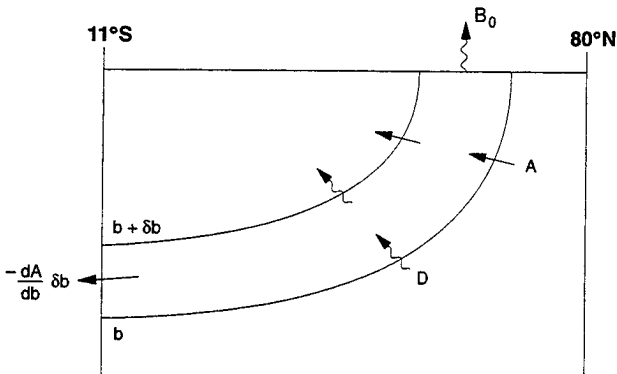


Figure 5. A schematic showing the control volume for the diagnostic calculation carried out by Speer (1997).

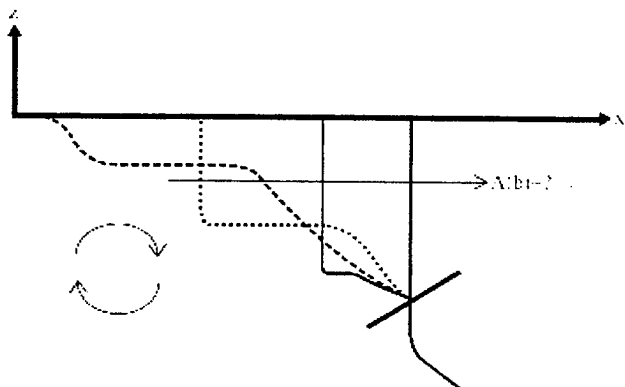


Figure 6. The ideal algorithm can no longer be expected to be valid if time-dependent effects are taken into account with entrainment at the mixed layer base.

Figure 5. These diagnostic calculations showed that the residual between $A(b)$ and $F(b)$ is significant, and therefore transformation due to the diffusive flux term $dD(b)/db$ must be considered. While this diagnostic calculation cannot be used to pinpoint which processes contribute to the D term, Speer (1997) showed that the calculations are consistent with diapycnal mixing in the thermocline.

The formulation considered thus far has assumed steady state, but an accumulation within the isopycnals can be interpreted as a net inflow, and (2) can still be used. A steady state scenario neglects the role of diapycnal advection due to time dependent deepening and shallowing of the mixed layer, at both seasonal and diurnal timescales. Conceptual modifications are required to relax the steady state assumption for the water mass transformation balance as shown in Figure 6.

The next section considers diapycnal advection due to the ubiquitous process of mixed layer deepening and entrainment. Upwelling at the base of the mixed layer

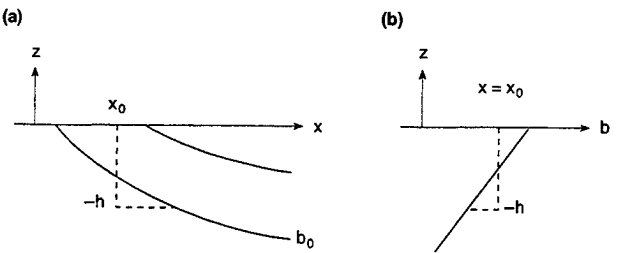


Figure 7. A schematic showing isopycnal distribution (left) and buoyancy distribution (right). The solid lines are before the mixing event and the dashed lines are after the mixing event.

and subsequent mixing results in water mass transformation which is conceptually very similar to that due to mixed layer deepening and entrainment at the base of the mixed layer. Regions of significant upwelling such as those found near submesoscale instabilities near fronts are considered next via an example from FASINEX (Weller 1991). The final section considers whether the stirring due to mesoscale processes should be considered as an independent process for water mass formation and hence considered to be independent of the transformation due to the mixed layer entrainment, or, do the two processes happen together, in series and are interdependent. The water mass transformation rates would only be additive in the former case. We conclude with a summary and unanswered questions.

2. Transformation Due to Mixed Layer Deepening

Garrett and Tandon (1997) show that buoyancy redistribution in the vertical by mixing achieves diapycnal advection across an isopycnal surface. Figure 7 shows an isopycnal that outcrops at position x_0 due to vertical mixing, and the buoyancy balance is shown on the right. x is taken to be the direction normal to the outcrop towards less dense waters.

With a uniform buoyancy gradient in the vertical and in the horizontal everywhere, the volume between the successive isopycnals does not change, i.e., there is no diapycnal advection. However, a departure from these conditions implies a net diapycnal advection. In particular, if a pre-existing mixed layer of depth $-h + dh$ deepens to $-h$, as shown in Figure 8, Garrett and Tandon (1997) show that the net diapycnal advection F_{ML} is given by

$$F_{ML} = \frac{1}{T} \int_0^T \left[\left(\frac{1}{b_{xi}} - \frac{1}{b_{xs}} \right) \Delta b - \frac{1}{2} b_{xx} b_x^{-3} (\Delta b)^2 \right] \left(w + \frac{\partial h}{\partial t} \right) dt \quad (4)$$

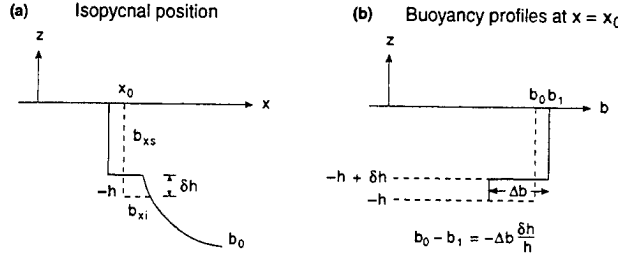


Figure 8. A schematic showing isopycnal distribution (left) and buoyancy distribution (right) for a pre-existing mixed layer in presence of both b_{xx} and b_{zz} . The solid lines are before the mixing event and the dashed lines are after the mixing event.

per unit outcrop length, the subscripts i and s refer to the gradients below the mixed layer (interior) and surface mixed layer respectively, Δb is the buoyancy change at the mixed layer base before a deepening event, h is the mixed layer depth, w is the vertical velocity at the mixed layer base, b_{xx}, b_z are buoyancy derivatives calculated at the surface, t is the time and $T = 1$ yr. F_{ML} is the integrated diapycnal advection over the year for each deepening event $w + \frac{\partial h}{\partial t} > 0$, since the upwelling with vertical velocity w has an effect similar to mixing and subsequent deepening by $w \delta t$.

The F_{ML} expression above consists of two terms, the first depending on vertical variation of horizontal buoyancy gradients and the second depending on the curvature or the horizontal variation of the surface buoyancy gradients. *Garrett and Tandon (1997)* remark on several cases in the limit as b_{xi} , the buoyancy gradient at the mixed layer interface and b_{zs} , the buoyancy gradient at the surface vanish, showing that the singularity in (4) is no worse than the singularity in $F_{air-sea} = -B_0(dS/db)$. The formulae need information on both large-scale horizontal gradients and vertical cycling of the mixed layer.

Tandon and Zahariev (2001) have used the Marine Light Mixed Layer (MLML) experiment mooring observations (*Plueddemann et al. 1995*) which include both spring and fall mixed layer transitions and used a combination of mixed layer model results and hydrography (*daSilva et al. 1994*) to calculate the b_{xx} terms to get an order of magnitude estimate of F_{ML} . The sensitivity to averaging of synoptic events is also explored. Their calculations indicate that if hourly winds are used, the water mass transformation due to mixed layer entrainment has annual peak contributions of about $O(4)$ Sv for $\sigma_t = 24.0$. This is comparable to the annual transformation attained by diapycnal mixing in the upper ocean water masses by *Zhang and Talley (1998)*. However, with daily averaged winds and without diurnal

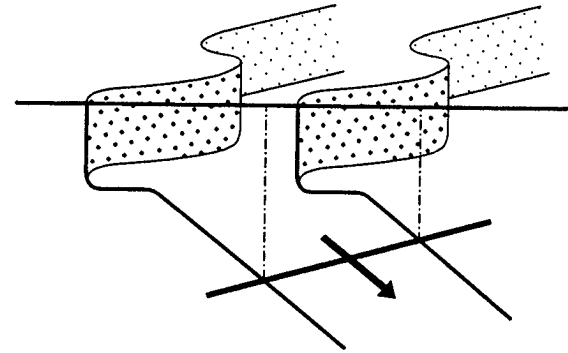


Figure 9. With meanders superposed on a mean isopycnal distribution, F_{ML} estimates are higher, both due to the variation in buoyancy gradient and the increased length of the isopycnal over which water masses get transformed.

variation in buoyancy forcing, this contribution is up to an order of magnitude smaller. Another set of mixed layer simulations includes an annual cycle with a shallow and strong summer thermocline. Inclusion of synoptic summer forcing for this scenario leads to transformation values several times larger than above, about $O(14)$ Sv at $\sigma_t = 24.0$. The peak contribution in this case is almost two orders of magnitude smaller if the synoptic forcing is averaged daily and the diurnal cycle is not resolved. The upper bound for the b_{zz} term at the MLML experiment site is $O(3)$ Sv. These estimates are likely to be underestimates since hydrographic data average over isopycnal meanders, due to both increase in the curvature terms and an increase in the isopycnal length (Figure 9). More details are presented in the appendix of *Tandon and Zahariev (2001)*. Contribution due to mesoscale and sub-mesoscale meanders is also conceptually considered later in more detail in section 4.2 of this paper.

3. Transformation Due to Upwelling Near Fronts

While the b_{zz} term was found to be small in *Tandon and Zahariev (2001)* away from the fronts, this need not be the case near fronts. Mesoscale eddies (wavelength ~ 500 km) strain the surface into $O(100$ km) tongues, which leads to sub-mesoscale features of 20-50 km diameter which induce vertical velocities of $O(40$ m/day) thereafter (e.g. *Pollard and Regier (1992)* for Frontal Air-Sea Interaction Experiment site, *Rudnick (1996)* and *Rudnick and Luyten (1996)* for the Azores front).

Due to the rapid upwelling near the fronts, the upwelling at the base of the mixed layer $\int_{w \text{ } dt > 0} w \text{ } dt$ dominates the deepening $\int_{dh > 0} dh$ in the F_{ML} term. Using typical FASINEX values of $b_{xs} = 1.5 \times 10^{-7} \text{ s}^{-2}$ (for temperature gradient of 1K/20 km), $b_{xz} = 1.5 \times 10^{-12} \text{ m}^{-1}\text{s}^{-2}$ and $\Delta b = 10^{-3} \text{ m s}^{-2}$. With upwelling of $O(40 \text{ m/day})$ along half the length of a convoluted frontal length of 3000 km, the annualized transformation values are $O(0.2 \text{ Sv})$ for the b_{xz} term and $O(5 \text{ Sv})$ for the b_{xs} term. The F_{ML} term is therefore likely to have a greater contribution from b_{xz} term and upwelling near sub-mesoscale features.

To summarize, while F_{ML} estimates are $O(5 \text{ Sv})$, they are particularly sensitive to the resolution of synoptic events and sub-surface density structure near fronts. It is also reasonable to ask whether these effects are already assumed to be present in a horizontal diffusive flux due to mesoscale stirring. Inspired by *Garrett's review* (this volume) as well as *Nakamura (1996)* and *Winters and D'Asaro (1996)*, we next ask, under what circumstance can these two processes result in water mass transformation independent of each other and when must they be considered interdependent.

4. Mesoscale Stirring and Mesoscale-Mixed Layer Interaction

Horizontal stirring due to mesoscale eddies and subsequent mixing would contribute to $D(b)$, and submesoscale upwelling contributes to $F_{ML}(b)$. How should the distinction be made between water mass transformation due to these two processes? How do we ensure that the transformation isn't being diagnosed multiple times under different processes which are in series (and hence not independent)? These questions are clearly related to the how the resolved and unresolved processes are defined.

Recent understanding (*Speer et al. 1997; Garrett and Tandon 1997; Marshall et al. 1999, Nurser et al. 1999*) has concentrated on expanding (2) heuristically in terms of the physical processes, which can be written as

$$A(b) = A_{\text{Ekman}}(b) + A_{\text{eddy}}(b) + A_{\text{mean}}(b) \quad (5)$$

$$= F_{\text{air-sea}} + F_{ML} - \frac{dD_{\text{eddy}}}{db} - \frac{dD_{\text{int}}}{db} \quad (6)$$

with (5) for the dynamics which must balance (6) for the thermodynamics. The dynamical processes are the diapycnal volume flux due to wind forcing (Ekman), mesoscale diapycnal volume flux, and the mean geostrophic flow across isopycnals. The thermodynamic processes are the air-sea transformation $F_{\text{air-sea}}$, the contribution due to mixed layer entrainment F_{ML} , horizontal mixing due to eddies dD_{eddy}/db , and the interior

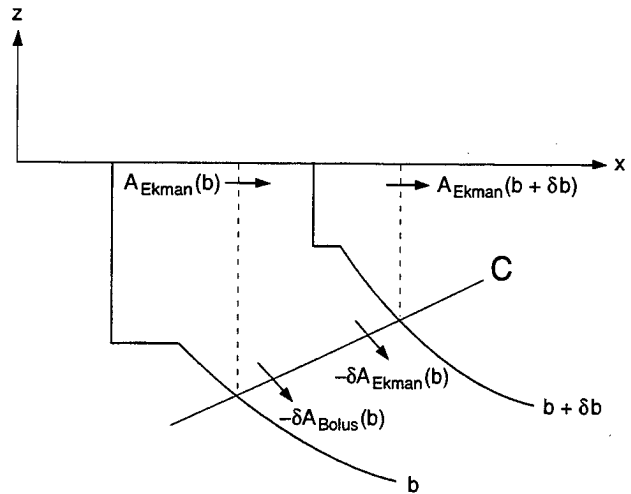


Figure 10. An illustration showing the modified control volume. $A_{\text{Ekman}}(b)$ refers to the wind-driven diapycnal volume flux past the control volume surface b , while $A_{\text{Bolus}}(b)$ or $A_{\text{eddy}}(b)$ refers to the diapycnal volume flux due to the mesoscale eddies past this control surface. The lower control surface C is the base of the winter mixed layer. Dashed vertical lines show the lateral control surfaces for the dynamic method; the instantaneous isopycnal positions shown as solid lines form the lateral control surfaces for the thermodynamic method.

diapycnal mixing dD_{int}/db . This procedure is naturally isopycnic/diapycnic and allows comparison of these diverse physical processes under a single framework.

The terms that are most readily calculated from climatological data in the above framework are A_{Ekman} and $F_{\text{air-sea}}$, e.g. the recent evaluations of A_{Ekman} and $F_{\text{air-sea}}$ for the Southern Ocean by *Speer et al. (1997)*. The evaluation of A_{Ekman} is generally done following isopycnal surfaces around the annual cycle. However, the control volumes for the dynamic and thermodynamic methods can be chosen differently as long as they coincide at the winter mixed layer depth. Thus, a modified control volume for the dynamic calculation can be chosen (*Garrett and Tandon 1997*) such that this consists of the volume between the vertical projections of the isopycnal surfaces below the winter mixed layer to the surface (Figure 10). Therefore, this modified controlled volume does not change much during the annual cycle.

4.1. The triple decomposition into mean, eddy, and turbulent flow

While choosing a fixed control volume as described above simplifies the diagnostic evaluations of the dynamic terms in (5), the issues concerning the decompo-

sition and overlap of the thermodynamic terms in (6) still remain. To clarify the role of horizontal stirring dD_H/db and mixed layer entrainment F_{ML} , following *Davis* (1994) and *Garrett* (this volume), we apply the triple decomposition to the water mass transformation ideas. As these authors stress, such a decomposition necessarily presupposes a gap in time (or space) scales such that a three-way decomposition can be defined. For the water mass transformation diagnostics the buoyancy field is split into the mean, eddy, and turbulent parts. The diapycnal advection u_n is also split into three parts, each representing the mean, eddy, and turbulent advection (subscripts m, e , and t respectively) across the mean buoyancy surface, i.e.,

$$b = b_m + b_e + b_t \quad \text{and} \quad (7)$$

$$u_n(b_m) = u_{nm}(b_m) + u_{ne}(b_m) + u_{nt}(b_m). \quad (8)$$

Here we envisage the mean buoyancy field b_m to be the modified mean buoyancy field (*Killworth* 2001, *McDougall* and *McIntosh* 2001) although for the large scale water mass transformation diagnostics the difference with Eulerian mean buoyancy field is probably small. We denote $(\bar{\ })$ for averaging over a time scale large compared to turbulence but small compared to that of the eddies and $\langle \rangle$ for averaging over a time scale large compared to that of the eddies but short compared to that of the mean. Substituting into the instantaneous buoyancy equation and subsequent averaging over the turbulent time-scales and the eddy time scale yields

$$u_{nm} \cdot \frac{\partial b_m}{\partial n} + \langle u_{ne} \cdot \frac{\partial b_e}{\partial n} \rangle = - \overline{\langle u_{nt} \cdot \frac{\partial b_t}{\partial n} \rangle} \quad (9)$$

if the mean flow is considered steady at long time-scales. The right hand side of eq.(9) is the $-\frac{\partial D}{\partial n}$ term and the terms on the left hand side are mean and eddy advection of mean and eddying isopycnals respectively. This equation is subject to the surface boundary condition

$$\langle w_e b_e \rangle + \langle \overline{w_t b_t} \rangle = B_0 \quad (10)$$

thus suggesting that the surface buoyancy flux is balanced by both the vertical buoyancy flux due to eddies and turbulent flux at the surface. *Garrett* (this volume) discusses the buoyancy variance budget for this decomposition.

4.2. Mesoscale transformation and the entrainment contribution: In series or parallel?

If the diagnostics are done in a framework that does not resolve eddies, then the transformation relationship can be written in terms of buoyancy balance about b_m :

$$A(b_m) = A_{\text{mean}}(b_m) + A_{\text{eddy}}(b_m) + A_{\text{Ekman}}(b_m) \quad (11)$$

$$= F(b_m) - \frac{dD_H}{db}(b_m) - F_{ML}(b_m) - \frac{dD_V}{db}(b_m) \quad (12)$$

where the contribution $\frac{dD_H}{db}(b_m)$ is due to the convergence of the eddy stirring horizontal diffusive flux and $F_{ML}(b_m)$ is the contribution to water mass transformation due to mixed layer deepening and entrainment, both evaluated about the mean isopycnal positions.

Following the triple decomposition suggested above, if the eddies are resolved in this framework, the water mass transformation balance becomes

$$A(b_m) = A_{\text{mean}}(b_m) + A_{\text{eddy}}(b_m) + A_{\text{Ekman}}(b_m) \quad (13)$$

$$= F(b_m + b_e) - F_{ML}(b_m + b_e) - \frac{dD_V}{db}(b_m + b_e) \quad (14)$$

and the eddy-stirring component $\frac{dD_H}{db}$ does not arise. The contributions in eq. (11) and eq. (13) are the same due to the choice of control volume in Figure 10. However, the contributions in eq. (12) and eq. (14) are different. In this case, the diapycnal advection due to horizontal mixing by the eddies and the contribution due to mixed layer entrainment are in *parallel* if the budgets are considered about the mean buoyancy surfaces (b_m) that do not resolve the eddies as in eq. (12). However, these two processes are in *series* if budgets are considered for eddying buoyancy surfaces ($b_m + b_e$) as in eq. (14), where eddying isopycnals are defined by modified mean density that averages over a time scale long compared to the turbulence but short compared to the eddies. Thus the F_{ML} estimates computed by *Tandon* and *Zahariev* (2001) (section 2) which are based on mean monthly isopycnals that average over the eddies correspond to the estimates for $F_{ML}(b_m)$, while the estimates earlier near frontal zones (section 3) correspond to the latter case $F_{ML}(b_m + b_e)$.

5. Discussion

The uncertainty in F_{ML} remains unacceptably high in both model based estimates of coarse non-eddy resolving simulations (e.g. *Nurser et al.* 1999) and data based evaluations which are based on localized mixed layer simulations (*Tandon* and *Zahariev* 2001). More accurate basin wide estimates are necessary to make progress. While considering budgets in an eddy resolving framework, the water mass transformation due to eddies happens in *series* with diapycnal mixing and entrainment. In this case, another significant concern is identifying the rate controlling process for diapycnal transformation in the upper ocean—do the mesoscale eddies define the rate at which net diapycnal advection will happen or does it primarily depend on the rate at

which diapycnal mixing occurs? The mesoscale stirring would be dominant for water mass transformation if the mixing processes are so efficient in the upper ocean that they act to dissipate the eddies quickly and transform water masses on a fast time scale. In this case, it is the baroclinic instability and larger scales that would set the net diapycnal advection rates. On the other hand it is possible that the mixed layer processes allow non-linear interactions amongst eddies, and the net diapycnal advection is then significantly dependent on mixing processes in the upper ocean. While recent eddy resolving simulations have concentrated on adiabatic properties of mesoscale paramaterizations (e.g., articles by Marshall, Killworth, and McDougall from this volume) diabatic interactions in the upper ocean remain unexplored, and the question above remains unanswered. Determining which process is dominant for water mass transformation rate should be feasible with multiple eddy-resolving simulations whose sensitivity to mixing in the upper ocean and air-sea interaction is explored systematically.

Acknowledgments. AT is grateful to the National Science Foundation (OCE-9996260 and OCE-9910446) for supporting this work, Office of Naval Research for supporting the Aha Huliko'a series and to Peter Müller for inviting him to this workshop. AT is also thankful to Chris Garrett and Trevor McDougall for their comments.

References

- daSilva, A. M., C. C. Young, and S. Levitus, Atlas of surface marine data 1994, vol. 1: Algorithms and procedures, U.S. Department of Commerce, NOAA, NESDIS, 1994.
- Davis, R. E., Diapycnal Mixing in the Ocean: The Osborn-Cox model, *J. Phys. Oceanogr.*, **24**, 2560–2576, 1994.
- Garrett, C., and A. Tandon, The effects on water mass formation of surface mixed layer time-dependence and entrainment fluxes, *Deep-Sea Res.*, **44/12**, 1991–2006, 1997.
- Garrett, C., K. Speer, and E. Tragou, The relationship between water mass formation and circulation, with application to Phillips' Red Sea model, *J. Phys. Oceanogr.*, **25**, 1696–1705, 1995.
- Marshall, J., D. Jamous, and J. Nilsson, Reconciling thermodynamic and dynamic methods of computation of water-mass transformation rates, *Deep-Sea Res.*, **46**, 545–572, 1999.
- Niiler, P. P., and J. Stevenson, On the heat budget of tropical warm pools, *J. Mar. Res.*, **40**(Suppl.), 465–480, 1982.
- Nurser, A. J. G., R. Marsh, and R. G. Williams, Diagnosing water mass formation from air-sea fluxes and surface mixing, *J. Phys. Oceanogr.*, **29**, 1468–1487, 1999.
- Plueddemann, A. J., R. A. Weller, M. Stramska, T. D. Dickey, and J. Marra, Vertical structure of the upper ocean during the Marine Light-Mixed Layers experiment, *J. Geophys. Res.*, **100**, 6605–6620, 1995.
- Pollard, R. T., and L. A. Regier, Vorticity and vertical circulation at an ocean front, *J. Phys. Oceanogr.*, **22**, 609–625, 1992.
- Rudnick, D. L., Intensive surveys of the Azores Front., 2, Inferring the geostrophic and vertical velocity fields, *J. Geophys. Res.*, **101**, 16,291–16,303, 1996.
- Rudnick, D. L., and J. R. Luyten, Intensive surveys of the Azores Front, 1, Tracers and dynamics, *J. Geophys. Res.*, **101**, 923–939, 1996.
- Speer, K., and E. Tziperman, Rates of water mass formation in the North Atlantic Ocean, *J. Phys. Oceanogr.*, **22**, 94–104, 1991.
- Speer, K., S. Rintoul, and B. Sloyan, Sub-antarctic Mode Water Formation by Air-Sea Fluxes, *International WOCE Newsletter*, December, 29–31, 1997.
- Speer, K. G., A note on average cross-isopycnal mixing in the North Atlantic ocean, *Deep Sea Res.*, **44/12**, 1981–1990, 1997/.
- Tandon, A., and K. Zahariev, Quantifying the role of mixed layer entrainment for water mass transformation in the north atlantic, *J. Phys. Oceanogr.*, **31**, 1120–1131, 2001.
- Tziperman, E., On the role of interior mixing and air-sea fluxes in determining the stratification and circulation of the oceans, *J. Phys. Oceanogr.*, **16**, 680–693, 1986.
- Walsh, G., On the relation between sea-surface heat flow and thermal circulation in the ocean, *Tellus*, **34**, 187–195 1982.
- Weller, R. A., Overview of the Frontal Air-Sea Interaction Experiment (FASINEX): A study of air-sea interaction in a region of strong oceanic gradients, *J. Geophys. Res.*, **96**, 8501–8516, 1991.
- Zhang, H.-M., and L. Talley, Heat and buoyancy budgets and mixing rates in the upper thermocline of the Indian and global oceans, *J. Phys. Oceanogr.*, **28**, 1961–1978, 1998.
-
- A. Tandon, Department of Physics, College of Engineering, University of Massachusetts, North Dartmouth MA 02747. (e-mail: atandon@umassd.edu)

Biogeochemical variability in the upper ocean

A. Mahadevan

Atmospheric and Environmental Research, Lexington, MA - USA

Abstract. Differences in the response times of different biogeochemical tracers to upper ocean forcing processes can lead to substantial differences in their patterns of variability. An idealized tracer with a steep vertical concentration gradient is modeled in a flow field representative of an upper ocean front. The surface distribution of the tracer is studied as a function of its response or restoration time scale.

Introduction

Many quantities, such as temperature, salinity, dissolved inorganic carbon (DIC), nitrate, phosphate, radiocarbon and dissolved oxygen, have strong vertical concentration gradients in the upper 500 or so meters of the ocean. These substances are often forced in the upper ocean, and vertical mixing and transport processes that convey the resulting concentration changes to the ocean interior are extremely small. Horizontal advection, on the other hand, is relatively efficient at mixing and homogenizing substances, and hence concentration gradients are relatively weak in the horizontal. Anomalous concentrations of many biogeochemical quantities in the upper ocean, are therefore, largely a result of upwelling that brings to the surface, water with a substantially different concentration than its surroundings. The substances may also be altered by processes like biological production, remineralization, and air-sea exchange. Such processes could induce horizontal variability, but the variability induced by upwelling is typically smaller scaled, more intermittent, and responsible for most of the variance in the sea-surface distributions of the biogeochemical quantities.

In an earlier modeling study (*Mahadevan and Archer, 2000*), it was observed that the nutrient upwelling rate in the pelagic ocean is very sensitive to model resolution. Increasing the model resolution from 0.4 degrees to 0.1 degrees in a domain situated in the interior of subtropical gyre, resulted in a two- to three-fold increase in not only the mean rate of nutrient supply, but also in the variance of the field. The mean and variance of other model variables like temperature and pCO₂ at the sea surface are not as sensitive to model resolution as new production. The density field in the coarse and fine resolution model runs looks very similar in its mean and variance, but the fine resolution simulation shows more folds in the isopycnal surfaces and greater convolutedness in the frontal outcrop formed by the intersec-

tion of such density surfaces with the euphotic layer. The transport of nutrients from the thermocline into the mixed layer is primarily an isopycnal process. Resolving the length of the front at which the flow field is also highly strained, is thus extremely important for capturing the vertical transport which occurs on scales of the order of 10 km or less.

Even though all the biogeochemical tracers in such a model are affected by vertical motion, the surface distribution of some, for example oxygen and H₂O₂, appears more fine scaled, i.e., there is more variance at a given length scale than in others like DIC and temperature. While there are many reasons for differences in the distributions of different tracers, I believe that this is largely a result of the difference in the response times of the tracers to various forcing processes. Substances that respond quickly to upper ocean forcing appear in small and intermittent anomalous patches representative of the upwelling scale. When substances are slow to adjust, the anomalous patches introduced by upwelling are stirred and spread by horizontal advection. Hence the distribution of such substances is not as fine-scaled. Carbon dioxide, for example, is very slow to equilibrate with the atmosphere on account of the buffering effect. While the oxygen in a 100m deep mixed layer may typically take one month to equilibrate with the atmosphere, the DIC would take about a year. The surface distribution of oxygen is, as a result, much more patchy or intermittent than DIC.

Modeling Study

The change in distribution of a tracer *c* in the ocean can be modeled using the equation

$$\frac{\partial c}{\partial t} + \mathbf{u} \cdot \nabla c = S, \quad (1)$$

where \mathbf{u} is the velocity of the fluid and *S* is a source or sink term. *S* may parameterize processes like air-sea exchange and biological production that alter the

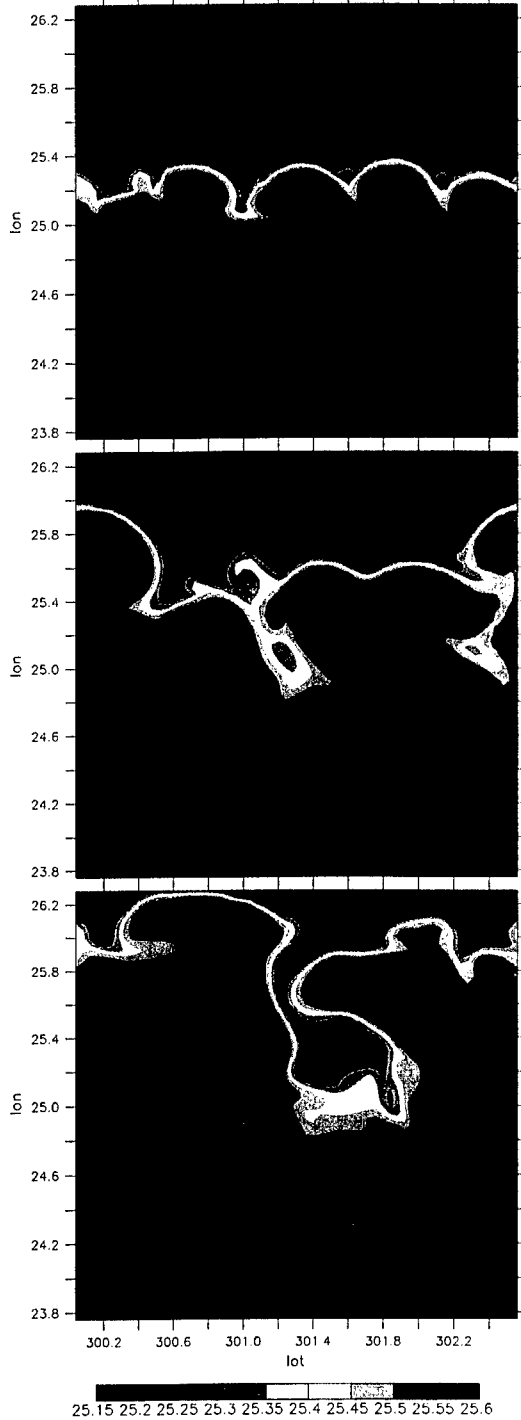


Figure 1. Snapshots of the surface density field in the model shown on days 46, 69 and 93 of the simulation help visualize the evolving flow field. The flow is from west to east along the the density contours.

quantity c . Often S can be expressed in terms of a characteristic response time or adjustment time. In the case of salinity and temperature, S could represent the effect of the heat or evaporation-precipitation flux, and may be expressed as $\lambda^{-1}(c - c_0)$, where c is the temperature or salinity, c_0 is the value to which it is restored at the surface, and λ is the restoration time scale. In the case of nutrients, S may be written as $\lambda^{-1}c_0$, where c_0 may be a combination of the nutrient and light, and λ a biological uptake time. In the case of gases that are subject to air-sea exchange at the ocean surface, S would represent the gas flux, for which the characteristic time scale λ is the ratio of the mixed layer depth to piston velocity. Thus the quantification of the source or sink term S in terms of an adjustment time λ is general to many tracers and processes.

In what follows, we use a three-dimensional numerical model of an idealized ocean front to analyze the surface distribution of a tracer as a function of its response time λ . The tracer c is qualitatively similar to other tracers in the ocean; it has a steep concentration gradient in the upper 500 m. It is modeled using equation (1) which is coupled to the dynamical model described in *Mahadevan et al. (1996)*. The source term on the right right hand side of (1) is modeled as

$$S = \begin{cases} 0, & \text{if } z < z_m \\ \lambda^{-1}[c - (1 - \exp(-\frac{z-z_m}{z_0}))], & \text{if } z \geq z_m. \end{cases} \quad (2)$$

Here z is the depth below the surface, z_m can be thought of as a mixed layer or euphotic layer depth, and z_0 is a reference depth. In the absence of advection, the tracer has the steady state profile $c = 1 - \exp(-(z - z_m)/z_0)$ at depths greater than z_m , and a value of 0 at depths less than z_m . The tracer can thus be thought of as depleted in the euphotic layer (z, z_m), and beneath it, increasing exponentially with depth so as to approach 1 over an e-folding distance $z_0 - z_m$. The euphotic depth z_m and e-folding distance $z_0 - z_m$ are each taken to be 100 m in these experiments. Advection disturbs this steady-state distribution to which it is constantly restored with a characteristic adjustment time λ . When λ is small, values of the tracer anomalous from the steady-state exponential distribution are rapidly annihilated. When λ is large, the anomalous values that are introduced primarily by vertical motion, persist for longer, are reinforced by further upwelling, and are spread horizontally by horizontal advection. Diffusion is negligible at the scales considered and is not explicitly included in the model.

The model is set up in a periodic channel with solid north-south boundaries. The domain is approximately 256×284 km in dimension and centered at 25°N . It is initialized with lighter fluid in the upper 100 m of the southern half and denser fluid in the upper northern

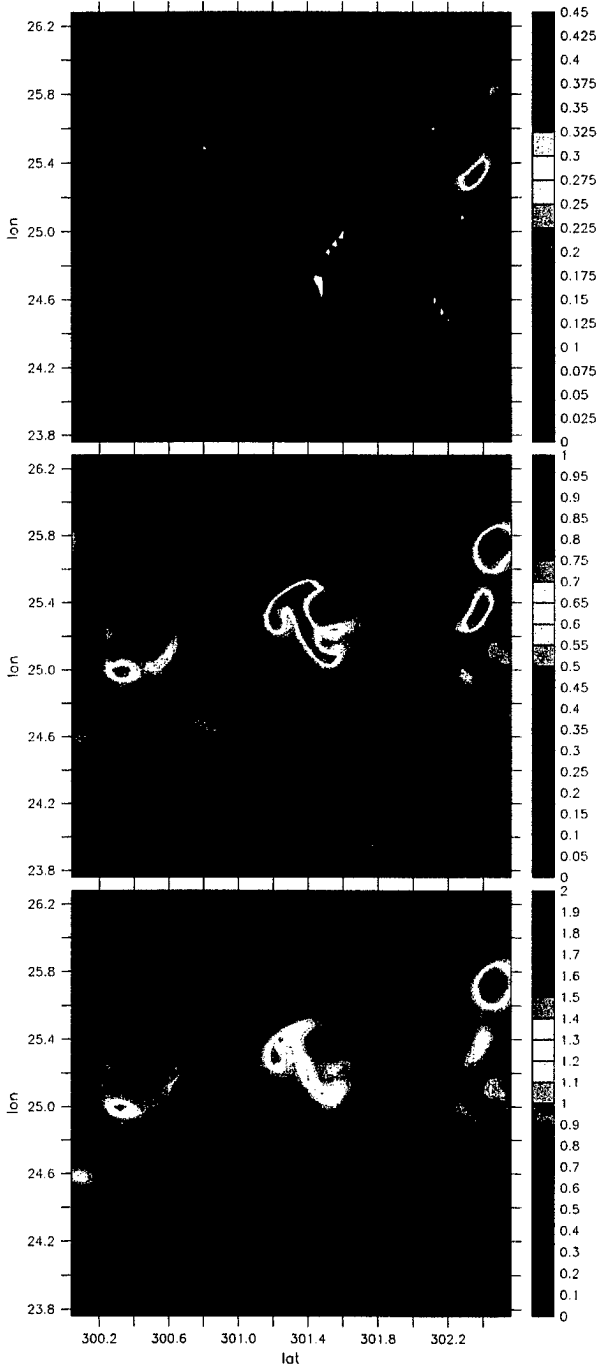


Figure 2. The tracer concentration in the upper 100m viewed on day 69 of the simulation (middle panel of Fig. 1) for three different values of the adjustment time λ : 2.5, 20 and 80 days. The tracer distribution is more patchy and the tracer concentration less for smaller values of λ . The concentration is displayed as a percentage of the maximum concentration, i.e. it is multiplied by 100.

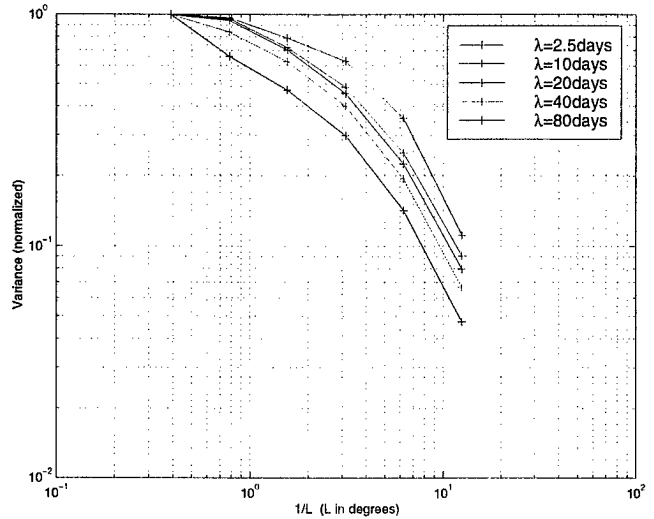


Figure 3. The variance $V(L)$ of the surface distribution of tracer shown in Fig. 2 plotted against wavelength (inverse of the length scale L) on log-log axes for different values of λ . $V(L)$ is the average variance contained in regions of area $L \times L$. Smaller values of λ result in more variance within a given length scale and a shallower curve in the log-log space. The relationship between $V(L)$ and λ seen in this distribution is qualitatively the same at other times in the simulation.

half. Beneath this surface layer, the density in both halves converges to a mean stratification that is representative of the thermocline. The model resolution is 0.04° (approximately 4 km) in the horizontal and varies in the vertical from 10 m near the surface to 125 m at depth. The tracer is initialized to its steady state distribution and allowed to evolve with the flow field. We use five different values of λ : 2.5, 10, 20, 40 and 80 days, and observe differences in the surface distributions of the tracer as a function of λ .

Results

The initial density front gives rise to a geostrophic jet in the along-front direction. The jet and the front meander as the flow evolves giving rise to a more complicated eddy field that gradually decays (Fig. 1). The surface distribution of the tracer that evolves with this flow field varies with λ . It is more patchy and has more variance at a given length scale for smaller values of λ (see Fig. 2). The tracer distributions are analyzed by calculating the variance as a function of length scale [J.W. Campbell, personal communication]. The variance is computed over the whole domain, and then over subregions of size L , by partitioning and re-partitioning the original domain. $V(L)$ is the average variance over all the subdomains of size L that occupy the whole do-

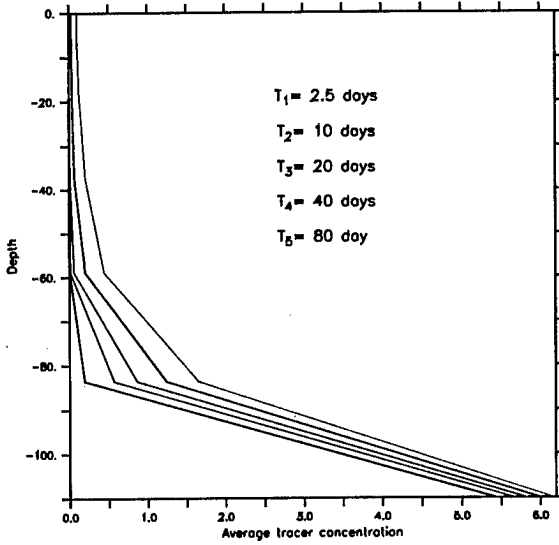


Figure 4. Vertical profiles of the tracer at a late stage (day 93) of the simulation averaged over the domain for different values of λ . The upper ocean tracer concentration increases (at a less than linear rate) with increasing λ .

main. $V(L)$ is normalized by the total variance and plotted as a function of the length scale L on a log-log plot (see Fig. 3). We obtain shallow curves that have small slope when λ is small and steeper curves for large λ . The approximate slope of these curves, denoted by p , is a measure of the intermittency or patchiness of the tracer distribution. Small values of p correspond to a more intermittent or patchy distribution with a large amount of variance at a given length scale. This kind of distribution results from rapid adjustment or small λ . The converse is true for large values of p and λ . The interesting thing is that the increase in p scales roughly as the logarithm of λ .

The same is true for the average anomalous concentration of tracer. Fig. 4 shows the mean vertical distribution of the tracers with different λ towards the end of the simulation. The total amount of tracer in the upper layer ($z < z_m$) increases with λ , but the increase scales roughly as the logarithm of λ for reasons that are not well understood.

balance

Conclusions

Thus it is shown that the distributions of biogeochemical quantities in the upper ocean are sensitive to

their time scale of response to various forcing processes. This ought to be taken into account when trying to design algorithms that quantify the surface distribution of one biogeochemical quantity in terms of another. The patchiness or intermittency of the distribution, quantified here in terms of the approximate slope p of the variance curve in log-log space, increases more or less logarithmically with the adjustment time λ .

Acknowledgments. I am very grateful for the opportunity to be able to participate in this Aha Hulikuo Workshop. My thanks to the conveners of the workshop and to ONR for funding this research.

References

- Mahadevan, A., and D. Archer, Modeling the impact of fronts and mesoscale circulation on the nutrient supply and biogeochemistry of the upper ocean, *J. Geophys. Res.*, **105**, 1209–1225, 2000.
- Mahadevan, A., J. Olinger, and R. Street, A non-hydrostatic mesoscale ocean model 2: Numerical implementation, *J. Phys. Oceanogr.*, **26**, 1181–1900, 1996.
- A. Mahadevan, Atmospheric and Environmental Research, 131 Hartwell Avenue, Lexington, MA 02421 (e-mail: amala@aer.com)

This preprint was prepared with AGU's L^AT_EX macros v4, with the extension package 'AGU++' by P. W. Daly, version 1.6a from 1999/05/21, with modifications by D. E. Kelley, version 1.0 from 2001/03/26, for the 'Aha Huliko'a Hawaiian Winter Workshop.

Stirring and mixing of biologically reactive tracers

K. J. Richards, S. J. Brentnall, P. McLeod, and A. P. Martin

Southampton Oceanography Centre, Southampton, UK

Abstract. We examine the effect of stirring and mixing on the marine planktonic ecosystem. We present a number of models investigating the impact of patchiness in the population, diffusion, and fluid stirring on the spatial structure of the population and the overall production rates of the system. It is found that the heterogeneity of the system significantly affects the way the system behaves. The response of the ecosystem to the action of the fluid flow is a function of not only the topology of the flow but also the dynamics of the ecological model itself.

1. Introduction

The marine ecosystem plays an important role in the cycling of carbon. In particular it acts as a ‘carbon pump,’ utilising atmospheric CO₂ through photosynthesis, a proportion of the carbon being exported to the deep ocean, and thus moderating levels of CO₂ in the atmosphere. Ecological models are now incorporated into models of climate change to predict global warming scenarios (see, e.g., it Cox et al., 2000). A physical/ecological model used in climate studies needs to incorporate both the appropriate ecological dynamics and the right physics impacting on the biological production.

Primary production in the ocean is dominated by phytoplankton. A feature of the distribution of phytoplankton distributions is that it is very heterogeneous or ‘patchy’ (Bainbridge, 1957). Structure is observed on scales ranging from metres to the basin scale (Mann and Lazier, 1996) with this structure often observed to be associated with physical features such as eddies and fronts (e.g., (The Ring Group, 1981; Falkowski et al., 1991; Strass, 1992). A number of important questions arise:

- Does the patchiness affect the dynamics of the ecological system?
- Does the heterogeneity of the system impact on the overall production rates and/or community structure?
- Does the structure affect the way the biological system responds to changes to the environment?

Here we will use a number of relatively simple models of both the ecological dynamics and the fluid flow in order to try and understand some of the more fun-

damental issues related to the problem of marine biological patchiness. The models should be thought of as caricatures of the more complex system, but we hope they will provide the building blocks for understanding of that system. The work is very much ‘in progress’ and so this not a presentation of a ‘complete theory’ but rather some initial attempts and their results.

2. Biological reactions and fluid flow

Fluid flow can impact on the marine ecological system in two distinct ways: (a) through the vertical movement of nutrients and biological species in or out of the euphotic zone, and (b) the stirring and mixing of components of the system. A good example of when both are important is baroclinic instability (*Spall and Richards, 2000*). Associated with the instability process is a permanent vertical displacement carrying nutrient rich waters into the sunlit surface layers. These nutrients are then stirred and mixed with the surrounding water and are utilised by the biota. Here we will concentrate on this second process, the stirring and mixing by lateral fluid flow.

2.1. General advection-diffusion-reaction equation

We shall model the ecological system using the advection-diffusion-reaction equation

$$\frac{\partial \mathbf{E}}{\partial t} + (\mathbf{u} \cdot \nabla) \mathbf{E} = \mathbf{f}(\mathbf{E}) + \nabla \cdot (D \nabla \mathbf{E})$$

where, for example, the state vector may take the form

$$\mathbf{E} = \begin{bmatrix} N \\ P \\ Z \end{bmatrix}$$

with the elements representing the concentration of nutrients (N), phytoplankton (P) and zooplankton (Z) expressed in terms of a currency, such as nitrogen.

The elements are advected by the flow \mathbf{u} and diffused. The reaction between elements is represented by $\mathbf{f}(\mathbf{E})$. (How well the field equation approach models the marine ecological system is a matter of debate. There is some evidence that it fails if behavioural aspects of the zooplankton are important (Flierl et al., 1999).

A measure of the relative 'strength' of the reaction terms to either diffusion or advection can be gauged by considering the ratio of timescales, i.e.

$$\beta_\kappa = \frac{\mu L^2}{\kappa}$$

and

$$\beta_u = \frac{\mu L}{U}$$

respectively, where U and L are typical velocity and length scales, κ a diffusion coefficient, and μ the reaction rate. The nondimensional parameters β_κ and β_u are equivalent to diffusive and advective inverse Damköhler numbers. Large values imply that the reaction dominates.

We present three models using (2.1). The first looks at the case of no flow and the structure that evolves simply through the combination of reaction and diffusion. The second considers simple biology in a simple flow, a pure strain, and examines the structure of filaments of biological material. The third takes a 2D geostrophic turbulent flow and investigates the impact the stirring has on biological production. The underlying message is that the response of the ecology to the action of the fluid flow is a function of not only the topology of the flow but also the dynamics of the ecological model itself.

2.2. Model 1: Intrinsic structure

Consider the case of no flow ($\mathbf{u} \equiv 0$). We shall consider a two compartment model:

$$\mathbf{E} = \begin{bmatrix} P \\ Z \end{bmatrix}$$

where $P \in [0, 1]$, and the reaction terms are

$$\mathbf{f} = \begin{bmatrix} \mu P(1 - P) - \frac{ZP^2}{\nu^2 + P^2} \\ \gamma \left(\frac{ZP^2}{\nu^2 + P^2} \right) - wh(Z) \end{bmatrix}$$

The reaction terms for the phytoplankton, P , include limited growth (known as logistic growth) and grazing by zooplankton (the functional form used here is known

as Holling type III). The zooplankton, Z , grow at a reduced rate $\gamma \ll 1$. The mortality term $h(Z)$ is taken to be either a linear or quadratic function of Z , corresponding to the zooplankton dying of old age or being consumed by a higher predator, respectively.

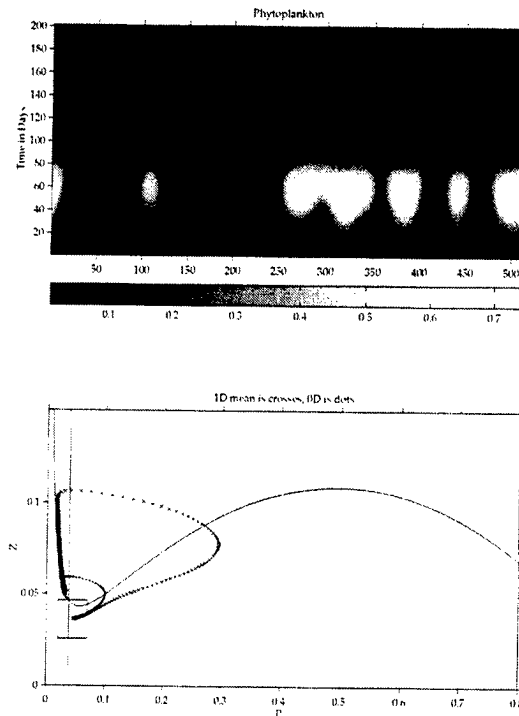


Figure 1. Model 1 with linear mortality. Upper panel, plot of phytoplankton concentration as a function of distance (given in tens of metres) and time. Lower panel, trajectories of the mean values of P and Z for the randomly perturbed (crosses) and unperturbed (dots) cases. Also shown are the null-clines of the reaction equations (i.e., $\partial P / \partial t = 0$ and $\partial Z / \partial t = 0$). The null-clines intersect giving a single stable equilibrium point

The model for the reaction terms is that of Truscott and Brindley (1994). It is chosen because of its simplicity and because the mathematical structure of the ecological dynamics is known. In particular the system becomes excitable (i.e., small but finite perturbations from an equilibrium point can lead to large excursions in model phase space) if both γ and ν are small enough.

The diffusion tensor is taken to be

$$D = \begin{bmatrix} \kappa & 0 \\ 0 & r\kappa \end{bmatrix}$$

so that zooplankton may diffuse at a different rate to phytoplankton (allowing cross diffusion, i.e., zooplankton diffusing up the phytoplankton gradient, has also been investigated).

Here we present two examples to illustrate the different behaviour of the system for linear (Figure 1) and quadratic (Figure 2) mortality (further details of the behaviour of the system are given in *Brentnall et al.* (2001)). We take a one-dimensional case, i.e., variables only vary in one horizontal direction. The system is initialised on a grid with random values of P and Z about some mean value. The size of the rectangular box in the lower panel of each figure gives an indication of the spread of values. In both the linear and quadratic mortality cases a structure appears. The difference is that this structure persists for a longer time for the quadratic mortality case. The length scale of the structure scales with $\sqrt{\mu/\kappa}$ (i.e., the diffusive inverse Damköhler number, β_κ is the relevant parameter). With a growth rate of 1 day⁻¹ and diffusion coefficient of 10⁻² m²s⁻¹ the emergent scale is of order $\simeq 500$ m.

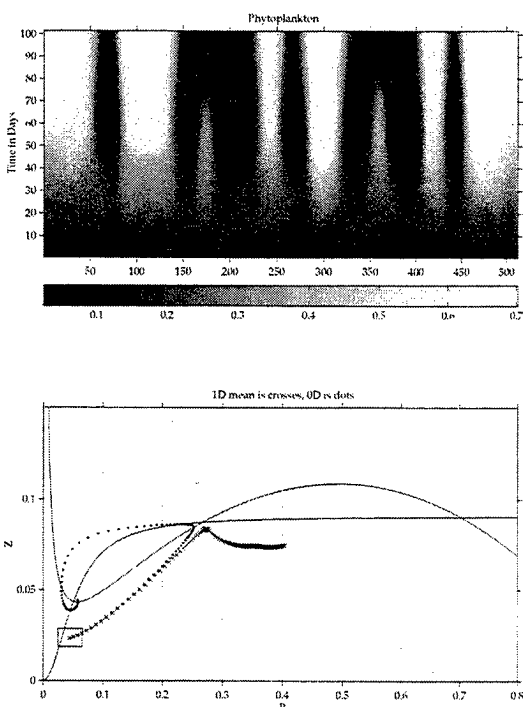


Figure 2. Model 1 with quadratic mortality. As for Figure 1, but in this case the null-clines intersect at three points, with two stable equilibria at $P = 0.05$ and 0.7 and an unstable equilibrium point at $P = 0.27$.

The trajectory in P/Z phase space changes significantly when horizontal structure is introduced. The trajectories for the mean P and Z with and without the small random perturbation are shown in the lower panel of Figures 1 and 2. With linear mortality, although the two trajectories converge to the same stable equilibrium, the excursion in P is much greater when

the perturbation is introduced. With quadratic mortality, the two trajectories converge to two different stable equilibria, with the perturbed case converging very slowly. Clearly the heterogeneity of the biology (with diffusion acting) is playing a significant role in the time evolution of the system. It is also clear that we need to consider what happens when there is a flow, which we do in the next section

2.3. Model 2: filaments

We now consider a pure strain flow

$$\mathbf{u} = (-\lambda x, \lambda y)$$

Such a flow will tend to pull a tracer into a thin filament.

For an inert tracer the filament width attains a value

$$W_i = \sqrt{\frac{\kappa}{\lambda}}$$

when the straining of the flow is balanced by diffusion. (34 (@)) has shown that filaments of an exponentially growing tracer have the same width as an inert tracer)

The biology we will use is a simplified version of that used above, namely

$$\mathbf{E} = [P]$$

with

$$\mathbf{f} = [\mu P(1 - P)]$$

A feature of this system is that the combination of logistic growth and diffusion allows the existence of reactive travelling waves (or Fisher waves) which have a minimum speed $2\sqrt{\kappa\mu}$ (c.f., *Murray*, 1993). These waves are important in transmitting ‘information’ and means that the biological population can advance faster than through pure diffusion. The waves are important in setting the width of filaments.

We may expect the travelling wave to be brought to rest when its speed matches that of the converging flow, such that the width of the filament

$$W_r \sim \frac{\sqrt{\kappa\mu}}{\lambda}$$

Indeed this is found to be the case for sufficiently large values of $\beta_u = \mu/\lambda$, an inverse advective Damköhler number (see the lower panel of Figure 3). The shape of the distribution of concentration changes with increasing β_u (upper panel Figure 3) from a Gaussian to a square wave as shown by the kurtosis of the distribution (lower panel Figure 3) (*McLeod et al.*, 2001).

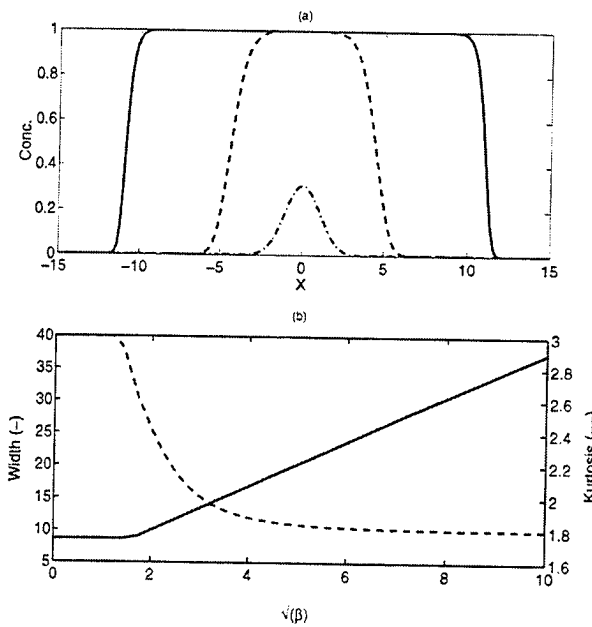


Figure 3. Model 2, filament structure. Upper panel: the distribution of phytoplankton across the filament for three values of β_u : dash-dot $\beta_u=2$, dash $\beta_u=10$ and solid $\beta_u=50$. The horizontal distance has been scaled with $\sqrt{\kappa\mu}/\lambda$. Lower panel: the filament width (scaled with $\sqrt{\kappa/\lambda}$) and kurtosis as a function of β_u .

It is interesting to note that

$$\frac{W_r}{W_i} = \sqrt{\beta}$$

i.e., the filament width for a reactive tracer will be greater than that of an inert tracer for $\beta_u > 1$. Using an observed filament width, and strain rate, to estimate κ will lead to an overestimate by a factor β if the reaction is not taken into account.

2.4. Model 3: fluid stirring

Lastly we consider the case of the ecosystem being stirred by a turbulent flow field. We use the 2D geostrophic turbulence model of Babiano *et al.* (1987) in a 512 km^2 periodic domain. The flow is forced to give a statistically steady state. An example of the potential vorticity is given in Figure 4. A characteristic of 2D turbulence is that the flow is inhabited by strong coherent vortical structures surrounded by a straining flow in the intervening regions. The coherent structures act as transport barriers inhibiting the mixing of tracers between the eddies and surrounding fluid (Provenzale, 1999).

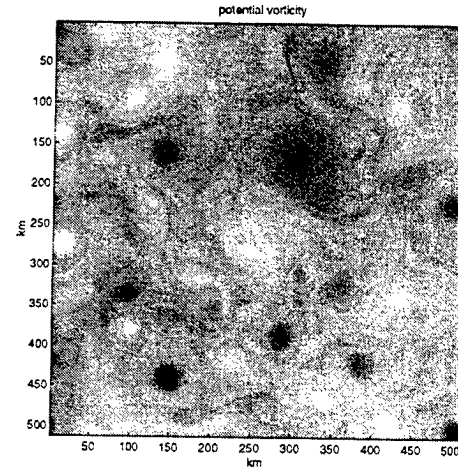


Figure 4. Model 3, fluid stirring. The potential vorticity field.

The biological model is slightly more complicated than before.

$$\mathbf{E} = \begin{bmatrix} N \\ P \\ Z \\ D \end{bmatrix}$$

with

$$\mathbf{f} = \begin{bmatrix} -\mu \left(\frac{N}{k_N + N} \right) P + \mu_D D + \gamma_2 Z \\ \mu \left(\frac{N}{k_N + N} \right) P - \left(\frac{g\epsilon P^2}{g + \epsilon P^2} \right) Z - \mu_P P \\ \gamma_1 \left(\frac{g\epsilon P^2}{g + \epsilon P^2} \right) Z - \gamma_2 Z - \mu_Z Z^2 \\ (1 - \gamma_1) \left(\frac{g\epsilon P^2}{g + \epsilon P^2} \right) Z + \mu_P P + \mu_Z Z^2 - \mu_D D \end{bmatrix}$$

where D represents detritus and there is an additional sinking term $-w_s D/h$ in the equation for detritus. The biological model is that of Oschlies and Garçon (1999) and has been chosen because it has been shown to capable of reproducing the seasonal cycle in both oligotrophic (nutrient depleted) and nonoligotrophic regions with the same set of parameter values. Details of the biological and flow model, including the parameter values, are given in Martin *et al.* (2001).

The biological system is forced by a source of nutrient

$$\Gamma_s = s(N_o - N)$$

where s is a function of position or some property of the flow, and can be thought of as modelling the input of nutrients to the euphotic zone through upwelling. Martin *et al.* (2001) investigate how the productivity depends upon the distribution of the upwelling by comparing

spatially stationary sources with sources correlated or decorrelated with flow features. They conclude that the increased productivity brought about by upwelling is a function of the rate of upwelling, the distribution of the sources, and the mixing efficiency of the flow.

We consider two cases, the first with the source confined to a single patch (Figure 5) and the second with the source distributed over 64 smaller patches but such that the total area is the same as in the first case (Figure 6). The figures show the distribution of primary production at a time when the biology is in a statistical equilibrium.

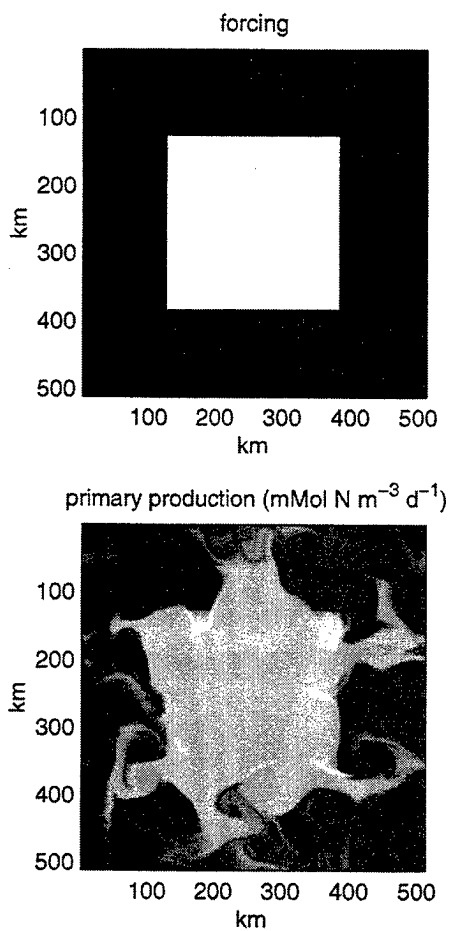


Figure 5. Model 3, fluid stirring. The forcing of nutrient and primary production resulting from stirring by a 2D turbulent field. The production ranges from 0.1 (black) to 0.45 (white) $\text{mMol N m}^{-3} \text{ d}^{-1}$.

Referring to the single source case (Figure 5), the nutrient forcing has produced elevated rates of production above the background level of $0.1 \text{ mMol N m}^{-3} \text{ d}^{-1}$. Compared to the case with the same forcing but no fluid stirring ($\mathbf{u} \equiv 0$) the areal average of produc-

tion has increased by 36%. The fluid motion has the effect of increasing the surface area between the nutrient enriched and surrounding waters. A striking feature of the distribution of production is that it is limited to the vicinity of the forcing (an inert tracer will be spread quickly across the entire domain). The reaction limits the extent of the region of high nutrients and hence the area of contact with the surrounding waters. Reducing the reaction rate (reducing β_u) will allow greater stirring to take place before the nutrients are consumed and hence increase the area of contact, counteracting the decrease in overall production because of the decreased production rate. Experiments varying β_u show that the two effects may balance each other.

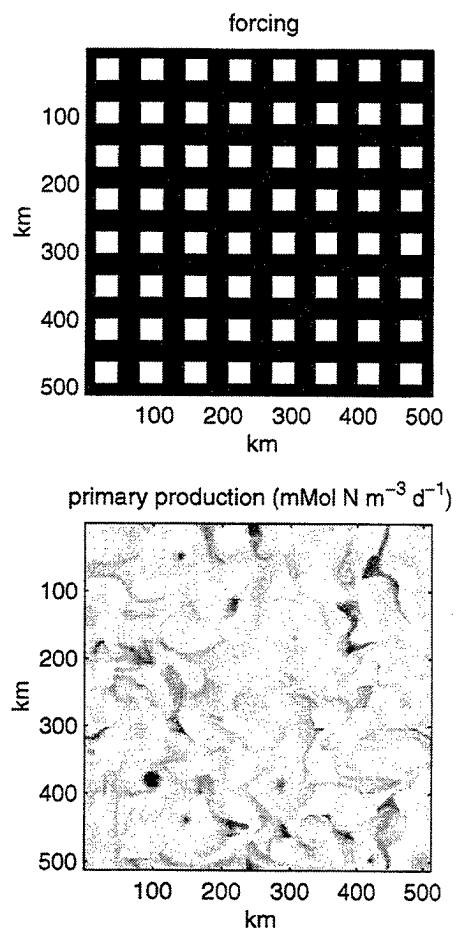


Figure 6. As for Figure 5 but for a distributed source.

As expected, distributing the source increases the mixing and hence production rate (Figure 6). In this case the overall production rate has been increased by 137% above the case with no mixing.

3. Concluding remarks

We have reported on a number of investigations into the impact of heterogeneity of the marine ecological system on the behaviour of that system as a whole. The results demonstrate that the heterogeneity cannot be ignored. Applying the results from studies such as those presented here is difficult. We freely admit that the results of our studies to date are somewhat of an anecdotal character. There are caveats on the methodology such as the exclusion of the diurnal and in particular the seasonal cycle, both of which impose a strong pacing of the system, and which need to be included in future studies.

It is disconcerting that the results are very dependent on the form of the ecological model (as an additional example, the enhancement of productivity found in model 3 was significantly reduced when a simpler [N,P] was used). Perhaps not a surprising remark but one which is often ignored. This issue needs to be explored further, but it does make the task of developing 'robust' ecological models that much more difficult.

What is clear is that viewing marine ecology as a simple 1D system (the space dimension being vertical) may well be erroneous and produce misleading results. Ecological models are often 'fitted' or rejected on the basis of the performance of a 1D version of the model compared to observations. At best the 'fitted' parameters may be dependent on the physical environment, implicitly including the effects of unresolved physical and ecological processes. At worst the functional form of the model chosen through this comparison may be wrong. In either case, in using an ecological model to predict changes to the ecological system as the physical environment changes, we need to ensure that the model captures the correct impact of those changes.

References

- Bainbridge, R., The size, shape and density of marine phytoplankton concentrations, *Biol. Rev.*, **32**, 91-115, 1957.
- Cox, P.M., R.A. Betts, C.D. Jones, S.A. Spall, and I.J. Totterdell, Acceleration of global warming due to carbon-cycle feedbacks in a coupled climate model, *Nature*, **408**, 184-187, 2000.
- Falkowski, P.G., D. Zieman, Z. Kolber, and P.K. Bielenfang, Role of eddy pumping in enhancing primary production in the ocean, *Nature*, **352**, 55-58, 1991.
- The Ring Group, Gulf Stream cold-core rings: their physics, chemistry and biology, *Science*, **212**, 1091-1100, 1981.
- Strass, V.H., Chlorophyll patchiness caused by mesoscale upwelling at fronts, *Deep-Sea Res.*, **39**, 75-96, 1992.
- Mann, K.H., and J.R.N. Lazier, *Dynamics of Marine Ecosystems*, Blackwell Science, Oxford, 1996.
- Flierl, F.G., D. Grunbaum, S. Levin, and D. Olsen, From individuals to aggregations: The interplay between behaviour and physics, *J. Theor. Biol.*, **196**, 397-454, 1999.
- Spall, S.A., and K.J. Richards, A numerical model of mesoscale frontal instabilities and plankton dynamics: I Model formulation and initial results, *Deep-Sea Res.*, **47**, 1261-1301, 2000.
- Truscott, J.E., and J. Brindley, Ocean plankton populations as excitable media, *Bull. Math. Biol.*, **56**, 981-998, 1994.
- Brentnall, S.J., K.J. Richards, and J. Brindley, Plankton patchiness and its effect on larger-scale production, Submitted to *J. Plankton Res.*, 2001.
- Murray, J.D., Biological Waves: Single species models, pp. 274-310, in *Mathematical Biology*, ed. S.A. Levin, Springer-Verlag, New York, 1993.
- McLeod, P., A.P. Martin, and K.J. Richards, Minimum length scale for growth limited oceanic plankton distributions, Submitted to *Proc. Roy. Soc. B*, 2001.
- Martin, A.P., K.J. Richards, A. Bracco, and A. Provencale, Patchy productivity in the open ocean, Submitted to *Global Biogeochem. Cycles*, 2001.
- Babiano, A.C., P. le Roy, and R. Sadourny, Single-particle dispersion, Lagrangian structure function and Lagrangian energy spectrum in two-dimensional incompressible turbulence, *J. Mar. Res.*, **45**, 107-131, 1987.
- Provenzale, A., Transport by coherent barotropic vortices, *Ann. Rev. Fluid Mech.*, **31**, 55-93, 1999.
- Oschlies, A., and V. Garçon, An eddy-permitting coupled physical-biological model of the North Atlantic, 1. Sensitivity to advection numerics and mixed layer physics, *Global Biogeochem. Cycles*, **13**, 135-160, 1999.
- Martin, A.P., On filament width in oceanic plankton distributions, *J. Plankton Res.*, **22**, 597-602, 2000.
-
-
- This preprint was prepared with AGU's L^AT_EX macros v4, with the extension package 'AGU++' by P. W. Daly, version 1.6a from 1999/05/21, with modifications by D. E. Kelley, version 1.0 from 2001/03/26, for the 'Aha Huliko'a Hawaiian Winter Workshop.

Brownian bugs and superprocesses

W.R. Young

Scripps Institution of Oceanography, University of California at San Diego, La Jolla 92093-0213

Abstract. Advection-diffusion-reaction (ADR) models link physical oceanography and biological oceanography. These models, which describe biology using continuous concentration fields, usually neglect individual-scale fluctuations. I describe a stochastic individual-based model, called the Brownian bug process, which illustrates some of the surprising issues associated with the neglect of fluctuations by ADR descriptions. The Brownian bug model is an ensemble of random walkers which suffer birth and death at constant mean rates. (Probabilists will recognize the Brownian bug model as the simplest example of a “superprocess.”) Binary division puts two bugs (parent and progeny) at the same position and the accumulation of these small-scale density fluctuations can produce palpable nonuniformities on large scales. In other words, provided that the diffusion is not too strong relative to the reproduction rate, a spatially homogeneous initial condition spontaneously develops patches and voids. The wavenumber signature of these reproductive pair correlations is that the spectrum of density fluctuations remains white but rises linearly with time. Diffusion opposes this reproductive forcing, most effectively at large wavenumbers, so that a red spectrum develops.

1. Introduction

Individuals are the fundamental unit of ecology but it is not feasible to model ecological processes by tracking single organisms. Instead, ecologists often employ advection-diffusion-reaction (ADR) approximations which describe biology using the ‘concentration’ $C(\mathbf{x}, t)$ (e.g., Flierl *et al.* 1999). The concentration is defined via a sample area¹ dA surrounding any \mathbf{x} at time t :

$$C(\mathbf{x}, t) dA = \text{expected number of organisms in } dA. \quad (1)$$

The dimensions of dA are such that the strong nonuniformities characteristic of scales comparable to that of an individual are greatly reduced by averaging.

Ecological ADR models originated with papers by Fisher (1937), Kolmogorov *et al.* (1937) and Skellam (1951). These authors independently proposed

$$C_t = \gamma C - \lambda C^2 + D \nabla^2 C \quad (2)$$

as a model for the growth, saturation and dispersion of a population. This chapter of theoretical ecology is either a slide down from this summit, as the ADR model is applied to specific cases, or an ascent as the ADR

approximation is derived and its limitations are better understood. The 1997 compilation edited by Tilman and Kareiva gives a good overview of both these endeavours. In this review we will admire some scenery on the climb-up to the ADR approximation by describing a maximally simplified model—the Brownian bug process.

Ocean ecology is a natural setting for ADR descriptions because the spatial domain is large and the populations of some species are enormous. Population size matters because C in (1) is an average or expectation. The actual number of organisms in dA , say N , is a random variable and using the definition in (1) $\bar{N} = CdA$. The difference $N' = N - \bar{N}$ is a fluctuation. Deterministic ADR equations ignore these fluctuations. The naive justification for discarding fluctuations is that N is a Poisson random variable (e.g., Durrett and Levin 1994) so that

$$\frac{N'}{\bar{N}} \sim \frac{1}{\sqrt{\bar{N}}} \ll 1. \quad (3)$$

Thus a deterministic description like (2) may be useful for copepods, but not for whales.

In oceanography, ADR models are a main line of communication between physicists and biologists. Physical oceanographers put the A into the ADR equation (2) by adding the term $\mathbf{u} \cdot \nabla C$ to the left hand side. The ve-

¹In this note I will work in two-dimensions so that in (1) I am using a control area rather than a control volume.

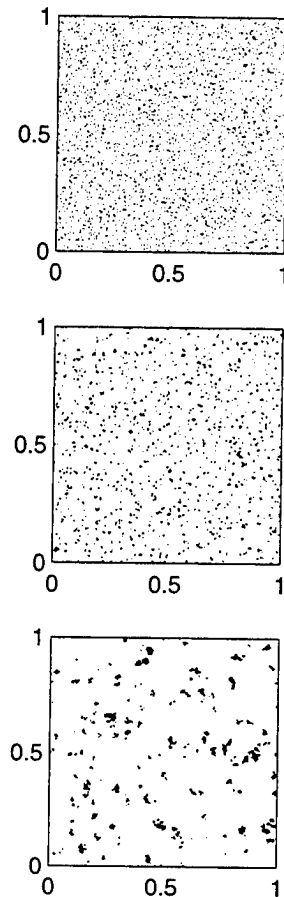


Figure 1. A Brownian bug simulation using $\Delta = 0.001$, $p = q = 1/4$, $N_0 = 4000$, and $U = 0$ (no advection). The position of each bug is plotted as a point in the unit square. The top panel shows the initial condition, the middle panel is after 10 cycles and the bottom after 100 cycles.

locity $\mathbf{u}(\mathbf{x}, t)$ is supplied by some physical model. (For example, see the paper by Kelvin Richards in these proceedings.) Physicists find this type of model appealing because the mathematical structure is familiar, and because it is easy to plug biology into existing ocean models. This is also my excuse for discussing these issues in a meeting devoted to oceanographic stirring and mixing.

When I described the Brownian bug process in my presentation at the 2001 'Aha Huliko'a meeting, Mel Briscoe pointed out that the same model had been independently presented at the 1997 'Aha Huliko'a meeting by Robert Adler and identified as a *superprocess*. Adler approaches this subject from the perspective of

a probabilist and the references in his article provide an entry into the extensive and very mathematical literature on superprocesses. A Google search on "superprocess" gives about 250 hits, most of which are on the homepages of mathematicians. Table stakes in the superprocess community are an understanding of measure theory and branching processes—most oceanographers can't ante.

Another closely related class of problems is diffusion-limited reactions, e.g., see the review by *Mattis and Glasser (1998)*, which emphasizes the utility of quantum field theory in these problems. There seems to be little communication between physicists interested in diffusion-limited reactions and probabilists studying superprocesses.

Ecologists and oceanographers will not find it easy to understand the review articles written by either of these communities. This review, which is intended for my oceanographic colleagues, might then be titled "Superprocesses for pedestrians, with no quantum field theory and no measure theory."

2. Brownian bug simulations

The Brownian bug process is an ensemble of random walkers (idealized as points) milling around in continuous time and space and simultaneously reproducing and dying at constant mean rates. Reproduction is random in time and occurs via binary division, so that parent and progeny are at the same point for just an instant before their independent random walks start to produce \sqrt{Dt} separation. Death is also random and dead bugs are removed from the ensemble. The addition of advection to this scenario (*Young 2001*) results in the simplest model of a planktonic species reproducing and dying in a turbulent fluid.

To simulate the continuous process described above on a computer one must discretize. There are several ways of doing this, and I describe in the appendix an individual-based Monte Carlo procedure which produces Figure 1. The top panel shows the homogeneous initial condition and the middle and bottom panels the results after 10 and 100 cycles of birth, death and diffusion. Patches of bugs spontaneously form out of the spatially uniform initial conditions.

Failure of deterministic ADR. The ADR approximation of the simulation in Figure 1 is simply

$$C_t = D\nabla^2 C + (\lambda - \mu)C, \quad (4)$$

where D is the diffusivity, λ is birth rate, and μ the death rate. (For the relation between D , λ , and μ and the parameters in the simulation see the appendix.) But in Figure 1 birth and death are equiprobable, $\lambda = \mu$,

and consequently (4) collapses to the diffusion equation. Thus, with the initial condition $C(\mathbf{x}, 0) = N_0/L^2$, the solution of the ADR description is $C(\mathbf{x}, t) = N_0/L^2$. Uniform concentration is not a good characterization of Figure 1 and we conclude that the ADR approximation fails to describe the Brownian bug process.

A stochastic ADR equation. Although deterministic ADR fails, there is a stochastic partial differential equation model which does capture the fluctuations exhibited by the individual-based model. This stochastic equation is something like

$$C_t = D\nabla^2 C + \sqrt{C} w(\mathbf{x}, t) \quad (5)$$

where w is a white Gaussian noise. The \sqrt{C} in (5) occurs because in the control volume d the stochastic imbalance between births and deaths is proportional to \sqrt{C} . I qualified the introduction of (5) with “something like” because mathematicians (e.g., Adler 1997) tell us that (5) makes sense only in one dimension, $d = 1$, but not when $d \geq 2$: in that case the concentration $C(\mathbf{x}, t)$ cannot be defined. I do not fully understand this point. In any event, Adler proceeds to introduce an integrated version of (5) which he claims is sensible even in $d \geq 2$. We press on...

Density fluctuations. The spatial clumping in Figure 1 occurs because birth is always next to a living bug, while death can occur anywhere. Alternatively, in some regions because of bad luck there is local extinction of the bug population. Diffusion from the surviving centers of population is not fast enough to recolonize the voids. This suggests that to produce patches the diffusion D must be weak relative to the growth rate $\lambda = \mu$. We can identify the nondimensional parameter that controls this transition by noting that the initial separation distance between bugs (the “specific” length) is $\ell_s = L/\sqrt{N_0}$. On the other hand, using the diffusivity D and the growth rate λ , we can define a “reproductive” length $\ell_r \equiv \sqrt{D/\lambda}$, which measures the separation that develops between parent and progeny before there is another reproductive event. We expect that patchiness will be strong if the nondimensional number

$$\frac{\ell_s}{\ell_r} = L \sqrt{\frac{\lambda}{N_0 D}}, \quad (6)$$

is large. If the ratio ℓ_s/ℓ_r is small then density fluctuations should be small because the diffusion will be effective at mixing a family into the background of unrelated, and therefore uncorrelated, bugs.

To illustrate these considerations, the $L \times L$ square is divided, like a chessboard, into smaller squares (“boxes”), each of size

$$\ell_p \equiv 2^{-p} L. \quad (7)$$

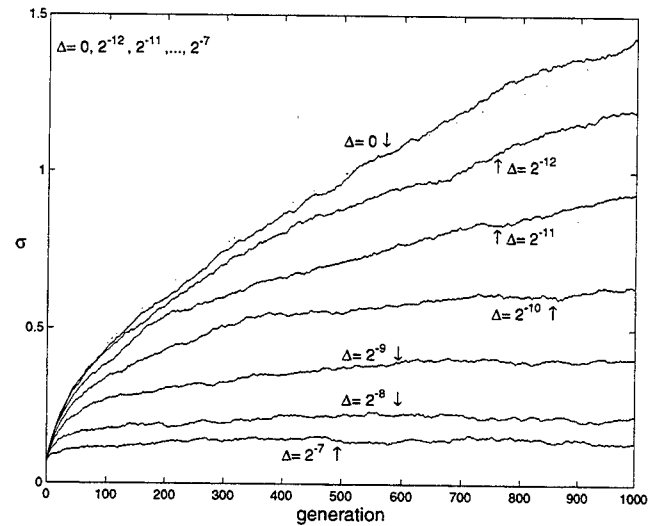


Figure 2. Results of 7 simulations each with $N_0 = 2^{18}$ bugs at $t = 0$. The unit square is divided into a lattice of 32×32 boxes (i.e., $p = 5$) and $\sigma(5, t)$ defined in (10) is computed. The parameters in section 5 are $p = q = 1/4$ and the step-length of the random walk, Δ , is varied as indicated. When the diffusion is strong σ remains close to its initial Poisson value, $\sigma(5, 0) \approx 1/16$. The dotted curve is $\sigma_{\text{GW}} \equiv \sqrt{(1 + 2\mu t)/n_p}$, which is computed using the Galton-Watson solution in (18) and (19) below.

There are 2^{2p} boxes so that the expected number of bugs per box is

$$n_p \equiv 2^{-2p} N_0. \quad (8)$$

The occupation number of box b is the fluctuating quantity

$$n_b(t) \equiv \text{the number of bugs in box } b \text{ at } t, \quad (9)$$

where $b = 1, \dots, 2^{2p}$ indexes the boxes. To measure the size of fluctuations in n_b relative to the expected value n_p we use the ratio of the RMS value of $n(b, t)$ to n_p :

$$\sigma(p, t) \equiv \sqrt{\sum_{b=1}^{2^{2p}} [n(b, t) - n_p]^2 / n_p}. \quad (10)$$

If $\sigma(p, t) \ll 1$ then $n(b, t)$ is fluctuating weakly around the expected value n_p .

Figure 2 shows $\sigma(p, t)$ for a set of simulations with various diffusivities and $p = 5$. The $\sigma(p, 0)$ is small because the box size $\ell_p = 1/32$ is much greater than the specific length, $\ell_s = 1/512$. If the diffusivity is strong enough (for example, $\Delta > 2^{-8}$ in Figure 2) then $\sigma(p, \infty) \ll 1$. In this case the diffusivity is arresting reproductively driven fluctuations. On the other hand, if the diffusivity is small then the growth of σ proceeds till $\sigma(p, \infty) \geq O(1)$, which

indicates large fluctuations in the density defined using the box-scale ℓ_p . In particular, if there is no diffusion ($\Delta = 0$) then one can show using the Galton-Watson solution in (18) and (19) that $\sigma(p, t) \approx \sqrt{(1 + 2\mu t)/n_p}$. Notice that by decreasing the diffusivity we are increasing the nondimensional parameter in (6).

It would be useful to be able to give a scaling law for the saturated value, $\sigma(p, \infty)$, in terms of D , μ , ℓ_p and the other external parameters. I have not been able to achieve this.

3. Galton-Watsonology

The Brownian bug model combines two classical stochastic processes: Brownian motion and a Galton-Watson branching process. Brownian motion is familiar to most oceanographers, but the Galton-Watson process is not. This section summarizes some basic properties of Galton-Watson process.

Suppose that we switch off the motion of the bugs, i.e., we set the step length of the random walk to zero. In this case each bug founds a family which sits at the initial spatial location. Newly born bugs pile up and build a tower on top of their ancestors. The towers go up and down as bugs are born and die. Towers can disappear forever (extinction) if a run of bad luck wipes out the family. The statistics of these families, particularly the probability of extinction, were studied by Galton and Watson in the nineteenth century (see *Harris*, 1963, and chapter XVII of *Feller*, 1968). In this review we closely follow Feller's continuous-time formulation of the Galton-Watson process.

The fundamental variables of the Galton-Watson process are the probabilities

$p_k(t)$ = the probability that there are k bugs at t .

We study the proliferation of a family descended from a single urbug using the initial condition $p_1(0) = 1$ and $p_k(0) = 0$ if $k \neq 1$. The probability that a family is extinct at t is $p_0(t)$. Given $p_k(t)$, one calculates the average of a function of k according to the definition

$$\bar{f}(k, t) \equiv \sum_{k=0}^{\infty} f(k, t)p_k(t). \quad (11)$$

Normalization of probabilities requires $\bar{1} = 1$ and the mean population of a family is $\bar{k}(t)$.

The family becomes extinct when a family with one surviving member suffers a death; accordingly the probability of extinction p_0 increases like

$$\dot{p}_0 = \mu p_1. \quad (12)$$

The evolution of the other probabilities with $k \geq 1$ is obtained from the hierarchy of differential equations

$$\dot{p}_k = \lambda(k - 1)p_{k-1} - (\lambda + \mu)kp_k + \mu(k + 1)p_{k+1}. \quad (13)$$

The term $-(\lambda + \mu)kp_k$ on the right hand side of (13) appears because a family of k bugs might make a transition to $k + 1$ bugs if any of its k members reproduce (probability per time λk) or make a transition to $k - 1$ bugs if any of the k members die (probability per time μk). Analogous reasoning is used to deduce the other terms containing $k - 1$ and $k + 1$ on the right hand side of (12).

Mean and variance. From (12) and (13) one can show using the definition (11) that $\bar{1} = 1$ and

$$\frac{d\bar{k}}{dt} = (\lambda - \mu)\bar{k}. \quad (14)$$

This result establishes the connection between the Galton-Watson process and the ADR equation (3): both \bar{k} and C are expectations defined by ensemble averages and $\lambda - \mu$ is the growth rate of the expected population. In fact, if we start with N_0 bugs, each of which is a family with one member, then because the evolution is independent $\int C dA = N_0 \bar{k}$.

The statistic \bar{k} contains no information concerning the fluctuations in population. That is, at times $t > 0$ some families are extinct, while others are very large. A coarse description of these fluctuations is provided by the variance $\bar{k}^2 - \bar{k}^2$, or better by the ratio

$$v = \sqrt{\bar{k}^2 - \bar{k}^2}/\bar{k}, \quad (15)$$

which, like (3), compares the fluctuations to the mean.

Assiduous summation of (12) and (13) shows that

$$\frac{d\bar{k}^2}{dt} = 2(\lambda - \mu)\bar{k}^2 + (\lambda + \mu)\bar{k}. \quad (16)$$

If the death rate balances the birth rate, so that $\lambda = \mu$ and $\bar{k} = 1$, then the solution of (16) is

$$\bar{k}^2 = 1 + 2\mu t, \quad (\lambda = \mu). \quad (17)$$

In this case $v = \sqrt{2\mu t}$, indicating that the system is dominated by fluctuations as $t \rightarrow \infty$.

The special case $\lambda = \mu$ in (17) is the critical point of the branching process. If $\gamma \equiv \lambda - \mu > 0$ then $\bar{k} \sim \exp(\gamma t) \rightarrow \infty$ and $v \sim \exp(-\gamma t/2) \rightarrow 0$. On the other hand, if $\gamma < 0$ then $v \sim \exp(-\gamma t/2) \rightarrow \infty$. The conclusion is that the system is dominated by fluctuations if the growth rate γ is less than or equal to zero.

A solution with $\lambda = \mu$. The variance is only a rough guide to behaviour of fluctuations. A much more informative result is provided by an explicit solution of (12) and (13) which is obtained using the generating function method (Feller 1968):

$$p_0(t) = \frac{\mu t}{1 + \mu t}, \quad (18)$$

and if $k \geq 1$:

$$p_k(t) = \frac{(\mu t)^{k-1}}{(1 + \mu t)^{k+1}}. \quad (19)$$

At large times, $\mu t \gg 1$, see that most families are extinct, $p_0(t) \rightarrow 1$. That is, at large times the *most probable* number of members in any given family is zero — in fact extinction is certain. On the other hand $\bar{k} = 1$ so that the expected number of members in a family (counting extinct families as having zero members) is always constant.

To reconcile the extinction of most families with a constant expected population, we make a distinction between surviving families (meaning a family with at least one member) and extinct families. Suppose that we start with a large number $N_0 \gg 1$ of individuals, each of which founds a family. At t the number of surviving families is a random variable, $F(t)$. The expected number of surviving families is $\bar{F} = (1 - p_0)N_0$, or using (18)

$$\bar{F}(t) = \frac{N_0}{1 + \mu t}. \quad (20)$$

Let the random variable n be the number of individuals in a surviving family. From (18) and (19), the probability distribution of n , conditioned on the survival of a family, is

$$p_n = \frac{(\mu t)^{n-1}}{(1 + \mu t)^n}, \quad (n = 1, 2, \dots). \quad (21)$$

and consequently

$$\bar{n}(t) = \mu t + 1, \quad \bar{n}^2 = (2\mu t + 1)(\mu t + 1). \quad (22)$$

Thus, the number of surviving families decreases like t^{-1} , while the membership of a surviving family grows like t^1 to keep the total population fixed.

These remarks illustrate Galton and Watson's conclusion that the "observed diminution of surnames among families whose history we can trace, is not a sign of their diminished fertility." Instead the extinction of most families, and the apparent fecundity of a few exceptions, is a result of "the ordinary law of chances."

4. Spectral dynamics

We began section 3 by imagining that the bugs were immobile so that the surviving families formed towers on top of the urbug. We then ignored the spatial aspects of the model, and focussed simply on the statistics of the bug population. Now let us return to the spatial domain and study the spectrum of concentration fluctuations.

For the moment, we continue to assume that the bugs are immobile ($D = 0$). The discussion surrounding (20) through (22) shows that the height of a typical family tower grows like $1 + \mu t$ and the average separation between towers grows like $\ell_s/\sqrt{1 + \mu t}$, where $\ell_s \equiv L/\sqrt{N_0}$. We can write the microscopic density of bugs in a single realization of the process as

$$\rho(\mathbf{x}, t) = \sum_{f=1}^F n_f \delta(\mathbf{x} - \mathbf{x}_f), \quad (23)$$

where $F(t)$ is the number of surviving families, n_f is the number of members in family f and \mathbf{x}_f is the location of the family. Notice that the concentration is

$$C = \langle \rho \rangle = N_0/L^2, \quad (24)$$

where the $\langle \rangle$ denotes an ensemble average over the random locations ² \mathbf{x}_f and an average over the n_f 's using (21). The average $C = \langle \rho \rangle$ is trivial — just like \bar{k} in the previous section. To learn something about the fluctuations we must study quadratic quantities such as the spectrum.

Continuing with the $D = 0$ assumption, we now make a standard calculation of the spectrum by ensemble averaging the density in (23). The Fourier series representation of (23) is

$$\rho(\mathbf{x}, t) = L^{-2} \sum_{\mathbf{k}} \rho_{\mathbf{k}} \exp(i\mathbf{k} \cdot \mathbf{x}), \quad (25)$$

where

$$\rho_{\mathbf{k}} = \sum_{f=1}^F n_f \exp(-i\mathbf{k} \cdot \mathbf{x}_f). \quad (26)$$

The spectrum is related to

$$\langle \rho_{\mathbf{k}} \rho_{\mathbf{k}}^* \rangle = \left\langle \sum_{f=1}^F n_f^2 + 2 \sum_{f' > f} n_f n_{f'} e^{i\mathbf{k} \cdot (\mathbf{x}_{f'} - \mathbf{x}_f)} \right\rangle, \quad (27)$$

where the $\langle \rangle$ is an ensemble average over both the random and uncorrelated positions \mathbf{x}_f of the surviving families and over the random variable n_f . Because there are

²The family locations \mathbf{x}_f are uniformly distributed in the domain. Thus $\langle \delta(\mathbf{x} - \mathbf{x}_f) \rangle = L^{-2}$ and if $\mathbf{k} \neq 0$ then $\langle \exp(i\mathbf{k} \cdot \mathbf{x}_f) \rangle = 0$.

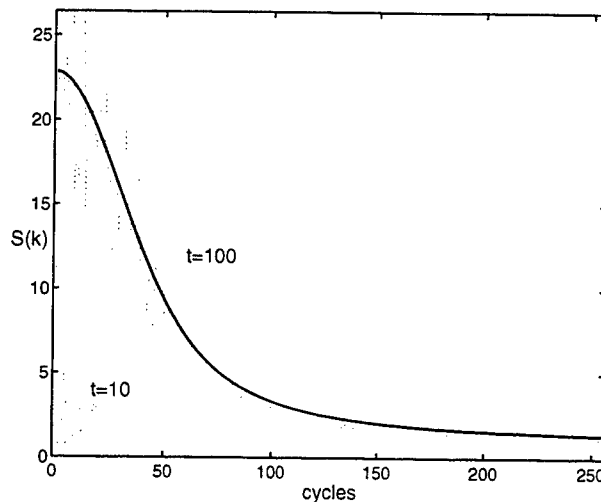


Figure 3. Comparison of the analytic prediction (31) (the smooth solid curve) with the results of simulation. We show estimated spectra (the three dotted curves) from the simulation at $t = 1$, $t = 10$ and $t = 100$; the comparison with (31) is made only at $t = 100$. The simulation used $N_0 = 10^5$ bugs with $\Delta = 2^{-11}$ and $p = q = 7/64$. The spectra are estimated by azimuthally averaging in the wavenumber plane.

no correlations between the positions of the families the final term, involving the double sum with $f \neq f'$ vanishes. Using \bar{F} from (20), and \bar{n}^2 from (22), shows that the remaining term on the right hand side of (27) is

$$\langle \rho_{\mathbf{k}} \rho_{\mathbf{k}}^* \rangle = \bar{F} \bar{n}^2 = N_0(1 + 2\mu t). \quad (28)$$

This simple calculation indicates that the spatial signal of a diffusionless Galton-Watson process is a white spectrum which rises at a constant rate.

How is the conclusion above affected by diffusion? With $D \neq 0$ the members of a family move as independent random walkers and the family towers blur into spreading clouds of bugs. We could write down a microscopic density, analogous to (23), in which the position of each individual bug is represented with a δ -function. But then the calculation founders at (27) because the $\langle \rangle$ no longer kills the off-diagonal terms: there are correlations between the positions of bugs which belong to the same family. Instead we can argue heuristically that the evolution of the spectrum, defined as

$$S(k, t) \equiv N_0^{-1} \langle \rho_{\mathbf{k}} \rho_{\mathbf{k}}^* \rangle, \quad (29)$$

is given by

$$S_t = 2\mu - 2Dk^2 S, \quad S(k, 0) = 1, \quad (30)$$

where $k \equiv \sqrt{\mathbf{k} \cdot \mathbf{k}}$. The first term on the right hand side of (30) is a source of variance which produces the uniform rise of the spectral level in (28). The final

term is the diffusive sink of variance which ultimately balances the source.

The solution of (30)

$$S(k, t) = \frac{\mu}{Dk^2} \left(1 - e^{-2Dk^2 t} \right) + 1, \quad (31)$$

exhibits a k^{-2} range at high wavenumbers. (If we isotropize by using $2\pi k S(k)$ then this is a k^{-1} spectrum.) Figure 3 shows good comparison of (31) with a spectrum estimated from a simulation.

5. Conclusions

In this note we have studied a model which focuses attention on the role of fluctuations in the spatial development of populations. It is remarkable that Euler, Navier and Stokes formulated the basic equations of fluid mechanics before the reality of atoms was established. This history indicates that for most purposes atomic fluctuations are unimportant in fluid mechanics. The Brownian bug model suggests that the problem of biological fluctuations is more severe, and that events on microscopic scales can impact macroscopic observations. Indeed, the source term 2μ on the right hand side of (30) is due to reproduction and has no analog in fluid mechanics.

Appendix: A recipe for simulations

The initial condition, $t = 0$, is prepared with a large number N_0 of bugs, strewn randomly into an $L \times L$ square domain. The initial condition is a Poisson point process in which there are no correlations between the positions of the bugs.

The simulation is advanced through time in increments of a "cycle" of duration τ . Each cycle consists of two steps: (a) random birth and death; (b) Brownian motion. In step (a) each bug reproduces by binary fission (probability p) or dies (probability q) or remains unchanged (probability $1 - p - q$). When a lucky bug divides the offspring is placed on top of the parent. In step (b), bug k is displaced to a new position $\mathbf{x}_k(t + \tau) = \mathbf{x}_k(t) + \delta \mathbf{x}_k(t)$. The components of $\delta \mathbf{x}_k$ are independent and identically distributed Gaussian random variables, each with RMS value Δ (i.e., Brownian motion with the diffusivity $D = \Delta^2/2\tau$). These independent displacements separate the coincident parent-progeny pairs created by step (a).

In principle, one can approach the continuous limit by taking $\tau \rightarrow 0$ while holding the parameters $\lambda \equiv p/\tau$, $\mu \equiv q/\tau$, and $D \equiv \Delta^2/2\tau$ fixed.

We can also use $p_0(t)$ in (18) to calculate the probability that an initial population of N_0 bugs becomes extinct at time t : each bug produces a family which

evolves independently of the other families, so that the probability that all N_0 families are extinct at t is

$$p_{\text{ext}} = p_0^{N_0} \approx \exp(-T_{\text{ext}}/t), \quad (\text{A1})$$

where the extinction time-scale is $T_{\text{ext}} \equiv N_0/\mu$. (The exponential approximation in (A1) assumes that N_0 is large and t/T_{ext} is of order unity.) In simulations we avoid extinction by making N_0 much larger than the number of generations. The suppression of extinction is a consequence of approaching the “thermodynamic limit” in which $N_0 \rightarrow \infty$ with N_0/L^2 fixed.

Acknowledgments. I am grateful to many people for discussions of this problem. My research is supported by the National Science Foundation, most recently by NSF OCE96-16017.

References

- Adler, R., Superprocesses and plankton dynamics, pp. 121–127 in *Monte Carlo Simulation in Oceanography*, Proceedings of the 'Aha Huliko'a Hawaiian Winter Workshop, University of Hawaii at Manoa. 1997.
- Durrett, R. and S. Levin, The importance of being discrete (and spatial). *Theor. Population Biol.*, 46, 363–394, 1994.
- Feller, W., *An Introduction to Probability Theory and its Applications, Volume I*, 3rd edition, Wiley, 1968.
- Fisher, R.A., The wave of advance of advantageous genes, *Ann. Eugenics*, 7, 355–369, 1937.
- Flierl, G., D. Grünbaum, S. Levin, and D. Olson, From individuals to aggregations: the interplay between behaviour and physics. *J. Theor. Biol.*, 196, 397–454, 1999.
- Harris, T.E., *The Theory of Branching Processes*, Springer-Verlag, Berlin, 1963.
- Kolmogorov, A., I. Petrovsky, and H. Piscunov, Study of the diffusion equation with growth of the quantity of matter and its application to a biology problem. Originally published in *Bulletin de l'université d'état à Moscou Série internationale*, section A, 1, 1937. For an english translation, see *Dynamics of Curved Fronts* edited by P. Pelcé. Academic Press, San Diego, 1988.
- Mattis, D.C., and M.L. Glasser, The uses of quantum field theory in diffusion-limited reactions. *Rev. Mod. Phys.*, 70, 979–1001, 1998.
- Skellam, J.G., Random dispersion in theoretical populations. *Biometrika*, 38, 196–218, 1951.
- Tilman, D., and P. Kareiva, (editors) *Spatial Ecology: the Role of Space in Population Dynamics and Interspecific Interactions*, Monographs in Population Biology, 30, Princeton University Press, 1997.
- Young, W.R., Reproductive pair correlations and the clustering of organisms, *Nature*, 412, 328–331, 2001.

This preprint was prepared with AGU's LATEX macros v4, with the extension package 'AGU++', by P. W. Daly, version 1.6a from 1999/05/21.

Describing intermittent processes in the ocean: Univariate and bivariate multiscaling procedures

Laurent Seuront

Ecosystem Complexity Research Group, CNRS UPRESA 8013 ELICO, BP 80, F-62930, Wimereux, France

François Schmitt

Department of Fluid Mechanics, Vrije Universiteit Brussel, Pleinlaan 2, B-1050 Brussels, Belgium

Abstract. Univariate and bivariate procedures for investigating the properties of single and joint intermittent stochastic processes are presented. They allow the characterization of all the statistics of intermittent variables using a set of three basic parameters in the multifractal framework, whatever the scales and the intensity. The multifractal formalism is then extended to more than one variable to investigate the degree of dependence among random fields by examining the nature of their joint distribution. These formalisms, which do not require any assumption about the spectrum or the probability distribution of the data sets under consideration, are finally illustrated, first, by studying the properties of turbulent velocity fluctuations recorded in a laboratory grid-generated turbulence experiment and in the ocean using a high-frequency free-fall profiler. Second, we investigate the distributions of temperature, salinity and *in vivo* fluorescence (a proxy of phytoplankton biomass) time series recorded in the coastal waters of the Southern Bight of the North Sea, as well as their potential correlation.

Introduction

Considering the current awareness of the intermittent nature of both physical and biological patterns and processes in marine sciences (Gibson, 1991; Pascual *et al.*, 1995; Seuront *et al.*, 1996a, 1999; Jou, 1997; Jiménez, 2000), and the emergence of hot topics such as those related to thin-layer properties (Cowles *et al.*, 1998; Osborn, 1998), there is a real need to focus on the precise nature of both single intermittent variables and the degree of correlations between joint intermittent variables, especially those related to physics and biology.

Recent theoretical and empirical developments, conducted both on turbulent energy dissipation rates and on the associated passive scalars distributions, have demonstrated the multiscale properties of intermittent processes (Pascual *et al.*, 1995; Seuront *et al.*, 1996a, b, 1999, 2001a, b; Lovejoy *et al.*, 2001). The large numbers of modeling approaches devoted to the structure of turbulent flows have only provided description at a very limited range of scales. Indeed, neither Gaussian diffusion models (Visser, 1997) nor direct numerical simulations (Yamazaki *et al.*, 1991) possess a way to change the scale upward or

downward. In contrast, scale change is natural for multifractal processes (Seuront *et al.*, 1999). Moreover, Gaussian processes are determined by only two moments, while the first three moments of empirical processes are usually provided to characterize them. In the statistical framework of multifractals, we propose a more global approach since we provide all the moments (even non-integers), giving as much statistical information as the study of probability density directly.

The procedures used to test for independence between two processes, based on second order statistics analysis (i.e., correlation), become fallacious for intermittent non-Gaussian fields. It is then necessary to test for independence by studying joint moments of all orders. In addition, more recent procedures based on examination of probability density functions do not deal with the multiscaling properties of intermittent fields.

In this paper, first we define the concept of intermittency and then review briefly the multifractal framework. Second, we will introduce an innovative objective technique for determining if two stochastic processes can be regarded as being independent or not, and for investigating the nature of their potential coupling. Finally, we provide

some illustrative case studies demonstrating how these multifractal formalisms can improve our understanding of the structures and functions in marine systems.

Intermittency

The concept of intermittency has been initially described in the framework of turbulence, where experimental records of the kinetic energy dissipation rate ϵ showed strong and unpredictable bursts instead of a steady behavior of the fluctuations (Fig. 1). It has thus been known for a long time that the assumption of a spatially uniform turbulent cascade used by Kolmogorov (1941) is not satisfied for the increments of turbulent velocity at distances in the inertial subrange or shorter, and that strong gradients are more common than they would be for a Gaussian distribution (Batchelor and Townsend, 1949). This means that most of the time the gradients would still be of the order of their standard deviation, but that occasionally we should expect stronger burst, much more often than in the Gaussian case. This is the phenomenon of intermittency, which, as with other turbulent phenomena, is found at all scales.

This may be understood from a geometrical point of view considering that the turbulent regions do not fill the whole space, but only a subpart, in a very irregular way. This erroneous picture of a non-space filling turbulence takes the intermittent nature of turbulence into account by assuming that subeddies in the inertial subrange are either ‘dead’ (inactive) or ‘alive’ (active), and leads to a (mono-) fractal description of turbulence. However, it is now known that both turbulent velocity and passive scalars fluctuations are intermittent in the sense that strong (i.e. ‘more active’) subeddies occupy tiny fractions of the space available. This led to a multifractal description of turbulence, each intermittency level being associated with its own fractal dimension [see Frisch (1995) for more details].

In the following we quickly review how to characterize the statistics of a multifractal intermittent field.

Investigating single intermittent distributions: a brief review of the multifractal framework

Spectral analysis has been widely used in ecology to separate and measure the amount of variability occurring at different wavenumbers. In particular, assuming local isotropy and three-dimensional homogeneity of turbulence in the inertial subrange, the velocity fluctuations and the fluctuations of a passive scalar quantity P can be described in Fourier space by the spectral densities $E_v(k)$ and $E_p(k)$:

$$E_v(k) \propto k^{-\beta_v} \quad (1)$$

$$E_p(k) \propto k^{-\beta_p} \quad (2)$$

where k is a wavenumber, and with $\beta_v = \beta_p = 5/3$ for a non-intermittent turbulence (Kolmogorov, 1941; Obukhov, 1941, 1949; Corrsin, 1951). However, spectral analysis and related techniques are implicitly based on Gaussian hypothesis untenable in an intermittent framework (Seuront *et al.*, 1999, 2001a). Thus, while random variability has been often modeled in marine ecology in the Gaussian framework, through, e.g., Gaussian distributions and Brownian motion (e.g., Yamazaki and Okubo, 1995; Visser, 1997), we will here generalize this approach fully taking into account the intermittency of turbulent velocity and passive scalar fluctuations.

Under fairly general conditions, the probability distribution of a random variable X is equivalently specified by its statistical moments. Here we consider the moments of the increments of a random field at all scales; this corresponds to the introduction of the structure functions exponents $\zeta_v(q)$ and $\zeta_p(q)$, which describe the multiscaling of the statistical moments of order q of turbulent velocity and passive scalar fluctuations:

$$\langle (\Delta V_i)^q \rangle \propto l^{\zeta_v(q)} \quad (3)$$

$$\langle (\Delta P_i)^q \rangle \propto l^{\zeta_p(q)} \quad (4)$$

where l is the spatial scale and the angle brackets “ $\langle \cdot \rangle$ ” indicate ensemble averaging. For monoscaling (i.e., monofractal) processes, the function $\zeta(q)$ is linear: $\zeta(q) = q/2$ for Brownian motion, and $\zeta(q) = q/3$ for Kolmogorov-Obukhov-1941. For multiscaling processes, this exponent is non-linear and concave.

While the functions $\zeta_v(q)$ and $\zeta_p(q)$ could depend on a very large number of parameters (a priori an infinite number of both integer and non-integer values of q), in the framework of universal multifractals they can be determined by only three parameters, with the general form $\zeta(q) = Aq + Bq^\alpha$ (Schertzer and Lovejoy, 1987). For turbulent velocity, the normalization conditions corresponding to the conservation of turbulent kinetic energy within the inertial subrange give $\zeta_v(3) = 1$, so that the resulting function can be written as

$$\zeta_v(q) = \frac{q}{3} - \frac{C_{1c}}{\alpha_c - 1} \left(\left(\frac{q}{3} \right)^\alpha - \frac{q}{3} \right). \quad (5)$$

For a passive scalar P , there is no such a relation, and we

must keep three parameters, writing the expression as (*Seuront et al.*, 1996a, b, 1999, 2001a)

$$\zeta_p(q) = qH - \frac{C_{1P}}{\alpha_p - 1} (q^{\alpha_p} - q). \quad (6)$$

H is the degree of non-conservation of the average process: $H=0$ for a conservative process (i.e., scale-independent) and $H\neq 0$ for a non-conservative process (i.e., scale-dependent). H is given by $H=\zeta_p(1)$, while it can be seen from Eq. (5) that $\zeta_p(1)>1/3$. C_1 is the codimension that characterizes the intermittency of the process and satisfies $0\leq C_1 \leq d$ (d is the dimension of the observation space): $C_1=0$ for a homogeneous process, and C_1 increases with the intermittency of the process, indicating that the field values corresponding to any given level of variability are more scarce. The Lévy index α is the degree of multifractality, bounded between $\alpha=0$ and $\alpha=2$, corresponding to the monofractal case and to the maximum, or log-normal, multifractal case, respectively.

In other words, the second terms of Eqs. (5) and (6) express the multifractal intermittent deviation from monofractality, in which case $\zeta_v(q)=q/3$ and $\zeta_p(q)=qH$. The “distance” between monofractality and multifractality is then a function of C_1 and α . The knowledge of these parameters is enough to characterize all the one-point statistics of the fields. In particular, we see from Eqs. (5) and (6) that C_1 is given by $C_{1e}=1-3\zeta_e(3)$ for velocity fluctuations, and $C_{1e}=H-\zeta_p(1)$ for a passive scalar quantity P . α and α are estimated as the best nonlinear fit of Eqs. (5) and (6) for values between 0 and 2, using a simplex procedure.

Finally, we note here that in the multiscaling framework, intermittency is taken into account noting that

$$\beta_v = 1 + \zeta_v(2) \quad (7)$$

$$\beta_p = 1 + \zeta_p(2). \quad (8)$$

We thus see that the intermittency corrections introduced by the second term of Eq. (5) lead to $\beta_v > 5/3$. Furthermore, in order to conduct direct quantitative comparisons between the velocity and passive scalar intermittent corrections associated to C_1 values, let us note that the coefficients in front of the non-linear terms in Eqs. (5) and (6) are similar only if we compare C_{1v} and C_{1P} , with C_{1v} estimated as (*Schmitt et al.*, 1996; *Seuront et al.*, 1996a)

$$C_{1v} = 3^{-\alpha_v} C_{1e}. \quad (9)$$

Investigating joint intermittent distributions: the “Generalized Correlation Functions”

Previous standard procedures devoted to test for independence between two given processes were generally based on second order statistics (i.e., covariance and correlation functions), even when they were conducted in scaling framework related to spectral analysis (*Legendre and Legendre*, 1984) or geostatistical analysis (*Kitanidis*, 1997). More recent procedures are based on probability density functions examination (*Lueck and Wolk*, 1999). The former are implicitly based on Gaussian hypothesis (uncorrelation implying independence), untenable in an intermittent framework characterized by a high-order statistical behavior. The latter do not deal with the intrinsic multiscaling properties of intermittent fields. We then propose here an original testing procedure based on a high-order generalization of the correlation concept between two variables X and Y .

Instead of random variables X and Y , we consider here two stochastic processes ΔX_i and ΔY_i (e.g., *Parzen*, 1962). For more convenience, let us note $x=\Delta X_i=e^{G_1}$ and $y=\Delta Y_i=e^{G_2}$. The joint moments can be written as the moments of a vectorial process:

$$\langle x^p y^q \rangle = \langle e^{pG_1+qG_2} \rangle = \langle e^{\bar{Q}\cdot\bar{G}} \rangle \propto l^{S(\bar{Q})} \quad (10)$$

where the vectors \bar{Q} and \bar{G} are given by $\bar{Q}=(p,q)$ and $\bar{G}=(G_1, G_2)$, and the exponents $S(\bar{Q})$ characterize the multiscaling properties of the joint moments $\langle x^p y^q \rangle$. The “Generalized Correlation Function” (GCF hereafter) we introduce is then simply a normalization of the joint moments following:

$$c(p,q) = \frac{\langle x^p y^q \rangle}{\langle x^p \rangle \langle y^q \rangle} \propto l^{-r(p,q)}. \quad (11)$$

The “Generalized Correlation Exponent” (GCE hereafter), estimated as the slope of the linear trend of $c(p,q)$ vs. l in a log-log plot, is then expressed as

$$r(p,q) = \zeta_x(p) + \zeta_y(q) - S(p,q) \quad (12)$$

where $\zeta_x(p)$ and $\zeta_y(q)$ characterize the multiscaling properties of the single fluctuations $\langle x^p \rangle$ and $\langle y^q \rangle$ as defined in Eqs. (3) and (4), and $S(p,q)$ characterizes the multiscaling properties of the joint fluctuations $\langle x^p y^q \rangle$, see Eq. (11). Both $c(p,q)$ and $r(p,q)$ are generalization of correlation functions. They express the correlation between

x^p and y^q and their scale and moment dependence. In the particular case $p=q=1$, Eq. (11) recovers the classical expression of the correlation coefficient between x and y . We nevertheless need to emphasize here that, whereas independence implies uncorrelation, uncorrelation does not imply independence.

Indeed, uncorrelation corresponds simply to the relation $r(1,1)=0$. Uncorrelation implies independence only in special cases such as for Gaussian processes. To show this, let us consider the joint scaling function for lognormal multifractals x and y . Using results for multivariate Gaussian processes (see any text book on multivariate stochastic processes, e.g., *Samorodnitsky and Taqqu*, 1994), one has the general expression for a lognormal process:

$$S(p,q) = a_1 p + a_2 q - a_3 q^2 - a_4 p^2 - \sigma pq \quad (13)$$

so that

$$r(p,q) = S(p,0) + S(0,q) - S(p,q) \quad (14)$$

giving

$$r(p,q) = \sigma pq. \quad (15)$$

In this case, it is clear that $r(1,1)$ or $r(2,2)$ is enough to estimate the only parameter, namely the correlation coefficient σ , so that if $r(1,1)=0$ or $r(2,2)=0$ it can be concluded that the two processes are independent. In the general case, this is no more true: independence between the stochastic processes x and y means that the GCE verifies $r(p,q)=0$ whatever the values of p and q , while uncorrelation corresponds to $r(1,1)=0$.

A function related to our $c(p,q)$ has also been independently introduced in the lognormal multifractal framework for financial time series by *Muzy et al.* (2000), where it was called “joint scaling exponent”.

The function $c(p,q)$ and its related scaling exponent $r(p,q)$ can be used as an analysis tool to study some complex relationship between two multifractal fields x and y . To provide some basis for discussion and interpretation of experimental results, let us consider some limit cases.

If x and y are independent, as was said above, $r(p,q)=0$. On the other hand, in case of perfect proportionality $x=K.y$, where K is a constant, or for “random proportionality” $x=\kappa.y$, where κ is a random variable independent on y , it is readily seen that

$$r(p,q) = \zeta_y(p) + \zeta_y(q) - \zeta_y(p+q). \quad (16)$$

In particular, one may note that $r(p,q)>0$ due to the convexity of the scaling functions $\zeta(p)$. This relation can be

directly tested to verify the random proportionality hypothesis. Furthermore, the shape of the surface obtained is symmetric in the p - q plane.

Other simple situations may be considered: if $x=K.y^b$ with $b>0$ and K constant, or if $x=\kappa.y^b$ with κ random and independent of y , then one has

$$r(p,q) = \zeta_y(bp) + \zeta_y(q) - \zeta_y(bp+q). \quad (17)$$

Eq. (17) is still positive, but no more symmetric in the p - q plane; it is symmetric in the bp - q plane. In this framework, the value of b may be first estimated as the positive value such that

$$r(p,0) = r(0,bp) \quad (18)$$

Using the value estimated this way, this framework is then tested by verifying that $r(p/b,q)$ is indeed symmetric in the p - q plane. More generally speaking, the more $r(p,q)$ is positive, the more the $x=\Delta X_i$ and $y=\Delta Y_i$ are dependent random variables.

The main advantages of this framework are the following: (i) it makes no assumptions about the spectrum or the distribution of either data sets; (ii) it takes fully into account their intrinsic multiscaling properties; (iii) it may be used to provide much more fundamental relations between two patterns/processes; and iv) more generally it fully explores qualitatively and quantitatively the correlations of the fields x^p and y^q , revealing the correlations of large and low fluctuations of both processes.

Turbulent velocity fields

Turbulence measurements

Laboratory experiments

Turbulence has been generated by means of fixed PVC grids (diameter 2 mm, mesh size 1 cm) in a circular flume. Considering the dimensions of the flume and the flow velocities considered in the experiment (Table 1), we were dealing with a fully developed turbulence. A high-frequency (100 Hz) time series of instantaneous horizontal turbulent velocity was measured by hot-film velocimetry 10 and 20 cm behind the grid. The average turbulent energy dissipation rate was derived following the isotropic formula (*Tennekes and Lumley*, 1972):

$$\varepsilon = 15\nu \int_{k_{\min}}^{k_{\max}} k^2 E(k) dk \quad (19)$$

where ε is the turbulent energy dissipation rate ($m^2 s^{-3}$), k the wavenumber ($k = 2\pi/\lambda$, m^{-1}), λ the eddy wave-

length (m), k_{\min} and k_{\max} respectively the smallest and largest wavenumber resolved, and $E(k)$ the turbulence spectrum (m s^{-2}). The spectrum $E(k)$ is regarded as the mean-square amplitude of velocity fluctuations associated with a wavenumber of turbulent motion.

Table 1. Main characteristics of the grid-generated turbulence experiment (d : distance from the grid; Re : Reynolds number; N : numbers of time series analyzed).

d (cm)	Speed (m s^{-1})	ϵ ($\text{m}^2 \text{s}^{-3}$)	Re	N
20 cm	0.15	$2.86 \cdot 10^{-8}$	$45 \cdot 10^3$	5
	0.20	$3.54 \cdot 10^{-6}$	$60 \cdot 10^3$	5
	0.25	$9.14 \cdot 10^{-6}$	$75 \cdot 10^3$	5
	0.30	$1.36 \cdot 10^{-5}$	$105 \cdot 10^3$	5
	0.35	$1.64 \cdot 10^{-5}$	$105 \cdot 10^3$	5
	0.40	$1.82 \cdot 10^{-5}$	$120 \cdot 10^3$	5
10 cm	0.15	$1.01 \cdot 10^{-7}$	$45 \cdot 10^3$	4
	0.20	$1.24 \cdot 10^{-5}$	$60 \cdot 10^3$	5
	0.25	$3.2 \cdot 10^{-5}$	$75 \cdot 10^3$	5
	0.30	$4.75 \cdot 10^{-5}$	$105 \cdot 10^3$	5
	0.35	$5.75 \cdot 10^{-5}$	$105 \cdot 10^3$	5
	0.40	$6.36 \cdot 10^{-5}$	$120 \cdot 10^3$	5

To investigate potential differences in the structure of velocity fields in relation to the different levels of the turbulent kinetic energy, we analyzed here 5 time series of 1 min duration (i.e., 6000 data points) for 5 flow velocities at the two locations considered behind the grid.

Field experiments

Measurements of the turbulence fields were done using TurboMAP (Turbulence Ocean Microstructure Acquisition Profiler), a free-fall integrated system housed in an HCR treated aluminum pressure case, specifically designed for concurrent measurements of turbulent parameters (shear, $\partial u / \partial z$, where u and z are the turbulent fluctuating cross-stream velocity component and the depth, respectively), hydrographic parameters (pressure, temperature and conductivity) and bio-optical parameters (*in vivo* fluorescence and backscatter). All sensors are set into a parabolically shaped cap at the top of the pressure case. This arrangement ensures that these sensors point into an undisturbed flow. All signals are simultaneously sampled at 256 Hz and stored internally in a PCMCIA memory card. More details on the description and evaluation of both design and performance of this instrument can be found in Wolk

et al. (2001 a,b).

In this paper, we focus only on the ability of this new high-resolution biophysical profiler to measure the shear signal, $\partial u / \partial z$. In that way, we use 8 vertical shear profiles, recorded on 21 August 1998 in a tidal channel located between Neko-Seto and Meneko-Seto Straits (Japan). The sampling location has been chosen because this area is characterized by very strong tidal currents (up to 180 cm s^{-1}), associated with channel narrowing, and a subsequent high tidal mixing (Takasugi et al., 1994a, b).

The turbulent velocity fluctuations are measured with a standard piezo-ceramic shear probe, which has extensively been described elsewhere (e.g., Lueck et al., 1997). The probe is associated with three orthogonal accelerometers mounted inside the pressure case and is used to quantify noise level of velocity shear and to clean the shear signal of possible narrow-band contaminations from vehicle vibrations (Levine and Lueck, 1999).

To recover the turbulent fluctuating velocity u from $\partial u / \partial z$, we run an anti-derivative digital filter over the shear data, which consists of a scaled single-pole low-pass filter with a cut-off frequency f_c . The f_c is a function of the integration time scale t_i as $f_c = 1/2.3t_i$ [see Wolk and Lueck (2001) for further details]. Here we used $t_i = 7.5 \text{ s}$ and $f_c = 0.06 \text{ Hz}$, leading to a maximum wavelength resolved to 10 m. The lowest frequency resolved is determined by the high-pass filtering of the shear probe signal to minimize pyro-electric effects (70 Hz).

The vertical distribution of the turbulent kinetic energy dissipation rates ϵ has been estimated, after systematic denoising and despiking, from shear power spectra computed for 512 successive segments of shear (i.e., every meter considering an average profiler sinking velocity of 0.5 m s^{-1}) following the isotropic formula defined above in Eq. (19).

Considering the extreme fluctuations observed in the vertical distribution of the dissipation rates ϵ (Fig. 1), our analysis has been conducted on all the 512 data point segments available within each vertical profile (Table 2).

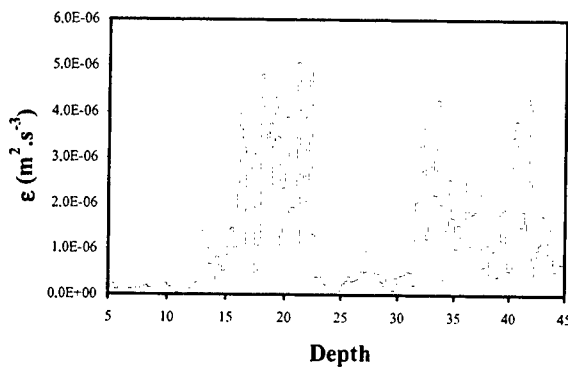


Figure 1. Example of the intermittent character of the vertical distribution of the kinetic energy dissipation rate ε , which has been estimated every meter using Eq. (19).

Table 2. Depth, numbers of 512 data points subsections, and mean of the turbulent kinetic energy dissipation rate ε ($\text{m}^2 \text{s}^{-3}$), for each of the eight vertical profiles.

Data set	N	n	ε
1	14463	28	$1.80 \cdot 10^{-8}$
2	20479	40	$1.87 \cdot 10^{-7}$
3	21887	43	$6.98 \cdot 10^{-8}$
4	18431	36	$6.43 \cdot 10^{-8}$
5	10495	20	$9.61 \cdot 10^{-8}$
6	22911	45	$1.33 \cdot 10^{-6}$
7	29949	58	$3.72 \cdot 10^{-7}$
8	17279	34	$5.65 \cdot 10^{-8}$

Characterizing turbulent velocity fields

The velocity spectra exhibit a scaling behavior ranging between 0.185 ± 0.1 m and 0.013 ± 0.015 m for velocity fluctuations measured in our circular flume, and between 1.0 ± 0.1 m and 0.050 ± 0.005 m for the velocity fluctuations estimated from shear data recorded in the field (Fig. 2). These scaling behaviors are qualitatively close (we try a quantification later) to the theoretical $-5/3$ Kolmogorov's power law over roughly 1.1 and 1.3 decades, respectively, with $\beta_v \approx 1.70$ in both cases. The ranges of scales defined that way will be regarded as the inertial subrange.

The estimates of the velocity structure functions $\langle (\Delta V_i)^q \rangle$ confirm the scaling regimes previously shown by spectral analysis for different orders of moment q (Fig. 3). Estimated scale ratios, highest and lowest wavenumbers of scaling ranges observed for the 512 data points subsections considered within each profile, exhibit very similar patterns to those observed in the spectral framework. We

refer the reader to Table 1 for further details. We subsequently computed the scaling exponents $\zeta(q)$ for several values of q between 0 and 10 (i.e. with 0.1 increments) for the range of scales where $\zeta_v(3)=1$ is valid; this range of scales characterizes here the inertial subrange. The scaling of the second-order moments $\zeta_v(2)$ confirms the estimates of the spectral exponents β_v [$\beta_v = 1 + \zeta_v(2)$, Eq. (7)]: $\zeta_v(2) = 0.710 \pm 0.010$ for grid-generated turbulence and $\zeta_v(2) = 0.705 \pm 0.005$ for ocean turbulence.

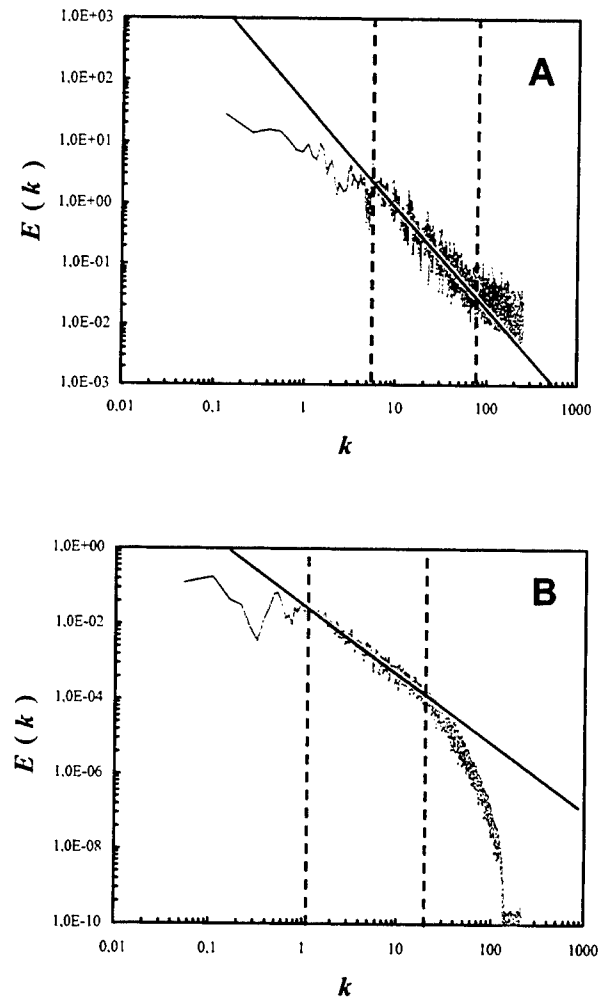


Figure 2. Samples of the power spectral density $E(k)$ of turbulent velocity fluctuations recorded with a hot-film velocimeter (A) located behind a grid in a circular flume, and (B) in a tidally mixed tidal channel, shown in log-log plots as a function of the wavenumber k (m^{-1}). The vertical dotted lines indicate the inertial subrange over which the spectra roughly follow the power-law form $E(k) \propto k^{-\beta_v}$, with $\beta_v \approx 5/3$ (continuous lines).

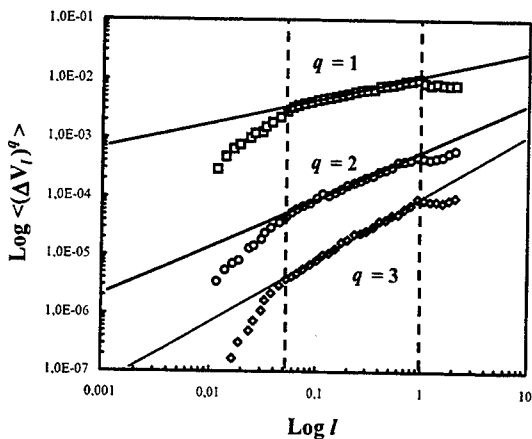


Figure 3. The velocity structure functions $\langle(\Delta V_i)^q\rangle$ of ocean velocity versus the length scale l in a log-log plot for various values of the statistical order of moment q (i.e., $q = 1, 2$ and 3 , from top to bottom). Linear trends are clearly visible, whatever the order of moment q (continuous lines), and indicate the multiscaling nature of our datasets. The vertical dotted lines correspond to the upper and lower limits of the inertial subrange. Note that the different scaling ranges (estimated from the profile shown in Fig. 2a) are indistinguishable from the one estimated from spectral analysis.

More generally, the clear nonlinearity of the functions $\zeta_v(q)$ (Fig. 4) is direct evidence for the multifractal nature of the velocity fluctuations. Moreover, within experimental error, the functions $\zeta_v(q)$ for grid-generated and ocean turbulent velocity fluctuations cannot be qualitatively shown as being different. While the similarity observed in the shape of the functions $\zeta_v(q)$ qualitatively suggests some convergent behavior in the high-order structure of velocity fluctuations, the values of the universal multifractal parameters C_{1e} and α_e lead to specifying these results. These parameters have been estimated as $C_{1e} = 0.18 \pm 0.02$, and $\alpha_e = 1.52 \pm 0.03$ for grid-generated turbulence, and $C_{1e} = 0.16 \pm 0.02$ and $\alpha_e = 1.55 \pm 0.04$ for ocean turbulence. That leads to confirmation that the structure of velocity fluctuations recorded in the field and in the laboratory cannot be regarded as being significantly different.

On the other hand, the parameters C_{1v} , estimated using C_{1e} and α_e in Eq. (9) as $C_{1v} = 0.032 \pm 0.02$, appear slightly smaller than the values reported in the literature for the parameters C_{1v} characterizing the intermittent behavior of temperature and salinity in highly dissipative areas:

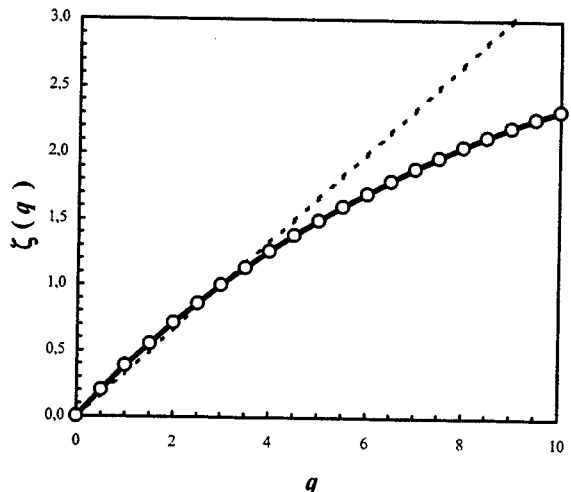


Figure 4. The scaling exponents structure function $\zeta_v(q)$ empirical curves (open dots) estimated from grid-generated turbulent velocity fluctuations, compared to the monofractal curve $\zeta_v(q) = q/3$ (dashed line), and to the universal multifractal curve (thick continuous curve) obtained with $C_{1e} = 0.18$ and $\alpha_e = 1.52$ in Eq. (5).

$C_{1v} \in [0.035 - 0.060]$ and $C_{1s} \in [0.035 - 0.062]$ (Seuront *et al.*, 1996a,b, 1999, 2001a). This implies that the temperature and salinity fields are much more intermittent than the velocity field; this high intermittency can be related to the strong discontinuities ("ramps") observed in the temperature signals (Sreenivasan, 1991; Pumir, 1994b). Intermittency for passive scalars, in both two and three dimensions, has also been studied in direct numerical simulations (Holzer and Siggia, 1994; Pumir, 1994a,b). Such simulations often reveal extended regions of almost uniform temperature separated by boundary layers (ramps) with strong gradients.

We should finally note that the multifractal parameters C_{1e} and α_e obtained here for the very first time for oceanic turbulence are very similar to the parameters estimated for atmospheric turbulence: $C_{1e} = 0.15 \pm 0.03$ and $\alpha_e = 1.50 \pm 0.05$ (Fig. 5; Schertzer *et al.*, 1995; Schmitt *et al.*, 1992a, b, 1993, 1996; Chigirinskaya *et al.*, 1994). As previously noticed by Seuront *et al.* (2001b), these results suggest a strong similarity of the intermittent nature of turbulent velocity fluctuations in the atmosphere and the ocean. The resolution of this particular issue, well beyond the scope of the present paper, is in progress. In particular, the question is whether atmospheric and oceanic temperature fields behave in a similar fashion (Seuront and Yamazaki, 2001; Seuront *et al.*, 2001c).

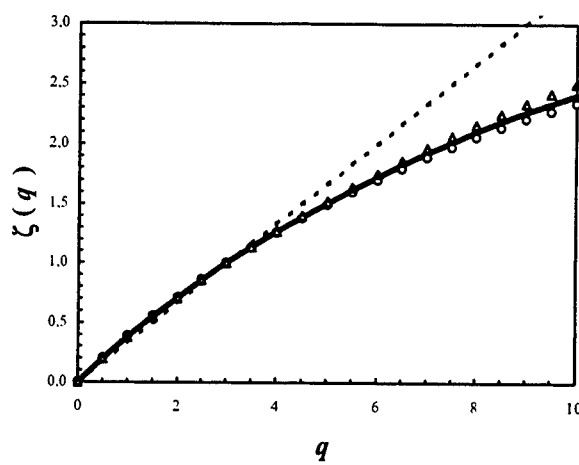


Figure 5. Comparison of the empirical values of the functions $\zeta_v(q)$ estimated from grid generated turbulence (open dots) and field ocean turbulence (open triangles), with the universal multifractal fit obtained with C_{1e} and α_e values characteristic of atmospheric turbulence, i.e. $C_{1e} = 0.15$ and $\alpha_e = 1.50$ in Eq. (5). The linear curve $\zeta_v(q) = q/3$ expected in case of non-intermittent turbulence is shown for comparison (dashed line).

Ocean passive and “biologically active” scalars

Phytoplankton of the Eastern English Channel

In a recent paper, Seuront *et al.* (1999) showed that the small-scale intermittent distribution of temperature (a scalar quantity passively advected by turbulent fluid motions) and phytoplankton biomass recorded in the coastal waters of the Eastern English Channel were indistinguishable, both in spectral and multifractal framework (Fig. 6). They subsequently concluded their study stating that phytoplankton biomass could be regarded as a purely passive scalar at small scales. Here, small scales correspond to temporal scales bounded between 1 and 20 seconds. Using the Taylor’s theory of frozen turbulence, these temporal scales can be related to spatial scales bounded between 0.1 and 22 meters. For larger scales, the phytoplankton biomass exhibits a very specific heterogeneous distribution, dominated by biological processes resulting from complex interactions between the turbulence level of fluid motions (mainly different tidal conditions related to both ebb/flood and neap/spring tidal cycles), the phytoplankton biomass concentration, and the specific composition of phytoplankton assemblages (Seuront *et al.*, 1996b; Seuront *et al.*, 1999). These larger scales are not investigated in the present work.

Table 3. Mean values of the empirical estimates of the spectral exponent β_F , and the universal multifractal parameters H_F , C_{1F} and α_F for subsets of *in vivo* fluorescence time series recorded under different levels of turbulence.

$\epsilon (\text{m}^2 \cdot \text{s}^{-3})$	β	H	C_1	α
$1 \cdot 10^{-6}$	1.76	0.43	0.060	1.80
$5 \cdot 10^{-6}$	1.76	0.43	0.055	1.82
$1 \cdot 10^{-5}$	1.77	0.42	0.050	1.80
$5 \cdot 10^{-5}$	1.78	0.42	0.045	1.81
$1 \cdot 10^{-4}$	1.78	0.41	0.040	1.80

Turbulence and phytoplankton patchiness

Considering the role played by turbulence in the formation and disruption of particle aggregates [e.g., Kiørboe (1997) and references therein], and the highly varying dissipation rates of turbulent energy observed over a tidal cycle in this area (between 10^{-6} and $10^{-4} \text{ m}^2 \cdot \text{s}^{-3}$; Seuront *et al.*, 2001a), the question here is whether the local hydrodynamic conditions have an effect on both temperature and phytoplankton biomass local distributions.

The original 46 h 24 min time series recorded at 1 Hz (i.e., 167040 data; Seuront *et al.*, 1999) has then been divided into 46 subseries of 1 h (i.e., 3600 data). We then built 5 sets of 7 subseries, each set corresponding to a different level of dissipation rates ranging from $\epsilon = 10^{-6} \text{ m}^2 \cdot \text{s}^{-3}$ to $\epsilon = 10^{-4} \text{ m}^2 \cdot \text{s}^{-3}$. We then conducted both spectral and multifractal analyses on each subseries of temperature and *in vivo* fluorescence within a given subset, and the resulting observations led to different comments (Table 3).

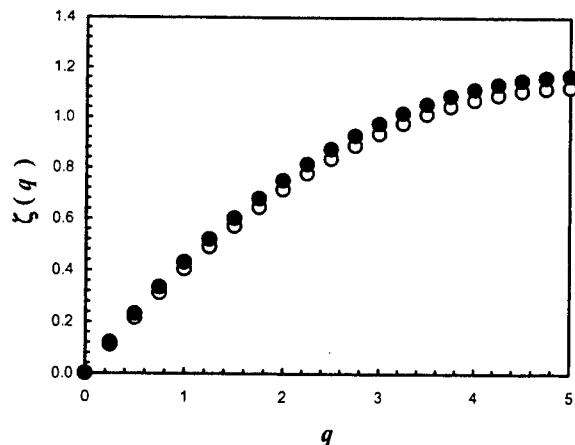


Figure 6. Comparison of the functions $\zeta_T(q)$ (open dots) and $\zeta_F(q)$ (black dots) estimated from small scale (<20 seconds) temperature and *in vivo* fluorescence fluctuations; (adapted from Seuront *et al.*, 1999).

The slopes β_T and β_F , estimated for the frequency bands that maximized the coefficient of determination and minimized the total sum of squared-residuals for the regression in log-log plots of the temperature and fluorescence power spectra [cf. Eq. (2)], cannot be statistically distinguished within each set of temperature and fluorescence subseries (analyses of covariance, $p > 0.05$), nor between the 5 sets considered ($p > 0.05$). These results, fully congruent with previous studies conducted in the same area (Seuront *et al.*, 1996a, b, 1999, 2001a), suggest extreme similarity between the single scaling properties of small-scale temperature and fluorescence distributions. At this stage, phytoplankton biomass can then still be regarded as being a passive scalar.

The nonlinear behavior of the functions $\zeta(q)$ confirms and generalizes in different hydrodynamic regimes the multifractal nature of temperature and *in vivo* fluorescence observed by Seuront *et al.* (1999) using a global approach of the same data set (Fig. 6). However, the functions $\zeta_T(q)$ obtained for temperature time series remain similar whatever the external hydrodynamic forcing (i.e., the values of the dissipation rate ε), while the nonlinearity (i.e., convexity) of the functions $\zeta_F(q)$ characterizing phytoplankton biomass clearly increases when the value of the dissipation rate ε decreases (Fig. 7).

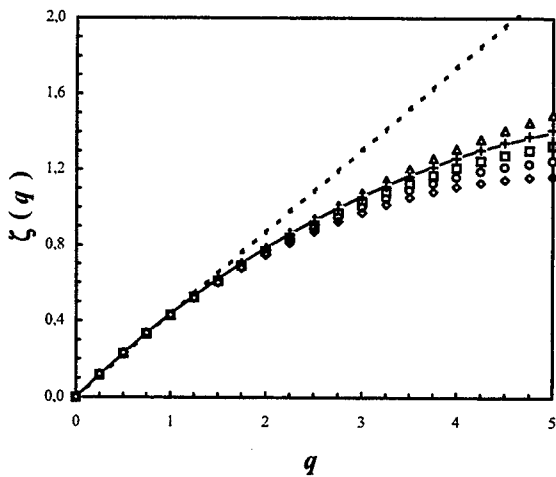


Figure 7. Comparison of the empirical values of the functions $\zeta(q)$ estimated for temperature (continuous curve) and *in vivo* fluorescence for different values of the turbulent kinetic energy dissipation rate ε ($\varepsilon = 10^{-6} \text{ m}^2 \text{s}^{-3}$, rhombs; $\varepsilon = 5 \times 10^{-6} \text{ m}^2 \text{s}^{-3}$, circles; $\varepsilon = 10^{-5} \text{ m}^2 \text{s}^{-3}$, squares; $\varepsilon = 5 \times 10^{-5} \text{ m}^2 \text{s}^{-3}$, crosses; $\varepsilon = 10^{-4} \text{ m}^2 \text{s}^{-3}$, triangles). The linear curve $\zeta_T(q) = qH$ expected in case of non-intermittent turbulence is shown for comparison (dashed line).

The distribution of temperature then remains the same whatever the hydrodynamic conditions. This result is convergent with our previous observations regarding the distribution of turbulent velocity fields, and it confirms the passive scalar behavior of temperature.

On the other hand, the distribution of phytoplankton biomass is less intermittent and is closer to that of temperature in high turbulent conditions (Fig. 7). This suggests that phytoplankton cells behave more like a passive scalar under high hydrodynamic conditions but exhibit very specific properties under lower levels of turbulence.

The universal multifractal parameters H , C_1 , and α confirm these qualitative observations (Table 3). Let us remember here that the parameters H , C_1 , and α have been obtained by fitting the universal multifractal model detailed in Eq. (6) to the empirical function $\zeta(q)$ as described above. These parameters remain constant for temperature time series with $H_T = 0.40$, $C_{1T} = 0.05$ and $\alpha_T = 1.90$. On the other hand, it is shown that only H and C_1 remain roughly constant for fluorescence, with $H_F = 0.42 \pm 0.01$ and $\alpha_F = 1.81 \pm 0.01$ [values compatible with the $H_F = 0.43$ and $\alpha_F = 1.80$ found by Seuront *et al.* (1999)]. However, the parameter C_{1F} is highly variable. It increases 33% when the dissipation rate ε decreases from the highest to the lowest values experienced over a tidal cycle, i.e. from $\varepsilon = 10^{-4}$ to $\varepsilon = 10^{-6} \text{ m}^2 \cdot \text{s}^{-3}$. Under low hydrodynamic conditions the higher values of C_{1F} indicate the occurrence of few patches of high phytoplankton concentrations that are several orders of magnitude above background levels. Under higher hydrodynamic conditions the lower values of C_{1F} indicate that phytoplankton cells are more homogeneously distributed and behave as a passive scalar. Here the so-called homogenization effect is thought to be associated with the disruption of these phytoplankton patches. This hypothesis is supported by the C_{1F} values observed for fluorescence time series under high hydrodynamic conditions, which cannot be distinguished from the C_{1F} values estimated for temperature irrespective of hydrodynamic conditions, and by the extreme similarity of the empirical functions $\zeta_T(q)$ and $\zeta_F(q)$ in high hydrodynamic conditions (Fig. 7).

Turbulence and biophysical couplings

In order to investigate the nature of the dependence between temperature and phytoplankton distributions, we subsequently computed the Generalized Correlation Functions, $c(p,q)$ and the related Generalized Correlation Exponents, $r(p,q)$, between temperature and fluorescence

time series, within each subset defined above.

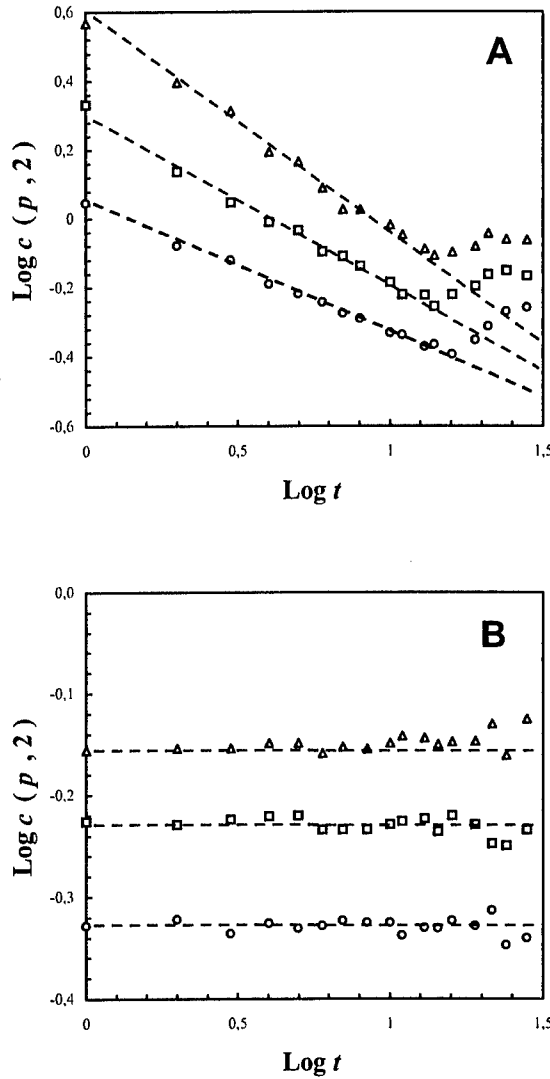


Figure 8. The Generalized Correlation Functions (GCF) $c(p,q)$ versus the time scale t in log-log plots, for (A) simultaneously and (B) independently sampled temperature and *in vivo* fluorescence time series. The function $c(p,q)$ shown here has been estimated for a constant value of the statistical order of moment q of temperature fluctuations ($q = 2$), and various values of the statistical order of moment p of *in vivo* fluorescence (i.e. $p = 1, 2$ and 3 , from bottom to top). The slopes of the linear regression estimated over the scaling ranges (dashed lines) provide estimates of the Generalized Correlation Exponents (GCE) $r(p,q)$.

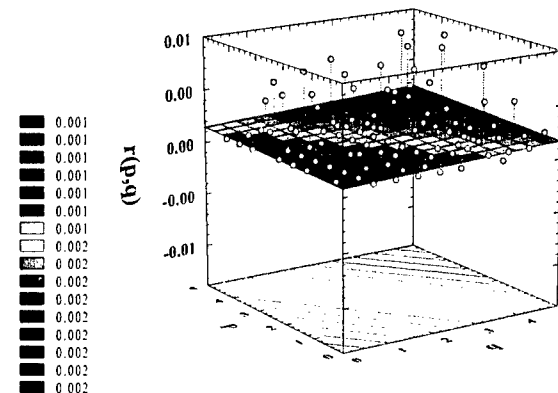


Figure 9. The Generalized Correlation Exponents (GCE) $r(p,q)$, shown as a function of both p and q , which characterize *in vivo* fluorescence and temperature fluctuations, respectively. The function $r(p,q)$ is estimated here between time series of temperature and fluorescence independently sampled (C).

Figure 8 shows the GCF, $c(p,q)$, plotted in log-log plots versus the time scale t , for simultaneously recorded temperature and fluorescence time series (Fig. 8a), as well as for temperature and fluorescence time series taken at different moments of the tidal cycle, and *a fortiori* independent (Fig. 8b). Both the linear behavior of the functions $c(p,q)$ over scales ranging between 1 and 20 seconds, and the positive values taken by the GCE, $r(p,q)$, estimated as the slope of the linear trend of the GCF $c(p,q)$ vs. t in a log-log plot, whatever the combinations of p and q values (Fig. 8a) confirm the validity of Eq. (11). On the other hand, the weak values taken by the functions $c(p,q)$ estimated between independent temperature and fluorescence time series (Fig. 8b) indicate a low correlation between the temperature and phytoplankton biomass fluctuations, $\langle(\Delta T_i)^q\rangle$ and $\langle(\Delta F_i)^p\rangle$. This is confirmed by the related values of the functions $r(p,q)$, which remain close to zero, whatever the combinations of p and q values (Fig. 9).

We subsequently refined these observations, comparing the functions $r(p,q)$ obtained between temperature and fluorescence time series in different turbulent conditions. Figure 10 then shows the $r(p,q)$ obtained for all the combinations of p and q values with 0.1 increments, for three levels of turbulence (10^{-4} , 10^{-5} and $10^{-6} \text{ m}^2 \text{ s}^{-3}$). It appears that the correlation between temperature and *in vivo* fluorescence fluctuations increases with hydrodynamic conditions and is weaker, even nil, in low turbulent conditions.

We confirm here the increased physical control suggested under strong turbulent conditions from the analysis of the shape of the function $\zeta_r(q)$, and its comparison

with the function $\zeta_r(q)$; see Figure 7. On the other hand, the decorrelation between temperature and phytoplankton fluctuations under weak turbulent conditions suggests an increase in the biological contributions to the control of phytoplankton biomass distribution, and confirms previous observations (cf. Fig. 7). Phytoplankton distribution then appears independent of the temperature distribution under the lowest turbulence levels investigated here, i.e., $10^{-4} \text{ m}^2 \text{ s}^{-3}$ (Fig. 10a).

More precisely, the shape of the function $r(p,q)$ indicates that large phytoplankton fluctuations are associated—under strong enough turbulent conditions—to weak temperature gradients, and conversely. This tendency seems to reflect, over a slightly wider range of scales, findings of Desiderio *et al.* (1993); they observed the occurrence of 0.1-0.2 meter thick fluorescent layers just above local temperature gradients. While these qualitative comments suggest a proportionality relationship between temperature and phytoplankton fluctuations, the relation (16) has never been verified. The phytoplankton fluctuations then cannot be regarded as strictly proportional or randomly proportional to the fluctuations of temperature, i.e., $\Delta F = K \cdot \Delta T$ and $\Delta F = \kappa \cdot \Delta T$, respectively. In contrast, the relation (17) has been verified testing the validity of Eq. (18) over a wide range of b values. Using b values ranging between 0.05 and 5 (with 0.05 increments), we then showed that Eq. (18) is verified for three of the five levels of turbulence investigated here: $\varepsilon = 10^{-4} \text{ m}^2 \text{ s}^{-3}$ with $b = 2.69$, $\varepsilon = 5.10^{-4} \text{ m}^2 \text{ s}^{-3}$ with $b = 2.25$, and $\varepsilon = 10^{-5} \text{ m}^2 \text{ s}^{-3}$ with $b = 1.76$. Figure 11 shows the relation $r(p,0)$ vs. $r(0,bp)$ corresponding to the functions $r(p,q)$ shown in Fig. 10b and c, with $b = 2.69$ and $b = 1.76$, respectively. The correlation shown between temperature and phytoplankton fluctuations under high turbulent conditions, is then related to a power-law dependence relationship, i.e. $\Delta F = \kappa \cdot (\Delta T)^b$.

Let us mention here that at this stage of the development of the multiscaling techniques illustrated in the present paper, the presence and the absence of evidence for power-law dependence between phytoplankton and temperature fluctuations cannot (*a priori*) be regarded as a general rule driving biophysical couplings in pelagic ecosystems. Indeed, the relationship between temperature and *in vivo* fluorescence or, more generally, biophysical couplings, can be influenced, and then complexified, by both the processes related to phytoplankton cells ecology and to the sampling strategy. Over the range of scales investigated in the present study, *in vivo* fluorescence fluctuations can indeed result from nonlinear interactions between the physiological state of phytoplankton cells, their related coagulation ability, the specific composition of phytoplankton assemblages, the grazing impact of copepods

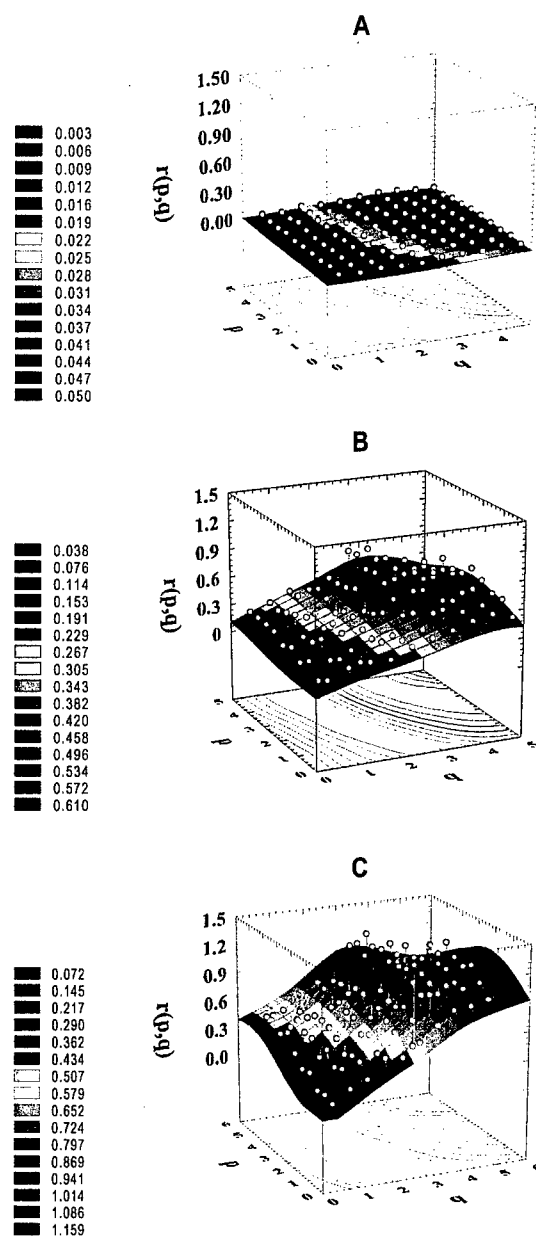


Figure 10. The Generalized Correlation Exponents (GCE $r(p,q)$), shown as a function of both p and q . Here the statistical orders of moment p and q characterize temperature and *in vivo* fluorescence fluctuations, respectively. The functions $r(p,q)$ correspond to three different levels of turbulence, i.e. (A) $\varepsilon = 10^{-6}$ (B), 10^{-5} , and (C) $10^{-4} \text{ m}^2 \text{ s}^{-3}$.

(shown recently to influence both spectral and multifractal properties of phytoplankton biomass; *Seuront*, 1999; *Lovejoy et al.*, 2001), and the turbulent processes. The resulting fluctuations can then be potentially more complex than those observed for a purely passive scalar such as temperature.

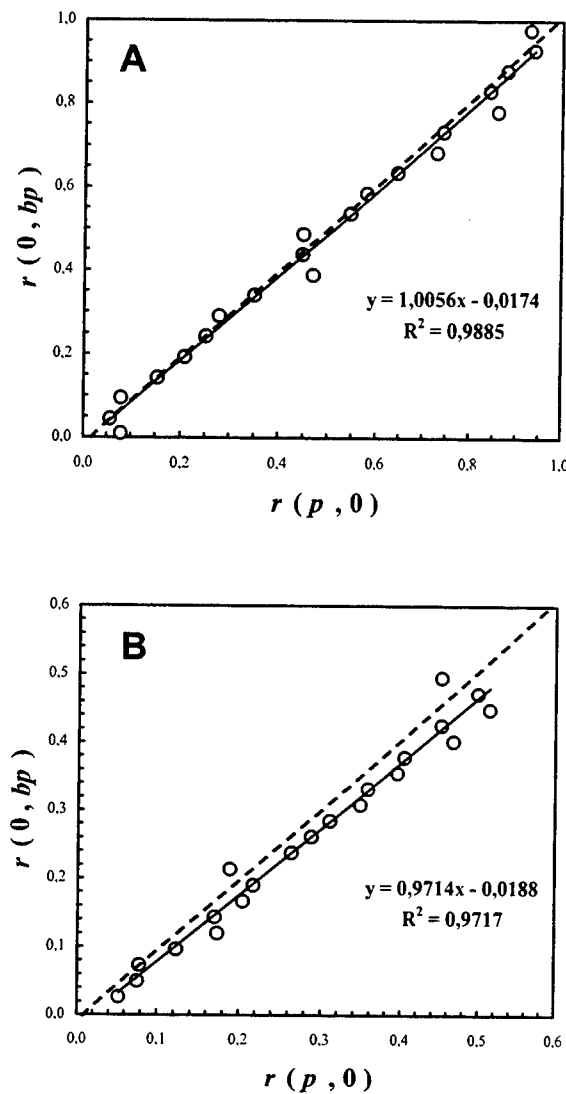


Figure 11. Plots of the Generalized Correlation Exponents $r(p,0)$ versus $r(0,bp)$ for two levels of turbulence, $\epsilon = 10^{-4}$ with $b = 2.69$ (A) and $\epsilon = 10^{-5}$ with $b = 1.76$ (B). The slopes of the regression lines (continuous line) cannot be distinguished from that of the relation $bp = q$ (dashed line). This shows the validity of Eq. (18) and the symmetry of the functions $r(p,q)$ in the $bp-q$ plane.

On the other hand, considering (i) the highly intrusive character of the sampling device used to record temperature and *in vivo* fluorescence (a Sea-Bird 25 Sealogger CTD probe and a Sea Tech fluorometer, respectively), and (ii) the spatial separation of the temperature and fluorescence sensors (≈ 10 cm), it is reasonable to think that the most extreme events, which are also the most infrequent and contribute to the highest values of the moments p and

q , are not necessarily simultaneously sampled in a proper way, leading to spurious joint high-order properties. In particular, this could explain the weakening of the Generalized Correlation Exponents, $r(p,q)$, for values of the moments p and q such as $p \geq 4$ and $q \geq 4$. The latter limitation will be easily fixed in the near future with the increasing development and availability of microstructure profilers able to record both physical and biological parameters with a high-spatial resolution from mildly intrusive sensors (Seuront *et al.*, 2001d,e). The former limitation will be difficult to overcome, because of the intrinsic physiological, biological, and ecological processes affecting phytoplankton populations.

Conclusions: the cost and gain of increasing analysis complexity

Our results demonstrate that single scaling properties of temperature and phytoplankton would have erroneously led to conclude that the latter could be regarded as a purely passive scalar. However, investigations of their detailed variability in the universal multifractal framework lead to consideration that phytoplankton biomass presents very specific properties, depending on the intensity of local turbulent processes. This suggests a differential control of phytoplankton biomass distribution involving complex interactions between turbulent velocity fields and the involved particles properties such as buoyancy, size, density or aggregative properties. In particular, this assertion is supported by the specific behavior of phytoplankton multiscaling properties under low turbulent conditions, suggesting the prevalence of phytoplankton cells specific properties on turbulent processes.

This has been confirmed and specified by the introduction of the Generalized Correlation Functions/Exponents. The correlation—and then the couplings—between temperature and phytoplankton biomass fluctuations are thus higher under high hydrodynamic forcing and decrease progressively to collapse under low hydrodynamic forcing. In particular, careful examination of the functions $r(p,q)$ indicates that large phytoplankton fluctuations are associated—under strong enough turbulent conditions—with weak temperature gradients, and conversely. These results are fully congruent with more intuitive and qualitative results by Desiderio *et al.* (1993) over similar scales and Wolk *et al.* (2001) at smaller scales. Whatever that may be, even if additional work and data sets will be needed to achieve more definitive functional scenarios, the joint multifractal framework introduced here provides the first objective method to characterize, both qualitatively and quantitatively, the details of the relationships between any pair of simultaneously recorded patterns or processes. In

particular, this framework makes no assumptions about the spectrum or the distribution of either data sets, and it takes fully into account their intrinsic multiscaling properties. We should also note here that this work provides the very first evidence of the multifractal character of ocean turbulent velocity fluctuations, and reveals their extreme similarity in the ocean and the atmosphere.

Finally, regarding the additional quantity of information brought by the univariate and bivariate multiscaling procedures described here to our understanding of the structure of velocity, temperature and phytoplankton fluctuations, as well as of the couplings between temperature and phytoplankton biomass, we claimed, as already stressed elsewhere (e.g., Yamazaki, 1993; Seuront, 2001; Seuront *et al.*, 2001c), that taking into account the reality of the intermittent nature of bio-physical microstructures could be the first step towards a general understanding of structures and functions in marine pelagic ecosystems. The quite elevated cost associated with making use of the single and joint multifractal tools presented here in terms of algorithmic developments and computation time consumption will then be easily overcome by the priceless gain in emerging knowledge.

Acknowledgments. We are grateful to Prof. C. Garrett for his kind invitation to participate to the 'Aha Huliko'a winter workshop, and for his interest and constructive comments on the earliest version of this work. This work has been initiated while LS was a postdoctoral fellow granted by the Japan Society for the Promotion of Science (grant JSPS99756), and hosted by Prof. H. Yamazaki at the Tokyo University of Fisheries. We especially thank F. Wolk for his help in recovering the turbulent velocity from the shear signal and computing the dissipation rates, as well as for his highly stimulating conversation. We also greatly acknowledge Drs. F. Chavez, M.B. Matthews, J.G. Mitchell, R.G. Lueck, S. Souissi, PG Strutton and H. Yamazaki for constructive discussions about the GCF/GCE framework. We finally acknowledge all the participants of the 'Aha Huliko'a winter workshop for their stimulating scientific company, especially M. Barry, A. Mahadevan, A. Natarov, R. Ferrari, G. Holloway, D.L. Rudnick and W. Young.

References

- Batchelor G.K., and A.A. Townsend, The nature of turbulent motion at large wavenumbers. *Proc. Roy. Soc. A*, **199**, 238-250, 1949.
- Chigirinskaya, Y., D. Schertzer, S. Lovejoy, A. Lazarev, and A. Ordanovich, Unified multifractal atmospheric dynamics tested in the tropics: horizontal scaling and self criticality. *Nonlinear Proc. Geophys.*, **1**, 105-114, 1994.
- Corrsin, S., On the spectrum of isotropic temperature in an isotropic turbulence. *J. Appl. Phys.*, **22**, 469, 1951.
- Cowles, T.J., R.A. Desiderio, and M.E. Carr, Small-scale planktonic structure: persistence and trophic consequences, *Oceanography*, **11**, 4-9, 1998.
- Desiderio, R.A., T.J. Cowles and J.N. Moum, Microstructure profiles of laser-induced chlorophyll fluorescence spectra: evaluation of backscatter and forward-scatter fiber-optic sensors, *J. Atmos. Oceanic Tech.*, **10**, 209-224, 1993.
- Frish, U., *Turbulence*, Cambridge University Press, 1995.
- Gibson, C.H., Kolmogorov similarity hypotheses for scalar fields: sampling intermittent turbulent mixing in the ocean and galaxy, *Proc. R. Soc. London A*, **434**, 149-164, 1991.
- Holzer, M., and E.D. Siggia, Turbulent mixing of a passive scalar. *Phys. Fluids*, **6**, 1820-1837, 1994.
- Jiménez, J., Intermittency and cascades, *Sci. Mar.*, **409**, 99-120, 2000.
- Jou, D., Intermittent turbulence: a short introduction, *Sci. Mar.*, **61**, 57-62, 1997.
- Kiørboe, T., Small-scale turbulence, marine snow formation, and planktivorous feeding, *Sci. Mar.*, **61**, 141-158, 1997.
- Kitanidis, P.K., *Introduction to Geostatistics. Applications in Hydrogeology*. Cambridge University Press, 1997.
- Kolmogorov, A.N., The local structure of turbulence in incompressible viscous fluid for very large Reynolds numbers. *Dokl. Akad. Nauk. SSSR*, **30**, 299-303, 1941.
- Legendre, L., and P. Legendre, *Ecologie numérique*, Masson, 1984.
- Lovejoy, S., W.J.S. Currie, Y. Teissier, M.E. Claereboudt, E. Bourget, J.C. Roff and D. Schertzer, Universal multifractals and ocean patchiness: phytoplankton, physical fields and coastal heterogeneity. *J. Plankton Res.*, **23**, 117-141, 2001.
- Levine, E.R., and R.G. Lueck, Turbulence measurement from an autonomous underwater vehicle. *J. Atmos. Oceanic Technol.*, **16**, 1533-1544, 1999.
- Lueck, R.G., and F. Wolk, An efficient method for determining the significance of covariance estimates. *J. Atmosp. Ocean. Tech.*, **16**, 773-775, 1999.
- Lueck, R.G., D. Huang, D. Newman, and J. Box, Turbulence measurements with an autonomous moored instrument. *J. Atmos. Oceanic Technol.*, **14**, 143-161, 1997.
- Muzy, J.F., J. Delour, and E. Bacry, Modelling fluctuations of financial time series: from cascade process to stochastic volatility model. *Eur. J. Phys. B*, **17**, 537-548, 2000.
- Obukhov, A.M., Spectral energy distribution in a turbulent flow. *Dokl. Akad. Nauk. SSSR*, **32**, 22-24, 1941.
- Obukhov, A.M., Structure of the temperature field in a turbulent flow. *Izv. Akad. Nauk. S.S.R. Geogr. I Jeofiz.*, **13**, 55, 1949.
- Osborn, T., Finestructure, microstructure, and thin layers, *Oceanography*, **11**, 36-43, 1998.
- Parzen, E. *Stochastic Processes*, Holden day, 1962.
- Pascual, M., F.A. Ascioti, and H. Caswell, Intermittency in the plankton: a multifractal analysis of zooplankton biomass variability, *J. Plankton Res.*, **17**, 1209-1232, 1995.
- Pumir, A., A numerical study of the mixing of a passive scalar in three dimension in the presence of a mean gradient. *Phys. Fluids*, **6**, 2118-2132, 1994a.
- Pumir, A., Small-scale properties of scalar and velocity differences in three dimensional turbulence. *Phys. Fluids*, **6**, 3974-3984, 1994b.
- Samorodnitsky, G., and M.S. Taqqu, *Stable Non-Gaussian Random Processes: Stochastic Models with Infinite Variance*, Chapman & Hall, New York, 1994.

- Schertzer, D., and S. Lovejoy, Physical modeling and analysis of rain and clouds by anisotropic scaling multiplicative processes. *J. Geophys. Res.*, 92, 96-99, 1987.
- Schertzer, D., S. Lovejoy, and F. Schmitt, Structures in turbulence and multifractal universality. In *Small-scale Structure in 3D Fluid and MHD Turbulence*, (M. Meneguzzi, A. Pouquet and P.L. Sulem, eds.), Springer-Verlag, New York, 137-144, 1995.
- Schmitt, F., D. Lavallée, D. Schertzer, and S. Lovejoy, Empirical determination of universal multifractal exponents in turbulent velocity fields. *Phys. Rev. Lett.*, 68, 305-308, 1992a.
- Schmitt, F., D. Lavallée, S. Lovejoy, D. Schertzer, and C. Hooge, Estimations directes des indices de multifractals universels dans le champ de vent et de température. *C. R. Acad. Sci. Paris Sér. II*, 314, 749-754, 1992b.
- Schmitt, F., D. Schertzer, S. Lovejoy, and Y. Brunet, Estimation of universal multifractal indices for atmospheric turbulent velocity fields. *Fractals*, 1, 568-575, 1993.
- Schmitt, F., D. Schertzer, S. Lovejoy, and Y. Brunet, Multifractal temperature and flux of temperature variance in fully developed turbulence. *Europhys Lett.*, 34, 195-200, 1996.
- Seuront, L., Space-time heterogeneity and biophysical couplings in pelagic ecosystems, PhD Thesis, Université des Sciences et Technologies de Lille, 1999.
- Seuront, L., Microscale processes in the ocean: why are they so important for ecosystem functioning?, *La Mer*, 39, 1-8, 2001.
- Seuront, L., and H. Yamazaki, Testing multiscaling statistics of ocean velocity fields in the inertial subrange, *in preparation*, 2001.
- Seuront, L., F. Schmitt, D. Schertzer, Y. Lagadeuc, and S. Lovejoy, Multifractal intermittency of Eulerian and Lagrangian turbulence of ocean temperature and plankton fields. *Nonlin. Proc. Geophys.*, 3, 236-246, 1996a.
- Seuront, L., F. Schmitt, Y. Lagadeuc, D. Schertzer, S. Lovejoy, and S. Frontier, Multifractal analysis of phytoplankton biomass and temperature in the ocean, *Geophys. Res. Lett.*, 23, 3591-3594, 1996b.
- Seuront, L., F. Schmitt, Y. Lagadeuc, D. Schertzer, and S. Lovejoy, Universal multifractal analysis as a tool to characterize multiscale intermittent patterns: example of phytoplankton distribution in turbulent coastal waters, *J. Plankton Res.*, 21, 877-922, 1999.
- Seuront, L., V. Gentilhomme, and Y. Lagadeuc, Small-scale nutrient patches in tidally mixed coastal waters. *Mar. Ecol. Prog. Ser.*, *accepted*, 2001a.
- Seuront, L., F. Schmitt, and Y. Lagadeuc, Turbulence intermittency, small-scale phytoplankton patchiness and encounter rates in plankton: where do we go from here?, *Deep-Sea Res.*, I, 48, 1199-1215, 2001b.
- Seuront, L., F. Wolk, H. Yamazaki, and F. Schmitt, Universality of turbulent velocity and scalar fields fluctuations in the atmosphere and the ocean, *in preparation*, 2001c.
- Seuront, L., H. Yamazaki, A. Nihongi, and F. Wolk, Bio-physical properties of a tidal channel. I. Observations of phytoplankton and turbidity fine-scale distributions, *in preparation*, 2001d.
- Seuront, L., H. Yamazaki, J.G. Mitchell, and F. Schmitt, Bio-physical properties of a tidal channel. II. Analysis of phytoplankton and turbidity microscale distributions *in preparation*, 2001e.
- Sreenivasan, K.R., Fractals and multifractals in turbulence. *Ann. Rev. Fluid Mech.*, 23, 539-600, 1991.
- Takasugi, Y., A. Hoshika, H. Noguchi, and T. Tanimoto, The role of tidal vortices in material transport around straits. *J. Oceanogr.*, 50, 65-80, 1994a.
- Takasugi, Y., T. Fujiwara, and T. Sugimoto, Formation of sand banks due to tidal vortices around straits. *J. Oceanogr.*, 50, 81-98, 1994b.
- Tennekes, H., and J.L. Lumley, *A First Course in Turbulence*, MIT Press, Boston, 1972.
- Visser, A.W., Using random walks models to simulate the vertical distribution of particles in a turbulent water column, *Mar. Ecol. Prog. Ser.*, 158, 275-281, 1997.
- Yamazaki, H., Lagrangian study of planktonic organisms: perspectives, *Bull. Mar. Sci.*, 53, 265-278, 1993.
- Yamazaki, H., T. Osborn, and K.D. Squires, Direct numerical simulation of planktonic contact in turbulent flow, *J. Plankton Res.*, 13, 629-643, 1991.
- Wolk, F., and R.G. Lueck, Heat flux and mixing efficiency in the surface mixing layer, *J. Geophys. Res.*, *submitted*, 2001.
- Wolk, F., L. Seuront, and H. Yamazaki, Spatial resolution of a new micro-optical probe for chlorophyll and turbidity. *J. Tokyo University. Fish.*, 87, 13-21, 2001.
- Wolk, F., H. Yamazaki, L. Seuront, and R.G. Lueck, A new free-fall profiler for measuring biophysical microstructure. *J. Atmos. Oceanic Tech.*, *accepted*, 2001.

Laboratory experiments on diapycnal mixing in stratified fluids

M.E. Barry¹, G.N. Ivey¹, K.B. Winters², and J. Imberger¹

¹ Centre for Water Research, The University of Western Australia, Australia

² Applied Physics Laboratory, University of Washington, USA

Abstract. Our turbulent lengthscale, velocity and diffusivity scalings are compared with data from other numerical, laboratory and field experiments. Comparison is made with reference to the turbulence intensity measure $\epsilon/\nu N^2$. We showed that our turbulent lengthscale and velocity results are consistent with measurements from the experiments considered, and that the rms turbulent lengthscale L_t is independent of the rate of dissipation of turbulent kinetic energy when $\epsilon/\nu N^2 > 300$. A diffusivity modelled in terms of an advective buoyancy flux, b , is found to reproduce our direct measurements of K_ρ in the experiments considered when $\epsilon/\nu N^2 > 300$. It is shown that modelling K_ρ as $0.2\epsilon/N^2$ is a poor parameterisation of the advective buoyancy flux model in all the experiments considered, and that at large $\epsilon/\nu N^2$, this parameterisation can over-predict the true K_ρ by two orders of magnitude. This overprediction is discussed in terms of a mixing efficiency and it is shown that in the experiments considered the mixing efficiency decreases rapidly with increasing $\epsilon/\nu N^2$. Finally, the application of our diffusivity scaling to other geophysical flows is discussed, and it is shown that a necessary requirement for the use of this scaling is that L_t is independent of the rate of dissipation of turbulent kinetic energy.

Introduction

A clear understanding of the irreversible vertical transport of mass in a stably stratified turbulent flow is fundamental to quantifying the dynamics of density stratified fluids. The rate at which this transport occurs has been widely modelled as a turbulent diffusivity for mass, K_ρ . Since K_ρ influences the distribution of heat, mass, contaminants and biota throughout a turbulent fluid (e.g. Tennekes and Lumley, 1972), an understanding of this quantity is essential to the management of aquatic systems such as lakes, estuaries and the oceans.

The simplest model describing turbulent transport in homogeneous isotropic turbulence relates a turbulent diffusivity K to a turbulent velocity scale U and a turbulent integral lengthscale L (Tennekes and Lumley, 1972),

$$K \sim U \times L. \quad (1)$$

This expression for K is considered to represent a bulk eddy diffusivity. Taylor (1935) found that the rate of dissipation of turbulent kinetic energy per unit mass, ϵ ,

is

$$\epsilon \sim \frac{u^3}{l}, \quad (2)$$

where u is the fluctuating component of velocity and l is a linear dimension defining the scale of the turbulent field. If we assume that U , u and L , l are well represented by their root mean square (ms) velocity and length scales U_t and L_t respectively, (1) and (2) can be combined to give

$$K \sim \epsilon^{1/3} L_t^{4/3}. \quad (3)$$

The rate at which a stratifying scalar θ is irreversibly mixed in a turbulent flow has generally been modelled using an average vertical advective flux $\overline{\theta' w'}$, where θ' and w' are the instantaneous scalar and vertical velocity fluctuations respectively (see Gregg, 1987, for a full review). This advective flux has been formulated in terms of an eddy coefficient (or diffusivity) K_θ as

$$K_\theta = \frac{\overline{\theta' w'}}{\frac{\partial \theta}{\partial z}}, \quad (4)$$

where $\partial\bar{\theta}/\partial z$ is the mean vertical scalar gradient on which the advective flux acts. *Osborn* (1980) used (4) to model K_ρ in the shear driven environment of the ocean thermocline. By using the turbulent kinetic energy equation, *Osborn* (1980) suggested that $K_\rho \leq 0.2\epsilon/N^2$, where the multiplicative constant is equal to $R_f/(1 - R_f)$, and R_f is a mixing efficiency taken to be less than or equal to 0.15. This model for K_ρ has often been used in geophysical applications other than originally intended, and with the inequality written as an equality such that

$$K_\rho = 0.2 \frac{\epsilon}{N^2}. \quad (5)$$

Winters and D'Asaro (1996) argued that rather than modelling K_ρ with (4), it can be computed directly as

$$K_\rho = \frac{\phi_d}{\left| \frac{d\rho}{dz_*} \right|}, \quad (6)$$

where ϕ_d is the irreversible diffusive flux of density across an isoscalar surface in a turbulent flow and $d\rho/dz_*$ is the resorted density gradient. Using this definition, *Barry et al.* (2001) conducted controlled laboratory experiments that directly and independently measured K_ρ , the rate of dissipation of turbulent kinetic energy ϵ , a turbulent lengthscale L_t and the buoyancy frequency $N^2 = -(g/\rho_0)(d\rho/dz)$ in a closed, shear free, linearly salt stratified fluid. Turbulence was generated in the entire fluid volume by the steady motion of a horizontally oscillating vertical rigid grid comprising 1-cm bars at a 5-cm spacing. A schematic diagram of the experimental configuration is shown in Figure 1, and full details are given in *Barry et al.* (2001). *Barry et al.* (2001) described the behaviour of K_ρ with reference to the turbulence intensity parameter $\epsilon/\nu N^2$, where ν is the kinematic viscosity of the fluid. Two regimes were identified: regime E (energetic turbulence, $\epsilon/\nu N^2 > 300$) and regime W (weak turbulence, $\epsilon/\nu N^2 < 300$). It was found that

$$K_\rho = 24\nu^{2/3}\kappa^{1/3} \left(\frac{\epsilon}{\nu N^2} \right)^{1/3} \text{ and} \quad (7)$$

$$K_\rho = 0.9\nu^{2/3}\kappa^{1/3} \left(\frac{\epsilon}{\nu N^2} \right) \quad (8)$$

for regimes E and W respectively. For regime E, *Barry et al.* (2001) also found that

$$L_t = 20 \frac{(\nu\kappa)^{1/4}}{N^{1/2}}, \quad (9)$$

where $(\nu\kappa)^{1/4}/N^{1/2}$ is the convective lengthscale, L_{co} . This lengthscale was related to U_t using (2) (and assuming that l and u are well represented by their respective

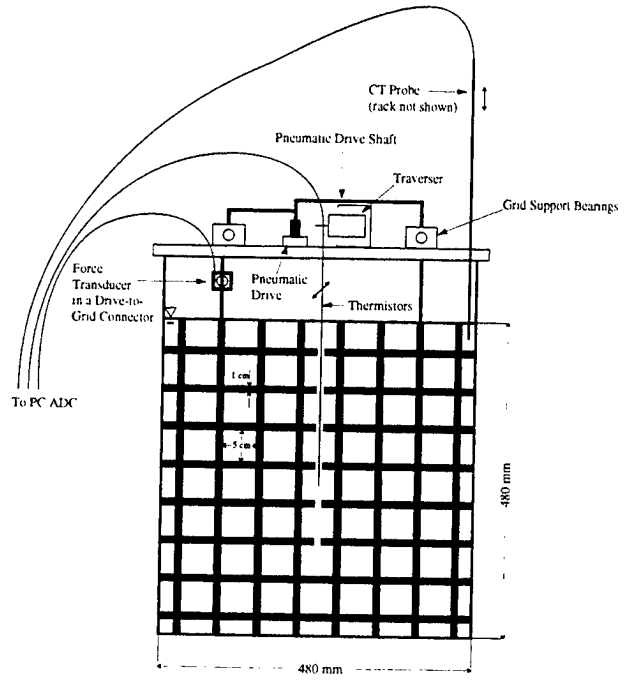


Figure 1. Schematic diagram of the front view of the experimental setup. The tank is 520 mm long, and was filled with a linearly salt stratified fluid. The vertical rigid grid stirred the entire fluid volume.

rms quantities) such that

$$U_t = 3.3 \left(\frac{\epsilon}{\nu N^2} \right)^{1/3} (\nu N)^{1/2} Pr^{-1/12}, \quad (10)$$

where $Pr = \nu/\kappa$ is the Prandtl number of the fluid. This rms velocity scaling is the same as that obtained by using the direct measurements of K_ρ and L_t and solving for U_t in (1). No velocity or lengthscale relations were identified in regime W.

The primary focus of this paper is to compare the *Barry et al.* (2001) direct diffusivity measurements in regime E with those inferred (via (4)) using the numerical data of *Ivey et al.* (1998), the laboratory data of *Stillinger et al.* (1983b), *Rohr* (1985), and *Itsweire et al.* (1987), and the field data of *Saggio and Imberger* (2001). We also use the same data sets to assess the generality of the *Barry et al.* (2001) lengthscale and velocity relations in the same regime.

The data sets

Direct numerical simulations

Using the code described by *Holt et al.* (1992), *Ivey et al.* (1998) undertook a series of direct numerical simulations (DNS) of stratified shear flows using a 128^3 point computational domain in which N^2 and the square of

the mean vertical shear $S^2 = (\partial U / \partial z)^2$ were held constant. Although only one value of S^2 was used for all the simulations discussed here, N^2 was varied between simulations such that the Richardson number, $Ri = N^2 / S^2$, varied from 0.075 to 1.0. The experiments were run for non-dimensional shear time, $0 < St < 8$, however we consider the results from only $St > 2$ where the turbulence becomes self-adjusted and has lost memory of the initialisation (Ivey et al., 1998). At each time-step within a simulation, all turbulent quantities were calculated as ensemble averages over the entire fluid volume. With the application to geophysical flows in mind, we consider only the DNS experiments with $Pr \geq 1$.

Laboratory experiments

The experiments of Stillinger et al. (1983b), Rohr (1985), and Itsweire et al. (1987) measured turbulent quantities at different points downstream of a fixed grid at the head of a water tunnel (see Stillinger et al., 1983a, for a full description of the experimental configuration). These experiments used a variety of grids with bars of diameter 0.318 to 0.635 cm at spacings of 1.905 to 3.81 cm. In all the experiments, salt stratified water was continually recirculated through the tunnel, allowing the collection of timeseries data at several positions downstream of the stationary grid. Average turbulent quantities were computed at these positions by averaging the collected timeseries at each point. The Rohr (1985) experiments included mean shear. From numerical simulations, Itsweire et al. (1993) found that in these experiments, ϵ was underestimated by approximately a factor of 2. We have applied this correction factor to the data sets for this analysis.

Field experiments

Saggio and Imberger (2001) measured turbulent properties in the metalimnion of Lake Kinneret, Israel, during three consecutive summer periods. During these experiments, a portable flux profiler (PFP) capable of resolving all three turbulent velocity components was traversed vertically through the water column at approximately 10 cm/s. This probe also allowed the measurement of the instantaneous vertical advective buoyancy flux $\rho'w'$, and the rate of dissipation of turbulent kinetic energy, ϵ .

Results

Turbulent lengthscales and velocities

In Figure 2 we plot U_t against $(\epsilon L_t)^{1/3}$, for the above numerical and laboratory data sets where $\epsilon / \nu N^2 > 300$. This rms quantity was computed as

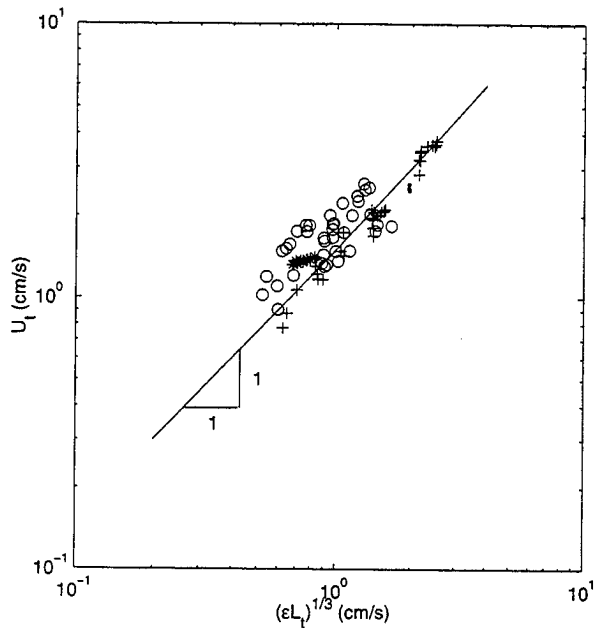


Figure 2. Root mean square turbulent velocity U_t vs $(\epsilon L_t)^{1/3}$, in cm/s; ·, Stillinger et al. (1983b); o, Rohr (1985); +, Itsweire et al. (1987); *, Ivey et al. (1998). The solid line is slope 1, with the equation given by (13).

$$U_t = \sqrt{2(u'^2) + w'^2} \quad (11)$$

for the laboratory data and

$$U_t = \sqrt{u'^2 + v'^2 + w'^2} \quad (12)$$

for the DNS data. The solid line in Figure 2 is slope 1 and has

$$U_t = 1.5(\epsilon L_t)^{1/3} \quad (13)$$

consistent with Ivey et al. (1998). Figure 3 shows the normalised turbulent velocity scale against $\epsilon / \nu N^2$ for the same data, where the solid line is given by

$$\frac{U_t}{(\nu N)^{1/2} Pr^{-1/12}} = 4.9 \left(\frac{\epsilon}{\nu N^2} \right)^{1/3}. \quad (14)$$

Equations (13) and (14) imply that the rms turbulent lengthscale L_t in the DNS and laboratory data is described by

$$L_t = 35 \frac{(\nu \kappa)^{1/4}}{N^{1/2}} = 35 L_{co}. \quad (15)$$

Similarly, Saggio and Imberger (2001) found for field data in a heat stratified lake that

$$\frac{U_t}{(\nu N)^{1/2} Pr^{-1/12}} = 3 \left(\frac{\epsilon}{\nu N^2} \right)^{1/3} \quad (16)$$

and

$$L_t = 15 L_{co}, \quad (17)$$

where U_t was computed using (12).

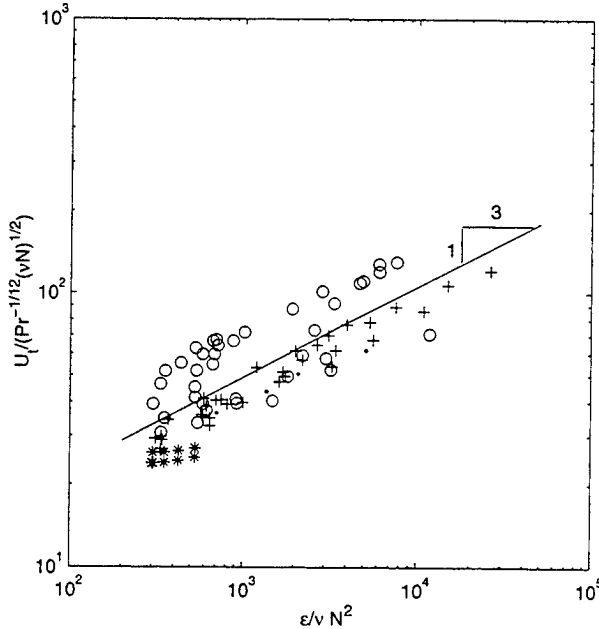


Figure 3. Normalised turbulent velocity $U_t / ((\nu N)^{1/2} \Pr^{-1/12})$ vs $\epsilon / \nu N^2$; ·, Stillinger et al. (1983b); ○, Rohr (1985); +, Itsweire et al. (1987); *, Ivey et al. (1998). The solid line is slope 1/3, with the equation given by (14).

Buoyancy flux estimates of K_ρ

In Figure 4 we plot the quantity $(b/N^2)/(\nu^{2/3} \kappa^{1/3})$ against $\epsilon / \nu N^2$, where $b = (g/\rho_0) \rho' w'$ is the buoyancy flux. The solid lines are given by

$$\frac{b}{N^2(\nu^{2/3} \kappa^{1/3})} = 24 \left(\frac{\epsilon}{\nu N^2} \right)^{1/3} \quad (18)$$

for the laboratory data and

$$\frac{b}{N^2(\nu^{2/3} \kappa^{1/3})} = 6 \left(\frac{\epsilon}{\nu N^2} \right)^{1/3} \quad (19)$$

for the DNS data where $\epsilon / \nu N^2 > 300$.

Saggio and Imberger (2001) found from field data in Lake Kinneret that when $\epsilon / \nu N^2 > 36$,

$$\frac{b}{N^2(\nu^{2/3} \kappa^{1/3})} = 12 \left(\frac{\epsilon}{\nu N^2} \right)^{1/3}. \quad (20)$$

Discussion

The functional forms of equations (14), (16) and (15), (17) are consistent with the Barry et al. (2001) scalings in (10) and (9), respectively. In particular, (15) and (17) demonstrate that in all these data sets the turbulent lengthscale is not a function of the rate of dissipation of

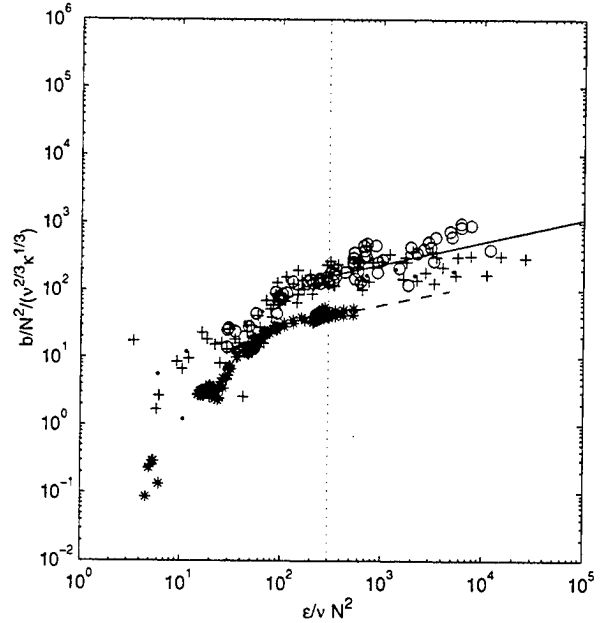


Figure 4. $(b/N^2)/(\nu^{2/3} \kappa^{1/3})$ vs $\epsilon / \nu N^2$; ·, Stillinger et al. (1983b); ○, Rohr (1985); +, Itsweire et al. (1987); *, Ivey et al. (1998). The equations of the lines are given in the text.

turbulent kinetic energy when $\epsilon / \nu N^2 > 300$. Further, these velocity scales are consistent with the results of Barry et al. (2001) who suggested that for a given N in regime E, an increase in ϵ does not result in an increase in the turbulent overturn scale but, rather, leads to an increase in the magnitude of the rms turbulent velocity.

Although we note some variation in the constant coefficient, the agreement between the turbulent velocity and lengthscale relations of Barry et al. (2001) and those of the data sets presented here suggests that, to first order, the configuration of the turbulence generation mechanism does not influence the physics of the turbulence when $\epsilon / \nu N^2 > 300$. Since all data sets are reasonably well described by $L_t \sim L_{co}$ and $U_t / ((\nu N)^{1/2} \Pr^{-1/12}) \sim (\epsilon / \nu N^2)^{1/3}$, we assume that (1) also applies to the experiments detailed above and, if it were directly measured, K_ρ would be well described by (7) in regime E.

Figure 4 shows that for regime E there is good agreement between (7) (given by the solid line) and $b / (N^2 \nu^{2/3} \kappa^{1/3})$ computed using the laboratory data. Although there is some scatter in the laboratory data (consistent with the scatter in the velocity and lengthscale measurements shown in Figures 2 and 3), the trend in $b / (N^2 \nu^{2/3} \kappa^{1/3})$ is consistent with (7) in regime E. We conclude that in these laboratory experiments, (4) can be used to satisfactorily approximate the true diffusivity measured by Barry et al. (2001) when $\epsilon / \nu N^2 > 300$.

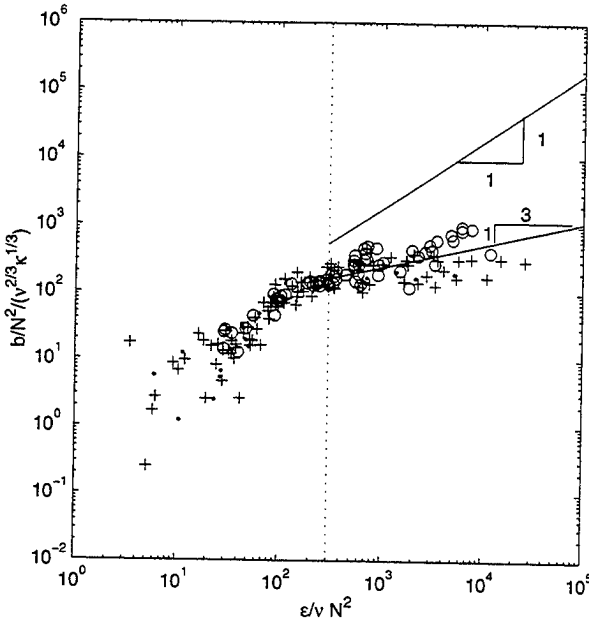


Figure 5. $(b/N^2)/(\nu^{2/3}\kappa^{1/3})$ vs $\epsilon/\nu N^2$; ·, Stillinger et al. (1983b); ○, Rohr (1985); +, Itsweire et al. (1987). The solid line is $(0.2\epsilon/N^2)/(\nu^{2/3}\kappa^{1/3})$, with $Pr = 700$.

The quantity $b/(N^2\nu^{2/3}\kappa^{1/3})$ computed from both DNS and Saggio and Imberger (2001) data shows the same functional dependence on $(\epsilon/\nu N^2)^{1/3}$ as (7) when $\epsilon/\nu N^2 > 300$. This implies that the physics of the turbulence in regime E (i.e. the relationship between K_ρ , U_t and L_t) is well described by the scale forms of the Barry et al. (2001) results. We note, however, that the constant coefficients in the DNS and field data sets are different from those of the Barry et al. (2001) measurements. It is currently not clear why this should be the case.

Figure 5 shows the estimates of K_ρ from the laboratory data sets using (4) compared with the prediction from Osborn (1980) in (5) for $Pr = 700$. The figure shows that for $\epsilon/\nu N^2 > 300$, the model predictions from (4) and (5) diverge. For highly energetic turbulence, the two estimates are widely disparate, such that at $\epsilon/\nu N^2 \approx 10^5$ they are different by more than two orders of magnitude.

Barry et al. (2001) argued that the most likely cause of this divergence for large $\epsilon/\nu N^2$, is the selection of a constant mixing efficiency R_f in deriving (5). Ivey and Imberger (1991) described the behaviour of this mixing efficiency in terms of the turbulent Froude number,

$$Fr_T = \left(\frac{L_o}{L_C} \right)^{2/3}, \quad (21)$$

and the turbulent Reynolds number,

$$Re_T = \left(\frac{L_C}{L_k} \right)^{4/3}, \quad (22)$$

where $L_o = (\epsilon/N^3)^{1/2}$ is the Ozmidov scale, L_C is a centred displacement scale equivalent to L_t , and $L_k = (\nu^3/\epsilon)^{1/4}$ is the Kolmogorov scale. In particular, Ivey and Imberger (1991) found that R_f has a maximum of approximately 0.2 at $Fr_T \approx 1.2$ (or $L_o \approx L_t$), and that R_f decreases rapidly when Fr_T deviates from this value, such that for $Fr_T > 1.2$,

$$R_f = \frac{1}{1 + 3Fr_T^2} \quad (23)$$

for large Re_T . If we assume that L_t (and hence L_C) is well described by $27.5L_{co}$ for $\epsilon/\nu N^2 > 300$ (where the coefficient of 27.5 is a representative value from the Stillinger et al. (1983b), Rohr (1985), Itsweire et al. (1987) and Barry et al. (2001) data sets), we can substitute $27.5L_{co}$ for L_C in (21) and (22) to give

$$Fr_T = 0.11 \left(\frac{\epsilon}{\nu N^2} Pr^{1/2} \right)^{1/3} \text{ and} \quad (24)$$

$$Re_T = 83 \left(\frac{\epsilon}{\nu N^2} Pr^{-1} \right)^{1/3}, \quad (25)$$

respectively. Ivey and Imberger (1991) argued that any two of the non-dimensional parameters Fr_T , Re_T and $\epsilon/\nu N^2$ are necessary and sufficient to describe the dynamics of a general turbulent field. However, equations (24) and (25) show that for regime E in the above experiments we need only one.

We plot Fr_T against $\epsilon/\nu N^2 Pr^{1/2}$ in Figure 6, for $\epsilon/\nu N^2 > 300$, where the solid line is given by (24). Equations (23) and (24) show that R_f necessarily decreases with increasing $\epsilon/\nu N^2$,

$$R_f = \frac{1}{1 + 0.04 \left(\frac{\epsilon}{\nu N^2} \right)^{2/3} Pr^{1/3}}. \quad (26)$$

Figure 7 shows R_f against $\epsilon/\nu N^2$ for these data sets, and clearly demonstrates that a diffusivity modelled as $K_\rho = R_f/(1-R_f)\epsilon/N^2$ with R_f constant at 0.15 (shown in Figure 7 as a horizontal solid line) will overestimate the true diffusivity at large $\epsilon/\nu N^2$ in these experiments. This result is consistent with the divergence of the estimates of K_ρ from (4) and (5) shown in Figure 5.

Application to geophysical flows

Equations (24) and (26) hold if, and only if, the turbulent lengthscale L_t is well described by L_{co} . Several field investigations however, (e.g. Crawford, 1986; Gregg, 1987; Peters et al., 1988; Imberger and Ivey,

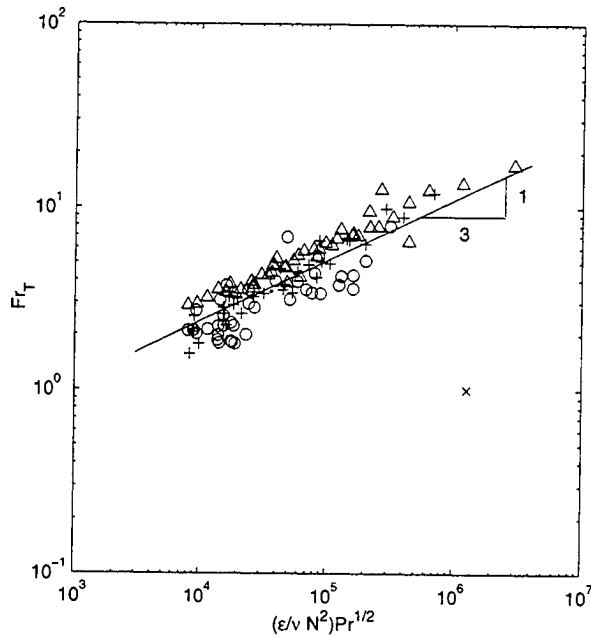


Figure 6. Turbulent Froude number Fr_T vs $(\epsilon/\nu N^2 Pr^{1/2})^{1/3}$; ·, Stillinger et al. (1983b); ○, Rohr (1985); +, Itsweire et al. (1987); △, Barry et al. (2001); ×, Ferron et al. (1998). The solid line is $0.11(\epsilon/\nu N^2 Pr^{1/2})^{1/3}$.

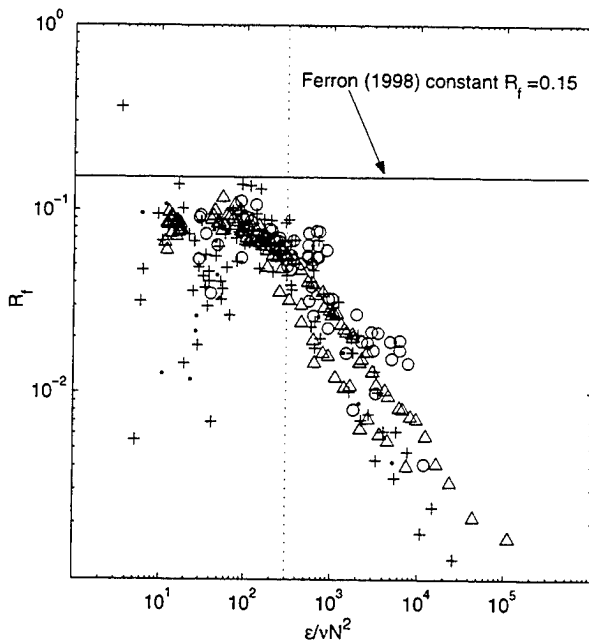


Figure 7. R_f vs $\epsilon/\nu N^2$; ·, Stillinger et al. (1983b); ○, Rohr (1985); +, Itsweire et al. (1987); △, Barry et al. (2001).

1991; Peters et al., 1995; Ferron et al., 1998) have found that in some geophysical flows $L_t \sim L_o$, or equivalently, that $Fr_T \approx 1$. In these situations, this relationship between L_t and L_o has been found to hold regardless of the value of $\epsilon/\nu N^2$. For instance, Ferron et al. (1998) observed that in the Romanche fracture zone,

$$L_o = 0.95(\pm 0.6)L_T, \quad (27)$$

even when $\epsilon/\nu N^2 \approx 500,000$, where L_T is the Thorpe displacement scale and is a measure of L_t . The corresponding value of Fr_T is order 1 and is shown in Figure 6 as an ×. The Ferron et al. (1998) measurements clearly do not conform to the trends of the data sets previously considered here, fundamentally because L_t does not scale like L_{co} .

The measurements of Ferron et al. (1998) imply that Fr_T is *always* approximately unity, regardless of the magnitude of $\epsilon/\nu N^2$. The arguments of Ivey and Imberger (1991) then require that the mixing efficiency in the Romanche fracture zone is constant and maximal, and hence the large value of $\epsilon/\nu N^2$ cannot be used in isolation to infer that R_f is vanishingly small. Rather, either Fr_T or Re_T must also be included in a description of the turbulent dynamics. In such cases, the scaling results of Barry et al. (2001) should not be expected to hold.

Conclusions

We have compared the turbulent lengthscale, velocity and diffusivity scalings presented by Barry et al. (2001) with data from Ivey et al. (1998) DNS experiments, laboratory experiments of Stillinger et al. (1983b), Rohr (1985), and Itsweire et al. (1987) and the field experiments of Saggio and Imberger (2001). For $\epsilon/\nu N^2 > 300$, the Barry et al. (2001) velocity and lengthscale results are good descriptors of the physics of the turbulence in all these experiments, to constant coefficient. We have shown that the turbulent lengthscales in all these experiments in this regime are independent of the rate of dissipation of turbulent kinetic energy. This in turn suggests that for a given N , an increase in ϵ does not increase the turbulent lengthscale, but rather, leads to an increase in the magnitude of the turbulent velocity.

We have shown that when $\epsilon/\nu N^2 > 300$, a diffusivity modelled using (4), is a good representation of the direct measurements of Barry et al. (2001) for the experiments considered, to constant coefficient.

We have discussed the parameterisation of (4) as $K_p = 0.2\epsilon/N^2$ and have shown that, in the data sets considered, this overestimates the true diffusivity for $\epsilon/\nu N^2 > 300$. We have suggested that this is a consequence of selecting a constant mixing efficiency $R_f =$

0.15, as for increasing $\epsilon/\nu N^2$, R_f necessarily decreases in the data sets considered.

Finally, we have discussed the application of the *Barry et al.* (2001) scalings to geophysical flows and have suggested that a necessary requirement for the use of these scalings is that the turbulent lengthscale L_t is independent of ϵ . If this constraint is satisfied (i.e. $L_t \sim L_{co}$) then K_p , and indeed all the turbulent dynamics, can be described in terms of only a single parameter $\epsilon/\nu N^2$. When this lengthscale constraint is not satisfied, the *Barry et al.* (2001) scalings do not apply. Future work must now investigate the circumstances under which this lengthscale constraint is satisfied in a variety of geophysical flows.

Acknowledgments. The first author is grateful to Peter Müller and Chris Garrett for the opportunity to participate in the workshop. M. Barry was supported by an Australian Postgraduate Award and a Samaha Research Scholarship. This forms Centre for Water Research reference ED1400-MB.

References

- Barry, M.E., G.N. Ivey, K.B. Winters and J. Imberger, 2001, Measurements of diapycnal diffusivities in stratified fluids, *J. Fluid Mech.*, **442**, 267–291, 2001.
- Crawford, W.R., A comparison of length scales and decay times of turbulence in stably stratified flows, *J. Phys. Oceanogr.*, **16**, 1847–1854, 1986.
- Ferron, B., H. Mercier, K. Speer, A. Gargett, and K. Polzin, Mixing in the Romanche Fracture Zone, *J. Phys. Oceanogr.*, **28**, 1929–1945, 1998.
- Gregg, M.C., Diapycnal mixing in the thermocline: A review, *J. Geophys. Res.*, **92**, 5249–5286, 1987.
- Holt, S.E., J.R. Koseff, and J.H. Ferziger, A numerical study of the evolution and structure of homogeneous stably stratified shear turbulence, *J. Fluid Mech.*, **237**, 499–540, 1992.
- Imberger, J., and G.N. Ivey, On the nature of turbulence in a stratified fluid. Part II: Application to lakes, *J. Phys. Oceanogr.*, **21**, 659–680, 1991.
- Itsweire, E. C., K. N. Helland, and C.W. Van Atta, The evolution of grid-generated turbulence in a stably stratified fluid, *J. Fluid Mech.*, **162**, 299–338, 1987.
- Itsweire, E.C., J.R. Koseff, D.A. Briggs, and J.H. Ferziger, Turbulence in stratified shear flows: implications for interpreting shear-induced mixing in the ocean, *J. Phys. Oceanogr.*, **23**, 1508–1522, 1993.
- Ivey, G.N., and J. Imberger, On the nature of turbulence in a stratified fluid. Part I: The energetics of mixing, *J. Phys. Oceanogr.*, **21**, 650–658, 1991.
- Ivey, G.N., J. Imberger, and J.R. Koseff, Buoyancy fluxes in a stratified fluid, in *Physical Processes in Lakes and Oceans*, American Geophysical Union, ed. J. Imberger, 54, *Coastal and Estuarine Studies*, 377–388, 1998.
- Osborn, T. R., Estimates of the local rate of vertical diffusion from dissipation measurements, *J. Phys. Oceanogr.*, **10**, 83–89, 1980.
- Peters, H., M.C. Gregg, and J.M. Toole, On the parameterization of equatorial turbulence, *J. Geophys. Res.*, **93**, 1199–1218, 1988.
- Peters, H., M.C. Gregg, and T.B. Sanford, Detail and scaling of turbulent overturns in the Pacific Equatorial Undercurrent, *J. Geophys. Res.*, **100**, 18,349–18,368, 1996.
- Rohr, J.J., An experimental study of evolving turbulence in uniform mean shear flows with and without stable stratification, PhD. thesis, Engineering Sciences, University of California San Diego, California, USA, 1985.
- Saggio, A., and J. Imberger, Mixing and turbulent fluxes in the metalimnion of a stratified lake, *Limnol. Oceanogr.*, **46**, 392–409, 2001.
- Stillinger, D.C., M.J. Head, K.N. Helland, and C.W. Van Atta, A closed-loop gravity-driven water channel for Density-stratified shear flows, *J. Fluid Mech.*, **131**, 73–89, 1983a.
- Stillinger, D.C., K.N. Helland, and C.W. Van Atta, Experiments on the transition of homogeneous turbulence to internal waves in a stratified fluid, *J. Fluid Mech.*, **131**, 91–122, 1983b.
- Taylor, G.I., Statistical theory of turbulence, *Proc. Roy. Soc. London*, A151, 421 pp., 1935.
- Tennekes, H., and J.L. Lumley, *A First Course in Turbulence*, MIT Press, 300 pp., 1972.
- Winters, K. B., and Eric A. D'Asaro, Diascalar flux and the rate of fluid mixing, *J. Fluid Mech.*, **317**, 179–193, 1996.

This preprint was prepared with AGU's LATEX macros v4, with the extension package 'AGU⁺⁺' by P. W. Daly, version 1.6a from 1999/05/21, with modifications by D. E. Kelley, version 1.0 from 2001/03/26, for the 'Aha Huliko'a Hawaiian Winter Workshop.

Simulations of internal-wave breaking and wave-packet propagation in the thermocline

G.F. Carnevale

Scripps Institution of Oceanography, University of California San Diego, 9500 Gilman Drive, La Jolla, California 92093, USA

P. Orlandi

Dipartimento di Meccanica e Aeronautica, University of Rome, "La Sapienza," via Eudossiana 18, 00184 Roma, Italy

M. Briscolini

IBM Italia S.p.A., Via Shangai 53, 00144 Roma, Italy

R.C. Kloosterziel

School of Ocean and Earth Science and Technology, University of Hawaii, Honolulu, 1000 Pope Rd, Hawaii 96822

Abstract. An investigation into density and velocity fluctuations in the oceanic thermocline is presented. Two kinds of numerical simulation are reported. In the first, an attempt is made to capture the transition from breaking internal waves to the small-scale turbulence they generate. The model used for this is based on a continual forcing of a large-scale standing internal-wave. Evidence is presented for a transition in the energy spectra from the anisotropic k^{-3} buoyancy range to the small-scale $k^{-5/3}$ isotropic inertial range. Density structures that form during wave breaking are analyzed and regions of mixing associated with the breaking events are visualized. In the second kind of simulation, internal-wave packets are followed as they propagate through the thermocline. It is found that the breaking of crests within the packet can lead to overturning events on the scale observed in the ocean, and the subsequent turbulence can form a continuous wake.

Introduction

In recent observations of fluctuations in the oceanic thermocline, *Alford and Pinkel* (1999, 2000) found many overturns with vertical scale of about 2 m and these were highly correlated with the presence of energetic waves with vertical wavelengths on the order of 10 m. Large scale fluctuations, say 10 m and above in vertical scale, can be described reasonably well as internal waves. For much smaller scales, say 1 m and below, the flow is probably better described in terms of nearly isotropic turbulence. Intermediate between the large-scale wave dynamics and the small-scale turbulence is a transition regime in which there is a competition between waves and turbulence. It is this intermediate range, often called the buoyancy range, that contains the overturning activity observed by Al-

ford and Pinkel. Since the observations are essentially one-dimensional in space, a direct numerical simulation which could faithfully describe events in this range would help toward understanding the full three-dimensional flow structures behind the observations. The first part of our investigation will focus on the production of overturns by an idealized internal wave forcing.

The second part of our investigation concerns the propagation of internal-wave packets through the thermocline. *Alford and Pinkel* (1999, 2000) observed coherent regions of strong oscillatory vertical strain rate that travel vertically through 100 m or more of the thermocline. These propagating structures had an internal wave structure with vertical wavelength of about 10 m, and the entire coherent region could be described by

an envelope of about 50 m in vertical extent. These coherent structures were strongly correlated with 2 m overturns. Given the complicated nature of the flow, with strong components of large-scale advection, it was difficult to know precisely what kind of structures to associate with these coherent localized oscillations. *Alford and Pinkel* suggested that these were internal-wave packets. Here we hope to validate that identification to a certain extent by showing how an idealized packet would propagate through a simplified model of the thermocline, and by showing that the observed overturning scales could be consistent with internal-wave packet propagation.

Given current computer resources, it would not be practical to simulate all of the scales that are relevant to the breaking of waves in the buoyancy range. The forcing of the waves is thought to result from a complicated interaction of many internal waves with scales ranging in the vertical from 10's of meters to hundreds of meters and more, and typical horizontal internal wave scales can be even much greater than these. On the small-scale end of the spectrum, the observed breaking is occurring on vertical scales of the order of 1 m, and these breaking events produce turbulence that extends down to a viscous cutoff on the order of 1 cm. Thus direct numerical simulation of the entire range of scales is still impractical. We will use a combination of LES modeling and an artificial model of the large scale forcing in order to reduce the spectral range that we will need to cover. To attack our first problem of investigating how waves at the short-scale end of the Garrett-Munk (1975) spectrum go unstable and break in the buoyancy range, we have used an artificial forcing with length-scales fixed at 20 m in the vertical and 20 m in the horizontal to represent the effect of all larger scales. At the small-scale end of the simulation, we have introduced an eddy viscosity with a cutoff at the 16 cm level in both horizontal and vertical directions. Thus our model does some violence to the true physics at the large and small-scale ends of the simulated range. However, the hope is that it will do justice to the evolution in the buoyancy range. This model does prove capable of capturing the transition from the buoyancy to the inertial range. For the problem of wave-packet propagation, which is perhaps the source of the order 10 m scale variability most correlated with overturning, we needed to expand our domain size in order to allow for the propagation and evolution of the packet.

Forced 20-meter wave

Our first goal is to determine to what extent our simulations can capture the transition from the buoyancy range to the inertial range in the energy spec-

tra. Constructing a theory of this transition is complicated because of the anisotropy of the buoyancy range. To make progress, some theoretical formulations have represented the entire spectrum as depending only on wavenumber k . The model for the kinetic energy spectrum in the buoyancy range is then

$$E(k) = \alpha N^2 k^{-3} \quad (1)$$

where α is an empirical constant and N is the Brunt-Väisälä frequency, which measures the strength of the stratification. The Brunt-Väisälä frequency is defined by

$$N^2 = -\frac{g}{\rho_0} \frac{\partial \bar{\rho}}{\partial z} \quad (2)$$

where g is the acceleration of gravity, $\bar{\rho}$ is the background density profile, assumed stable (i.e. $\partial \bar{\rho} / \partial z < 0$), and ρ_0 is the volume average of $\bar{\rho}$. From the observed spectra of vertical shear, the constant α is determined to be about 0.47, but it will be more convenient for us to consider the two components of the horizontal velocity (u, v) separately, and, assuming horizontal isotropy in the observations, this would suggest $\alpha \approx 0.2$ for the spectrum of either component (cf. *Gibson* 1986, *Gargett et al.* 1981). The inertial range kinetic energy spectrum is given by

$$E(k) = C_K \epsilon^{2/3} k^{-5/3} \quad (3)$$

where ϵ is the turbulent dissipation rate of total kinetic energy and C_K is the empirical Kolmogorov constant. A reasonable value to assume for C_K is 1.5 (cf. *Lesieur*, 1997). For the energy of one component of the velocity field, there would simply be a prefactor of 1/3 multiplying this isotropic spectrum. The Ozmidov (or buoyancy) wavenumber is then estimated by simply matching these two spectra at wavenumber k_b . The result is, up to an order one multiplicative constant,

$$k_b \equiv \sqrt{N^3 / \epsilon}, \quad (4)$$

(cf. *Holloway*, 1981; *Gibson* 1986).

The model for the potential energy spectrum in the buoyancy range is similar to that for the kinetic energy spectrum. The empirical constant α for the temperature spectrum is found to have value of about 0.2 (cf. *Gibson* 1986, *Gregg* 1977). The spectral model for the inertial range of density fluctuations is the Corrsin-Obukhov spectrum, which involves the decay rate of density fluctuations as well as ϵ . For our purposes, we prefer to write the spectrum directly in terms of the turbulent decay rate of potential energy, which we shall write as ϵ_{pe} . Then the Corrsin-Obukhov spectrum for the potential energy takes the following form:

$$PE(k) = C_o \epsilon_{pe} \epsilon^{-1/3} k^{-5/3}, \quad (5)$$

where C_o is the Corrsin constant.

For all of the simulations presented here, we have used the Boussinesq approximation. The evolution equations may be written as

$$\frac{\partial \mathbf{u}}{\partial t} + \mathbf{u} \cdot \nabla \mathbf{u} + \frac{1}{\rho_0} \nabla p' - \frac{\rho'}{\rho_0} \mathbf{g} = \nu(\nabla^2) \nabla^2 \mathbf{u}, \quad (6)$$

$$\nabla \cdot \mathbf{u} = 0. \quad (7)$$

$$\frac{\partial \rho'}{\partial t} + \mathbf{u} \cdot \nabla \rho' + w \frac{\partial \bar{\rho}}{\partial z} = \kappa(\nabla^2) \nabla^2 \rho', \quad (8)$$

where $\nu(\cdot)$ and $\kappa(\cdot)$ are considered functions of the Laplacian operator and are used to represent eddy parameterizations in general (cf. *Herring and Matalas* 1992) and $\mathbf{g} = -g\hat{\mathbf{z}}$. We have neglected the effect of rotation, which should not play a major role at the small scales with which we are concerned. The total density is given by

$$\rho = \bar{\rho}(z) + \rho'(x, y, z, t), \quad (9)$$

where $\rho'(x, y, z, t)$ is the deviation from the horizontally averaged density $\bar{\rho}(z)$. ρ_0 is the average of $\bar{\rho}(z)$ over z . The pressure p' is the deviation from the background mean pressure. p' can be determined in terms of \mathbf{u} by taking the divergence of (6) under the assumption that the velocity field is divergenceless.

We simulate these dynamical equations with a spectral code with triply periodic boundary conditions. As a sub-grid scale parameterization, we have used the large-eddy simulation model of *Lesieur and Rogallo* (1989). This eddy viscosity $\nu_t(k)$ is approximately constant throughout the buoyancy range and the large-scale end of the inertial range, but increases rapidly with k in the vicinity of the spectral cutoff k_c . Due to the spectral shape of the eddy viscosity, this model is sometimes called the cusp model. It seems reasonable in modeling the buoyancy range to use such a model since it does not completely neglect the effects of unresolved eddies on the buoyancy range, but, at the same time, it puts the strongest eddy viscosity in the inertial range near the cutoff.

We should emphasize the point that the size of the eddy viscosity depends on the amount of energy at the cutoff scale. If the resolution of the simulation of a given physical flow is increased, that is if k_c is increased, then the eddy viscosity will be correspondingly smaller. The total viscosity used in the simulations is the sum of the eddy viscosity and the constant molecular viscosity ν_{mol} . Thus the $\nu(\nabla^2)$ in equation (6) in the spectral simulation is taken as the total viscosity:

$$\nu(k) = \nu_{mol} + \nu_t(k) \quad (10)$$

The choice of turbulent diffusion depends on the choice of values for various parameters that enter into

the closure model for stratified turbulence. For simplicity, we have just taken the turbulent Prandtl number $Pr_t(k)$ to be a fixed constant independent of k in our simulations. We determined this constant by examining the evolution of the potential energy spectrum for decaying stratified turbulence that is initially highly excited at all scales. More specifically, we started with an initial spectrum in which the GM spectrum was continued to scales below 10 m as in the decay simulations of *Siegel and Domaradzki* (1994). With $Pr_t = 0.55$ our simulations of decaying turbulence produced spectra with the high wavenumbers obeying the $k^{-5/3}$ law for both velocity and density fluctuations.

Next we turn to the question of the forcing. The large-scale flows that actually drive the buoyancy range are predominantly the waves of the Garrett-Munk range. The full range where internal wave dynamics dominates includes scales of kilometers in the horizontal and hundreds of meters in the vertical. Because of lack of resolution, we cannot provide a full representation of the effects of all large-scale internal wave forcing on the buoyancy range. In our model, of necessity, we perform a drastic reduction in modeling the forcing; we replace the driving of all of the GM waves by a linear standing wave at one wavelength. *Bouruet-Aubertot et al.* (1995, 1996), in two-dimensional simulations of a stratified turbulence, excited a standing wave of the type we use, but they allowed this wave to decay, whereas we maintain its amplitude at the same level throughout the simulation.

To give the form of the forcing used, let us first introduce nondimensional units. We will take all lengths to be scaled by $2\pi/L$, where L is the length of one side of our computational domain. Time will be scaled by $1/N$. Then the frequency of linear internal waves is given by

$$\sigma = \pm \frac{k_h}{k}, \quad (11)$$

where $k_h = \sqrt{k_x^2 + k_y^2}$ is the horizontal wavenumber. One particular linear standing wave is

$$\mathbf{u} = (u, v, w) = A \frac{g^*}{\sqrt{2}} (0, \sin y \sin z, \cos y \cos z) \sin \frac{t}{\sqrt{2}}, \quad (12)$$

$$\frac{\rho'}{\rho_0} = A \cos y \cos z \cos \frac{t}{\sqrt{2}}, \quad (13)$$

where A is an arbitrary amplitude and g^* is the nondimensional gravity. Note that the dimensional period of this wave, which is the forcing period, is given by

$$T_F = \sqrt{2} \frac{2\pi}{N}. \quad (14)$$

To give some idea of the structure of this standing wave, we show in Figure 1 a contour plot of the density

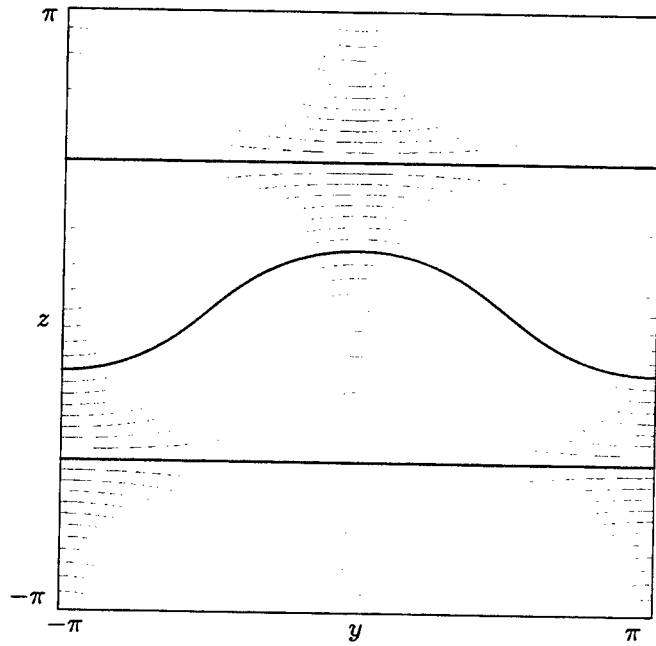


Figure 1. Contour plot of the density field in a vertical $y-z$ cross section through the center of the domain. The width and height of the cross section are each 20 m, which corresponds to 2π in nondimensional units. The instant shown corresponds to maximum displacement of the isopycnals for the forced standing wave.

field in a vertical $y-z$ cross section. Note that the density field in this standing wave has no variation along the x direction. In this figure, we see an instantaneous representation of the iso-density surfaces. When $t/\sqrt{2}$ is an odd multiple of $\pi/2$, these isopycnals will all be flat. The degree to which they deviate from that at other times depends on the value of A as well as t . The instant of time represented here is such that $t/\sqrt{2}$ is an integer multiple of π and, hence, one of maximum distortion of the density contours. Note that the density field in (13) has two nodal planes, represented by two thick contour lines in the figure, at $z = \pm\pi/2$ (nondimensional). During the forcing cycle, these planes remain flat and fixed in position. The fluid above and below these planes vertically approaches and retreats from them depending on the phase in time and the y position considered. Thus the points on the nodal planes at $y = 0$ and $y = \pm\pi$ are the centers of regions of oscillating high strain rate. On the other hand the points where the isopycnals are steepest, that is where $y = \pm\pi/2, \pm 3\pi/2$ and $z = 0, \pm\pi$ the magnitude of the shear $\partial v/\partial z$ is highest. Thus one advantage of the standing wave forcing is that the points of highest shear and highest strain rate remain fixed in space making it easier to differentiate the kinds of overturning events associated with these extremes. This will be convenient for making comparisons with Alford and

Pinkel's (2000) analysis. In particular, they noted that there were regions of high shear where classical shear instabilities often, but not always, resulted in overturning. Even more interestingly, there were regions of high Ri in which overturns were also observed. In more than half of these cases Ri was even greater than 2 suggesting that the typical shear instability ($Ri < 1/4$) is unlikely. Many of these overturns were in regions of high vertical strain rate. With our standing wave forcing, the regions of high shear and high strain rate are separate and each occur in the same location during each forcing oscillation. This helps simplify the analysis.

In two-dimensional numerical studies of Bouruet-Aubertot *et al.* (1996), the standing wave becomes unstable and generates turbulence. This would also happen in our three-dimensional simulation, but the turbulence would be highly constrained since there is yet no source of x -variation in our flow. To break the two-dimensional symmetry of the flow, while maintaining the basic structure of the large scale, we add a weak component of forcing with x -variation. We have tried this in various ways: adding a random initial perturbation at all scales, randomly forcing the modes with $k = 1$ at each time step, adding another large-scale standing wave, adding a propagating wave, and so on. The results are similar to each other if the perturbations are sufficiently weak. For the simulations discussed below, we have added to the primary forcing wave only a small amplitude standing wave of the same spatial scale. Specifically, we added the following perturbation:

$$\mathbf{u} = A' \frac{g^*}{\sqrt{2}} (\cos(x+z), 0, -\cos(x+z)) \sin \frac{t}{\sqrt{2}}, \quad (15)$$

$$\frac{\rho'}{\rho_0} = A' \cos(x+z) \cos \frac{t}{\sqrt{2}}. \quad (16)$$

Thus in the simulations discussed below the forcing occurs only at $k = \sqrt{2}$. The coefficient A' was taken to be $A/20$, and, hence, the energy in the perturbation is only 1/400 that of the primary forcing wave.

We performed a series of experiments in which the size of the computational domain and the amplitude of the forcing were varied. The initial studies were at resolution 64^3 and showed that for sufficiently large amplitudes A for which the forcing wave itself was overturning, a $k^{-5/3}$ spectrum extending over most of the spectral range could be established. For weaker forcing, a steeper spectrum approximating k^{-3} was found (Carnevale and Briscolini, 1999). For intermediate amplitude forcings, we were able to observe, at least intermittently, cases which do appear to exhibit the transition from the buoyancy range to the smaller scale inertial range. Weak and strong forcings are measured relative to shear amplitudes typical in the thermocline.

The best results were obtained with a forcing amplitude that could actually be considered representative of wave amplitudes in the thermocline. Specifically, the forcing amplitude that we refer to as intermediate, is for a value of A in equations (12) and (13) such that the maximum shear during a cycle of the forcing is equivalent to the rms shear of the GM spectrum at the scale of our computational domain. The rms shear is calculated by integrating the shear of the GM spectrum from the kilometer scale down to the scale of interest (cf., Gregg, 1989). Our best results tended to be for cases in which the vertical wavelength of the forcing was 20 m. For $N = 3$ cph, the net rms shear from the GM spectrum for this scale is $S_{GM}(20 \text{ m}) \approx 3 \times 10^{-3} \text{ s}^{-1}$ (cf., Gregg, 1989). Taking this value to determine the amplitude of our forcing, we obtain a standing wave in which the largest deviation of the density isosurfaces are as illustrated in Figure 1. Thus we have a standing wave that does not itself overturn during the forcing cycle, and, in addition, the Richardson number of the forcing wave, defined by

$$Ri \equiv -\frac{\frac{g}{\rho_0} \frac{\partial \rho}{\partial z}}{\left(\frac{\partial u}{\partial z}\right)^2 + \left(\frac{\partial v}{\partial z}\right)^2}, \quad (17)$$

does not drop below 3.125. Therefore, the forcing wave itself is convectively stable and not subject to shear instability. This kind of forcing is consistent with the picture that the GM waves themselves are not convectively or shear unstable, but through wave-wave interactions will produce smaller scale waves that are unstable by these criteria. Choosing a stronger forcing wave that is itself convectively or shear unstable would miss the important cascade process that produces the unstable waves of the buoyancy range, but would rather produce turbulence directly resulting in an inertial range (cf. Carnevale and Briscolini, 1999).

For all of the simulations discussed below, we used a resolution 128^3 and a computational cube of 20 m on a side. Our isotropic spectral cutoff is at wavenumber 60, and the smallest resolved wavelength is about 33 cm (with grid spacing $20 \text{ m}/128 \approx 16 \text{ cm}$). The forcing amplitude was fixed so that the max shear in the forced wave is $S_{GM}(20 \text{ m})$, and the Väisälä frequency was taken to be 3 cycles per hour, which is a typical oceanic value.

A long simulation was performed with realistic values for the molecular viscosity and diffusivity. The kinematic viscosity was set to $\nu_{mol} = 0.01 \text{ cm}^2/\text{s}$ and the molecular Prandtl number at $Pr_{mol} = 7$ (cf. Gargett, 1985). We can calculate a Reynolds number for the oceanic flow for vertical motions on the 20 m scale by using the rms shear. Thus we can write

$$Re = S_{GM}(L)L^2/\nu_{mol}. \quad (18)$$

For $L = 20 \text{ m}$, this Reynolds number would be approximately 10^5 . By including the molecular viscosity, the simulation is an attempt to represent flow with this Reynolds number. We will see that there is not much difference with results obtained by neglecting the molecular components of viscosity and diffusivity. That is to say that over the range of scales simulated (20 m to 33 cm) the difference between infinite Reynolds number flow and that for $Re = 10^5$ is small.

We can think of our standing wave forcing as the linear superposition of a set of propagating internal waves. To be precise, the combination of the two standing waves given in (12) and (15) consists of 12 propagating plane waves. These wave interact nonlinearly producing smaller-scales that eventually fill out the entire spectrum. The early evolution is essentially just that of the nearly two-dimensional standing wave. During this time there are only sinusoidal waves on the most disturbed isosurface, but these waves then fold over forming elongated overturns. These regions are convectively unstable and break. At this point the three dimensionality of the flow becomes evident.

After about five cycles of the forcing, the large-scale wave breaks repeatedly, however, not necessarily during each forcing period. The wave breaking on the most disturbed isopycnal occurs roughly symmetrically with large-scale overturning occurring nearly at the same values of y and z each time and along lines of constant x , respecting in the large scales the symmetry of the main part of the forcing. However, no two breaking events with the subsequent evolution during the forcing cycle are the same. In Figure 2, for one such cycle, we show eight instantaneous images of this isosurface using a perspective three-dimensional plot. The frames are ordered temporally from left to right and top to bottom. The first frame in the upper left hand corner corresponds to $t = 11.39T_F$, and the interval between frames is $\Delta t = T_F/7$. Thus the first and last frames correspond to the same phase of the forcing. The first frame captures the moment when breaking is just beginning. Let us say that the first four frames represent the breaking event, and the last four the aftermath. We see that during the breaking event, heavy fluid spills over lighter fluid, crashing down with the creation of small-scale structures all along the lines of the two breaking regions. Similar behavior is in laboratory experiments with standing-wave forcing (Taylor 1992, McEwan 1983a). Afterwards, the region of the small-scale turbulent structures spreads, eventually 'contaminating' the entire isosurface. If we compare the final frame with the first frame, we see that the final surface is much rougher, filled with small-scale structures everywhere, and that there is no larger scale folding-over of the surface as there was in the first frame. In the

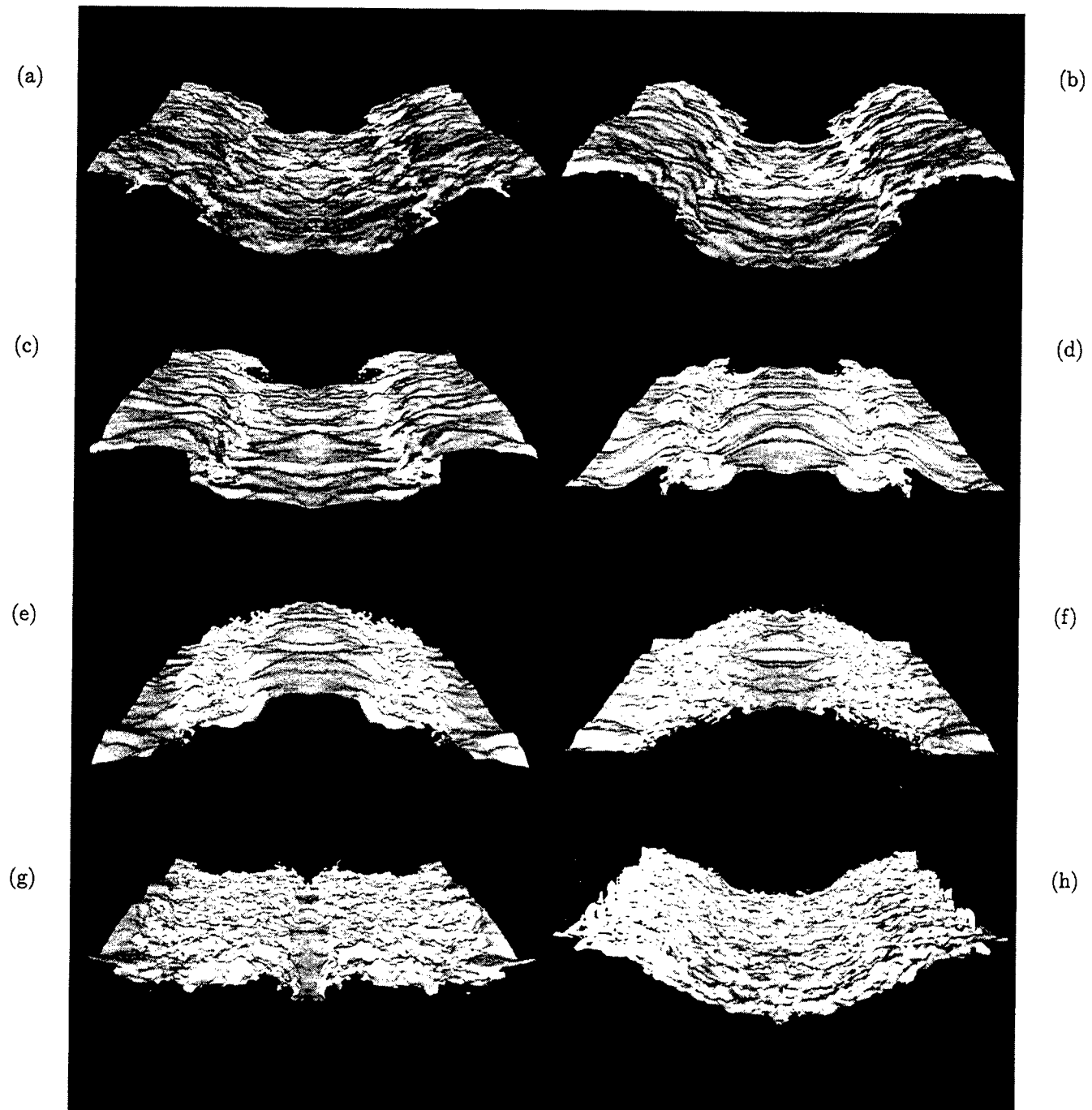


Figure 2. The evolution of the $\rho = \rho_0$ isopycnal during one cycle of the forcing. The frames are ordered by time from left to right and top to bottom. The first corresponds to $t = 11.39T_F$, and the interval between frames is $\Delta t = T_F/7$.

later evolution, the wave will break again, but only after a refractory period, in this case of about two forcing cycles.

Next we will consider the energy spectra for the flow at the same times as those illustrated in Figure 2. Since the energy is highly anisotropic at scales larger than those in the inertial range, plotting the total energy as a function of the isotropic wavenumber tends to obscure the transition between small and large scales. To most clearly display the transition, we have found it useful to consider the spectrum $E_v(k)$ of v , the y component of velocity, which is the horizontal component that is directly affected by the forcing. Along with the spectra, we have also drawn lines corresponding to the inertial range spectrum $(1/3)C_K \epsilon^{2/3} k^{-5/3}$ and buoyancy range spectrum $0.2N^2 k^{-3}$. For each frame, ϵ is taken as the total kinetic energy dissipation rate at that time. We have included a factor of $(1/3)$ which is appropriate for a single component in the isotropic inertial range. For the Kolmogorov constant, a value of 1.5 was used in each case. We should emphasize that no attempt is made here to fit the data, but the coefficient is just taken as this standard value *a priori*. For the buoyancy range spectrum, we have used the coefficient $\alpha = 0.2$ in all cases. In each frame shown in Figure 3, we see a fairly good match at wavenumbers greater than about 20 (that is for scales below about 1 m) to the Kolmogorov inertial range spectrum. The main deviation is at wavenumbers near $k = 60$, the cutoff wavenumber, and this is to be expected from previous experience with the cusp model (cf. *Lesieur and Rogallo*, 1989). The spectrum below wavenumber 20 is naturally far more irregular than that above due to the much smaller number of modes in the lower spectral bands. If we neglect the first few wavenumbers, then there is some evidence here for a steeper spectral range for wavenumbers below about $k = 20$, that is for scales larger than about 1 m, at least in the frames that correspond to times during the breaking of the wave (first four panels). In the aftermath of breaking, the spectra tend to be somewhat flatter (the last four panels). The best representative of the transition between buoyancy and inertial range is found in panel (c), which corresponds to a time when the enstrophy is near a local maximum. Here the buoyancy range spectrum makes a reasonably good fit in the range of scales from about 4 m down to about 1 m. From the forcing scale (20 m vertical) to about the 5 m scale, there is a dip in the energy that has also been seen in the spectra from similar two-dimensional simulations of the decay of a standing wave (*Bouruet-Aubertot et al.* 1996).

In this experiment it appears that the expected spectral signature of a transition between a buoyancy range at large scale and the inertial range at small scale oc-

curs only for periods during which there is active breaking. Indeed, it appears that wave-wave interactions repeatedly build up energy in the buoyancy range until a k^{-3} spectrum is achieved. At that point significant breaking occurs and energy drains from the buoyancy range. Let us focus on the breaking event. In Figure 4a is the image of the $\rho = \rho_0$ isosurface at the time identified as the best for illustrating the spectral transition from the buoyancy to the inertial range. It shows the curling over and spilling down or plunging of the heavier fluid over lighter, while Figure 4b suggests mixing by the appearance of many small-scale structures along the two parallel lines of the breaking wave. The corresponding spectra for all three components of kinetic and for the potential energy are shown in Figure 5. First we notice that although the spectra are highly anisotropic from the forcing scale (20 m) down to about the 1 m scale, there is an approximate ‘return’ to isotropy for the smaller scales. This is particularly evident in the kinetic energy spectra for $t = 11.82 T_F$ (panel c). In panels (a) and (c), we have made an attempt to draw the best fit inertial range spectra to determine the appropriate Kolmogorov constants (C_K) that fit these data. We did this for the $E_v(k)$ spectra, obtaining the best fit ‘by eye’ from enlarged portions of the small scale spectra. The result that was used to draw the inertial range model spectra in panels (a) and (c) is $(C_K) = 1.4$. In panels (b) and (d), the potential energy spectra are drawn. In these panels the small scales were fit to the Corrsin-Obukhov spectrum to determine the appropriate Corrsin constant. In panels (b) and (d) the Corrsin constants used to draw the model Corrsin-Obukhov spectrum were $C_o = 0.83$ and 0.8 respectively. In all panels the model buoyancy range spectrum drawn is $0.2N^2 k^{-3}$. Thus the Kolmogorov constant found here is somewhat smaller than the empirical values of 1.5 and the Corrsin constant is somewhat larger than the empirical value of 0.67. Nevertheless, the values are remarkably close to the empirical values, given that the spectral width of the inertial range here only covers wavelengths from about 1 meter to about 33 cm. Also the near collapse of the three kinetic energy spectra for small scales is encouraging. Thus it seems that the subgrid scale model is working well at small scales and that the dynamics of the transition from anisotropic buoyancy to the isotropic inertial range is acting as imagined in theoretical models. Finally, we should note that the value of ϵ from the simulations is about one third of the value observed by *Alford and Pinkel* (2000) associated with values of $N = 3$ cph. This appears quite reasonable given the level of modeling we have had to employ for the forcing and subgrid scale vortices.

Besides the kinetic and potential energy spectra, we

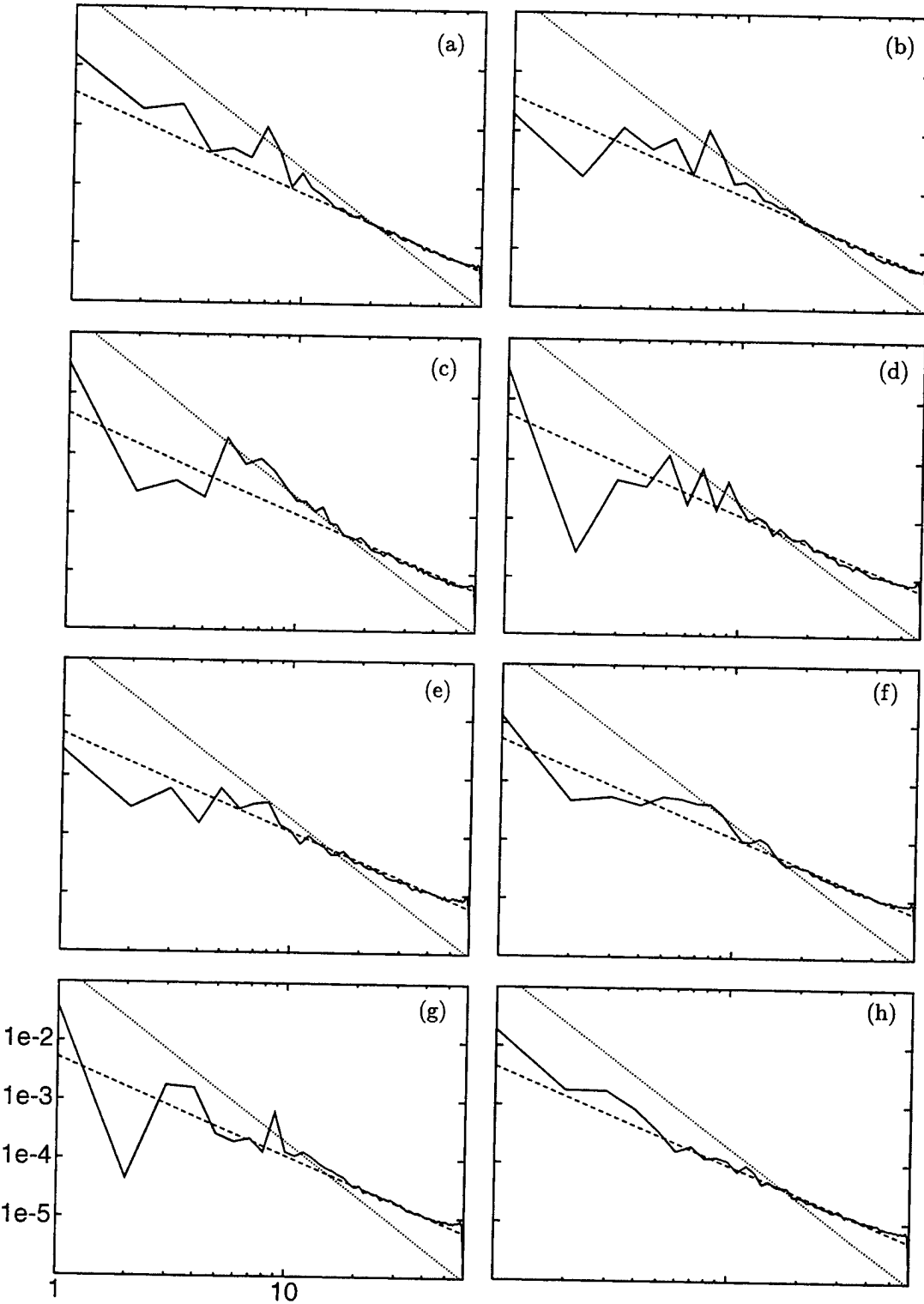


Figure 3. Kinetic energy spectra for the v component of the velocity during one cycle of the forcing. The dashed lines correspond to the Kolmogorov spectrum $(1/3)C_K \epsilon^{2/3} k^{-5/3}$ with $C_K = 1.5$ and the saturation spectrum $0.2N^2 k^{-3}$. The time interval between frames is $\Delta T_F/7$ and the first frame corresponds to time $t = 11.39T_F$. These are log-log plots of $E(k)$ in units of $N^2(L/2\pi)^3$ vs. k in units of $2\pi/L$. All plots have the scales as indicated in panel (g).

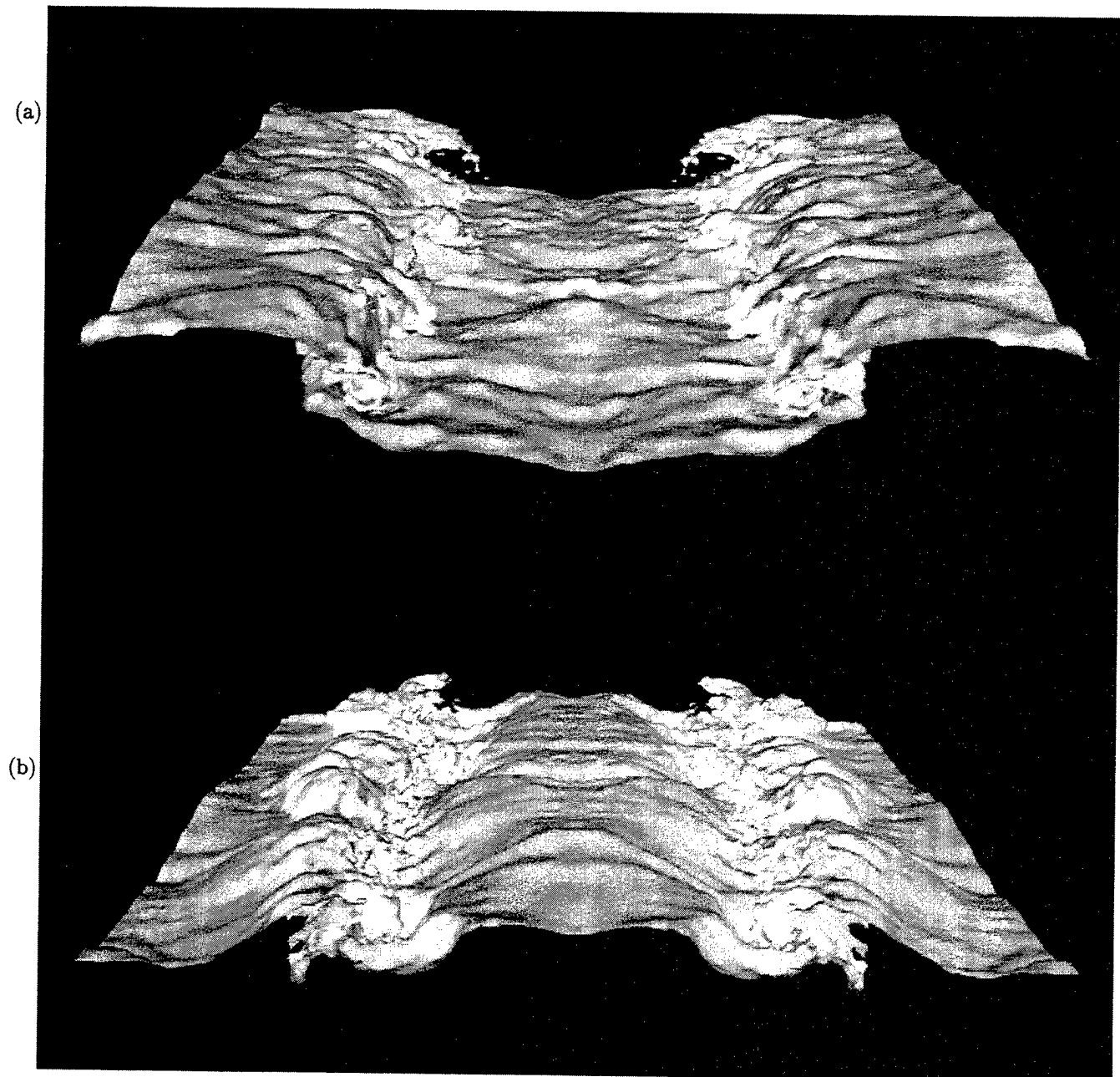


Figure 4. A breaking event visualized on the $\rho = \rho_0$ isopycnal. These are enlargements of the images shown in the composite Figure 2 in panels 3 and 4, corresponding to times (a) 11.68 and (b) 11.82 T_F (one seventh of a forcing period apart).

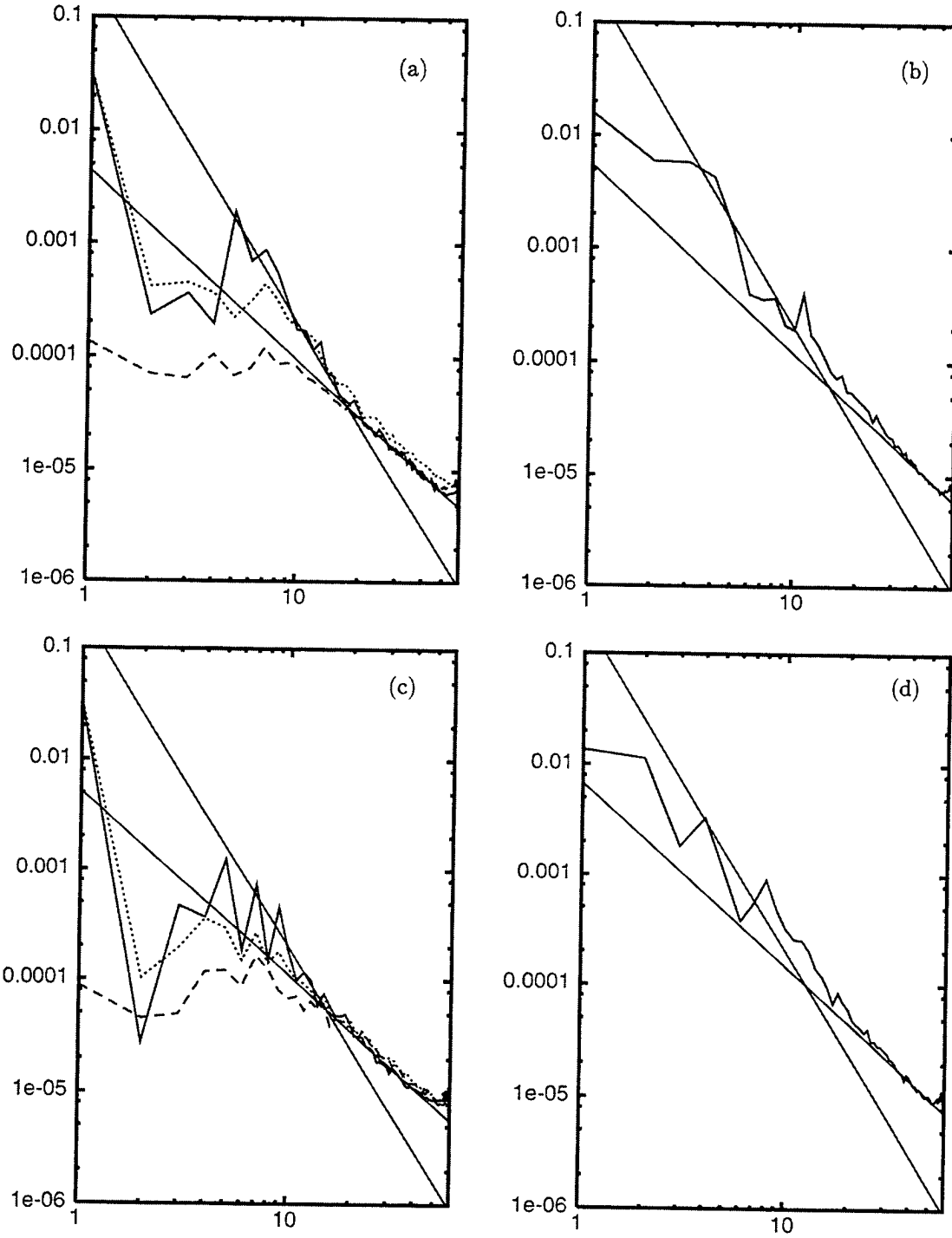


Figure 5. (a) Kinetic energy spectra for all three components of the velocity at time $t = 11.68T_F$. The thick long dashed, solid and short dashed lines correspond to the energy spectra for the u , v , and w components respectively. The thin solid lines correspond to the Kolmogorov spectrum $(1/3)C_K \epsilon^{2/3} k^{-5/3}$ with $C_K = 1.4$ and the saturation spectrum $0.2N^2 k^{-3}$. (b) Potential energy spectrum at time $t = 11.68T_F$. The thick solid line corresponds to the potential energy spectrum. The thin solid lines correspond to the Corrsin-Obukhov spectrum $C_o \epsilon_{pe} \epsilon^{-1/3} k^{-5/3}$ with $C_o = 0.83$ and the saturation spectrum $0.2N^2 k^{-3}$. (c) As in (a) but for $t = 11.82 T_F$ and $C_K = 1.4$. (d) As in (b) but for $t = 11.82 T_F$ and $C_o = 0.80$.

can also find predictions for the buoyancy flux spectrum in both the theory of Lumley-Shur (cf. Lumley 1964, 1967, Phillips 1967, Weinstock 1985) and the theory of Holloway (1983, 1986). The modal spectrum of the buoyancy flux can be written as

$$-g\mathcal{R} < w_{\mathbf{k}}^* \rho'_{\mathbf{k}} > / \rho_0. \quad (19)$$

If this quantity is positive, then for wavevector \mathbf{k} there is conversion of potential energy to kinetic energy, and vice versa if it is negative.

The prediction of the Lumley-Shur theory for the buoyancy flux spectrum in the buoyancy and inertial ranges is

$$BF(k) = -2D \frac{\epsilon_0}{k_b} \left(1 + D(k_b/k)^{4/3}\right)^{1/2} (k_b/k)^{7/3} \quad (20)$$

where k_b is as defined in (4) and D is a constant. Lumley (1964) assumed the buoyancy flux to be negative and, hence, D to be positive. In displaying his final result, Lumley incorporated D into his definition for k_b , but we will leave it explicit. Lumley's prediction of negative buoyancy flux through the buoyancy and inertial ranges is just the opposite of what we have found numerically for our wave-forced problem. All of the ingredients for an alternative prediction of the buoyancy flux are given in Holloway (1983), and based on this we have derived the same prediction as given in (20, but with the sign of D clearly arbitrary (for details see Carnevale et al., 2001).

In Figure 6a, we plot the buoyancy flux spectrum from our simulation as a function of k . This is a time averaged spectrum, where we have averaged over a period of $6T_F$, with time increment of $0.1T_F$. The time averaging is necessary to remove temporal fluctuations in the large-scales. Note that the buoyancy flux spectrum is negative for large scales ($1 < k < 3$), and positive for smaller scales. This implies a transformation of kinetic to potential energy at large scales (closest to the forcing scale $k = \sqrt{2}$) and a transfer of potential to kinetic energy at all smaller scales. Since our observed buoyancy flux spectrum is positive through both the buoyancy and inertial ranges, it can be compared to the theoretical prediction given by (20) only by choosing a negative value for D . To define the constant D , we note that the wavenumber where the buoyancy flux vanishes is determined by D . Here we shall choose D so that the zero value occurs at $k = 3.5$ (corresponding in our simulation to a wavelength of 5.7 m) since our buoyancy flux was found to vanish between $k = 3$ and $k = 4$. The theory will apply only above this wavenumber, and we can think of this as the lower limit on the buoyancy range, or the upper wavenumber of the Garrett Munk spectrum in the schematic shown in our introduction. To compute k_b , given by (4), we use the

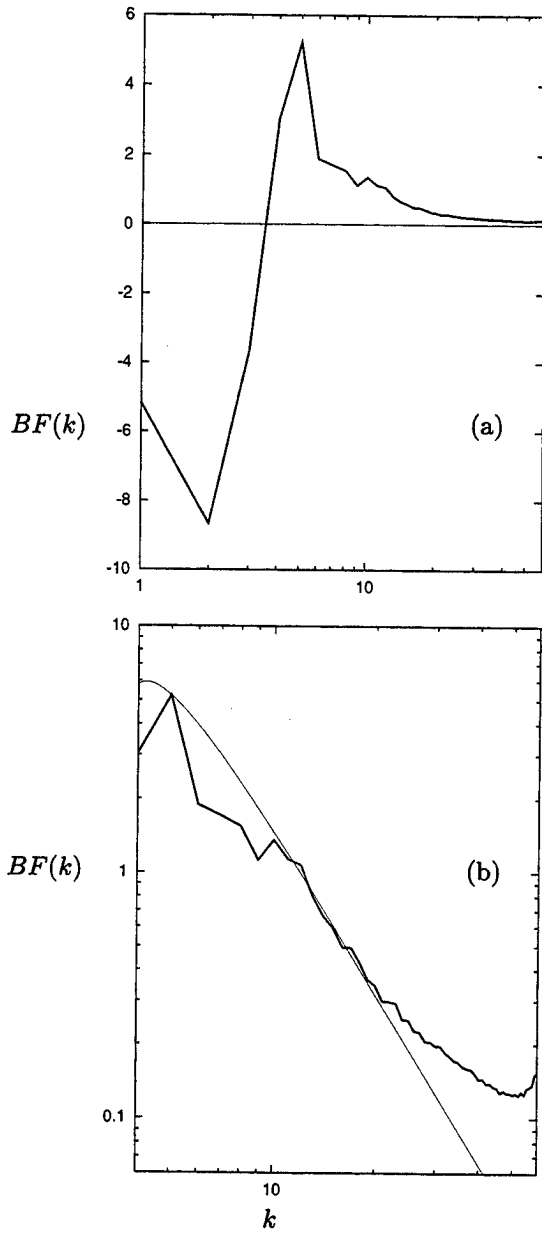


Figure 6. (a) Graph of the buoyancy flux spectrum averaged over 6 periods of the forcing, with 10 samples per period. (b) as in (a) but only the positive portion of the spectrum plotted in log-log format to compare with the theoretical spectrum of equation (20) with negative coefficient D . The result from the simulation is represented by the thick line, while the theoretical spectrum, based on $\epsilon_0 = \bar{\epsilon}$ where the overbar represents time averaging, is drawn as a thin line. All graphs in (a) and (b) are normalized by $\bar{\epsilon}/\kappa_b$.

time averaged dissipation rate $\bar{\epsilon}$. Thus all parameters in the theory are determined by the wavenumber where the buoyancy flux vanishes and the values of N and $\bar{\epsilon}$ (in this case $k_b \equiv (N^3/\bar{\epsilon})^{1/2} \approx 34.1$). The resulting theoretical buoyancy flux spectrum is compared in Figure 6b to the results from our simulation. For wavenumbers in the buoyancy range, the match between theory and simulations is reasonably good. For the theoretical curve, the decay with k is approximately $k^{-7/3}$ for all k above about 10. The simulation data follow the theoretical curve fairly well up to about wavenumber 20, where the simulation spectrum begins to deviate from $k^{-7/3}$, and is clearly much shallower than this for $k \geq 30$. This shallowness of the simulation spectrum for k greater than about 30 is probably an indication that the buoyancy flux is not captured properly by the SGS model near the high wavenumber cutoff. The cusp model viscosity grows rapidly with k for wavenumbers above about $k = 30$ and is largest at k_{max} . This is just the range where our buoyancy flux spectrum becomes very shallow. It is very possible that the artificial damping of the high k modes that the model performs to mimic transfer of energy beyond k_{max} does not allow for the proper treatment of the buoyancy flux in that region. But this is not unexpected for such a subgrid-scale model.

Positive buoyancy flux for small scales has also been found in other simulations. In direct numerical simulations (i.e. simulations without subgrid scale modeling) of forced stratified turbulence in both two and three-dimensions, *Holloway* (1988), and *Ramsden and Holloway* (1992) showed that the buoyancy flux was negative only at large scales and positive at small scales. These results were interpreted as meaning negative buoyancy flux for $k < k_b$ (i.e. in the buoyancy range) and positive buoyancy flux for higher k . However, the forcing used in their simulations was spectrally fairly broad, and it would not be inconsistent with their results to say that the buoyancy flux was negative at the strongly forced modes and positive for smaller scales as in our findings. Additionally, we have repeated our numerical simulations with a finite difference code using a Smagorinsky eddy viscosity, a very independent test, and also found positive buoyancy flux through the buoyancy and inertial ranges. In their finite difference LES study of shear driven stratified turbulence, *Kaltenbach et al.* (1994) also found positive buoyancy flux at small scales and negative at large scales, although we must note that the region of negative buoyancy flux in their simulations is spectrally very broad compared to ours. In two-dimensional flow simulations of the decay of a standing wave of just the type that we use for forcing our flow, *Bouruet-Aubertot et al.* (1996) found that the buoyancy flux was positive through most of the range

that they identified with the buoyancy range, and also that the flux followed a $k^{-7/3}$ spectral law in a run with grid resolution 256^2 and a slightly steeper law at resolution 512^2 (note that those simulations did not include an inertial range).

There was some discussion at the 'Aha Huliko'a meeting about the possibility that the sign of the buoyancy flux found in these simulations is affected by the type of forcing used. Our forcing inputs both potential and kinetic energy, while it may be more suitable to consider a source of kinetic energy alone in these problems. If there were no explicit external forcing of the density evolution, then the net buoyancy flux (averaged over time) would have to be negative to balance the drain of potential energy due to diffusion. This however does not mean that the buoyancy flux would have to be negative for all scales. Further simulations would be helpful to define how the buoyancy flux spectrum varies as the mix of kinetic and potential energy sources are changes.

Structures in regions of high strain rate

The main structure of interest in the buoyancy range evident in the density isosurfaces presented in the last section is the overturn produced by the curling over of the isosurface in a manner familiar from surface wave breaking. The overturning region shown in the breaking wave illustrated in Figure 2c has a vertical scale of about 2 meters. This is similar in size to overturns found in oceanographic measurements in the buoyancy range. *Alford and Pinkel* (2000) made an inventory of more than 2200 overturns. They found a median Thorpe scale, a measure of the vertical extent of the overturn, of 1.88 m. Note that this is not greatly different from the scale suggested by the transition point in the spectra shown in Figure 5, where the associated length scale is about 1.2 m. Since the observational data are primarily one-dimensional in space, it is difficult to form a three-dimensional image of those overturns. The ability to perform three-dimensional analysis of such structures is one of the benefits of numerical simulation.

Examining the full density field more thoroughly, we also find interesting structures of a rather different nature than those associated with strong vertical shear. These can be represented well by the deformations of the density surfaces that are the flat nodal surfaces of the forcing wave. We shall just refer to these surfaces as the nodal surfaces even when perturbed and deformed by eddies. The most basic motion of the fluid in the nodal surfaces is alternately toward and away from the centers of high strain; however, the combination of the large-scale background straining motion and small-scale eddies produces localized deformations of the nodal surface that can result in overturning and mixing in a man-

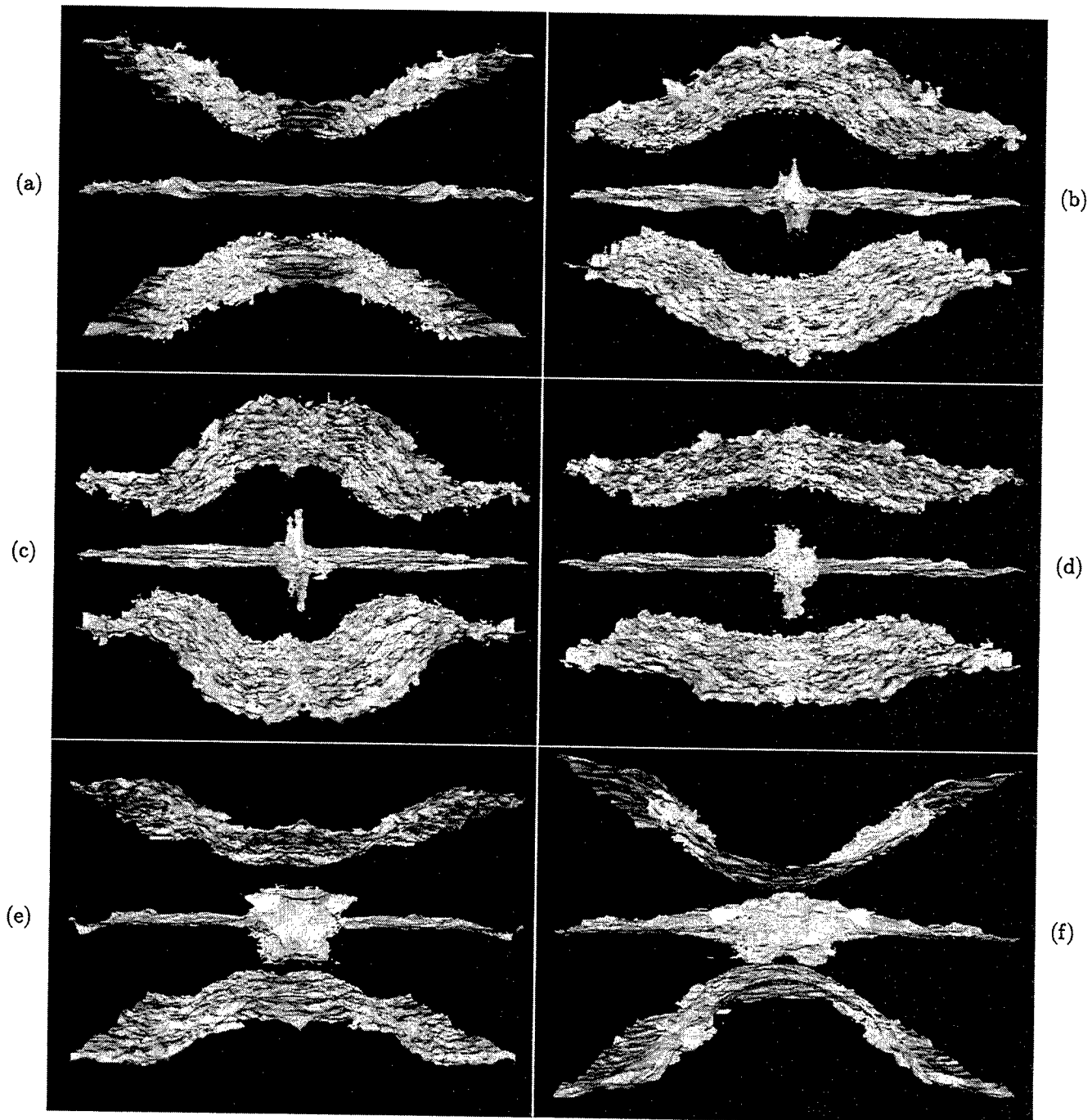


Figure 7. The evolution of three density isosurfaces ($g^*(\rho - \rho_0)/\rho_0 = 0, \pi/2, \pi$) showing the evolution of 'spouts' from a 'nodal surface' and their subsequent collapse with considerable broadening and mixing. Times represented are $t = 12.1, 12.4, 12.5, 12.7, 12.8$, and $13.1 T_F$.

ner different from the overturns discussed in the last section. By plotting simultaneously three density isosurfaces (one 'nodal surface' and the most strongly perturbed isosurfaces above and below it) for a sequence of times during the forcing cycle, we can get some understanding of the nature, formation, evolution, and fate of these structures. In Figure 7, the sequence proceeds from left to right, top to bottom. We have shifted our view of the computational domain by an amount in the vertical sufficient to center the upper 'nodal surface' in the image. Above and below the 'nodal surface,' the most strongly displaced isosurfaces are shown. The upper and lower isosurfaces move vertically but always in opposite directions at any horizontal location. The combined effect of the motion of these surfaces above and below the 'nodal surface' produces vertical 'dilation' and 'compression' centered on the 'nodal surface' without producing large-scale sinusoidal displacement of that surface. In panels (a), (b) and (c), the upper/lower surface is moving upward/downward in the middle of the domain (i.e. at $y = 0$, where y is the horizontal coordinate), and oppositely at the left and right ends of the domain. This is associated with the vertical straining of the nodal surface in the middle and at the left and right ends of the domain. In panel (b) the isosurface 'erupts' with elements moving up and down along a midline pointing into the plane. The eruption reaches its maximum extension when the upper and lower surfaces stop their motion, and reverses direction around the time of panel (c). At $y = 0$ on the 'nodal surface' this is a time of maximum vertical dilational strain but zero strain rate (where $\partial w / \partial z$ is the vertical strain rate). The structures formed by these eruptions represent localized intrusions of heavy fluid into light fluid and vice versa. We shall refer to them as 'spouts.' As the upper and lower isosurfaces move back toward the 'nodal surface,' the sense of straining motion is reversed and the spouts that were formed are flattened. This causes a spreading out of these structures, which in some cases results in tossing elements of the spouts to the right and left of the midline. This leads to the kind of pattern seen in panel (e) which is in part an elongated horizontal structure as opposed to the elongated vertical structures originally produced during the vertically dilational phase of the large-scale straining motion. The final panel (f) shows the isosurface a short time after the upper and lower surfaces have again reversed their direction of vertical motion. This is a phase of the motion near to that of the initial panel (a), but now there is a mixed patch of fluid at the mid section ($y=0$) of the 'nodal surface.'

To summarize, we can say that the 'spouts' originate from small-scale deviations of the nodal surface created by turbulent flow at the nodal surface. Once

perturbations pull structures from the nodal planes vertically, these elements are subject to advection due to the large-scale straining motion of the forcing wave. At times and positions where the straining is highly dilational in the vertical, these deviations from the flat plane elongate vertically and narrow horizontally, forming 'spouts.' Then, during the vertically compressional and horizontally dilational phase of the forcing, the spout is elongated horizontally creating regions of convectively unstable overturned fluid. Note that if the large-scale forcing were the only field acting on the spout, than the growth of the spout would simply have been reversed when the sense of the straining motion was reversed. Thus the presence of the eddy field must play an important role in this irreversible process. The distortions of the spout by the eddy field are enhanced during the horizontally dilational phase of the evolution.

Internal-wave packets

The observations of *Alford and Pinkel* (2000) show vertically propagating structures at depths from 150 to 350 m which they suggest may be internal wave packets. These structures have vertical extent of about 50 m with internal vertical wavelengths of about 12 m and are associated with overturning events with vertical scales of about 2 m. Recent theoretical analysis by *Thorpe* (1999) provides a criterion for determining whether the small-scale turbulence generated by the overturns in a packet will be left behind in just small patches or in continuous 'scars' much longer than the size of the packet. Stimulated by these developments, we have embarked on a numerical investigation of internal wave packets.

Assuming a constant background Brunt-Väisälä frequency N and ignoring the effects of the earth's rotation, the intrinsic dimensional frequency for internal waves is

$$\sigma = N \frac{k_h}{k}. \quad (21)$$

The observed frequency for one of the wavepackets in the *Alford and Pinkel* (2000) data is 4 cph. This is higher than the ambient $N \approx 3$ cph. Since $\sigma_{max} = N$, it is assumed that the observed frequency for this packet is the sum of the intrinsic frequency plus a Doppler shift. To predict this shift, it is necessary to know the wavelength of the packet, the magnitude of the ambient current and its direction relative to the packet propagation direction. *Alford and Pinkel* (2000) suggest that the intrinsic frequency for their packet with observed frequency of 4 cph is near 0.14 cph which leads one to a wavelength of 180 m. This suggests that the horizontal wavelengths in both directions are much larger than the vertical wavelength. For our numerical modeling, this

represents a difficulty. We are reluctant to introduce anisotropic grids for fear of the distortions that might result, especially when applying simple sub-grid scale models. Thus, in this preliminary work, we decided to consider only the case in which horizontal and vertical wavelengths were equal. The corresponding intrinsic frequency would then be about 2 cph which would still be consistent with the observed packet, just requiring less of a Doppler shift to match the observed frequency.

As for the amplitude of the observed packets, this can be given in terms of the peak magnitude of the observed strain rate $\partial w/\partial z$. The maximum value of vertical strain rate in the *Alford and Pinkel* (2000) observations is approximately N , and in the case of the particular packet discussed above, it seems that the maximum is about $0.38N$.

In what follows, we will examine the evolution of a particular wave packet with two-dimensional simulations. In an attempt to reproduce the kind of behavior evident in the observations, we used simulations in a domain of 200 m in both width and depth. We used a packet with non-dimensional wavenumbers of 12 in both directions, corresponding to vertical and horizontal wavelengths of $(200 \text{ m})/12 \approx 17 \text{ m}$. Our 2D simulations had an effective resolution corresponding to a cut-off wavelength of $\approx 0.8 \text{ m}$. To follow this phenomenon in DNS with all relevant scales well resolved would require resolution from 200 m down to a few cm, which is somewhat impractical. Since the subgrid scale model used in the 3D simulations is not appropriate in 2D, we had recourse to hyperviscosity (with the Laplacian taken to the eighth power). The simulations illustrated here are from a spectral code dealiased with the 3/2 rule (*Orszag* 1971). Although there are 768 wavevectors used in each direction, after application of the 3/2 rule this leaves only 512 active modes in each direction.

Linear dispersion of packets

The linearized version of the Boussinesq evolution equations can be used to obtain a model of the internal wave packet. The vorticity and density of a plane internal wave can be written dimensionally as

$$(\omega_x, \omega_y, \omega_z, \rho') = A\mathbf{e}_k \exp i(\mathbf{k} \cdot \mathbf{r} - \sigma t), \quad (22)$$

where A is an arbitrary amplitude and \mathbf{e} is the eigenvector

$$\mathbf{e}_k = (gkk_y/Nk_h, -gkk_x/Nk_h, 0, \rho_0). \quad (23)$$

Taking a linear superposition of such waves distributed continuously in wavevector space and centered on a particular wavevector, say \mathbf{k}_0 , would produce an internal

wave packet. For example,

$$(\omega, \rho') = \mathcal{R} e \int G(\mathbf{k} - \mathbf{k}_0) \mathbf{e}_k e^{i(\mathbf{k} \cdot \mathbf{r} - \sigma t)} d^3 k, \quad (24)$$

with

$$G(\mathbf{p}) \equiv A \exp (-a^2 p_x^2 - b^2 p_y^2 - c^2 p_z^2), \quad (25)$$

where a , b , and c are length scales, represents a propagating ellipsoidal packet. A slight generalization based on simple coordinate rotations will also permit an arbitrary choice for the orientation of the ellipsoidal envelope relative to the crests internal to the packet. Within the envelope, the vorticity and density fields will have a phase velocity in the direction of \mathbf{k}_0 and group velocity

$$\mathbf{c}_g = \nabla_{\mathbf{k}} \sigma_{\mathbf{k}}, \quad (26)$$

which is perpendicular to the phase velocity.

By varying the dimensions a , b and c , we can change the shape of the packet as needed. A likely candidate for the packets whose effects are observed in *Alford and Pinkel's* (2000) data would suggest that at least one of these lengthscales is very large. For the present calculations we take a to be infinite. Then we chose b and c and the orientation of the system to be such that the envelope is an ellipse with major axis aligned along the direction of propagation. Other choices may also be of interest, but that will be explored in future work. With the ellipse as chosen, the phase velocity is directed along the short axis and the group velocity along the long axis. In a numerical simulation, the packet can only be approximated, with the integral replaced by a discrete sum of wavevectors. By using (24) and (25) with $t = 0$, we are able to construct the initial condition for a packet that is both reasonably confined in space and well resolved internally.

The first issue that we need to address is the dispersive spreading of the wave packet. Simple arguments suggest that the physical extent of the wave packet will grow as $\Delta c_g t$ in the direction of the group velocity, where Δc_g represents the spread in group velocities calculated for the individual wavevectors that contribute significantly to the wave packet. We can make some crude dimensional estimates for the rate of dispersion by setting $c_g \sim N/k_0$ and $\Delta c_g \sim (N/k_0^2)\Delta k_0$, where Δk_0 measures the spread of wavenumbers in the packet. If we call Δx_0 , the initial length of the wavepacket, then the change in the size of the packet can be crudely taken as

$$\Delta x - \Delta x_0 = \Delta c_g t. \quad (27)$$

The packet would then double in size by a time $t_d \sim \Delta x_0/\Delta c_g$, and the distance that the packet can travel before doubling is

$$x/\Delta x_0 \sim k_0/\Delta k_0. \quad (28)$$

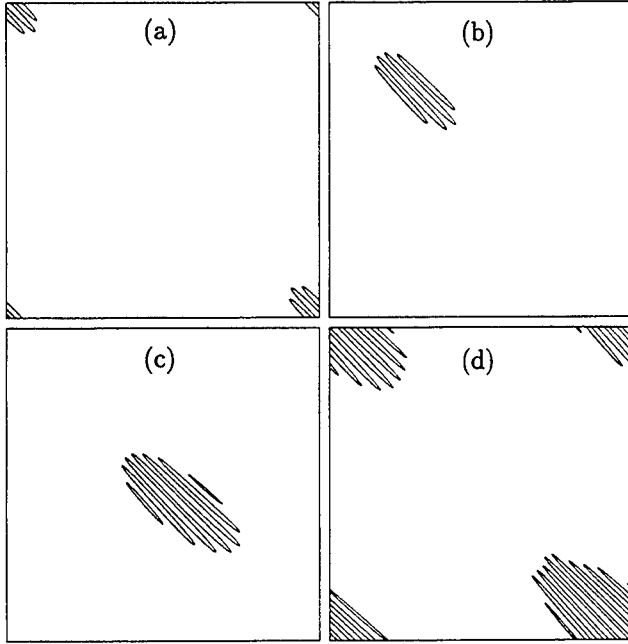


Figure 8. Contours of the magnitude of the perturbation density $|\rho'/\rho_0|$ from a simulation of the linear propagation of a wavepacket. The domain size is 200 m on each side. The vertical axis is depth. The only contour level drawn is that at 0.5 of the maximum field value. The time sequence of the panels is (a) $t=0$, (b) $t=3$ hr, (c) $t=6$ hr, and (d) 11 hr.

For the packet used in the simulations this predicts a doubling after propagation of about 200 m.

In Figure 8, we show the evolution of the density perturbation field during the propagation of our packet following purely linear dynamics. In each panel, only the contour level corresponding to $0.5|\rho'/\rho_0|$ is drawn. Positive and negative values have not been indicated, but clearly the sign of ρ' will alternate from one wave crest to the next. We see the packet propagates along the diagonal. This is in agreement with the fact that the wavevector is $\mathbf{k} = (12, 12)$ and that the group velocity is perpendicular to this. It is less obvious from the few panels that we can include here that the phase of the waves within the packet advances in the direction of \mathbf{k} . The average speed of the packet in propagating from one corner of the domain to the opposite corner is correctly given by $|c_g|$. Furthermore, we see that the width and length of the packet grow to a little more than double their original values in the time it takes to cross from one corner of the domain to the other, and this is correctly predicted by the formula (28). During the period of evolution illustrated, the peak amplitude of the packet decays to 25% of its initial value.

Although the amplitude of the packet can be changed

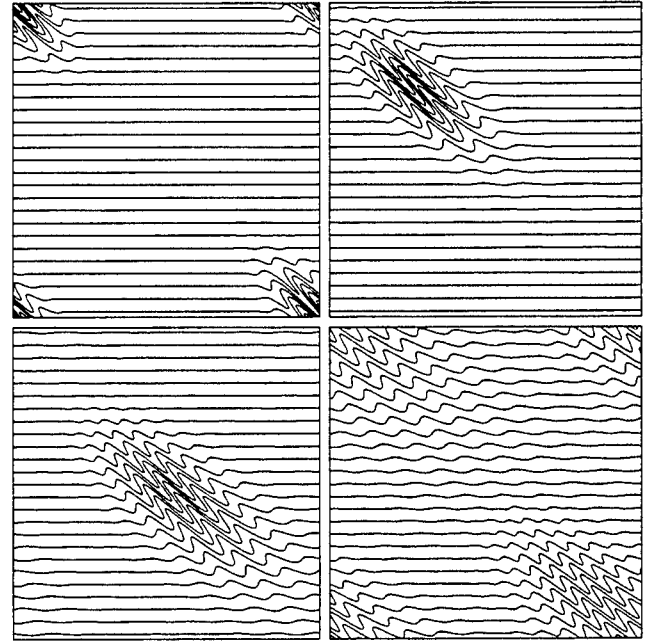


Figure 9. Contours of ρ/ρ_0 from a simulation of the linear propagation of a wavepacket. The domain size is 200 m on each side. The vertical axis is depth. The time sequence of the panels is the same as in Figure 8. The contour increment is such that the vertical separation between unperturbed isopycnals is 8 m.

arbitrarily in this purely linear simulation, we may simply assign an amplitude to see the effect of such a packet on the full density field. This is done in Figure 9. The amplitude used represents fluctuations in $\partial w/\partial z$ about five times the maximum actually observed in the Alford and Pinkel (2000) data. Nevertheless, we have used this packet with exaggerated amplitude to more clearly illustrate the nature of the linear propagation. In such a strong packet, there are regions of strong overturning, which, if the packet is not propagating too rapidly, would develop convective instability under the full nonlinear dynamics.

Nonlinear propagation of packets

Having determined that our packet propagates correctly under linear dynamics, we then investigated its evolution with the complete Boussinesq equations. The amplitude of the observed packet discussed in the introduction is such that the maximum value of the strain rate $\partial w/\partial z$ is about $0.38N$. With the packet amplitude set to match this value as its maximum $\partial w/\partial z$, we performed the simulation illustrated by contour plots of ρ'/ρ in Figure 10. This figure should be compared to

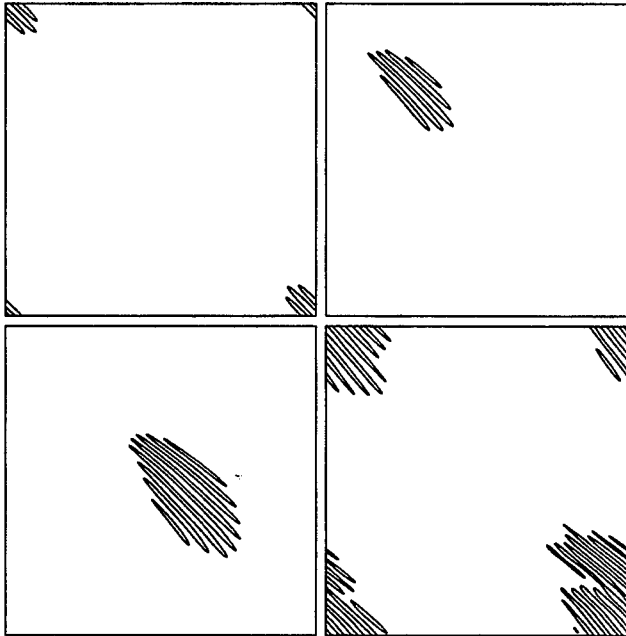


Figure 10. Contours of the magnitude of the perturbation density $|\rho'/\rho_0|$ from a simulation of the nonlinear propagation of a wavepacket with $\max \partial w/\partial z \approx 0.38N$. The domain size is 200 m on each side. The vertical axis is depth. The only contour level drawn is that at 0.5 of the maximum field value. The time sequence of the panels is the same as in Figure 8.

the corresponding figure for linear evolution, Figure 8. The times represented are the same in each figure. By the time of panel (b) a clear asymmetry in the form of the packet has developed in the nonlinear case and there is some clear distortion of the packet in the final panel. Nevertheless, the overall evolution of this nonlinear packet is not very different from the linear case. This packet is so weak that the initial condition is not overturning anywhere and the Richardson number is above 1 everywhere. Thus, the classical criteria for convective instability and shear instability are not satisfied in this packet. This continues to be the case throughout the simulation in spite of small-scale generation by nonlinear wave-wave interactions. An idea of how weak this packet is can be obtained graphically from the plots of the density contours as illustrated in Figure 11.

The next case that we will treat is one for which the amplitude of the packet is just above the threshold for overturning. The amplitude of this packet in terms of its maximum strain rate is $\partial w/\partial z = 0.76N$. In Figure 12,

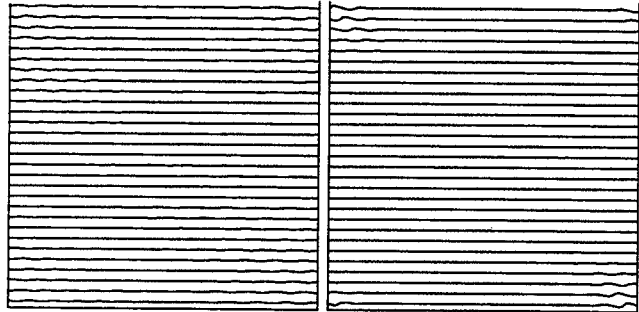


Figure 11. Contours of ρ/ρ_0 from the same simulation as represented in Figure 10. The domain size is 200 m on each side. The vertical axis is depth. The two times illustrated correspond to the first and last times of Figure 10. The contour increment is such that the vertical separation between unperturbed isopycnals is 8 m.

we display the contour plots for the perturbation density at the same times as in the previous figures. We see that there is some early production of small scales that are evident in the wake of the packet. By $t = 6$ hr the packet itself has become badly distorted, and by $t = 11$ hr, it has degenerated into small-scale structures, although these still retain to some extent an organization and alignment related to the original structure of the packet. To better illustrate the decay of this packet, we display contour plots of the full density field from $t = 2.5$ hr to $t = 4.8$ hr in Figure 13. Each frame is an enlarged image centered on the wave packet, showing only a portion of the domain (a square of size 200/3 m on a side). In panel (a) we see an early stage in which the wave is overturning at points, but there has not yet been any strong production of energy in scales smaller than 2 m (note that the spacing between the unperturbed isopycnals is 2 m). There are four relatively strong crests evident in panel (a). These crests

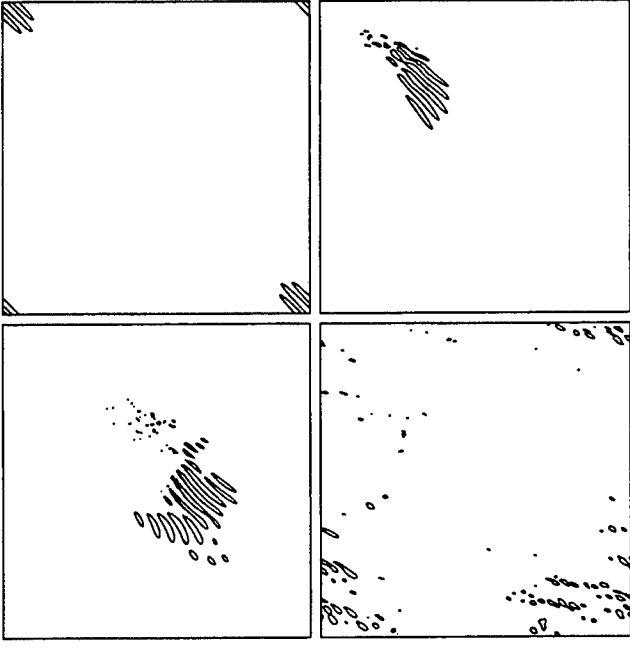


Figure 12. Contours of the magnitude of the perturbation density $|\rho'/\rho_0|$ from a simulation of the nonlinear propagation of a wavepacket with $\max \partial w/\partial z \approx 0.76N$. The domain size is 200 m on each side. The vertical axis is depth. The only contour level drawn is that at 0.5 of the maximum field value. The time sequence of the panels is the same as in Figure 8.

are advancing from bottom-left to top-right in these figures. The weakest crest (bottom-left) is just entering the packet in panel (a). In the linear evolution as each crest passes through the packet from bottom-left to top-right, its amplitude first increases and then decreases. As envisioned by Thorpe (1999), the crests amplify as they move toward the center of the packet and break leaving small-scale perturbations behind that link up with the ‘debris’ produced by the passage of previous crests. The period of the sequence of panels shown here is long enough for the weak crest on the lower-left side of the packet in panel (a) to move completely through the packet, finally becoming the weak crest on the upper-right side. In the case we have simulated here, the crests do produce overlapping zones of small-scale perturbations that form a somewhat continuous scar, a possibility suggested by Thorpe (1999). One should note, however, that during the period when a particular crest is actually breaking, the overturning and small-scale production is not uniform along the length of the crest, as assumed in Thorpe’s idealized model, but rather appears in spots along the crest (see panels (c) and (d)). Also the breaking and subsequent scar formation does

not continue indefinitely. The strength of the packet is both dispersed and dissipated, so that by $t = 210N^{-1}$ the process of scar formation has ceased.

We have also performed 3D simulations of the propagation of these wave packets. The general evolution exhibited in the 2D simulations is also found in 3D, although in 3D we did not have sufficient resolution adequately capture the 2 m overturns. Further details can be found in Carnevale and Orlandi (2000).

Theory of packet evolution

We have addressed here questions about the longevity of wave groups. A theory for the evolution of the packet envelope has been developed by Shrira (1981) via multiscale analysis in both space and time. His result for the evolution of the amplitude A of the packet in the two-dimensional case studied above is

$$\begin{aligned} & iA_\tau + \{\sigma_{k_y k_y} A_{yy} + 2\sigma_{k_y k_z} A_{yz} + \sigma_{k_z k_z} A_{zz}\} \\ & - \frac{i}{6} \{ \sigma_{k_y k_y k_y} A_{yyy} + 3\sigma_{k_y k_y k_z} A_{yyz} + 3\sigma_{k_y k_z k_z} A_{yzz} \\ & + \sigma_{k_z k_z k_z} A_{zzz} \} = -i\gamma A(AA_s^* - A^*A_s), \end{aligned} \quad (29)$$

where k_y and k_z are components of the central wavevector of the packet, σ is the intrinsic frequency corresponding to the central wavevector, s is the coordinate in the direction of propagation of the packet, $\partial/\partial\tau = \partial/\partial t + c_g\partial/\partial s$, c_g is the magnitude of the group velocity, and

$$\gamma = k^3/(\sigma k_y k_z). \quad (30)$$

The typical equation that arises for the evolution of a wave-packet envelope is the cubic Schroedinger equation which is significantly different from (29). It turns out that the term corresponding to the nonlinearity in the cubic Schroedinger vanishes identically here due to the fact that a plane wave cannot interact with itself. Thus Shrira had to go to third order in the multiple scale analysis to obtain the first contributions of the nonlinearity to the evolution. This still involves a cubic term for the nonlinearity, but now not the simple $A|A|^2$ of the cubic Schroedinger equation, and the presence of the third order spatial derivatives from the linear terms further complicates matters. Notice that the coefficients depend in magnitude and sign on the orientation of the central wavevector of the packet. Thus we can anticipate interesting results as this wavevector is varied. In addition, there are nonlocal nonlinear terms that arise if the flow is three dimensional that further greatly complicate the evolution. In future work, we plan to investigate the evolution of the packet analytically based on Shrira’s equations, and make a comparison with our numerical results.

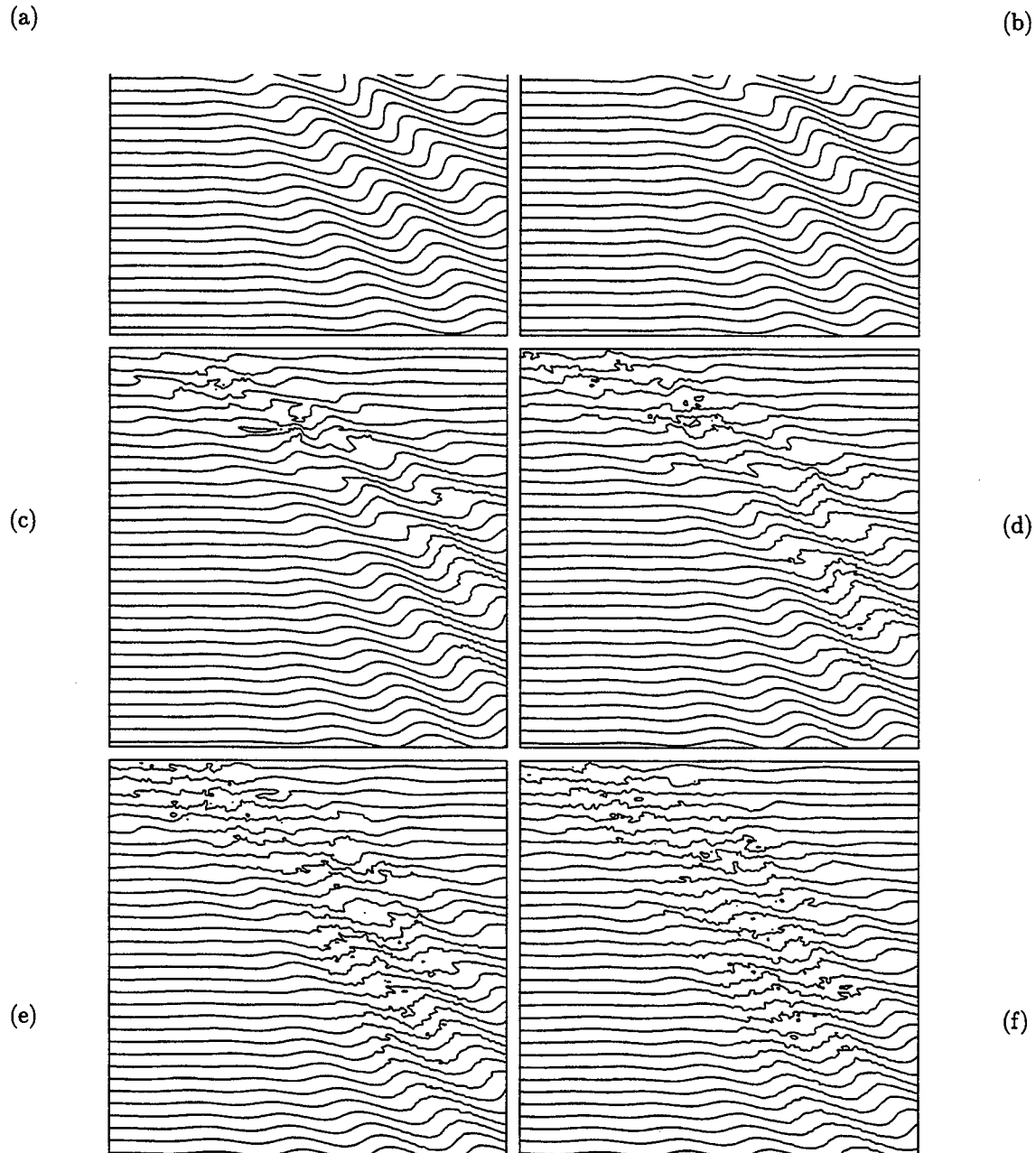


Figure 13. Contours of ρ/ρ_0 from a simulation of the nonlinear propagation of a wavepacket with initially max $\partial w/\partial z \approx 0.76N$. Only a portion of the computational frame is shown, and this corresponds to a square $200/3$ m on each side. The contour increment is such that the vertical separation between unperturbed isopycnals is 2 m. The times corresponding to the panels are (a) 2.5, (b) 2.9 (c) 3.5, (d) 3.9, (e) 4.4 and (f) 4.8 hr.

Conclusions

We have attempted with some very idealized numerical modelling to shed some light on the structures that may be responsible for the variability observed in the oceanic thermocline. This attempt has been successful to a certain extent. We were able to show a transition from buoyancy to inertial range that follows the features of the observed spectra, but only during a breaking event. To what extent this simulated transition is related to the actual transition in the oceanic observations is still not clear. We were able to give three-dimensional structure to a classical shear type instability much as found in the observations and at about the correct vertical scale. In addition, we described an unexpected kind of overturning and mixing that occurs in regions of high strain rate. The correlation for overturns and high strain rate was suggested by *Alford and Pinkel* (2000), and yet it is not clear at this point whether the structures we were able to simulate are directly related to any of the overturns reported in that paper. Finally, two-dimensional simulations demonstrated that a packet with approximately the correct vertical structure can propagate through a substantial portion of a thermocline as observed by *Alford and Pinkel* (2000) without dispersing radically and with the production of overturns on the scale of about 2 m which is entirely consistent with Alford and Pinkel's observations. Unfortunately, these simulations could not also capture the large horizontal scales nor the rapid advection of packets that is suggested by *Alford and Pinkel* (2000). Thus, we feel that there has been some progress in demonstrating the possibility of analyzing the small-scale fluctuations in the thermocline with numerical simulations using subgrid scale parameterizations, and look forward to advancing this work so that closer comparisons with observations may be possible.

Acknowledgments

This research has been supported by Office of Naval Research grants N00014-97-1-0095 and N00014-96-0762. Numerical simulations were performed at the San Diego Super Computer Center and the Center for Turbulence Research, Stanford. We thank the staff of the San Diego Supercomputer Center for help in preparing the three-dimensional images for this paper and the animation used in this research. Additional computing support was provided by the Office of Naval Research and the University of Rome. We thank Matthew Alford, Lou Goodman, Myrl Hendershott, Greg Holloway, James Lerczac, Robert Pinkel and David Siegel for very helpful discussions and suggestions.

References

- Alford, M., and R. Pinkel, Observations of overturning in the thermocline: the context of ocean mixing. *J. Phys. Oceanogr.*, 30, 805-832, 2000.
- Bouruet-Aubertot, P., J. Sommeria, and C. Staquet, Breaking of standing internal gravity waves through two-dimensional instabilities. *J. Fluid Mech.*, 285, 265-301. 1995.
- Bouruet-Aubertot, P., J. Sommeria, and C. Staquet, Stratified turbulence produced by internal wave breaking: two-dimensional numerical experiments. (4th International Symposium on Stratified Flows, Grenoble, France, 29 June-2 July 1994). *Dyn. Atmos. Oceans*, 23, 357-69, 1996.
- Carnevale, G.F., and M. Briscolini, Large Eddy Simulation of Oceanic Fine Structure, '*Aha Huliko'a, Internal Wave Modeling, Proceedings, Hawaiian Winter Workshop, University of Hawaii, January 19-22, 1999*' eds. P. Muller and D. Henderson, pp. 279-288, 1999.
- Carnevale, G.F. and P. Orlandi, Propagation of internal wave packets in the thermocline, Proceedings of the 2000 Summer Program, Center for Turbulence Research, Stanford University pp. 119-130, 2000.
- Carnevale, G.F., M. Briscolini, M., and P. Orlandi, Buoyancy to inertial range transition in forced stratified turbulence *J. Fluid Mech.*, 427, 05-239, 2001.
- Gargett, A.E., P.J. Hndricks, T.B. Sanford, T.R. Osborn, and A.J. Williams, A composite spectrum of vertical shear in the upper ocean. *J. Phys. Oceanogr.*, 11, 1258-1271, 1981.
- Gargett, A.E., Evolution of scalar spectra with the decay of turbulence in a stratified fluid. *J. Fluid Mech.*, 159, 397-407, 1985.
- Garrett, C., and W. Munk, Space-time scales of internal waves: A progress report. *J. Geophys. Res.*, 80, 291-297, 1975.
- Gibson, C.H., Internal waves, fossil turbulence, and composite ocean microstructure spectra. *J. Fluid Mech.*, 168, 89-117, 1986.
- Gregg, M.C., Variations in the intensity of small-scale mixing in the main thermocline (Pacific Ocean). *J. Phys. Oceanogr.*, 7, 436-454, 1977.
- Gregg, M.C., Scaling turbulent dissipation in the thermocline. *J. Geophys. Res.*, 94, 9686-9698, 1989.
- Herring, J.R., and O. Metais, Spectral transfer and bispectra for turbulence with passive scalars. *J. Fluid Mech.*, 235, 103-121, 1992.
- Holloway, G., Theoretical approaches to interactions among internal waves, turbulence and finestructure. in *Nonlinear Properties of Internal Waves*, AIP conference proceedings No. 76, (ed. B.J. West, AIP, New

- York), 1981.
- Holloway, G., A conjecture relating oceanic internal waves and small-scale processes. *Atmos. Ocean.*, 21, 107-122, 1983.
- Holloway, G., Considerations on the theory of temperature spectra in stably stratified turbulence. *J. Physical. Oceanogr.*, 16, 2179-2183, 1986.
- Holloway, G., The buoyancy flux from internal gravity wave breaking. *Dyn. Atmos. Oceans*, 12, 107-125, 1988.
- Kaltenbach, H.-J., T. Gerz, and U. Schumann, Large-eddy simulation of homogeneous turbulence and diffusion in stably stratified shear flow. *J. Fluid Mech.*, 280, 1-40, 1994.
- Lesieur, M., and R. Rogallo, Large-eddy simulation of passive scalar diffusion in isotropic turbulence. *Phys. Fluids A*, 1, 718-722, 1989.
- Lesieur, M.. *Turbulence in Fluids*, Dordrecht; Boston, Kluwer Academic Publishers, 1997.
- Lumley, J.L., The spectrum of nearly inertial turbulence in a stable stratified fluid, *J. Atmos. Sci.*, 21, 99-102, 1964.
- Lumley, J.L.. 1967 Theoretical aspects of research on turbulence in stratified flows, in *Atmospheric Turbulence and Radio Wave Propagation*, Proceedings of the International Colloquium, Moscow 1965 (A.M. Yaglom and V.I. Tatarsky, Eds), *Nauka*, Moscow, 121-128, 1967.
- McEwan, A.D., The kinematics of stratified mixing through internal wavebreaking, *J. Fluid Mech.*, 128, 47-57, 1983.
- Orszag, S.A., On the elimination of aliasing in finite-difference schemes by filtering high-wavenumber components, *J. Atmos. Sci.*, 28, 1074, 1971.
- Phillips, O.M., On the Bolgiano and Lumley-Shur theories of the buoyancy subrange. *Atmospheric Turbulence and Radio Wave Propagation* Proceedings of the International Colloquium, Moscow 1965 (A.M. Yaglom and V.I. Tatarsky, Eds), *Nauka*, Moscow, 121-128, 1967.
- Ramsden, D., and G. Holloway, Energy transfers across an internal wave-vortical mode spectrum. *J. Geophys. Res.*, 97, 3659-3668. 1992.
- Siegel, D.A., and J.A. Domaradzki, Large-eddy simulation of decaying stably stratified turbulence, *J. Phys. Oceanogr.*, 24, 2353-86, 1994.
- Shrira, V.I., On the propagation of a three-dimensional packet of weakly non-linear internal gravity waves. *Int. J. Non-Linear Mech.*, 16, 129-138, 1981.
- Taylor, J.R., The energetics of breaking events in a resonantly forced internal wave field, *J. Fluid Mech.*, 239, 309-340, 1992.
- Thorpe, S.A., On internal wave groups, *J. Phys. Oceanogr.*, 29, 1085-1095, 1999.
- Weinstock, J., On the theory of temperature spectra in a stably stratified fluid. *J. Phys. Oceanogr.*, 15, 475-477, 1985.

Mixing and diapycnal advection in the ocean

Louis C. St. Laurent

School of Earth and Ocean Sciences, University of Victoria, Victoria, British Columbia, Canada

John M. Toole and Raymond W. Schmitt

Woods Hole Oceanographic Institution, Woods Hole, Massachusetts, USA

Abstract. In the stratified ocean, vertical motions arise from both adiabatic and diabatic mechanisms. Diapycnal advection is the vertical component of flow across an isopycnal surface which occurs when mixing produces a divergent flux of buoyancy. Buoyancy forcing of the lateral flow by vortex stretching occurs when diapycnal advection rates vary with depth. Microstructure observations of enhanced turbulence above rough topography are presented. These data allow us to distinguish the influence of diabatic forcing on the circulation. Estimates of diapycnal advection are used to quantify the diabatic flow, and the role of diapycnal advection as a mechanism of vortex stretching on the circulation is assessed. The divergence of diapycnal mass flux is found to be a significant forcing mechanism for the circulation occurring above fracture zone topography. Moreover, both the direction and magnitude of diapycnal advection are dependent on the efficiency of turbulence at generating a buoyancy flux. Depth variations of diapycnal advection suggest the mixing efficiency is reduced in weakly stratified abyssal canyons.

Introduction

The sun heats the Earth's atmosphere and ocean, driving the winds, evaporation, and rain. These act over global scales to input mechanical energy and variance to the scalar fields of the ocean. Turbulence acts at the smallest scales of fluid motion, where variance is dissipated by molecular processes. Stirring is the mechanism that acts at the intermediate range of scales, advecting variance both in physical and wavenumber space.

The input of variance at the largest scales is related to the mechanical and buoyancy forcing that drives the so-called "large-scale circulation". However, circulations can be forced by mechanisms occurring anywhere along the variance cascade. For example, Spall (1994) describes large-scale abyssal recirculations driven by the eddy fluxes of topographic waves. Examples of eddy driven mean flows are described by Lozier (1997) and Alves and Colin de Verdiere (1999). Buoyancy forcing may also originate at any scale. In particular, turbulent mixing at the smallest scales of motion can give rise to

divergent fluxes of heat and salt. If the buoyancy forces that result from turbulence are significant relative to other forcing, a large-scale circulation may develop by the direct influence of small-scale mixing. Spall (2000) demonstrates that mixing near large-scale topography is particularly effective at driving strong buoyancy-forced circulations.

Stommel (1957) first proposed that the abyssal circulation of the ocean may be driven by buoyancy forcing, and a model proposed by Stommel and Arons (1960) described a simple set of dynamics governing the buoyancy driven flow. The Stommel-Arons model is still central to our view of the abyssal circulation problem, and the important role of buoyancy forcing in the abyss is not questioned. However, the nature of deep buoyancy forcing has only recently come to light, with observations providing new insight into the mechanisms driving abyssal circulations. Observations of turbulence across the Brazil Basin show that abyssal mixing rates are spatially nonuniform, with enhanced mixing occurring above regions of rough topography (Polzin *et al.*,

1997). *Ledwell et al.* (2000) and *St. Laurent et al.* (2001) suggest that energy from internal tides sustains the elevated turbulence in these regions.

In the report that follows, the implications for buoyancy forcing by small-scale mixing are discussed. Observations from the abyssal Brazil Basin described by St. Laurent et al. (2001) are summarized here. Estimates of cross-isopycnal motion, termed diapycnal advection, are used to quantify the diabatic flow. The diapycnal advection serves as a primary measure of buoyancy forcing.

Diapycnal advection

We wish to consider the diabatic flow in the ocean interior driven by a divergent buoyancy flux. The equation for buoyancy ($b = -(g/\rho_0)\rho'$) is

$$\frac{\partial b}{\partial t} + \mathbf{u} \cdot \nabla b + wN^2 = -\nabla \cdot \mathbf{F} - \frac{\partial J_b}{\partial z}, \quad (1)$$

where $\mathbf{u} = (u, v)$ is the lateral flow, $\nabla = (\partial/\partial x, \partial/\partial y)$ is the lateral differential operator, and (\mathbf{F}, J_b) are the lateral and vertical components of buoyancy flux. To distinguish diabatic from adiabatic flow, it is useful to consider the buoyancy budget along a neutral surface. Along a neutral surface whose depth is described by $z_i(x, y, t)$, buoyancy is subject to the relations

$$\begin{aligned} \nabla b_i &= \nabla b + \nabla z_i N^2 = 0, \\ \frac{\partial b_i}{\partial t} &= \frac{\partial b}{\partial t} + \frac{\partial z_i}{\partial t} N^2 = 0, \end{aligned} \quad (2)$$

where $(\cdot)_i$ denotes an isopycnal function of (x, y, t) , and $N^2 = \partial b / \partial z$. Additionally, since buoyancy flux across an isopycnal occurs only by small-scale turbulence, all fluxes may be expressed in terms of a turbulent diffusivity k_ρ such that

$$\begin{aligned} \mathbf{F}_i &= -k_\rho \nabla b_i = -k_\rho \nabla b - k_\rho \nabla z_i N^2 = 0, \\ J_b &= -k_\rho N^2. \end{aligned} \quad (3)$$

Thus, the equation for buoyancy on a neutral surface can be expressed as

$$\left(w - \frac{\partial z_i}{\partial t} - \mathbf{u} \cdot \nabla z_i \right) N^2 = \frac{\partial(k_\rho N^2)}{\partial z} - \nabla \cdot (k_\rho \nabla z_i N^2). \quad (4)$$

We define the vertical advection quantity $w_* = w - \partial z_i / \partial t - \mathbf{u} \cdot \nabla z_i$ as the "diapycnal advection". As discussed by *McDougall* (1987, 1995) and *Pedlosky* (1996),

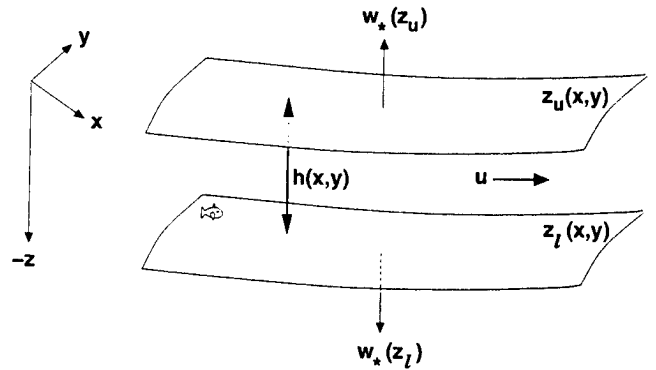


Figure 1. Diagram showing the parameters of a steady-state density layer.

w_* is the vertical component of flow through (not normal to) isopycnals, and w is the vertical motion that is caused by a divergent buoyancy flux. The divergent buoyancy flux is comprised of two terms; a standard vertical divergence term $-\partial J_b / \partial z$, and a lateral divergence of vertical buoyancy flux $\nabla \cdot (\nabla z_i J_b)$. It is useful to consider the ratio of these terms, with scaling $\partial J_b / \partial z \sim \delta^{-1} J_b$, and $\nabla \cdot (\nabla z_i J_b) \sim \ell^{-2} \delta J_b$ for characteristic lateral and vertical scales (ℓ, δ). The ratio of the vertical to lateral divergence terms is $(\ell/\delta)^2$. In general, we will assume that the aspect ratio δ/ℓ of isopycnals is small, such that $(\ell/\delta)^2 \gg 1$, and (4) can be approximated as

$$w_* N^2 \cong -\frac{\partial J_b}{\partial z}. \quad (5)$$

Dynamical Considerations

Consider a large-scale geostrophic and inviscid flow. The potential-vorticity equation for flow in a steady-state density layer (Fig. 1) is

$$\beta v = \frac{f}{h} \mathbf{u} \cdot \nabla h + \frac{f}{h} (w_*(z_u) - w_*(z_l)), \quad (6)$$

where $h(x, y)$ is the thickness of the density layer, and (z_u, z_l) denote the upper and lower bounding isopycnal surfaces. The above expression is the density-layered version of the *Stommel and Schott* (1977) beta-spiral equation, and is discussed by *McDougall* (1988) and *Hautala and Riser* (1993). In (6), the advection of planetary vorticity is balanced by vortex stretching. Vortex stretching may occur adiabatically by flow along sloping isopycnals, or diabatically by the divergence of diapycnal advection. Diabatic vortex stretching is related to

the divergence of buoyancy flux by (5). During mixing events, vertical exchanges of buoyancy are accompanied by dissipation of turbulent kinetic energy (TKE), and the energy budget for an ensemble of turbulent events is

$$(1 - R_f) J_b + R_f \bar{\epsilon} = 0, \quad (7)$$

where ϵ is the dissipation rate, and R_f is the efficiency of the mixing. The TKE budget expressed in (7) assumes steady-state and homogeneous statistics of the Reynolds stress tensor. This equation is discussed by Osborn (1980), and an expression for the eddy diffusivity is readily derived by substituting $J_b = -k_p N^2$ into (7),

$$k_p = \left(\frac{R_f}{1 - R_f} \right) \left(\frac{\bar{\epsilon}}{N^2} \right). \quad (8)$$

The fraction $\Gamma = R_f (1 - R_f)^{-1}$ (equivalently $\Gamma = -J_b/\bar{\epsilon}$), the ratio of buoyancy flux to energy dissipated, is typically taken to be $\leq 20\%$ for stratified turbulence. With use of (5) and (7), the diapycnal advection can be expressed as

$$w_* \cong N^{-2} \frac{\partial(\Gamma \bar{\epsilon})}{\partial z}, \quad (9)$$

and the potential vorticity equation (6) can be expressed as

$$\beta v = \frac{f}{h} \mathbf{u} \cdot \nabla h + \frac{\partial}{\partial z} \left(\frac{f}{N^2} \frac{\partial(\Gamma \bar{\epsilon})}{\partial z} \right), \quad (10)$$

where we have taken $(w_*(z_u) - w_*(z_l))/h = \partial w_*/\partial z$.

As a clear way of demonstrating the importance of the diabatic forcing term in (10), it is useful to consider the following scaling relations. Using standard notation, we scale $(x, z) \sim (L, H)$, $\mathbf{u} \sim U$, $\beta \sim U/L^2$ and define the deformation radius as $R_d = NH/f$. The scaling for the term ∇h is taken from the geostrophic relation $fU \sim g' \nabla h$, where the reduced gravity is $g' \sim N^2 H$. Additionally, we scale the energy dissipation term as $\epsilon \sim fE$, where E is the scale of the kinetic energy associated with the forcing for the vertical mixing. This scaling for ϵ is proposed on solely dimensional grounds, noting that a time scale f^{-1} is relevant for many dynamical regimes. Application of these scaling relations in (10) yields the following nondimensional equation,

$$\beta v = \frac{L^2}{R_d^2} \mathbf{u} \cdot \frac{\nabla h}{h} + \frac{E}{U^2} \frac{\partial}{\partial z} \left(\frac{L^2}{R_d^2} \frac{\partial(\Gamma \bar{\epsilon})}{\partial z} \right), \quad (11)$$

where the lower-case variables are now dimensionless. The ratio of the diabatic to adiabatic stretching is

$$\frac{\text{diabatic stretching}}{\text{adiabatic stretching}} = \Gamma \frac{E}{U^2}. \quad (12)$$

The relative importance of the diabatic-forcing term will be set by the energy level of the process controlling the vertical mixing. In the case of dissipating internal-tide energy, the energy flux scales as U_{tide}^2 . In the abyss where geostrophic flow is weak, typical geostrophic velocities are $U \sim 5 \text{ mm s}^{-1}$, while tidal velocities are generally $U_{\text{tide}} \sim 20 \text{ mm s}^{-1}$. Thus a ratio of $O(1)$ for the diabatic to adiabatic vorticity forcing is easy to justify, demonstrating the strong dynamical link between mixing and circulation in the abyss.

Observations of turbulence in the Abyssal Brazil Basin

In the period between January 1996 and April 1997, two microstructure surveys were made in the Brazil Basin. The 1996 survey consisted of a basin-scale survey and the initiation of a tracer dispersion experiment at a site near the Mid Atlantic Ridge (MAR). During the 1997 survey, a detailed survey was conducted over a $5 \times 10^5 \text{ km}^2$ region of rough topography near the tracer release site. The primary focus of the 1996 survey was the spatial variability of mixing levels, and a report on the observed variability is given by Polzin *et al.* (1997). Results from the tracer release experiment are described by Ledwell *et al.* (2000).

The presentation here will focus on the dissipation data collected over the fracture zone (FZ) topography near the MAR (Fig. 2). All profiles consist of conventional hydrographic variables (e.g., Θ, S, U, V) in addition to microstructure, and generally extend from the surface mixed layer to within 20 m of the bottom. The bathymetric data shown in Fig. 2 were derived from satellite measurements of the marine gravity field Smith and Sandwell (1997). The map clearly shows the network of FZs leading east to the MAR. This system of FZs is characterized by a series of canyons bounded latitudinally by crests that rise up to 1 km above the canyon floors.

Turbulent kinetic energy dissipation rates were derived from observations of velocity microstructure. Only two components of the strain tensor are measured, and isotropy is assumed to express the dissipation rate as $\epsilon = (15/4) \cdot (\langle u_z^2 \rangle + \langle v_z^2 \rangle)$. A summary of the observed deep-dissipation data was made by collapsing the latitudinal spread of the profiles (Fig. 3).

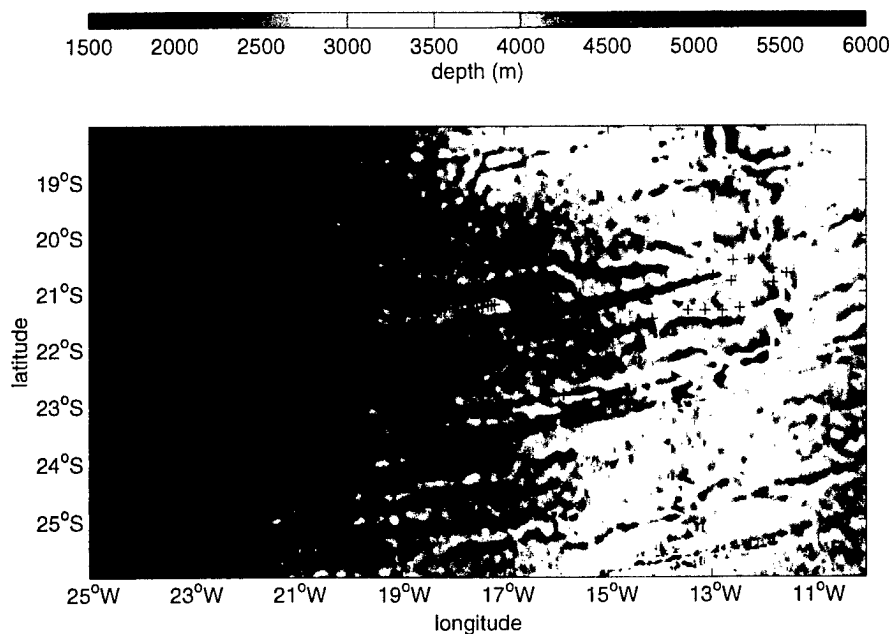


Figure 2. Map of the 1997 survey site with the 2 arc-minute resolution bathymetric estimates of /it Smith and Sandwell (1997). A total of 129 profiles of dissipation rate observations (crosses) were collected in this region.

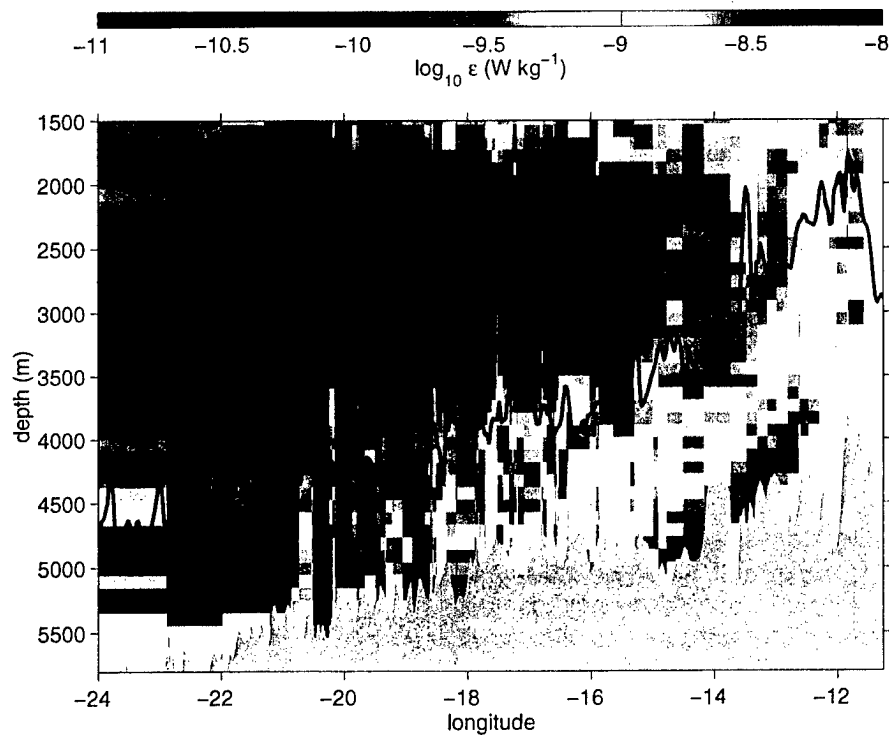


Figure 3. A zonal section of TKE dissipation rate ϵ . The individual profiles are shown as columns, and dissipation rate observations were vertically averaged into 100 m-bins. The shaded bathymetry is representative of canyon floors, while the shallower trace represents the level of ridge crests.

To simplify the presentation, only the depth range deeper than 1500 m is shown. The dissipation data were depth averaged into 100-m intervals, and individual profiles are shown as columns of binned dissipation. Since the latitudinal extent of the survey has been collapsed, no particular section of bathymetry is entirely appropriate. Instead, two classes of representative bathymetry are shown: the bathymetry of FZ crests and the bathymetry of canyon floors, as sampled from the latitude range 21°S to 23°S. Within about 500 m of the bottom, there is an enhancement of dissipation by more than two orders of magnitude over values observed at mid depth. Enhanced dissipation generally occurs between the level of FZ crests and canyon floors, suggesting the largest mixing rates occur in canyons.

An inverse estimate of circulation

Surveyed hydrography was used to divide the flow regime into a series of density layers. In these layers, geostrophic advection is related to isobaric gradients of geopotential anomaly (φ) by

$$\mathbf{u} = \hat{\mathbf{z}} \times \frac{\nabla \varphi}{f} + \mathbf{u}_0, \quad (13)$$

where \mathbf{u}_0 is a reference level velocity. Thus, the advection of potential vorticity through a density layer of thickness $h(x, y)$, as previously stated in (6), may be expressed in the form

$$\begin{aligned} \frac{h_x}{h} u_0 + \left(\frac{h_y}{h} - \frac{\beta}{f} \right) v_0 &+ \frac{1}{h} (w_*(z_u) - w_*(z_l)) \\ &= -u_r \frac{h_x}{h} - v_r \left(\frac{h_y}{h} - \frac{\beta}{f} \right), \end{aligned} \quad (14)$$

where (u_r, v_r) are the components of relative geostrophic velocity given by $(u - u_0, v - v_0)$ in (13). Thus, the problem of determining the lateral flow \mathbf{u} is reduced to determining the reference level velocity, i.e., the vertical integration constants (u_0, v_0) of a thermal-wind balance.

In layers where flow encounters topography, the use of the geostrophic balance is questionable. A modified momentum balance, such as that of the bottom Ekman layer, may be called for in regions where a density layer comes within $O(100)$ m of the bottom. Additionally, the difficulty of defining the geopotential anomaly along pressure surfaces interrupted by bathymetry severely limits the practical use of (13) and (14) in deep layers. For these reasons, it is necessary to employ additional dynamical constraints on the flow. This is

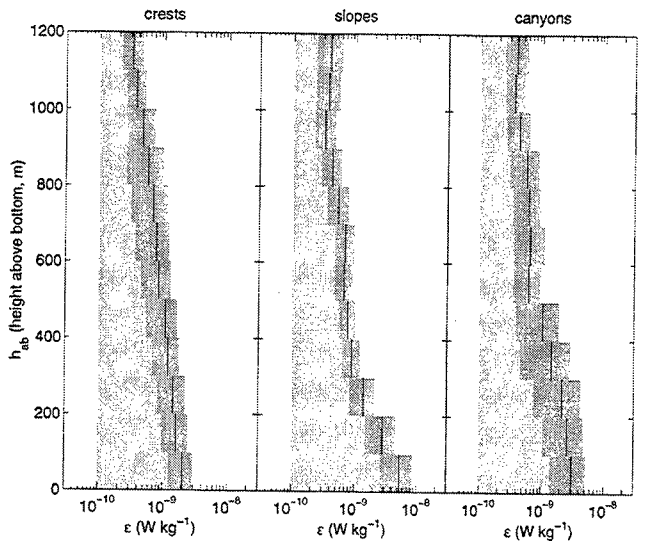


Figure 4. Dissipation profiles averaged according to bathymetric classification. Bathymetric classes were assigned as crests, canyons, or slopes. All profiles are shown relative to a reference dissipation of $\epsilon = 1 \times 10^{-10} \text{ W kg}^{-1}$. The 95% confidence interval is shown for each 100-m average.

achieved through the use of integrated advective budgets for mass,

$$\begin{aligned} \iint dy dz u|_x^{x+\gamma} + \iint dx dz v|_y^{y+\Delta} \\ + \iint dx dy w_*|_{z_l}^{z_u} = 0 \end{aligned} \quad (15)$$

and for potential temperature

$$\begin{aligned} \iint dy dz u\Theta'|_x^{x+\gamma} + \iint dx dz v\Theta'|_y^{y+\Delta} \\ + \iint dx dy w_*\Theta'|_{z_l}^{z_u} = \\ \iint dy dz \kappa\Theta_x|_x^{x+\gamma} + \iint dx dz \kappa\Theta_y|_y^{y+\Delta} \\ + \iint dx dy k_p\Theta_z|_{z_l}^{z_u}. \end{aligned} \quad (16)$$

The integrated expressions (15) and (16) are bounded in control volumes of meridional and zonal extent (γ, Δ), and vertically bounded in a density layer by the surfaces $z_u(x, y)$ and $z_l(x, y)$.

Relations for the diapycnal diabatic terms are expressed using the dissipation rate with the use of (8) and (9). For use in the inverse model, the mixing efficiency

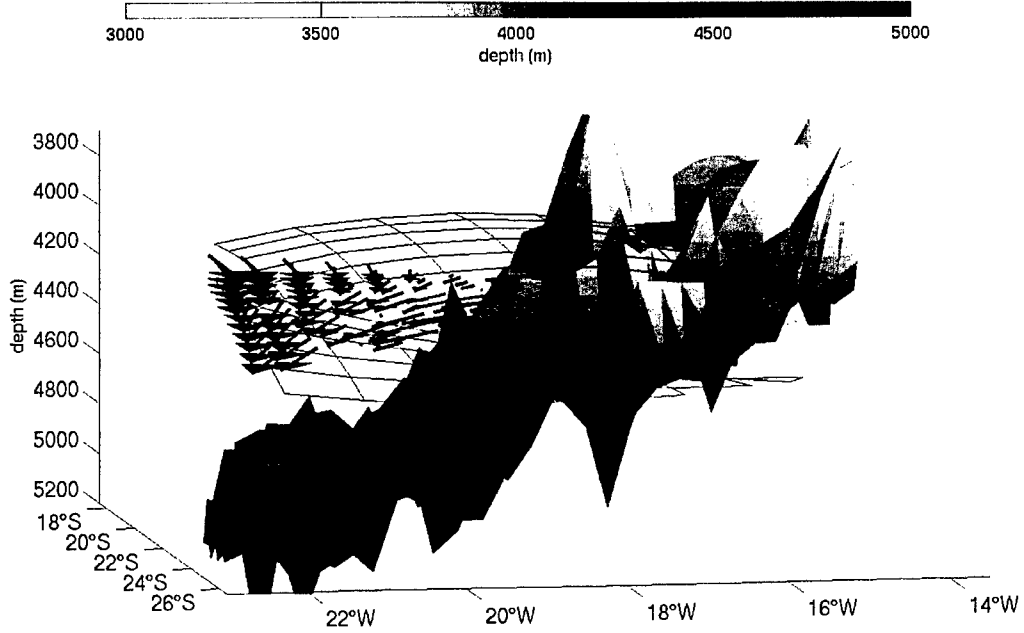


Figure 5. Layer-averaged flow for the density layer $28.16 < \sigma_n < 28.20$. The gridded surfaces show the $\sigma_n = 28.16$ (upper) and $\sigma_n = 28.20$ (lower) isopycnals. Bottom bathymetry was subsampled onto a $0.25^\circ \times 0.25^\circ$ Mercator grid. The largest vectors are $(5\text{-}6) \text{ mm s}^{-1}$.

parameter Γ is treated as constant, $\Gamma_0 = 0.20 \pm 0.04$. This allows us to specify the diapycnal diffusivity for turbulence as

$$k_\rho \cong \frac{\Gamma_0}{N^2} \bar{\epsilon}, \quad (17)$$

and the diapycnal advection as

$$w_* \cong \frac{\Gamma_0}{N^2} \frac{\partial \bar{\epsilon}}{\partial z}. \quad (18)$$

We emphasize that (17) and (18) are approximations, where a constant mixing efficiency has been assumed. While oceanic observations of turbulence from well stratified regions suggest $\Gamma_0 \cong 0.2$ (*Moum, 1996; St. Laurent and Schmitt, 1999*), observations from fjords suggest $\Gamma \cong 0.05$ (*Stigebrandt and Aure, 1989*). Additionally, laboratory measurements of turbulence suggest $0.05 < \Gamma < 0.25$ characterizes the variation of mixing efficiency over a wide range Reynolds, Richardson, and Froude numbers (*Ivey and Imberger, 1991; Hug and Britter, 1995*). In our inverse model estimates, we accept that using $\Gamma_0 = 0.2 \pm 0.04$ may lead to a specification of k_ρ that is biased high. The use of a constant mixing efficiency in (18) is more problematic, as variations in Γ with depth will not only influence the magnitude of the w_* estimate, but also the sign ($w_* > 0$

for upwelling, $w_* < 0$ for downwelling). For this reason, w_* is regarded as an unknown in the inverse model, and (18) serves as a “constraint” in the inversion. In this manner, (18) provides an a priori estimate, while full inversion of (14), (15), and (16) determines the best estimate of w_* .

In expressions (17) and (18), $\bar{\epsilon}$ is meant to denote some suitably averaged function of the dissipation data. Averaging over multiple profiles is necessary to achieve statistical stability in the mean dissipation estimates. Since our inverse model utilizes the steady-state forms of the advective budgets, we seek an averaging procedure that yields an estimate of the time-mean dissipation rate. Thus, the dissipation data were averaged in both space and time. The time averaging was weighted by a function of the squared barotropic tidal-current speed to remove biases associated with a spring-neap modulation. Furthermore, dissipation data were spatially averaged according to a bathymetric classification scheme. Dissipation profiles above FZ canyons, crests, and the sloping topography between, were treated separately in the averaging. The profile data, classified in this manner, are shown in Fig. 4. Each ensemble profile results from data that has been vertically averaged into 100-m bins. Dissipation decreases with height above

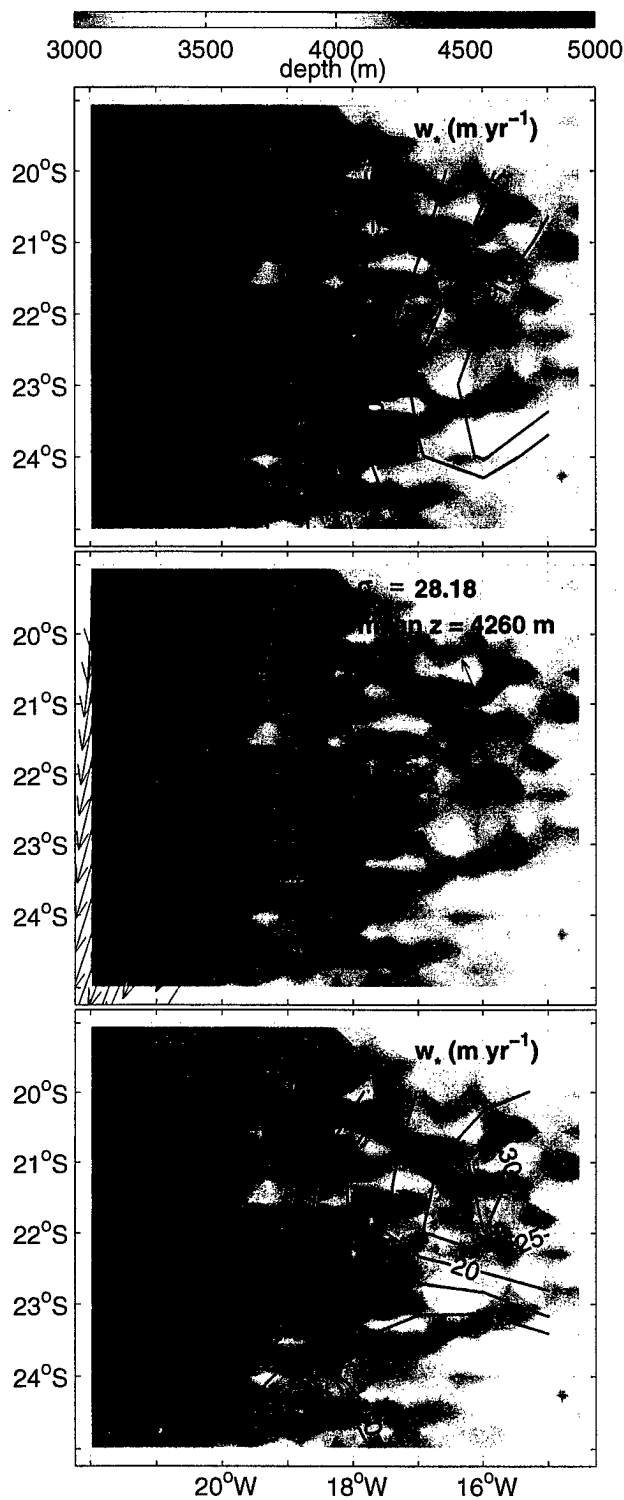


Figure 6. Diapycnal advection estimates for the $\sigma_n = 28.16$ (upper panel) and $\sigma_n = 28.20$ (lower panel) isopycnals. The lateral flow for this density layer (from Fig. 5) is shown in the middle panel. Contoured estimates of diapycnal advection have been averaged over $1^{\circ} \times 1^{\circ}$ Mercator cells which include regions blocked by topography.

bottom in each of the 3 classes, and all profiles reach background levels of dissipation, $\epsilon \cong 3 \times 10^{-10} \text{ W kg}^{-1}$, at heights greater than 1000 m. The slope profile is notably different from the other two, in both the magnitude of the maximum dissipation and the scale of decay. The slope profile has a bottom value of $\epsilon \cong (3 - 9) \times 10^{-9} \text{ W kg}^{-1}$ and decays with an e-fold scale of (150 ± 50) m. The crest and canyon profiles peak at $\epsilon \cong (2 - 5) \times 10^{-9} \text{ W kg}^{-1}$ and decay over a larger scale, (500 ± 100) m.

A matrix model for a 6 density layer system consisting of about 7000 equations for 3200 unknowns was formed using (14), (15), (16), (17), and (18). The details of the linear inversion are given by *St. Laurent et al.* (2001). In a series of initial calculations, lateral diffusivity κ was treated as constant along each density surface used in the inversion. Using this approach, the estimates of κ were inconsistent with the a priori estimates of $\kappa \sim 100 \text{ m}^2 \text{ s}^{-1}$ derived from float observations (*Hogg and Owens*, 1999). Spatial variations of κ on isopycnals intersecting topography may account for this discrepancy. Additionally, diagnostic scaling with $\kappa \sim 100 \text{ m}^2 \text{ s}^{-1}$ indicated that a primary thermal-advection balance (16) occurs between the terms involving advection (both lateral and vertical) and the vertical diffusion term. Scale estimates suggest that the magnitude of the lateral diffusive flux terms in (16) are less than 10% of the diapycnal diffusive flux of potential temperature. For these reasons, terms involving the lateral diffusivity were dropped from the thermal advection equations, leaving the three dimensional flow field (\mathbf{u}, w_*) as the model unknowns.

Flow in and above abyssal canyons

Here, we present the estimated circulation in and above the FZ canyons. A more complete discussion of the circulation at all depths in this region of the Brazil Basin is given by *St. Laurent et al.* (2001). In the layers deeper than 3000 m, bottom bathymetry has a clear influence on the flow dynamics. In particular, proximity to the bottom is the controlling factor for the magnitude of the diabatic forcing. The vertical diffusivity characterizing these layers is $k_p \sim 1 \times 10^{-4} \text{ m}^2 \text{ s}^{-1}$ or greater, and this corresponds to an increased importance of the diabatic terms in the governing equations. Flow was estimated in the neutral density layer $28.16 < \sigma_n < 28.20$ (Fig. 5). The upper isopycnal for this layer ($\sigma_n = 28.16$) rests just above the level of the FZ crests at 16°W . Near the MAR, there is westward flow out of canyons with average current magnitudes of

$(2-4) \text{ mm s}^{-1}$. Further west, the density layer's average height above bottom increases, and flow at 500 m above the level of FZ crests is southward with average current magnitudes of $(5-6) \text{ mm s}^{-1}$.

Diapycnal advection estimates are presented in Fig. 6. These contoured fields of w_* have been highly smoothed. Where FZ crest topography intersects each density surface, there is no flow, and the contoured maps show estimates of w_* that have been averaged in $1^\circ \times 1^\circ$ cells which often include regions blocked by topography. The $\sigma_n = 28.16$ and $\sigma_n = 28.20$ isopycnals are characterized by diapycnal downwelling to the west and diapycnal upwelling to the east. Estimates of upward advection in canyons exceed $w_* \cong 30 \text{ m yr}^{-1}$, and are as large as $w_* \cong 100 \text{ m yr}^{-1}$ in some local regions. Uncertainty estimates for the diapycnal flow are typically less than $\pm 40\%$ of the contoured values.

To produce a clearer summary of the deep circulation in and above canyons, a zonal stream function (ψ) was defined by latitudinally integrating the velocity so that $\bar{u}\delta_y = -\psi_z$ and $\bar{w}_*\delta_y = \psi_x$, where the latitudinal limits of integration were taken over the inverse domain (19°S - 25°S),

$$\begin{aligned} \bar{u}(x, z) &= \frac{1}{\int dy} \int dy u(x, y, z), \\ \bar{w}_*(x, z) &= \frac{1}{\int dy} \int dy w_*(x, y, z). \end{aligned} \quad (19)$$

An objective analysis technique was used to interpolate the inverse solution and compute the stream function. The resulting smoothed stream-function is shown in Fig. 7 relative to representative bathymetry and the density field. These estimates suggest eastward flow in canyons. Diapycnal upwelling occurs at sites where isopycnals in-crop along canyon floors, and this upwelling feeds the westward flow at the level of the FZ crests.

Deep upwelling and mixing efficiency

As presented above, strong diapycnal upwelling is required to close the heat and mass budgets in regions where density surfaces intersect canyon floors. Figure 8 presents a comparison of the a priori estimates of w_* to the inverse solutions for w_* on the $\sigma_n = 28.20$ neutral surface. Inverse estimates are generally consistent with the a priori estimates of w_* at sites where the $\sigma_n = 28.20$ surface is more than 300 m above the bottom. However, the inverse estimates suggest diapycnal upwelling is favored at sites where the $\sigma_n = 28.20$ surface is within 300 m of the bottom.

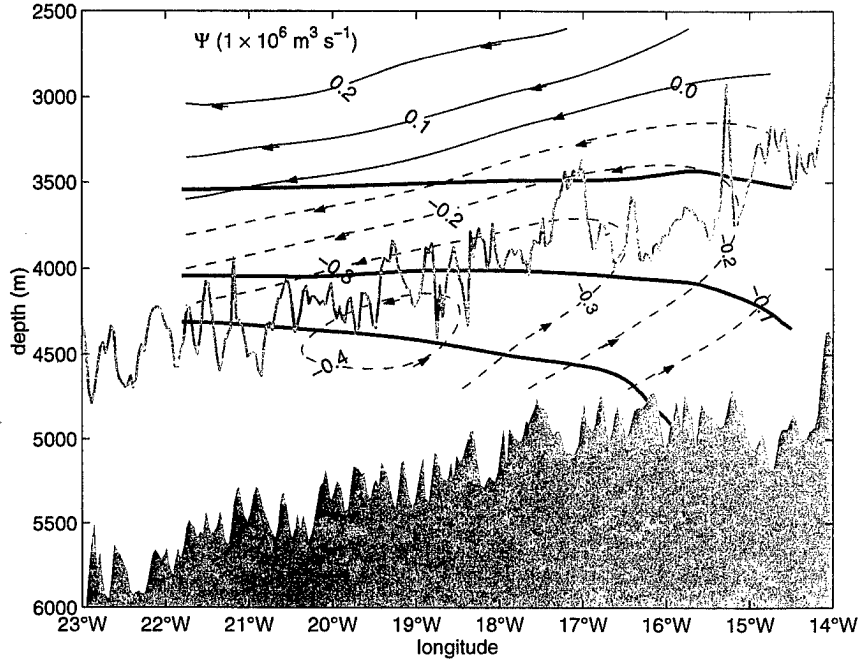


Figure 7. The meridionally integrated stream function as estimated through objective analysis of the inverse model solution. Dimensional values of the stream function are contoured, and uncertainties are roughly $\pm 40\%$. Representative bathymetry of the canyon floors (shaded) and crests (gray line) is shown, as are the $\sigma_n = 28.10, 28.16$ and 28.20 isopycnals.

Diapycnal upwelling must be occurring in regions where turbulence supports a convergent buoyancy flux: $w_*N^2 \cong -\partial J_b / \partial z > 0$. This condition is satisfied by turbulence occurring close to the bottom, since the buoyancy flux must decrease with depth to meet a no-flux condition at the sea floor. Within the context of (7), the buoyancy flux is related to the dissipation rate by a mixing efficiency parameter, $J_b = -\Gamma\bar{\epsilon}$. We believe that a reduction in mixing efficiency near the bottom allows the no-flux condition to be met at the sea floor. This reduction may occur in a 1 to 10 m thick boundary layer (i.e., the “log layer”), which was unresolved by our measurements. However, variations in mixing efficiency may extend to greater heights in the canyons. The physical mechanisms controlling the efficiency of mixing near topography are not well understood, but turbulent mixing in regions enclosed by topography may favor mixing with reduced efficiency. Stigebrandt and Aure (1989) found that mixing in fjords occurred at 0.05 efficiency. Given our observations of dissipation and stratification along canyon slopes, a decrease in mixing efficiency from 0.2 to 0.05 in the bottom most 100 m above FZ slopes would account for diapycnal upwelling as large as $w_* \cong +300 \text{ m yr}^{-1}$.

Discussion

We have described buoyancy forcing and circulation occurring in a region of the abyssal ocean. Our calculations suggest that enhanced levels of turbulence above rough bathymetry lead to enhanced levels of diabatic flow. Divergence of the diabatic flow acts as a mechanism of buoyancy forcing for the lateral circulation through the vortex stretching term $(f/h)(w_*(z_u) - w_*(z_l))$ in the vorticity budget. The significance of diabatic vortex stretching as a forcing mechanism must be assessed relative to other forcing agents for the flow. From the inverse estimates, we may compare the strength of buoyancy forcing to the adiabatic mechanism of vortex stretching, represented by $(f/h)\underline{u} \cdot \nabla h$ in the vorticity budget.

Above the level of FZ crests, adiabatic vortex stretching is cyclonic, while diabatic vortex stretching is anti-cyclonic. In the region where mixing rates are largest, these two mechanisms are comparable in magnitude and the vortex stretching terms in (6) nearly cancel. Since $\beta v \cong 0$, there is little meridional flow just above the level of FZ crests (Fig. 5). The divergence of diapycnal mass flux is clearly a significant forcing agent on the

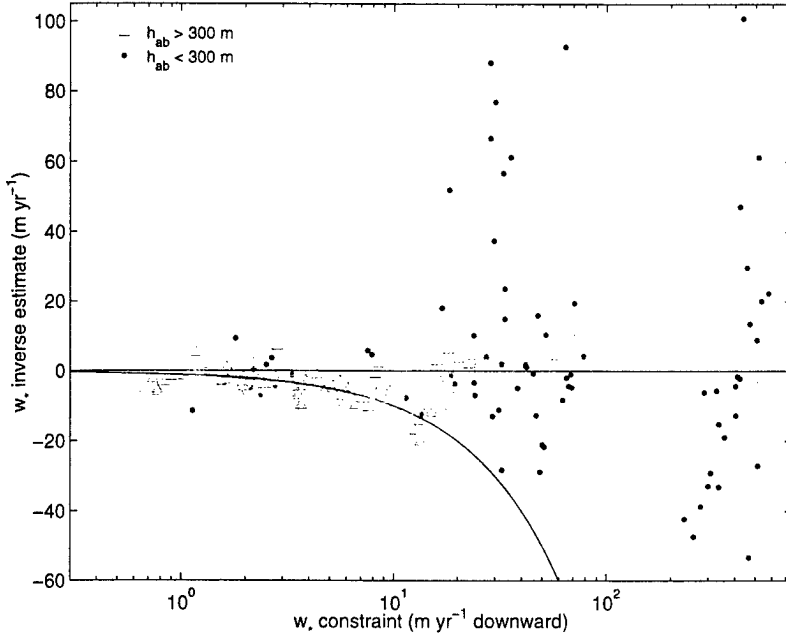


Figure 8. Comparison of the a priori estimates of w_* with the inverse estimates for the $\sigma_n = 28.20$ neutral density surface. Estimates at sites where the $\sigma_n = 28.20$ surface is more than 300 m above the bottom are plotted using triangles, and estimates from sites where $\sigma_n = 28.20$ is less than 300 m above the bottom are plotted as points. The curve along which the inverse and a priori estimates are equal is shown. Standard errors are shown for all estimates.

lateral circulation in this region. Further west of the Mid Atlantic Ridge where mixing rates are weaker, the adiabatic stretching exceeds the diabatic stretching, resulting in the southward flow where the largest lateral velocities occur. In addition to the stretching mechanisms, friction imposed by topography may also be a significant forcing mechanism near the bottom, though we have not attempted to assess this contribution.

The diapycnal advection estimates presented here are clearly sensitive to assumptions made about turbulent mixing efficiency. As indicated by (9), depth variations in mixing efficiency will influence both the magnitude and direction of the diabatic mass flux. We note that most data are consistent with a mixing efficiency R_f near 15% (equivalently, $\Gamma \cong 0.20$). For example, diffusivity estimates from (17), which assume $\Gamma = 0.2 \pm 0.04$ agree with the turbulent diffusivity estimated from the tracer dispersion experiment (Ledwell *et al.*, 2000). Moreover, St. Laurent *et al.* (2001) find general agreement between a priori diapycnal advection estimates estimated with $\Gamma \cong 0.20$ in (18) and diapycnal advection estimates deduced from inversion of the steady-state budgets. Variations in mixing efficiency

are only inferred from estimates deep in FZ canyons, in regions where isopycnal slopes increase as density layers in-crop along the bottom. Our evidence for reduced mixing efficiencies is indirect, but the diapycnal advection estimates are consistent with a reduction from $\Gamma \cong 0.20$ to $\Gamma \cong 0.05$ over a depth of 100 m above the sloping walls of FZ canyons.

While the study strictly considered data from a small geographic region, the bathymetric features present are ubiquitous over the basins of the global ocean, as are the tides. If, as suggested by Munk and Wunsch (1998), the tides are the dominant source of mechanical energy for abyssal mixing, the pattern of enhanced turbulence observed over Brazil Basin fracture zones may be representative of turbulence occurring in other regions. Diabatic forcing above rough topography may be a primary forcing mechanism for the abyssal circulation.

Acknowledgments. We thank K. Polzin and J. Ledwell for helpful discussions. The authors also thank E. Montgomery, D. Wellwood, T. Bolmer, and the officers and crew of the R/V Seward Johnson for their efforts in the Brazil Basin field program, which was supported by grant OCE94-15589 of the National Science Foundation. The support of

the Office of Naval Research is also acknowledged.

References

- Alves, M.L.G.R., and A. Colin de Verdiere, Instability dynamics of a subtropical jet and applications to the Azores Front Current System: Eddy-driven mean flow. *J. Phys. Oceanogr.*, 29, 837-864, 1999.
- Hautala, S.L., and S.C. Riser, A nonconservative β -spiral determination of the deep circulation in the Eastern South Pacific. *J. Phys. Oceanogr.*, 23, 1975-2000, 1993.
- Hogg, N.G., and W.B. Owens, Direct measurements of the deep circulation within the Brazil Basin. *Deep-Sea Res. II*, 46, 335-353, 1999.
- Huq, P., and R.E. Britter, Turbulence evolution and mixing in a two layer stably stratified fluid. *J. Fluid Mech.*, 285, 41-67, 1995.
- Ivey, G.N., and J. Imberger, On the nature of turbulence in a stratified fluid. Part 1. The energetics of mixing. *J. Phys. Oceanogr.*, 21, 650-658, 1991.
- Ledwell, J.R., E.T. Montgomery, K.L. Polzin, L.C. St. Laurent, R.W. Schmitt, and J.M. Toole, Mixing over rough topography in the Brazil Basin. *Nature*, 403, 179-182, 2000.
- Lozier, S.M., Evidence for large-scale eddy-driven gyres in the North Atlantic. *Science*, 277, 361-364, 1997.
- McDougall, T.J., Thermobaricity, cabbeling, and water-mass conversion. *J. Geophys. Res.*, 92, 5448-5464, 1987.
- McDougall, T.J., Neutral-surface potential vorticity. *Prog. Oceanogr.*, 20, 185-221, 1988.
- McDougall, T.J., The influence of ocean mixing on the absolute velocity vector. *J. Phys. Oceanogr.*, 25, 705-725, 1995.
- Moum, J.N., Efficiency of mixing in the main thermocline. *J. Geophys. Res.*, 101, 12,057-12,069, 1996.
- Munk, W., and C. Wunsch, Abyssal recipes II: energetics of tidal and wind mixing. *Deep-Sea Res. I*, 45, 1977-2010, 1998.
- Osborn, T.R., Estimates of the local rate of vertical diffusion from dissipation measurements. *J. Phys. Oceanogr.*, 10, 83-89, 1980.
- Pedlosky, J., *Ocean Circulation Theory*, Springer-Verlag, 453 pp., 1996.
- Polzin, K. L., J.M. Toole, J.R. Ledwell, and R.W. Schmitt, Spatial variability of turbulent mixing in the abyssal ocean. *Science*, 276, 93-96, 1997.
- St. Laurent, L.C., J.M. Toole, and R.W. Schmitt, Buoyancy forcing by turbulence above rough topography in the abyssal Brazil Basin. *J. Phys. Oceanogr.*, in press, 2001.
- St. Laurent, L., and R.W. Schmitt, The contribution of salt fingers to vertical mixing in the North Atlantic Tracer Release Experiment. *J. Phys. Oceanogr.*, 24, 1404-1424, 1999.
- Smith, W.H.F., and D.T. Sandwell, Global sea floor topography from satellite altimetry and ship depth soundings. *Science*, 277, 1956-1962, 1997.
- Spall, M. A., 1994: Wave-induced abyssal recirculations. *J. Mar. Res.*, 52, 1051-1080, 1994.
- Spall, M.A., Buoyancy-forced circulations around islands and ridges. *J. Marine. Res.*, 58, 957-982, 2000.
- Stigebrandt, A., and J. Aure, Vertical mixing in basin waters of fjords. *J. Phys. Oceanogr.*, 19, 917-926, 1989.
- Stommel, H., The abyssal circulation of the ocean. *Nature*, 180, 733-734, 1957.
- Stommel, H., and A.B. Arons, On the abyssal circulation of the World Ocean-I: Stationary planetary flow patterns on a sphere. *Deep-Sea Res.*, 6, 140-154, 1960.
- Stommel, H. and F. Schott, The beta spiral and the determination of the absolute velocity field from hydrographic station data. *Deep-Sea Res.*, 24, 325-329, 1977.

This preprint was prepared with AGU's L^AT_EX macros v4, with the extension package 'AGU++' by P. W. Daly, version 1.6a from 1999/05/21, with modifications by D. E. Kelley, version 1.0 from 2001/03/26, for the 'Aha Huliko'a Hawaiian Winter Workshop.

Differential diffusion in bistable conditions

Greg Holloway, Ann Gargett, and Bill Merryfield

Institute of Ocean Sciences, Sidney BC, Canada

Abstract. Double diffusive phenomena, due to the difference in molecular conduction coefficients for heat and for ion concentrations in sea water, are widely known. These include salt fingering and diffusive convection which occur when either temperature or salinity is destabilizing while the other (salinity or heat) is stabilizing. Less well known, less dramatic in their occurrence, but far more widespread are circumstances where both temperature and salinity are stabilizing and yet the differences in molecular conduction lead to systematic differences in turbulent transport rates. “Differential diffusion” has been seen in laboratory experiments, in ocean observations and in numerical simulations. Here we examine differential diffusion in terms of turbulence-induced restratifying (up-gradient) fluxes.

Introduction

Double diffusion occurs in the ocean because heat and salt (ion concentration) experience very different coefficients of molecular conduction. Heat conduction has about $100 \times$ larger coefficient than ionic conduction. As both heat and salt determine density, circumstances arise where the potential density profile $\rho(z)$ is stable although the contribution from either temperature $T(z)$ or salinity $S(z)$ would, by itself, be gravitationally unstable. Many studies and a large literature have addressed these doubly diffusive phenomena, as *Kelley* (2001) has reviewed at this workshop.

Over the major part of the ocean interior, both $T(z)$ and $S(z)$ are stabilizing. While lateral intrusive instabilities may occur, most double diffusive phenomena are not allowed. The prevailing view is that both T and S are simply mixed by occasional background turbulence. Turbulent diffusivities for T and for S are assumed to be equal. However prevalent this view, it may not be quite so.

Do the differences of molecular conduction cause differences for the turbulent (advective part) fluxes? Laboratory evidence and numerical experiments show that they do. In early experiments, *Turner* (1968) mechanically agitated a fluid stratified with respect to T and, separately, a fluid stratified with respect to S , taking care that the two stratifications were initially the same. Under the same mechanical agitation, it was found that T was mixed more efficiently than S by an amount greater than could be attributed to molecular conduction. Later, *Altman and Gargett* (1980) performed similar experiments in which a tank

was initially stably stratified with respect to both T and S , arranged so that both made the same initial contribution to stratification. Again it was seen that T mixed more readily than S by amounts exceeding molecular conduction. Direct observation of differential diffusion in the ocean is hugely technically difficult, and first results are just now being reported by *Nash and Moum* (2001).

Attempting to quantify differential diffusion, one may employ direct numerical simulations. A major challenge to this approach is the necessity to resolve widely disparate scales, with the dissipation scale for S nearly 100 times smaller than the dissipation scale for T , itself already 10 times smaller than the dissipation scale for the advecting velocity field. A limited investigation based upon numerical simulations was performed by *Merryfield et al.* (1998) employing the idealization that all fields were independent of one horizontal coordinate, *i.e.*, two-dimensionalizing the problem. By not resolving three dimensions, more computing resource could be applied to wider range of scales in two dimensions.

Forcing with random velocity fields, *Merryfield et al.* found results consistent with laboratory observations, namely that turbulent fluxes (not including explicit diffusive fluxes driven by background gradients) transferred heat more rapidly than salt. Differential transfer rates were explored as dependent upon flow parameters. However, these results were subject to doubt because the two-dimensionalization very much alters the nature of “turbulence”, trapping kinetic energy in large, non-dissipating scales.

As far as computing resources have allowed, we have now performed a suite of experiments in fully three dimen-

sions. In this note we report preliminary results from these experiments and a schematic explanation to account for the occurrence of differential diffusion.

Direct simulations in 3D

We solve the Boussinesq equations without Earth's rotation:

$$\frac{\partial \mathbf{u}}{\partial t} + (\mathbf{u} \cdot \nabla) \mathbf{u} = -\frac{1}{\rho_0} \nabla p + \frac{\rho}{\rho_0} g + \nu \nabla^2 \mathbf{u} \quad (1)$$

$$\nabla \cdot \mathbf{u} = 0 \quad (2)$$

$$\frac{\partial T}{\partial t} + (\mathbf{u} \cdot \nabla) T = \kappa_T \nabla^2 T \quad (3)$$

$$\frac{\partial S}{\partial t} + (\mathbf{u} \cdot \nabla) S = \kappa_S \nabla^2 S \quad (4)$$

where $\mathbf{u}=(u,v,w)$ is velocity, T is temperature, S is salinity, ρ is density, p is pressure, g is gravity, ν is viscosity, κ_T and κ_S are coefficients of explicit diffusion, and we assume a linear equation of state

$$\rho = \rho_0 [1 - \alpha(T - T_0) + \beta(S - S_0)] \quad (5)$$

T and S are expanded about a prescribed (non-varying) background

$$T(x, y, z) = \Gamma_T z + T'(x, y, z) \quad (6)$$

$$S(x, y, z) = \Gamma_S z + S'(x, y, z) \quad (7)$$

such that

$$R_p = \alpha \Gamma_T / \beta \Gamma_S = -1$$

Equations (1) through (4) are solved pseudo-spectrally, with dealiasing, using filtered leapfrog timestepping. Viscous and diffusive terms are represented by exponential integrating factors in Fourier space. The great difficulty, even in our age of modern computing, is that the requisite range of scales one should wish to resolve in 3-space exceeds computational resource. At our highest resolution, we employ 160 gridpoints in each dimension for velocity and temperature fields while employing twice that (320 gridpoints) for salinity. Even so, for $\nu = 0.01$ cm²/s, $\kappa T = 0.0014$ cm²/s and $\Gamma T = 10^{-4}$ °C/cm, we are compelled to work in a cube approximately 17 cm tall with grid spacing about 0.1 cm for u and T and 0.05 cm for S . For salinity dissipation scales to be resolved, we must limit $\tau = \kappa S / \kappa T$ to 0.1 where a more realistic value would be near 0.01.

We then randomly select an isotropic initial \mathbf{u} with energy spectrum approximately k^3 , while initial T' and S' are nil. Amplitude of the initial \mathbf{u} are adjusted for experiments in which a turbulent Froude number takes values from 0.4 ("weak") to 48 ("strong"). During the subsequent decay, we diagnose vertical heat and salt fluxes, $w'T'$ and $w'S'$, evaluating their cross-spectra at selected times and evaluating time-integrated fluxes. A more complete account will be given by *Gargett et al.* (2001). Here we sketch only key results and an explanation.

Results

First, we've compared output with previous 2D experiments reported by *Merryfield et al.* (1998). For this comparison, we have rerun the earlier 2D simulations but with $\tau=0.1$, consistent with present 3D runs. Results (not shown here) are pleasantly reassuring, tending to confirm the value of earlier 2D simulations and suggesting that our 3D $\tau=0.1$ results can be extrapolated to $\tau=0.01$ by analogy with 2D results. For the purpose of this report, we show only a representative case from 3D simulations. Figures 1 and 2 show evolution in time of several spectral bands from cross-spectra $-w'T'$ and $w'S'$.

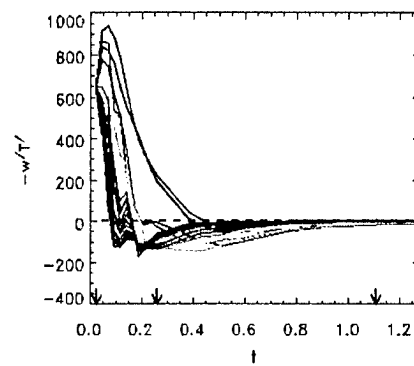


Figure 1. Timeseries of $-w'T'$ are shown for several vertical wavenumber bands from red=low kz to blue=high kz . We show $w'T'$ so that positive values represent downward flux, hence downgradient in T (usual "mixing"). A half-buoyancy period, π/N , occurs at about $t=0.8$. Arrows mark times displayed in Figure 3.

Why?

Numerical simulations, here in 3D and previously in 2D (*Merryfield et al.*, 1998), are consistent with the sense of laboratory observations. The less diffusive scalar is transported by velocity fluctuations less effectively than the

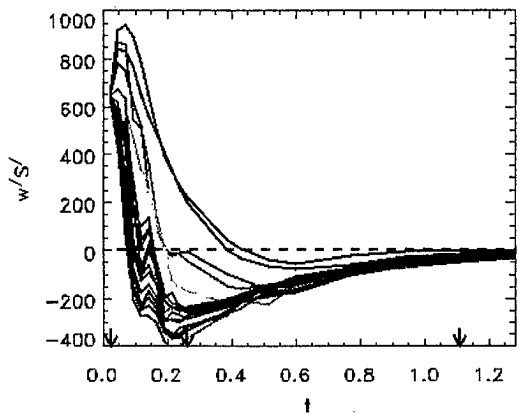
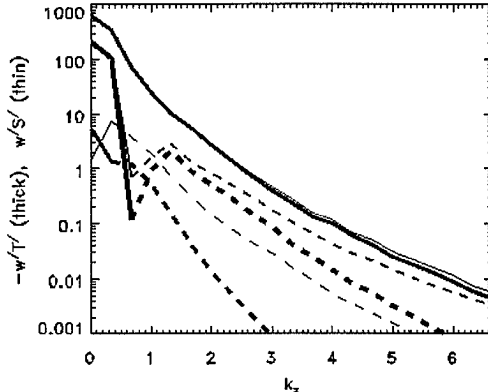


Figure 2. Timeseries of $+wS'$ are shown as in Figure 1, plotted so that positive is upward flux, hence downgradient in S . To aid comparison, fluxes in each spectral band have been rescaled just after initiation. While rescaling enables the higher wavenumber bands to be displayed, one is cautioned that this enhances perception of bands dominated by restratifying fluxes.

more diffusive scalar. 3D experiments were performed over a range of Froude numbers 0.4 to 48 and turbulent Reynolds numbers 1 to 80, all with $\tau=0.1$ (not 0.01). In the higher Fr and Re cases, we obtain flux ratios from 0.7 to 0.9. (At lower Fr and Re, flux ratios can be 0.2 and less approaching the theoretical limit $\tau=0.1$. However, in these low amplitude cases, the velocity fluctuation induced transports are smaller than direct conduction.) Taking account that active oceanic turbulence typically occurs with Re greater than we are able to realize in numerical simulations, and that actual salt-heat have nearer 0.01, our results are best described as not inconsistent with the observational inference from *Nash and Moum* who estimate flux ratio $0.7 \pm 20\%$. A more complete report will be given by *Gargett et al.* (A.E. Gargett, W.J. Merryfield, and G. Holloway, Differential diffusion of T and S : Three-dimensional numerical simulations, in preparation).

We pause to ask why differential diffusion happens at all, and why it has the sense it has. One might have thought *ab initio* that the sense of differential diffusion would be opposite to that observed. If we thought of “usual” turbulence transporting a “usual” (passive) scalar, say C , then flux cross-spectra $w'C'$ should remain of downgradient sense at all scales. Diffusivity of the scalar would cut off the high wavenumber range of $w'C'$ and thus a more diffusive scalar would feel less turbulent transport. Why is this not also the case for active (buoyant) tracer in stratified flow?

The answer is seen in Figures 1, 2 and 3 in the prevalence of upgradient (restratifying) fluxes. Are these fluxes



1 and 2 with blue=early, green=mid, red=late. Solid curves indicate downgradient (“mixing”) fluxes while dashed curves represent upgradient (“restratifying”) fluxes.

not also the fluxes reported by *Carnevale* (this proceedings)? If indeed restratifying fluxes are generic, and the restratifying sense dominates the higher wavenumber range, then diffusive suppression of higher wavenumber cross-spectra yields enhanced transprt of the more diffusive tracer simply because the more diffusive tracer experiences less restratification. In this case the question would move from “Why differential diffusion?” to “Why restratifying fluxes?” It is a question from ‘Aha Huliko’ā since more than a decade ago (*Holloway*, 1989), yet unresolved.

Conclusions

Until a far more confident dynamical basis is established, we are not able to propose a parameterization scheme for differential diffusion in the bistable environment. What we show is that numerical simulations, both in 2D and here in 3D, confirm laboratory and oceanic observations that heat and salt do not mix equally efficiently. This is contrary to modelling practice for which the mixing coefficients for heat and salt are equal except in rare instances where a double-diffusive parameterization has been considered. For the large fraction of world’s oceans where the environment is stable to double diffusion, the assumption of equal mixing of heat and salt is wrong.

Acknowledgments

We are grateful for support from the Office of Naval Research, grant N00014-99-1-0050.

References

- Altman, D.B., and A.E. Gargett, Differential property transport due to incomplete mixing in a stratified fluid, pp. 454-460, in *Stratified Flows*, E. List and G. Jirka, eds., Amer. Soc. Civil Engr., 1990.
- Holloway, G., Relating turbulence dissipation measurements to ocean mixing, p. 329-340 in 'Aha Huliko'a: Parameterization of Small-Scale Processes, P. Muller and D. Henderson, eds., Hawaii Inst. Geophysics, 1989.
- Merryfield, W.J., G. Holloway, and A.E. Gargett, Differential vertical transport of heat and salt by weak stratified turbulence, *Geophys. Res. Lett.*, 25, 2773-2776, 1998.
- Nash, J.D., and J.N. Moum, Microstructure estimates of turbulent salinity flux and the dissipation spectrum of salinity. *J. Phys. Oceanogr.*, submitted, 2001.
- Turner, J.S., The influence of molecular diffusivity on turbulent entrainment across a density interface. *J. Fluid Mech.*, 33, 639-656, 1968.

Six questions about double-diffusive convection

Dan E. Kelley

Dalhousie University, Halifax, Nova Scotia, Canada

Abstract. Double-diffusive convection, at first considered an “oceanographic curiosity,” has fascinated fluid dynamicists for a generation. This is partly because some early and basic questions have still not been answered. The most practical of these – whether double diffusion is important in the ocean – was raised in the defining paper, when Stern (1960) wrote “*future studies of this model ... will determine whether the proposed mechanism is significant in the vertical mixing of the sea.*” This question of significance has not been answered yet, and may not be until we can answer a host of fundamental questions about mechanisms and interactions, some of which are highlighted here.

Introduction

Double-diffusive phenomena¹ occur in diverse systems, ranging from stars to magma chambers, with oceans in between. Studies of cirrus clouds almost led to the discovery of the mechanism of double diffusion (DD henceforth²) in the 1800s (Schmitt, 1995), but it was a group of oceanographers who eventually made the discovery a full century later. While pondering whether they could measure deep ocean pressures by lowering pipes from the surface, the oceanographers conceived of a perpetual salt fountain (Stommel *et al.*, 1956), a fanciful idea that soon developed into a theory of SF and of DD convection in general (Stern, 1960). An analogy between convecting layers created in the laboratory and layers newly observed in the ocean (Stommel and Fedorov, 1967; Tait and Howe, 1968) suggested that DD was significant to the ocean, and this was supported by estimates of large oceanic DD fluxes, inferred using laboratory-based flux laws (Turner, 1965, 1967). In addition to this work on the case with background T and S fields³ varying vertically, attention was paid to the case of horizontal variation, as in the theory that divergent

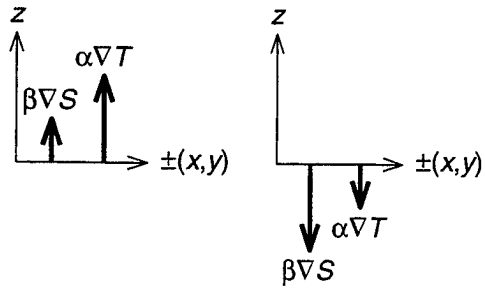


Figure 1. Definition sketch of background gradients in the linear instability view of “staircase” double diffusion (SF in left panel, DC in right panel), with salinity and temperature gradients aligned parallel in the vertical.

DD fluxes might drive interleaving across thermohaline fronts (Stern, 1967).

The dates in the last paragraph suggest that the key modern ideas about oceanic DD were developed in little more than a decade. However, even that may be an overestimate. Stommel (1995) summarized the thought progression from salt fountains to salt fingers under the remarkable heading “Exciting Ten Minutes at the Blackboard.” But, whether it took ten minutes or ten years, one thing is clear: the central ideas of DD research came to light in a short time. It might also be noted that these ideas were set out a full generation ago. A student could well ask whether there are significant research questions left for the next generation. I think there are, and I plan to outline some of them here, in hopes of encouraging discussion and future work.

¹I will assume readers are familiar with double diffusion in the ocean; see recent reviews by Schmitt (1994) and Fernando and Brandt (1994).

²Abbreviations: “DD” for double diffusion; “WS” for relatively warm and salty; “CF” for relatively cold and fresh; “SF” for the salt-finger mode of DD, possible when WS water overlays CF water; and “DC” for the reverse case of diffusive convection.

³Notation: T for temperature; S for salinity; α for thermal expansion coefficient; β for haline contraction coefficient; κ for thermal diffusivity; κ_S for haline diffusivity; ν for kinematic viscosity; z for upward coordinate; $R_\rho = (\alpha \partial T / \partial z) / (\beta \partial S / \partial z)$ for the density ratio in the SF case or its reciprocal for the DC case, or either in finite-difference form; Nu for Nusselt number, a nondimensional heat flux; Ra for Rayleigh number, etc., as in Turner (1973).

Q1. Where does DD exist in the ocean?

Staircases. Instability theory suggests that DD convection may occur if large-scale gradients of S and T are oriented vertically in the same direction (Figure 1). This sets a very wide domain indeed. For example, *Ingham* (1966) estimated that 90% of the Atlantic Ocean main thermocline has SF-unstable stratification. Furthermore, stratification at high latitudes is very commonly DC-unstable.

A possible test of whether DD is significant in a given region may be whether regular-shaped thermohaline staircases are observed there. This rests on the assumption that regular-shaped staircases can result only if up-gradient DD buoyancy fluxes, which create layers, exceed down-gradient turbulent buoyancy fluxes, which disrupt layers. If we had a solid conception of how DD signatures are formed, it might be feasible to test this notion by comparing spatial patterns of DD signatures with those of mixing rates. Unfortunately, we cannot claim certainty about how DD signatures are formed (see Q2 and Q3 below), nor can we map easily the spatial patterns of mixing rates. Even so, it might be useful to map DD occurrence patterns, in order to guide efforts to understand the DD processes.

For example, it has been noted that SF staircases are mainly seen when R_p is less than about 2. Why is this so, and what sets the critical value of R_p ? Several answers have been put forward. Most of these relate to competition, since instability theory suggests that SF should be possible up to $R_p = \kappa/\kappa_S \sim 100$. For example, perhaps the SF growth rate needs to exceed the buoyancy frequency N , if the latter sets a timescale for disruption. Or perhaps it needs to exceed the large-scale shear $\partial U/\partial z$, if SF tilting is the main issue. Or perhaps it needs to exceed the Coriolis parameter f , if inertial turning sets a limit. Other possibilities could be mentioned. While laboratory, theoretical and numerical work on each possibility would be welcome, efforts could be more focused if field studies were undertaken to hint at which physical effects are most relevant. For example, consider the coriolis parameter. *Schmitt* (1994) points out that the *Kunze* (1990) model of disruption by inertial waves implies that the observed maximum R_p for regular-shaped SF staircases should decrease with increasing latitude, and that this qualitative pattern seems to be hold in the ocean. Does this provide firm support for the hypothesis of inertial-turning limitation, or is it a coincidence?

The DC case provides a marked contrast to the SF case, since regular-shaped staircases are routinely observed for (DC-formulated) R_p values ranging up to at least 10. Is the nature of disruption different in the two cases, e.g. with shear inhibiting SF fluxes (*Kunze*, 1994)

but not DC fluxes (*Padman*, 1994)? Or is it just that DC survives to higher density ratios because disruption is weaker in regions where DC-unstable stratification exists, such as the Arctic?

Interleaving. Predicting regions in which DD interleaving might occur is more difficult than doing so for staircases. Interleaving has been observed near thermohaline fronts⁴ in many regions of the world ocean (*May*, 1999). A dramatic example is provided by the Arctic, which has interleaving signatures with remarkable spatial and temporal coherence (*Rudels et al.*, 1999). To date, sampling of the interleaving mode has been very limited. Extensive field programs are needed to develop a clearer picture of interleaving. It is important that such sampling be on a grid, not on isolated transects, since only then can the along-front and across-front slopes of intrusions be measured. These slopes are key dynamical indicators that might help us to select from competing theories, and select we must. For example, it is still unclear (see Q3 below) whether Arctic interleaving results from DD processes (*May and Kelley*, 2001) or from differential mixing (*Hebert*, 1999; *Merryfield*, 2001), and surely that is a first-order question!

Q2. What creates staircases?

Collective-instability mode. An early hypothesis for staircase formation was a collective-instability mode, in which the SF set up internal waves that in turn disrupt the SF, yielding a system of sheets and layers (*Stern*, 1969; *Stern and Turner*, 1969). Questions remain as to the relevance of the mechanism as a general cause of staircase formation. One is whether the idea can be reformulated for the DC case⁵. Others relate to the details of the proposed mechanism limiting SF length (*Kunze*, 1987, 1990, 1994).

Variable-diffusivity mode. The vertical mode of DD extracts potential energy from the gravitationally destabilizing component of density, transporting buoyancy in the up-gradient direction. Associated flux divergences have been hypothesized as a cause of staircase formation (*Ruddick*, 1997), by analogy to an hypothesis for the creation of steppiness in DD-stable fluids by flux divergences arising from turbulent diffusivities that depend on the buoyancy gradient (*Phillips*, 1972; *Ruddick et al.*, 1989). Preliminary tests along these lines have been carried out via 1D numerical simulations (*Merryfield*, 2000) but questions remain about flux parameterizations, boundary conditions, etc. Indeed, the impor-

⁴A thermohaline front is taken here to mean a front with covarying S and T fields, but not necessarily with flat isopycnals. See Figure 2.

⁵However, the search for parallelism between the SF and DC cases owes as much to aesthetic desire as to physical principle.

tance of boundary conditions is difficult to overstate: direct numerical simulations of the SF case show layer formation with insulating top/bottom boundary conditions (*Özgökmen et al.*, 1998) but not with periodic boundary conditions (*Merryfield and Grinder*, 2001).

Shear-modulated mode. The inhibition of SF fluxes by shear (*Linden*, 1971; *Kunze*, 1990, 1994) could lead to vertical variations of buoyancy flux associated with vertical variations in shear, and this has been hypothesized as a mechanism for the generation of fine-structure in SF-unstable regions (*Wells et al.*, 2001). A challenge in taking this to provide a full explanation of staircase formation is the requirement that the spatial pattern of shear match that of observed staircases. Whether that holds or not, this process could play a collaborative role in other mechanisms.

Applied-flux mode. *Turner* (1968a) proposed a mechanism for the creation of thermohaline staircases by the application of destabilizing buoyancy flux, e.g. when a salt gradient is heated from below. Further laboratory and theoretical treatments have added details to *Turner's* initial sketch of this mechanism (*Linden*, 1976; *Huppert and Linden*, 1979; *Fernando*, 1987) and 2D numerical simulations have added color to the picture (*Molemaker and Dijkstra*, 1997). However, questions remain about the directness of the analogy of the applied-flux scenario to the ocean, where staircases appear at mid-depth and where fluxes are likely not to be constant, but rather to depend on the DD response itself.

Modified-intrusion mode. The ideas outlined above are a generation old, but new ideas are now starting to surface. A prime example is the *Merryfield* (2000) proposal that staircases might result from intrusions. The theory produces reasonable predictions of oceanic staircase observations. Issues remaining to be resolved include the role of baroclinicity (*Kuzmina and Rodionov*, 1992; *May and Kelley*, 1997, 2001) and, as usual, the fundamental uncertainty about how to parameterize DD fluxes (see Q5 below). Another issue relates to context: what sets off the initial interleaving? In some cases we may answer that the interleaving results from the contact of watermasses of different *TS* characteristics. However, in other cases (e.g. perhaps in deep Arctic basins) there may not be a great deal of lateral variation in water properties to set off interleaving.

Q3. What creates intrusions?

Neighboring-watermass mode. It is common to observe interleaving across fronts separating WS and CF watermasses. *Stern* (1967) presented an instability theory for this process that has since been extended greatly, e.g. allowing for friction as well as diffusion

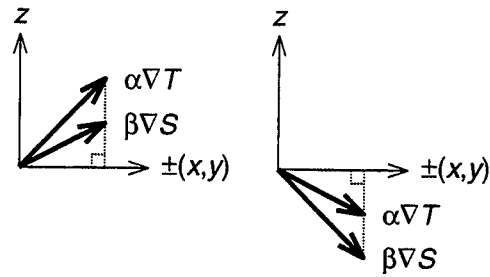


Figure 2. Background gradients in the *Stern* (1967) instability theory of double-diffusive interleaving across a barotropic thermohaline front, for background gradients of the SF (left) and DC senses (right). The dashed lines illustrate that density contributions from *S* and *T* are assumed to compensate laterally, yielding flat isopycnals. Is this a good model of ocean fronts?

(*Toole and Georgi*, 1981), allowing for more general frontal geometry (*Niino*, 1986), allowing for baroclinicity (*Kuzmina and Rodionov*, 1992; *May and Kelley*, 1997), etc. The “allowing for” phrases in the last sentence relate to some of the most basic aspects of ocean physics, and this might suggest that this theory has not borne its last fruit yet. If we think ocean fronts might be unsteady on the timescale of interleaving, if we think cross-frontal contrasts might vary with depth, if we think fronts vary in the downstream direction, if we think diffusivity-based flux laws are flawed, if we think SF and DC fluxes could act at the same time, . . . , then we may not be surprised to see more extensions of the *Stern* (1967) idea. Extending such analytical models of initial growth to the stage of finite-amplitude evolution will remain a challenge. Probably laboratory work will be crucial in guiding thinking, as it has been historically (*Ruddick and Turner*, 1979; *Ruddick et al.*, 1998). Intermediate-scale numerical simulations may play an increasing role in developing understanding, but until we are more certain how to parameterize DD fluxes (see Q5 below) a cloud will hang over such work, as it does now over theoretical treatments.

Sloped-boundary Mode. Sloped insulating boundaries have been shown to create interleaving structures even in fluids with no initial horizontal variations in water properties (*Turner*, 1973; *Linden and Weber*, 1977). This scenario deserves more study, because sloping boundaries are common in the ocean, and thermohaline currents are often steered along them. Might the two mechanisms, the watermass and boundary modes, be linked? A good place to investigate this question might be the Arctic, where interleaving is observed near currents of WS Atlantic waters that appear to be steered along mid-ocean ridges (*Rudels et al.*, 1999).

Differential-mixing mode. Incomplete turbulent mixing can yield differential mixing rates for heat and salt, owing to the difference between the molecular diffusivities of heat and salt acting on fluid parcels momentarily put into contact by the weak turbulence (*Turner*, 1968b; *Altman and Gargett*, 1987; *Ruddick*, 1997). It is not yet clear how to parameterize these mixing rates. The 2D direct numerical simulations of *Merryfield et al.* (1998) confirm the expected, *i.e.* that heat diffuses faster than salt and that the effect vanishes if mixing is vigorous. Soon, we may have flux laws that have been inferred from laboratory work and 3D direct numerical simulations being done today. In the meantime, it is worth noting that the idea of differential mixing may hold promise in answering a long-standing question in intrusion research, namely how to explain intrusions seen in locations that have DD-stable background vertical gradients. The conventional explanations are that (a) the initial lateral displacements were not infinitesimal, as in the theories, but were large enough to create inversions, (b) we are observing the “noses” of intrusions extending from DD-unstable regions into DD-stable regions, or (c) the intrusions are fossilized signatures in a background field that was previously DD-unstable. The idea of differential mixing provides a new hypothesis: that the differential mixing of S and T could yield density convergence analogous to the DD case, thus driving intrusions. This proposal has been put forward recently in a general context by *Hebert* (1999) and for the particular case of Arctic intrusions by *Merryfield* (2001). The former author points out that testing the scenario is problematic in terms of tests in the field, since a key diagnostic is the cross-frontal intrusion slope, which is difficult to measure.

Q4. Do staircases and intrusions interact?

Mixed modes. See the discussion of Q2 for issues relating to the *Merryfield* (2000) idea of transformation of intrusions into staircases.

Intrusions within staircases. Although some staircases display remarkable integrity in some respects (*e.g.* trends in layer TS properties), they are certainly not one-dimensional structures without lateral variation. This is revealed by high-resolution sampling (which is, unfortunately, rare). For example, *Padman and Dillon* (1988) found that station spacings of less than about 1 km were required to track individual layers in the DC staircase that they measured in the Arctic Canada Basin with microstructure temperature profiles. Similarly, towed-chain thermistor sampling of the SF staircase of the C-SALT experiment revealed rich variability on several scales and of several physical types (*Marmorino*, 1989, 1991). For example, within this SF stair-

case, *Marmorino* (1991) sees evidence of the expected convection plumes within the layers, but also signs of DC interfaces and of intrusions within the layers. These intrusions extend about 1 km laterally, and since they are found in the middle of the wide staircase zone, they seem not to have entered from the edges. What causes them? *Marmorino* (1991) speculates that they may arise because of lateral variations in DD vertical buoyancy fluxes or as a response to mesoscale stirring. These are an important issues to clarify. If lateral phenomena such as intrusions control interface substructures, and if these substructures control DD fluxes, then we won’t be able to parameterize DD fluxes in terms of large-scale properties until we can come to grips with lateral affects. Further tests in the field, and in the laboratory, are sorely needed.

Staircases within intrusions. High-resolution sampling sometimes reveals staircases, or at least steppy profiles, between interleaving intrusions (see *e.g.* *Perkin and Lewis* (1984) Figure 11b). These have received surprisingly little attention to date, probably because sampling has been so sparse. Until fuller understanding is developed, we should view analyses based on presumed DD flux laws between interleaves as being somewhat suspect. The issue may not be easy to resolve, since interleaving environments tend to be more dynamic than staircase environments, and we haven’t come to grips with the latter yet.

Q5. Can DD fluxes be parameterized?

Necessity. While diagnostic calculations for a given ocean region can be made using DD fluxes calculated by direct (*e.g.* microscale) measurements, prognostic calculations require a parameterization of DD fluxes in terms of large-scale properties.

Form of flux law. For the DC case it seems likely that layer-layer flux laws (in which fluxes are presumed to be determined by the contrasts ΔS and ΔT between layers) are valid in the ocean (*Padman and Dillon*, 1989; *Padman*, 1994). However, the SF case is apparently much more complicated⁶. It may be that the details of the SF interfaces, as opposed to the layer-layer contrasts, are important in setting fluxes. It may also be that external factors, such as large-scale shear, alter SF convection so much that they must be taken into account in trying to formulate a large-scale diffusivity (*Kunze*, 1994). Since I think we are closer to formulating large-scale parameterizations for the DC case than the SF case, I’ll concentrate on the DC case here.

Exponent in layer-layer flux law. Early laboratory work with sharp interfaces between well-mixed

⁶Or has the SF case just been better studied?

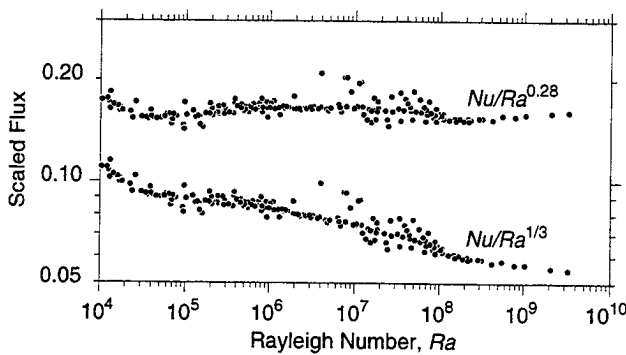


Figure 3. Failure of the 4/3 flux law for thermal convection in water. Dots indicate measurements from five laboratory studies, compiled by Kelley (1990). The 4/3 flux law predicts $Nu \propto Ra^{1/3}$ and the lower dots show this is not true; an exponent of 0.28 matches the measurements better.

layers suggested that vertical fluxes are proportional to $\Delta S^{4/3}$ or $\Delta T^{4/3}$, for the SF or DC cases respectively, with a proportionality factor $C = C(R_p)$. This 4/3 exponent was based on a dimensional analysis of single-component convection (Turner, 1965). However, measurements of single-component convection contradict the prediction (Figure 3), yielding an exponent nearer 5/4 than 4/3 (Kelley, 1990). A lower exponent is also predicted by convection theories (Castaing et al., 1989; Kelley, 1990) and by direct numerical simulations of thermal convection (Kerr, 1996). Does the same apply to DD convection? I am unaware of laboratory tests in the DC case, but in the SF case, the laboratory tests are somewhat contradictory. Schmitt (1979) reported support for an exponent of 4/3, with regression-based exponents in his Table 3 ranging from 1.24 to 1.37. McDougall and Taylor (1984) reported that an exponent of 1.23 matched their observations better than 4/3, but that distinguishing between the two values was problematic with their measurements. Taking these things together, the value of the exponent must be regarded as an open question. One might also ask whether some of the scatter in the empirical value of $C(R_p)$ might result from the extrapolation errors resulting from using an incorrect exponent (Kelley, 1990).

Linking large-scale properties to vertical fluxes. If fluxes are governed by layer-layer flux laws, as they appear to be in the DC case, then parameterizing fluxes is equivalent to parameterizing the thickness of layers within staircases, since layer thickness together with large-scale gradients yields the ΔS and ΔT values required in order to calculate fluxes. This idea is the gist of a proposed parameterization of large-scale diffusivities for the DC case (Kelley, 1984, 1988), illustrated in Figure 4 here. The original measurements are shown in this figure along with the closely matching values of Fedorov (1988). However, the values reported by Padman and Dillon (1987) are in systematic disagreement, yielding a reduction in the large-scale diffusivity by a factor of approximately 3. The reason for this discrepancy is unknown, and more observations would help to clarify whether the layer-thickness (and diffusivity) scaling presented by Kelley (1984) is generally valid. Along similar lines, it would help to examine the pattern of variation of layer thickness, looking for the “split” layers proposed by Kelley (1988) to be a signature of a process that controls layer thickness.

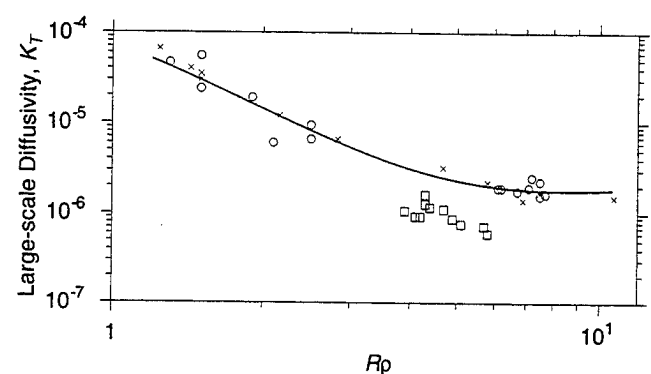


Figure 4. Effective large-scale thermal diffusivity for DC case. The open dots are from Kelley (1984), the crosses from Fedorov (1988), and the boxes are inferred from the G^* values graphed by Padman and Dillon (1987).

However, the values reported by Padman and Dillon (1987) are in systematic disagreement, yielding a reduction in the large-scale diffusivity by a factor of approximately 3. The reason for this discrepancy is unknown, and more observations would help to clarify whether the layer-thickness (and diffusivity) scaling presented by Kelley (1984) is generally valid. Along similar lines, it would help to examine the pattern of variation of layer thickness, looking for the “split” layers proposed by Kelley (1988) to be a signature of a process that controls layer thickness.

Interleaving fluxes. It is not clear how to parameterize interleaving fluxes since the dynamics are still not understood. Even energy-based arguments seem tenuous, given that the energy flow depends on whether the physics involves DD, differential mixing, baroclinic exchange, etc. As the C-SALT experiment set a firm foundation for analysis of the SF staircase mode, so might a dedicated field study enliven research on interleaving. In the meantime, gross sensitivity studies in a GCM would be welcome.

Q6. Is DD important?

Locally. In regions with regular-shaped staircase signatures, it seems reasonable to conclude that DD is important compared with other forms of mixing. It has been argued that these are regions with weak turbulent mixing rates, and that this might suggest that DD is not important. However, if a region is of enough interest to foster dynamical study, then the mixing in that region must also be of interest, whether it be large or small. (The Arctic is a prime example.) And what of regions that lack DD signatures? It may be that DD is significant nonetheless. For example, St.Laurent and Schmitt (1999) suggest that at the site of the NATRE experi-

ment, where thermohaline staircases were not present, up to half the diffusion of an injected tracer might have been transported by DD.

Globally. Does DD play an important global role, say to the rate of overturning circulation, or to the poleward heat flux, two quantities of great interest for climate studies? One way to tackle such questions is with GCM sensitivity studies. I am unaware of attempts to address the interleaving mode in global domains, either in terms of isopycnal fluxes or diapycnal fluxes (the latter being addressed theoretically by *Garrett* (1982)), but some preliminary studies have been done of the staircase mode. So far, the answer seems to be divided. Some studies suggest a large importance, others a negligible importance. For an example, the GCM simulations by *Zhang et al.* (1998) and *Merryfield et al.* (1999), using similar DD flux parameterizations, yielded very different results. The first study found that including DD mixing reduces the overturning circulation by 22 percent, while the second study found only about 1 percent. Why do these results differ so greatly? Stating differences between the model configurations is straightforward. The former focused on a single basin, the latter on the globe; the former used square walls and zonally-averaged surface forcing, the latter used realistic geography and forcing, etc. However, explaining the differences in results is not so straightforward, and may justify further study. Models of intermediate complexity and type might reveal why the *Zhang et al.* (1998) and *Merryfield et al.* (1999) results differ so much. As is usual in ocean models, the form of the surface boundary conditions may be crucial. A followup to the *Zhang et al.* (1998) study, which employed mixed surface boundary conditions instead of the relaxation conditions used by *Zhang et al.* (1998), found that DD had very little affect on the overturning circulation (*Zhang and Schmitt*, 2000). On the other hand, it revealed a heightened sensitivity of the circulation stability to freshwater forcing. Until the contradictory results of such coarse-resolution GCM studies are better understood, the importance of DD fluxes to the global overturning circulation rate remains less than certain.

Answers

Few of the questions listed above were unposed thirty years ago. When will we have answers, and how will we get them? It seems clear that the answers to some of the small-scale questions (e.g. how do salt fingers react to shear?) may soon be provided by direct numerical simulations. A new era of oceanographically relevant direct numerical simulations (which I think is imminent; see appendix) may free us from the uncomfortable posture of straddling oversimplified theories and richly-complex

laboratory simulations. However, it will be a long time before direct numerical simulations will have the scope to match laboratory (meter) scales, let alone oceanic scales that are orders of magnitude larger. Indeed, if history is any guide, future theoretical and laboratory work, as well as direct numerical simulations, will need field experiments to provide ground truth and also to suggest relevant problems to study. Until we learn how double-diffusive structures are formed in the ocean, and how double diffusion interacts with its competitors, we cannot assess the significance of double diffusion in the vertical mixing of the sea, fulfilling the goal that *Stern* (1960) stated in such sanguine words, so long ago.

Appendix: A computational laboratory?

A 3D numerical simulation on an $N \times N \times N$ grid requires AN^3 numerical operations per timestep, where $A \sim 10^3$ depends on the coding and computer architecture⁷. Thus, a computer that performs F operations per second can do a realtime simulation (directly competitive with a laboratory study) only if $N < (F\Delta t/A)^{1/3}$, where Δt is the model timestep.

Under laboratory conditions, the width of salt fingers is $\sim 3 \times 10^{-3}$ m. If $\sqrt{\kappa/\kappa_S} \sim 10$ gridpoints are required for adequate resolution, a reasonable computational mesh might have resolution $\Delta x \sim 3 \times 10^{-4}$ m and a diffusive-limit timestep $\Delta t \sim \Delta x^2/\nu \sim 10^{-1}$ s. A desktop computer can perform $F \sim 10^8$ operations per second, setting a realtime limit of $N \sim 20$, i.e. a domain that can hold under a dozen salt-fingers. This suggests that a desktop computer cannot produce useful realtime simulations. Switching to a supercomputer increases F by a factor of 10^3 , so $N \sim 200$ and thus the domain can hold hundreds of salt fingers. Such simulations may be of great utility, but even they span only 1/10th the scale of typical laboratory experiments.

What if the realtime constraint is relaxed? Matching the laboratory domain size by increasing N tenfold increases the computational requirement by 10^3 ; a year of CPU time would be required to simulate an afternoon in the laboratory. Thus, it seems that the laboratory is the better place for free-wheeling investigation, for exploring parameter space, etc.

When will this change? Assuming that computer power continues to double every 1.5 years (*Mann*, 2000), within a decade numerical simulations running at 1/10th realtime (arguably a practical limit) will match laboratory scales. Thus, we may soon enter a new era, in

⁷This estimate of A is perhaps accurate to an order of magnitude, but the accuracy is of little interest here. The main point is the cubic dependence of computational cost on N , which seems inarguable for models based on grids of fixed geometry.

which numerical simulation is a common adjunct to, or a replacement for, laboratory work.

The limiting factor may be software, not hardware. For example, a typical laboratory setup can be described in a few sentences and reproduced both broadly and swiftly, whereas model codes are not easily developed, reproduced, or modified. Formalized schemes for sharing code might prove useful, as they have in the open-source community (*Raymond and Young*, 2001). Funding agencies could help by requiring researchers to use open-source development practices, perhaps sharing codes only after a time delay, as is done with hydrographic data.

Acknowledgments. I thank the 'Aha Huliko'a organizers for inviting me to this stimulating meeting, as well as the Natural Sciences and Engineering Research Council of Canada and the U.S. Office of Naval Research for funding my work.

References

- Altman, D. B., and A. E. Gargett, Differential property transport due to incomplete mixing in a stratified fluid, in *Proceedings of the third international symposium on stratified flows*, Cal. Inst. of Technology, Pasadena, CA, USA, 1987.
- Castaing, B., G. Gunaratne, F. Heslot, L. Kadanoff, A. Libchaber, S. Thomae, X.-Z. Wu, S. Zaleski, and G. Zanetti, Scaling of hard thermal turbulence in Rayleigh-Bénard convection, *J. Fluid Mech.*, **204**, 1–30, 1989.
- Fedorov, K. N., Layer thickness and effective diffusivities in "diffusive" thermohaline convection in the ocean, in *Small-scale turbulence and mixing in the ocean*, edited by J. C. J. Nihoul and B. M. Jamart, pp. 471–479, Elsevier, Amsterdam, Netherlands, 1988.
- Fernando, H. J. S., The formation of a layered structure when a stable salinity gradient is heated from below, *J. Fluid Mech.*, **182**, 525–541, 1987.
- Fernando, H. J. S., and A. Brandt, Recent advances in double-diffusive convection, *Appl. Mech. Rev.*, **47**, c1–c7, 1994.
- Garrett, C., On the parameterization of diapycnal fluxes due to double-diffusive intrusions, *J. Phys. Oceanogr.*, **12**, 952–959, 1982.
- Hebert, D. H., Intrusions: what drives them?, *J. Phys. Oceanogr.*, **29**, 1382–1391, 1999.
- Huppert, H. E., and P. F. Linden, On heating a stable salinity gradient from below, *J. Fluid Mech.*, **95**, 431–464, 1979.
- Ingham, M. C., The salinity extrema of the world ocean, Ph.D. thesis, Oregon State Univ., Corvallis, OR, USA, 1966.
- Kelley, D. E., Effective diffusivities in ocean thermohaline staircases, *J. Geophys. Res.*, **89**, 10, 484–10, 488, 1984.
- Kelley, D. E., Explaining effective diffusivities within diffusive oceanic staircases, in *Small-scale turbulence and mixing in the ocean*, edited by J. C. J. Nihoul and B. M. Jamart, pp. 481–502, Elsevier, Amsterdam, Netherlands, 1988.
- Kelley, D. E., Fluxes through diffusive staircases: a new formulation, *J. Geophys. Res.*, **95**, 3365–3371, 1990.
- Kerr, R. M., 1996, Rayleigh number scaling in numerical convection, *J. Fluid Mech.*, **310**, 139–179.
- Kunze, E., Limits on growing, finite-length salt fingers: a Richardson number constraint, *J. Mar. Res.*, **45**, 533–556, 1987.
- Kunze, E., The evolution of salt fingers in inertial wave shear, *J. Mar. Res.*, **48**, 471–504, 1990.
- Kunze, E., A proposed flux constraint for salt fingers in shear, *J. Mar. Res.*, **52**, 999–1016, 1994.
- Kuzmina, N. P., and V. B. Rodionov, Influence of baroclinicity on formation of thermohaline intrusions in ocean frontal zones, *Izvestiya, Atm. & Oce. Phys.*, **28**, 804–810, 1992.
- Linden, P. F., Salt fingers in the presence of grid-generated turbulence, *J. Fluid Mech.*, **49**, 611–624, 1971.
- Linden, P. F., The formation and destruction of fine-structure by double-diffusive processes, *Deep-Sea Res.*, **23**, 895–908, 1976.
- Linden, P. F., and J. E. Weber, The formation of layers in a double-diffusive system with a sloping boundary, *J. Fluid Mech.*, **81**, 757–773, 1977.
- Mann, C. C., The end of Moore's law?, *MIT Enterprise Technology Review*, May issue, online at www.technologyreview.com/magazine/may00/mann.asp. 2000.
- Marmorino, G. O., Substructure of oceanic salt finger interfaces, *J. Geophys. Res.*, **94**, 4891–4904, 1989.
- Marmorino, G. O., Intrusions and diffusive interfaces in a salt finger staircase, *Deep-Sea Res.*, **38**, 1431–1454, 1991.
- May, B. D., Double-diffusive interleaving in baroclinic ocean fronts, Ph.D. thesis, Dalhousie Univ., Halifax, NS, Canada, 1999.
- May, B. D., and D. E. Kelley, Effect of baroclinicity on double-diffusive interleaving, *J. Phys. Oceanogr.*, **27**, 1997–2008, 1997.
- May, B. D., and D. E. Kelley, Growth and steady state stages of thermohaline intrusions in the Arctic Ocean, *J. Geophys. Res.*, **106**, 16,783–16,, 2001.
- McDougall, T. J., and J. R. Taylor, Flux measurements across a finger interface at low values of the stability ratio, *J. Mar. Res.*, **42**, 1–14, 1984.
- Merryfield, W. J., Origin of thermohaline staircases, *J. Phys. Oceanogr.*, **30**, 1046–1068, 2000.
- Merryfield, W. J., 2001, Intrusions in double-diffusively stable Arctic waters: evidence for differential mixing?, *J. Phys. Oceanogr.*, submitted.
- Merryfield, W. J., and M. Grinder, 2001, Salt fingering fluxes from numerical simulations, *J. Phys. Oceanogr.*, submitted.
- Merryfield, W. J., G. Holloway, and A. E. Gargett, Differential vertical transport of heat and salt by weak stratified turbulence, *Geophys. Res. Lett.*, **25**, 2773–2776, 1998.
- Merryfield, W. J., G. Holloway, and A. E. Gargett, A global ocean model with double-diffusive mixing, *J. Phys. Oceanogr.*, **29**, 1124–1142, 1999.

- Molemaker, M. J., and H. Dijkstra, The formation and evolution of a diffusive interface, *J. Fluid Mech.*, **331**, 199–229, 1997.
- Niino, H., A linear stability theory of double-diffusive horizontal intrusions in a temperature-salinity front, *J. Fluid Mech.*, **171**, 71–1100, 1986.
- Özgökmen, T. M., O. Esenkov, and D. Olson, 1998, A numerical study of layer formation due to fingers in double-diffusive convection in a vertically-bounded domain, *J. Mar. Res.*, **56**, 463–487, 1998.
- Padman, L., Momentum fluxes through sheared oceanic thermohaline steps, *J. Geophys. Res.*, **99**, 22, 491–22, 499, 1994.
- Padman, L., and T. Dillon, Vertical heat fluxes through the beaufort sea thermohaline staircase, *J. Geophys. Res.*, **92**, 10, 799–10, 806, 1987.
- Padman, L., and T. M. Dillon, On the horizontal extent of the Canada Basin thermohaline steps, *J. Phys. Oceanogr.*, **18**, 1458–1462, 1988.
- Padman, L., and T. M. Dillon, Thermal microstructure and internal waves in the canada basin diffusive staircase, *Deep-Sea Res.*, **36**, 531–542, 1989.
- Perkin, R. G., and E. L. Lewis, Mixing in the West Spitsbergen current, *J. Phys. Oceanogr.*, **14**, 1315–1325, 1984.
- Phillips, O. M., Turbulence in a strongly stratified fluid – is it unstable?, *Deep-Sea Res.*, **19**, 79–81, 1972.
- Raymond, E. S., and B. Young, *The Cathedral and the Bazaar: Musings on Linux and Open Source by an Accidental Revolutionary*, O'Reilly and Associates Press, Sebastopol, CA, USA, 2001.
- Ruddick, B., Differential fluxes of heat and salt: implications for circulation and ecosystem modelling, *Oceanography*, **10**(3), 122–127, 1997.
- Ruddick, B. R., and J. S. Turner, The vertical length scale of double-diffusive intusions, *Deep-Sea Res.*, **26A**, 903–913, 1979.
- Ruddick, B. R., T. J. McDougall, and J. S. Turner, The formation of layers in a uniformly stirred density gradient, *Deep-Sea Res.*, **36**, 597–609, 1989.
- Ruddick, B. R., O. Phillips, and J. Turner, A laboratory and quantitative model of finite-amplitude intrusions, *Dyn. Atmos. Oceans*, **30**, 71–99, 1998.
- Rudels, B., G. Björk, R. D. Muench, and U. Schauer, Double-diffusive layering in the Eurasian Basin of the Arctic Ocean, *J. Mar. Sys.*, **21**, 3–27, 1999.
- Schmitt, R. W., Flux measurements on salt fingers at an interface, *J. Mar. Res.*, **37**, 419–436, 1979.
- Schmitt, R. W., Double diffusion in oceanography, *Ann. Rev. Fluid Mech.*, **26**, 255–285, 1994.
- Schmitt, R. W., The salt finger experiments of Jevons (1857) and Rayleigh (1880), *J. Phys. Oceanogr.*, **25**, 8–17, 1995.
- St.Laurent, L., and R. W. Schmitt, The contribution of salt fingers to vertical mixing in the north atlantic tracer release experiment, *J. Phys. Oceanogr.*, **29**, 1404–1424, 1999.
- Stern, M. E., The “salt-fountain” and thermohaline convection, *Tellus*, **2**, 172–175, 1960.
- Stern, M. E., Lateral mixing of water masses, *Deep-Sea Res.*, **14**, 747–753, 1967.
- Stern, M. E., Collective instability of salt fingers, *J. Fluid Mech.*, **35**, 209–218, 1969.
- Stern, M. E., and J. S. Turner, Salt fingers and convecting layers, *Deep-Sea Res.*, **16**, 497–511, 1969.
- Stommel, H., and K. N. Fedorov, Small scale structure in temperature and salinity near Timor and Mindanao, *Tellus*, **14**, 306–325, 1967.
- Stommel, H., A. B. Arons, and D. Blanchard, An oceanographical curiosity: the perpetual salt fountain, *Deep-Sea Res.*, **3**, 152–153, 1956.
- Stommel, H. M., The sea of the beholder (excerpt of unpublished autobiography), in *Collected works of Henry M. Stommel*, edited by N. G. Hogg and R. X. Huang, vol. 1, American Meteorol. Soc., Boston, MA, USA, 1995.
- Tait, R. I., and M. R. Howe, Some observations of thermohaline stratification in the deep ocean, *Deep-Sea Res.*, **15**, 275–280, 1968.
- Toole, J. M., and D. T. Georgi, On the dynamics and effects of double-diffusively driven intrusions, *Prog. Oceanogr.*, **10**, 123–145, 1981.
- Turner, J. S., The coupled turbulent transports of salt and heat across a sharp density interface, *Int. J. Heat Mass Transfer*, **8**, 759–767, 1965.
- Turner, J. S., Salt fingers across a density interface, *Deep-Sea Res.*, **14**, 599–611. 1967.
- Turner, J. S., a, The behaviour of a stable salinity gradient heated from below, *J. Fluid Mech.*, **33**, 183–200, 1968.
- Turner, J. S., b, The influence of molecular diffusivity on turbulent entrainment across a density interface, *J. Fluid Mech.*, **33**, 639–656, 1968.
- Turner, J. S., *Buoyancy Effects in Fluids*, Cambridge University Press, Cambridge, UK, 1973.
- Wells, M. G., R. W. Griffiths, and J. S. Turner, The generation of density fine-structure by salt fingers in a spatially periodic shear, *J. Geophys. Res.*, *in press*, 2001.
- Zhang, J., and R. W. Schmitt, The impact of salt fingering on the thermohaline circulation under mixed boundary conditions, *J. Phys. Oceanogr.*, **30**, 1223–1231, 2000.
- Zhang, J., R. W. Schmitt, and R. X. Huang, Sensitivity of the GFDL modular ocean model to parameterization of double-diffusive processes, *J. Phys. Oceanogr.*, **28**, 589–605, 1998.
-
- Dan E. Kelley, Dalhousie University, Halifax, NS, Canada (email: Dan.Kelley@Dal.Ca)
-

Meeting report: From stirring to mixing in a stratified ocean

Peter Müller

University of Hawaii, Honolulu, Hawaii, USA

Chris Garrett

University of Victoria, Victoria, British Columbia, Canada

Over fifty years ago, Carl Eckart described the sequence of processes as a passive scalar is stirred and mixed in a turbulent flow (*Eckart, 1948*). At first, during the stirring phase, the variance of the scalar gradient is greatly increased, but later, during the mixing phase, the gradients become sufficiently sharp that molecular diffusion becomes important and the gradient variance rapidly decreases. The process is of great practical importance in many engineering situations as well as being familiar from adding cream to coffee.

The interplay of stirring and mixing is also important in the ocean for temperature, salinity, chlorophyll and other naturally occurring tracers as well as for introduced material. The situation is complicated by the numerous physical processes that can cause stirring and by the interplay of processes that act along isopycnals (surfaces of constant mean density, where "mean" requires careful definition) with "diapycnal" processes acting across the density surfaces.

The Twelfth 'Aha Huliko'a Hawaiian Winter Workshop was convened from 15 to 19 January 2001 to review this theme, with the support of the Office of Naval Research and the participation of 25 invited speakers. The general topics included in presentations and discussions were (1) mesoscale eddy parameterization, (2) general approaches to stirring, including the application of ideas from dynamical systems theory, (3) inertial instability, submesoscale motions and vortical motions, (4) the interplay of isopycnal and diapycnal processes, (5) processes in the surface mixed layer, (6) the stirring and mixing of active, particularly biological, tracers, (7) mixing efficiency, i.e. the fraction of energy lost from the mean flow which produces a vertical buoyancy flux, and (8) differential mixing of heat and salt in doubly-stable environments as well as those which permit double diffusion. Before summarizing the discussions on these topics, we first review the general approach to parameterizing unresolved processes.

The need for parameterization

Ocean general circulation models used in climate studies lack the resolution to treat small-scale processes explicitly and so must parameterize their effects in terms of the

average properties that are resolved. If the eddy flux of a scalar is related by a tensor to the local gradient of the mean concentration of the scalar, as for a mixing length argument, the symmetric part of the tensor is diagonalizable and may be thought of as anisotropic diffusion. The general assumption is that two principal directions are along the "neutral" surfaces of constant mean potential density, with very much greater diffusivity in these directions than in the direction normal to the surfaces. The isopycnal diffusion along the neutral surfaces is largely associated with mesoscale eddies, whereas the diapycnal mixing across them is caused by breaking internal waves and, in some locations, double-diffusive processes.

The antisymmetric part of the tensor describes a "skew flux" normal to the mean gradient of the scalar. Part of this flux is non-divergent and does not affect the mean scalar concentration. The remaining, divergent, part may be expressed as simple advection of the scalar by an additional mean flow, the "skew velocity", over and above that which would be recorded by current meters at a fixed location. To some extent the skew flux can be thought of as representing an eddy flux of thickness, or spacing between neighbouring isopycnals, but it is actually a more subtle representation, in a coordinate system using z as the vertical coordinate, of a flux that would appear in a coordinate system using the potential density instead.

These results are purely kinematic. Specific numerical values for the diffusivities and skew velocities could be obtained from suitable measurements in the present ocean. Any model that aspires to predictive capability, however, requires an understanding of the dynamical processes responsible for the transports to which the model output is sensitive. The parameterizations must then be specified as formulae rather than just numerical values. Consider diapycnal mixing by internal wave breaking. If it is to be characterized not by a number but by a formula then the origin of the wave field becomes important. Vastly different feedback loops can be obtained in climate studies depending on whether the intensity of the wave field and hence diapycnal mixing is determined by the ocean circulation, cascading energy via eddies to the waves, or by the atmospheric wind field generating waves at the sea surface, or by the surface tide generating waves at the sea floor.

The need to parameterize subgrid processes is not idiosyncratic to oceanic general circulation models but generic to all models. There are always unresolved processes.

Mesoscale eddies

So-called mesoscale eddies, with a spatial scale of the order of 100 km and a time scale of the order of a month, are a dominant feature of oceanic variability. They are dynamically analogous to synoptic-scale eddies in the atmosphere. The deformation of an air layer by such eddies is depicted in Pierre Welander's (1955) now famous checkerboard figure, here reproduced as Figure 1. The figure also depicts the stirring along oceanic isopycnals if time and space are appropriately rescaled.

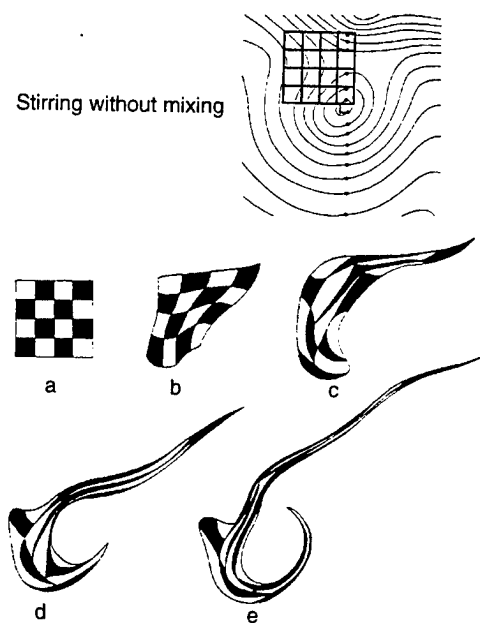


Figure 1. Stirring without mixing of passive tracer. The initial streamlines of the two-dimensional turbulent flow are shown on top. The flow deforms the checkerboard pattern into elongated filaments. In the atmospheric case, the length of the checkerboard is 1200 km and the deformation is shown after 6, 12, 24 and 36 h. In the oceanic case, the length of the checkerboard is 100 km and the deformation is shown after 3, 6, 12 and 18 d. (After Welander, 1955).

Determining the magnitudes of the isopycnal diffusivity and skew velocity associated with oceanic mesoscale eddies requires an understanding derived from a combination of general principles, dynamical studies of processes such as baroclinic instability, and numerical models that resolve the eddies in various idealized situations. There are no simple answers. Invoking general principles, such as mixing potential vorticity, can imply unphysical sources of

momentum and energy; eddy parameterizations should not do what eddies cannot do! To some extent the eddies serve to release available potential energy from the mean state, as in the popular scheme of Gent and McWilliams (1990), but this will lead to an ocean at rest in a situation, without forcing or dissipation, where a steady, stable, circulation is more likely. Moreover, idealized eddy-resolving runs have mostly been used to produce numerical values for the free parameter in the Gent and McWilliams scheme, rather than the formula in terms of resolved variables which we really need for predictive models.

The extant parameterizations of mesoscale eddies really just treat the stirring effect of the eddies. One unanswered question is whether this stirring connects directly to molecular mixing at very fine scales, or whether there is an intermediate mechanism, in series with the eddy stirring, which accomplishes the transfer to mixing. Another question concerns the ultimate fate of the energy released from the mean state. Parameterization schemes essentially assume that this is dissipated adiabatically, but this may not be true. We return to both these issues later.

Another very serious question is whether the effect of mesoscale eddies can be represented as a purely local effect, with eddy fluxes just proportional to local mean gradients. This may be reasonable in some regions, such as the Antarctic Circumpolar Current, but inappropriate for non-zonal flows such as the Gulf Stream from which radiating Rossby waves and coherent rings may carry properties over large enough distances to invalidate any local mixing length approach. In such situations eddies may drive, rather than dissipate, the mean flow.

Ocean models may remain inadequate until mesoscale eddies are resolved explicitly. Quite apart from the difficulties associated with mesoscale eddies, high resolution also seems to be required to produce a sufficiently high effective Reynolds number for the correct representation of phenomena such as the separation, variability, and penetration of the Gulf Stream. Although results stabilize with increasing resolution, they remain sensitive to choices in forcing and viscosity parameterization, even at the finest grid spacing used today.

General approaches to stirring

Turbulent stirring leads to the distortion of a tracer field. The exact distortion is determined by the complete Lagrangian evolution of the flow field, but much can be inferred from the velocity gradient tensor. If the relative motion near a point is dominated by vorticity, then tracer gradients tend to align with the shear and not increase. If, on the other hand, the rate of strain dominates the relative

motion, then a tracer tends to become elongated along the principal axis having the largest rate of strain and the tracer gradient grows exponentially.

Simulations of two-dimensional flows show additional phenomena such as barriers to mixing and areas of filament production. These barriers and areas can be identified when additional information is used. In one approach, the vorticity (from the velocity field) is combined with the rotation of the rate of strain tensor (from the acceleration field) into an effective rotation to characterize the flow field. Another approach uses concepts from dynamical systems theory. It identifies hyperbolic regions in the flow field (characterized by strong deformations in the velocity gradient tensor) to calculate special material curves, or manifolds, that determine the stirring and mixing. A blob of tracer can advect without much distortion, but then be ripped apart rather abruptly when it encounters these hyperbolic regions in a flow. Realistic simulations of the surface currents in the Gulf of Mexico illustrate this process (Figure 2).

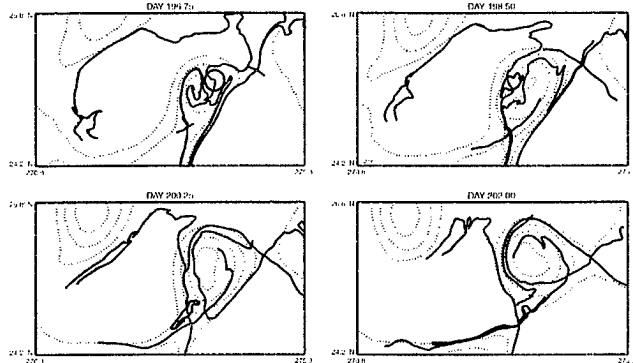


Figure 2. Evolution of a blob of tracer in a simulation of the surface currents in the Gulf of Mexico. The Loop Current is located in the lower right corner and a cyclone to the northwest. Height anomalies are shown as dashed lines. The red and blue lines are inflowing and outflowing manifolds. There are two hyperbolic regions associated with the cyclone and the Loop Current. On day 196.75 a circular blob (black) straddles an inflowing manifold (blue). This manifold delineates which portion of the blob will travel west into the central Gulf and which portion will travel east through the Straits of Florida. The blob is stirred with modest deformation for the next 3.5 days as it rotates around the cyclone. On day 200.25, however, the blob approaches the hyperbolic point created by the intersecting inflowing and outflowing (blue) manifolds to the southwest of the cyclone. Here it begins to show strong compression along the inflowing manifold direction and strong distortion along the outflowing manifold direction. Day 202.00 shows the fate of the blob when it reaches this intersection. It has collapsed along the outflowing manifold. (Courtesy of A.D. Kirwan and L. Kantha).

Inertial instability, submesoscale motions, and vortical motions

Mesoscale motions may arise from baroclinic instability of large-scale flows in the ocean and may, in turn, be unstable to submesoscale eddies an order of magnitude smaller. Near the sea surface it seems that these eddies, often visible at the sea surface via beautiful spiral patterns (Figure 3), are mainly cyclonic, quite possibly because anticyclonic ones would break down rapidly via an inertial, or barotropic, instability. These small eddies may be a link in the pathway from stirring to mixing, but this has not been quantified. Similarly, in the ocean interior there seems to be a family of "vortical modes", of largely unknown scale range and intensity, which play a role in lateral stirring. They can be generated by frictional effects in flow past topographic features and, possibly, by the collapse and geostrophic adjustment of regions mixed by breaking internal waves.

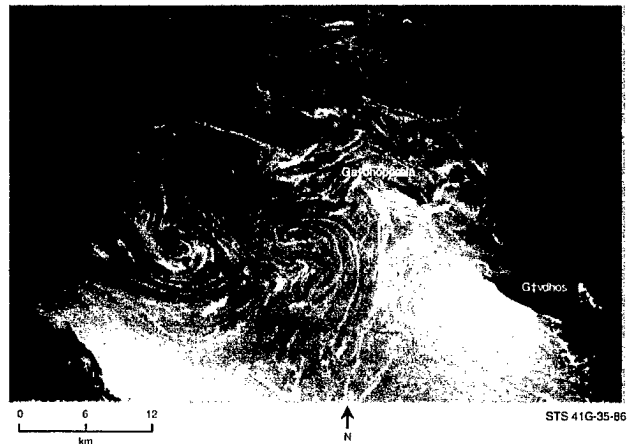


Figure 3. A pair of interconnected spirals in the Mediterranean Sea south of Crete. The vortex pair has a clearly visible stagnation point between the two spirals, the cores of which are aligned with the preconditioning wind field. Picture taken on October 7, 1984. (Courtesy of W. Munk).

A general question about the links between low frequency eddies and higher frequency motions concerns the extent to which the mesoscale or submesoscale eddies generate internal waves, particularly in situations where the eddies generate sharp fronts. Theoretically, the mesoscale and submesoscale eddies are assumed to satisfy some sort of balanced dynamics, such as geostrophy. These balanced motions are also called the "slow manifold". Balanced turbulent flows exhibit an upscale energy cascade and are very inefficient in dissipating energy. Internal gravity waves and other more nearly isotropic flows, on the other hand, exhibit a downscale cascade with effective dissipation. The structure of the equations governing bal-

anced flows is such that they can be integrated forward in time only if certain conditions are met. Analysis of several classical instability problems shows that the fluid-dynamical transition occurs in the neighborhood of these integrability conditions. It is hypothesized that violation of these conditions characterizes in general the flow regimes where energy is transferred from balanced to unbalanced motions.

The interplay of isopycnal and diapycnal processes

When a scalar is stirred by high Reynolds number turbulence in homogeneous water, the eddy flux is mainly determined by the turbulent stirring and is largely independent of the small value of molecular diffusivity. Reducing the latter would merely lead to finer scales in the tracer field, without significantly affecting the turbulent transport. The situation is more subtle in the ocean because of the need to quantify both isopycnal and diapycnal transports. One issue, already raised, is the extent to which energy released by mesoscale eddies is dissipated in the ocean interior, perhaps by breaking internal waves which have drawn some of that energy from the eddies. This could partly tie diapycnal mixing rates to the lateral stirring rates.

Another issue concerns the ultimate mechanism for the destruction of fine-scale lateral gradients of temperature and salinity created by stirring on isopycnals. One possibility is that vertical shear of the stirring process leads to very strongly tilted frontal regions, so that pre-existing diapycnal mixing can remove the strong gradients. This could be described as a "passive" destruction of the strong lateral gradients. A more active process is possible: thermohaline fronts caused by lateral stirring on isopycnals could become unstable to a double-diffusive interleaving process. This would introduce further diapycnal mixing at the same time as it destroyed lateral gradients.

The relative importance of these scenarios has not been established. Preliminary estimates favor the latter process, the signature of which should be internal double-diffusive interleaving regions in the ocean. These are certainly known to occur, but a systematic catalog of their locations and characteristics has not been developed. If the process is important it may provide significant diapycnal mixing in regions with strong lateral gradients of potential temperature, and compensating salinity, on isopycnals. Moreover, the diapycnal mixing is upgradient for density, as is necessary in any double-diffusive process.

A significant sub-theme which emerged on this and other issues concerns the extent to which different stirring and mixing processes are in parallel or in series. If two

processes are in parallel, their strengths may be compared to decide which is more important. If processes are in series, one might need to know which is the rate-controlling one. In the usual case of the stirring of a tracer in a homogeneous fluid, molecular mixing clearly operates in series, but with the ultimate mixing rate being controlled by the turbulent stirring. In the ocean, where there might be some intermediate process between the stirring agents and the final molecular diffusion, the answer may be more complicated. For example, the flux of warm water across the Gulf Stream may be controlled by the amount of air-sea interaction that occurs in warm-core rings before they are reabsorbed by the Stream; the flux is not necessarily controlled just by the ring formation rate. The general issue of series or parallel processes needs to be borne in mind in any attempt to focus on processes that are important, and may be aided by a triple decomposition into mean, eddies and turbulence (Figure 4).

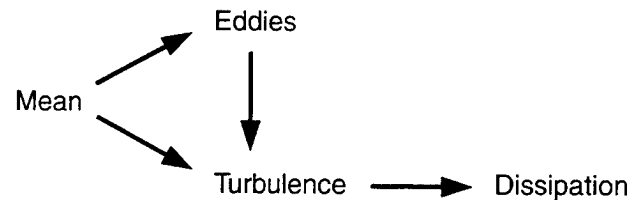


Figure 4. A simple schematic of the path of scalar concentration variance from mean to dissipation via eddies and turbulence. (Courtesy of C. Garrett).

Processes in the surface mixed layer

Because of intense vertical mixing there, the surface mixed layer of the ocean provides many examples of the interplay of stirring and mixing processes. One such process relies on the fact that the density of sea water is determined by both temperature and salinity.

Typical of the surface mixed layer are compensated fronts that are warm and salty on one side and cold and fresh on the other side such that the density contrast is small. Figure 5 shows an example along a longitude line in the subtropical North Pacific. The existence of the fronts has been rationalized as follows (Young, 1994): Nonhomogeneous atmospheric forcing and entrainment of thermocline waters generate horizontal gradients in temperature, salinity, and density. Density fronts slump by the action of horizontal density-driven shear currents which are eventually arrested by vertical mixing. This process can be

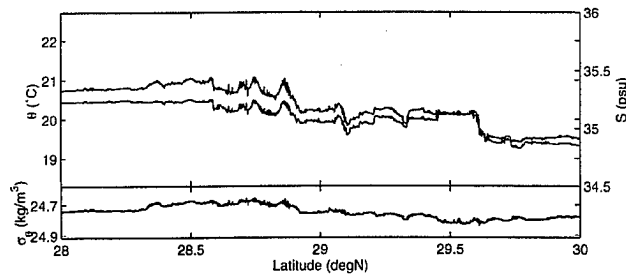


Figure 5. Potential temperature (red line), salinity (blue line) and potential density (black line) from a horizontal Sea Soar tow at 50 m in the subtropical North Pacific, at 140°W, between 28 and 30°N. The depth is in the middle of the local mixed layer. The vertical axes for temperature and salinity are scaled by the expansion coefficients so that excursions of temperature and salinity show the change they imply for density. (Courtesy of R. Ferrari).

thought of as shear dispersion. Compensated fronts do not experience such shear dispersion. The result is that density fronts diffuse whereas compensated fronts persist. The ubiquitous existence of compensated fronts suggest that horizontal mixing in the surface mixed layer is very much larger for density than for "spice", the combination of temperature and salinity that is "orthogonal" to density. Indeed, eddy-resolving models that diffuse temperature and salinity and hence density and spice with the same coefficient are unable to reproduce the observed tendency towards thermohaline compensation.

Air-sea fluxes and the behavior of the surface mixed layer are also involved in a thermodynamic approach to water-mass formation. Basically, water must flow across isopycnals to balance surface buoyancy loss or gain, and the convergence of this volume flux provides an estimate of the subduction rate. This rate may be compared with a dynamically-based prediction from Ekman convergence. Both the thermodynamic and dynamic approaches, however, require allowance for the role of eddies and diurnal and seasonal cycling of the mixed layer depth. The problem is thus complicated by the interplay of various stirring and mixing processes which need to be understood.

The stirring and mixing of non-conservative tracers

Remote sensing of the sea surface from space has made us aware of beautiful and complex patterns in biologically active variables such as chlorophyll (Figure 6). One question is whether the observed patchiness is a consequence of biological processes or merely of the passive stirring of large-scale gradients. Some clues come from comparing the shapes of the wavenumber spectra of active and pas-

sive scalars, such as chlorophyll and temperature respectively. If the former shows comparatively more variance at small scales, this is evidence for the importance of scalar growth processes.

Accounting for such patchiness in a model is particularly difficult if the non-conservative processes are nonlinear. In that case it is clearly inadequate to proceed with a model that deals only with an ensemble average variable; a Lagrangian approach which follows the development of individual patches is necessary. A very basic model of this kind is the "Brownian bug model". It describes an ensemble of bugs that perform random walks and experience random birth and death processes along the way. Mathematically, this is a "superprocess." A homogeneous initial distribution spontaneously develops patches and voids.

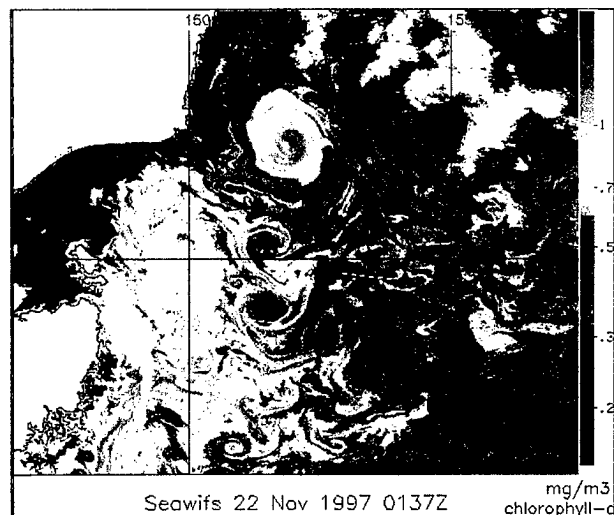


Figure 6. Chlorophyll concentration in the Tasmanian Sea as observed by SeaWiFS. (Courtesy of B.L. Hua).

Examining data for evidence of patchiness or intermittency can be aided by examination of high order structure functions. For a variable $C(x, t)$ the q th order structure function is defined as $\langle (\delta C(l))^q \rangle$, where $\delta C(l)$ is the difference in C over a separation l and $\langle \rangle$ denotes an ensemble average. The structure function exponent $\zeta(q)$, defined by fitting a power law $l^{\zeta(q)}$ to the structure function, characterizes the degree of intermittency for multifractal processes. It is a linear function of q for non-intermittent processes and becomes a nonlinear concave function for intermittent processes. Calculation of this exponent from oceanic observations suggests that, in the scale range of nearly isotropic turbulence, passive scalars such as temperature are more intermittent than the advective velocity field. This is a result also obtained in numerical simulations of 3D homogeneous turbulence (e.g., Jiménez, 2000). Biologically

active tracers show intermittency beyond that associated with turbulent stirring. The excess increases with decreasing turbulence intensity (Figure 7). These observational results need to be corroborated and understood. Further to this, the possibility of a relationship between biological and physical variables can be studied through examination of the behavior of joint structure functions, though caution is required to avoid over-interpretation of artifacts introduced by particular sampling schemes or noise.

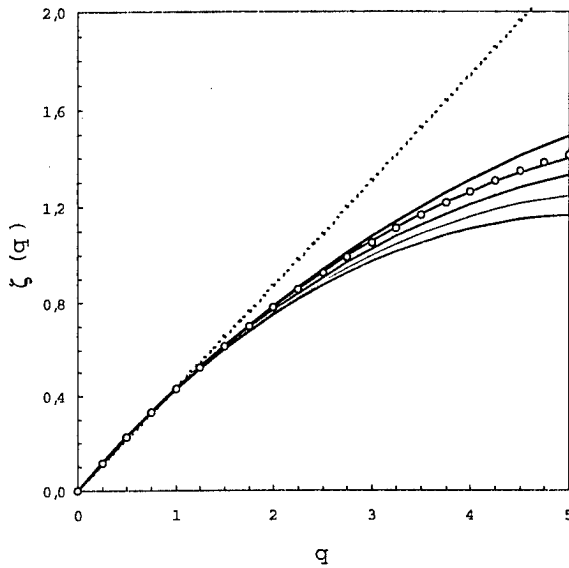


Figure 7. Empirical values of the structure function exponent $\zeta(q)$ for temperature (circles) and in vivo fluorescence for different values of the turbulent dissipation rate ϵ (red $\epsilon = 10^{-6} \text{ m}^2 \text{ s}^{-3}$; orange $\epsilon = 5 \times 10^{-6} \text{ m}^2 \text{ s}^{-3}$; blue $\epsilon = 10^{-5} \text{ m}^2 \text{ s}^{-3}$; dark green $\epsilon = 5 \times 10^{-5} \text{ m}^2 \text{ s}^{-3}$; light green $\epsilon = 10^{-4} \text{ m}^2 \text{ s}^{-3}$). The linear curve (dotted line) is expected for non-intermittent turbulence. The data were collected in the eastern English Channel. (Courtesy of L. Seuront).

Mixing efficiency

Much of the diapycnal mixing in the ocean is associated with the shear instability of internal waves. The subsequent overturning and stirring leads to finescale patterns of density which then disappear through the action of molecular thermal diffusivity or the molecular diffusion of salt. The turbulent eddies are being dissipated by molecular viscosity at the same time as they are working against buoyancy forces; a major question concerns the relative fractions of turbulent kinetic energy lost to dissipation at a rate ϵ and converted to mean potential energy at a rate $K_v N^2$, where K_v is the eddy diffusivity and N the buoyancy frequency. The ratio $\Gamma = K_v N^2 / \epsilon$ is generally thought to be about 0.2, largely based on calibration against other methods of esti-

mating K_v . There is no reason to suppose that Γ is a universal constant, however, but it has not been established what environmental parameters might determine its value.

Some evidence reported at the meeting, based largely on a laboratory experiment but with some field support, suggests that Γ is less than the value of about 0.2 quoted above if the turbulence is weak with a “turbulent Reynolds number” $Re_T = \epsilon/vN^2$ less than about 100. This is not surprising: weak turbulence dies away before it has accomplished much buoyancy flux. What was a surprise was a claim that Γ also falls off again for values of Re_T greater than about 1,000. This dependence is hard to accept; it may transpire that Re_T in these experiments was actually a proxy for an input variable that does not involve the viscosity v . One variable that might lead to reduced Γ in the ocean is the duration of high shear compared with the buoyancy time N^{-1} . A long-lived mixing event might produce all its buoyancy flux at first and subsequently stir water that is already mixed, dissipating energy but with little further buoyancy flux. More study is required, with high resolution 3D numerical simulations of breaking internal wave fields becoming increasingly feasible and informative.

The question of mixing efficiency is important in any assessment of the amount of mixing that might be associated with, for example, the energy loss from the barotropic tide to internal tides. There are also implications for the circulation that is diagnosed from measured dissipation rates ϵ and the observed mean density structure. The mean diapycnal velocity w_* may be obtained from the mean buoyancy equation (e.g., St. Laurent *et al.*, 2001)

$$w_* N^2 = \partial(\Gamma\epsilon)/\partial z$$

so that the value of w_* can depend on gradients of Γ . Vortex stretching given by $f \partial w_*/\partial z$ then affects the mean flow along isopycnals.

Differential mixing

The rapid decay of turbulent kinetic energy at small values of the turbulent Reynolds number $Re_T = \epsilon/vN^2$ can also lead to less turbulent transport of salt than heat, given the very small molecular diffusivity of the former. Although the effect is clearly established in 2D and 3D numerical simulations and in laboratory experiments that mimic the breaking of internal waves in a stratified ocean, it is somewhat counterintuitive at first sight. If the turbulent fluxes were downgradient at all scales then the more diffusive tracer would lose its higher wavenumber fluctuations and would experience less turbulent transport. It seems, however, that the fluxes are upgradient at high wavenumbers, as a simple consequence of the secondary

instability and collapse of an overturning billow. The more diffusive tracer thus loses some upgradient flux and therefore experiences more downgradient transport.

The importance of differential mixing for the ocean is not yet known. It may turn out that in regions where mixing matters it is at high enough Re_T that the eddy diffusivities of heat and salt are the same. This is particularly likely to be true given the intermittent nature of mixing in the ocean compared with the rather steady stirring in the numerical experiments; Re_T based on ϵ during a mixing event in the ocean may be much larger than that based on the average ϵ .

Different rates of mixing for heat and salt are, however, firmly established for regions of the ocean where double-diffusive processes are significant. These regions include places, such as the C-SALT region near Barbados (Schmitt, 1994), where the vertical profiles of temperature and salinity are nearly compensating in density, and places such as the Arctic Ocean where internal wave activity is low. Even in these regions there are significant puzzles, partly because laboratory results seem not to be readily applicable, and partly because we lack adequate theoretical guidance. One obvious problem is to explain the step size in thermohaline staircases. In the diffusive regime (with warm salty water below cooler fresher water), some useful predictions come from a local water column model, whereas in the salt fingering regime (with the opposite stratification) it seems that the step size might be set by lateral intrusive processes. The issue is certainly not fully resolved, and the interfaces in the fingering regime also seem more complex in the ocean than in the laboratory.

Importantly, many regions of the ocean which might support double-diffusive processes seem to have these disrupted by things like the shear of internal waves, with the breaking of these waves then dominating diapycnal transports. Even these regions can show some evidence for double diffusive transports, however, so that the phenomena warrant continued attention.

Summary

There are typically nearly 10^{20} spatial degrees of freedom between the smallest scales being resolved by numerical models of ocean circulation and the smallest scales of variability. The meeting was therefore being ambitious in attempting to survey a vast range of scales and phenomena. Some general, if rather platitudinous, principles do seem clear: (1) Studying the processes at work in the ocean is worthwhile science. (2) There is a need not just to understand these processes but also to parameterize them in a form that can be implemented in models for the large-scale behavior of the ocean. (3) These models should be

used in sensitivity tests to determine which parameterizations need improvement.

It is not really clear what issues have the highest priority. After a sometimes tumultuous discussion the participants arrived at the following ranking by vote:

1. What are the constraints on eddy parameterization and how should they be implemented?
2. What nonlocal effects matter and how can they be parameterized?
3. How uniform are stirring and mixing processes? Are there any "hotspots," particularly in association with topographic features?
4. What are the effects of diapycnal boundary processes on eddy parameterization?
5. What is the parameter dependence of the mixing efficiency or flux Richardson number?
6. How does energy leak from the slow manifold?
7. What aspects of stirring and mixing affect biological processes? What do patterns of biological tracers tell us about fluid dynamics?
8. Under what circumstances do we need different diffusivities for different tracers?
9. What are the effects of adiabatic stirring on diapycnal mixing?
10. Do subgrid scale processes provide stochastic forcing?

The last question addresses a very fundamental aspect of the Reynolds decomposition. A second fundamental aspect is that the simple Reynolds decomposition ideally requires a spectral gap, in time or space, separating the unresolved processes to be parameterized from the slowly changing "mean." Both these issues were discussed at the meeting, but without any profound new insights.

Stirring and mixing in a stratified ocean is the physics that needs to be parameterized in ocean circulation models. Challenging open problems remain at all levels, from very fundamental to highly applied aspects.

Acknowledgments. We thank the participants of the workshop for their input into this report and for their permission to quote unpublished material. Copies of the proceedings are available from Peter Müller, University of Hawaii, School of Ocean and Earth Science and Technology, Department of Oceanography, 1000 Pope Road, Honolulu, Hawaii, 96822, and can also be viewed at <http://www.soest.hawaii.edu/PubServices/AhaWebPage.html>. The twelfth 'Aha Huliko'a Hawaiian Winter Workshop was supported by the Department of the Navy grant number N00014-00-1-0168, issued by the Office of Naval Research.

References

- Eckart, C., An analysis of the stirring and mixing processes in incompressible fluids, *J. Mar. Res.*, 7, 265–275, 1948.
- Gent, P.R., and J.C. McWilliams, Isopycnal mixing in ocean circulation models, *J. Phys. Oceanogr.*, 20, 150–155, 1990.
- Jiménez, J., Turbulence. In *Developments in Fluid Mechanics*, ed. G.K. Batchelor, K. Moffatt and G. Worster, C.U.P., 231–288, 2000.
- St. Laurent, L., J. Toole, and R. Schmitt, Buoyancy forcing by turbulence above rough topography in the abyssal Brazil Basin, *J. Phys. Oceanogr.*, in press, 2001.
- Schmitt, R.W., Double diffusion in oceanography, *Ann. Rev. Fluid Mech.*, 26, 255–285, 1994.
- Welander, P., Studies of the general development of motion in a two-dimensional, ideal fluid, *Tellus*, 7, 141–156, 1955.
- Young, W.R., The subinertial mixed layer approximation, *J. Phys. Oceanogr.*, 24, 1812–1826, 1994.